UNIVERSITY OF ADELAIDE LIBRARY
25/2/82

THE DETERMINATION OF MOLECULAR OXYGEN DENSITY PROFILES FROM THE ABSORPTION OF SOLAR UV RADIATION

by

L. A. Davis, B.Sc (Hons)

A Thesis
presented for the degree of
DOCTOR OF PHILOSOPHY
AT THE
University of Adelaide
Physics Department
December 1980

awarded Nov/81

C O N T E N T S

		Page
SUMMARY		x
PREFACE		xiii
ACKNOWLEDGEMENTS		xiv
CHAPTER 1.	INTRODUCTION	1
1.1	INTRODUCTION	1
1.2	ATMOSPHERIC PARAMETERS STUDIED	5
	1.2.1 Molecular Oxygen	5
	1.2.2 Dayglow	8
1.3	SPECIFIC RESEARCH AIMS	14
	1.3.1 Molecular Oxygen	14
	1.3.2 Water Vapour	16
	1.3.3 Airglow	17
1.4	LIMITATIONS OF STUDY	19
1.5	ORGANIZATION OF THESIS	20
CHAPTER 2	THE MEASUREMENT OF MOLECULAR OXYGEN IN THE LOWER THERMOSPHERE - A REVIEW	23
2.1	MEASUREMENT OF $n(O_2)$ BY UV ABSORPTION TECHNIQUES	23
	2.1.1 Introduction	24
	2.1.2 Non-Dispersive Instrumentation	26
	2.1.3 Dispersive Instrumentation	35
2.2	MEASUREMENT OF $n(O_2)$ BY MASS SPECTROSCOPIC TECHNIQUES	39
	2.2.1 Introduction	39

CONTENTS Continued.... Page

2.2.2 General Problems in the Experimental Determination of Mass Densities by Rocket or Satellite-borne Mass Spectrometers 40

2.2.2.1 Contamination 41

2.2.2.2 Uncertainty in the Flight Mass Sensitivity 41

2.2.2.3 Limited Operational Height Range 44

2.2.3 Experimental determination of $n(O_2)$ by Rocket-borne Mass Spectrometers 45

2.2.4 Experimental Determination of $n(O_2)$ by Satellite-borne Mass Spectrometers 50

2.3 OTHER METHODS 53

2.4 THE RESULTS 54

2.4.1 A Comparison of $n(O_2)$ measured by UV Absorption Techniques with $n(O_2)$ measured by Mass Spectroscopy 55

2.4.2 Variation of Lower Thermospheric Molecular Oxygen Densities 57

2.4.2.1 Seasonal Variations 58

2.4.2.2 Diurnal Variations 60

2.4.2.3 Magnetic Variations 62

2.4.2.4 Semi-Annual, Annual, Latitudinal Variations 63

2.4.2.5 Solar Flux Variation of $n(O_2)$ 65

2.5 SUMMARY 67

CONTENTS Continued.....

		Page
CHAPTER 3	THE CHOICE, CONSTRUCTION AND CALIBRATION OF THE INSTRUMENTATION TO MEASURE $n(O_2)$	69
3.1	CHOICE OF TECHNIQUE AND INSTRUMENTATION	69
3.2	ION CHAMBERS	71
	3.2.1 Introduction	71
	3.2.2 Construction of Body Shell	73
	3.2.3 Window Materials	75
	3.2.4 The Filling Gases and their Preparation	78
	3.2.5 The Filling Procedure	79
	3.2.6 Calibration Procedures	81
	3.2.6.1 Light Source and Beam Monitor	82
	3.2.6.2 Characteristics of Sodium Salicylate	83
	3.2.6.3 The Spectral Response	86
	3.2.6.4 Absolute Quantum Efficiencies	88
	3.2.7 Angular Response	97
	3.2.8 Temperature Effects	99
	3.2.9 Long Wavelength Sensitivity	100
	3.2.10 Lifetimes and Stability of Chambers	100
3.3	THE SPECTROPHOTOMETER	108
	3.3.1 Description of Spectrophotometer	108
	3.3.2 Calibration of Spectrophotometer	110
	3.3.2.1 Determination of the Passband	110

CONTENTS Continued..... Page

3.3.2.2 The Spectral Response and the Absolute Quantum Efficiency 111

3.3.3 Temperature Effects 114

CHAPTER 4. THE METHODOLOGY 115

4.1 THE BASIC EQUATIONS 115

4.2 THE EFFECTIVE ABSORPTION CROSS-SECTION 119

4.2.1 Introduction 119

4.2.2 Calculation of $\sigma_{EFF}(z)$ 120

4.2.3 The Sensitivity of σ_{EFF} to the assumed Flux Function $\phi(\lambda, \infty)$ 126

4.2.4 The Uncertainty in σ and its Effect on σ_{EFF} 128

4.2.5 Uncertainty in $\varepsilon(\lambda)$ and its Effect on σ_{EFF} 132

4.2.6 The Effect of Other Wavelengths on the Effective Absorption Cross-Section of $L\alpha$ Chambers 136

4.2.7 The Effect of Other Absorbers on the Effective Absorption Cross-Sections of the Ion Chambers 143

4.3 THE OPTICAL DEPTH FACTOR 147

4.4 THREE POSSIBLE METHODOLOGIES BASED ON THE USE OF THE BEER-LAMBERT LAW 150

4.4.1 Introduction 150

4.4.2 Hand-Drawn Curves 151

4.4.3 The use of Weighted Differences 154

CONTENTS Continued..... Page

4.4.4 Curve Fitting and the Method of Maximum Likelihood 162

4.5 CHOICE OF METHODOLOGY 166

4.6 SUMMARY OF UNCERTAINTY IN MOLECULAR OXYGEN PROFILE ARISING FROM METHODOLOGY 170

CHAPTER 5 THE ROCKET EXPERIMENTS 172

5.1 SUMMARY OF ROCKET FLIGHTS 172

5.2 THE SKYLARK ROCKETS 172

5.2.1 The Vehicle 172

5.2.1.1 General Description 173

5.2.1.2 The Environment 175

5.2.2 SL 1005 176

5.2.2.1 The Experiments 176

5.2.2.2 Preflight Checks 178

5.2.2.3 The Flight 179

5.2.2.4 The Results 179

5.2.3 SL 1207 180

5.2.3.1 The Experiments 180

5.2.3.2 The Flight 181

5.2.3.3 The Results 182

5.3 AEROBEE 13.123 IS 183

5.3.1 The Vehicle 183

5.3.2 The Experiments 184

5.3.3 The Flight 186

5.3.4 The Results 186

CONTENTS Continued....

			Page
CHAPTER 6	LOWER THERMOSPHERIC MOLECULAR OXYGEN DENSITIES		188
6.1	THE RESULTS		189
	6.1.1	Introduction	189
	6.1.2	Presentation of Individual $n(O_2)$ Profiles and General Comments	190
	6.1.3	Comparison of the Molecular Oxygen Density Profiles Determined by Lα and QT Chambers	191
	6.1.4	Comparison of the $n(O_2)$ Profiles Determined by SX and QT Ion Chambers and by the Spectrometer	193
	6.1.5	Broad Band Estimates of Flux Levels	195
6.2	THE MEAN PROFILES		199
	6.2.1	Selection of Profiles for the Mean Profile	199
		6.2.1.1 SL 1005	199
		6.2.1.2 SL 1207	200
		6.2.1.3 Aerobee 13.123 IS	200
	6.2.2	Uncertainties Associated with Mean Profiles	201
	6.2.3	Comparisons of Densities obtained with Ion Chambers against those obtained with a Mass Spectrometer and a UV Spectrophotometer	203
	6.2.4	Comparison of $n(O_2)$ Profiles with Earlier Woomera Measurements	204

CONTENTS Continued.... Page

6.3	OBSERVED VARIATIONS IN MOLECULAR OXYGEN DENSITIES	207
	6.3.1 Horizontal Variations	207
	6.3.2 Seasonal/Latitudinal Variations	209
	6.3.3 Magnetic Variations	209
6.4	THE MODEL PROFILES	210
	6.4.1 Comparison with CIRA 72 and Jacchia 77	210
	6.4.2 Comments on Models	212
6.5	SUMMARY	213
6.6	FUTURE WORK	213
CHAPTER 7	THE AIRGLOW EXPERIMENTS	216
7.1	INTRODUCTION	216
7.2	THE PHOTOMETERS	218
	7.2.1 The SL 1005 Photometers	218
	7.2.2 The SL 1207 Photometers	220
7.3	CALIBRATION OF THE PHOTOMETERS	221
	7.3.1 Alignment of Photometers	221
	7.3.2 Filter Selection	222
	7.3.3 Angular Response	222
	7.3.4 White Light Calibration	223
	7.3.5 Calibration for Airglow Lines	223

CONTENTS Continued..... Page

7.4	FLIGHT PERFORMANCES	224
	7.4.1 SL 1005	224
	7.4.2 SL 1207	224
7.5	SUMMARY	225
CHAPTER 8	THE WATER VAPOUR EXPERIMENT	227
8.1	INTRODUCTION	227
8.2	CONCEPT OF EXPERIMENT	229
8.3	COMPUTER SIMULATION OF EXPERIMENT	232
8.4	THE ROCKET EXPERIMENTS	233
	8.4.1 Description of the Cockatoo Vehicle	233
	8.4.2 Performance of Vehicles	236
	8.4.2.1 C 1044 and C 1046	237
	8.4.2.2 C 4009 and C 4007	237
	8.4.2.3 C 4017 and C 4018	237
8.5	THE VIABILITY OF THE WATER VAPOUR EXPERIMENT AND SOME COMMENTS ON LIKELY DENSITIES	238
	8.5.1 Viability of Experiment	238
	8.5.2 A Comment on Likely Densities	241
APPENDIX 1	THE EFFECT OF CONTAMINATION ON THE STANDARD ION CHAMBER CALIBRATIONS	242
APPENDIX 2	TABULATIONS OF MOLECULAR OXYGEN DENSITIES	245

CONTENTS Continued.....

	Page
APPENDIX 3 DETERMINATION OF DETECTOR ASPECT	276
PUBLICATIONS	281
BIBLIOGRAPHY	282

SUMMARY

This thesis descibes rocket-borne experimental investigations of the upper atmosphere. These studies were carried out as part of a continuing rocket programme conducted by the University of Adelaide at Woomera, Australia. The principal aim was to extend, to higher altitudes (i.e. 170 kms), the previous measurements of molecular oxygen densities made at the Southern Hemisphere location.

This aim was achieved by experiments flown on three stabilized and pointed rockets which were launched on the 11.12.1972, 23.4.1974, and 22.2.1977. These rockets were code-named SL 1005, SL 1207 and Aerobee 13.123 IS respectively.

The molecular oxygen density was measured by the technique of absorption spectroscopy in the vacuum ultraviolet. Ion chambers were used to measure the attenuation profile of solar UV radiation. The construction and calibration of these detectors is fully described. Some developmental work was carried out on these chambers during the course of this work and this is also described.

The densities obtained are presented in graphical form in the main body of the thesis and are fully tabulated in Appendix 2. The present results are compared with earlier determinations of the molecular oxygen density profiles above Woomera.

The experimental payload of Aerobee 13.123 IS included a mass spectrometer. Comparison is made between the molecular oxygen densities determined by this instrument and those determined by the

UV absorption techniques of the present work.

The magnetic conditions at the time of launch of the rockets SL 1005 and SL1207 was such that comparison was possible between molecular oxygen densities measured at different levels of magnetic activity. The possible effect of magnetic disturbances on molecular oxygen densities above Woomera is considered.

In the results obtained from Aerobee 13.123 IS differences were observed between the measured upleg and downleg densities. Between the altitudes 130 to 156 kms these differences were well outside the statistical uncertainty of the results and indicated that horizontal structure was being observed.

The apogees of the rockets were above the atmospheric absorbing layers for the wavelengths of the passbands of the chambers, and estimates of the flux levels in these broad bands are presented.

As an adjunct to the main experiment,and in an attempt to increase the physical understanding of the lower thermospheric region by the simultaneous measurement of more than one parameter, airglow photometers were flown on SL 1005 and SL 1207. No useful data was, however, gained from these and discussion on them is limited to a brief justification of the experimental concept and a description of the design and calibration of the instrumentation.

As stated, the molecular oxygen measurements were an extension of the lower altitude work done by the Adelaide University. These lower altitude measurements were carried out in small spin stabilized rockets. An attempt was made to devise a small, rugged, simple experiment that could be carried on these vehicles and was capable of measuring water vapour densities in the upper mesosphere-

lower thermosphere (70km - 110km). The discussion of the experiment is confined to the concept of the experiment and the performance of each experimental payload since the data obtained did not allow qualitative assessment of water vapour densities. Results from the molecular oxygen experiment have, however, been used to make a tenative comment on the likely magnitude of such densities.

P R E F A C E

This thesis contains no material which has been accepted for the award of any other degree or diploma in any University. To the best of the author's knowledge and belief it contains no material previously published or written by another person, except where due reference is made in the text.

L. A. DAVIS.
DECEMBER 1980.

ACKNOWLEDGEMENTS

The author would like to thank her supervisor, Dr B. H. Horton for his help and encouragement throughout the research programme. In addition she acknowledges, with gratitude, the work of Messrs. S. Dowden, R. Hurn and R. Walker and the staff of the Physics Workshop, especially G. Eames, in constructing the rocket payloads.

Thanks are also due to Dr L. W. Torop and Dr David Gigney for their helpful critiques of the initial drafts of this thesis.

Finally, sincere thanks are due to Patricia Coe for her help during the preparation of the manuscript.

UNIVERSITY OF ADELAIDE

CHAPTER 1

INTRODUCTION

1.1 INTRODUCTION

The lower thermosphere, defined here as the atmospheric region between 90 to 170 kms, is a region of intense aeronomic interest. In this region molecular oxygen is dissociated by solar UV radiation and this absorption of solar UV radiation by molecular oxygen is one of the major sources of heating for the thermosphere (Chandra and Sinha, 1973). In addition, over this altitude range, the distribution of individual atmospheric constituents is expected to change from one dominated by mixing to one dominated by diffusion (Colegrove *et al*, 1965; Keneshea *et al*, 1979).

Up to the early seventies, however, this region was largely unexplored. Moe (1973) stated that one of the most important problems of aeronomy was the lack of information about the lower thermosphere.

Most of the information that was available was derived from a relatively small number of sounding rockets (Dalgarno *et al*, 1973; Offerman, 1974). While satellites had been used at lower thermospheric heights to obtain total densities by atmospheric drag measurements (King Hele and Walker, 1969) consideration of useful lifetimes generally kept the perigees of instrumented satellites above 250 kms. The high altitude measurements from these satellites could not really be used to infer low altitude parameters (Mayr *et al*, 1974). Some use was made of satellite-borne occultation experiments (Norton and Warnock, 1968; Lockey *et al*, 1969; Stewart and Wildman, 1969). These were capable of deducing information about the atmosphere at lower thermospheric heights while the satellite itself was in a high altitude, stable orbit.

However, such measurements were limited to satellite sunrise or sunset and as pointed out by Felske *et al* (1974) the finite angular width of the sun can imply a large error in the derived grazing height. This latter uncertainty would not only degrade the altitude resolution but would also lead to large uncertainties in the densities obtained from this type of experiment.

In addition to the rocket and satellite experiments some ground based methods had been developed. For example, Noxon and Johanson (1972) investigated the changes in molecular oxygen density at 120 kms by monitoring the change in the twilight intensity of the airglow line at 6300Å; incoherent scatter techniques were used to obtain information on the temperature and winds above 100 kms (Evans, 1972) and to determine atomic oxygen densities at 120 kms (Alcayde *et al*, 1972). Both these techniques were, however, limited by the fact that interpretation of the raw data was dependent on the particular set of assumptions made about the lower thermosphere. To obtain atomic oxygen concentrations Alcayde *et al* (1972) had to assume a temperature profile, a value for the temperature at 120 kms and that diffusive equilibrium existed above 120 kms. Noxon and Johanson (1972) had to assume an initial lower thermospheric density profile for molecular oxygen.

The inadequacy of the data base in the early seventies is evident in the construction of one of the most widely used models - Jacchia '71 (Jacchia, 1971). The model was a development of the author's 1965 model. (Jacchia, 1965). In the earlier model, Jacchia had formulated, by trial and error, a variable thermospheric temperature profile that did not differ strongly from the theoretical profiles of Nicolet (1961) and Harris and Priester (1962 a & b) and

which was capable of implying, at satellite heights, total densities that matched those measured by satellite drag techniques. Diffusive equilibrium was assumed to exist above 120 kms and lower thermospheric values for parameters such as total density, molecular oxygen density ($n(O_2)$), atomic oxygen density ($n(O)$) and molecular nitrogen density ($n(N_2)$) were deduced from the diffusion equation and the above temperature profile. In the 1971 model, diffusion was assumed to exist from 100 km up rather than 120 kms. The expanded data base available for total densities allowed refinement of the temperature profile and its variations but the basic reliance of the model on high altitude total densities was still evident. The only constraints used which reflected actual lower thermospheric measurements were the values of $n(O_2)$, $n(O)$, $n(N_2)$ and the ratio $n(O)/n(O_2)$ at 150 kms. These came from the results of rocket-borne experiments launched during the sixties (von Zahn, 1970). Jacchia manipulated the temperature profile so that predicted values of $n(O)$, $n(O_2)$, $n(N_2)$ and $n(O)/n(O_2)$ for 150 kms were consistent with those of von Zahn (1970), but it is significant that at no other altitude within the thermosphere did he apply similar experimentally derived constraints to his model.

Therefore, in summary, looking generally at the lower thermosphere it can be seen that up to the early seventies most of the investigations of this region had been carried out by rocket-borne instrumentation and that the subsequent data base was inadequate.

Since then, however, the data base has expanded rapidly with much of the information coming from satellite and ground-based research programs (Carignan, 1975; Hedin, 1979). Despite the limitation of the ground-based methods - mainly incoherent scatter techniques - their

capacity for long term monitoring of the lower thermosphere has led to their increasing use. In situ, lower thermospheric measurements by satellite borne instrumentation became possible with the launching of the AE series of satellites (Dalgarno *et al*, 1973; Spencer *et al*, 1973). For a short period these satellites were able to follow orbits with perigees as low as 130 kms because they carried propulsion units which could boost them back to higher, more stable, long lived orbits.

However, despite the expanding use of satellites and ground stations, rocket-borne instrumentation has continued to play a significant though diminished role in lower thermospheric research. The results from rocket-borne instrumentation have been used to provide new calibration factors for instrumentation on long lived satellites (Heroux and Swirbalus, 1976; Hinteregger, 1976). With the development of cryo-cooled mass spectrometers (Offerman and Trinks, 1971; Offerman and Tartarczyk, 1973) rocket-borne mass spectrometers have become capable of in-situ determination of atmospheric composition at altitudes as low as 85 km (Scholz and Offerman, 1974).

For solar UV absorption experiments the use of rockets does have some advantages. Experiments carried on rockets are not limited to local sunrise and sunset as are the solar UV occultation experiments on satellites. Nor does the $\frac{1}{2}^{\circ}$ width of the sun degrade the altitude resolution of a rocket-borne UV experiment; provided that the rocket is fired at a solar zenith angle less than 90°. (Higgins and Heroux, 1977). Although Garriott *et al* (1977) overcame the problem of the poor altitude resolution in satellite occultation experiments by designing a spectro-helio-meter with an angular field of view of 5×5 (arc. secs)^2 their solution yielded a new source of uncertainty. Vernazza *et al* (1975) have shown that regions on the solar disc with angular dimensions less than

30 x 30 (arc. secs)^2 can have random intensity fluctuations as large as 50% in times as short as one minute. These fluctuations are evident in the results of Garriott *et al* (1977).

Therefore rocket-borne instrumentation, although it cannot match the capability of satellite-borne instrumentation to provide wide spread geographical and long term data can be said to compensate for this in two ways,

(1) it has the ability to obtain low altitude data

(2) it can easily provide data with high altitude resolution.

The major work done for this thesis is based on payloads carried on three rockets launched between 1972 and 1977 from Woomera (31° S) Australia.

1.2 ATMOSPHERIC PARAMETERS STUDIED

1.2.1 Molecular Oxygen

The major research objective was the measurement of the lower thermospheric density profile of molecular oxygen. Accurate knowledge of lower thermospheric concentrations is essential for any realistic discussions of the heat budget since the main source of heating in the region arises from the absorption of solar UV light by molecular oxygen (Hunt, 1972; Chandra and Sinha, 1973).

The behaviour of molecular oxygen was not well understood at the start of the current rocket programme. The collations by von Zahn (1970) and Offerman (1974) of thermospheric data from rocket-borne experiments showed large variations in the values obtained for the molecular oxygen concentration at a specific height, e.g. 150 kms. To some extent this may have been expected since the values quoted were obtained over a 9-10 year period and therefore encompassed different

solar conditions as well as different latitudes of measurement, different times of measurement and different magnetic conditions and season at the time of measurement. Variations of all of these had been linked with variations in total densities (Jacchia, 1970; 1971). However, with so few measurements any such trends were difficult to detect and justify with statistical certainty.

It was not just the scarcity of data that made the discerning of trends difficult. Hall *et al* (1967) pointed out that large uncertainties in the data also obscured likely dependencies. Associated with their instrumentation and with each type of instrumentation used were unique systematic uncertainties which, coupled with the statistical uncertainties of a rocket-borne experiment led to total uncertainties ranging from ± 25% to ± 50% (Hall *et al*, 1967; Jursa *et al*, 1965; Müller and Hartman 1969; Hedin *et al*, 1964). These estimates may have been conservative. For example, Champion (1970) considered the absorption coefficients used by Hall *et al* (1967) could have been a factor of two out. Discussion on the uncertainties associated with some of the rocket experiments mentioned above is given in Chapter 2.

The collations of von Zahn (1970) and Offerman (1974) of rocket-borne experimental investigations of the thermosphere were not a complete coverage of the studies that had been undertaken. However, since at this time the majority of the research had been done by rocket-borne payloads, they do highlight the poor latitude coverage of experimental investigations up to the early seventies. Most of the rockets had been launched from sites between 28°N and 68°N. The only southern hemisphere data quoted by Offerman (1974) was that of

Weeks and Smith (1968) and Wildman *et al* (1969). Although these were not the only southern hemispheric studies at thermospheric heights - the work of Carver *et al* (1969) is not mentioned, and the very nature of the collation precludes the satellite based work of Stewart and Wildman (1969), Norton and Warnock (1968) and Lockey *et al* (1969) - at this time very few Southern Hemisphere measurements had been made.

The previously mentioned work of Carver *et al* (1969) only obtained measurements up to 120 km. This altitude limitation was reflected in reverse by many of the experimental payloads mentioned in the two collations (von Zahn, 1970; Offerman, 1974). The rocket-borne mass spectrometers of such researchers as Hedin *et al* (1964); Hedin and Nier (1966); Kasprzak *et al* (1968) and Krankowsky *et al* (1968) could only take measurements above approximately 120 kms. The authors considered measurements below this height as unreliable because the mean free path of the atmospheric constituents was no longer large with respect to the dimensions of the ion source of the mass spectrometer and the passage of the ion source itself would disturb the ambient gas density. A further complication arose from the possible formation of a shock wave in front of the ion source of a mass spectrometer (Offerman and Tatarczck, 1973). In the high temperature and high density region behind such a shock wave many chemical reactions would occur and the air sample going into the mass spectrometer would be highly modified.

However, it wasn't only the mass spectroscopy experiments that were limited in their altitude coverage. Because of the wavelengths chosen the EUV absorption experiments of Hall *et al* (1963; 1965; 1967) were normally limited to altitudes above 150 kms.

To summarize, the inadequacies of the data base for molecular oxygen were at the start of this program.

(a) too few measurements

(b) large uncertainties associated with most measurements

(c) very few measurements in the Southern Hemisphere

(d) individual measurements only covered limited altitude ranges within the lower thermosphere.

1.2.2 Dayglow

The behaviour of one component of the atmosphere cannot be considered in isolation. For example, Schaeffer *et al* (1971) considered that between 120 km to 140 kms the intensity of the 6300Å line of daytime airglow (also called dayglow) was dependent on the local concentration of molecular oxygen.

Airglow is a general term describing radiation emitted when an excited state of an atmospheric atom or molecule returns to the ground state. The airglow line mentioned above arises from the 'D state of atomic oxygen:

$$O('D) \rightarrow O(^3P) + h\nu \ (6300Å) \qquad (1)$$

The observed intensity depends on the concentration of O('D) atom and the radiative probability of this state. O('D) can come from several sources. During the day two possible mechanisms are

photodissociation $O_2 + h\nu \ (\lambda < 1751Å) \rightarrow O('D) + O(^3P)$ (2)

dissociative recombination $O_2^+ + e \rightarrow O('D) + O(^3P)$ (3)

(Wallace & McElroy, 1966; Hunten and McElroy, 1966).

If reaction (2) is the dominant source as is suggested for the 120 - 140 km region by Schaeffer *et al* (1971) and Rusch *et al* (1975) the concentration of O('D) and hence the intensity of the 6300Å line will depend on the local $n(O_2)$ - the example already mentioned. However, not all the O('D) produced will return to the ground state by radiating. The excited state is metastable with a lifetime of approximately 100 secs. During this lifetime the atomic oxygen may be deactivated before it can radiate. Hunten and McElroy (1966) postulated that molecular nitrogen is capable of collisionally de-activating or quenching the excited atomic oxygen state. Therefore the amount of quenching, the number of O('D) atoms surviving to radiate, and hence the intensity of the 6300 line will also depend on the local concentration of N_2.

Therefore, the intensity of the 6300 depends directly or indirectly on the local concentration of O_2 and N_2 between 120 kms and 140 kms. But nitrogen may be ionized by solar radiation $\lambda < 796$Å

$$N_2 + h\nu\ (\lambda < 796\text{Å}) \rightarrow N_2^+ + e \qquad (4)$$

and this ion may resonantly scatter solar radiation.

$$N_2^+\ (X^2\ \Sigma_g^+) + h\nu\ (3914\text{Å}) \rightarrow N_2^+\ (B^2\ \Sigma_u^+) \rightarrow N_2^+\ (X^2\ \Sigma_g^+) + 3914\text{Å} \qquad (5)$$

This links 3914Å emissions with 6300Å for if $n(N_2)$ is adjusted in order to make the mechanisms postulated for 6300Å produce the observed intensity, then the adjusted $n(N_2)$ must still be able to explain the observed airglow at 3914Å.

Of course, as with O('D) the N_2^+ ion may be quenched. Wallace and McElroy (1966) postulated three possible quenching reactions

$$N_2^+ + e \rightarrow N + N \quad (6)$$

$$N_2^+ + O \rightarrow NO^+ + N \quad (7)$$

$$N_2^+ + O_2 \rightarrow N_2 + O_2^+ \quad (8)$$

These reactions indicate further interaction - $n(O_2)$ and $n(O)$ will influence the intensity of 3914Å. However, the interaction extends beyond this again. Reactions (6) and (7) may produce $N(^2D)$ (Wallace and McElroy, 1966; Oran *et al*, 1975).

i.e. $$N_2^+ + e \rightarrow N(^2D) + N(^4S) \quad (9)$$

$$N_2^+ + O \rightarrow NO^+ + N(^2D) \quad (10)$$

This excited state of atomic nitrogen gives rise to an airglow line at 5200Å. Not all the reactions of the type (6) and (7) will give the products illustrated in (9) and (10). For example, if the electron does not have sufficient energy to produce an excited state then reaction (6) could lead to the production of two ground state atoms ($N(^4S)$). This highlights the requirement to know electron energies and therefore temperatures in order to be able to evaluate the importance of such reactions in the production of $N(^2D)$.

The above gives a hint of the complexity of the relationship between three airglow lines and the neutral and ionized constituents of the atmosphere. The complexity can increase. Reaction (8) produces O_2^+. A further quenching reaction of N_2^+

$$N_2^+ + O \rightarrow N_2 + O^+ \quad (11)$$

followed by $$O^+ + O_2 \rightarrow O_2^+ + O \quad (12)$$

may provide a further source (Dalgarno and Walker, 1964). However, dissociative recombination of O_2^+ can produce $O('D)$ (reaction (3)) i.e. the excited state that produces 6300Å airglow. This further links

airglow at 6300Å and 3914Å.

However, reaction (3) can also produce O('S) if the electron is energetic enough.

$$O_2^+ + e \rightarrow O('S) + O(^3P) \qquad (13)$$

O('S) decays to O('D) emitting radiation at 5577Å.

$$O('S) \rightarrow O('D) + 5577Å \qquad (14)$$

The O('D) state can either undergo collision deactivation or return to the ground state by radiating at 6300Å.

Apart from quoting Schaeffer *et al's* (1971) statement that photodissociation was the dominant source for 6300Å between 120-140 kms, no attempt has been made to state at what height the various reactions occur. Papers by Wallace and McElroy (1966), Schaeffer *et al* (1971), Rusch *et al* (1975) and Oran *et al* (1975) contain diagrams showing the relative importance of many of the functions mentioned as a function of altitude.

It can be seen from the brief discussion above that simultaneous measurements of as many parameters as possible can only enhance physical interpretation of the atmospheric phenomena since many are closely inter-related and dependent on each other.

Airglow measurements can also be used in a less direct way. A proposed source for the production of the (1^s) excited state of atomic oxygen at altitudes less than 120 kms is the mechanism first proposed by Chapman (1931c).

i.e. $$O + O + O \rightarrow O('S) + O_2 \qquad (15)$$

While laboratory measured values of the rate coefficient for (15) have varied, leading to controversy over the ability of this mechanism to explain the 5577Å observed (Barth and Hildebrandt, 1961; Barth, 1964; Young and Black, 1966; Felder and Young, 1972) the results obtained by Dandekar (1969) and Reed and Chandra (1975) are consistent with (15) being the source for O('S) at these heights. Note that further work by Slanger and Black (1977), published after the flights of the present experiments, once again casts doubts on the validity of the Chapman mechanism; but because of the difficulty of simulating the lower thermospheric environment in the laboratory the authors did not believe they could positively exclude this method of generating O'S. However if the Chapman mechanism is assumed to be the one operating then measurement of the airglow at 5577Å together with knowledge of the rate coefficient of (15) and the radiative probability of O('S) allows an estimate of the concentration of atomic oxygen to be made at altitudes < 120 kms.

If $n(O_2)$ is also being measured, as it was in the current work, this means that the ratio $n(O)/n(O_2)$ can be calculated. This ratio is very important for discussions of the heat budget of the region since the dominant heat mechanism (photodissociation) and heat loss mechanisms (conduction and radiation) are basically governed by the O_2 and O densities (Chandra and Sinha 1973). If it is accepted that the dominant source for O('D) (6300Å) between 120-140 kms is photodissociation (Schaeffer *et al*, 1971; Rusch *et al*, 1975) then by measuring the concentration of O_2 and the intensity of the airglow at 6300Å, and using laboratory measured rate coefficients for (2) and any possible quenching reactions, the estimate of the atomic oxygen concentration can be extended to cover the range 120 kms to 140 kms.

Therefore the simultaneous measurement, in the lower thermosphere, both of the intensity of several airglow lines and of the concentration of molecular oxygen can yield more than an evaluation of the magnitude of these intensities and the concentration of O_2 . From such measurements an estimate for the concentration of atomic oxygen can also be made and a limited check on the self consistency of the proposed mechanisms for the airglow can be carried out.

1.3 SPECIFIC RESEARCH AIMS

1.3.1 Molecular Oxygen

The measurement of lower thermospheric molecular oxygen densities has been described as the basic research objective (1.2.1). Consideration of the inadequacies of the data base and the availability of a Southern Hemisphere launch site (Woomera, 30°56'S, 136°27E) led to an attempt being made to measure molecular oxygen densities over an altitude range encompassing the whole of the lower thermosphere. Noxon and Johanson (1972) had pointed out that an accurate density profile for O_2 from the region where the atmosphere was mixed (80-90 kms) to a region -h > 160 - where the atmosphere could be considered to be controlled by diffusion would be useful for attempts to explain the observed 6300Å airglow intensity. There were large uncertainties associated with the published values of lower thermospheric molecular oxygen densities (Section 1.2.1). Therefore a systematic attempt was made to reduce the uncertainty that would be associated with the current results e.g. experiments were duplicated to improve data statistics.

To some degree the uncertainty is dependent on the technique and the type of instrumentation used. In the present research the technique of Solar UV absorption using broad band detectors was employed. The reasons for the choice of this technique, and the uncertainties involved with it are discussed in Chapters 3 and 4.

It has been mentioned previously (Section 1.1) that the finite width of the sun does not degrade the altitude resolution of rocket borne UV absorption experiments, as it does similar instrumentation carried on satellites, provided the solar zenith angle at the time of flight is less than 90°. This advantage can be lost if the motion of

the rocket during flight restricts the number of times the rocket borne detector views the sun,and therefore,restricts the number of times the density of O_2 can be determined. In the current program this problem was avoided by using attitude controlled rockets - the detectors view the sun continuously throughout the region of interest.

If the basic research objective of obtaining a lower thermospheric molecular oxygen profile with good altitude resolution and small absolute uncertainties was achieved then there were several questions which could be addressed. These were

(1) Was there a statistically significant difference between profiles obtained on the upleg and downleg ?

(2) Did this difference denote observation of horizontal structure in the atmosphere or was it an instrumental effect ?

(3) How well did the experimentally derived profiles agree with the current theoretical models ?

This then formed the core of the research program. Because of the fortuitous timing of the launching of two of the rockets it was also possible to investigate the effect of a magnetic disturbance on the density of lower thermospheric molecular oxygen. One other aspect of lower thermospheric O_2 measurements was looked at. Champion (1965) had postulated that variations in the published data could as easily be attributed to instrumentally induced effects as they could to genuine atmospheric phenomena. Ackerman *et al* (1974), measuring molecular oxygen by UV absorption techniques and mass spectroscopic techniques

simultaneously,found significant differences between the two density profiles. Which was the more reliable seems to be in some doubt. While Ackerman *et al* (1974) preferred the UV absorption data, Nier *et al* (1976) saw no reason why the mass spectrometer data should be downgraded. A chance to compare the results from UV absorption and mass spectroscopic techniques was provided by the last rocket in the current program.

1.3.2 Water Vapour

As previously mentioned the methodology chosen for the research into molecular oxygen densities is discussed in Chapter 4. One facet discussed is the uncertainty arising from atmospheric constituents, other than O_2, absorbing the solar UV being monitored, (Section 4.2.7). The basic assumption of the solar UV technique is that any real change in the detected UV can be attributed to a change in the amount of O_2 between the detector and the sun. The adjective"real" is used because if changes in the signal are caused by differing detector aspect then they must be calculated and allowed for before any further analysis can precede. If other constituents such as CO_2, H_2O, N_2 or NO absorb the solar radiation and this is not allowed for in the analysis, an erroneously high $n(O_2)$ will be derived from the rocket data. The magnitude of the systematic error that can be introduced if these other absorbers are ignored varies with the wavelength being observed, (see Section 4.2.7). Of interest here is the effect at $L\alpha$ and while it has been estimated (Hall, 1972; Carver *et al*, 1977b) that 6% to 7% of the total $L\alpha$ flux is absorbed by the constituents listed above, water vapour alone may account for more absorption than this at 100 kms.

In comparing the absorption coefficients at Lα (Section 4.2.7) the value for water vapour is outstanding. At Lα the absorption cross section for water is some three orders of magnitude greater than that for O_2 (Watanabe *et al*, 1953). Therefore even a small concentration of water vapour could have a significant effect on the absorption that occurs. For example, if the water vapour concentration at 110 km was such that $n(H_2O) : n(O_2)$ equalled approximately $1 : 10^4$ then up to 10% of the Lα absorption at this height could be attributed to water vapour. This value for the relative concentration of H_2O is not unreasonable. It corresponds to a local density of $10^7/cm^3$ which is consistent with the theoretical estimates of Fukuyama (1974).

The possibility and the probable size of the water vapour effect led to an attempt to obtain an upper limit to the water vapour concentration from approximately 80-120 kms, i.e. encompassing most of the altitude range over which Lα is absorbed even at high zenith angles.

1.3.3 Airglow

The importance and desirability of measuring airglow at the same time as molecular oxygen has been stressed in Section 1.2.2. In the current work there were two airglow experiments built.

Because of limited space the first of these only looked at 5577Å and 3914Å . 5577Å was chosen so an estimate of the $n(O)/n(O_2)$ ratio could be made up to ≈ 120 kms. The heights of the emitting layers and their maximum emission rates were also of interest. For λ5577Å there would appear to be three emitting layers, one at 98 kms, one at 170 kms and a third, above the lower thermosphere, at 200 kms, (Dandekar, 1969). After comparing his own work with that of other

experimenters, Dandekar (1969) speculated on the possibility of the maximum emission rate of the 170 km layer being dependent on the solar zenith angle (SZA). Since the proposed SZA for the rocket on which this airglow instrumentation was to be flown was approximately 40° - different from any of the flights considered by Dandekar (1969) - it was hoped the results would help in attempting to confirm or deny the suggestion.

The measurement of 5577Å implied that over a limited altitude range both n(O) and $n(O_2)$ were being determined. Wallace and McElroy (1966) had stated that the biggest source of uncertainty in their work on the possible mechanisms for 3914Å were the values assumed for these two quantities. Therefore since they were being determined and an estimate of the concentration of molecular nitrogen was also possible because the total density was also being measured (Bibbo, 1977), 3914Å was the second line looked at. While a definitive answer on the validity of the mechanisms proposed by Wallace and McElroy (1966) was not expected from the data it was hoped that the results would provide a test of the suggested mechanisms' self consistency.

The second airglow photometer block looked at all the airglow lines discussed in Section 1.2.2. i.e. 6300Å, 5577Å, 5200Å and 3914Å. The aim of the experiment was similar to the one already mentioned: - n(O) was to be estimated from atomic oxygen airglow and it was hoped to test the feasibility and consistency of some of the proposed mechanisms for the airglow being observed.

1.4 LIMITATIONS OF STUDY

The availability of a Southern Hemisphere launch site in part confirmed the decision to investigate lower thermospheric molecular oxygen (Section 1.3). However, despite the advantage of the geographical location of the launch site, launching all the rockets from only one site immediately limited the scope of the research to an investigation of lower thermospheric $n(O_2)$ above this one fixed geographical location.

Rocket borne experiments supplement satellite borne experiments as has been shown in Section 1.1. However, one disadvantage they do suffer is the limited sampling time. In the present work, time spent within the lower thermosphere was only three to five minutes depending on the vehicle. This small sampling time increases the risk of the results obtained being non-typical.

While the above are broad limitations which must be considered if the results obtained are used to support or refute any general atmospheric theory there are two others which have a more immediate effect; both on the experiment itself and on the subsequent data. Both these limitations are common to satellites and rockets.

The first airglow experiment illustrates the first limitation:- the space available for instrumentation. This space is limited by the size of the rocket or satellite and/or other experiments being carried on the same payload. Limited space can lead to a reduction in the scope of the experiment. In the example quoted this meant only observing two airglow lines. It can also become one of the dominant specifications for the mechanical design of the experiment. This leads to compromises which are not always successful. An example of this is

is the airglow photometer which measured 3914Å and 5577Å.

The second limit is the accuracy to which the telemetry reproduces, at the ground station, the signal it receives from the experiment. For any satellite or rocket-borne experiment this property of the telemetry is an unavoidable source of uncertainty in the data. In the present work the telemetry was accurate to ± 25 mV. The effect of this uncertainty is discussed in Chapter 4 and Chapter 6.

1.5 ORGANIZATION OF THESIS

Although in previous sections there has been some indication of the location of various parts of the thesis, the sign-posting has not been complete. This section explains the construction of the thesis as well as giving a broad outline of the content of each chapter.

The investigation of lower thermospheric O_2 densities was the primary research aim. As such this is treated in depth, in Chapters 2 through to 6. Chapter 2 reviews the techniques used to measure lower thermospheric molecular oxygen and discusses the results that have been obtained. Chapter 3 starts with a brief rationale as to why broad band UV detectors were chosen and then describes their construction and calibration. Chapter 4 discusses fully the methodology used. The basic technique is explained but the main emphasis lies in an attempt to assess quantitatively all the systematic and statistical errors that are associated with this technique. Chapter 5 describes the molecular oxygen experiments, the payloads with which they were associated, the vehicles on which they were flown and their flight performance. The information gained is presented in the form of computer drawn plots of signal vs. altitude. Some comment is made on the observable quality of the data.

Chapter 6 presents the $n(O_2)$ determined by the flights. Included in this presentation is an analysis of the errors. This analysis looks at the uncertainties arising from the methodology (Chapter 4), the uncertainty of the telemetry and the radar plotting of the altitude together with the statistical variation displayed in the $n(O_2)$ derived from the individual detectors. In addition the density profiles are looked at with a view to answering the three core questions posed in Section 1.3.1, plus whether or not changing magnetic fields affect lower thermospheric densities and whether or not systematic differences can be seen between O_2 densities derived by different instrumentation. The present work is also compared with the work of other researchers and with current models.

Section 1.2.2 indicated the interest of simultaneous airglow measurements. Chapter 7 describes the instrumentation used and its calibration. The chapter also contains a description of the instrumentation's flight performance. Because the data received was unsatisfactory the discussion on airglow measurements is not pursued beyond this.

Discussion in Chapter 8 on the water vapour experiments is also limited because of the unsatisfactory nature of the data received. The instrumentation used were broad band detectors similar to those used in the molecular oxygen research. As these are discussed fully in Chapter 3, no further discussion is included in Chapter 8. However, the concept of the experiment is discussed as is the computer based feasibility study of the technique used. Flight performances of the experiments are also included, as is a description of the vehicles used.

Although the actual water vapour experiment didn't yield any numbers for $n(H_2O)$ in the lower thermosphere some very tentative conclusions about the density of water vapour at lower thermospheric heights were deduced from the differences in the molecular oxygen density profiles determined by different types of broad band detectors. These are discussed in Chapter 8.

CHAPTER TWO

THE MEASUREMENT OF MOLECULAR OXYGEN IN THE LOWER THERMOSPHERE - A REVIEW

This Chapter reviews the experimental determinations of lower thermospheric molecular oxygen densities. The review can be considered to be divided into two parts. In the first, which includes Section 2.1, 2.2 and 2.3 the techniques used to make the measurements and analyse the subsequent data are considered. In the second (Section 2.4) the discussion centres on the results obtained. A summary is also given (Section 2.5).

The majority of the experiments have been based on either U V absorption spectrophotometry/spectroscopy (the distinction is explained in Section 2.2.1) or on mass spectroscopy. These two techniques are discussed separately in 2.1 and 2.2 respectively. The third section in part one deals with determinations which utilized methods falling outside of either of the above categories.

The lower thermosphere is not a static system. A constant molecular oxygen profile is not expected. Section 2.4 discusses the types of variations observed in 30 years. Also included in Section 2.4 is a comparison of results from U V absorption and mass spectroscopic techniques. Mean densities were calculated for each technique and these are both tabulated and presented in graphical form.

In all sections reference may be made to measurements outside the defined limits of the lower thermosphere (Chapter 1). These have been included for completeness of the discussion.

2.1 MEASUREMENT OF $n(O_2)$ BY U V ABSORPTION TECHNIQUES

It has already been stated in Chapter 1 that U V absorption techniques were used in the current research program. Because of this

the methodology is fully discussed in Chapter 4. However to facilitate discussion in this review, some basic concepts and parameters are defined in a short introduction (Section 2.1.1).

Both non-dispersive and dispersive instrumentation has been built to exploit U.V. absorption techniques and these are considered in Sections 2.1.2 and 2.1.3 respectively.

2.1.1 Introduction

All U V techniques involve measuring the intensity of solar, stellar or lunar U V radiation as a function of height. The resultant curve is known as the extinction curve. The radiation is "extinguished" because of atmospheric absorption. At a particular height h, the absorption of the radiation at wavelength λ that will occur over a given interval about h is dependent on the density of the absorbing gases at h and the absorption cross sections, at λ, of those gases. If it is assumed that only one gas absorbs significantly, then the change in intensity can be expressed as

$$I = I_0 \exp(- \sigma n x) \qquad 2.1$$

where x is the length of the interval over which change in intensity is being observed; n is the density of the absorbing gas (it is normally held constant and approximated to that at h); σ is the absorption cross section of the gas; I_0 is the intensity of the initial radiation and I is the intensity after the radiation has travelled the length x.

Although, as will be shown in Chapter 4, the relationship is not usually used in this form it does illustrate how n the number density, may be obtained. I and I_0 can be read off the extinction curve once a choice has been made for length x of the absorbing path, and if σ is known from laboratory measurements the only unknown is n.

The Equation 2.1 applies to the expected change in intensity of radiation at a fixed wavelength. In practice, however, the intensity of a band of radiation will be observed. It can still be used if σ is replaced by a quantity known as the effective cross-section σ_{EFF} which allows for the finite width of the detector passband and its non-uniform response, with respect to wavelength. This parameter is defined as

$$\sigma_{EFF} = \frac{\int_{\lambda_1}^{\lambda_2} \phi\ (\lambda,\ h).\ S(\lambda).\ \sigma(\lambda).d\lambda}{\int_{\lambda_1}^{\lambda_2} \phi\ (\lambda,\ h).\ S(\lambda).d\lambda} \qquad 2.2$$

where

(a) λ_1 and λ_2 are the wavelength limits of the passband,

(b) $\phi(\lambda,\ h)$ is the flux at h,

(c) $S(\lambda)$ is the spectral response of the detector,

(d) $\sigma(\lambda)$ is the absorption cross-section of the absorbing gas.

It is important to note that the definition implies that absolute values are not required either for $\phi(\lambda,\ h)$ or $S(\lambda)$. Normalized curves will suffice.

If $\sigma(\lambda)$ varies strongly across the passband differential absorption of the radiation takes place. Radiation for which $\sigma(\lambda)$ is high, is preferentially absorbed leaving the more penetrating radiation. This is normally referred to as "radiation hardening". The shape of the flux function therefore changes as radiation is absorbed. This implies σ_{EFF} is also a function of the absorption and therefore the correct numerical value of σ_{EFF} to use in Equation 2.1 depends on the amount of absorption that has occurred by h.

As a measure of the absorption, the parameter μ, which is known as the extinction coefficient, is introduced. μ is defined as

$$\mu_h = \frac{\text{intensity of radiation @ h } (I_h)}{\text{intensity of unattenuated radiation } (I_\infty)} \qquad 2.3$$

where the unattenuated intensity is that measured well above the absorbing layer. Both I_h and I_∞ can be read from the extinction curve. Further detail is given in Chapter 4, but σ_{EFF} can be expressed as a function of the extinction coefficient and therefore by using 2.3 to find μ_h the value σ_{EFF} required for Equation 2.1 can be ascertained for any height h.

It is clear from the above that the basis of U V absorption techniques is the measurement of the extinction curve. However, the method adopted for the measurement varies and in the present work these experimental methods have been classified according to the way in which the radiation has been detected. Techniques where the intensity of the solar radiation is recorded on film are termed U V absorption spectroscopy while the name U V absorption spectrophotometry covers those techniques where the intensity of the radiation is translated to a current or series of pulses.

2.1.2 Non-Dispersive Instrumentation

The simplest instrumentation developed to exploit the U V absorption technique is the ion chamber. (Chapter 3). These are broad band, non-dispersive spectrophotometric detectors and an early prototype of this type of instrumentation was used in the first attempt to measure molecular oxygen densities *in situ* (Friedman *et al*, 1951). This rocket

borne experiment was not successful, partly because of the failure of some of the detectors and partly because the lack of aspect information (i.e. knowledge of the angle between the sun vector and the look direction of the detector) meant that the signal from those detectors which responded and did not saturate could not be corrected for their angular response (Section 3.2.7). The detectors were improved (Chubb and Friedman, 1955) and using them, successful attempts to measure molecular oxygen were made by Byram *et al* (1954, 1955) and Kupperian *et al* (1959).

From these early detectors, Friedman *et al* (1958) developed the copper bodied chamber on which are based the ion chambers, both of the present work and of many of the experimenters mentioned in this review. Other chambers used have been of similar design but have been constructed of different materials : the internally plated ceramic chambers first manufactured by Stober (1962) and the glass ion chamber of Lockey (1972).

Other instrumentation which is capable of measuring the atmospheric density profile of molecular oxygen has been developed (see Section 2.1.3). However, ion chambers still have several advantages. They are rugged, small and cheap enough to use in non-recoverable payloads.

These features plus their wide angle of view make them suitable for use on small spin stabilized sounding rockets. Most of the experiments reviewed have been carried on this type of vehicle. With spin stabilization, the aspect changes continually throughout the flight and aspect sensors need to be flown as well. Extinction curves are built up either by using the known angular response of the chamber to correct all signals back to zero aspect, or by only using the signal taken at a particular value of the aspect.

The most frequently used version of the ion chambers measured the extinction curve of solar Lα. Molecular oxygen densities resulting from the analysis of extinction curves measured by rocket-borne Lα chambers were reported by authors such as Carver *et al* (1964, 1966); Weeks and Smith (1968); Quessette (1970); Hall (1972); Subbaraya *et al* (1972, 1974); Weeks (1975 a); Carver *et al* (1977b) and Bibbo *et al* (1979). Lα chambers were also used in satellite-borne experiments (Norton and Warnock, 1968; Lockey *et al*, 1969; Knuth *et al*, 1976 and Sonneman *et al*, 1977).

To interpret the data obtained it was assumed that molecular oxygen was the only significant absorber within the passband (see Section 4.2.7 for further discussion). The broad band response of the chamber (200Å - 300Å) implies the need to use an effective absorption cross-section. This has been done in the present work (Section 4.2.6) but in the literature research groups have adopted varying methods to avoid the complexity of σ_{EFF}. They have justified this approach by pointing out that the strength of the solar Lα line implies that the bulk of the signal of a Lα chamber is derived from the incident Lα radiation.

Some have tried to correct for the non Lα radiation (Kupperian *et al*, 1959; Weeks and Smith, 1968). These experimenters flew a second ion chamber with a passband of λλ1235Å - 1350Å (the Lyman alpha ion chambers themselves had passbands of either λλ1050Å - 1350Å or λλ1140Å - 1350Å, see Chapter 3). The signal from this second chamber which had a window of Calcium fluoride and a filling gas of NO. (CaF_2- NO) was deducted from that of the Lα chamber. Kupperian *et al* (1959) also deducted another 2½% for the contribution of the solar line at 1206.5Å. The curve produced by this reduced signal was assumed to be

solely due to the decreasing intensity in $L\alpha$ as a result of its absorption by molecular oxygen. Laboratory measured absorption coefficients (Watanabe *et al*, 1953 ; Watanabe, 1958) were then used to determine $n(O_2)$.

From their results, Weeks and Smith (1968) also estimated the percentage fraction of the ion chambers maximum signal (i.e. when the ion chamber is viewing the unattenuated radiation) derived from the $L\alpha$ line. Their results implied a level of 80% to 90%. Another group (Smith and Millar, 1974) reported a level of $89 \pm 5\%$. In addition the results suggested the chamber could be considered monochromatic in $L\alpha$ and the extinction curve could be considered to only reflect the changing absorption of $L\alpha$ until these signal levels were reached.

The height at which the 80% to 90% signal level will occur will vary with the solar zenith angle (SZA) at the time of flight. Weeks and Smith (1968) suggested that the assumption of monochromaticity would only be valid if $h < 94$ for SZA = 60° and $h < 112$ kms if SZA = 90°.

Carver *et al* (1964, 1966) had already noted that the absorption cross sections (Watanabe, 1958 ; Blake *et al*, 1966) for the non-Lyman-alpha radiation in the passband are much greater than the absorption cross section for $L\alpha$. This they had argued implied that the non-Lyman-alpha radiation is absorbed first. Therefore to avoid the need to use σ_{EFF} they restricted their analysis to heights below which they estimated only $L\alpha$ would remain. $h < 90$ was chosen and the results of Weeks and Smith (1968) corroborate their choice.

Failure to account for the non-Lyman-alpha radiation can produce severe anomalies in the $n(O_2)$ profile (Quessette, 1970; Lockey *et al*, 1969) and the two approaches to avoiding both the introduction of these anomalies and the need to use σ_{EFF} have continued. While Carver

et al (1969, 1977b) have continued to just restrict all their analysis to $h < 90$, other experimenters (Weeks, 1975a; Brannon and Hoffman, 1971) have used the work of Weeks and Smith (1968) to assess the likely effect of the non $L\alpha$ radiation on their experimental determinations of $n(O_2)$. For their flight conditions Brannon and Hoffman (1971) found the effect was $< 3\%$ and they ignored it. However, Weeks (1975a)did not use some high altitude data because the earlier flights of Weeks and Smith (1968) suggested this would reflect the extinction of radiation in the passband $\lambda\lambda$1225Å - 1350Å.

Early experimenters (Kupperian *et al*, 1959; Carver *et al*, 1964, 1966; Weeks and Smith, 1968) used a single absorption cross section for $L\alpha$. However, the work of Ogawa (1968) showed that the absorption cross-section of molecular oxygen varies across the solar $L\alpha$ line. Therefore not only is an effective cross section needed for the Lyman-alpha line itself but since radiation hardening will occur as the radiation passes through the atmosphere this effective cross section ($\sigma_{EFF}(L\alpha)$) must change with absorption. Hall (1972) using the results of Ogawa (1968) calculated an absorption dependent $\sigma_{EFF}(L\alpha)$ and predicted errors as large as 30% if a single $\sigma_{L\alpha}$ was used.

This contrasts strongly with the suggestions of Brannon and Hoffman (1971) who considered the use of $\sigma_{EFF}(L\alpha)$ to be unnecessary and of Quessette (1970) who predicted errors no larger than 12% being introduced by not using $\sigma_{EFF}(L\alpha)$. However, when Subbaraya *et al* (1974) re-analysed some of their earlier data (Subbaraya *et al*, 1972) they found that, consistant with Hall's predictions, their computed molecular oxygen densities changed by 15% to 30% when the more correct absorption dependent $\sigma_{EFF}(L\alpha)$ was used.

Use of a variable effective cross section is now standard procedure. (Ackerman *et al*, 1974; Weeks, 1975a; Felske and Sonnemann, 1976; Ilyas, 1976; Norton and Roble, 1974) but until the work of Carver *et al* (1977a) it was still subject to unknown systematic errors because it was calculated with $\sigma(\lambda)$ measured at room temperature. Carver *et al* (1977a) measured the absorption cross section of molecular oxygen across the $L\alpha$ line at 82°K, 195°K and 294°K. They have since published a review of many of the previous $L\alpha$ results (Carver *et al*, 1977b). These results have been adjusted by using the new data at T = 195°K and the authors now predict a systematic error of no more than 5%. This arises because of the range of temperatures over the height range covered by the extinction curve and because 195°K may still be an inappropriate mean temperature for the region.

There is one other source of uncertainty that can be associated with $\sigma_{EFF}(L\alpha)$ and this has also been discussed in the literature. From Equation 2.1 $\sigma_{EFF}(L\alpha)$ will depend on the line shape of the solar $L\alpha$ line. This will vary (Meier, 1969; Vidal Madjar, 1975). Ion chambers cannot resolve the shape of the line and therefore calculation of the effective cross section for $L\alpha$ usually relies on the adoption of a line profile measured at some other time. Garriott *et al* (1977) dismissed the uncertainty introduced by line profile variation as negligible but Carver *et al* (1977a) calculated $\sigma_{EFF}(L\alpha)$ with the line profiles of Purcell and Tousey (1960) and of Quessette (1970) and found systematic differences between the two of up to 5%. However, they have not taken this source of uncertainty into account in their application of their $\sigma_{EFF}(L\alpha)$ (Carver *et al*, 1977b). That is, variation in the shape of the solar-Lyman-alpha line has not been considered a significant source of

uncertainty in $\sigma_{EFF}(L\alpha)$ and consequently in $n(O_2)$ profiles derived from $L\alpha$ chambers. This contrasts with the attitude adopted in the present work (Section 4.2.3).

Although used extensively the $L\alpha$ ion chamber is not the only type that has been flown. As is shown in Figure 2.1 it can only provide information across a limited height range. The three extinction curves in this diagram were all measured by chambers flown aboard Aerobee 13.123 IS launched with an approximate zenith angle of 84.4° and, even at this zenith angle, the $L\alpha$ chamber is only useful for altitudes < 120 kms. Of the other two chambers the SX ion chamber is considered first. The SX refers to the window material, Sapphire and the filling gas, Xylene and it has a passband of $\approx \lambda\lambda 1425Å - 1490Å$.

Kupperian *et al* (1959) flew the first ion chamber with a passband in this wavelength range in order to extend their measurements to higher altitudes. The use of these has continued, both on rockets, (Weeks and Smith, 1968; Carver *et al*, 1969; Weeks, 1975b; Higgins and Heroux, 1977; Carver *et al*, 1978a; and Bibbo *et al*, 1979) and satellites (Stewart and Wildman, 1969; Lockey, 1972; Parker and Stewart, 1972).

Although Figure 2.1 shows the extinction curve of a particular chamber flown on a rocket launched at a particular zenith angle, it is representative of the height range Δh over which SX chambers can operate and of h_1, h_2, the upper and lower limits of Δh. All these parameters Δh, h_1 and h_2, however, do change with the sensitivity of the ion chamber and the solar zenith angle (SZA) at the time of flight and further examples of the extinction curves of SX chambers are given in

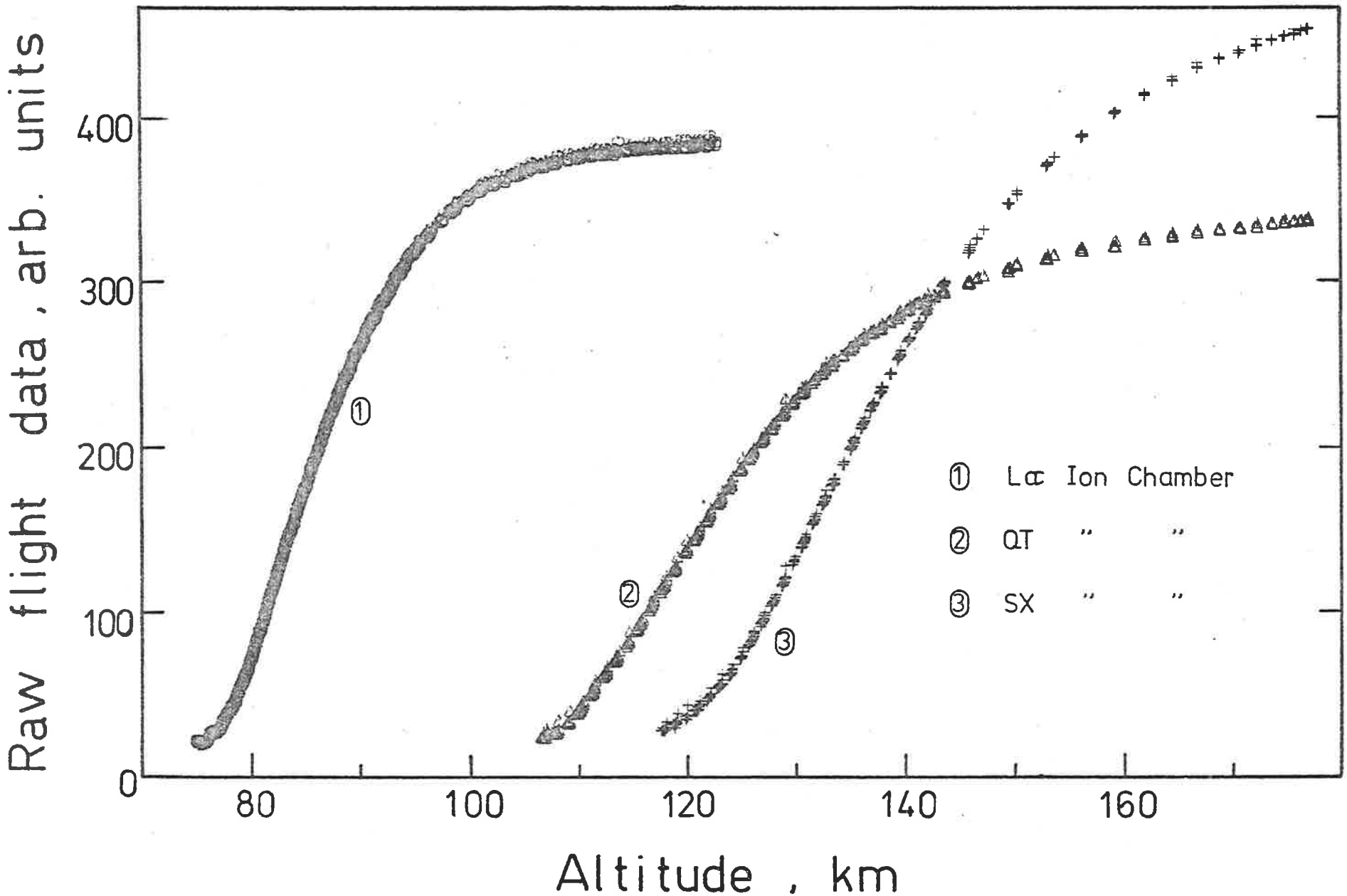

Fig 2.1 Sample extinction curves of the three types of ion chambers used in the present work. (see text for explanation of code)

Chapter 5; e.g. Figures 5.8, 5.18 and 5.27.

There is no dominant line within the passband of an SX chamber and these chambers are not considered to be monochromatic over any part of the extinction. However, because the cross-section of molecular oxygen does not change markedly across the wavelengths of the passband, the σ at λ1450Å, rather than an effective cross-section has normally been used (Weeks and Smith, 1968; Weeks, 1975b; Higgins and Heroux, 1977).

The use of $\sigma_{1450Å}$ implies that neither individual differences in the chamber nor possible radiation hardening across the passband have been taken into account (see Section 4.2). Nor has the laboratory measured $\sigma_{1450Å}$ been corrected for possible temperature effects before applying it to *in situ* atmospheric measurements where the temperatures could reach 600°K to 700°K (Jacchia, 1977). The likely effect of these temperatures on the absorption cross section can only be estimated from the theoretical work of Evans and Schexynader (1961). No experimental measurements have been taken.* Their work predicts a change of less than 4% and this has not been considered large enough to warrant attempting the corrections (Weeks, 1975b; Carver *et al*, 1978a; Bibbo *et al*, 1979).

The chambers have exhibited apparent changes in sensitivity over apogee (Weeks and Smith, 1968; Wildman *et al*, 1969). Outgassing of H_2O from the payload has been suggested as a possible cause (Weeks 1975b)and this has lead to thorough pre-launch dry nitrogen purging of payloads containing SX chambers (Weeks, 1975b; Higgins and Heroux, 1977). (In relation to the present work this was already an established practice for all payloads). Where asymmetry around apogee is still observed downleg data is considered to be the more reliable. In some cases only

* Experimental measurements have now been taken, see note with table 4.7. on Page 171a.

downleg measurements have been attempted. (Higgins and Heroux, 1977).

Reduction in outgassing leads to an apparently increasing sensitivity but decreasing sensitivities have also been observed. Breakdown of the Xylene gas under irradiation has been suggested as the cause (Wildman *et al*, 1969) but no preventive or corrective measures have been put forward in the literature. (See Chapter 6 for further discussion).

Photoelectric emission has been observed from the body of the chamber (Stober *et al*, 1963; Weeks, 1975b; Higgins and Heroux, 1977) and it can be a significant source of uncertainty. This is caused by the intense solar radiation above λ2000Å but it is easily avoided by holding the body of the chamber at a positive potential (see Section 3.2.9). Authors such as Carver *et al* (1969), Lockey (1972) and Ilyas (1976) have adopted this preventative measure and have not reported any photoelectric emissions in these or any of the other chambers they used.

Referral to Diagram 2.1 will show that the two chambers that have already been discussed do not provide a complete coverage of the lower thermospheric region. The Lα extinction curve effectively flattens out before the start of the SX extinction curve. The third curve, does, however, complete the coverage. The chamber has a Quartz window and a Triethylamine filling gas which gives it a passband of λλ1560Å - 1650Å. Δh for this chamber is approximately 50 kms and h_1, h_2 vary with the solar zenith angle, (see further examples of extinction curves in Chapter 5) but the QT chamber by operating between the Lα and the SX chamber enables a continuous measurement of $n(O_2)$ from ≈ 80 kms to ≈ 170 km.

Molecular oxygen densities derived from QT chambers have been published by Lockey (1972), Carver *et al* (1969),

Ilyas (1976), Carver *et al* (1978a) and Bibbo *et al* (1979).

The absorption cross section of molecular oxygen varies significantly across the QT chamber passband and the adoption of an effective X-section for the chamber has been considered essential by the authors listed above. Radiation hardening occurs and use of a constant effective absorption cross section rather than one dependent on the amount of absorption that has occurred leads to errors in the derived $n(O_2)$ of the order of $\pm$ 20% (Lockey, 1972). However, only the later authors mentioned (Ilyas, 1976; Carver *et al*, 1978a and Bibbo *et al*, 1979) have used an absorption dependent σ_{EFF}.

Lockey (1972) and Ilyas (1976) adopted a typical response curve ($S(\lambda)$) to calculate a standard σ_{EFF} for all QT chambers. The QT derived $n(O_2)$ published by Carver *et al* (1978a and Bibbo *et al* (1979) were determined by the use of individually calculated σ_{EFF}. The need or otherwise to adopt individual spectral responses is discussed further in Chapter 4.

The effect of temperature on $\sigma(\lambda)$ for the wavelengths within the passband of a QT chamber has been measured. (Hudson and Carter, 1968; Rogers, 1979). Although using $\sigma(\lambda)$ measured at room temperature has been estimated to introduce up to $\pm$ 10% uncertainty, (Carver *et al*, 1978a no attempts have been made to use $\sigma(\lambda)$ measured at a more appropriate temperature. Once again because these chambers were used in the research programme for this thesis further discussion is included in Chapter 4.

2.1.3 Dispersive Instrumentation

Dispersive instrumentation has also been used to measure the U V extinction curves necessary for determining $n(O_2)$. In contrast to

ion chambers these instruments are large, non-rugged because of the need to maintain accurate alignment of optical paths, and they require attitude controlled rockets or satellites. Two basic forms have been used, the spectrograph and the spectrophotometer.

The spectrograph records the information received on film (a spectrogram) and is therefore by the definition in 2.1.1 a spectroscopic instrument. Spectrographs were flown by Jursa *et al* (1963, 1965) on several rockets launched from White Sands missile range (32° N). These spectrographs were the development of an earlier instrument (Jursa *et al*, 1959) which although designed for the measurement of n(NO) by U V absorption techniques had also enabled "rough" measurements of $n(O_2)$ to be made from 62 to 87 kms. From all their flights Jursa *et al* (1965) were able to publish a composite $n(O_2)$ profile from 65 to 160 kms.

Despite this success, the spectrograph of Jursa *et al* (1963, 1965) did have some serious disadvantages. These were -

(a) the length of exposure time for the film implied that the intensity registered was an average of the intensity observed over an altitude range of 2-3 kms,

(b) the instrument only took 7 spectrograms during each flight. This limited altitude resolution,

(c) the film used was only capable of recording a limited range of intensities thus limiting the altitude range over which $n(O_2)$ could be determined,

(d) calibration of the film introduced a ± 50% uncertainty into the derived $n(O_2)$.

Some of these problems appear to be intrinsic to the use of a spectrograph. The much later spectrograph of Prinz and Bruecker (1977)

was capable of taking more spectrograms but film exposure times still implied averaging over 2 or 3 kms and the uncertainties introduced by the film calibration still ranged up to ± 50%.

The E.U.V. monochromator of Hinteregger (1962) avoided some of the problems outlined above. In this spectrophotometric instrumentation the film was replaced by a photoelectron counter which scanned right across the spectrum but detected only a ≈ 2Å wide band of it at any one time. The response time of this counter was such that the signal received represented an instantaneous solar intensity measurement rather than an average over 3 or 4 kms. (cf with point (a) above). In addition uncertainties arising from photoelectron counter calibration were smaller than those arising from the film calibration. Hall *et al* (1963) considered uncertainties from this source to be of the order of ± 10% to ± 25%.

Despite these improvements, extinction curves measured by the monochromator were still unsatisfactory. The instrument scanned from 250Å to 1300Å with a wavelength resolution of 1Å to 2Å. Subsequently because of the length of time taken to complete one scan the extinction curve for any particular wavelength could be made up of fewer than 10 points. Therefore,although individual points were not averaged,altitude resolution was still limited because the points were many kilometers apart.

To obtain better defined extinction curves with higher altitude resolution the EUV monochromator was altered so that instead of scanning across a 1050Å range only a few selected wavelengths were observed (Hall *et al*, 1965). This markedly increased the number of times

the intensity of a particular wavelength radiation was measured as the rocket passed through the atmosphere. However, it was still considered that the definition of the extinction curve could be improved. This was achieved by Reid and Withbroe (1970) by simply exploiting the extended observation time available to satellite-borne instrumentation. Instead of a continuous scanning across all the wavelengths of interest they only needed to look at one wavelength during any one occultation, and could rely on the repeated occultations to get measurements for all the different wavelengths. They were able, therefore, to obtain an extinction curve whose definition or altitude resolution was limited only by the speed of the telemetry. Garriott *et al* (1977) also achieved this but they did it by having a separate detector for each line they wished to observe. This latter technique can be adopted to rocket-borne experiments if space is available.

Using a satellite as the observation platform can however, have its effect on the altitude resolution obtainable and the results of Reid and Withbroe (1970) in common with those from satellite-borne ion chambers were still limited in this because of the $\frac{1}{2}^{\circ}$ width of the sun. (Felske *et al*, 1974; Felske and Sonnemann 1976).

The problem of the finite size of the sun was overcome by Garriott *et al* (1977) by restricting the field of view of their instrument. The small field of view chosen (5 arc secs x 5 arc secs) enabled a final altitude resolution of $\approx$ 1 km but it introduced further uncertainties. Vernazza *et al* (1975) have shown that solar regions with angular dimensions of < (30 x 30) arc secs^2 will exhibit random fluctuations in intensity of up to 50% in time scales as short as 1 min. This must be considered as an uncertainty associated with the results of Garriott *et al*

(1977). The authors themselves suggested, as a compromise, a field of view of (1 x 1) arc min^2 for future instruments. This would reduce the effect of the intensity fluctuations while maintaining good altitude resolution. However, such instruments do not appear to have been flown as yet.

2.2 MEASUREMENT OF $n(O_2)$ BY MASS SPECTROSCOPIC TECHNIQUES

While a general discussion on the design and theory of operation of rocket or satellite-borne mass spectrometers is not relevant to the present work - the reader is referred to papers by Schaefer and Nichols (1964a), von Zahn (1968) and Hedin *et al* (1973) and the references they contain - some basic definitions and concepts are defined in Section 2.2.1. This is simply to facilitate the discussion in the sections that follow.

Section 2.2.2 considers some of the general difficulties of using mass spectrometers to measure atmospheric constituent densities while Section 2.2.3 looks at the extra problems encountered when attempts are made to measure the atmospheric $n(O_2)$ profile with a rocket borne mass spectrometer. $n(O_2)$ measurements made with satellite-borne mass spectrometers are discussed separately in Section 2.2.4. The distinction has been made because the different restraints and opportunities of the different environments can lead to quite different techniques of operation for satellite and rocket-borne mass spectrometers.

2.2.1 Introduction

Although called mass spectrometers many instruments in fact discriminate for mass number either by momentum selection (magnetic analysers) or by velocity selection (time of flight analysers). The quadrupole mass spectrometer is the only mass selector.

Irrespective of type, if a neutral gas sample is to be analysed the neutral particles must first be ionized. This is usually achieved by bombarding the gas sample with electrons from a hot cathode filament. The filament together with its supportive structure is known as the ion source.

If the atmospheric particles entering the ion source can intersect the electron beam, be ionized and pass into the analysing region without suffering any wall collisions the geometry of the source is described as open. In practice ideal open sources are not obtainable. (von Zahn, 1968). If they suffer many collisions following this path then the geometry of the source is described as closed. A closed source is normally obtained by enclosing the ion source in a cavity which is only connected to the ambient atmosphere by a small orifice (von Zahn, 1968).

In discussing the uncertainties associated with mass spectrometers and the different types of ion source geometry, the uncertainty in the thermal accommodation coefficient of the wall of the ion source is mentioned. This coefficient is a measure of the energy transfer that occurs when a particle collides with a wall of the ion source. Its value may range from zero, if there is specular reflection of the impinging particle, to one, if the particle, having suffered the collision, has been thermalized.

2.2.2 General Problems in the Experimental Determination of Mass Densities by Rocket or Satellite-borne Mass Spectrometers.

This section briefly looks at some of the general problems encountered when mass spectrometers are used to measure the mass densities of atmospheric constituents. Some of these difficulties have not been

overcome but where progress has been made mention is given to the development.

2.2.2.1 Contamination

No results were obtained from the first flight of a mass spectrometer because of massive contamination of the instrument by vapour from the rocket fuel. (Townshead *et al*, 1954). This did not appear to affect the mass spectrometer launched from White Sands in 1955 (Meadows & Townshead, 1956) nor the four mass spectrometers flown during the International Geophysical Year by Meadows and Townshead (1960). In fact, although some researchers have taken the precaution of separating their mass spectrometer from the spent rocket motor before exposing it to the atmosphere (Schaefer and Nichols, 1964a) contamination from this source no longer appears to be significant. Contamination from outgassing of the payload itself is, however, still reported, (Krankowsky *et al*, 1968; Mauersberger *et al*, 1968; Offerman and Grossman, 1973) but this only seems to prevent measurement of $n(H_2O)$.

2.2.2.2. Uncertainty in the Flight Mass Sensitivity

A serious problem, and one which affects all rocket-borne mass spectrometers designed to measure neutral constituents, is the difficulty in determining the flight mass sensitivity of the instrument. Laboratory calibrations cannot be used without correction because these are taken with the mass spectrometer "at rest" with respect to the gas sample, whereas in flight the mass spectrometer is moving, with high velocity, through the gas. This correction factor for what is known as the "ram effect" depends on the velocity vector of the rocket (more correctly the velocity vector of the mass spectrometer), the temperature

of the atmosphere and the ion source, the ion source geometry and the condition of the source walls (Offerman and Trinks, 1971). As is shown below each of these parameters introduces uncertainty into the correction factor and therefore contributes to the uncertainty of the number densities derived from the data.

The velocity vector of the mass spectrometer with respect to the opening of the mass spectrometer defines the instrument's angle of attack. If the mass spectrometer is on a spinning rocket the continual changing of the angle of attack modulates the instrument's signal (Nier *et al*, 1964). Failure to allow for the effects of this modulation may introduce inaccuracies into derived number densities. An example of this is the work of Hedin *et al* (1964) and Nier *et al* (1964). They both analysed the same mass spectrometer data but the number densities they obtained differed by up to a factor of 2. Hedin *et al* (1964) had carefully analysed the effects of spin while Nier *et al* (1964) had only used the nodal points of the modulated signal. If the mass spectrometer has been separated from the rocket and is tumbling, the angle of attack also changes but this time not necessarily in a uniform way. It may only be possible to estimate the angle of attack (Schaefer and Nichols, 1964a; Schaefer 1969) and this immediately introduces uncertainty into the analysis.

The flight temperature of the mass spectrometer can be monitored but the atmospheric temperature must quite often be estimated from an atmospheric model and this is another source of uncertainty. This can be reduced if it is possible to obtain temperatures derived from simultaneous radar back scatter measurements (Trinks *et al*, 1978a).

The condition of the ion source walls has a bearing on the "ram effect" correction factor because in part it determines the thermal

accommodation coefficient of the walls. Uncertainty is introduced because the way the history of the ion source affects the surface of the wall and subsequently the thermal accommodation coefficient is, in itself, uncertain. Further uncertainty arises because the effect on the coefficient of the differing temperatures between the ion source and the ambient atmosphere is also uncertain (Nier, 1970).

The magnitude of the uncertainty that can be introduced into the derived number densities by estimating the thermal accommodation coefficient is illustrated by the example of von Zahn (1968). For an open ion source mass spectrometer changing the thermal accommodation coefficient from 0 to 1 changes the implied number densities by a factor of 2.

The problems in correcting the results of an open mass spectrometer for dynamic effects were recognized early (Schaefer & Nichols, 1964a; Nier *et al*, 1964). Closed ion sources were considered because it was thought the repeated collisions undergone by the incoming particle would make valid the assumption of a value of 1 for the thermal accommodation coefficient. This may have removed one source of uncertainty but the use of a closed source introduces other problems into the analysis. With the repeated collisions there is a greatly increased probability of reactions at the wall (Hedin and Nier, 1966). The possibility of wall loss is also increased. Moe and Moe (1969) have stated that adsorption is a problem even for an inert gas.

The difficulties in the analysis and correction of the data from either closed or open sources led to the development of the cryo-cooled mass spectrometer (Offerman and Trinks, 1971). The walls of a nearly closed ion source are kept to a temperature of 8°K. Therefore

any particle hitting the wall sticks there, and the sample analysed is unmodified by partly or wholly thermalized particles. Nor is it affected by wall reactions or desorption from the walls. A flight of this instrument (Offerman and von Zahn 1971; Offerman and Grossman, 1973) appears to have been very successful. Some of the results are considered later in Section 2.4.

2.2.2.3 Limited Operational Height Range

Instrumental sensitivity determines the highest altitude at which the mass spectrometer still detects atmospheric constituents but since this can be made well above lower thermospheric heights it is not of relevance here. The lower altitude limit for most mass spectrometers, however, has reduced their usefulness for lower thermospheric measurements since this limit has been approximately 120 kms. Rocket-borne mass spectrometer measurements below 120 kms have been considered unreliable because the passage of the rocket disturbs the free molecular flow (Hedin and Nier, 1966; Krankowsky *et al*, 1968), and satellite-borne mass spectrometers have been limited by the capabilities of the vehicle on which they are carried, to heights well above this.

Progress has been made, however, in reducing the lower limit for rocket-borne mass spectrometers. Offerman and Tartarczck (1973) argued that mass spectrometer measurements were possible at altitudes less than 120 kms if the shock wave created by the mass spectrometer's passage through the atmosphere could be dissipated. They achieved this by modifying the front plate of the cryogenically cooled ion source which had already been developed (Offerman and Trinks, 1971). The advantages

of this earlier version have already been mentioned in Section 2.2.2.2.

In practice all parts of the ion source are cooled to 10°K to 20°K by supercritical helium. Ambient particles hitting the front plate,(see Figure 2.2) which acts like a very efficient heat exchanger, stick to it. This prevents the high pressure, high density and temperature region which normally builds up immediately in front of the ion source at these lower altitudes i.e. < 120 kms. Without the build-up of this region the gas sample remains unmodified and the mass densities measured by the instrument will be indicative of true ambient densities.

2.2.3 Experimental determination of $n(O_2)$ by Rocket-Borne Mass Spectrometers

The preceding discussion has centred on the general problems faced by rocket-borne mass spectrometers. These difficulties influence all results obtained by them and add to the experimental uncertainty of all derived number densities. However, there are some problems which are unique to attempts to measure the density profile of O_2.

One of these is once again related to the difficulty in applying laboratory calibrations to data collected during the flight. von Zahn and Gross (1969) found that if a rhenium filament is used it pumps molecular oxygen at a speed equivalent to about 10% of the total speed obtainable under laboratory conditions. However, the pumping of the rhenium filament will be negligible compared to the pumping speed of the upper atmosphere and this implies laboratory calibrations are not applicable and have to be revised. Bitterberg *et al* (1970) reported a similar problem.

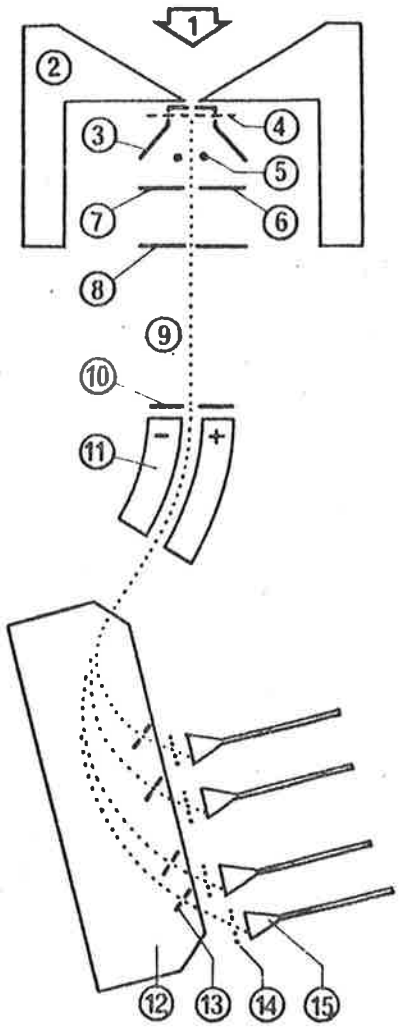

Fig. 2.2 Schematic of the mass spectrometer layout. 1. is the ambient gas particles, 2. is the helium-cooled front part removing the shock in front of the ion source, 3. is the ion box (helium cooled), 4. is the electron beam, 5. is the ion lens (helium cooled, 6. is the ion-focusing plate J+ (helium cooled), 7. is the ion-focusing plate J- (helium cooled), 8. is the object slit, 9. is the ion beam, 10. is the total ion-counting monitor, 11. is the electric analyzer, 12. is the magnetic analyzer, 13. is the exit slits, 14. is the suppressor grids and 15. is the Spiraltron multipliers. (Figure 1. of Trinks *et al*, 1978a).

It has been suggested that O_2 is lost at the walls of a mass spectrometer (Kasprzak *et al*, 1968; Mauersberger *et al*, 1968; Müller and Hartman, 1969). However, the major doubt about the validity of reported mass spectrometer measurements of $n(O_2)$ arises from the continuing controversy on whether or not atomic oxygen recombines at the walls of the ion source and re-appears as molecular oxygen.

The design of the ion source of the Bennet radio frequency mass spectrometer flown by Pokhunkov (1962) was such that incoming atmospheric molecules and atoms could not reach the ionizing space without hitting the source walls. The author considered that many of the atomic oxygen atoms would recombine on the walls to produce molecular oxygen, an opinion shared by Meadows-Reed and Smith (1964) who flew a similar type of instrument. These latter authors suggested less recombination would occur in an open ion source.

The work of Nier *et al* (1964) appeared to support the conjecture of Meadows-Reed and Smith (1964). Nier *et al* (1964) flew a mass spectrometer with a semi-open ion source and not only did they obtain higher $n(O)/n(O_2)$ ratios than had been derived from Bennet radio frequency mass spectrometers (Meadows and Townshead, 1960) but the implied $n(O_2)$ profile agreed surprisingly well with the profile determined by Byram *et al* (1955) by UV absorption techniques. They therefore considered their results were not significantly influenced by recombination.

However, Schaefer and Nichols (1964b) obtained even higher values for the $n(O)/n(O_2)$ ratios. Their results came from a mass spectrometer with a more open ion source than that of Nier *et al* (1964) and while the differences may have represented genuine atmospheric

variation they may also have been indicative of the occurrence of recombination in the semi-open source. It is noted that for a later measurement (Gross *et al*,1968), which also used a Nier type semi-open ion source, recombination,to molecular oxygen, of up to 40% of the atomic oxygen was consistent with the data obtained.

If recombination was occurring then not only should $n(O_2)$ determinations by Bennet radio frequency mass spectrometers be considered uncertain but also those carried out by mass spectrometers with semi-open ion sources.

In an attempt to test the importance of recombination in a mass spectrometer Hedin and Nier (1966) flew three mass spectrometers on one payload. They flew two with closed sources and one with a semi-open source. Their interpretation of the data implied the following:-

(a) the wall loss of atomic oxygen in the closed source was almost total but probably less than 15% could be contributed to the recombination of O to O_2,

(b) there was no significant wall loss of atomic oxygen in the mass spectrometers with the semi-open ion sources.

The inference that can be drawn from these statements is that Hedin and Nier (1966) considered only those $n(O_2)$ measurements taken with a semi-open source to be reliable but $n(O_2)$ could be reliably derived from the data of mass spectrometers with either closed or semi-open ion sources. Data from further flights of a mass spectrometer with a semi-open ion source were analysed under assumption (b) (Kasprzak *et al*, 1968; Krankowsky *et al*, 1968).

Assumption (b) contrasts strongly with the conclusions of von Zahn and Gross (1969) who flew a modified Nier type ion source. They

not only considered that atomic oxygen was being lost on the walls of their ion source but they also suggested that the $n(O_2)$ profile was being enhanced by up to 1 in 3 oxygen atoms recombining to form molecular oxygen.

The consequences of the different interpretations placed upon the mass spectrometer data shows up in a review of $n(O)$, $n(O_2)$ and $n(N_2)$ measurements (von Zahn, 1970). In comparison with other experimenters (Hall *et al*, 1967; Bitterberg *et al*, 1970) the $n(O)$ of the University of Minnesota group (Hedin and Nier, 1966; Kasprzak *et al* 1968; Krankowsky *et al*, 1968) are low. Although von Zahn (1970) considered the difference in the $n(O)$ to be too large to be genuine atmospheric variations, Nier (1972) could see no reason why the University of Minnesota's measurements should be selectively in error and, in a later paper (Nier *et al*, 1976), stated "there is absolutely no evidence that atomic oxygen is converted to molecular oxygen" in the mass spectrometers flown on the rockets considered by von Zahn. However, he could not reconcile his group's results with those of the cryogenically cooled mass spectrometer (Offerman and Grossman, 1973). This instrument, which should not have been troubled by any selective wall loss or recombination at all, obtained significantly higher $n(O)$ and $n(O)/n(O_2)$.

A third group attempted to resolve the question by looking at the results of a simple mass spectrometer and comparing them with simultaneous measurements taken by incoherent radar backscatter methods. In order to reconcile the results from the two different methods, Giraud *et al* (1972) were forced to assume wall loss of O did occur within the mass spectrometer and that the loss mechanism was recombination to O_2.

This however, didn't stop the controversy. Mauersberger and Nier (1973) pointed out that in seven of their flights launched from White Sands (32°N) (Hedin and Nier, 1965; Kasprzak *et al*, 1968; Krankowsky *et al*, 1968) O_2 had been found to be in diffusive equilibrium. Not only that but the densities obtained were less than those proposed by the diffusive equilibrium model of Jacchia (1971). They did not consider either of these results would be expected if $n(O_2)$ was being enhanced by the recombination of O. In this context it is interesting to note that the University of Minnesota's average $n(O_2)$ for 150 kms was in fact only about 20% greater than that determined by the Bonn group (von Zahn, 1970 and references therein) which was insisting recombination was occurring.

The laboratory work of Lake and Nier (1973) supported the "no recombination" claims of Mauersberger and Nier (1973) but Giraud (1973) re-affirmed the comments of the earlier paper (Giraud *et al*, 1972) and continued to insist O_2 densities were over-estimated by mass spectrometers and mass spectrometer determinations of $n(O_2)$ could not be regarded as completely reliable.

Since this interchange the work of Ackerman *et al* (1974) has been published. They flew a U V Spectrometer on two rockets launched from Sardinia (40°N). The $n(O_2)$ derived from the U V experiment was significantly less than the $n(O_2)$ derived from the mass spectrometer and the authors considered their U V results to be the more valid of of the two. However, the downgrading of mass spectrometer results was questioned by Nier *et al* (1976).

An answer to the controversy and therefore by implication an assessment of the reliability of mass spectroscopic measurements of $n(O_2)$

has still not been determined. As mentioned in Chapter 1, one of the rocket payloads in the present research program carried a mass spectrometer as well as U V absorption experiments. The results from this payload provide what is believed to be only the second opportunity to directly compare molecular oxygen densities obtained by U V and mass spectroscopic techniques. The discussion is contained in Chapter 6.

2.2.4 Experimental Determination of $n(O_2)$ by Satellite-Borne Mass Spectrometers

Satellite-borne mass spectrometers are discussed separately because although some of their problems are similar to those experienced by rocket-borne mass spectrometers, their extended data collecting time enables several different approaches to a solution.

Whether or not O recombines to O_2 does not seem to be controversial with regards to satellite-borne mass spectrometers. It has been assumed that there is almost total recombination to molecular oxygen (Newton *et al*, 1974; Taeusch *et al*, 1971). This assumption appears to be correct only after an initial conditioning of the internal surfaces of the ion source, (Hedin *et al*, 1973). The conditioning takes about 20 days and after this the surface appears to stabilise.

Since considerations of lifetimes kept early instrumented satellites at altitudes where molecular oxygen densities would be insignificant, the inability to distinguish between O and O_2 was not a limitation, although it did prevent Newton *et al* (1974) from measuring lower thermospheric $n(O_2)$ during the last week of their satellite's life when the orbital perigee came as low as 137 kms. However, the advent of the self powered A.E. series of satellites

(Spencer *et al*, 1973; Dalgarno *et al*, 1973) specifically designed to measure number densities at low altitudes - orbit perigees could be made as low as 130 kms for short periods of time - meant that this inability had to be circumvented. Considerable ingenuity has been shown in obtaining $n(O_2)$ from the mass spectrometers aboard the A.E. series of satellites.

To enable determination of $n(O_2)$, Nier *et al* (1974, 1976) developed the fly-through mode for the neutral mass spectrometer on the A.E.C.satellite. In the fly-through mode the mass spectrometer discriminated against particles which had suffered collisions with the walls, and therefore was expected to reject any O_2 arising from recombination of O. $n(O_2)$ was determined by measuring the mass 32/mass 28 ion current ratio in the fly-through mode, adjusting this on the basis of the laboratory measured relative mass sensitivities of the mass spectrometer and multiplying it by the number density obtained for N_2 (i.e. mass 28) measured on orbits where the mass spectrometer was in the "normal" mode. Normal mode values were used because in this mode the mass spectrometer behaved essentially like a closed source instrument which made correction of instrument densities to ambient densities easier.

Although the fly-through mode was successful in determining $n(O_2)$ it was only used on a limited number of orbits (Nier *et al*, 1976). The majority of passes were made with the mass spectrometer in the normal mode. In the normal mode only total oxygen, i.e. $n(O) + 2n(O_2)$ can be determined but the availability of such a large amount of data prompted Kirby-Docken and Oppenheimer (1977) to seek an indirect method

to obtain $n(O_2)$ from measurements of the total oxygen density.

At altitudes greater than 260 kms the measured oxygen density will be less than 5% molecular oxygen. Kirby-Docken and Oppenheimer (1977) used these total oxygen densities to create a model of the $n(O)$ distribution. They then assumed the difference at low altitudes between the model and the measured total O resulted from ambient O_2. In this way they obtained an $n(O_2)$ profile down to 140 kms. The method was however, only valid if diffusive equilibrium could be assumed for molecular oxygen.

A different solution also utilizing the data from the normal mode of a mass spectrometer was developed for the instrument on AE-D. This instrument was a modified version of the instrument flown on AE-C. The effect of one of these modifications, a gold insert, was less than complete recombination of $O \rightarrow O_2$ even after the conditioning period. Kayser and Potter (1978) were therefore, able to develop a technique to measure $n(O_2)$ while the mass spectrometer was in the "normal" mode. Interpreting the mass 32 peak as the result of ambient $n(O_2)$ and some definite percentage of $n(O)$ they were able to obtain a $n(O_2)$ profile which seemed compatible with that determined by the mass spectrometer in the fly-through mode.

A final technique is of interest, even though the $n(O_2)$ were not obtained at lower thermospheric heights. It illustrates the degree of sophistication that knowledge of the ion chemistry of the thermosphere has reached. Most of the $n(O_2)$ profiles obtained by the AE-C and AE-D satellites were determined from the data from the neutral mass spectrometers they carried. However, Oppenheimer *et al* (1976) used the data from the

Bennet ion mass spectrometer on AE-C. They obtained their $n(O_2)$ by combining the measured concentration of the O_2^+ ion with a comprehensive scheme of the ion's daytime chemistry in the thermosphere. They concluded that the ion chemistry was sufficiently well known to be able to use measurements of $n(O_2^+)$ to probe the concentration of $n(O_2)$.

This conclusion is supported by the general agreement found by Potter *et al* (1977) between the results of Oppenheimer *et al* (1976) and those derived from the neutral mass spectrometer in the fly-through mode (Nier *et al*, 1976; Kayser and Potter, 1976). However it may not be valid for all solar and magnetic conditions. Potter *et al*, (1977) restricted their discussion to measurements made during times of relatively low solar flux and little magnetic activity and were hesitant to imply that similar agreement would be obtained for other solar and magnetic conditions.

2.3 OTHER METHODS

There have been very few measurements of atmospheric molecular oxygen densities that used neither mass spectroscopic nor UV absorption techniques. Noxon and Johanson (1972) and Schaeffer and Noxon (1975) discussed a method for monitoring $n(O_2)$ by measuring twilight 6300Å airglow intensities. This airglow line arises from the excited $O('D)$ state of atomic oxygen. Their method was based on the assumption that the major source for the $O('D)$ is the photodissociation of molecular oxygen

$$O_2 + h\nu \rightarrow O('D) + O('P)$$

Relative changes in the O_2 densities rather than absolute numbers are

obtained.

Alcayde *et al* (1974) discussed an indirect method for determining $n(O_2)$ based on incoherent scatter observations. Once again the technique appears to be more suited for monitoring relative changes in $n(O_2)$ rather than obtaining absolute numbers.

The only other method that seems to have been employed in measuring $n(O_2)$ relies on inducing fluorescence in the ambient atmosphere by electron bombardment. The emission is then looked at in selected wavelength ranges (Haasz *et al*, 1976), and $n(O_2)$ deduced from the measured intensity.

2.4 THE RESULTS

The controversy surrounding the supposition that atomic oxygen recombines within the ion source of a mass spectrometer to form molecular oxygen has been discussed in Section 2.2.3. In Section 2.4.1. a comparison of UV and MS derived lower thermospheric $n(O_2)$ is undertaken in order to ascertain whether or not any systematic difference exists between the two sets of data.

Diurnal, geomagnetic, seasonal, latitudinal and solar flux variations of the molecular oxygen densities have been reported. Semi-annual variations observed in $n(O)/n(O_2)$ would suggest the possibility of a semi-annual variation as well. Annual variations have also been discussed in the literature though the distinction, if any, made between these and seasonal or latitudinal variations is ambiguous. This is considered further in Section 2.4.2.4.

The small number of rockets (3) and the timing of the launches has meant that the author has been unable to look for such variations in the present work, (Information was however, gained about the geomagnetic variation, see Chapter 6), but the available data on $n(O_2)$ is discussed

by referencing it to the particular variation it has supported or contradicted. This approach to reviewing the measurements of lower thermospheric molecular oxygen densities has been adopted because it clearly shows the complexity of the behaviour of molecular oxygen. A complexity which highlights the need, already stressed in Chapter 1, for additional data.

This has obviously led to the omission of some experimental determinations of $n(O_2)$ and the reader is referred to the quantitative reviews of von Zahn (1970) and Offerman (1974). The discussion in Chapter 6 introduces further experiments.

The complexity of its behaviour and the inadequate data base has made modelling of $n(O_2)$ difficult. It has been further complicated by the suggestions that there are systematic instrument related differences between profiles determined by mass spectrometers or U V absorption techniques. However, the models and their agreement with experimental measurements is not discussed here but left until Chapter 6 where the present results are considered.

2.4.1 A Comparison of $n(O_2)$ measured by U V Absorption Techniques with $n(O_2)$ measured by Mass Spectroscopy

The, as yet, unresolved controversy about the importance of the recombination of O to O_2 within mass spectrometer ion sources has been discussed in Section 2.2.3. It is considered that if the recombination of O has been important it will manifest itself in a systematic difference between $n(O_2)$ determined by mass spectroscopic techniques and $n(O_2)$ determined by U.V. absorption techniques.

To test this premise a total of 21 published density profiles of O_2 have been selected, one group of 11 using U V absorption

REFERENCE	LAUNCH COORDS \ ALTITUDE (kms)	90	95	100	105	110	115	120	125	130	135	140	145	150	155	160	165	170	COMMENTS
		Mult. by 10^{18}					Mult. by 10^{16}						Mult. by 10^{15}						
Byram *et al*, 1955	32° 24'N 106° 21'W						6.4	2.9	1.6	1.0									Ion chamber pass-band 1425-1500Å.
Jursa *et al*, 1965	as above	7		1		.27		7.8		1		.56		2.8		1.9			Spectrograph. Nos. interpolated from composite profile. Fig 1 of paper.
Hall *et al*, 1965	as above													3.3		2.1		1.2	EUV monochromator. $n(O_2)$ derived from extinction curve of 1206.5Å.
Weeks & Smith, 1968	37° 50'N 75° 29'W		4.6	2.1	.9	.34		2.8		.97		.49		1.8					Lα & SX ion chambers. h ⩽ 110 rocket 14.145 h ⩾ 110 rocket 14.244
Carver *et al*, 1969	30° 56'S 136° 31'E	14	4.8	1.1	.37	.13													Lα & QT ion chambers. Interpolated from Fig 2 of paper.
Wildman *et al*, 1969	as above					.19	6.3	2.3	1.4	.97	.6	.43	3						SX ion chambers. Rocket SL407 inter-polated from Fig. 4 of paper.
Norton & Roble, 1974	N/A	3.7		.72	.14			4.7		1.3		.57		2.7		1.4		.7	Lα, 1225-1350Å and 1450-1600Å ion chambers. Averaged 14 occultations. Solrad 10 satellite.

[continued over page]

REFERENCE	LAUNCH COORDS \ ALTITUDE (kms)	90	95	100	105	110	115	120	125	130	135	140	145	150	155	160	165	170	COMMENTS
		Mult. by 10^{18}					Mult. by 10^{16}						Mult. by 10^{15}						
Ackerman *et al*, 1974	39° 36'W 9° 11'E						9.5	4.3	2.1	1.1	.64	.41	2.7	1.9	1.35	1	.74	.54	UV Monochromator. Looked at 1216Å, 1450Å & 1710Å Rocket - S84.
Weeks, 1975a/b	32° 24'N 106° 21'W	8.9	3.9	1.9								1.6		7		3.2		1.6	Lα & SX ion chambers. Rocket A09.102-1. Magnetically disturbed conditions.
Garriott *et al*, 1977	N/A		4.1	1.6	.5		5	2.9	1.8	1.0	.62	.4	2.6	1.7	1.2	.82			Lα, 1032Å, 1335Å. High resolution spectrophotometer. Skylab.
Higgins & Heroux, 1977	32° 24'N 106° 21'W					.2	12	5.3	2.3	1.2	.67	.45	3.0	2.0	1.5	1			SX ion chamber. Spring launch. Magnetically disturbed conditions.

TABLE 2.1 O_2 number densities determined by UV Absorption techniques ($n(O_2)/m^3$).

REFERENCE	LAUNCH COORDS \ ALTITUDE (kms)	90	95	100	105	110	115	120	125	130	135	140	145	150	155	160	165	170	COMMENT
		Mult. by 10^{18}					Mult. by 10^{16}						Mult. by 10^{15}						
Hedin *et al*, 1964	32° 24'N 106° 21'W				.45	.18	7.7	3.8	2.1	1.2	.75	.49	3.1	2.1	1.4	.9	.62	.44	Analysis considered by authors to be less reliable for h < 120 kms.
Hedin & Nier, 1966	as above							3.9	2.0	1.7	.74	.5	3.5	2.6	1.9	1.4	1.1	.80	O_2 number densities determined from data of semi-open and closed ion source.
Kasprzak *et al*, 1968	as above							4.5	2.5	1.5	.95	.62	4.1	2.9	2.1	1.5	1.1	.85	Instrumentation same as Hedin & Nier 1966. $n(O_2)$ from morning flight.
Mauersberger *et al*, 1968	39° 36'N 9° 26'E						8.5	3.7	2.0	1.1	.93	.46	2.2	1.5	1.1				Considered O_2 loss occurring, loss taken to be 20%
Muller & Hartman, 1969	58° 44'N 93° 49'W					.35	13.	7.0	3.8	2.2	1.4	1.0	7.9	5.7	4.4				Authors consider $n(O_2)$ may be 25% high at 155 kms & 5% high at 120 kms.
Hickman & Nier, 1972	58° 44'N 93° 49'W							6.4	3.3	1.9	1.2	.76	5.1	3.5	2.5	1.8	1.4	1.1	Instrumentation similar to Hedin & Nier 1966. M.S. affected by vibration.

[continued over page]

REFERENCE	LAUNCH COORDS \ ALTITUDE (kms)	90	95	100	105	110	115	120	125	130	135	140	145	150	155	160	165	170	COMMENT
		Mult. by 10^{18}					Mult. by 10^{16}						Mult. by 10^{15}						
Offerman & Grossman, 1973	39° 36'N 9° 26'E							2.7		.96		.38		1.6		.78		.43	Cryo-cooled mass spectrometer.
Ackerman *et al*, 1974	39° 36'N 9° 11'E						9.8	4.9	2.7	1.7	1.0	.69	4.8	3.3	2.4	1.7	1.3		Flown in same payload as U.V. expt. of authors in Table 2.1.
Kayser & Potter, 1978	N/A											1.1	5.3	4.7	2.7	2.5	1.7	1.5	Satellite-A.E.-D Below 165 km - normal mode, 165 km & above fly-through mode.
Trinks *et al*, 1978a	37° 50'N 75° 29'W		4.2	1.5	.32	.06*	2.3	1.6	1.2	.95	.71	.50	3.4	2.4	1.6	1.1	.73	.51	Cryo-cooled M.S. with heatexchanger to dissipate shock wave at lower alts.

* Deduced from smooth curve no expt. measurement.

TABLE 2.2 O_2 number densities determined by mass spectrometer ($n(O_2)/m^3$).

techniques and one group of 10 using mass spectroscopic techniques. The choice was dictated only by a desire to have measurements which spanned the entire period over which $n(O_2)$ had been measured and to have many different research groups, locations and variants of the two techniques represented. Tables 2.1 and 2.2 give the details of the experimental determinations chosen.

It was intended to calculate the mean and standard deviation for each group but several experiments were so atypical it was felt their inclusion would obscure any pattern that might emerge. For this reason the calculations for UV molecular oxygen densities excluded the high altitude results of Weeks (1975b) since even allowing for the magnetically disturbed conditions (see Sections 2.4.2.4 and Chapter 6) the number densities reported by Weeks (1975b) are exceptionally high. In the M.S. group the results of the cryo-genically cooled mass spectrometers (Offerman and Grossman, 1973; Trinks *et al*, 1978a) have not been considered. It is highly unlikely that recombination will occur in cryo-genically cooled ion sources and the significantly lower molecular oxygen densities derived from these instruments appear to support this suggestion. These results are therefore not typical of mass spectrometer measurements of $n(O_2)$ over the years.

The mean and standard deviations calculated from the results of the remaining experiments are tabulated in Tables 2.3 and 2.4 and illustrated graphically in Figure 2.3. If the standard deviation is taken into account there is an overlap between M.S. and UV derived $n(O_2)$. However, it still seems clear that there is a systematic difference between the derived mean profiles. Over the altitude range 125 kms to

ALTITUDE (kms)	MEAN $n(O_2)/m^3$ - UV TECHNIQUES	NO. OF RESULTS IN MEAN	STANDARD DEVIATION	STD. DEV./MEAN
90	8.4×10^{18}	4	4.3×10^{18}	51%
95	4.35×10^{18}	4	4.2×10^{17}	10%
100	1.4×10^{18}	6	5.5×10^{17}	39%
105	5.9×10^{17}	3	2.76×10^{17}	47%
110	2.12×10^{17}	6	8×10^{16}	38%
115	7.84×10^{16}	5	2.85×10^{16}	36%
120	4.13×10^{16}	8	1.83×10^{16}	44%
125	1.84×10^{16}	5	3.6×10^{15}	20%
130	1.07×10^{16}	8	1.2×10^{15}	12%
135	6.35×10^{15}	4	3×10^{14}	5%
140	4.73×10^{15}	7	6.9×10^{14}	15%
145	2.83×10^{15}	4	2.1×10^{14}	7%
150	2.31×10^{15}	7	6.1×10^{14}	27%
155	1.35×10^{15}	3	1.5×10^{14}	11%
160	1.37×10^{15}	6	5.3×10^{14}	39%
165	7.4×10^{14}	1	NOT APPLICABLE	
170	8.13×10^{14}	3	3.4×10^{14}	42%

TABLE 2.3 Mean and standard deviation of $n(O_2)$ as measured by UV Absorption Techniques.

ALTITUDE (kms)	MEAN $n(O_2)/m^3$ MASS. SPECT.	No. OF RESULTS IN MEAN.	STANDARD DEVIATION	STD. DEV./MEAN
90	-			
95	-			
100	-			
105	4.5×10^{17}	1	NOT	APPLICABLE
110	2.65×10^{17}	2	1.2×10^{17}	45%
115	9.75×10^{16}	4	2.33×10^{16}	23%
120	4.89×10^{16}	7	1.32×10^{16}	27%
125	2.63×10^{16}	7	7×10^{15}	27%
130	1.62×10^{16}	7	3.8×10^{15}	24%
135	9.96×10^{15}	7	2.37×10^{15}	24%
140	7.03×10^{15}	8	2.4×10^{15}	34%
145	4.5×10^{15}	8	1.73×10^{15}	39%
150	3.29×10^{15}	8	1.37×10^{15}	42%
155	2.31×10^{15}	8	1×10^{15}	44%
160	1.63×10^{15}	6	5.3×10^{14}	32%
165	1.2×10^{15}	6	3.6×10^{14}	30%
170	9.38×10^{14}	5	3.9×10^{14}	42%

TABLE 2.4 Mean and Standard Deviation of $n(O_2)$ as measured by Mass Spectroscopic Techniques.

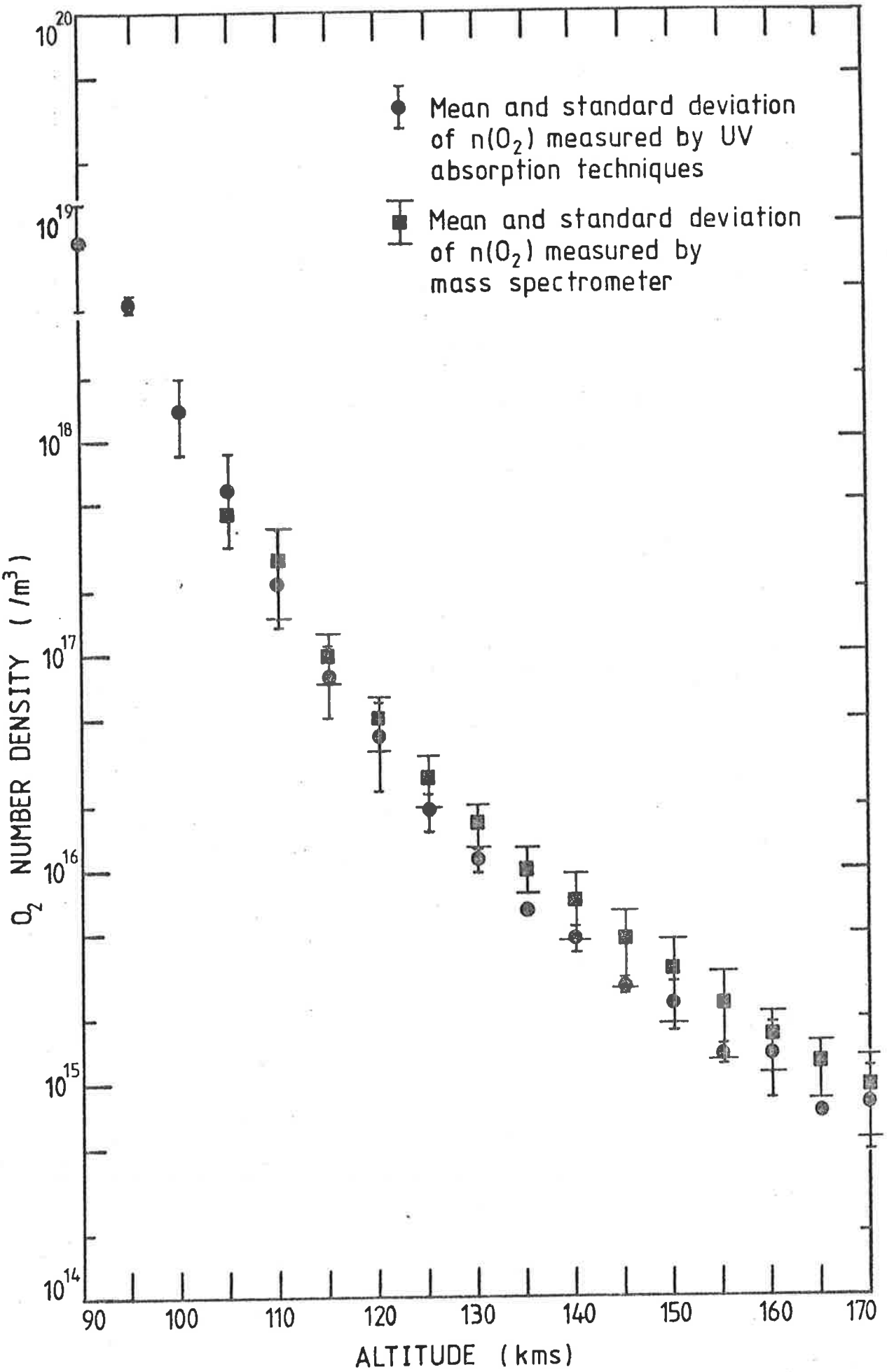

Fig 2.3 Comparison of $n(O_2)$ measured by mass spectrometer and UV absorption techniques.

150 kms the ratio mean mass spectrometer $n(O_2)$/mean U V $n(O_2)$ is 1.5 ± .07. In view of the period of time over which the measurements have been taken - 30 years - the magnitude of the uncertainties associated with each measurement and the genuine variations that occur in $n(O_2)$ the consistency of the ratio is unexpected. If the discrepancy is due to recombination in the mass spectrometer the ratio implies recombination of the order of 15% to 20%. This is not unrealistic when compared with the 10% suggested by Ackerman *et al* 1974 and the 33% suggested by von Zahn & Gross (1969).

Comparison of the mean of the mass spectroscopically determined $n(O_2)$ with the atypical results of the cryo-genically cooled M.S. (Figure 2.4) does not yield such a constant ratio. Instead the ratio, mean mass spectrometer $n(O_2)$/cryo-genically cooled M.S. $n(O_2)$, is as small as 1.32 and as large as 2.19 over this altitude range. However it still supports the premise that recombination occurs in conventional mass spectrometers.

Note that in the following sections the question of recombination is usually not important. Comparisons made in an attempt to identify variations have usually been carried out between results gathered by the same or similar instrumentation, and, for mass spectrometers, although levels of recombination are not expected to be constant (Offerman and Trinks, 1971), they should not vary enough to invalidate any conclusions that might be drawn.

2.4.2. Variation of Lower Thermospheric Molecular Oxygen Densities

Diurnal, geomagnetic, semi-annual, annual, seasonal, latitudinal and solar flux induced variations have been mentioned. The interaction between these variations is complex and separate effects are hard to

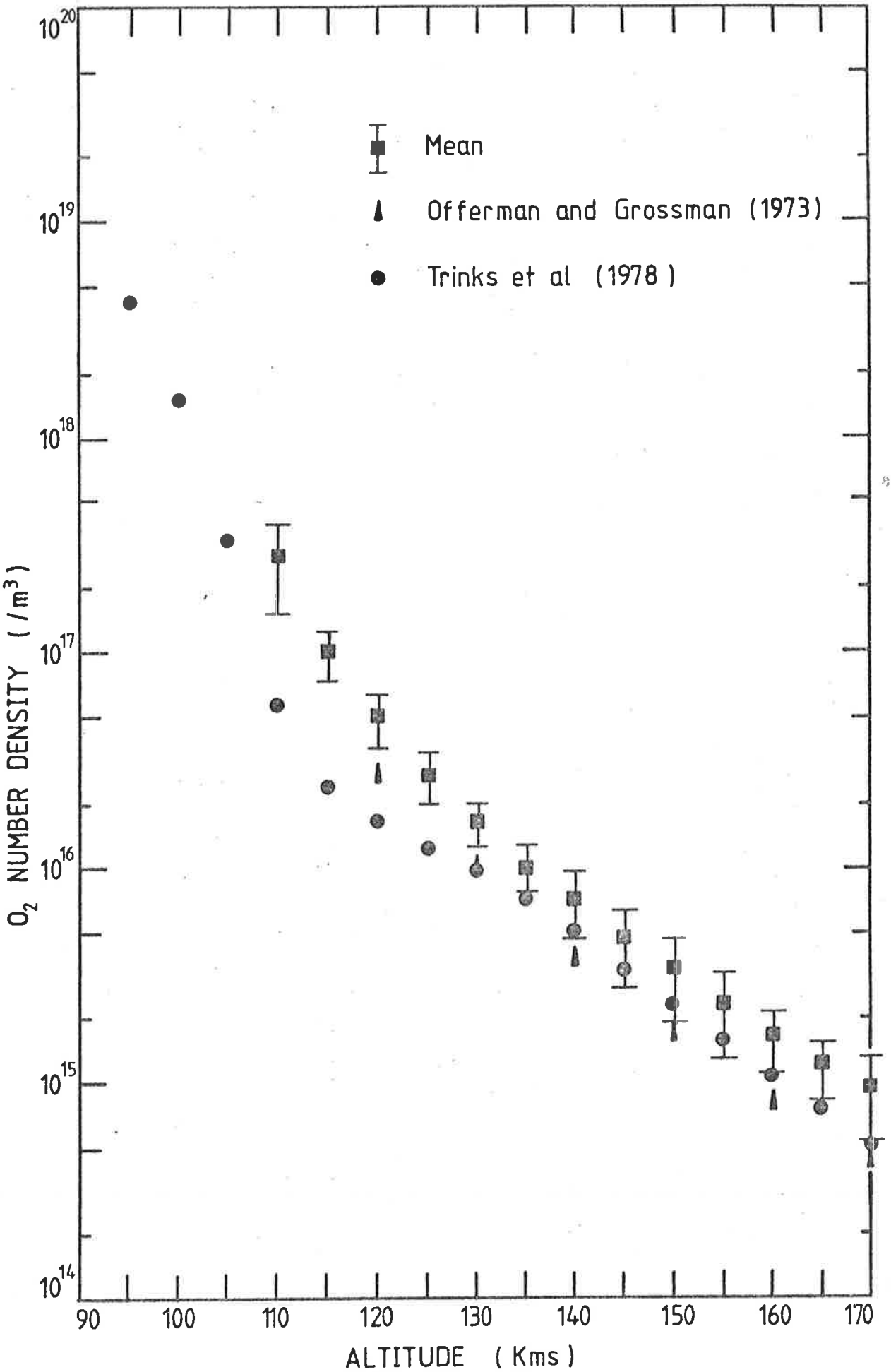

Fig 2.4 Comparison of mean of M.S. $n(O_2)$ (Table 2.3) with $n(O_2)$ measured by cryo-cooled mass spectrometers.

isolate. For example, Jacchia *et al* (1978) points out that a global picture of expected diurnal variations could give a psuedo seasonal-latitudinal effect. The very ambiguity of the notation, annual-latitudinal, seasonal-latitudinal hints at the uncertainty still existing in this field of investigation. An uncertainty heightened by the effect solar activity appears to have on the amplitudes of many of the listed variations (Oran and Strobel, 1976; Mayr *et al*, 1976; Norton and Roble, 1977; Mayr and Volland, 1971).

In the following, diurnal, seasonal and geomagnetic effects are discussed separately. Annual, semi-annual and latitudinal are considered together. Under the heading, Solar Flux Variations (Section 2.4.2.5) not only is direct experimental evidence for a solar flux - $n(O_2)$ link discussed but attention is given to the likely effect of solar activity on the variations considered in the sections prior to 2.4.2.5.

The subsections follow the given listing.

(1) Seasonal

(2) Diurnal

(3) Magnetic

(4) Semi-annual, Annual, Latitudinal

(5) Solar flux

2.4.2.1 Seasonal Variations

The first experimental evidence for seasonal variation in $n(O_2)$ was the spring/summer density ratio of 1.8 obtained by Kupperian *et al* (1959). Later, Norton and Warnock (1968) interpreted the differences between the summer and winter occultations measured by their satellite-borne Lα chambers as implying summer $n(O_2)$ were approximately 50% higher than winter $n(O_2)$. Roble and Norton (1972) claimed an even larger

summer enhancement. Their results indicated a summer/winter ratio of molecular oxygen densities of approximately 3:1.

All the above results were derived from Lα chambers and the effects were observed at heights ranging from 70 kms to 120 kms. Alcayde *et al* (1974) on the other hand, using incoherent backscatter methods, saw an apparent summer/winter ratio of 6:1 at 200 kms.

The spring/summer enhancements and the summer/winter enhancements were,however, not the only seasonal effects seen. Felske *et al* (1972) reported a spring/autumn ratio of approximately 2 at Lα chamber heights. The authors themselves refer to it as a winter/summer enhancement but since the results were taken in October, the spring/autumn label appears to be more appropriate. Winter/summer enhancements have, however, been reported elsewhere (Mayr *et al*, 1976).

These results differ sharply from the conclusions drawn by Offerman (1974). Reviewing lower thermospheric measurements of atmospheric constituents, including molecular oxygen, he considered that while the data might possibly suggest a seasonal effect at 200 kms it was very small. In addition, he felt the data did not support a seasonal variation at 150 kms and the small apparent summer minimum could be a fortuitous effect of the available data set rather than a genuine atmospheric phenomenon.

Other authors (Oppenheimer *et al*, 1976; Nier *et al*, 1976) have been in essential agreement with Offerman (1974) and have offered alternative explanations for the "seasonal effects" reported. Nier *et al* (1976) suggested increased magnetic activity (see Section 2.4.2.3) at the time of the summer measurements of Roble and Norton (1972) could explain their results. Oppenheimer *et al* (1976) suggested latitudinal

effects (Section 2.4.2.4). This latter explanation was dismissed by Norton and Roble (1977) and indeed the data of Garriott *et al* (1977) would imply little or no latitudinal variations at $L\alpha$ heights.

If separate groups are made of those experimenters for, and those against, seasonal variation in molecular oxygen densities, an extra fact emerges. Measurements supporting seasonal variation (Felske *et al*, 1972; Roble and Norton, 1972; Alcayde *et al*, 1974) were taken at solar maximum whereas those not supporting seasonal variation (Oppenheimer *et al*, 1976; Kayser and Potter, 1976; Schaeffer and Noxon, 1975) were taken at solar minimum. Norton and Roble (1977) included other experimenters in these groups, Noxon and Johanson (1972) in the former and Mayr *et al* (1976) in the latter. However, the reported seasonal effects of Noxon and Johanson (1972) are now attributed to differing levels of magnetic activity (Schaeffer and Noxon, 1975) and Mayr *et al* (1976) did in fact support seasonal variation as has already been mentioned. They only differed in the phase of the enhancement.

It is obvious that no firm conclusion can be drawn about the existence or otherwise of a seasonal dependence in lower thermospheric molecular oxygen. The possible influence of solar flux levels, which is suggested by the above results, leads to consideration of this effect in Section 2.4.2.5.

2.4.2.2 Diurnal Variations

Diurnal Variations in the concentration of $n(O_2)$ have been reported by Weeks and Smith (1968), Parker and Stewart (1972), Mayr *et al* (1976), Garriott *et al* (1977) and Hinteregger and Chaikin (1977). Other experimenters, (Hall *et al*, 1967; Kasprzak *et al*, 1968) while seeing a

difference between morning and afternoon data found that either it was smaller than the day-to-day differences observed or it could not be regarded as significant in view of the possible errors associated with the measurements. Norton and Roble (1977), claimed to have observed little or no diurnal variation in their satellite experiment (Roble and Norton, 1972).

The diurnal variations reported have not been consistent. A sunrise/sunset density ratio greater than 1 was observed by both Hinteregger and Chaikin (1977) and Parker and Stewart (1972). In contrast Garriott *et al* (1977) found sunset densities to be greater than sunrise densities. Although the rocket-borne experiments of Weeks and Smith (1968) did not observe sunset their results suggested daytime molecular oxygen densities would be greater than sunrise densities and the data from the rocket-borne experiments of Ilyas (1976) implied afternoon enhancements in $n(O_2)$.

These results may simply reflect the complexity of the response of the lower thermosphere. All those results mentioned as showing enhanced sunset or daytime densities were at approximately 90 kms to 120 kms, whereas the sunrise enhancements were seen at 150 kms and 180 kms. Further results of Garriott *et al* (1977) are consistent with the concept of going from a sunset to a sunrise enhancement as the altitude increases. Using the absorption of the U V lines at 1032Å and 1335Å to obtain oxygen densities in the altitude region $\approx$ 130 kms to 140 kms, they found no statistically significant difference between sunset and sunrise.

Unfortunately this consistency is destroyed by the results of Mayr *et al* (1976) who observed a density minimum in $n(O_2)$ at 120 kms at 1800 hrs local time.

As with seasonal variations there is evidence to suggest that the diurnal response of the atmosphere will differ with differing solar activity. The measurements of Roble and Norton (1972) were taken near solar maximum whereas the diurnal variations reported by Mayr *et al* (1976), Hinteregger and Chaikin (1977), Garriott *et al* (1977) and Weeks and Smith (1968) were in measurements taken at low levels of solar activity. No definite conclusions can be drawn however, since once again not all the results fit into the pattern. Parker and Stewart (1972) observed a sunrise/sunset difference in $n(O_2)$ during May to November of 1967, i.e. close to solar max.

2.4.2.3 Magnetic Variations

As with seasonal and diurnal variations there is experimental evidence for and against magnetically induced enhancements of lower thermospheric molecular oxygen. However, most of the evidence favours a magnetically induced enhancement of the density. This has been reported by Oppenheimer *et al* (1976), Weeks (1975b), Nier *et al* (1976), Garriott *et al* (1977) and Potter *et al* (1979).

The commonly used parameter to indicate the strength of the disturbance is the K_p index. The correlation considered is not that between the measured density and the K_p at the time of the measurement. Better correlation has been found between the density and the K_p index 6 to 7 hrs before the launch, (Jacchia, 1971). This agrees with the work of Hays *et al* (1969) who found that the exospheric temperature took around 3 hrs to respond to a magnetic storm and then it takes several hours for the high altitude heating to propagate down.

There was however, evidence that was contra-indicative of magnetic enhancement. Even allowing for the time lag, Parker and Stewart

(1972) found that the correlation between the index of magnetic activity and $n(O_2)$ was very poor for measurements within the latitudes - 30°S to 30°N. In fact they did not find much evidence for magnetic variation at all in this region.

Their conclusion is supported by the results of Higgins and Heroux (1977) who did not observe any significant changes in the data from two rockets launched at differing K_p's from The White Sands Missile Range (32°N) in 1973/1974. On the other hand, Weeks (1975b) reported a very large enhancement in densities measured above White Sands in April 1973. However, the enhancement was in comparison with results from a rocket launched at Wallops Island (38°N) in October 1971, and the possibility exists that seasonal, diurnal (1971-afternoon flight, 1973-morning flight) and even latitudinal influences affected the results.

The effect of magnetic activity on lower thermospheric molecular oxygen densities is considered again in Chapter 6. The discussion is more quantitative as an opportunity to investigate the effect was afforded by the fortuitous timing of the rockets launched during the present research.

2.4.2.4. Semi-Annual, Annual, Latitudinal Variations

The semi-annual effect is driven by the semi-annual migration of the Sun and by a second high latitude source, associated with magnetic storms, (Mayr and Volland, 1971). No direct measurements for $n(O_2)$ have been made but semi-annual variations in the $n(O)/n(O_2)$ ratio have been observed by Mayr and Mahajan (1971) at 120 kms and by Katyushina and Ivanov-Kholodny (1971) at 130 kms. More recently, Mahajan (1977) compiled all the data available on neutral composition at 120 kms and confirmed the existence of this variation.

It is considered unlikely that such variations would be generated solely by changing n(O) levels and therefore the results also indicate a semi-annual variation in $n(O_2)$ but this is yet to be confirmed by direct measurement. More data is required.

Mayr *et al* (1976) used the two terms Annual and Latitudinal synonymously. If these two terms are considered equivalent then the latitudinal variations in $n(O_2)$ observed by Garriott *et al* (1977) at approximately 130 kms and 140 kms, the latitudinal variation in the effect on $n(O_2)$ of magnetic storms (Parker and Stewart, 1972), and the increase with latitude of $n(O_2)$ observed by Mayr *et al* (1976) in the winter hemisphere may all be manifestations of the annual effect. The results of Garriott *et al* (1977) point to an altitude variation in the annual effect since no appreciable latitudinal variation is seen at 100 kms.

The terms Annual and Seasonal variations have also been used interchangeably (Hedin *et al* 1977b) but Barlier *et al* (1974) claim that the annual variation, arising in part from the sun earth distance, is a separate phenomenon, distinct from seasonal variations. Garriott *et al* (1977) appear to agree with the distinction.

Barlier *et al* (1974) consider asymmetry in the northern and southern hemisphere seasonal responses could be the result of the annual effect and it is possible that the seasonal effects already discussed (Section 2.4.2.2) have been modified by an annual effect. However, as pointed out by Garriott *et al* (1977) being able to distinguish between seasonal and latitudinal variations relies on a data base which has extensive spatial and temporal coverage. This is yet to be achieved for $n(O_2)$.

2.4.2.5 Solar Flux Variation of $n(O_2)$

If the data from the rocket based experiments summarized by Offerman (1974) is combined with that from The Atmospheric Explorer Satellites, there is some evidence to suggest an inverse relationship between low altitude O_2 densities and the solar flux as represented by $F_{10.7}$ (Kayser, 1980). While this suggested solar flux-density correlation contrasts with the conclusion drawn by Offerman (1974), and there is some question as to the validity of using direct $F_{10.7}$ measurements as an indicator of the amount of EUV and UV flux incident on the earth's atmosphere (Rawer *et al*, 1979; Schmidtke, 1979; Hinteregger, 1977), the suggestion that $n(O_2)$ decreases with increasing EUV and UV radiation is entirely consistent with the work of Oran and Strobel (1976). They postulated that both direct dissociation by radiation within the Schumann-Runge continuum and indirect dissociation from the absorption of EUV and the photochemistry of N_2 would significantly affect the molecular oxygen concentration in the lower thermosphere. Increased flux levels would be expected to enhance both processes thereby leading to decreased concentrations of molecular oxygen.

However, changes in the solar flux not only affect the photochemistry of the lower thermosphere, they also change the circulatory systems of this region. Enhanced EUV flux will increase the vertical velocity of the wind systems and since these will induce diffusion (Mayr and Volland, 1972), this will also influence $n(O_2)$. Reber and Hays (1973) have shown that the density of atmospheric constituents heavier

than the mean mass will be enhanced by an upward wind and an upward wind would be expected in the summer hemisphere (Mayr and Volland, 1971; Johnson and Gottlieb, 1970).

Therefore conflicting processes arise. Increased E U V and U V flux levels, but particularly U V flux levels will decrease $n(O_2)$ through photochemistry but increased E U V will enhance $n(O_2)$ through increased transport velocities. Not only that, but increased flux levels, by raising the temperature of the atmosphere, will cause expansion of the atmosphere, and this will lead to enhanced $n(O_2)$ (Kayser, 1980). The enhancement of $n(O_2)$ by thermal expansion is however, not generally important at lower thermospheric heights (Mayr and Harris, 1977c).

Although solar flux levels appear to have a direct effect on $n(O_2)$, of more interest is their apparent influence on the other variations previously considered in Sections 2.4.2.1 to 2.4.2.4.

Referring back to seasonal effects, studies (Hinteregger, 1976; 1979; Heath, 1973) have shown that while E U V flux levels fluctuate strongly with solar activity U V flux levels have varied very little - 10% - 15%. Therefore at low levels of solar activity it may be that dissociative losses are more important and a minimum could be expected in the summer hemisphere, but at high levels of solar activity the relatively larger enhancement in solar EUV flux may lead to a domination of transport effects (Mayr *et al*, 1976). This would lead to an enhancement in the summer hemisphere which is consistent with results such as those of Roble and Norton (1972). The summer enhancement at 200 kms (Alcayde *et al*, 1974) could possibly be explained as the result of thermal expansion. The lack of either summer or winter enhancement of any significance may be the result of a rough balancing of these two processes.

Mayr and Harris (1977a) have produced a theoretical model which can be made to reproduce the diurnal variations observed in the data of the AE-C satellite (Mayr *et al*, 1976). This model showed that while wind induced diffusion was the dominating influence in the diurnal variation of lower thermospheric molecular oxygen densities, the dissociation of O_2 and the photoionization of O_2 were also significant.

It would appear reasonable therefore, to expect the differing relative flux levels that occur at differing levels of solar activity to result in differing diurnal effects. As already pointed out in Section 2.4.2.2. with the exception of the work of Parker and Stewart (1972) a pattern has emerged with diurnal variations being more important during periods of low solar activity.

Magnetic storms result from solar activity but there is no evidence to suggest that the atmospheric response or more specifically the molecular oxygen response exhibits a solar cycle dependence.

Annual and semi-annual effects in $n(O_2)$ do not appear to be influenced by solar activity, (Mayr & Harris, 1977b; Mahajan, 1977).

2.5 SUMMARY

This Chapter has attempted to review thirty years of measurements of lower thermospheric molecular oxygen densities. In the first three major sections the emphasis in the discussion centred on the consideration of the different methods that have been used to measure $n(O_2)$; the problems encountered and the solutions, if any, devised. Solutions ranged from instrumental adaptation to an increase in the sophistication of the data analysis. Each type of instrument had its own problems and no optimal experiment can be nominated.

Section 2.4 looked at the variations seen in the molecular oxygen densities. For any one variation the evidence is often contradictory. Overall, however, it suggests that there are, as yet, unresolved complex interactions between the named effects rather than denying the existence of any of the effects. The discussion in 2.4 supports the veracity of the statements made by Carignan (1975) and Hedin (1979) about the lack of understanding of the behaviour of molecular oxygen and of the inter-relation between the sets of data.

CHAPTER THREE

THE CHOICE, CONSTRUCTION AND CALIBRATION OF THE INSTRUMENTATION TO MEASURE $n(O_2)$.

In the present work U V absorption spectrophotometry was used to determine lower thermospheric molecular oxygen densities. Section 3.1 discusses the rationale behind this choice. Two categories of broad band U V detectors were used to measure the radiation extinction curves from which $n(O_2)$ was calculated. Section 3.1 also discusses the choice of instrumentation. Each category of detector is then discussed in turn, in Sections 3.2 and 3.3.

3.1 CHOICE OF TECHNIQUE AND INSTRUMENTATION

It was concluded in Chapter 2 that there was no optimal technique for measuring lower thermospheric molecular oxygen. However, other factors, apart from the intrinsic advantages and disadvantages, can influence the choice of technique and instrumentation.

The present work was part of a continuing programme of research which had been carried out using U V absorption spectrophotometry (Carver *et al*, 1964, 1966; Lockey *et al*, 1969; Lockey, 1972; Ilyas, 1976) and thus a well equipped calibration laboratory was available. In addition there was a continuing laboratory based research program, capable of providing the necessary absorption cross sections, being carried out at Adelaide University (Blake *et al*, 1966; Carver *et al*, 1977a; Rogers, 1979). These two factors, together with the desire to keep any systematic differences between the various experimental results to a minimum, led to the

continued use of UV absorption spectrophotometry.

In the continuing research program ion chambers (I.C's) had been used because they were small, as was their supporting electronics package, rugged, and they had a broad angular response. This made them ideal for the small spin stabilized sounding rockets mainly used in the program. In these vehicles space was limited, launch accelerations were severe and unfavourable coning could imply large aspect angles. Not all the properties listed above were necessary for a detector in an attitude controlled vehicle - the broad angular response, for example, became superfluous. However, because the space available on the rockets for the $n(O_2)$ experiment was small (Chapter 5) the overall compactness of the ion chambers and their supporting electronics provided a strong argument for their continued use.

The ion chambers also had the capability to take full advantage of the fact that the rocket was attitude controlled. While the attitude control unit was operational they would be able to monitor continually the intensity of the solar radiation within their passband, thereby providing high altitude resolution data (see extinction curves, Chapter 5).

Because the current research was part of a continuing program the use of ion chambers had another advantage. It would enable a comparison to be made between the high altitude results gained in the present work and the previous low altitude results (Carver *et al*, 1964; Ilyas, 1976) without the need to consider systematic errors that could be introduced by different instrumentation.

Ion chambers can be constructed with many different passbands. Weeks and Smith (1968) and Carver (1969) list some of these. Several different types were used in the present work and these are listed in Section 3.2.1. Two of them, code named MEB, LEB and LEC (see 3.2.1

for explanation of code) were used in the water vapour experiment and were chosen because of the overlap in their passbands. Choice of the others was dictated by the desire to measure $n(O_2)$ throughout the lower thermosphere. The discussion in Chapter 2 has already indicated that Lα, QT and SX chambers would provide such coverage. These types of ion chambers were therefore chosen.

Mention was made in Chapter 2 of the apparent change in sensitivity of SX chambers during flight. This had been noted by Weeks and Smith (1968) and Wildman *et al* (1969). To investigate whether these effects were instrumental, or in fact actually reflected real changes in solar intensity, a second broad band UV detector was developed. The criterion for the design was the requirement that the passband of an SX ion chamber (λλ1425Å - 1490Å) must be simulated while using a completely different method of detection. This detector is discussed in Section 3.3.

3.2 ION CHAMBERS

3.2.1 Introduction

Ion chambers are non-dispersive, spectrally selective detectors with a passband defined by the transmission cut-off of the window material and the ionization potential of the filling gas. Detectors of this type were first made by Friedman *et al* (1958). The chamber bodies can be made of copper, (Friedman *et al*, 1958) internally plated ceramic, (Stober, 1962) or glass (Lockey, 1972). The bodies of the ion chambers built for the present work were made of copper tubing (Section 3.2.2). This material provided both ease of construction and a rugged finished product.

Ion chambers with 7 different passbands were constructed. They were used either in determining lower thermospheric molecular

oxygen concentrations or in the water vapour experiment (Chapter 8). The 7 are listed in Table 3.1.

TABLE 3.1 ION CHAMBERS

Code	Window Material	Filling gas
LNO	Lithium Fluoride (LiF)	Nitric Oxide (NO)
LEB	Lithium Fluoride	Ethyl Bromide (C_2H_5Br)
LEC	Lithium Fluoride	Ethyl Chloride ($C_2H_5C\ell$)
MNO	Magnesium Fluoride (MgF_2)	Nitric Oxide
MEB	Magnesium Fluoride	Ethyl Bromide (C_2H_5Br)
QT	Quartz	Triethylamine ($C_6H_{15}N$)
SX	Sapphire	p-Xylene (C_8H_{10})

The letters in the left hand column provide a code by which the chambers are identified. MNO and LNO chambers were collectively referred to as $L\alpha$ chambers in Chapter 2 but their distinct codes are used in the following sections.

Construction details which were similar for all the ion chambers are described in Section 3.2.2. The window materials are discussed in 3.2.3 while the preparation of the gas and the filling procedure are described in Sections 3.2.4 and 3.2.5 respectively.

Section 3.2.6 details calibration procedures. Topics covered are spectral response and absolute quantum efficienty. For the water vapour experiment (Chapter 8) the chambers were flown on spin stabilized sounding rockets. While, for this experiment it was not essential to know the angular response, knowledge of this parameter ensured maximum information retrieval. Their response was deduced from their flight

behaviour. The method is discussed in Section 3.2.7.

On some rockets, payloads may suffer severe heating and the likely effect of this heating on the performance of the detectors is considered in Section 3.2.8. The performance of the detectors may also be affected by photoelectric emission at the walls. The likelihood of photoelectric emission occurring is discussed in Section 3.2.9.

A requirement for all the ion chambers was long term stability (of the order of months) with respect to their sensitivity. Final integration of the payload, pre-launch testing and weather controlled launch windows can mean there are several weeks between the final laboratory calibrations and the launch. During these last few weeks, testing, and replacement of the ion chambers are not always possible. In the present work it was necessary to assume that the detector sensitivities would still be high enough at launch to provide good signal strength during the flight. Confidence in this assumption only seemed possible if randomly selected chambers in the less varied environment of a laboratory displayed a stability far in excess of requirements.

A study on the stability of the detectors was carried out and the results of this research are discussed in 3.2.10.

3.2.2 Construction of Body Shell

Two types of copper backed chambers were flown. Both chambers are modified versions of the original chambers of Carver and Mitchell (1964). They are referred to as type I and type II and are illustrated schematically in Figures 3.1 and 3.2.

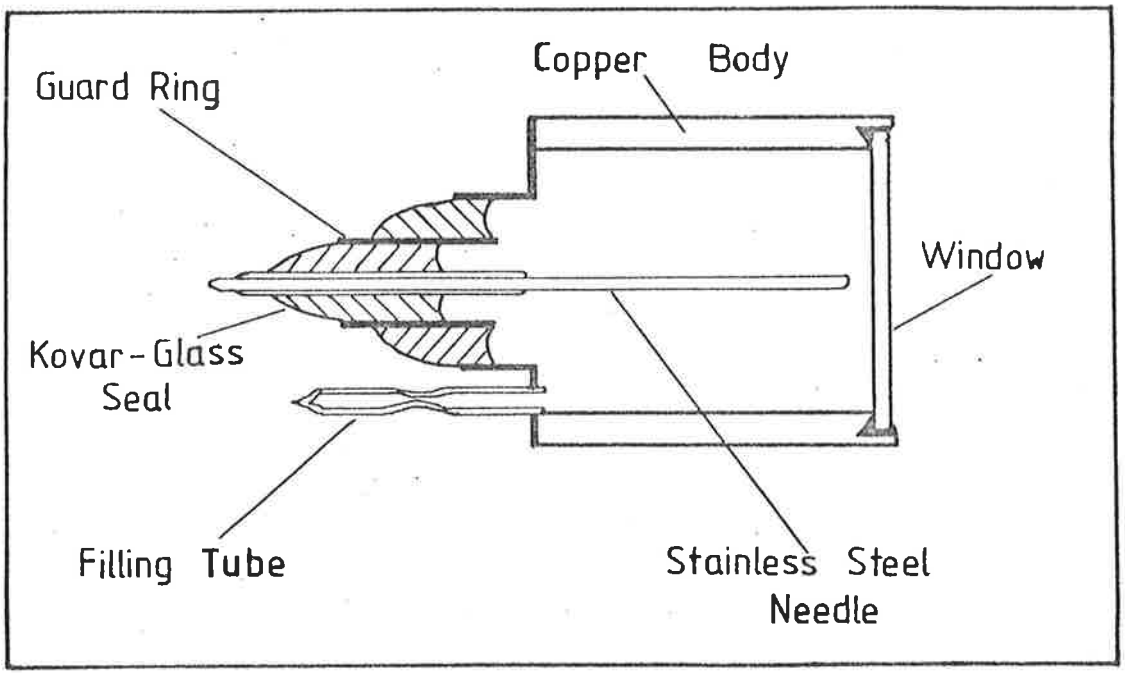

Fig 3.1 Schematic of Type I Ion Chamber - developed by Lockey (1972).

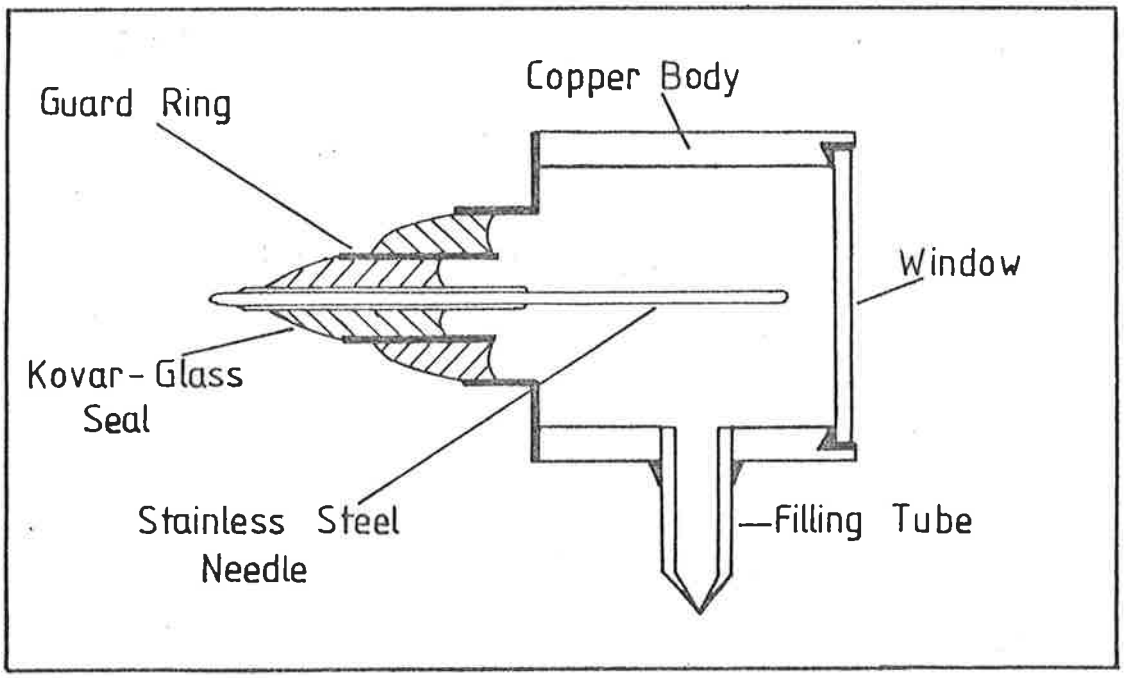

Fig 3.2 Schematic of Type II Ion Chamber - developed during present research.

The earlier chamber (Figure 3.1) was developed by Lockey (1972). A 2.5 cm length of copper tubing with an internal diameter of 2.1 cms and a wall thickness of .24 cms was used for the body of the chamber. Electrical connections were made through a Kovar glass to metal seal. This seal also supported a stainless steel cathode. The tip of the cathode was hard soldered and polished to provide a smooth hemispherical surface. The other end was then soft soldered into the seal. A length of annealed copper tubing (approx. 2.5 cms long) of i.d. 1.3 mm was soldered on to the metal flange of the seal at the same time. This was the chassis of the ion chamber.

The chamber chassis were then cleaned thoroughly. They were dipped into nitric acid, washed three times in an ultrasonic bath of distilled water and rinsed in acetone. After being cleaned the chassis were baked for several hours at approximately 90° C. This was well in excess of the temperatures they would be expected to experience during calibration and flight,and it was considered the baking would prevent further desorption of water vapour during normal use. The windows were also baked before being attached to the chamber with an epoxy resin (Araldite AV 100). To enable the chambers to be attached to the filling system (Figures 3.4, 3.5; Section 3.2.5) a glass tube was attached with epoxy resin to the annealed 1.3 mm i.d. copper tubing.

The second type of ion chamber flown (Figure 3.2) differed in two ways from the detectors of Lockey (1972). The first change arose from the need to fit two rows of chambers, diametrically opposite each other, in a small sounding rocket (see Figure 8.2). Since the necessary modification, shortening the body length by 3 mm did not affect the performance of the detectors, the shorter length was adopted as the standard specification.

Studies carried out by G. Bibbo (private communication) on the pumping speeds of small internal diameter tubes stimulated the second change. The chambers were evacuated before being filled with the desired gas (Section 3.2.5). G. Bibbo's results indicated that satisfactory evacuation of the chamber would not be obtained with the 1.3 mm tube normally used . The pressure inside the chamber was probably as high as 10^{-3} Torr even though the system pressure was 10^{-5} Torr.

The diameter of the annealed copper tube was increased to 3 mm. Since the conductance of a round pipe is proportional to the fourth power of the diameter the pressure differential along the pipe was expected to decrease by a factor of $(3/1.3)^4$ (≈ 28). This implied a chamber pressure well below 10^{-4} Torr if the system had been pumped down to a pressure of 10^{-5} Torr.

The 3 mm tube proved adequate. The long term stability of the chambers was greatly improved (Section 3.2.10). Because of its size the new filling tube had to be located on the side of the ion chamber. The positioning was not critical.

3.2.3 Window Materials.

The transmission limits of the window materials used are listed in Table 3.2. The transmission limit represents the shortest wavelength light transmitted by the window. It defines the short wavelength side of the passband. The numbers given in Table 3.2 are the mean of the values obtained for windows used in the flight chambers.

The lithium fluoride windows were unpolished cleaved crystals, while the sapphire, quartz and magnesium fluoride (MgF_2) were polished

TABLE 3.2 TRANSMISSION LIMITS OF WINDOW MATERIAL

Material	Transmission Limit (angstroms)
Lithium Fluoride	1040
Magnesium Fluoride	1129
Sapphire	1423
Quartz	1563

plates. The quartz was a synthetic fused variety known as Spectosil A.

Cleaved Lithium Fluoride (LiF) crystals have been widely used as the windows in constructing chambers to measure Lα (i.e. LNO chambers). (Byram *et al*, 1956; 1958; Kupperian *et al*, 1959; Carver *et al*, 1964, 1966; Weeks and Smith, 1968). Lithium Fluoride however, has a low but significant hygroscopic quality and this has a detrimental effect on both the stability and sensitivity of the ion chamber.

The sensitivity of an ion chamber depends upon the transmission of the window and the photoelectric yield of the filling gas. Patterson and Vaughan (1963) and Davis (1966) both showed that serious deterioration can be expected in the transmission of a LiF window as the window ages. Decreases in the transmission at Lα of up to 57% were observed (Davis, 1966). Patterson and Vaughan (1963) considered several mechanisms for the deterioration but finally concluded that the crystal was reacting with water vapour to form an absorbing surface film.

Davis (1966) found it was possible to remove the film and restore the transmission by ultrasonically cleaning the window in a bath

of absolute ethyl alcohol. This is not a practical solution for a fully constructed chamber because it was highly probable that the window seal (made with Araldite AV 100) would deteriorate under the combined action of the ultrasonic and the solvent. Fortunately in the present work absolute calibration was not necessary and deterioration in the transmission, while not desirable, could be tolerated as long as the overall chamber sensitivity remained high enough to provide good signal strength and the transmission could be considered as constant throughout the flight ($\leqslant$ 10 mins). There was nothing in the work of either Patterson and Vaughan (1963) or Davis (1966) to suggest that the assumption of short term stability with respect to window transmission would be invalid. In fact for the windows tested by Patterson and Vaughan (1963) the transmission appeared to drop to approximately 85% of the initial transmission within 10 days and then almost stabilize for the rest of their testing period. (30 days).

A more serious result of the solubility of LiF is the apparent diffusion of water vapour through the window into the chamber. Water vapour contamination led to continually reducing sensitivities. In a few cases the chambers stabilized at low sensitivities ($\approx$ 5%-7%), but in most cases the sensitivities of the chambers deteriorated until they no longer responded to irradiation.

The unreliability of these chambers led to the introduction of Magnesium Fluoride (MgF_2) windows (Masuoka and Oshio, 1974). MgF_2 is far less soluble in water. It is therefore less likely that a surface film of the type suggested for LiF would build up on an MgF_2 window. Masuoka and Oshio (1974) found that even if the MgF_2 window was dipped in water the transmission was unimpaired. They conducted the same test with an LiF window and the transmission was immediately reduced by 40%.

Water vapour did not appear to diffuse through a MgF_2 window and contaminate the filling gas. Experience showed that MgF_2 windowed chambers (MNO's) did remain more stable than those with LiF windows (Section 3.2.10).

3.2.4 The Filling Gases and their Preparation.

The ionization potential of the filling gas determines the long wavelength limit of the passband of the ion chambers. Table 3.3 shows typical cut-off points for each gas. These were obtained by averaging the response limits determined in the laboratory for several ion chambers of each type. They are expressed in terms of the equivalent wavelengths. The values obtained by Watanabe *et al* (1962) are included for comparison.

TABLE 3.3 IONIZATION POTENTIALS OF FILLING GAS.
(expressed as the equivalent wavelength)

Filling Gas	Typical Threshold (Angstroms)	Watanabe *et al* (1962) (Angstroms)
Nitric Oxide	1370	1341
Ethyl Bromide	1210	1205
Ethyl Chloride	1140	1129
P-Xylene	1489	1468
Triethylamine	1646	1654

No preparation was carried out for Ethyl Bromide, Ethyl Chloride, p-Xylene or Triethylamine. For all these compounds, which are liquids at standard temperature and pressure, the purity of A.R.

grade reagents was considered adequate. However, for nitric oxide (NO) which was also purchased commercially, removal of contaminants - mainly water vapour - was essential.

The purification system, schematically represented in Figure 3.3, contained no metal parts which might react with nitric oxide. To remove residual water vapour the all glass apparatus was simultaneously heated and evacuated for over an hour before it was used. In operation nitric oxide was passed from the source through the U tubes and into the reservoir. The purification system was then isolated and the reservoir used to fill several storage flasks. These flasks were fitted with cold finger tubes and breaker seals.

Because the main contaminant was water vapour, one tube contained silica gel, the other crushed glass (to increase the surface area on to which the water vapour could condense) and both were cooled to - 80° C.. The cooling was achieved by immersing the U tubes in a slush mixture made with equal parts of Chloroform and Carbon Tetrachloride semi-frozen by the addition of liquid air.

The cold finger tube of the storage flask allowed further purification before the NO was used. To remove any contaminants that may have outgassed from the walls of the flask during storage the flask was gently warmed while the cold finger tube was immersed in a slush mixture (approximately - 80° C). This concentrated any condensible contaminants in the cold finger tube which was then removed by flame seal off.

3.2.5 The Filling Procedure.

Figure 3.4 is a schematic of the equipment used to fill the LNO and the MNO ion chambers with nitric oxide. Figure 3.5 is a schematic of the equipment used to fill the LEC, LEB, SX and QT ion chambers.

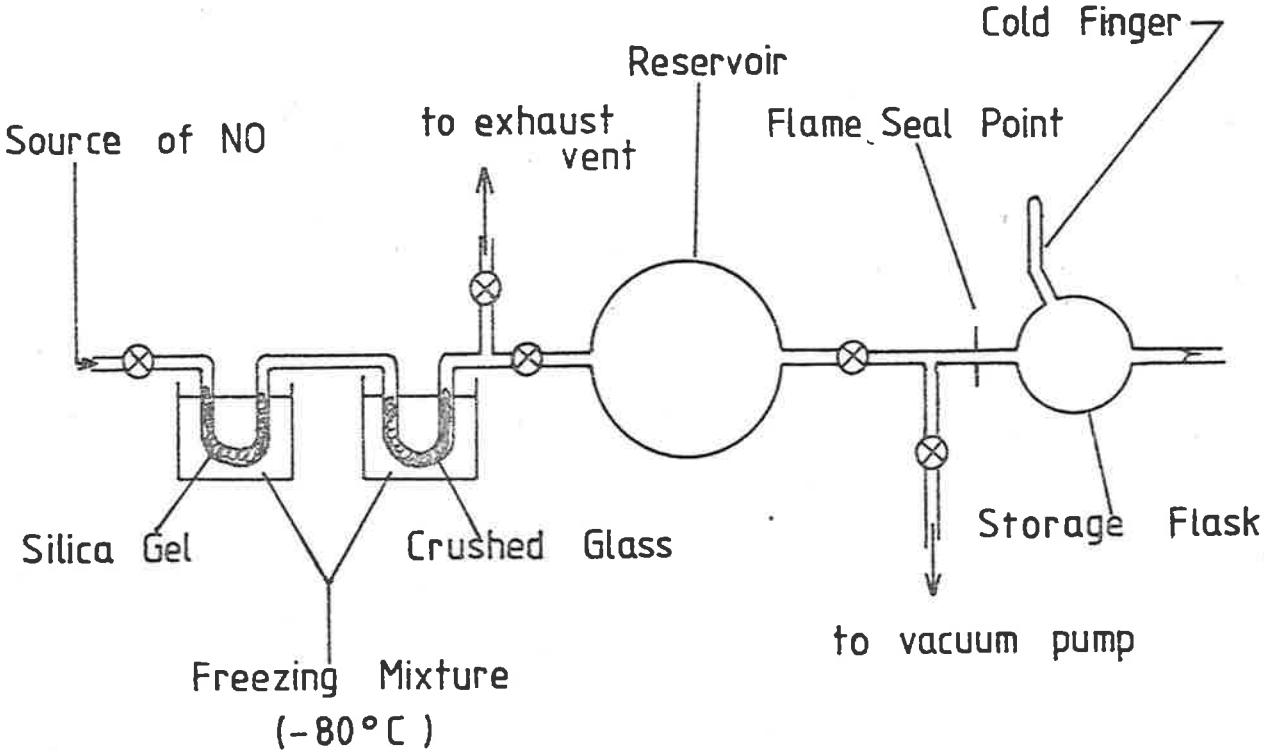

Fig 3.3 Gas Purification System (Nitric Oxide)

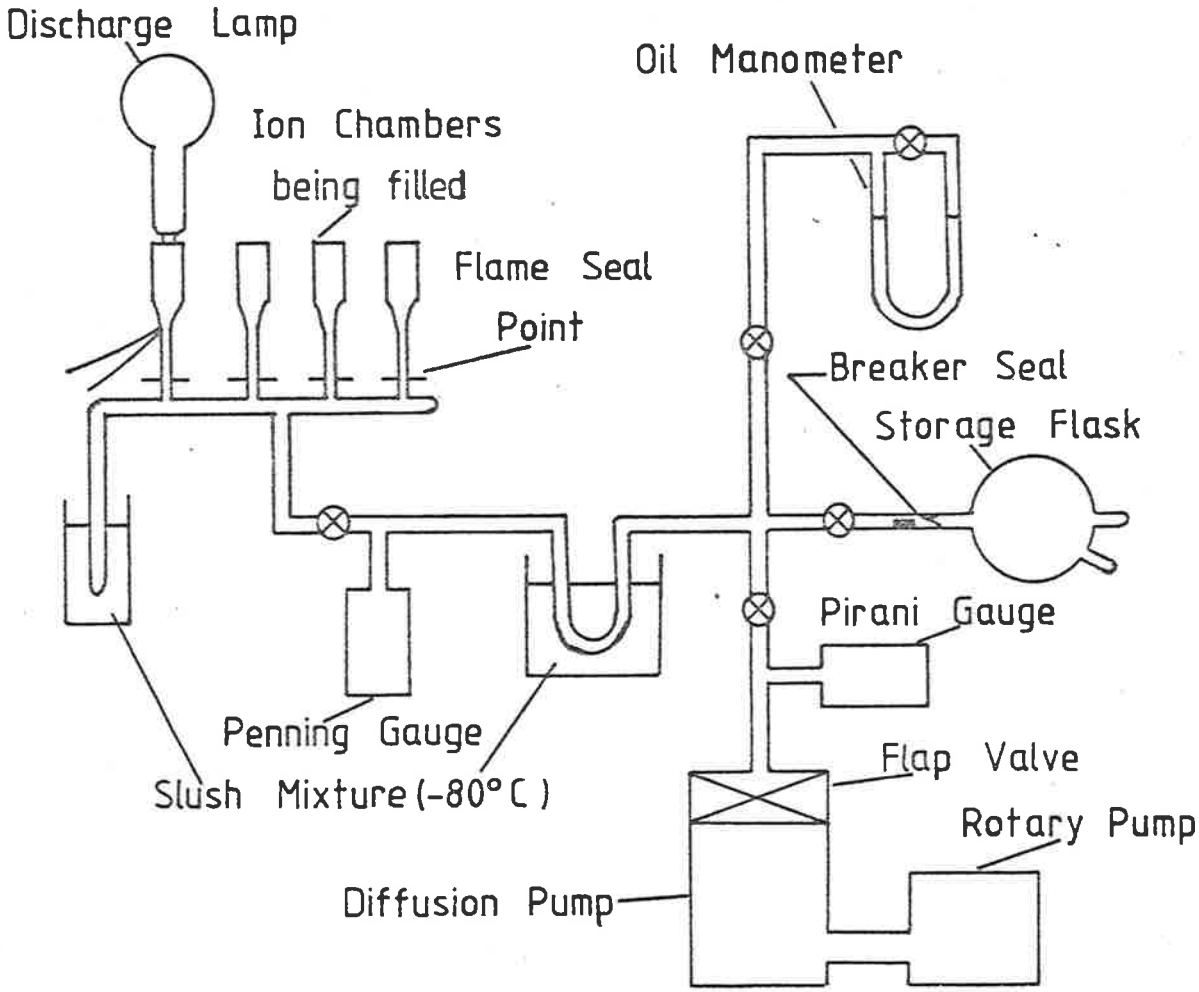

Fig 3.4 Filling System for gas (Nitric Oxide)

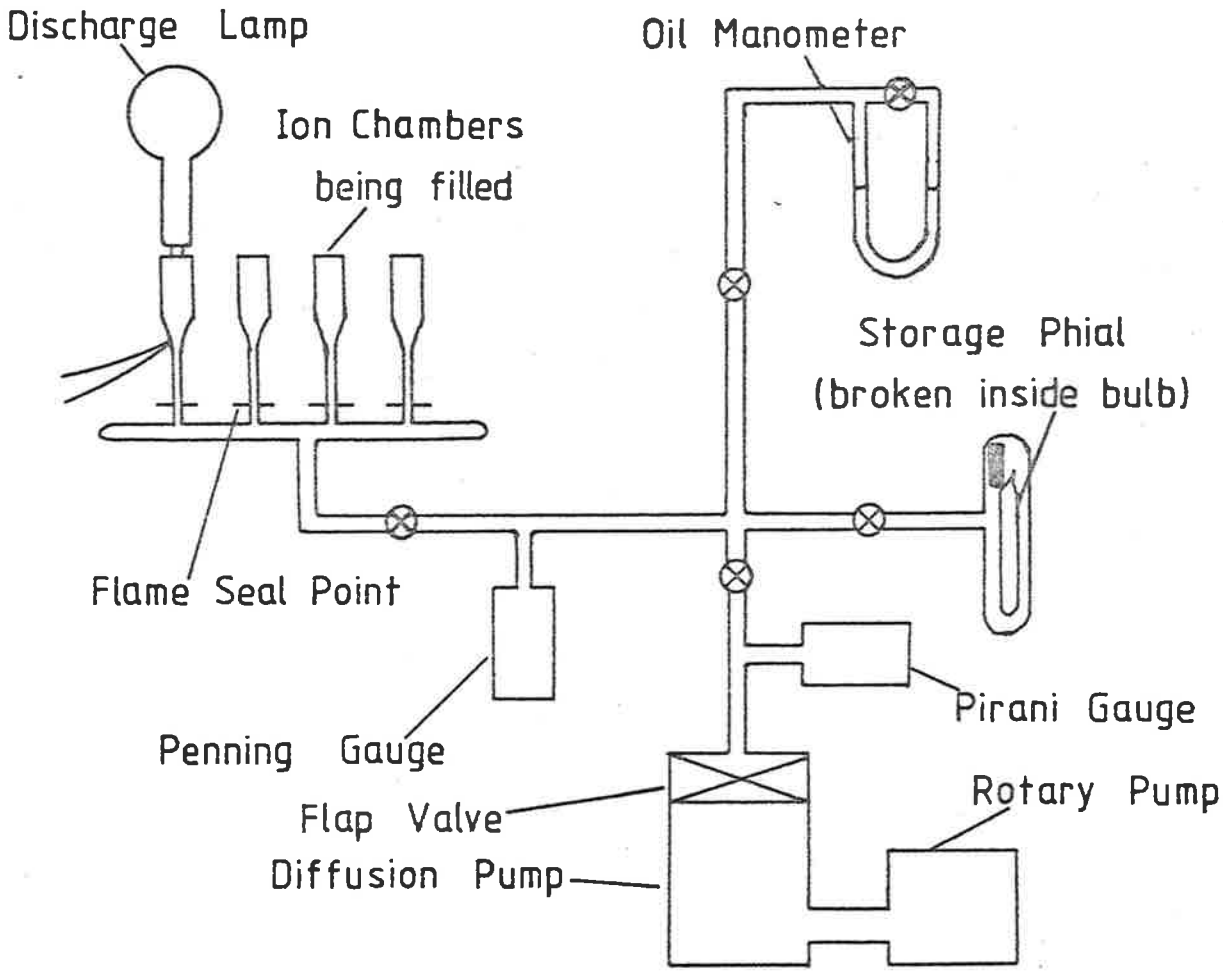

Fig 3.5 Filling System for Ethyl Bromide, Ethyl Chloride, p-Xylene and Tri-ethyl amine.

The differences arise because at normal temperature and pressures the filling gases of the latter four are liquids. Four sets of the equipment illustrated in Figure 3.5 were built; one set for each filling gas. The use of separate equipment eliminated the possibility of cross contamination arising from inadequate evacuation between chamber fillings.

As with the purification system the apparatus were built entirely of glass. Bakeable glass taps were used and therefore, with the exception of the oil manometer, the whole system up to the breaker seal of the storage flask (nitric oxide) or phial (liquids) could be heated. Heating was essential to ensure that contaminants which could arise from the walls of the filling system and the chambers were removed before filling began.

The chambers were attached to the filling system by their glass extension tubes and the whole was pumped out until the Penning gauge read 10^{-5} Torr. This pressure was maintained for several days during which time the system was periodically heated. The equipment was then isolated from the pumps and the seals on the flask or phial broken. The phials were gently warmed to produce an adequate pressure of vapour. Irrespective of the source, gas was allowed to fill the system to a pressure of 15-20 mm. The source was then isolated. This initial filling of gas was pumped away after approximately one hour. Fresh gas was re-admitted. However, this time as the gas was admitted a D.C. light source was pressed against the window of one of the ion chambers and the output of this chamber monitored. The chambers were filled to the pressure required for maximum sensitivity in the test ion chamber.

The ion chambers were not immediately removed from the system. They were first checked for short term stability (approximately one day). If they were stable over this time they were removed by flame seal-off. If not, the system was pumped down and the process of filling repeated.

3.2.6 Calibration Procedures

Ion Chambers are broad bandpass instruments. It was briefly described in Section 2.1 how this led to the use of an effective cross-section. The effective cross-section was defined as

$$\sigma_{EFF} = \frac{\int_{\lambda_1}^{\lambda_2} \phi(\lambda).\ S(\lambda).\ \sigma(\lambda)\ d\lambda}{\int_{\lambda_1}^{\lambda_2} \phi(\lambda).\ S(\lambda).\ d\lambda}$$

where $\phi(\lambda)$ is the incident flux. Only the shape, not the absolute magnitude of $\phi(\lambda)$, need be known.

$\sigma(\lambda)$ is the absorption cross section of the absorbing gas,

$S(\lambda)$ is spectral response of the detector,

and λ_1 and λ_2 are the bandpass limits.

It was, therefore, necessary to know the spectral response of the chamber. However, as is clear from the definition, this curve did not have to be absolutely scaled i.e. the absolute quantum efficiency of ion chamber as a function of wavelength was not needed. In fact as discussion of the methodology in Chapter 4 will make clear, absolute quantum efficiency of an ion chamber is not required at all for $n(O_2)$ determinations.

Despite this, however, scaling of the response curves was carried out (Section 3.2.6.4). Although it was not essential to know what flux the signal from the ion chamber represented it was essential to know what signal the expected flux would produce. Rocket telemetry systems have limited ranges and it was desirable to set the ion chamber amplifiers to give the maximum sensitivity while keeping their output signals within the range of the telemetry.

In addition, knowledge of the absolute calibrations did allow flux determinations from signal levels recorded when the rocket was above the absorbing layer. Although such work was not part of the present research program and, as will be explained in Chapter 6, the values obtained must be treated with some caution, this was still of interest.

There was one other reason for determining absolute efficiencies. The need for long term stability in the detectors has already been mentioned (Section 3.2.1). Chambers for flight had to be chosen on the basis of their behaviour during the calibration period. A more precise assessment of their likely stability could be made if the absolute sensitivities were noted each time.

3.2.6.1 Light Source and Beam Monitor.

The dispersed ultraviolet radiation needed for the calibration was obtained by passing the light from a hydrogen capillary discharge lamp through a ½ metre McPherson Vacuum Monochromator of the Seya-Namioka type. The grating was ruled at 1200 lines/inch and gave a dispersion of .017Å/u. The slit widths used were 300μ implying a resolution of 5Å. Differential pumping between the lamp and the

entrance slit was not used. The monochromator pumps were able to maintain an operational pressure of $< 10^{-4}$ Torr without this facility.

A photomultiplier, [EMI 95145] mounted at 90° to the beam and viewing a sodium salicylate coated wire grid placed in the beam, was used to monitor the beam strength. The light from the grid was transmitted to the multiplier by a polished perspex light pipe. The photomultiplier current was monitored with a Keithley Electrometer 610B.

The relationship between the photomultiplier current and the intensity of radiation in the beam depended on the response of sodium salicylate layer to U V radiation. This response is discussed in the following section.

3.2.6.2 Characteristics of Sodium Salicylate.

Sodium Salicylate (sometimes written as Na. Sal) used extensively as a detector for ultraviolet radiation. When irradiated by U V the substance gives off fluorescent radiation in a spectral band centred at approximately 4430Å (Figure 3.6). This matches the maximum sensitivity of many photomultipliers. Early researchers (Johnston *et al*, 1951; Watanabe and Inn, 1953) also reported that sodium salicylate was stable under vacuum and showed a good uniform response from λλ 900Å - 2300Å.

In 1964, a series of papers (Samson, 1964; Allison *et al*, 1964a; Knapp and Smith 1964 ; and Allison *et al*, 1964b) discussed the properties of Na Sal. From these papers were drawn the following general conclusions,

(a) that the response of the Na Sal layer decreases when it is exposed to the atmosphere of a vacuum monochromator,

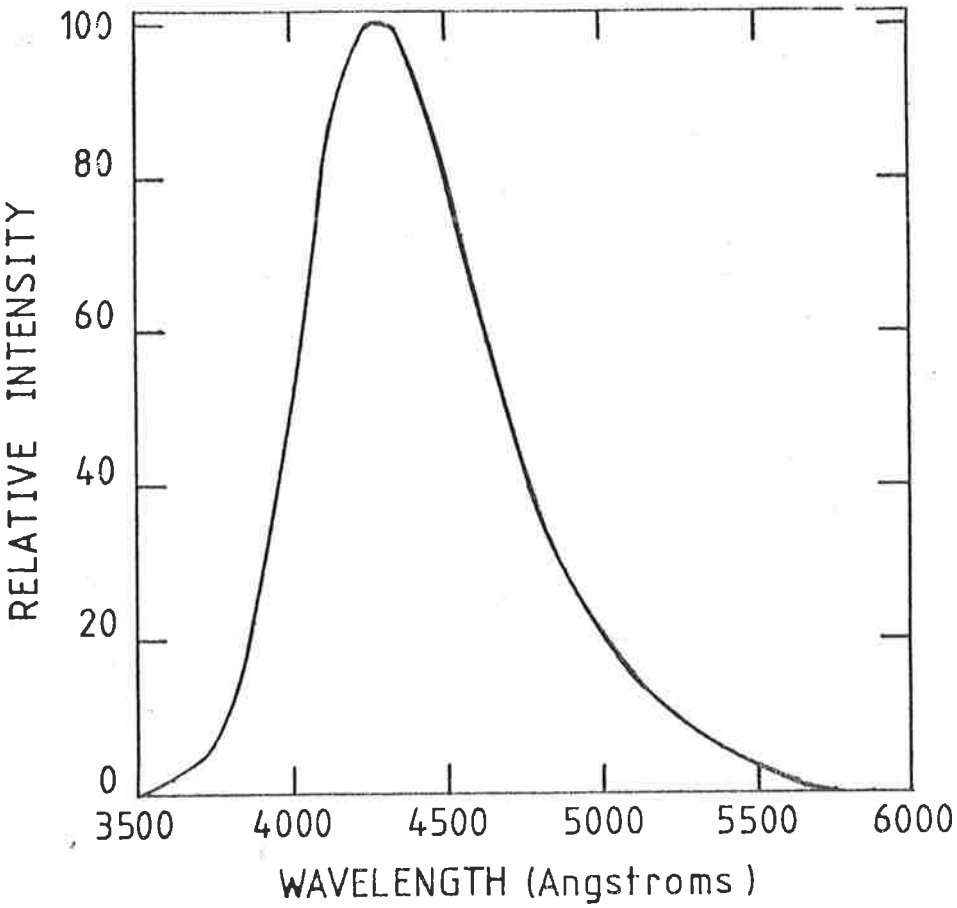

Fig 3.6 Spectral Distribution of Fluorescent Radiation from Sodium Salicylate.

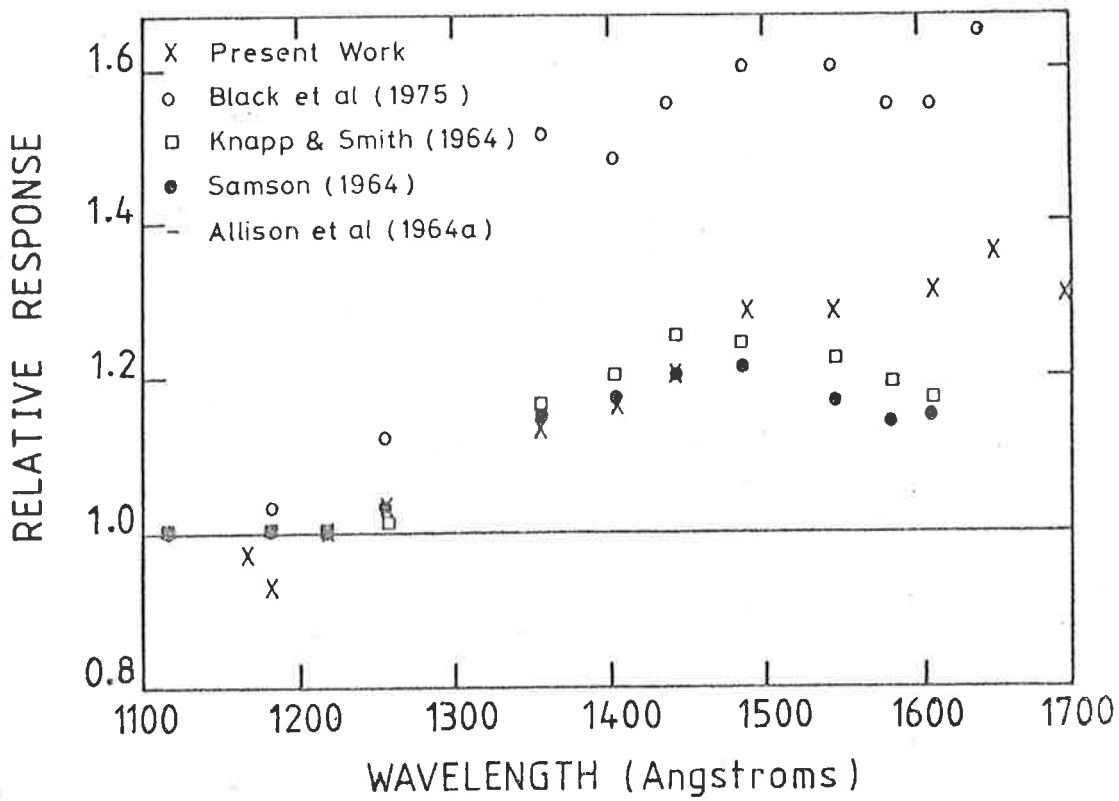

Fig 3.7 Relative Response of Sodium Salicylate as a Function of Wavelength. (All curves have been scaled to a value of 1 at Lα)

(b) that this deterioration is possibly due to contamination of the layer by the traces of diffusion pump oil found in a vacuum monochromator atmosphere under normal operating conditions,

(c) that further deterioration may be caused by the irradiation of the Na Sal layer by U V light at wavelengths $\lambda < 1600$Å.

Despite the unanimity of the researchers on the general conclusions already listed there was some controversy about the uniformity of the salicylate's response as the wavelength of the U V light varied. Both Samson (1964) and Knapp and Smith (1964) reported that the response increased as the wavelength increased. They found the initial response at λ1500Å was 20%-50% greater than that at λ1250Å. The dissimilarity worsened as the layer aged.

However, Allison *et al* (1964a) reported the response on fluorescent quantum yield of sodium salicylate was independent of wavelength. Their second paper (Allison *et al* 1964b) written after the work of Samson (1964) and Knapp and Smith (1964) had been published, reiterated this finding. In addition they noted that the aging effects reported by these authors were not evident when the layer was maintained, either in a dry atmosphere or an oil free vacuum.

The behaviour of sodium salicylate was investigated in the present work. Na Sal was sprayed on to a grid of approximately .5 mm spacing. The relative response was determined by comparing the output of the grid as measured by a photomultiplier with the adjusted signal

from an E.M.R. 543-09-00 photo-diode. The adjustment was necessary because the sensitivity of the photo-diode varied with wavelength. The "100%" signal was used as the standard.

The results are presented in Figure 3.7 where the relative response of the salicylate is plotted as a function of wavelength. The work of Black *et al* (1975), Samson (1964), Knapp and Smith (1964) and Allison *et al* (1964a) is also shown. To make comparison of the various results easier, all curves have been scaled to a value of 1 at Lα.

As can be seen from Figure 3.7 there is only limited agreement between the results. An increase of approximately 20% in the response of the Na Sal was observed by Samson (1964), Knapp and Smith (1964) and in the present work as the wavelength changed from 1216Å to 1490Å.

The work of Black *et al* (1975) is very dissimilar and is more consistent with the results obtained in the present work for a layer 13½ months old. Figure 3.8 shows the relative response curves of a Sodium Salicylate covered grid as the coating aged from 0 to 24 months. For each curve the value of the response is given the value of 1 at Lα and the response at the other wavelengths is expressed as a function of the Lα value.

Figure 3.9 shows the same response curves expressed in arbitrary units rather than as a function of the Lα value. The two figures together clearly illustrate that the overall sensitivity of the Na Sal coating decreases as it ages (Figure 3.9) but that the decrease in sensitivity is more marked at the lower wavelengths (Figure 3.8). This latter observation is consistent with the work of Knapp and Smith (1964).

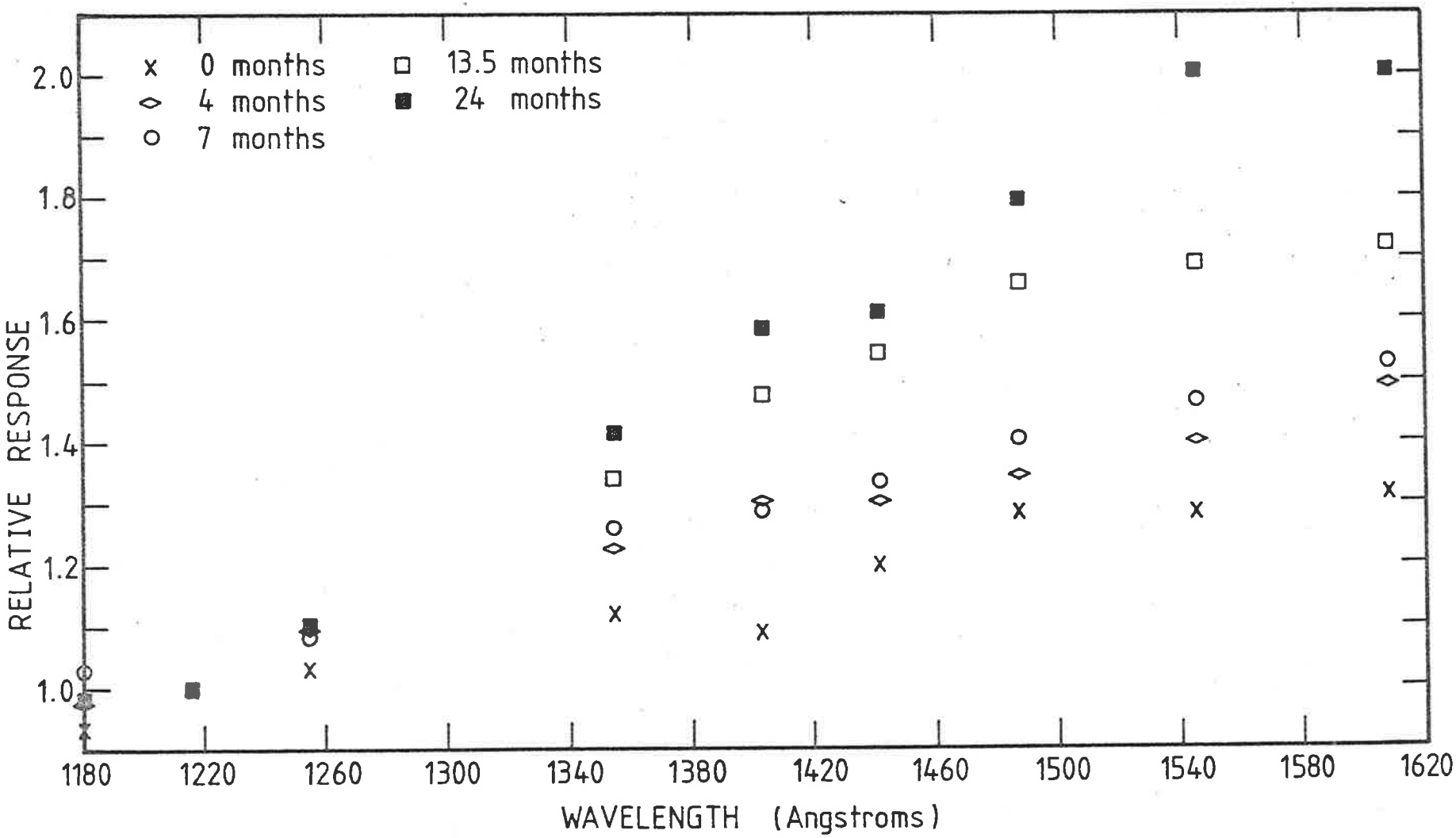

Fig. 3.8 Change in response of Na.Sal. as coating ages.

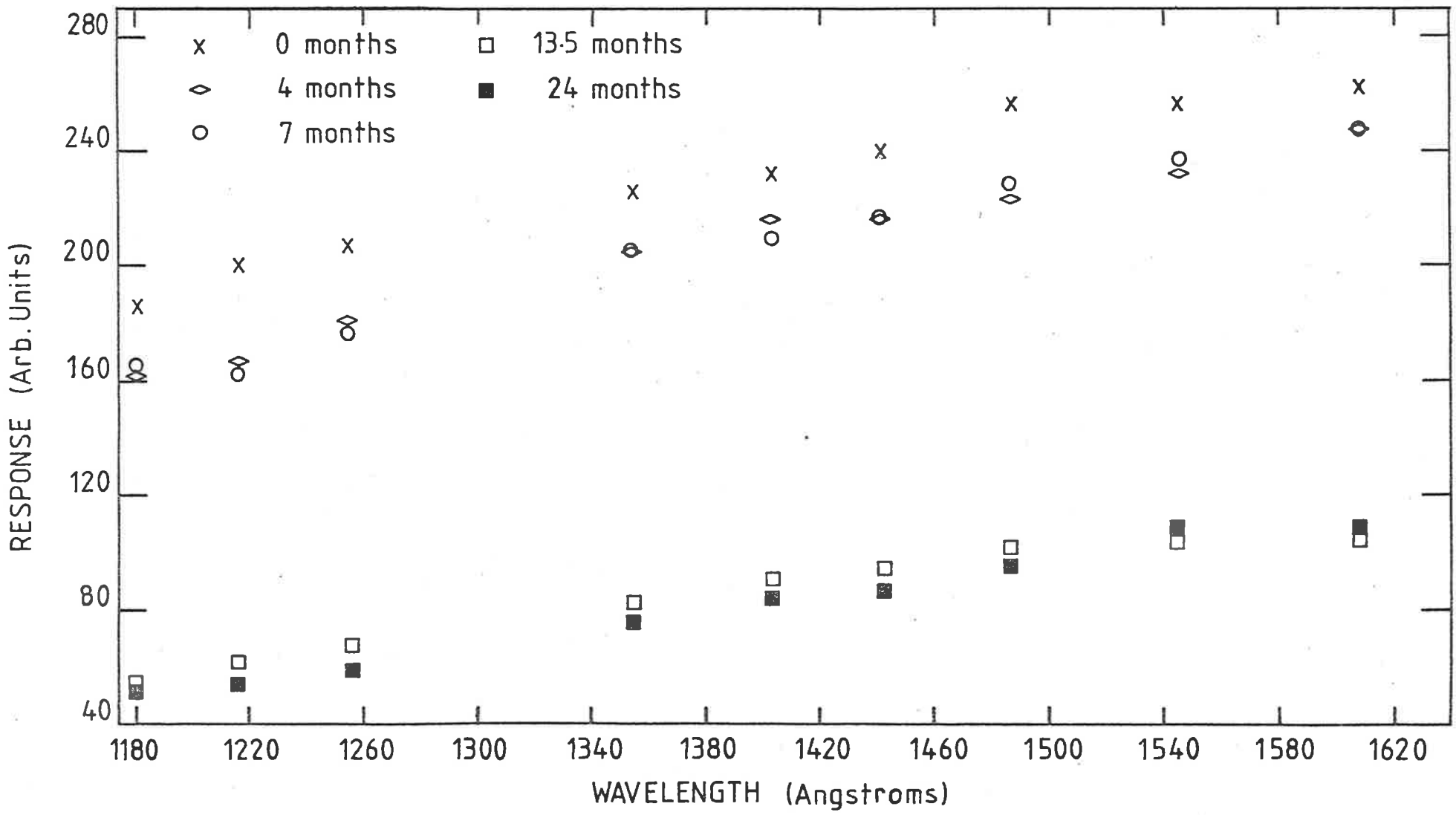

Fig 3.9 Deterioration in sensitivity of Na. Sal as coating ages.

Therefore the current from the beam monitor can only be considered strictly proportional to the intensity of the incident radiation if the wavelength is held constant. Attempted comparisons of intensities at different wavelengths by comparison of the beam monitor current will be invalid if allowance is not made for the differing response of the sodium salicylate. The size of the error introduced by the use of strict proportionality across all wavelengths will increase as the coating ages.

The effect of the non-uniform response of the beam monitoring system on measurements of spectral response and absolute quantum efficiency is discussed in the following sections.

3.2.6.3. The Spectral Response.

A schematic of the experimental equipment used for determining the spectral response of an ion chamber is shown in Figure 3.10. The ion chamber, held in an insulating clamp, was attached to a brass mount which mated with the exit port of the monochromator. As shown in Figure 3.10 the exit port is defined as the flange after the beam monitoring system. There were "O" ring seals between the brass mount and the monochromator exit port; the insulating clamp and the brass mount, and the ion chamber and the insulating clamp. The volume between the exit slits and the ion chamber was pumped with a single stage rotary pump. With this arrangement the monochromator could still be maintained at a working pressure of 10^{-4} Torr when the exit slits were opened.

Radiation from the exit slit of the monochromator passed through

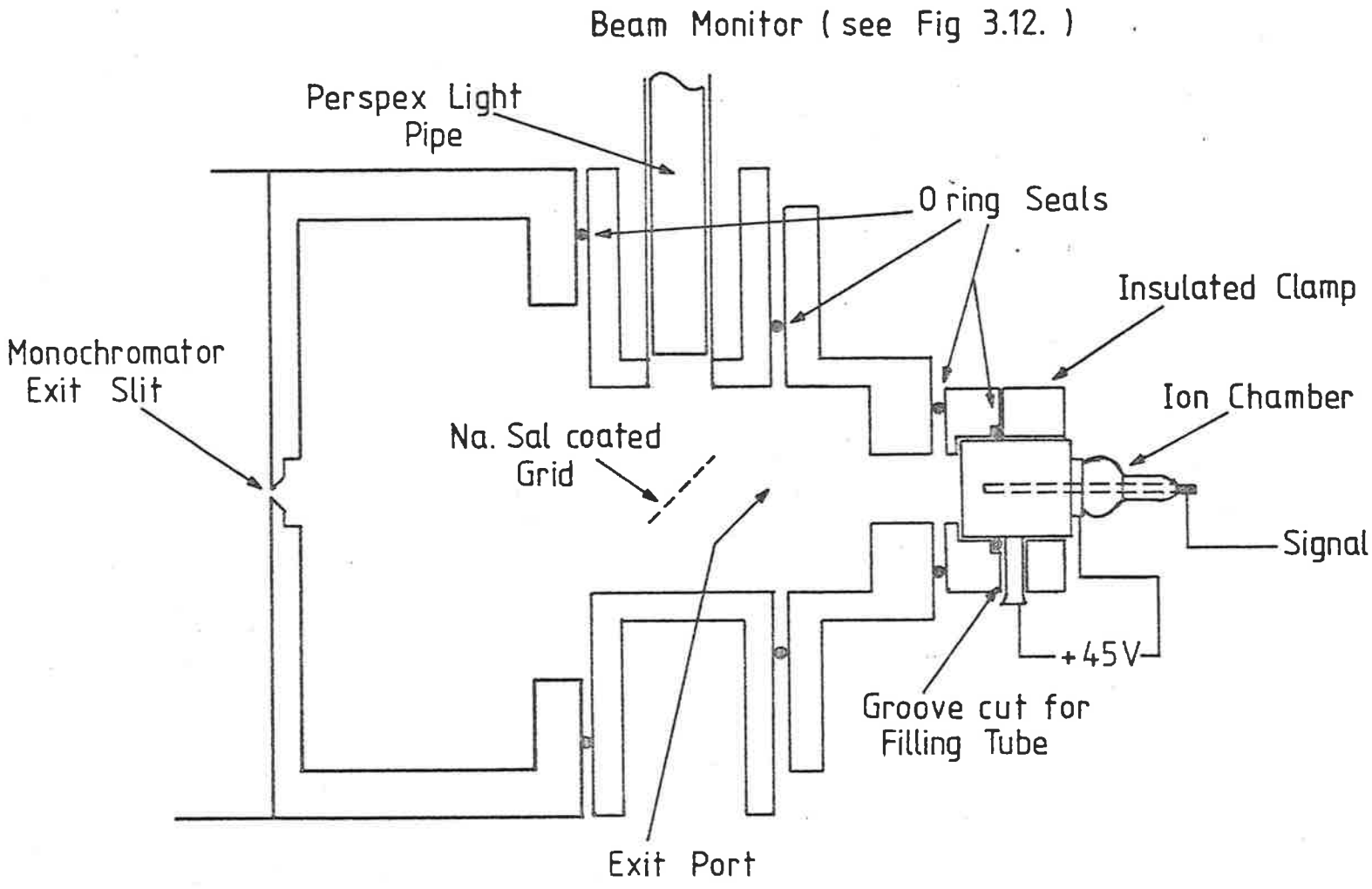

Fig. 3.10 Schematic of Experimental Apparatus for Spectral Response Measurement.

the monitoring system already described and entered the IC. A voltage of +45 volts was applied to the chamber. The signal was measured on a Keithley Electrometer 610C.

While the current of the monitor photomultiplier was corrected for the thermal emission current of the photo-cathode (i.e. the dark current) the current from the ion chamber was not corrected. If the noise signal from the ion chamber was significant it was not used but was cleaned, re-pumped and re-filled. The ratio of the ion chamber current over the corrected monitor current was taken as the spectral response of the chamber.

The validity of this procedure was, however, cast in some doubt after the investigation of the non-uniform response of sodium salicylate. (Section 3.2.6.2). The non-uniformity would introduce error. The spectral response would be biased towards the shorter wavelengths by the apparent increase in light intensity at the longer wavelengths. Because of the importance of the spectral response to the calculation of the effective cross section (Section 2.2 and 4.2.5) an attempt was made to estimate the magnitude of the uncertainty introduced.

If the measured spectral response of an ion chamber is called $\varepsilon_M(\lambda)$ a better estimate of the actual response $(\varepsilon(\lambda)$ will be given by

$$\varepsilon(\lambda) = \varepsilon_M(\lambda).R(\lambda) \qquad 3.1$$

where $R(\lambda)$ corrects for the biased response of the salicylate grid of the monitoring system.

$R(\lambda)$ was given the value 1 at λ_s where λ_s was defined as the short wavelength limit of the passband of any particular chamber. Then the value of $R(\lambda)$ at λ_ℓ, the long wavelength limit of the

chamber, was investigated. It was found for both SX and QT chambers,and for sodium salicylate coatings of all ages up to two years,that the mean (μ) of $R(\lambda_\ell) = 1.11$; standard deviation of distribution (s.d.) = .03. The implications of this result are discussed quantitatively in Section 4.2.5. but it was concluded that it was acceptable to adopt the more convenient $\varepsilon_M(\lambda)$.

Typical measured response curves for all the chambers used in the present work are shown in Figure 3.11 (a - g). The response curves are not absolutely scaled. For Figures 3.11a and 3.11b the curve is scaled to the response at 1200Å. For Figures 3.11 (c - g), the curves are normalized to a value of one at maximum efficiency. To convert these relative curves to spectral responses showing actual quantum efficiencies at each wavelength it was only necessary to obtain the absolute response at one wavelength. The procedure for this is described in the next section.

3.2.6.4. Absolute Quantum Efficiencies.

Prior to 1975 the basis of all absolute calibrations was a single parallel plate ion chamber filled with nitric oxide. This was used to calibrate, absolutely, an LNO chamber. The LNO chamber was then used as a secondary standard and all other chambers were calibrated against it.

Figure 3.12 shows the experimental apparatus. The standard ion chamber (SIC) was attached to the exit port of the monochromator. An LiF window mounted in a brass plate was used to seal the monochromator from the parallel plate ion chamber. The brass plate was

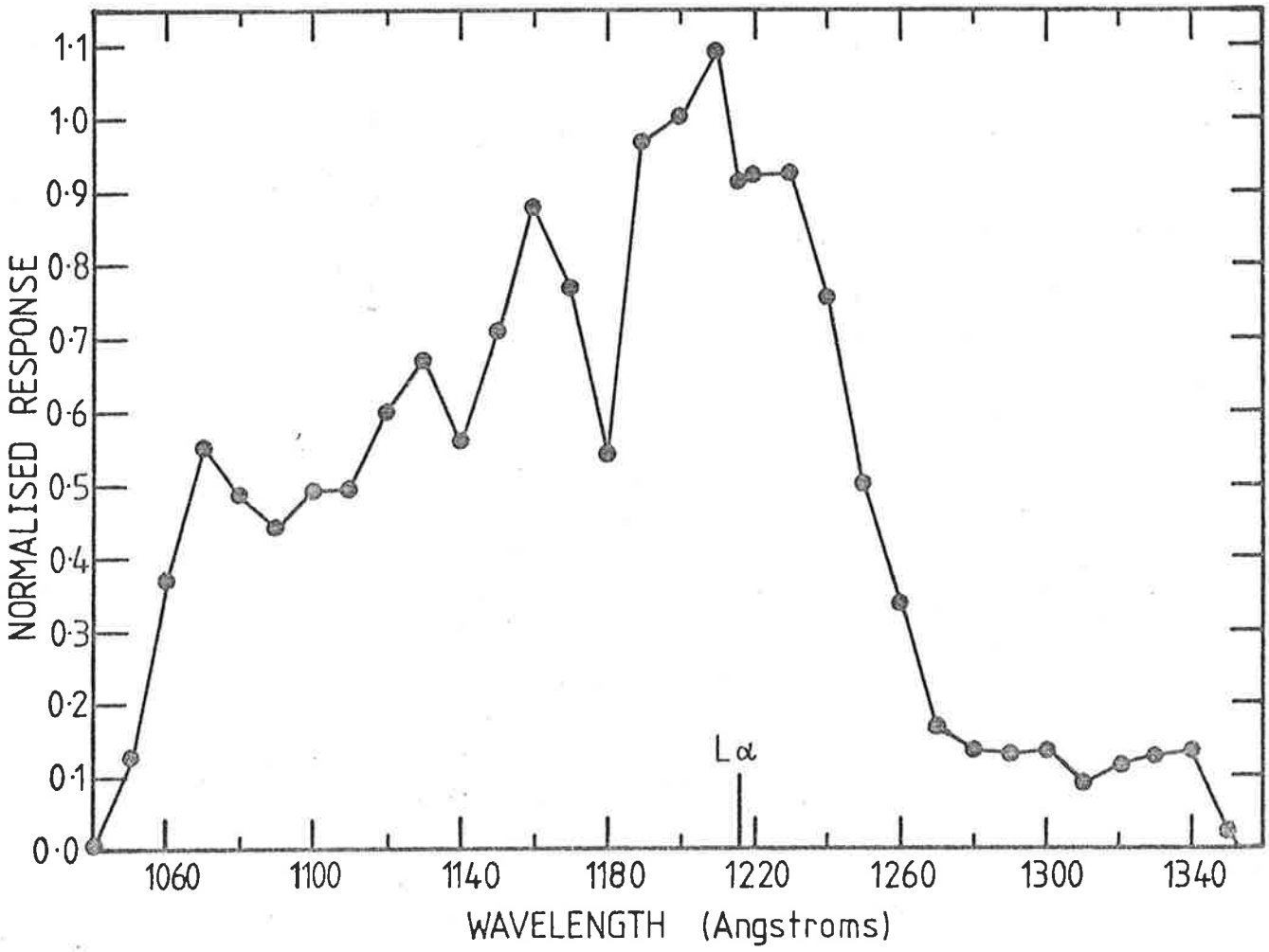

Fig 3.11a Spectral Response of LNO Ion Chamber.

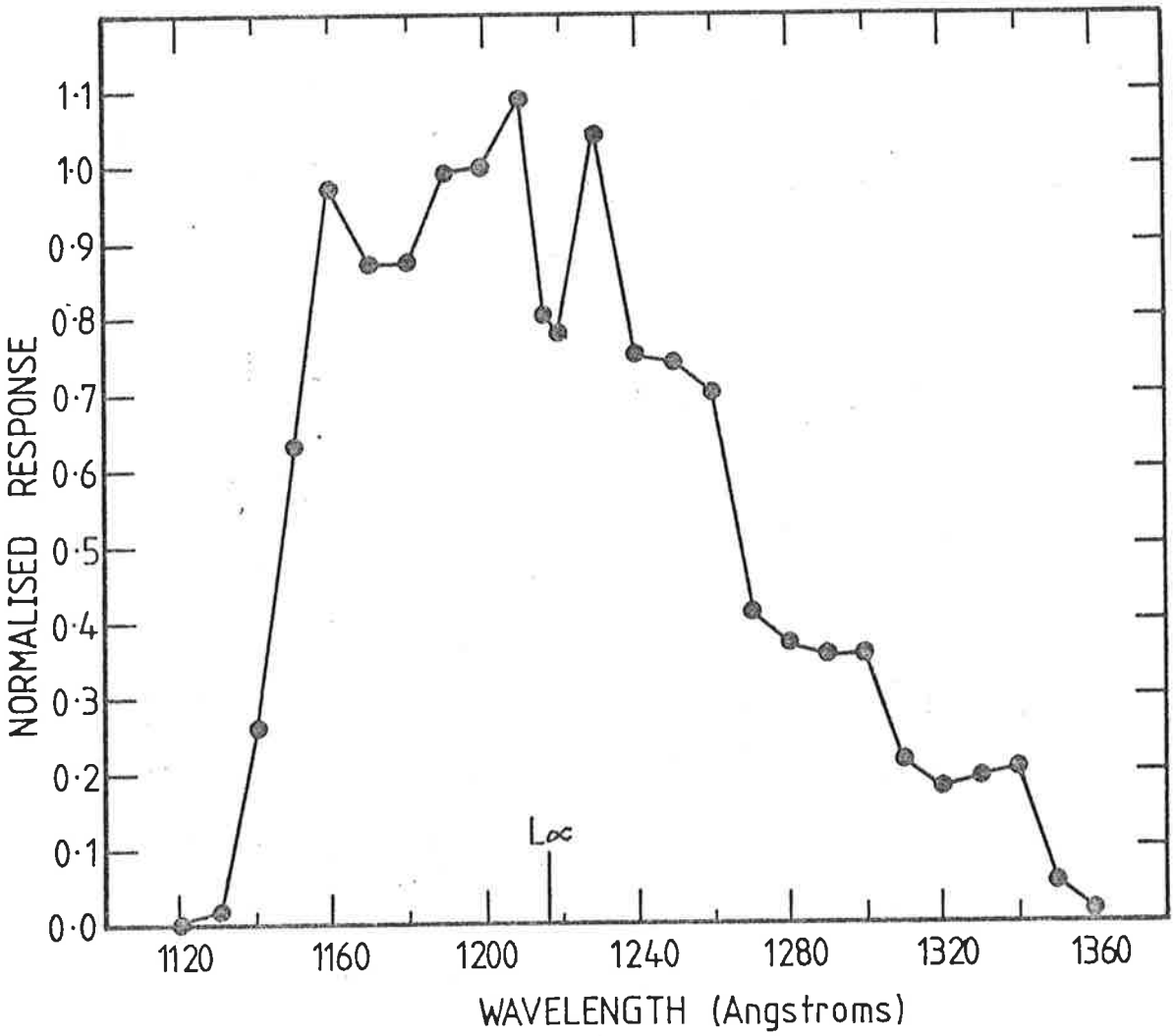

Fig 3.11b Spectral Response of MNO Ion Chamber.

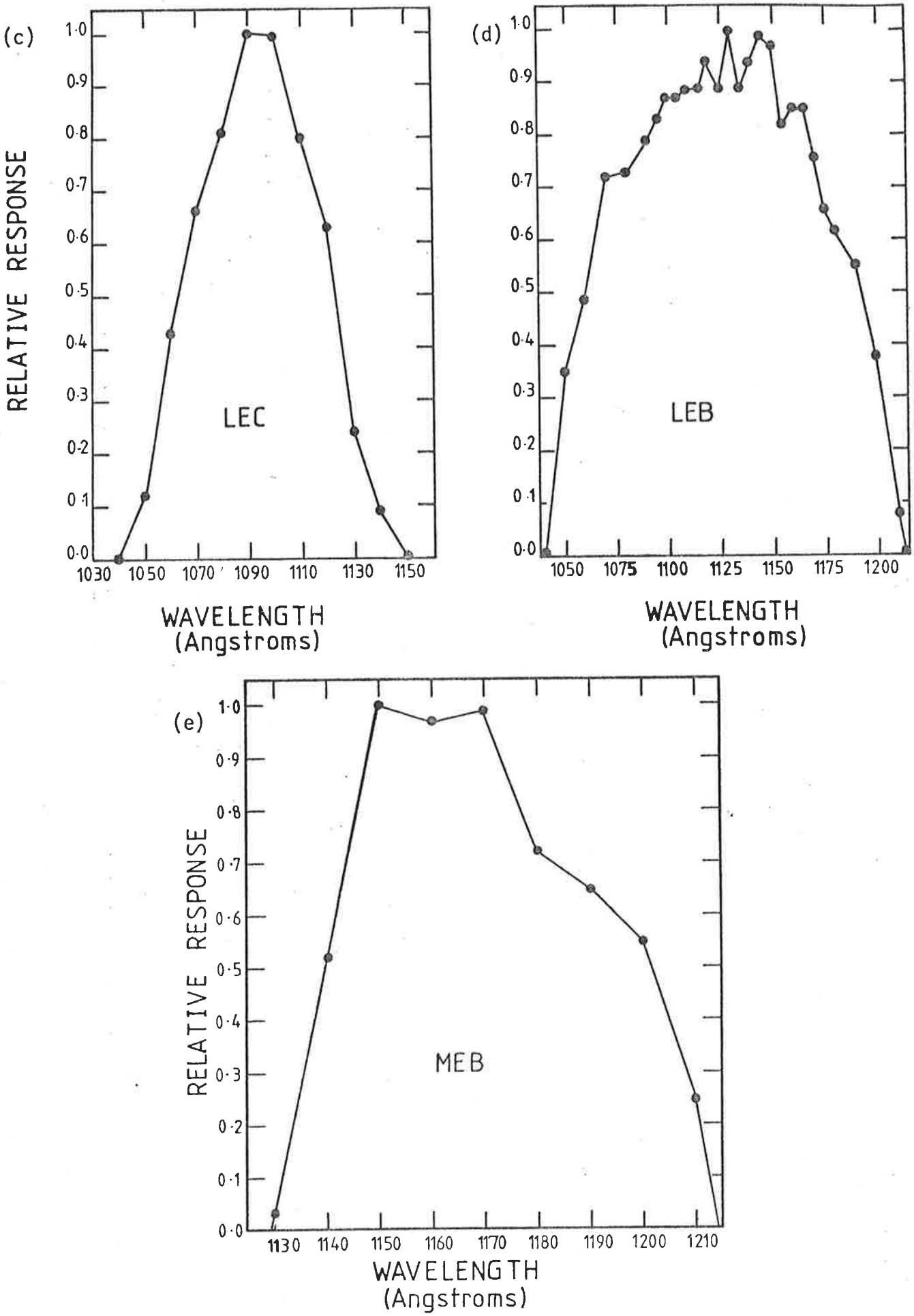

Fig 3.11 Spectral Responses of the Ion Chambers.

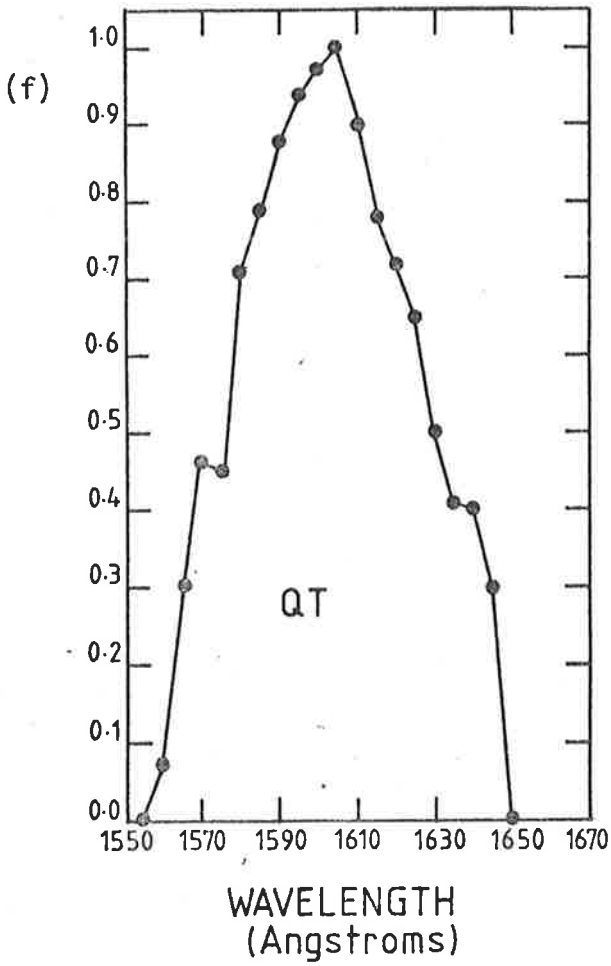

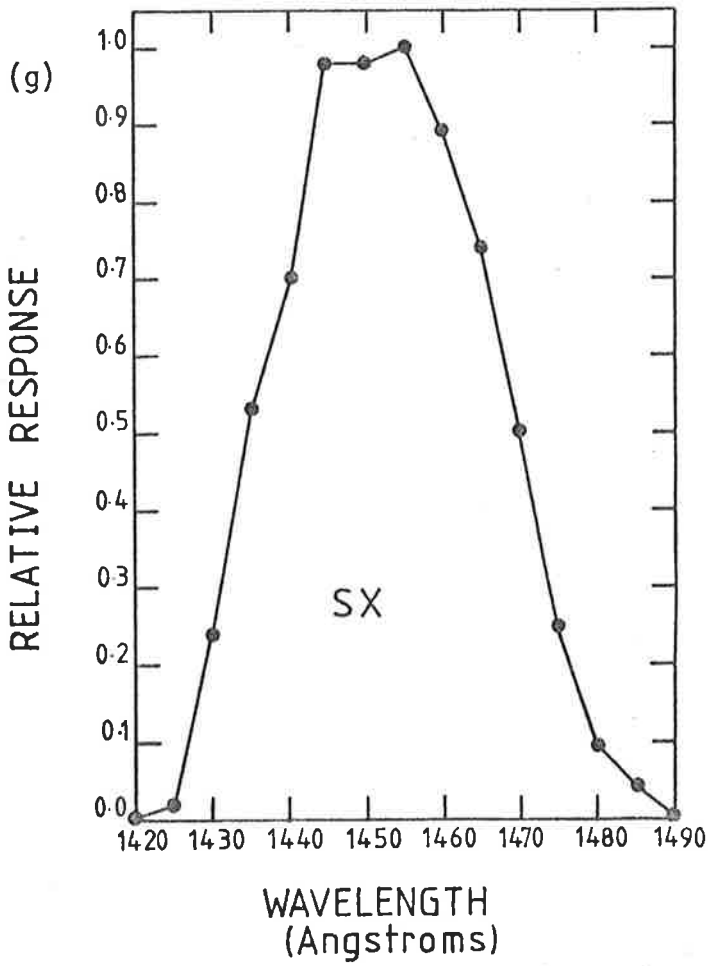

Fig 3.11 Spectral Response of the Ion Chambers.

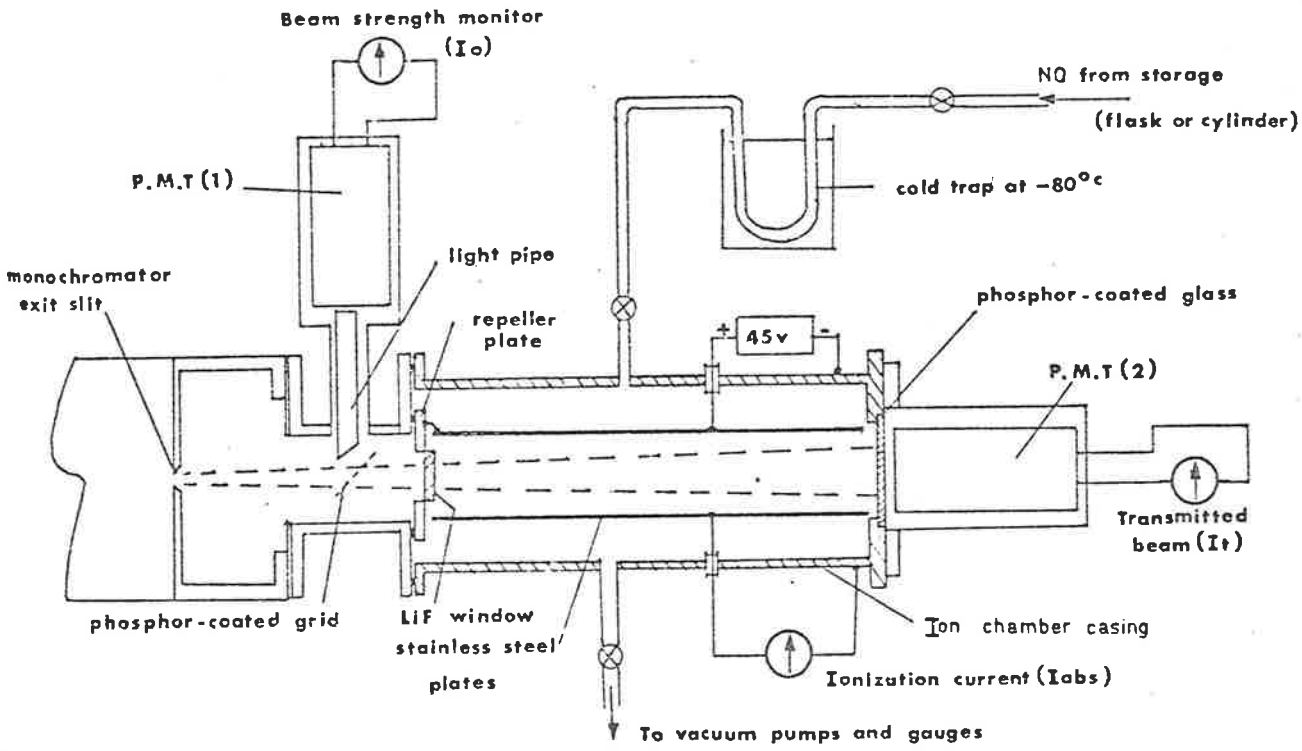

Fig. 3.12. Schematic of Standard Ion Chamber Calibration System. (Reproduced from O'Conner, 1973)

insulated from the main body of the monochromator and electrically connected to the positive plate (+ 45 volts) of the SIC. This created a field suitable for collecting ions formed near the window. The beam of light was monitored in two places. The monitoring system of the monochromator (PM1) recorded the intensity of $L\alpha$ produced by the monochromator. A second monitor (PM2), which looked at the fluorescence produced by sodium salicylate covered glass plate, recorded the intensity of radiation reaching the back of the parallel plate ion chamber. (In Figure 3.12 sodium salicylate is referred to as phosphor).

The monochromator, the space between the exit slits and the LiF window, and the SIC were all pumped separately. The space between the exit slits and the LiF window was pumped with a single stage rotary pump to approximately 10^{-2} Torr independently. Further pumping occurred when the exit slits of the monochromator were opened. No differential pumping was used but after a short stabilizing period an operating pressure of 10^{-4} could still be maintained in the monochromator. It was standard procedure to let the pressure stabilize before taking any measurements.

The SIC was pumped with a diffusion pump for at least 24 hours before use. During the pump-out it was periodically heated to aid out-gassing. Then calibration procedure was as follows:

(a) the monochromator was set to $L\alpha$,

(b) the SIC was isolated from the vacuum pumps,

(c) the dark currents of PM1 and PM2 were noted,

(d) the exit slit of the monochromator was opened; the pressure allowed to stabilize and then the response of the two monitors and the SIC recorded,

(e) a small amount of nitric oxide was admitted to the SIC and the signals of the three detectors recorded again,

(f) step (e) was repeated until the signal from the back monitor (PM2) remained unchanged and the signal from the SIC decreased when more NO was admitted,

(g) the source of the NO was now isolated and the above procedure reversed, i.e. the chamber was pumped out in steps and the detector signals recorded at each step,

(h) the standard ion chamber was replaced by an LNO chamber,

(i) the space between the LiF window and the ion chamber was evacuated using the SIC's pumping system i.e. diffusion pump, and the response of the chamber to irradiation by $L\alpha$ recorded. The signal from the beam monitor, PM1, was also recorded.

The basis of this method of absolute calibration lies in the work of Watanabe *et al* (1967). Watanabe and his co-workers measured the photoionization efficiency of nitric oxide as a function of wavelength. For Lα this efficiency was 81%. Therefore if all the light is absorbed by NO within the SIC and all the ions and electrons produced by photoionization reach their respective electrodes the current I_{ABS} (see Figure 3.12) will be representative of a detector of 81% efficiency. This will only occur at a particular concentration of nitric oxide within the SIC. Too low, and not all of the Lα radiation is absorbed. Too high, and scattering of the photoionization products will allow recombination to occur in the body of the chamber instead of just at the cathode. This will reduce the signal. The exact concentration is rarely achieved during a calibration run and therefore I_{ABS} must normally be found by extrapolation.

Figure 3.13 shows the graphical result of a calibration run. The signal from the back monitor PM2 is plotted against the signal from the SIC. Both detector signals are corrected for their dark currents. Before the admission of any NO all the light from the exit slit of the monochromator reaches the back sodium salicylate covered glass plate and the photomultiplier PM2 records its maximum signal. As NO is introduced absorption takes place. The signal from PM2 therefore decreases. The signal from the SIC however, increases since the absorption of the light leads to photoionization of the NO. The introduction of more nitric oxide leads to a further decrease in the signal from PM2 and a further increase in the SIC signal. This trend continues and is represented by the first linear section of the graph. Eventually the signal from the back monitor stabilizes and shows no

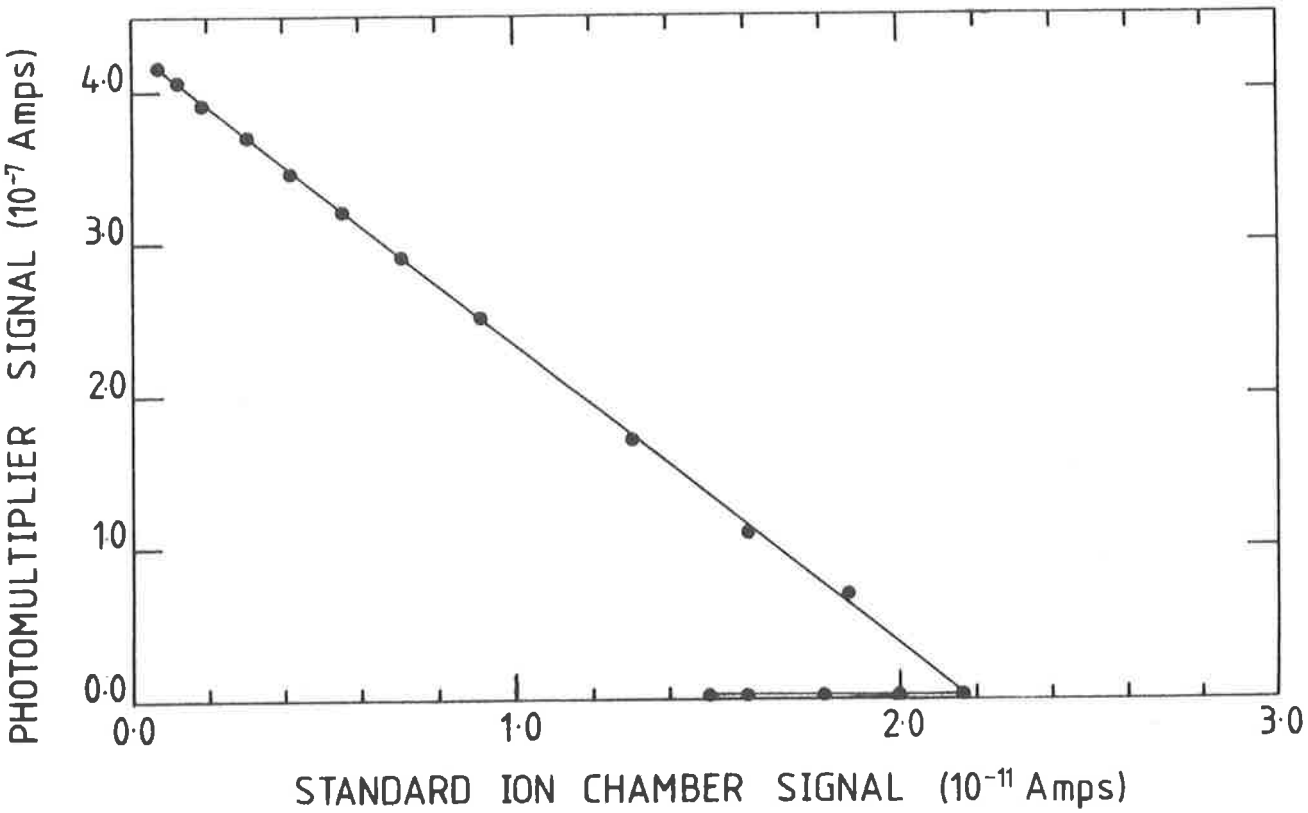

Fig 3.13 Calibration Curve for the Standard Ion Chamber.

further decrease, implying that all the incident $L\alpha$ radiation has been absorbed. The residual signal results from scattered visible light in the beam. Once the PM2 signal has stabilized further increases of the concentration of NO reduces the signal from the standard ion chamber because scattering occurs. This is represented by the horizontal section of the graph.

The best estimate of I_{ABS} will be the point at which the PM2 signal just reaches its minimum. The best estimate of this point will be the intersection of the two linear sections. As stated this normally requires extrapolation but for the set of results shown in Figure 3.13 the best estimate of I_{ABS} is given by a data point.

Once the I_{ABS} has been estimated, finding the quantum efficiency of the secondary standard is a simple procedure. Q_L, the efficiency, will be given by

$$Q_L = 81 \cdot \frac{I_L}{I_{ABS}} \qquad 3.4$$

where I_L is the signal from the LNO chamber. Q_L is given in terms of a percentage.

If the beam strength had changed between the measurement of I_L and I_{ABS} this could be allowed for by using the signal from PM1

$$\text{i.e. } Q_L = 81 \cdot \frac{I_L}{I_{ABS}} \cdot \frac{M_{ABS}}{M_L} \qquad 3.5$$

where M_{ABS} was the strength of the beam as measured by the monitor at the time I_{ABS} was observed and M_L was the strength of the beam at the time I_L was observed.

The efficiency of any other LNO chamber could therefore be calculated by

$$Q_c = Q_L \cdot \frac{I_c}{I_L} \cdot \frac{M_L}{M_c} \qquad 3.6$$

where the subscript c denotes the new ion chamber, the subscript L the secondary standard and the symbols Q, I and M have the definitions given previously for Equation 3.5.

Equation 3.6 was also used to obtain a figure for the absolute quantum efficiency of the other types of ion chamber. In this instance M_c became the intensity, as measured by the beam monitor, of the light at the wavelength appropriate to the chamber being calibrated.

From the discussion of Section 3.2.6.2 the use of Equation 3.6 for chambers other than LNO and MNO chambers is not valid. The non-uniform response of the sodium salicylate covered grid will imply that M_c is instrumentally enhanced and not directly comparable with M_L.

This systematic error in the absolute efficiencies of the chambers constructed and flown before 1975 did not affect the derived $n(O_2)$ densities. However, estimates of flux were made from signals recorded at apogee and these would have been affected. Table 3.4 shows the efficiencies of the chambers flown in the rockets SL1005 and SL1207. (Chapter Five). The first efficiency is that measured prior to flight and the second is a value based on the original measurement and the subsequent research into the behaviour of sodium salicylate. The numbers associated with the ion chambers are an identifying code and do not have any physical or analytical significance.

The solar fluxes in Chapter 6 are based on the estimated efficiencies.

TABLE 3.4 EFFICIENCIES OF THE ION CHAMBERS FLOWN ON THE SKYLARK ROCKETS, SL1005 AND SL1207

Rocket	Ion Chamber	Measured Efficiency (%)	Estimated efficiency (%)
SL1005	QT203	1.02	1.33
	QT204	1.19	1.55
	SX3	4.85	5.82
SL1207	QT1	1.05	1.52
	QT3	.36	.52
	SX5	.56	.74
	SX7	3.89	5.13

Calibration procedure was simplified by the acquisition of an E.M.R. 543P-09-00 photodiode. The diode had an end window of Magnesium fluoride and a semi-transparent photocathode of Rubidium Telluride. The multiplier tube was glass with venetian blind dynodes. It had been calibrated at selected wavelengths in the range λλ1160Å - 2537Å by the National Bureau of Standards Laboratory in Washington D.C., U.S.A. General calibration procedures followed by N.B.S. for this type of detector are outlined by Canfield *et al* (1973). The probable error for the calibrations was quoted as 6%-10%.

Before use the diode was fully enclosed in a protective brass tube. A flange, which mated with the exit port of the monochromator and provided a vacuum seal that was also light tight, had been brazed

onto one end of this tube, while a brass plate fitted with vacuum and light-tight electrical connectors had been brazed onto the other. The diode was run at 150 volts.

Experimental procedure was simple. The photo-diode had been calibrated at selected wavelengths. One was chosen that lay within the passband of the ion chamber being calibrated. Keeping the resolution to 5Å the monochromator was adjusted to the selected wavelength. The photodiode was positioned at the exit port of the monochromator, the space between the front of the diode and the exit slit of the monochromator evacuated, the slits opened, and the response of the photodiode to the irradiation measured on a Keithley Electrometer 610C. The monitor signal was also noted. The procedure was repeated with the ion chamber undergoing calibration.

With this procedure there was no ambiguity associated with the use of a sodium salicylate grid in the beam monitor. Both the standard and the ion chamber looked at the same wavelength radiation and it could, therefore, be assumed that any change in the beam monitor signal reflected a real change in the intensity of the radiation.

The absolute quantum efficiency of the tested ion chamber was given by

$$Q_c(\lambda) = Q_D(\lambda) . \frac{I_c(\lambda)}{I_D(\lambda)} \cdot \frac{M_D(\lambda)}{M_c(\lambda)} \qquad 3.7$$

where $Q_c(\lambda)$ is the quantum efficiency of the chamber at the wavelength λ ,

$Q_D(\lambda)$ is the quantum efficiency of the photodiode at the wavelength λ ,

$I_c(\lambda)$ and $I_D(\lambda)$ are the responses of the ion chamber and diode respectively to irradiation by light of wavelength λ ,

$M_c(\lambda)$ and $M_D(\lambda)$ are the intensity of the emitted beam , as represented by the signal of the monitor, at the time $I_c(\lambda)$ and $I_D(\lambda)$ respectively are measured.

To compare the two systems of calibration the photodiode was calibrated at $L\alpha$ against the standard parallel plate ion chamber. The National Bureau of Standards Laboratory quoted the efficiency of the diode at this wavelength as 7.52 with a probable absolute error of ± .45%. The value of the efficiency as measured by the SIC was 7.95 ± .32%. The error quoted here is a statistical one calculated by assuming that the answers gained in a series of calibrations fitted a normal distribution. The two results are within 6% of each other, well within the range of each others error bars. A similar degree of consistency between calibration systems based either on a standard ion chamber or on a photodiode was obtained by Nishi *et al* (1976).

In view of the agreement obtained, and because of the possibility of a systematic error occurring in the SIC value as a result of the contamination of the NO (see Appendix 1) the N.B.S. value for the efficiency at $L\alpha$ was adopted. i.e. 7.52 ± .45%.

The work done for this thesis on the non-uniform response of the sodium salicylate and the efficiencies of all chambers flown from 1975 onwards is based on the N.B.S. calibrations of the photodiode over the wavelengths $\lambda\lambda$1160Å - 1608Å.

3.2.7. Angular Response

The angular response of the ion chambers was not needed for the molecular oxygen density experiments of the present work. For these experiments the use of attitude controlled rockets meant that the aspect angle could be, and was, held at zero throughout the region of interest. It was not needed for the water vapour experiment either, but for completeness it was, however, measured.

The typical angular response of an ion chamber is gven in Figure 3.14. This was not measured in the laboratory, but deduced from the change in a detector's signals observed at altitudes where absorption of radiation within the passband was no longer significant and it could be assumed that the only change in the signal level was the result of differing aspect. This method is of course only possible where data from an ion chamber flown on a spinning rocket is available.

The ion chamber was flown on a small sounding rocket which spun at 11.5 revs/sec. The rotation of the rocket about its long axis swept the aspect in the plane, perpendicular to that which contained the long axis and the sun, from - 180° through to + 180°. Because the telemetry sampling rate of the detector output, just under twice/rev, was not synchronous with the spin rate, the aspect at the time of the sampling varied. Over a time scale of 1 to 1½ secs. a full curve of signal against aspect was built up. This will be referred to as the spin curve.

Information about the vehicle performance was obtained from the quad aspect sensors (see Appendix 3.) and the magnetometers included in the payload. The magnetometers indicated the rocket was reasonably stable and did not undergo any large scale rapid yawing. From the data of the

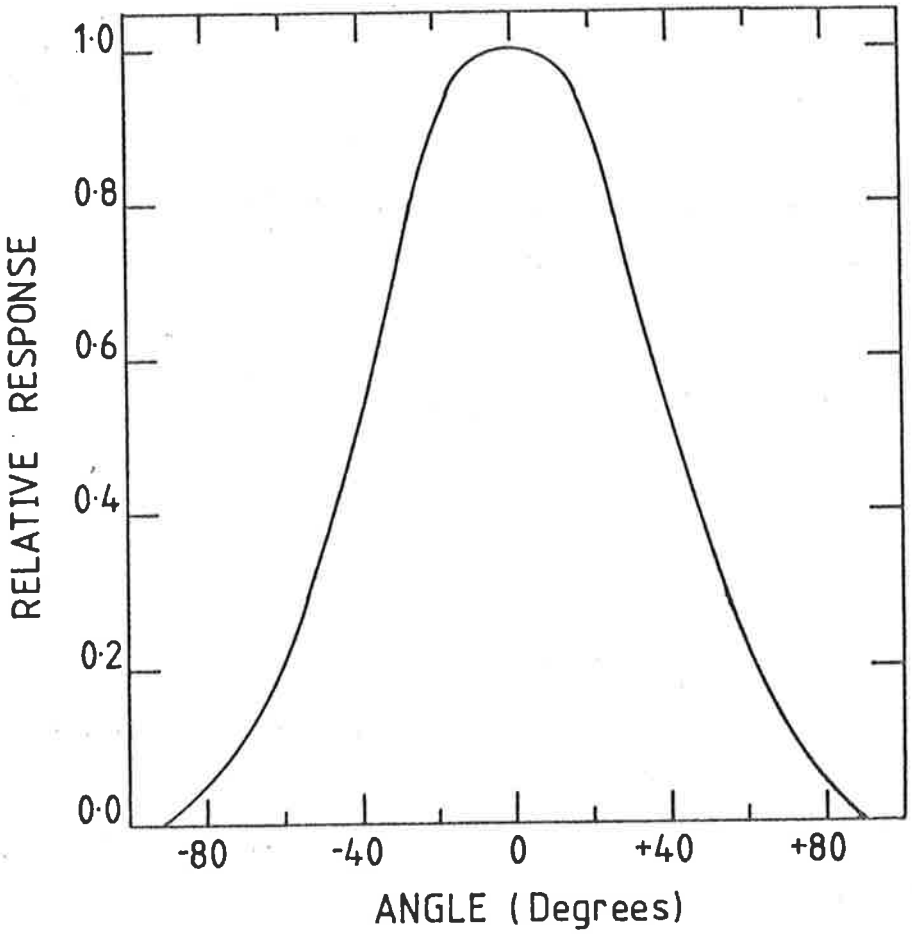

Fig 3.14 Angular Response of Ion Chamber.

quad aspect sensors it was deduced that the rocket coned at a rate of 1 cycle/14 secs. with a half angle of approximately 15° about a mean aspect of approximately 22°, i.e. aspect in the plane containing the long axis of the rocket and the sun varied slowly from ≈ 7° to ≈ 39°.

Therefore although, as stated, the spin curve reflected the change in aspect in the plane normal to the long axis, it was also influenced by the slowly varying aspect in the plane containing the long axis. This influence was seen as a slowly varying shallow, modulating envelope.

The spin curve is equivalent to the angular response of the ion chamber if the aspect in the other plane is constant and equal to zero. These conditions were not met on the rocket flight under consideration. It was clear, however, that at a maximum in the modulating envelope the aspect in the second plane could, without the introduction of significant error, be regarded as constant over the 1 to 1½ seconds taken to record the curve. The maximum in the modulating envelope corresponded to an aspect in the second plane of ≈ 7° rather than zero, but laboratory work done on angular response suggested this too could be ignored without the introduction of significant error.

Angular response curves had, in fact, been measured in the laboratory, and the general agreement between them and the spin curve at the maximum of the modulating envelope increased the confidence level in the validity of using the spin curve as the angular response. The advantage of the spin curve was that it showed none of the irregularities exhibited by the laboratory curves and believed to be the result of using a diverging, narrow beam, as the light source.

Therefore, the very small systematic errors resulting from the non-constant, non-zero aspect in the second plane were ignored and

the spin curve at the maximum of the modulating envelope was taken as the angular response of the ion chambers. All the chambers on the same flight exhibited similar behaviour and therefore, where required, Figure 3.14 was taken as the angular response of an ion chamber.

3.2.8 Temperature Effects

The effect of temperature on these chambers has been reported by Carver and Mitchell (1967). Table 3.5 summarizes the relevant results from this paper.

TABLE 3.5 THE EFFECT OF TEMPERATURE ON ION CHAMBERS

Chamber	Change in Threshold in Window	Changes in Photo-ionization Threshold
SX	.21Å/°C	.03Å/°C
QT	.16Å/°C	.03Å/°C
LNO	.22Å/°C	.02Å/°C

All the shifts are towards longer wavelengths. Increasing the temperature of the SX and QT chambers also shifted the position of the maximum of their spectral response. The LNO chamber showed no variation in the central portion of its spectral response.

The effect of temperature on the spectral response of LEC and LEB chambers was not reported by Carver and Mitchell (1967), nor was it investigated in the present work. Although these chambers were flown, the data obtained from them did not warrant analysis (see Chapter 8) and therefore such information was not needed.

Because LNO chambers showed no variation in the central portion of their response it was assumed that the effect of chamber temperature on the results from these chambers was negligible. The same assumption was made for the MNO chambers.

3.2.9 Long Wavelength Sensitivity.

If the response of an ion chamber is to have a sharp long wavelength cut-off,then its response due to photoelectric emission from its metal surfaces must be negligible. For the ion chambers used in the present work this can nearly always be assumed. The lack of photoelectric emission is due to the nature of the ion chambers themselves and the way in which they were used.

The photoelectric yield of a metal surface decreases rapidly as the wavelength of the irradiating light increases (Walker *et al* 1955). In an ion chamber only the longer wavelength light reaches exposed metal surfaces as any light of energy greater than the photoionization threshold of the filling gas is strongly absorbed.

Since under operating conditions the copper bodies of these chambers are held between + 37.5v and + 45v the only exposed metal surface at voltages favourable to photoelectron emission is that of the central electrode and the back seal. The photoelectron emission source area is therefore very small and any such currents which might arise will be correspondingly small.

3.2.10 Lifetimes and Stability of Chambers.

It has previously been mentioned (Section 3.2.1) that there was quite often weeks between final calibration and checking of the instrumentation and the launching of the payload. This made long term stability (in the present context long term implies months) a requirement for the detectors. For the earlier Type I version of the detectors (Figure 3.1) such stability was not always achieved. For example, the sensitivity of a QT ion chamber on the Skylark rocket SL1005 (Chapter 5) deteriorated badly in the final weeks before launch

UNIVERSITY OF ADELAIDE LIBRARY

and information about the statistical uncertainty associated with the $n(O_2)$ measurement was lost because the $n(O_2)$ experiment was no longer duplicated.

Stability of the sensitivity of a chamber during the actual flight is essential if the introduction of large errors into the derived $n(O_2)$ is to be avoided (Chapter 6). With type I chambers such stability was not always achieved. This can be seen in the plot of the raw data received from an SX chamber on the Skylark rocket SL1207 (Figure 3.15). There is a large scale change in the received signal even when the rocket is above the absorbing layer. This phenomenon was not unique to the present work. Wildman *et al* (1969) also observed sensitivity changes in SX chambers. Their chambers, like the type I chambers of the present work, had a small id. (1.3 mm) pump-out/filling tubes.

The loss of statistical information and the introduction of unnecessary error could not be tolerated. Some means of assessing the probable behaviour of an ion chamber was required. As an initial step, a sample group of ion chambers was monitored for periods of up to two years to gain statistical information. The sample consisted of type II chambers (Figure 3.2) only, since the work of G. Bibbo (private communication) had indicated strongly that at least some of the problem might arise from the poor evacuation of the type I chambers. (Section 3.2.2). This was supported by the fact that one of the very few early ion chambers to show any long term stability was a glass one with an oversize pump stem/filling tube.

Although no formal data had been kept by the author on the type I ion chambers, laboratory notebook records implied that, with the

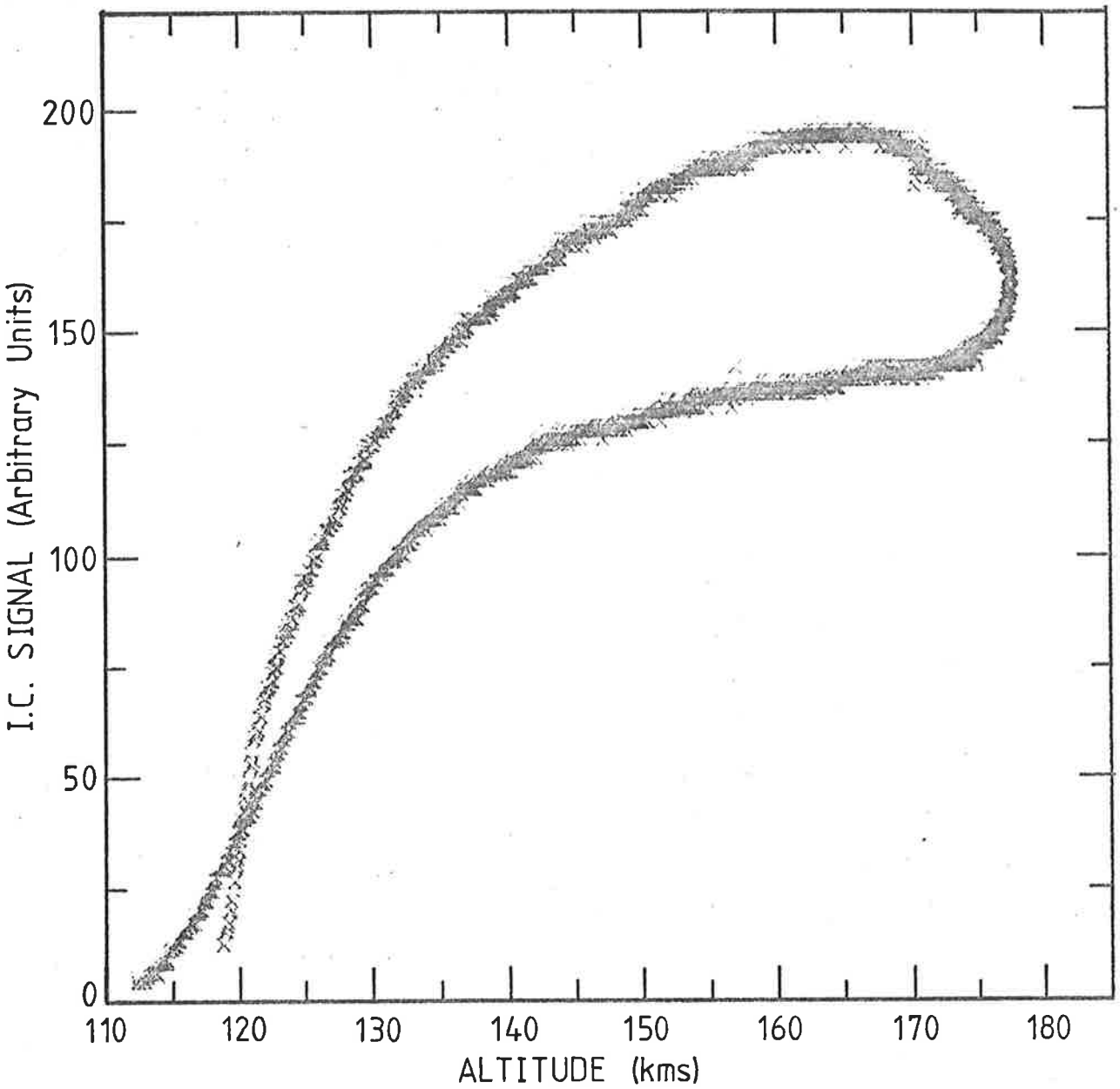

Fig 3.15 Telemetred Signal from SX 7 flown on SL 1207.
Signal levels are shown for whole flight.

odd exception, as mentioned above, lifetimes were measured in weeks. The "lifetime" in this context is defined as the period of time over which the chamber would have been sensitive enough to give a good signal to noise ratio under flight conditions.

The results with the new chambers were startlingly different. After two years a QT chamber was still at 90% of its original sensitivity. SX chambers, although showing a 50% reduction in sensitivity, were still sensitive enough for use after 12 months. Even LNO chambers, which had previously shown rapid deterioration, had sensitivities at the end of 2 years, which were at least 70% of their original absolute calibrations.

This was such a significant improvement, it was not expected that these chambers would seriously deteriorate during a prelaunch period, even though the environment would be less controlled than that which could be maintained in a laboratory. This confidence was justified by the performance of the ion chambers flown on Aerobee 13.123S (Chapter 5). Signal levels were as expected from all but one of the chambers. The two SX chambers survived re-entry and impact and when tested their sensitivities were well within the statistical range of sensitivities observed in preflight calibrations.

Because of their performance it was considered that the problem of long term stability had been solved and no general investigation was, therefore carried out. The one chamber that deteriorated under pre-launch holding conditions was the LNO chamber. Further consideration of this chamber was undertaken and it is discussed later in this section.

Overall, an improvement was also noted in the flight stability of the type II chambers (Figure 3.2) but the results were less

satisfactory than those for long term stability. The types of chamber affected by this problem had been SX, LNO and MNO chambers. Of these the SX chamber is discussed first.

Wildman *et al* (1969) suggested two different mechanisms for the changing sensitivities they observed in SX ion chambers. The first, which resulted in an apparent increase in sensitivity, was the removal, by the pumping action of the upper atmosphere, of a surface film of contamination from the window. This film supposedly built up during prelaunch preparation. The second was a de-sensitizing process resulting from the photo-dissociation of para-xylene under ultraviolet irradiation. Breakdown under irradiation has been observed in this laboratory. (Carrick, 1971).

A severe reduction in sensitivity was noted over apogee for the type I SX chamber flown on SL1207, (Figure 3.15), but it did not appear to occur in the type II SX ion chamber flown on Aerobee 13.123S (Figure 3.16). However, the Aerobee rocket, unlike SL1207, was not above the absorbing layer for any period of time and the change or lack of change in the sensitivity was hard to detect.

Because of this difficulty an attempt was made to determine trends by considering the $n(O_2)$ derived from the extinction curves. Changing sensitivities would produce anomalous densities. On the upleg section of the flight an increase in sensitivity would result in an enhancement of the derived $n(O_2)$. whereas a decrease in sensitivity would result in a reduction in the derived $n(O_2)$. These effects would be reversed on the downleg.

To be able to classify a particular value of the molecular oxygen density as an enhancement or a reduction, a standard is required. There was a large region where $n(O_2)$ could be determined either by QT

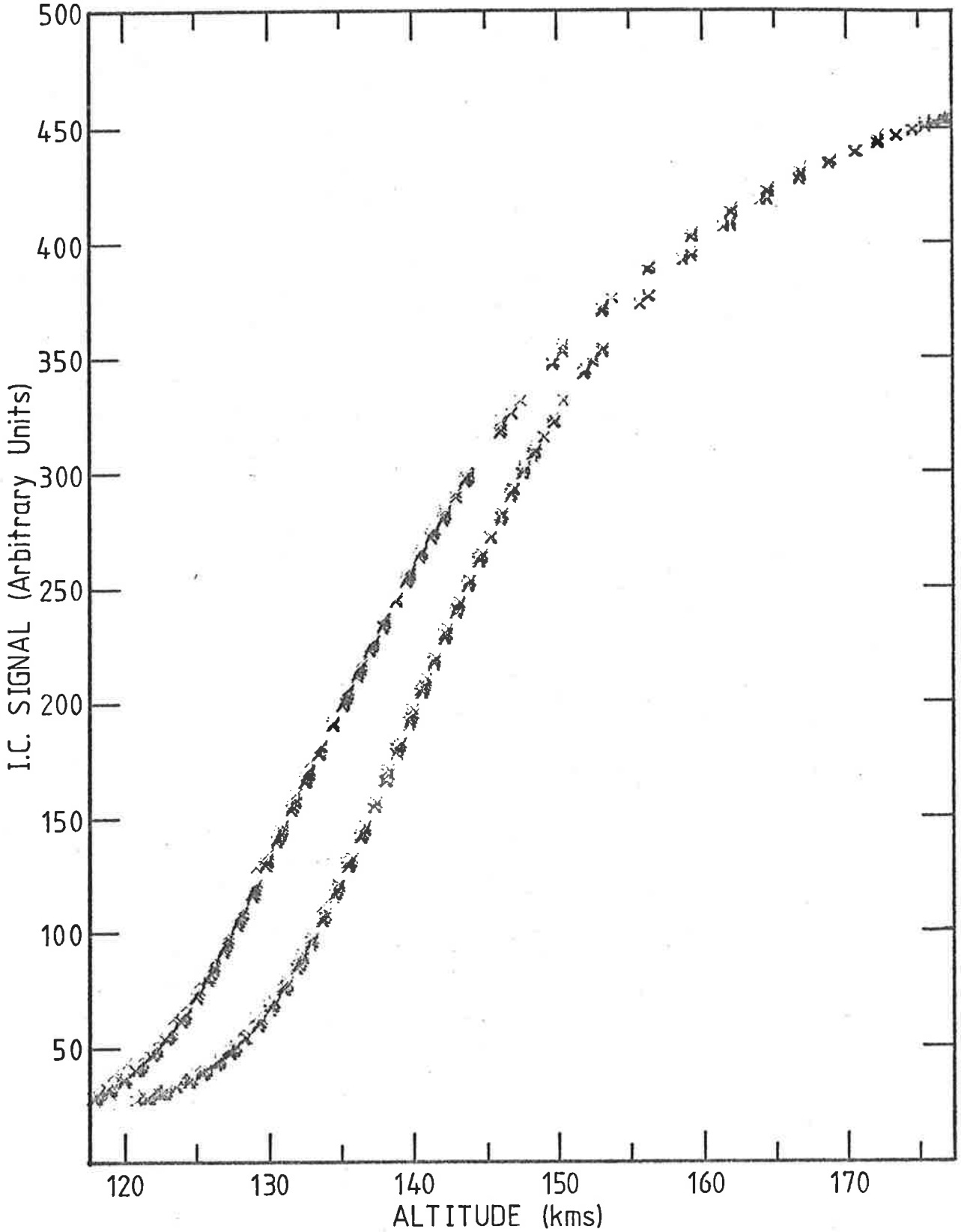

Fig 3.16 Telemetred signal from SX 202 flown on Aerobee 13.123 IS - Signal levels are shown for whole flight.

or by SX ion chambers. QT chambers, even type I, had not shown any sensitivity variations. Therefore the results from these chambers were adopted as standard.

The results were contradictory. The data from the SX chamber of SL1207 which showed such a clear decrease in sensitivity over apogee gave upleg $n(O_2)$ significantly greater than those determined from the data of the QT chamber. The SX3 chamber flown on the Skylark rocket SL1005 showed an anomalous feature between 115 to 125 kms which could only be explained by increasing sensitivity, and yet signal levels decreased by 10% over apogee. This could be explained by allowing both effects mentioned by Wildman *et al* (1969) to occur but with the de-contaminating effect temporarily masking the de-sensitization, or with the de-sensitizing region being above rather than below the absorbing layer.

Another anomaly arose in the downleg densities. Wildman *et al* (1969) had noted that the SX chambers appeared to stabilize before the downleg. This was also observed during the present work as is shown by the raw data of SX7. (Figure 3.15). However, in both flights of type I chambers (SL1005 and SL1207) the $n(O_2)$ derived from the downleg data of the SX chamber, although closer, were still above those derived from the QT chambers in the region where the two overlapped. The confidence in the QT results is high because of the symmetry of the raw data about apogee. Apogee was well above the absorbing layer for the wavelengths measured by QT chambers and any changes in the sensitivity would have shown up clearly in this portion of the flight.

The symmetry of the QT chambers about apogee invalidates, for these flights, the suggestion by Weeks (1975b)that signal variations

for the SX chambers were caused by the outgassing of water vapour from the payload. Outgassing would not have been expected on these payloads because both were purged almost continously with dry nitrogen for approximately three weeks before launch, but the QT results are the confirmation of this expectation.

The Aerobee payload did not have extensive dry nitrogen purging but signal symmetry about apogee was still observed for QT chambers. Whether this would have occurred for the type II SX chambers could not be determined because of the low apogee of the rocket. SX determined upleg O_2 densities were higher than those determined from the QT upleg data but for the better chamber (i.e. more efficient) the discrepancy wasn't as large as on the previous flights. The agreement between the various chambers on the downleg was excellent.

It was therefore concluded from the results of the three flights that SX chambers are more stable during the downleg and O_2 densities derived from the downleg data of an SX chamber are more reliable than those from the upleg. If type I chambers are used downleg results must still be treated with caution as there is some evidence of a continuing change of sensitivity. For type II chambers it would appear that stability is obtained before the downleg and downleg results are reliable and can be accepted with confidence.

The other chambers for which changing sensitivities had been reported were the LNO and MNO ion chambers. Ilyas (1976) had observed increases of up to 80% in sensitivity between the upleg and downleg sections of a rocket flight. These changes were seen in LNO and MNO chambers of both type I and type II design. He concluded,

however, that the change was not due to some intrinsic property of the chamber but resulted from atmospheric pumping removing a film of contamination from the window. It was conjectured that the film built up during the prelaunch period when a controlled environment for the ion chambers i.e. dry, oil free and dust free, was hard to maintain.

This increase in sensitivity did not occur in the chambers flown on Aerobee 13.123 IS. The MNO was stable over apogee and the LNO showed a 7% decrease. A decrease is hard to explain. It was unique to the LNO chamber, therefore it could not be due to the initial contamination of the NO filling gas. (MNO chambers were filled from the same source). Carver and Mitchell (1967) had irradiated LNO chambers but not noticed any detrimental effects over the time scale of a rocket flight. Heath and sacher (1966) had observed a large decrease in the transmission of an LiF window under electron bombardment, but their dosage rates were equivalent to a year's exposure and did not seem to indicate any deterioration from this source during a short rocket flight.

Post flight calibration showed the LNO chamber had deteriorated badly (24% to 7.5% efficiency). A possible cause for this reduction in efficiency at $L\alpha$ was the presence of water vapour within the chamber. Laboratory experience has shown that the spectral responses of ion chambers with poor efficiencylevels display features consistent with the absorption cross section values of H_2O, (Lockey, 1972; Ilyas, 1976). If the chamber was highly contaminated at launch, and this cannot be proven since lack of facilities prevented the checking of spectral responses during preflight preparation, then water vapour must have diffused through the LiF window since the spectral response taken during the calibration period did not indicate an initially high water vapour level.

If water vapour was present and it had diffused through the LiF window then it would appear reasonable to assume

(a) Some water vapour was adsorbed on to the walls of the chamber,

(b) There were significant amounts of water vapour in the LiF window.

This suggests a possible explanation for the small decrease in sensitivity observed over the apogee. During the initial stages of the flight the temperature of the chambers rose slightly (5°C to 10°C). This would cause some of the water absorbed on to the walls to be given off. The change in temperature along with the atmospheric pumping would alter the diffusion coefficient of the water vapour in the crystal. This may introduce more water vapour into the chamber. With the window having a vacuum on one side instead of one atmosphere, there would be a change in mechanical deformation. This might release water vapour into the chamber.

That is, it is argued that during flight there could conceivably be an increase in the amount of free water vapour within the chamber. Water vapour absorbs more strongly than NO at Lα, (Watanabe *et al*, 1953) but the ionization potential of H_2O (982.5Å - Herzberg, 1966) is well below the transmission limit of an LiF window. At wavelengths greater than the window transmission limit the dominant process is photo-dissociation, (Lee *et al*, 1978), and there will be no contribution to the signal from this source. This competing absorption process will, however, decrease the amount of light available to the NO with a consequent decrease in signal. The magnitude of the increase in contamination needed to explain the decrease in sensitivity is only 2% in absolute terms.

The effects mentioned may not be sufficient to produce a 2% change especially over the time scale of a rocket flight. The explanation is largely conjectural. It was, however, beyond the scope of the present work to investigate this phenomenon experimentally since the information was not needed to derive $n(O_2)$. The error introduced into the derived $n(O_2)$ by the sensitivity change is small compared with that from other sources (Chapter 4). In addition $n(O_2)$ densities could be obtained over the same altitude range by using MNO chambers which displayed much greater long term and inflight stability.

In summary, it is suggested that the lack of stability in QT and SX chambers was caused by insufficient evacuation of the chambers before filling. The improvement of the chambers after the introduction of the large pumpout tube supports this concept. LNO and MNO chambers of the new design also showed significant improvement. However, deterioration of LNO chambers was still observed if they were removed from a dry environment. The most significant cause of this deterioration is likely to be contamination of the filling gas by water vapour diffusing through the window.

These results imply that with the introduction of the large pumpout/filling tube and the use of MgF_2 windows rather than LiF windows, a range of detectors can be built which are capable of measuring $n(O_2)$ throughout the lower thermosphere and which are stable over long periods of time.

3.3 THE SPECTROPHOTOMETER

3.3.1 Description of Spectrophotometer

The spectrophotometer was designed to be an alternative to the SX ion chamber for measuring radiation in the wavelength range

λ 1425Å - λ 1490Å. It was hoped that comparisons of the extinction curves measured by the spectrophotometer and the ion chambers would remove some of the ambiguities surrounding the SX ion chamber results.

The instrument was flown on the Skylark rocket, SL1005. This rocket was fitted with a pointing control capable of locking on to the sun with an accuracy of ± 1 min of arc . Therefore a wide flat angular response did not have to be a feature of the design. Space was, however, limited on this rocket and the spectrophotometer was restricted in both length and width.

Figure 3.17 is a sketch of the instrument flown. The restrictions in size led to the use of mirrors to fold the optical path. The first mirror was adjustable, while the second and third mirrors were glued on to 45° planes, milled on the solid aluminium blocks, which held the motor and the grating. A third aluminimum block was milled out to accommodate the solar blind, EMR 541G - 05M - 14 photomultiplier used as a detector. These three blocks formed a rigid base for the instrument. The top section, which held the adjustable mirror,was an aluminium plate box which slid over the 3 milled blocks and was attached to the base. The box was kept rigid by the frame of the experimental package (Figure 5.2 b). To reduce light scattering the interior of this section was painted ultra matt black.

Light entered through an aperture in the top section. It was dispersed by the grating. The resultant spectrum was reflected by the adjustable mirror towards the base of the instrument. Just in front of the first 45° angled mirror, a pair of razor blades formed a slit. This slit allowed only the light from a small section of the spectrum to reach the detector. Adjusting the angle of the mirror altered the wavelength

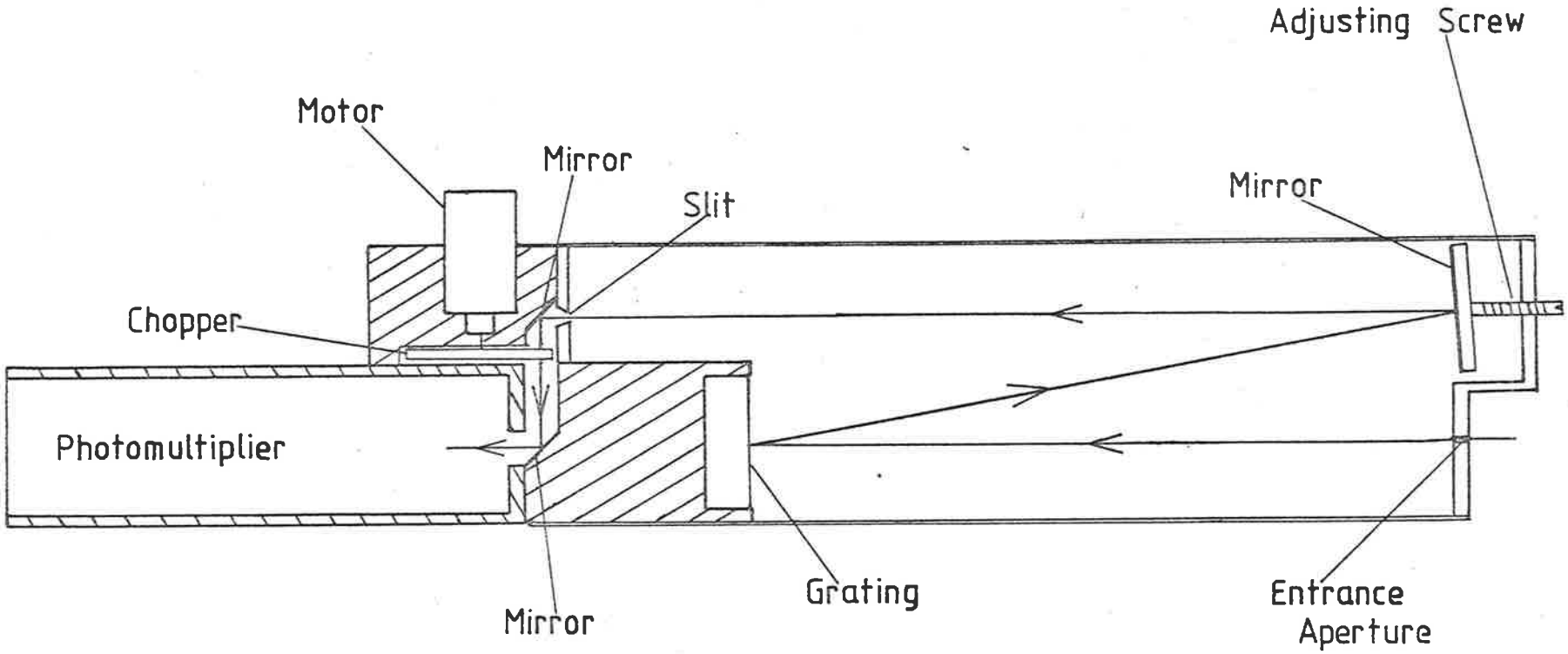

Fig. 3.17 Schematic of Spectrophotometer.

of the light falling on the slit and thus, the wavelength of light reaching the detector. A toothed wheel driven by a geared down Escap 15 motor at 1 rev/sec, was placed between the two 45° angled mirrors. This wheel chopped the light 3 times every revolution. During flight therefore, a check was made on the "dark current"approximately every 1/3 of a kilometre. The "dark current" was later subtracted from the signal to obtain a truer measurement of the signal due to the incoming radiation.

3.3.2 Calibration of Spectrophotometer.

3.3.2.1 Determination of the Passband.

If the spacing of a grating is known then the angle (θ) at which the first order maximum of light of any particular wavelength occurs may be calculated from

$$d \sin \theta = \lambda \qquad 3.8$$

where d is spacing between the lines of the grating. The reflection grating used in the spectrophotometer was nominally ruled at 1200 lines/mm. For this spacing the first order maximum of light at λ 1450Å , the desired midpoint of the instruments spectral response,would be at 10.02° to the normal to the grating. The passband was set up by aligning the mirror so that light coming from the grating at this angle was reflected through the middle of the slit. The required optical path is traced in Figure 3.17.

A laser beam was used to achieve the alignment. The photomultiplier was removed and the laser positioned such that the beam traced the shown optical path in reverse until it reached the grating. At the grating most of the energy of the beam was specularly reflected. The angle between the normal to the grating and the reflected beam was

measured. The mirror was adjusted until the measured angle of reflection was 10.02°.

Measurement of the spectral response at this mirror setting showed that the grating was not ruled at 1200 lines/mm and therefore an iterative process was used. This was as follows:

(a) the spectral response (Section 3.3.2.2.) of the instrument was measured,

(b) using the value of θ calculated from the previously assumed spacing and the wavelength, λ, of the maximum response of the instrument d was re-calculated from 3.8,

(c) the new value of d was used to re-calculate, from 3.8, the value of θ for light at λ 1450Å,

(d) the mirror of the spectrophotometer was adjusted to accommodate the new angle,

(e) (a) - (d) were repeated until the spectral response measured in (a) was satisfactory.

3.3.2.2. The Spectral Response and the Absolute Quantum Efficiency.

A schematic of the experimental equipment for the calibration of the spectrophotometer is shown in Figure 3.18. Radiation from the ½ metre McPherson monochromator passed through the monitoring system (Section 3.2.6.1) along the pipe and into the tank. The Spectrophotometer was inside the tank and was aligned such that its long axis was parallel to the direction of travel of the beam. At this distance (approximately 3 metres) from the exit slits of the monochromator

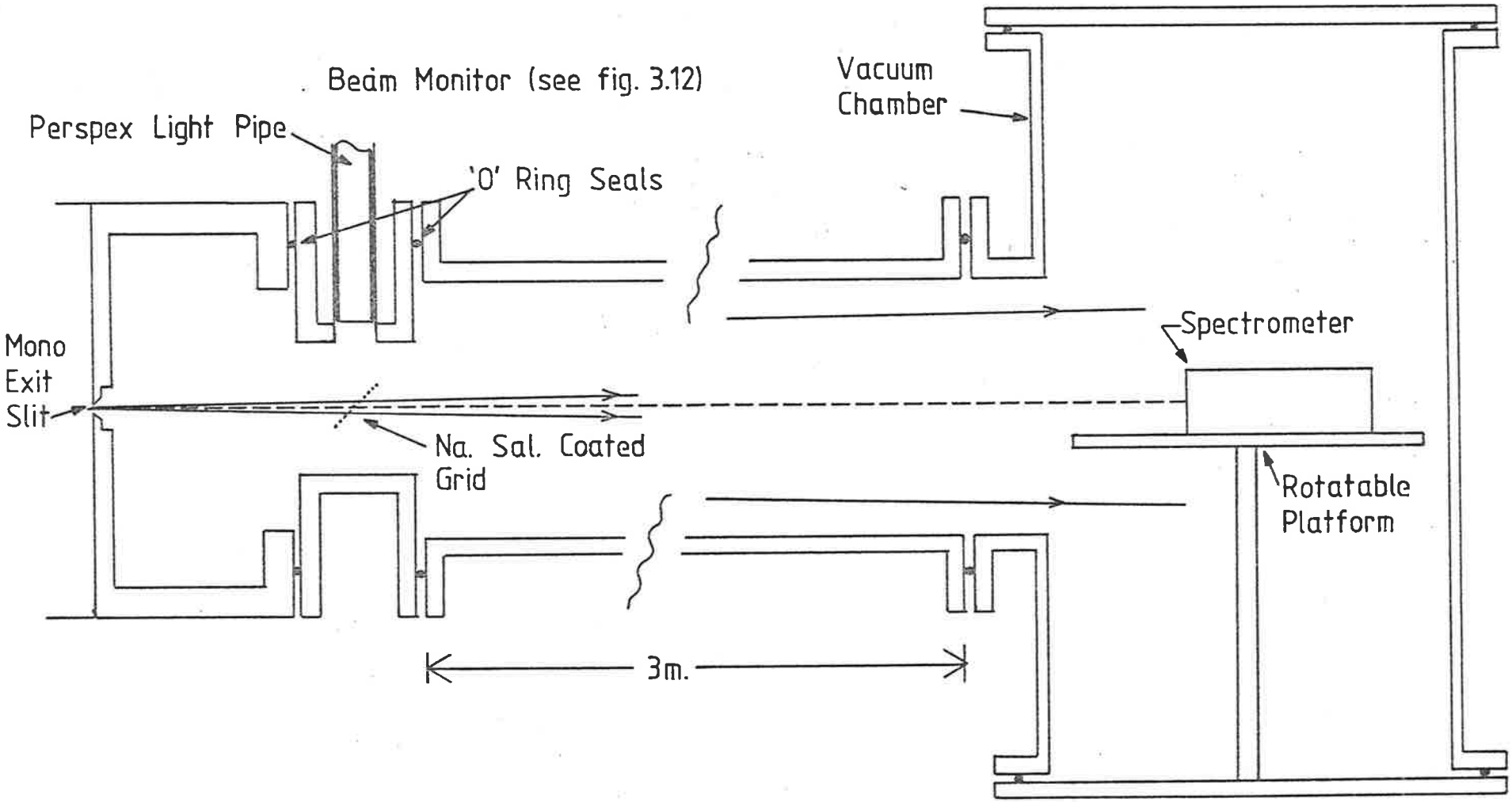

Fig. 3.18 Schematic of Experimental Apparatus for Calibration of Spectrophotometer.

the diverging beam was broad enough to irradiate the whole of the entrance aperture. (O'Connor, 1973).

Electrical connections were made through glass to metal seals in the lid of the tank. The EMR photomultiplier was run at - 3000V. The signal from the detector was measured on a Keithley 610C. Before taking a spectral response the pipe and tank were evacuated to 10^{-5} Torr.

The signals from the monitor and the spectrophotometer were each corrected for the dark current of their respective detectors. For the monitor signal, this correction was of the order of 10^{-10} amps, while for the spectrophotometer, the correction was of the order of 10^{-12} amps.

The spectral response of the spectrophotometer was the ratio of the corrected signal from that instrument over the corrected signal from the monitor as a function of wavelength. There is a small error in this calibration. The incoming light is not parallel but diverging. To estimate the effect of this divergence the spectral response of the instrument was also measured when the direction of the beam and the long axis of the instrument differed by $\pm \frac{1}{2}°$ and ± 1. These angles were much greater than the estimated divergence ($\frac{1}{4}°$) seen by the spectrophotometer. The similarity of the spectral responses at $\pm \frac{1}{2}°$ to that at $0°$ led to the conclusion that this source of error was negligible. It was ignored. The spectral response is shown in Figure 3.19.

The last step in the calibration was absolutely scaling the spectral response. This was done by comparing the signal from the spectrophotometer to that from a standard detector. The standard used was a glass bodied, LNO ion chamber, which had already been used to

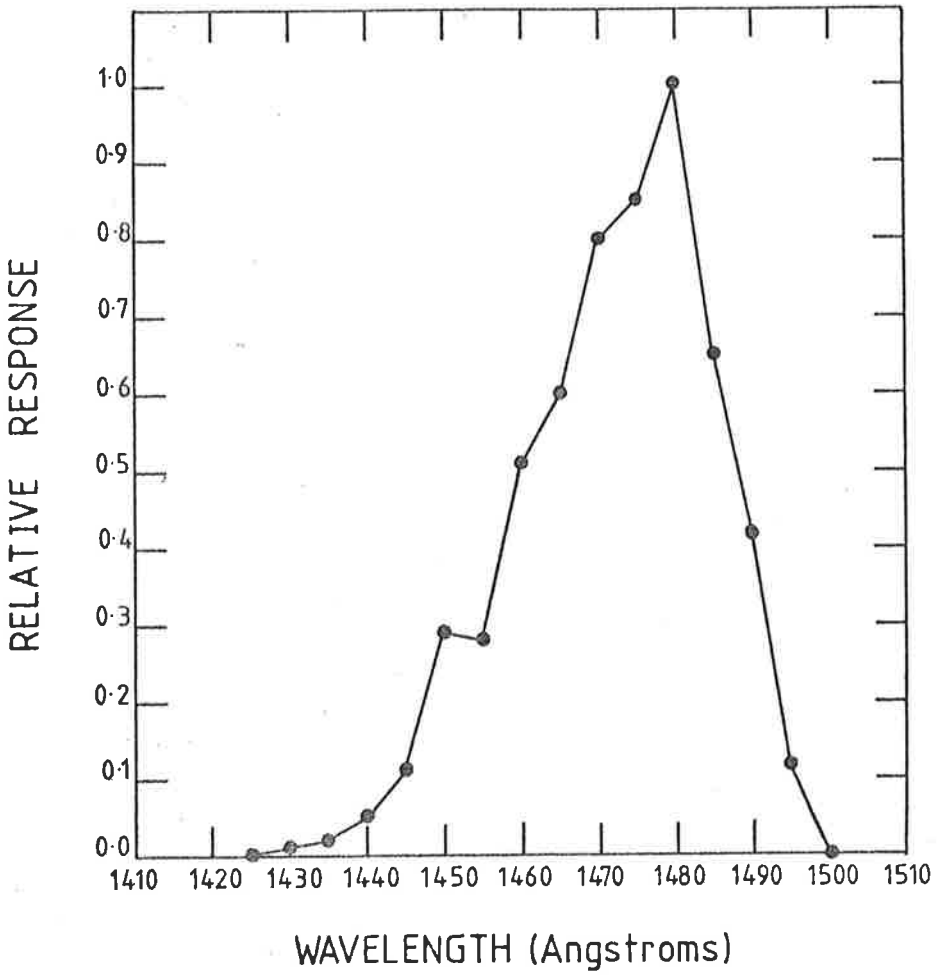

Fig 3.19 Spectral Response of Spectrophotometer.

calibrate the ion chambers to be flown on the same rocket. The wavelength scale of the monochromator was adjusted so that the emitted light was at the wavelength of the maximum response of the spectrophotometer. The signal from the spectrophotometer and from the beam monitor were noted. Then the spectrophotometer was replaced with the LNO chamber and the monochromator adjusted so that $L\alpha$ was emitted. The signals from the beam monitor and the ion chamber were noted. Where necessary corrections were made for the dark current signals of the detectors. Using these corrected signals, the quantum efficiency (Q_s) of the spectrophotometer was given by :

$$Q_s = Q_L \cdot \frac{I_s}{I_L} \cdot \frac{M_L}{M_s} \cdot \frac{A_L}{A_s} \qquad 3.9$$

where Q_L is the efficiency of the standard at $L\alpha$,

I_L is the signal from the standard when irradiated with $L\alpha$,

I_s is the corrected signal from the spectrophotometer when irradiated with light at the wavelength of its max. response,

M_L & M_s are the corrected beam monitor signals of the emitted beam at the time when I_L & I_s respectively were measured,

A_L is the window area of the ion chamber,

A_s is the area of the entrance aperture of the spectrophotometer.

A_L & A_s are introduced because at this distance only part of the beam is being observed and therefore the amount of light seen will depend on the size of the "aperture" of the instrument.

The discussion in 3.2.6.3 and 3.2.6.4, on the effect of the sodium salicylate of the monitoring system on measured spectral responses and quantum efficiencies,is also relevant here. It was stated that across the passband of a detector the changing sensitivity of the sodium salicylate did not significantly affect the measured spectral response (Section 3.2.6.3). The measured spectral response could therefore be taken as the best estimate of the true spectral response. Since the instrument was not used to obtain an absolute measurement of the solar flux the inaccuracy of the measured absolute quantum efficiency is not important. This parameter was only used to obtain estimates for the expected signal levels in flight so that amplifier levels could be set. For this purpose it was sufficient if the efficiency was known to an order of magnitude.

3.3.3 Temperature Effects

The dark current of a photomultiplier virtually consists of the thermal emission current of its photocathode. This current increases rapidly with any increase in the temperature of the multiplier. No attempt was made to insulate the photomultiplier of the spectrophotometer from the heating the payload would experience during flight. However, by checking the dark current every 1/3 kilometre, (Section 3.3.1) the consequences of such heating could be measured and the data corrected for this effect.

CHAPTER FOUR

THE METHODOLOGY

This chapter looks at the methodologies that were developed to analyze the data provided by the instrumentation described in Chapter 3. All the methodologies were derived from the Beer-Lambert law describing the absorption of radiation in a gas.

Section 4.1 shows the development of this law into forms suitable and convenient for use with the type of data obtained during the rocket experiments. Sections 4.2, 4.3 and 4.4 discuss in detail the factors of the basic equation derived in 4.1 and in particular Section 4.4 shows how the methodologies differed in their approach. Included in these sections is an attempt to isolate, and, where possible, quantitatively assess the sources of uncertainties associated with the methodologies. Some comment is also made as to how these sources of uncertainty have been handled by other research groups.

One methodology was chosen and used to analyze all the data available. Section 4.5 gives a brief rationale to the choice and Section 4.6 summarizes the magnitudes of the uncertainties introduced by the analysis technique.

4.1 THE BASIC EQUATIONS

Lambert's Law describes the absorption of a parallel beam of monochromatic light by an infinitesimally thin layer of absorbing material dS. The amount of absorped radiation $d\phi$ is given by

$$d\phi = -\mu \phi \, dS \tag{4.1}$$

where ϕ is the flux, measured in photons/sec/unit area, falling on the

layer dS, and the constant of proportionality, μ, is called the absorption coefficient. Beer found that μ was proportional to n the number density of the absorbing species

$$\mu = n.\sigma \tag{4.2}$$

This gives σ the dimensions of area and he called it the absorption cross-section. Therefore

$$d\phi = -\sigma.n.\phi.dS \tag{4.3}$$

Equation 4.3 is an expression of the Beer Lambert Law which can be used to describe the absorption of solar radiation in the atmosphere as long as the absorption can be attributed to one species. n becomes the altitude dependent concentration of the absorbing species, σ becomes $\sigma(\lambda)$ the wavelength dependent absorption cross-section and dS is an increment in the optical path length as is shown in Figure 4.1. dS is measured in the direction shown. dS can be expressed in terms of dz.

$$dS = -Fdz \tag{4.4}$$

where F is known as the "optical depth factor" and allows for the obliquity of the optical path (see Section 4.3). The negative sign arises because dz is defined upwards. Equation 4.3 therefore becomes

$$d\phi = \sigma(\lambda).\ n(z).\phi(\lambda,z).F.dz \tag{4.5}$$

where $\phi(\lambda, z)$ is still the incident flux on the layer but has been written to indicate it's independence of λ and z.

In the limit, equation 4.5 describes the absorption taking place at any height z = h. (see Figure 4.1). However, this only considers monochromatic radiation. The detectors used in the present work were

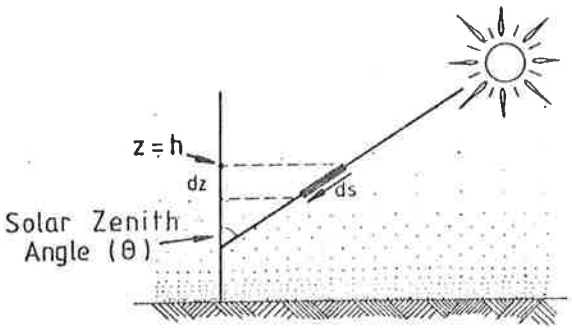

Fig. 4.1 The relationship between the lengths ds and dz in a plane stratified atmosphere.

(adapted from Fig. 17.2 of Banks and kockarts, 1973)

broad band. Any change in signal observed in them will be due to the absorption of a band of radiation. Equation 4.5 is still relevant and is used as shown below.

The signal $I(z)$ of an ion chamber will be given by

$$I(z) = \beta \int_{\lambda_1}^{\lambda_2} \varepsilon(\lambda).\phi(\lambda, z)d\lambda \qquad (4.6)$$

where $\phi(\lambda, z)$ is the flux at z. $\varepsilon(\lambda)$ is the relative sensitivity of the chamber to radiation at λ.

λ_1, λ_2 are the passband limits of the chamber and β, the constant of proportionality, allows for the absolute sensitivity of the chamber, the window area and the calibration of the amplifier. Therefore,

$$\frac{d(I(z))}{dz} = \beta \int_{\lambda_1}^{\lambda_2} \varepsilon(\lambda) \frac{\partial\phi(\lambda, z)}{dz} d\lambda \qquad (4.7)$$

Using Equation 4.5 =

$$\beta \int_{\lambda_1}^{\lambda_2} \varepsilon(\lambda).\ \sigma(\lambda).\ n(z).\ F.\ \phi(\lambda, z).d\lambda$$

$$= \beta.\ n(z).\ F. \int_{\lambda_1}^{\lambda_2} \varepsilon(\lambda).\ \sigma(\lambda).\phi(\lambda, z)d\lambda$$

$$\therefore \quad \frac{1}{I} \frac{dI(z)}{dz} = \frac{\beta.\ n(z).F. \int_{\lambda_1}^{\lambda_2} \varepsilon(\lambda).\sigma(\lambda).\phi(\lambda, z).d\lambda}{\beta \int_{\lambda_1}^{\lambda_2} \varepsilon(\lambda).\phi(\lambda, z).d\lambda}$$

This can be written as

$$\frac{1}{I} \frac{dI(z)}{dz} = n(z).\ F.\ \sigma_{EFF}(z) \qquad (4.8)$$

where $$\sigma_{EFF}(z) = \frac{\int_{\lambda_1}^{\lambda_2} \varepsilon(\lambda).\ \sigma(\lambda).\ \phi(\lambda,\ z).d\lambda}{\int_{\lambda_1}^{\lambda_2} \varepsilon(\lambda).\ \phi(\lambda,\ z)\ d\lambda} \tag{4.9}$$

(It can be seen that this definition of σ_{EFF}, the effective absorption cross-section, corresponds to that already given in Chapter 2. This parameter is further discussed in Section 4.2).

Therefore the local concentration of the absorbing species can be found from the behaviour of a broad band detector. That is

$$n(z) = \frac{1}{F} \cdot \frac{1}{\sigma_{EFF}(z)} \cdot \frac{1}{I} \cdot \frac{dI}{dz} \tag{4.10}$$

This derivation is only valid if it can be assumed that the absorption is all due to a single species, and equation 4.10 was used to determine $n(O_2)$ from the data of broad band rocket-borne detectors by assuming that solar radiation, from $L\alpha$ to 1650Å, was absorbed only by molecular oxygen. (Other atmospheric constituents do absorb this radiation and the magnitude of the error introduced by the assumption is discussed in Section 4.2.7).

The differential form was not always the form required for data analysis. An alternative form was easily derived. Equation 4.10 can be expressed as

$$\frac{dI(z)}{I} = n(z).\ F.\ \sigma_{EFF}(z).dz \tag{4.11}$$

Therefore the signal I at the height h can be found by integration

$$\int_{I(\infty)}^{I(h)} \frac{dI(z)}{I} = F \int_{\infty}^{h} n(z).\ \sigma_{EFF}(z).dz.$$

where $I(\infty)$ is the signal observed at the top of the atmosphere.

$$\ln \frac{I(h)}{I(\infty)} = - F \int_h^{\infty} n(z).\ \sigma_{EFF}(z).dz.$$

Taking the exponential of both sides,

$$\frac{I(h)}{I(\infty)} = e^{- F \int_h^{\infty} n(z).\ \sigma_{EFF}(z).dz.}$$

That is

$$I(h) = I(\infty)\ e^{- F \int_h^{\infty} n(z).\ \sigma_{EFF}(z).dz} \qquad (4.12)$$

If it is possible to choose an interval Δh at h over which $\sigma_{EFF}(z)$ may be regarded as a constant, σ_E, then equation 4.12 can be written as

$$I(h) = I(h + \Delta h)\ e^{- F.\ \sigma_E.\ \int_h^{h+\Delta h} n(z).\ dz} \qquad (4.13)$$

If the interval Δh is chosen as the resolution of the analysis, i.e. $n(z)$ is considered to be constant over Δh then calling the concentration at h, N

$$I(h) = I(h + \Delta h)\ e^{- (F.\ \sigma_{EFF}.\ N.\ \Delta h)} \qquad (4.14)$$

This was the basic equation used in the methodology described in Section 4.4.4.

4.2 THE EFFECTIVE ABSORPTION CROSS-SECTION

4.2.1 Introduction

The effective absorption cross-section was defined by equation 4.9, i.e.

$$\sigma_{EFF}(z) = \frac{\int_{\lambda_1}^{\lambda_2} \varepsilon(\lambda).\ \sigma(\lambda).\ \phi(\lambda,\ z).\ d\lambda}{\int_{\lambda_1}^{\lambda_2} \varepsilon(\lambda).\ \phi(\lambda,\ z).\ d\lambda}$$

It is an essential parameter in obtaining $n(O_2)$ from the data of broad band detectors and will, because of $\varepsilon(\lambda)$ and λ_1, λ_2, be unique to each chamber.*

In the following, how σ_{EFF} is calculated is described (Section 4.2.2). From the definition, σ_{EFF} will obviously be affected by uncertainties in $\phi(\lambda,\ z)$, $\sigma(\lambda)$ and $\varepsilon(\lambda)$, and the likely magnitude of the uncertainties associated with these parameters and the uncertainty they will introduce into σ_{EFF} is discussed (Sections 4.2.3, 4.2.4 and 4.2.5). Special consideration is given to the $L\alpha$ chambers in Section 4.2.6 where the validity of using the effective absorption cross-section, for $L\alpha$ alone,as the effective absorption cross-section for the chamber is investigated. In the last subsection of 4.2 an assessment is made of the magnitude of the systematic error introduced if it is assumed that the only atmospheric gas to significantly absorb the wavelengths of interest is O_2.

A summary is made at the end of each of the sub-sections 4.2.2 and 4.2.7. Where possible this sets out, for each type of ion chamber, the magnitude of the introduced uncertainty, or systematic error.

4.2.2 Calculation of $\sigma_{EFF}(z)$

To calculate $\sigma_{EFF}(z)$ numerical methods were used to approximate the integrals of equation 4.9. The numerical integration was based on a weighted averaging of 5 points. Allowance was made for the extreme regions where 5 points may not have been available by

*Note that in this chapter, the spectrophotometer (Section 3.3) will not be referred to separately. Unless otherwise stated the collective terms chambers/ion chambers/detectors also specifically encompasses the spectrophotometer. In addition, comments made for the SX ion chambers apply to the spectrophotometer as well.

including in the algorithm expressions for 2, 3 and 4 point numerical integration.

The values of the expressions $\sigma(\lambda).\varepsilon(\lambda).\phi(\lambda, z)$ and $\varepsilon(\lambda).\phi(\lambda, z)$ vary reasonably smoothly as λ varies from λ_1 to λ_2, the band-pass limits. Therefore a smoothly varying, analytical function was chosen to test the algorithm, and, it was found that, for this function ($\sin\theta$ was used), the difference between the analytical integration and the numerical approximation was $< .2\%$.

Subsequent investigation revealed that the choice of algorithm was not critical for the calculation of σ_{EFF}. The parameter was also calculated using a simple, unweighted summation, only accurate to 12%, to evaluate the integrals. The difference between the two evaluations was negligible at all heights. The algorithm was, however, retained, since it gave a better estimate of the maximum signal that could be expected in flight. This improved estimate allowed better optimization of amplifier settings.

$\sigma_{EFF}(z)$ depends on the flux $\phi(\lambda, z)$. With broad band detectors the function $\phi(\lambda, z)$ cannot be found from flight data but must be estimated. In the calculation of $\sigma_{EFF}(z)$ for QT and SX chambers, $\phi(\lambda, z)$ was estimated in the following manner.

$\phi(\lambda, \infty)$, the flux at the top of the atmosphere,was assumed to be that given by Delaboudiniere *et al* (1977). In practice it was found that $\phi(\lambda, \infty)$ was still valid at 200 kms, since for the wavelength ranges covered by the detectors ($\lambda\lambda$ 1425Å $\rightarrow$ 1490Å and $\lambda\lambda$ 1560Å $\rightarrow$ 1650Å) no significant absorption occurred above this height.

A model atmosphere was assumed (CIRA, 1972) and $\phi(\lambda, z)$ was obtained for all required altitudes by repeated evaluations of

$$\phi(\lambda, h_i) = \phi(\lambda, h_{i+1})\, e^{-(F.\sigma(\lambda).N.\Delta h)} \qquad (4.15)$$

where $h_{i+1} - h_i = \Delta h$

4.15 is similar to 4.14, but because individual wavelengths rather than a broad band are being looked at it is not necessary to use σ_{EFF}.

The optical depth factor, F, (Section 4.3) was taken to be 1; $\sigma(\lambda)$ were assumed to be as measured by Blake *et al* (1966) (see Section 4.2.3 for further discussion); N was the local concentration of O_2, as given by the model, and Δh was usually taken to be 1 km. Once $\phi(\lambda, z)$ had been obtained the effective abs. cross-sections of the QT and SX ion chambers were calculated by use of the numerical methods already discussed.

These calculations gave the effective absorption cross-section as a function of altitude. It was found that the effective absorption cross-sections calculated for the SX chambers, although unique to each chamber, did not vary greatly between chambers. In addition σ_{EFF} for each SX chamber was almost constant over the altitude region in which they operated and could, without the introduction of significant error, be considered as such. QT chambers, however, varied strongly with altitude and from chamber to chamber (Figure 4.2).

The change with altitude in the σ_{EFF} of a QT ion chamber arises because of the differential absorption of solar radiation. The absorption cross-section of molecular oxygen varies strongly for the wavelengths within the pass-band of this chamber. (Figure 4.3). Radiation for which σ is high will be absorbed first, biasing $\phi(\lambda, z)$ towards radiation for which the absorption cross-section of molecular oxygen is lower. This has already been referred to as radiation hardening in Chapter 2 and its effect is a decrease in σ_{EFF} as z decreases.

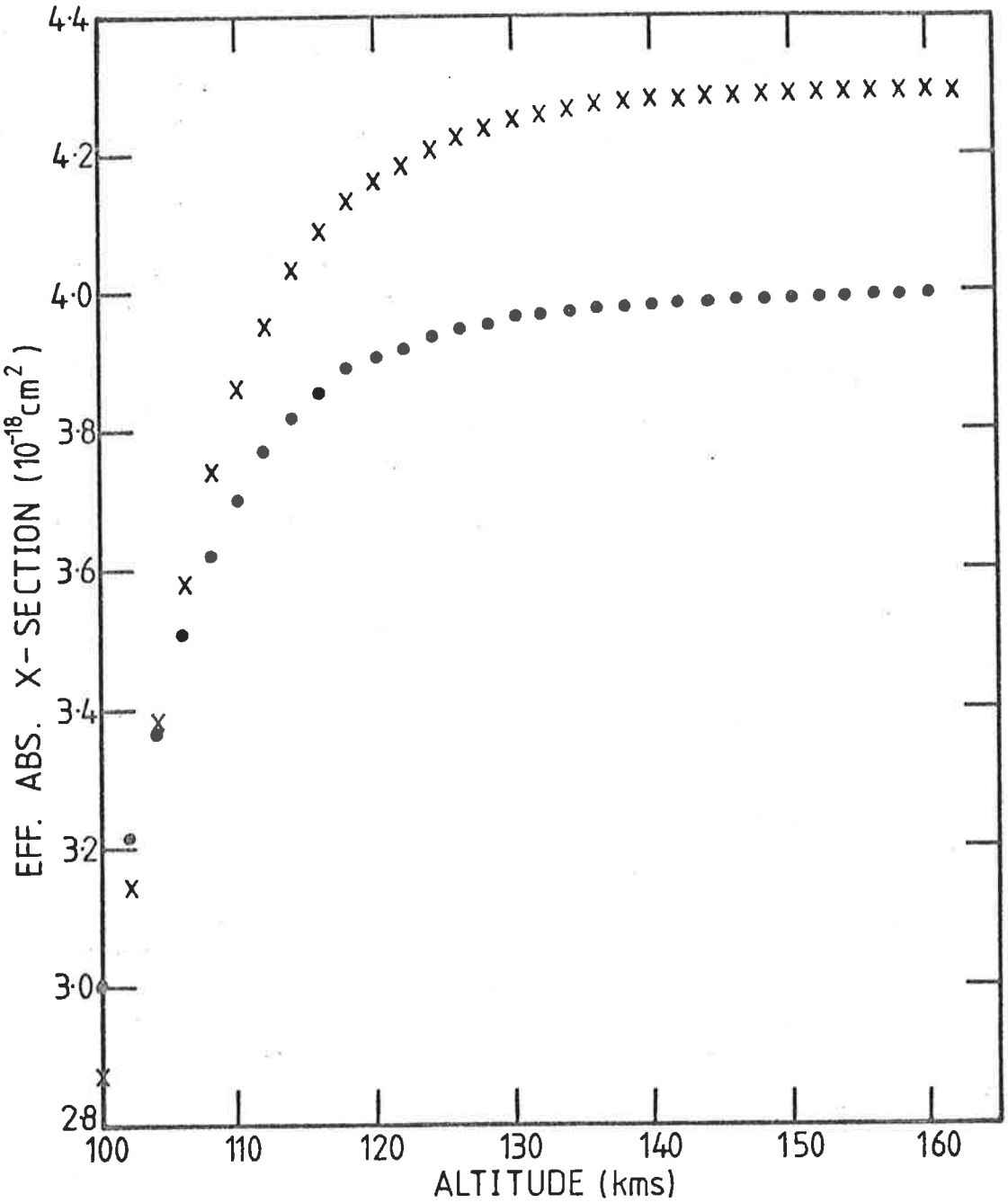

Fig. 4.2 Comparison of σ_{EFF} for two different ion chambers.

X - QT204 - SL 1005

● - QT1 - SL 1207

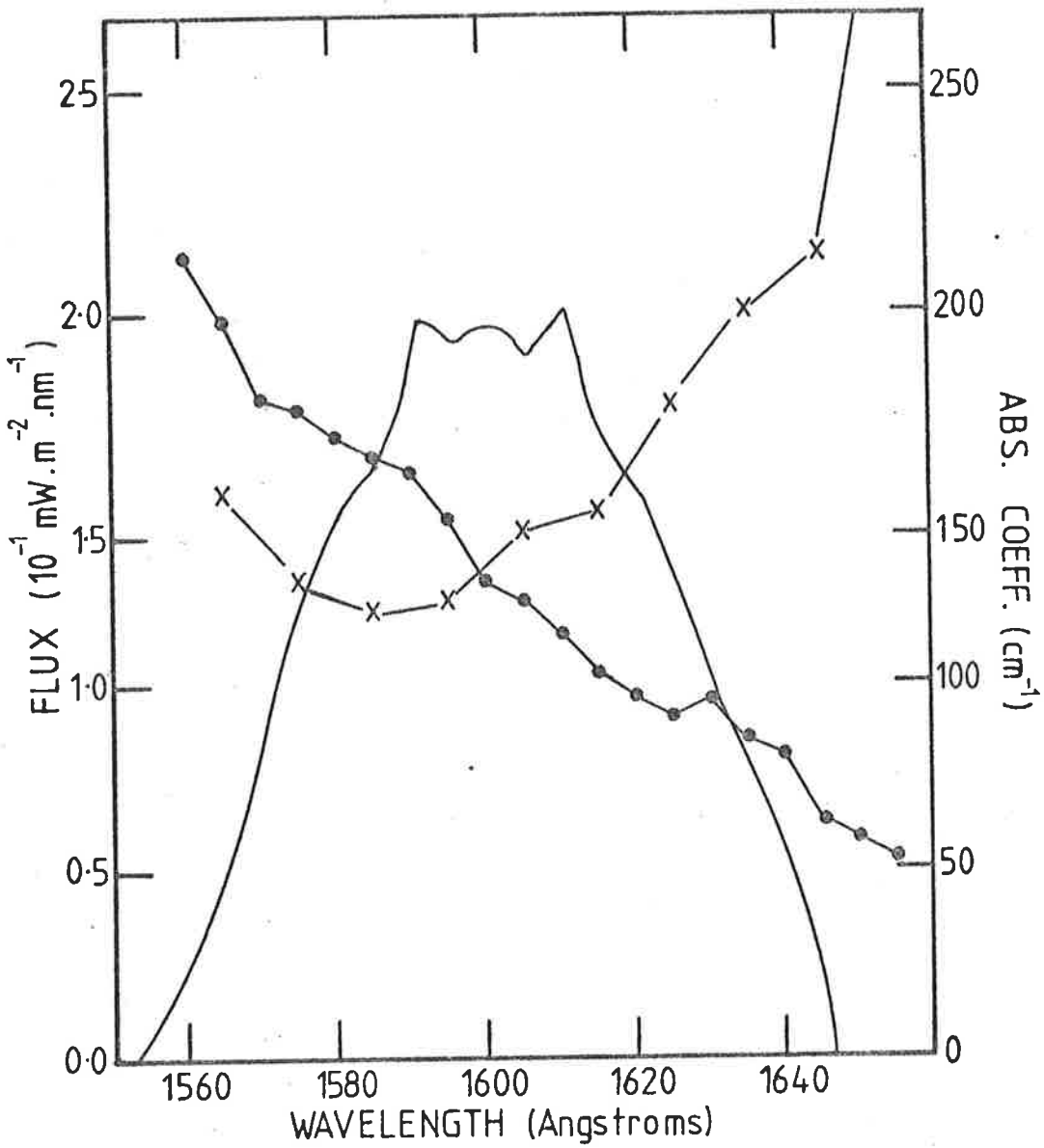

Fig. 4.3 Factors influencing σ_{EFF} for a QT ion chamber. In example given

—●-- Abs. X-section (Blake *et al*, 1977)

—X-- Ave flux from Delaboudiniere *et al* (1977)

——- Normalised response curve of ion chamber.

Because the effective cross-section of an SX ion chamber could be taken as $\sigma_{EFF}(\infty)$ the adopted value was independent, at all altitudes, of the values chosen for N and F. This was not so for the strongly varying effective cross-section of a QT ion chamber. The numerical value obtained for any particular height was strictly only valid for the assumed conditions; e.g. the model $n(O_2)$ profile chosen. But σ_{EFF} was required to enable experimental determination of $n(O_2)$. An effective absorption cross-section dependent on a model profile for $n(O_2)$ could not be used without the development of iterative procedures.

It was more convenient to develop another variable which could be used to express the effective absorption cross-section in a form that was independent of the assumed model. A variable known as the extinction coefficient, j, was used. For an ion chamber at $z = h$, j is defined as

$$j(h) = \frac{I(h)}{I(\infty)} \tag{4.16}$$

where $I(h)$ is the ion chamber signal at h and $I(\infty)$ is the ion chamber signal at the top of the atmosphere. The justification behind the use of j is given in the following.

For radiation at the wavelength λ_i an expression can be found which relates the flux at $z = h$, $\phi(\lambda, h)$ with the flux at top of the atmosphere, $\phi(\lambda_i, \infty)$. Ignoring the possible contribution of other gases to the absorption of radiation at λ_i where $1050Å < \lambda_i < 1660Å$, (see Section 4.2.7 for discussion on the probable magnitude of these contributions) equation 4.5 can be rewritten as

$$\frac{d\phi(\lambda_i, z)}{\phi(\lambda_i, z)} = F.\ n(z).\ \sigma(\lambda_i).\ dz \tag{4.17}$$

where $n(z)$ is taken as the local concentration of molecular oxygen [For explanation of other symbols see Page116]. The flux at $z = h$ can be found by integration

$$\int_{\phi(\lambda_i,\infty)}^{\phi(\lambda_i,h)} \frac{d\phi(\lambda_i,z)}{\phi(\lambda_i,z)} = \int_{\infty}^{h} F.\ n(z).\ \sigma(\lambda_i).\ dz$$

$$= -\ \sigma(\lambda_i) \int_{h}^{\infty} F.\ n(z).\ dz \qquad (4.18)$$

The R.H. integral is equivalent to the total number of O_2 molecules in the absorbing path above h. Calling this quantity $N_T(h)$ equation 4-18 becomes

$$\ln \frac{\phi(\lambda_i,h)}{\phi(\lambda_i,\infty)} = -\ \sigma(\lambda_i).\ N_T(h) \qquad (4.19)$$

Taking the exponential of both sides of 4.19

$$\frac{\phi(\lambda_i,h)}{\phi(\lambda_i,\infty)} = e^{-\ \sigma(\lambda_i).\ N_T(h)}$$

i.e. $$\phi(\lambda_i,h) = \phi(\lambda_i,\infty).\ e^{-\ \sigma(\lambda_i).\ N_T(h)} \qquad (4.20)$$

Using 4.6 and 4.20, the signal of an ion chamber at $z = h$ can therefore be expressed as

$$I_z(h) = \beta \int_{\lambda_1}^{\lambda_2} \varepsilon(\lambda).\ \phi(\lambda,\infty).\ e^{-\ \sigma(\lambda).\ N_T}\ d\lambda \qquad (4.21)$$

From the definition of j (4.16)

$$j(h) = \frac{I(h)}{I(\infty)} = \frac{\int_{\lambda_1}^{\lambda_2} \varepsilon(\lambda).\ \phi(\lambda,\infty)\ e^{-\ \sigma(\lambda).\ N_T(h)}\ d\lambda}{\int_{\lambda_1}^{\lambda_2} \varepsilon(\lambda).\phi(\lambda,\infty)\ d\lambda} \qquad (4.22)$$

and from the definition of σ_{EFF} (4.9)

$$\sigma_{EFF}(h) = \frac{\int_{\lambda_1}^{\lambda_2} \varepsilon(\lambda).\ \sigma(\lambda).\ \phi(\lambda.\ \infty)\ e^{-\sigma(\lambda).\ N_T(h)}\ d\lambda}{\int_{\lambda_1}^{\lambda_2} \varepsilon(\lambda).\ \phi(\lambda,\ \infty)\ e^{-\sigma(\lambda).\ N_T(h)}\ d\lambda} \tag{4.23}$$

As h increases N_T decreases monotonically and therefore h is a single valued function of N_T, i.e.

$$j(N_T) = \frac{\int_{\lambda_1}^{\lambda_2} \varepsilon(\lambda).\ \phi(\lambda,\ \infty).\ d^{-\sigma(\lambda).\ N_T}\ d\lambda}{\int_{\lambda_1}^{\lambda_2} \varepsilon(\lambda).\ \phi(\lambda,\ \infty).\ d\lambda} \tag{4.24}$$

$$\sigma_{EFF}(N_T) = \frac{\int_{\lambda_1}^{\lambda_2} \varepsilon(\lambda).\ \sigma(\lambda).\ \phi(\lambda,\ \infty)\ e^{-\sigma(\lambda).\ N_T} d\lambda}{\int_{\lambda_1}^{\lambda_2} \varepsilon(\lambda).\ \phi(\lambda,\ \infty)\ e^{-\sigma(\lambda).\ N_T} d\lambda} \tag{4.25}$$

from 4.24, j, for a particular ion chamber and a particular set of flux values, will depend monotonically on N_T, i.e. the value of N_T will define uniquely the value of j. Because the relationship is monotonic N_T is in turn uniquely defined by j. i.e. N_T is a single valued function of j.

$$N_T = N_T(j)$$

From 4.25, σ_{EFF} is a single valued function of N_T. Therefore σ_{EFF} is a single valued function of j

i.e.

$$\sigma_{EFF}(j) = \frac{\int_{\lambda_1}^{\lambda_2} \varepsilon(\lambda).\ \sigma(\lambda).\ \phi(\lambda,\ \infty)\ e^{-\sigma(\lambda).\ N(j)}\ d\lambda}{\int_{\lambda_1}^{\lambda_2} \varepsilon(\lambda).\ \phi(\lambda,\ \infty)\ e^{-\sigma(\lambda).\ N(j)}\ d\lambda} \tag{4.26}$$

and the value of j at z = h will define the appropriate σ_{EFF}.

To aid computation, a third order poly-nominal was fitted to $\log_{10}(\sigma_{EFF}(z))$ using $\log_{10}(j(z))$ as the variable. This simplified the selection of the appropriate effective absorption cross-section for use in equation 4.10 and the uncertainty introduced by the use of the

poly-nominal was less than ½%.

For the initial analysis of the data the effective absorption cross-section of the Lα ion chambers were not calculated by the author. The results of Carver *et al* (1977a) were used. As with σ_{EFF} for QT and SX ion chambers, assumptions about F and ϕ had to be made to enable evaluation of the parameter $\sigma_{EFF}(L\alpha)$. F was taken as one. The integration was not taken over the whole of the chambers response but only over the width of the solar Lα line. (The validity of this procedure is discussed in Section 4.2.6). $\phi(\lambda, \infty)$ was taken to be the function describing the shape of the solar Lα line and for their calculation Carver *et al* (1977a) used the profile of Purcell and Tousey (1960). The absorption cross-sections were those measured by themselves and given in the paper (Carver *et al* 1977a). The $\sigma(\lambda)$ were measured at several different temperatures and the effective absorption cross-sections adopted for the present work were those based on measurements of $\sigma(\lambda)$ at 195° K.

The absorption cross-section of molecular oxygen varies strongly across the solar Lα line and radiation hardening occurs. σ_{EFF} was given as a function of j(z) by Carver *et al* (1977a) and as with the other chambers, to aid computation, a third order poly-nominal was fitted to $\log_{10}(\sigma_{EFF})$ using $\log_{10}(j(z))$ as the variable. As before the uncertainty introduced by the use of a poly-nominal was less than ½%.

4.2.3 The Sensitivity of σ_{EFF} to the assumed Flux Function $\phi(\lambda, \infty)$.

From equation 4.20, $\phi(\lambda, h)$ depends on $\phi(\lambda, \infty)$, $\sigma(\lambda)$ and $N_T(h)$. Because σ_{EFF} is expressed as a value of j rather than h uncertainty in N_T is not relevant. The uncertainty arising in $\phi(\lambda, h)$

and consequently in σ_{EFF} from uncertainty in $\sigma(\lambda)$ can be considered to be included in the differences observed and allowed for in Section 4.2.4 where $\sigma_{EFF}(j)$ is calculated for different measurements of $\sigma(\lambda)$ (Figure 4.5). In this section only the effect of the uncertainty in $\phi(\lambda, \infty)$ is considered.

In calculating σ_{EFF} for QT and SX chambers, it was assumed that the flux incident on top of the atmosphere was the same as the mean of those given by Delaboudiniere *et al* (1977). But the rockets involved in the project were flown in 1972, 1974 and 1977. It is unlikely that the assumed flux was valid for all three. It was probably not valid for any of them. Therefore some estimation of the uncertainty that was introduced into σ_{EFF} by the assumption of these flux values was required.

Flux induced variations in σ_{EFF} only occurred if the shape of the flux function $\phi(\lambda, \infty)$ changed. The results listed by Delaboudiniere *et al* (1977) suggested that for the wavelengths 1425Å to 1490Å and 1560Å to 1650Å the shape of $\phi(\lambda, \infty)$ would not vary greatly. It was considered, therefore, that the flux functions given by the mean of the results quoted in the above paper, the 1972 Results of Rottman (also taken from the above paper) and the assumption that the sun was a black body at 4600°K would be adequate to represent the likely variability. σ_{EFF} was calculated for all three and an inter-comparison made in order to assess the likely uncertainty associated with the results.

For SX chambers the difference between the two calculations of σ_{EFF} were negligible. For QT chambers the difference varied from chamber to chamber but in all cases was less than 2%. This is

illustrated in Figure 4.4.

Carver *et al* (1977a) in their discussion of the effective absorption cross-section of a $L\alpha$ ion chamber also looked at the effect of the shape of the flux function on the calculated σ_{EFF}. As with SX and QT chambers, σ_{EFF} for $L\alpha$ proved relatively insensitive to changes in $\phi(\lambda, \infty)$. From their results the maximum uncertainty introduced is 5% for $\sigma_{EFF}(\infty)$. The uncertainty decreases so that for $j(z) \leqslant .5$ the uncertainty is $\lesssim 2\%$.

It would appear that the only other person in the literature to attempt a quantitative assessment of this source of uncertainty was Weeks (1975a). He obtained similar results. However, neither Weeks (1975a) nor Carver *et al* (1977b) who used the effective cross-sections calculated by Carver *et al* (1977a) included this uncertainty in the final assessment of their number densities.

The author believes this source of uncertainty cannot be dismissed, and therefore, in summary, the uncertainty introduced in σ_{EFF} by uncertainty in the assumed incident flux is, for the various chambers, as follows,

SX negligible

QT < 2% for all chambers

$L\alpha$ chambers < 2% for $j(z) \leqslant .5$ rising to a maximum of 5% at $j(z) = 1$.

4.2.4 The Uncertainty in σ and its Effect on σ_{EFF}

Uncertainty in σ arises from two sources. The first is the uncertainty in the laboratory measured cross-sections as expressed by quoted experimental uncertainties and illustrated by the scatter in the results from different research groups. The second arises from the validity or otherwise of applying room temperature laboratory cross-

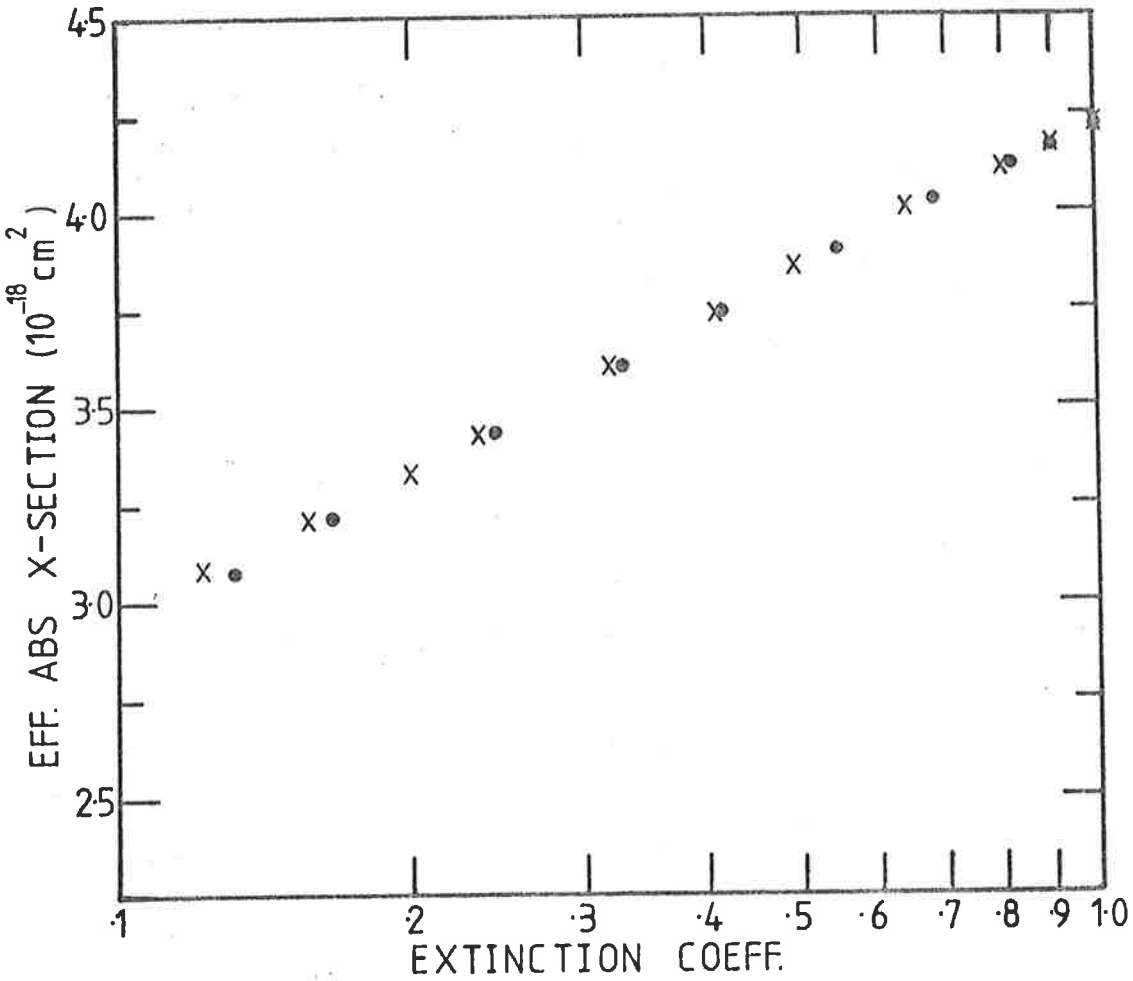

Fig. 4.4 The effect of different flux values on σ_{EFF} of a QT ion chamber.

X - Black body at 4600° K

● - Ave. flux from Delaboudiniere *et al* (1977)

sections to the atmosphere where, over the region of the lower thermosphere, the temperature ranges from 195° K to 570° K. Both these sources were looked at and the following discusses the possible magnitude of the uncertainty induced in σ_{EFF} by them.

For the wavelengths covered by the SX chambers the absorption cross-sections of Blake *et al* (1966) were used. The experimental uncertainty of these cross-sections is quoted as ± 5%. This would appear to be a reasonable estimate of the total uncertainty involved since a comparison of the experimental determinations of σ of molecular oxygen (Hudson, 1971) shows that the various results agree with each other well within their quoted experimental errors. Since uncertainties in σ are directly reflected in uncertainties in σ_{EFF} it was considered valid to assign from this source an uncertainty of ± 5% to the effective absorption cross-section of an SX ion chamber.

It is difficult to assign a magnitude to the uncertainty or perhaps more correctly the systematic error that occurs when laboratory measured absorption cross-sections for λλ 1425Å - 1490Å are used in atmosphere applications. Temperature dependent cross-sections have not, as yet, been measured at these wavelengths. Such work is presently being undertaken (A.J. Blake, private communication) and, if available in time, the results and their effect on the effective absorption cross-section of an SX chamber will be included in an appendix*. The theoretical work of Evans and Schexynader (1961) suggests a maximum systematic error of 4%. Because of the uncertainties involved in establishing a temperature profile at the time of each flight and the relatively small magnitude of the effect, no attempt was made to correct

* See note Table 4.7 at end of Chapter

for it.

This same approach was adopted by the author in preparing the results presented in Carver *et al* (1978a)and Bibbo *et al* (1979). Therefore the σ_{EFF} calculated and used for SX chambers in the present work may be systematically high by up to 4%.

Hudson's (1971) review shows that for the QT ion chamber passband (λλ 1560Å - 1650Å) there are systematic differences between different measurements of σ that are well outside quoted experimental errors. The significantly different values of σ were directly reflected in any effective absorption cross-sections calculated from them. For example, σ_{EFF} from the absorption cross-sections of Watanabe *et al* (1953) was smaller and differed by as much as 12% from σ_{EFF} calculated from the results of Blake *et al* (1966) (Figure 4.5). In the original analysis of the present results (Carver *et al*, 1978a) Bibbo *et al* 1979) no preference could be given to any one set of measurements and those of Blake *et al* (1966) were used. This implied a statistical error of ± 5% rising from the experimental uncertainty and a possible systematic error of as much as + 12%.

After publication,(Carver *et al*, 1978a) Bibbo *et al* 1979) new measurements of the absorption cross-section of molecular oxygen for the wavelengths within the passband of a QT chamber became available (Rogers, 1979). These measurements were made with the high resolution 6m monochromator described by Carver *et al* (1978b). The results showed an almost systematic discrepancy from those of Blake *et al* (1966) and lie much closer to those of Watanabe *et al* (1953). There is,however, still no criterion which can preferentially select one of the sets of values. The addition of the results of Rogers (1979) to those reviewed by Hudson (1971) does not alter the conclusions previously drawn about the magnitude of the uncertainty and the error introduced into the σ_{EFF}

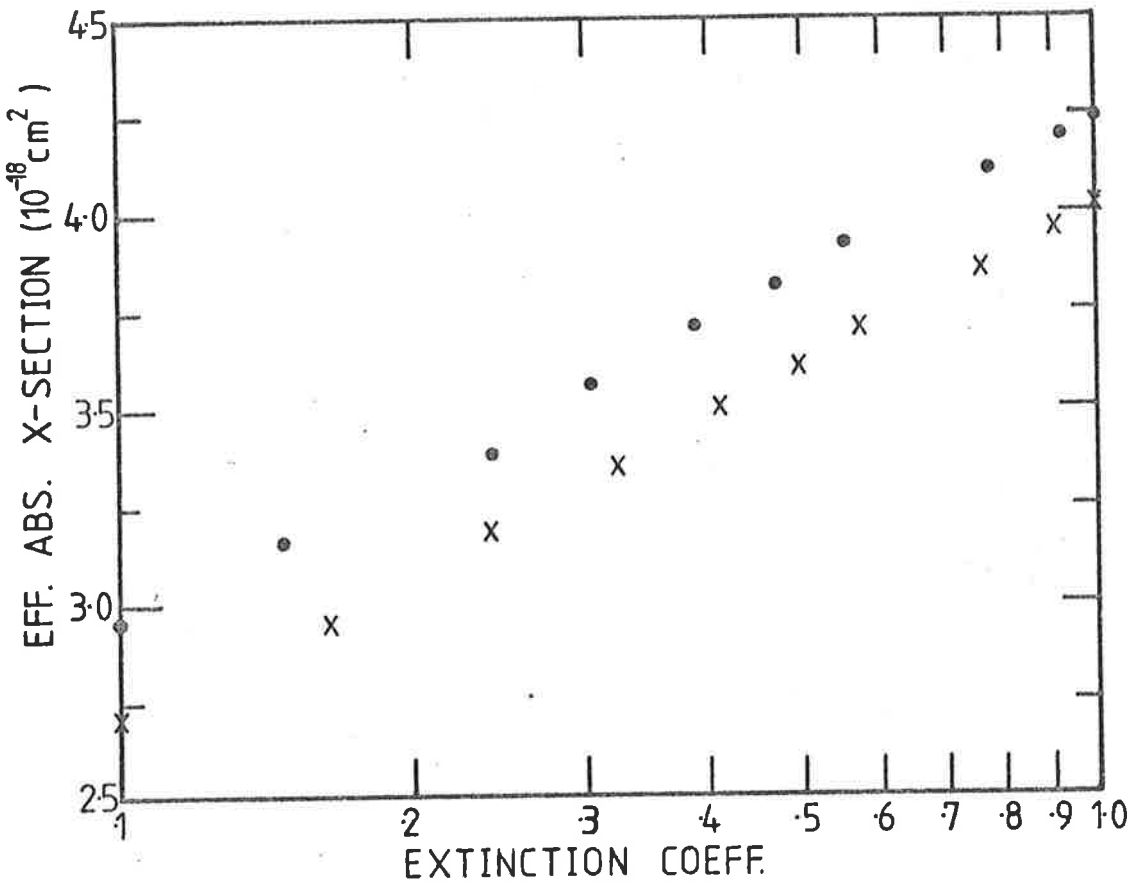

Fig. 4.5 Effect of differing absorption cross sections on the σ_{EFF} of a QT ion chamber.

X - Watanabe *et al* (1953)

● - Blake *et al* (1966)

of a QT ion chamber by the use of the absorption cross-sections of Blake *et al* (1966).

The experiment of Rogers (1979) is about to be repeated (A.J. Blake, private communication) and these results when available may be more conclusive. This information will be included in an appendix if it becomes available in time. (see contents listing).*

Rogers (1979) also looked at the temperature dependence of the absorption cross-sections at the QT ion chamber wavelengths. Measurements were taken at 95°K, 290°K and 570°K. Increased temperatures enhanced the absorption cross-section. Taking 570°K to be a reasonable estimate of the maximum temperature likely at 150 kms - the usual upper limit for QT ion chamber results - these new results implied that the maximum error that would be observed in σ_{EFF}, if room temperature absorption cross-sections were used throughout, would be 9%. That is the calculated σ_{EFF} would be up to 9% too small.

The enhancement seen in σ has the effect of bringing the results of Rogers (1979) in much closer agreement with those of Blake *et al* (1966). Therefore it was considered valid to assume that the 12% possible systematic error already postulated for the QT effective absorption cross-section could be taken as including temperature induced errors.

For Lα chambers, σ_{EFF} is once again associated both with uncertainty and with a possible systematic error. The uncertainty arises from the uncertainties in the experimental determination of σ and, for the σ_{EFF} used in the present work, this is $< 5\%$ (Carver *et al* 1977a). The systematic error arises because of lack of knowledge about the

* These measurements have now been taken, but they do not alter the conclusions drawn on this page and the next and therefore, the data set of Blake *et al* (1966) has still been used. Since they were not used the suggested appendix of the later measurements has not been included.

the temperature of the atmosphere at the time of flight. Carver *et al* (1977a), although using cross-sections measured at a temperature (195° K) applicable to the range of altitude over which Lα operated, still believed that the effective absorption cross-section could be systematically low by 4% to 5%.

Therefore in summary, uncertainties and possible systematic errors in σ are as listed in Table 4.1.

TABLE 4.1 UNCERTAINTIES AND POSSIBLE SYSTEMATIC ERRORS IN σ_{EFF} RESULTING FROM SAME IN σ

Chamber	Statistical Uncertainty	Max. Systematic Error
SX	± 5%	4% too low
QT	± 5%	12% too high
Lα	< ± 5%	4%-5% too low

4.2.5 Uncertainty in $\varepsilon(\lambda)$ and its Effect on σ_{EFF}

Because of the dependence of the effective absorption cross-section on the spectral response ($\varepsilon(\lambda)$) of the detector, (equation 4.10) σ_{EFF} is unique to each detector. The significance of this will, however, vary between detector types. For SX chambers, although individual σ_{EFF} were used, the use of a common mean σ_{EFF} would not have introduced any error > 1%.

The calculation of σ_{EFF} for SX chambers did, however, imply that the use of the absorption cross-section at 1450Å (Weeks and Smith 1968; Weeks, 1975b; Higgins and Heroux (1977)) could lead to a systematic error. This error was considered negligible in the literature but the calculations showed it to be of the order of 3% to 4% and the author considers the present approach of calculating and using an

effective absorption cross-section is more satisfactory.

For $L\alpha$ chambers lack of resolution in the calibration equipment means that $\varepsilon(\lambda)$ has to be taken as constant across the width of the solar $L\alpha$ line. This implies

$$\sigma_{EFF_{L\alpha}}(z) = \frac{\int_{\lambda_1}^{\lambda_2} C.\ \phi(\lambda,\ z).\ \sigma(\lambda).\ d\lambda}{\int_{\lambda_1}^{\lambda_2} C.\ \phi(\lambda,\ z).\ d\lambda}$$

where C is the response at $L\alpha$, and therefore

$$\sigma_{EFF,L\alpha}(z) = \frac{\int_{\lambda_1}^{\lambda_2} \phi(\lambda,\ z).\ \sigma(\lambda).\ d\lambda}{\int_{\lambda_1}^{\lambda_2} \phi(\lambda,\ z).\ d\lambda} \qquad (4.27)$$

i.e. $\sigma_{EFF_{L\alpha}}(z)$ is independent of $\varepsilon(\lambda)$ and one evaluation of σ_{EFF} applies to all chambers. The error, if any, introduced by this assumption is not known but is most likely far less significant than the error introduced by ignoring the other wavelengths within the chambers passband (see Section 4.2.6).

If the effective absorption cross-section at $L\alpha$ is independent of $\varepsilon(\lambda)$ then uncertainties in $\varepsilon(\lambda)$ will have no effect on it. If the σ_{EFF} of different SX ion chambers agree to within 1% of each other the uncertainty in the individual passband would not be expected to introduce a large uncertainty into the σ_{EFF} of that chamber. In the present work this assumption could be made because the total uncertainties in the passband were on a par or smaller than the differences between ion chambers. The only chambers expected to be sensitive to uncertainties in $\varepsilon(\lambda)$ were the QT ion chambers and the following discussion centres on their spectral responses.

The spectral response of a detector may be considered to have two characteristics; the magnitude of the response at a particular wavelength, and the wavelength limits of the response. While these two characteristics are obviously not independent of each other the concept is convenient when discussing sources of uncertainty.

Consider the magnitude of the response at a particular wavelength. Associated with any measured value of this will be an unavoidable statistical uncertainty. For the flight detectors, laboratory experience indicated that this was normally 10%. There was one exception. For QT chambers figure 4.6 shows that individual differences must be taken into account and illustrates clearly that the use by some researchers (see Chapter 2), of a common passband and consequently a common σ_{EFF} is not satisfactory. One chamber exhibited changes of up to 65% in the value of $\varepsilon(\lambda)$ for any particular λ. A 10% uncertainty in $\varepsilon(\lambda)$ implied an uncertainty of the order of $\pm$ 1½% to $\pm$ 2% in σ_{EFF}. Launch scheduling prevented further investigation of the one exception and so for that chamber an uncertainty of $\pm$ 12% has had to be included in the final assessment of the data.

Because a Sodium Salicylate (Na. Sal.) photomultiplier combination was used to monitor the flux in the calibration procedure (Sections 3.2.6.1) the magnitude of the response was also subject to a systematic error. It was stated in Section 3.2.6.2 that a truer measure of the response $\varepsilon(\lambda)$ was given by

$$\varepsilon(\lambda) = \varepsilon_M(\lambda) . R(\lambda) \qquad (3.1)$$

where $\varepsilon_M(\lambda)$ is the measured response and $R(\lambda)$ the correcting factor allowing for the enhanced sensitivity of Na. Sal. towards longer wavelengths. A correction factor was also given. Giving $R(\lambda)$ the value

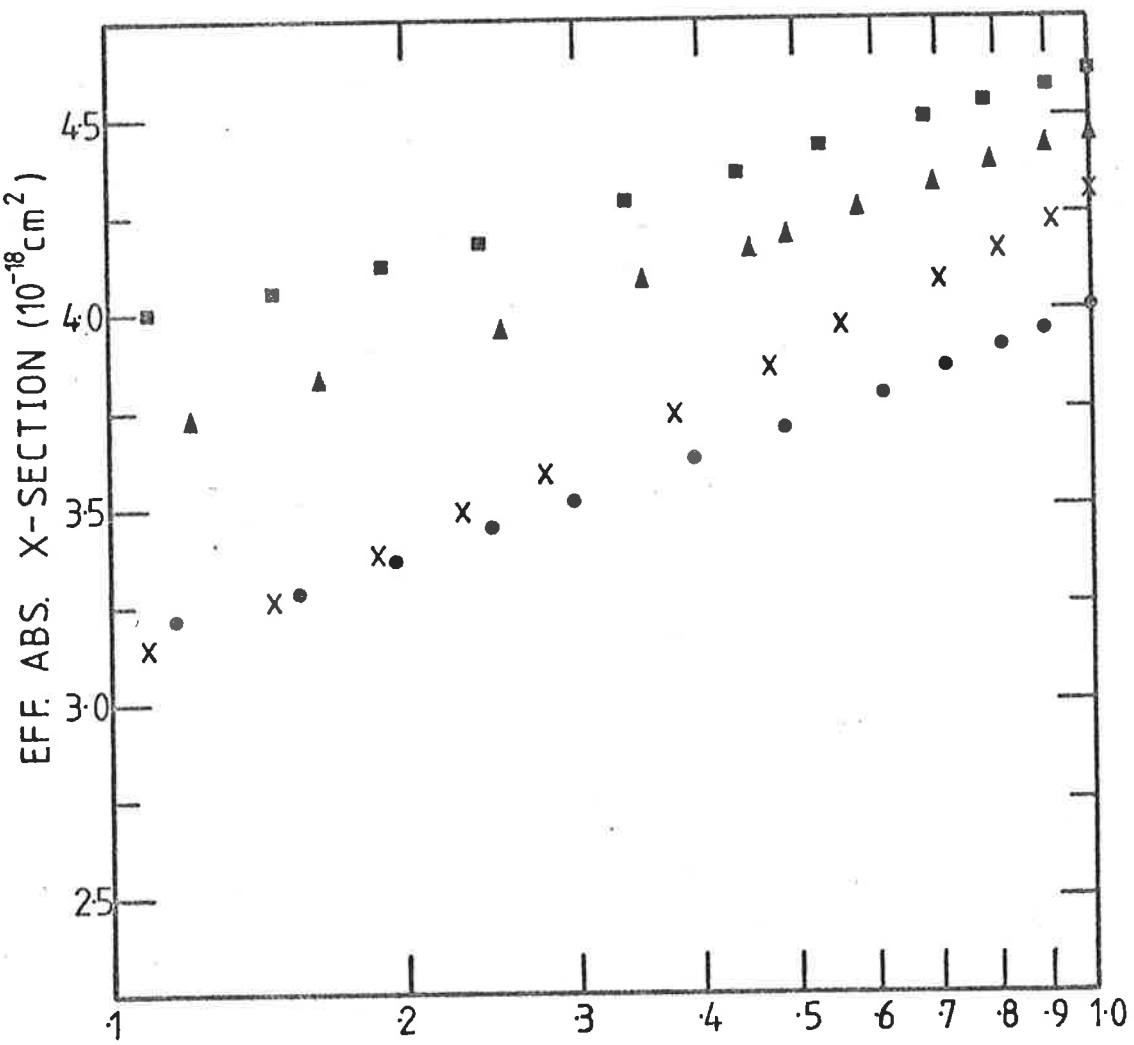

Fig. 4.6 Variation observed in σ_{EFF} for QT ion chambers flown in research programme.

X - QT204 - SL 1005

● - QT1 - SL 1207

■ - QT202 - Aerobee 13.123 IS

▲ - QT5 - Aerobee 13.123 IS

of 1 at λ_1 the short wavelength limit of the passband it was found that R, at the long wavelength limit, λ_2, was $1.11 \pm .03$. (This result was derived from looking at both SX and QT ion chambers). Corrected $\varepsilon(\lambda)$ curves were drawn up by assuming that the correction factor was a linear function of $(\lambda - \lambda_1)$. The ε_{EFF} calculated from these corrected curves was in all cases $< 1\%$ different from that calculated from the uncorrected curves.

It was stated in Section 3.2.8 that for QT and SX chambers heating could change the position of the maximum response. The chambers were heated during flight, but the small increase in temperature (flight temperatures were only 5°C to 10°C above calibration temperatures) implied the resultant change in magnitude, at any particular wavelength was far less than the experimental uncertainty of the calibration and this effect was ignored.

The second characteristic of an ion chamber was defined as the wavelength limits (λ_1, λ_2) of the passband. These too are subject to uncertainty. Experimental uncertainty in λ_1, λ_2 was of the order of 1Å to 2Å. λ_1, λ_2 were also affected by the heating suffered during flight. However, from the values quoted in Section 3.2.8 and with the minor nature of the heating, the effect, a shift towards longer wavelengths, was much less than the experimental uncertainty and was ignored.*

The change introduced by the temperature induced shift is regarded as an uncertainty rather than a systematic error because of the uncertainty in the flight temperature. Under these conditions the total

* This comment does not apply to the spectrophotometer. Heating does not produce a shift in the passband. It did introduce uncertainty because of the change in the dark current of the photomultiplier. Experimental uncertainty in λ_1 and λ_2 appeared negligible.

uncertainty introduced by uncertainty in λ_1, λ_2 was < 1.2% despite the apparent sensitivity of the QT ion chamber's effective absorption cross-section to changes in the passband.

Therefore in summary, uncertainties in the effective absorption cross-section caused by uncertainties in $\varepsilon(\lambda)$ are as listed in Table 4.2

TABLE 4.2

Chamber	Uncertainty
LNO, MNO	N/A if only Lα considered.
QT	< 3½% except for QT 1 which is approx. 13½%
SX	< 1%.

4.2.6 The Effect of Other Wavelengths on the Effective Absorption Cross-Section of Lα Chambers

The non-monochromaticity of the LNO and MNO chambers has already been discussed in Chapter 2. An attempt was made in the present work to qualitatively assess how the chambers response to wavelengths other than Lα affected the observed signal, and how the interpretation of the data should, therefore, be modified.

The investigation centred on an MNO chamber. Two parameters were calculated; the extinction coefficient, j(z), as a function of altitude and the effective absorption cross-section for the whole chamber [σ_{EFF} (λ_1, λ_2)]. The latter was expressed both as a function of altitude and of j(z). The procedure already described for QT and SX chambers was used to calculate both j(z) and $\sigma_{EFF}(\lambda_1, \lambda_2)$. Not all the basic assumptions were the same, however, because the MNO chamber

was a flight chamber and experimental data was available. The initial assumptions made for the Lα work were

1. The solar radiation flux, except for Lα, was taken as that given by Delaboudiniere *et al* (1977),

2. The initial Lα flux was calculated by assuming 85% of the maximum signal observed during the flight of the MNO chamber was due to Lα radiation only,

3. The absorption cross-section of molecular oxygen for Lα was the effective absorption cross-section given by Carver (1977a),

4. The absorption cross-sections of molecular oxygen for the non Lα wavelengths were those given by Blake *et al* (1966),

5. The initial oxygen profile was that derived from the data of the SX and QT ion chambers flown on the same rocket, together with the number densities obtained from the data of the MNO chamber itself by using the simple Lα effective abs. cross-section of Carver *et al* (1977a),

6. The optical depth factor (Section 4.3) was the one relevant to the actual rocket flight - Aerobee.

The percentage of the ion chambers signal due to Lα alone was defined by a simple criterion. The effective cross-section of the whole chamber was calculated and compared with that given by Carver (1977a) for Lα. When the two agreed to within 5% of each other the corresponding extinction coefficient, j(z), was interpreted as the Lα

part of the ion chamber's signal. $j(z)$ was used because this allowed comparison of the two parameters even though some of the initial assumptions differed.

Although the criterion was simplistic it does give a valid estimate of the $L\alpha$ induced signal. Since the absorption cross-section at $L\alpha$ itself is orders of magnitude smaller than σ for the other wavelengths within the passband, absorption of $L\alpha$ radiation is not significant at the 5% agreement level.

Initially agreement was reached at $j(z) \approx .75$ implying $L\alpha$ made up $\approx 75\%$ of the ion chambers signal. The assumed $L\alpha$ flux was adjusted and the calculations re-done. Once again the results implied a 75% contribution. The $\sigma_{EFF}(\lambda_1, \lambda_2)$ obtained in this second run were then used to correct the $n(O_2)$ derived from the results of the MNO chamber. The new profile was used to calculate $\sigma_{EFF}(\lambda_1, \lambda_2)$ a third time. Agreement was still reached at $j(z) = .75$.

It is interesting to note that this work confirmed the validity of calculating σ_{EFF} as a function of $j(z)$. Alterations of the flux level at $L\alpha$, or use of a model $n(O_2)$ rather than the flight $n(O_2)$ did not significantly vary the σ_{EFF} applicable to any particular value of $j(z)$, although the altitude at which the $j(z)$ and its associated $\sigma_{EFF}(\lambda_1, \lambda_2)$ occurred did differ up to 1 to 2 kms.

Because the 75% contribution seemed low compared with that given in the literature (see Chapter 2), and because it was expected this fraction would alter with differing flux levels and ion chamber efficiencies (Weeks, 1975a), both these parameters were varied. The efficiency of the MNO chamber at $L\alpha$ was known from pre-flight calibrations, but, to investigate the possible consequences, it was

enhanced by up to 25%. This did alter the percentage contribution. At 90% efficiency the contribution stood at $\approx 80\%$. The flux levels were enhanced up to 50%. Once again, the percentage contribution was increased ($\approx 81\%$). While for the ion chamber under study, and using the $n(O_2)$ profile derived at the time of flight, convergence could not be obtained with the enhanced level of flux, these results do confirm Week's (1975a) suggestion.

Therefore contributions of 89% ± 5% (Smith and Miller, 1974) or 95% (Roble and Norton, 1972), may have been valid for the particular chambers and flight conditions involved but it would appear the expected $L\alpha$ fraction of the signal must be calculated for each individual chamber. The present technique of doing this by testing for convergence appears to be valid and has an added advantage since it strengthens the credibility of the value obtained from the chamber, for the absolute flux, (for the present work, the flux equals 4.41 erg/cm^2/sec).

$\sigma_{EFF}(\lambda_1, \lambda_2)$ not only differs radically from $\sigma_{EFF}(L\alpha)$ for $j(z) > .75$ it also changes rapidly with $j(z)$ (Figure 4.7). If $\sigma_{EFF}(\lambda_1, \lambda_2)$ is used to correct the $n(O_2)$ derived from the MNO chambers any uncertainty in $j(z)$ will produce magnified uncertainties in $n(O_2)$, if $j(z) > .75$. Therefore, while it was not essential that the theoretical $j(z)$ versus altitude curve match the experimental one, it was considered, in view of the magnitude of the possible corrections and uncertainties, that matching, if possible, would provide support, both for the hypothesis that corrections were needed, and for the particular correction curve adopted. In reality, support for the necessity of correction factors can be said to be provided already by the lack of agreement between the theoretical curve using $\sigma_{EFF}(L\alpha)$ alone and the experimental curve (Figure 4.8).

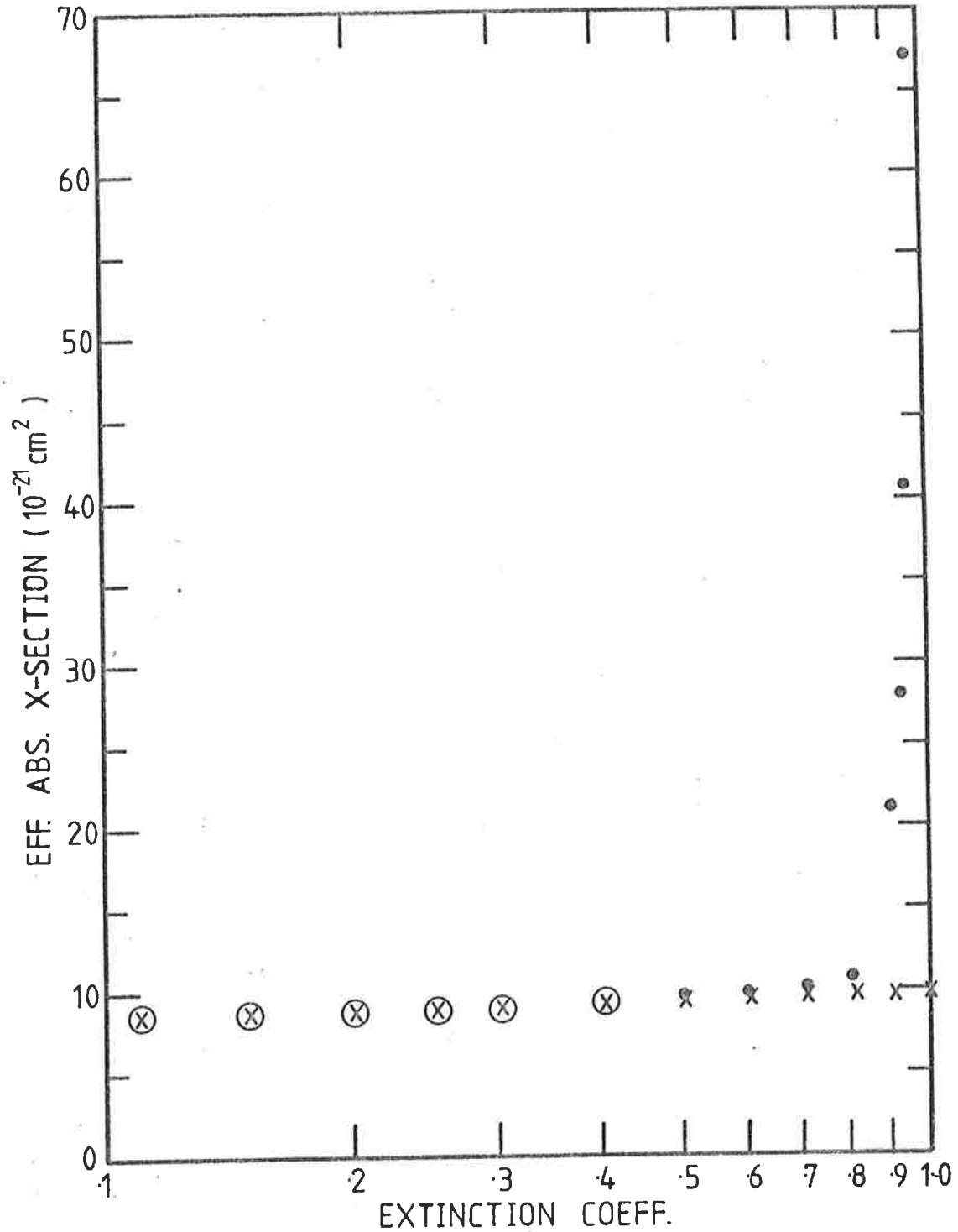

Fig. 4.7 Comparison of σ_{EFF} for an MNO chamber and σ_{EFF} for Lα

● -MNO chamber

x - Lα

⊗- coincident points

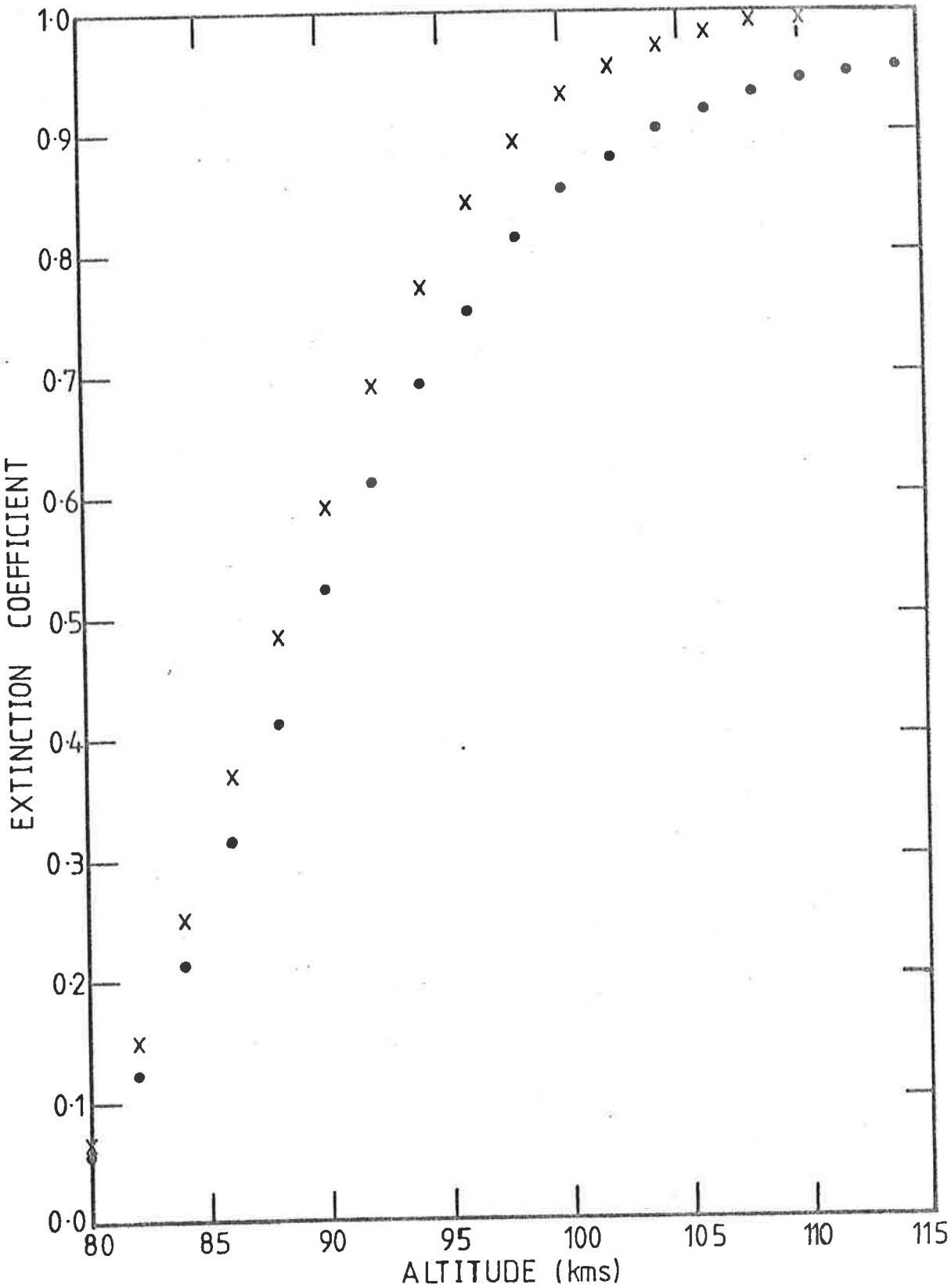

Fig. 4.8 Comparison of Experimental Extinction Coefficient with that generated by the use of $\sigma_{EFF}(L\alpha)$

● - Experimental

X - Theoretical

Neither variations in the flux level nor the chamber efficiency could be used to achieve the desired result. The best estimate of the flux had already been obtained by looking for convergence, and, even allowing for the uncertainty in the calibration, the range of possible efficiencies of the chamber did not provide a match. Other factors were, therefore, looked at.

Amplifier offsets will affect the apparent signal and these were carefully checked. The choice of maximum signal will affect the apparent $j(z)$ and this was also checked. Averaging of the signal received from above the absorption layer was carried out to obtain the best possible estimate of the max signal (the chamber only showed a 2.2% drift in signal over 3.5 minutes, so averaging over a much shorter time scale was valid). Some adjustment was necessary. The match then obtained between theoretical and experimental is shown in Figure 4.9.

While the closeness of the match - compared to that illustrated in Figure 4.8 - shows the validity of the procedures adopted, the use of these calculations to provide correction factors for the derived molecular oxygen densities is associated with large uncertainties. For example, a 1% uncertainty in the experimental $j(z)$, if $j(z)$ nominally equals .9, leads to a 16% uncertainty in the correction factor adopted while the same uncertainty when $j(z) = .96$ leads to an uncertainty of 45%.

The possible magnitude of the uncertainties is reflected in the results but the corrected numbers are more consistent than might be expected considering likely uncertainties in the experimental $j(z)$. Figure 4.10 shows three sets of data. These are :

(i) the mean and standard deviation of the $n(O_2)$ derived from the $L\alpha$ chambers (both MNO and LNO using the $\sigma_{EFF}(L\alpha)$ of Carver *et al* (1977a),

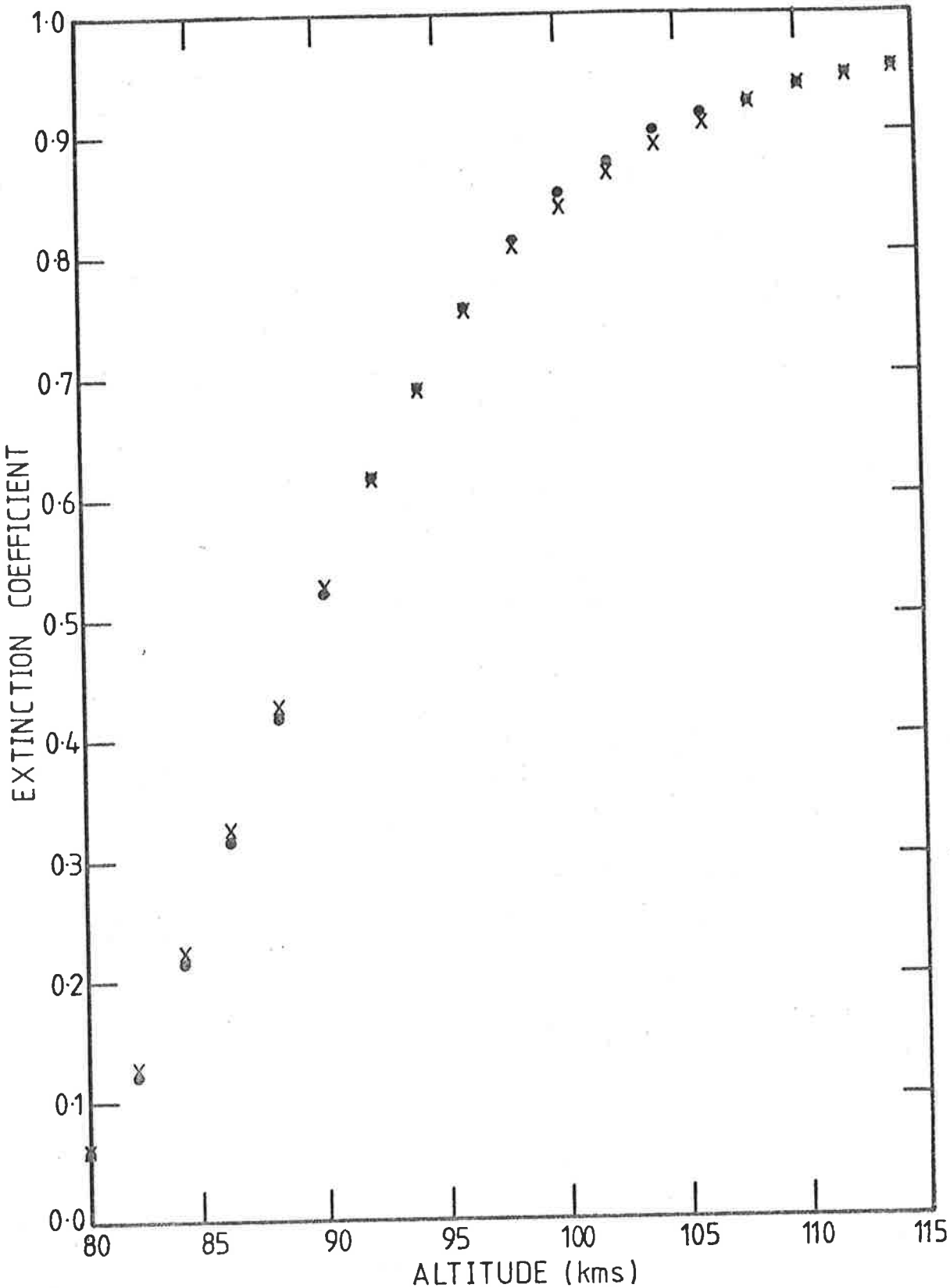

Fig. 4.9 Comparison of Experimental Extinction Coefficient with that generated by the use of $\sigma_{EFF}(\lambda_1-\lambda_2)$

● - Experimental
x - Theoretical

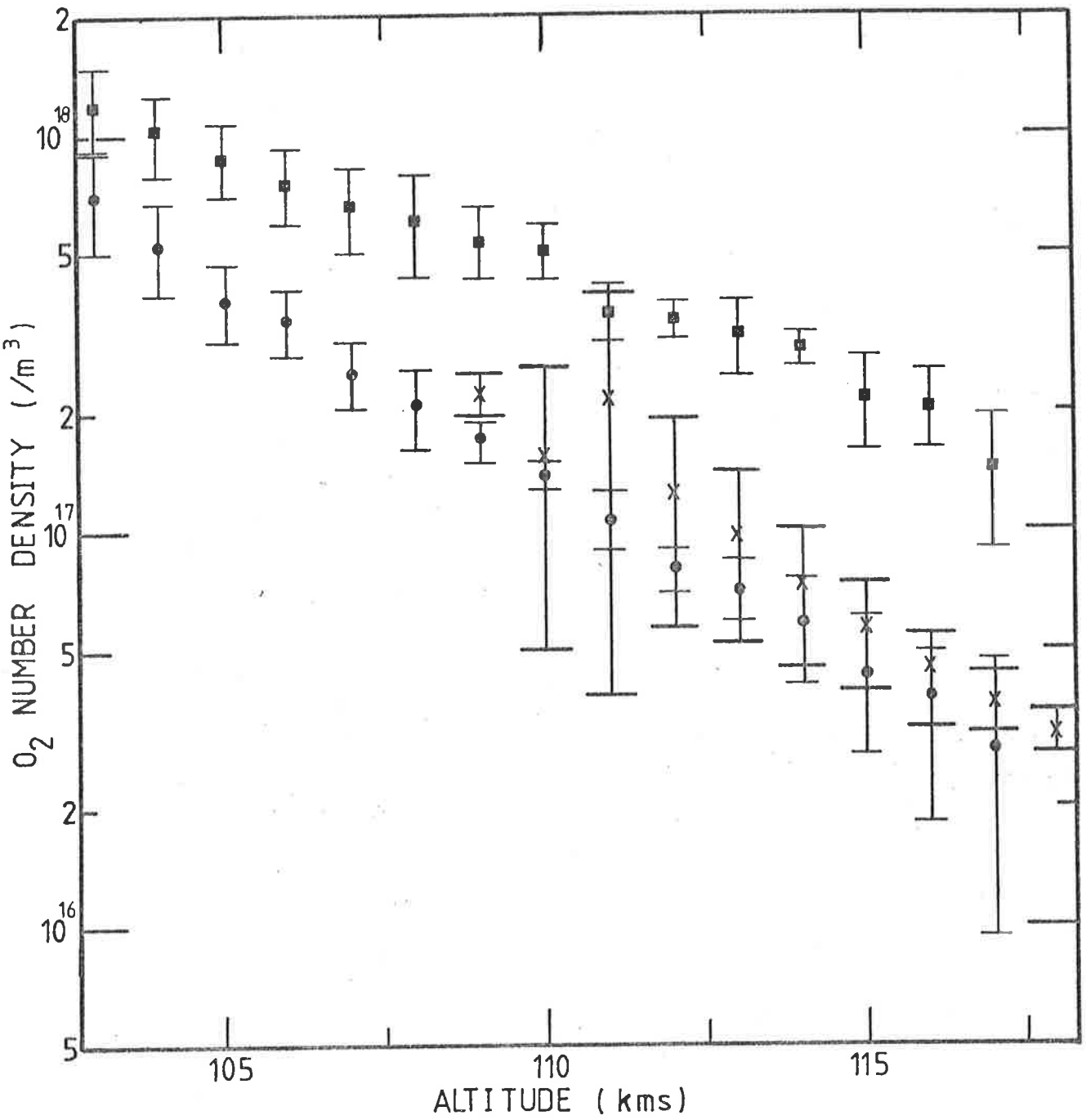

Fig. 4.10 Comparison of corrected and uncorrected (see text) oxygen numbers determined by an MNO ion chamber with those determined by a QT chamber.

mean of QT results

corrected MNO results

uncorrected MNO results.

(ii) the mean and standard deviation of the $n(O_2)$ determined from the $L\alpha$ chambers using a $\sigma_{EFF}(\lambda_1, \lambda_2)$,

(iii) the mean and standard deviation of the $n(O_2)$ profile determined from the QT ion chambers.

Both uplegs and downlegs have been included in the mean although this may have introduced an unnecessary spread in the results since there may be real differences in the two profiles.

It is clear from the diagram that

(a) the uncertainty in the corrected $n(O_2)$ is larger than that in the uncorrected $n(O_2)$ but the two profiles still show systematic differences,

(b) as would be expected these systematic differences increase at higher altitudes where less absorption of the other wavelengths has taken place,

(c) the use of $\sigma_{EFF}(\lambda_1, \lambda_2)$ in the analysis of $L\alpha$ chamber data gives densities which agree within their combined uncertainties with those independently derived from the QT chambers. If only the downlegs are considered the agreement is better again (see Chapter 6).

Examples have been given of how the uncertainty in $j(z)$ is reflected in magnified uncertainties in the correction factor. However, it is difficult to quantitatively assess the uncertainty that might be introduced into $n(O_2)$ by the use of the correction factor. If the mean and standard deviation of both the corrected and non-corrected $n(O_2)$ profiles are compared then it would appear that approximately an extra $\pm$ 15% spread in results is introduced. The only thing that differs between the two calculations is the use of the corrected effective abs.

cross-section. It is, therefore, considered that, as a rough estimate, the correction factors could be considered to add an uncertainty of ± 15% to the mean $n(O_2)$ profile derived from the $L\alpha$ chambers.

The graph indicates that curve a and curve b converge as z decreases. This is so and for $j(z) < .75$ the difference between the two is < 4%. For the Aerobee rocket with a zenith angle of approximately 85° $j(z) = .75$ occurred at 95 kms. This lends credence to the procedure adopted by Carver *et al* (1977b). In re-analyzing much of the published data, these authors only used $\sigma_{EFF}(L\alpha)$ but they restricted their analysis to $z < 90$ km. Irrespective of the zenith angle at the time of flight, no significant error would have been introduced. The less restrictive procedure adopted by Weeks and Smith (1968) where, for a zenith angle of 60°, monochromaticity was assumed up to a height of 94 kms (the height at which $j(z) = .85$) may have been valid for their particular chamber but cannot be universally applied. For the MNO chamber investigated $j(z)$ also equals .85 by 94 kms if the zenith angle equals 60°, but the assumption of monochromaticity would lead to systematic errors ranging up to 27%.

Therefore, in summary, while the magnitude of the associated uncertainties imply caution must be exercised in using the correction factors, and these factors can only be estimated where the full spectral response of the chamber is known, their use is justified. Adoption of alternative procedures outlined in the literature are either unnecessarily restrictive or may introduce large systematic errors. They would appear to extend, significantly, the range over which these chambers may be used, although, as is discussed in the next section, the restrictions connected with assuming monochromatic radiation may not be the limiting factor in determining this height range.

4.2.7 The Effect of Other Absorbers on the Effective Absorption Cross-Sections of the Ion Chambers.

It was stated in Chapter 2 that molecular oxygen was assumed to be the only significant absorber of radiation in the bands of radiation monitored by the ion chambers used i.e. nominally λλ 1050Å - 1350Å, λλ 1140Å - 1350Å, λλ 1425Å - 1490Å and λλ 1560Å - 1650Å. Other atmospheric constituents, however, do absorb this radiation and the significance or otherwise of this extra absorption varies with the type of chamber. Table 4.3 shows the absorption coefficients at representative wavelengths of the most dense of these constituents.

TABLE 4.3 ABSORPTION COEFFICIENTS OF ATMOSPHERIC GASES*

Gas	N_2	CO_2	H_2O	O_2	NO
Wavelength					
Lα	*.0002	1.97	387	***.26	68
1450	< .01	16	13.6	370	**
1600	< .01	5	95	1.28	**

Source of Absorption Coefficients of Atmospheric Gases - Watanabe *et al* (1953)

* quoted by Hall (1972) see comment in text,

** Complex wave structure, (Marmo, 1953) value at particular wavelength not useful,

*** New measurement (Carver *et al* 1977a).

The radiation within the passbands of the SX and QT chambers is considered first. Table 4.4 shows the relative magnitude of the absorption that will arise because of the gases listed in Table 4.3. The

* Note that for convenience absorption coefficients (cm^{-1}) rather than absorption cross-section (cm^2) have been used. For conversion $\mu = n\sigma$....(4.2) where n = Locshmit's number = $2.68715 \times 10^{19} cm^{-3}$.

oxygen number densities are those calculated from the data of the QT and SX chambers flown on Aerobee 13.123IS by assuming that molecular oxygen was the only absorber. The $n(CO_2)$ is that of Trinks and Fricke (1978); the $n(N_2)$ Trinks *et al* (1978a); the $n(H_2O)$ is based on the work of Martynkevich (1972) and the $n(NO)$ is from the mass spectrometer work of Trinks *et al* (1978b). The percentages given apply to all altitudes.

TABLE 4.4 THE POSSIBLE CONTRIBUTION OF ATMOSPHERIC GASES OTHER THAN O_2 TO THE ABSORPTION OF SOLAR RADIATION AT 1450Å AND 1600Å

	Gas	N_2	CO_2	H_2O	NO
WAVELENGTH					
1450Å (SX)		<< .1%	neg	neg	* < .1%
1600Å (QT)		< .1%	neg	neg	* < .2%

* These are rough estimates only. They are based on measurements of the absorption cross-section of NO by Marmo (1953). The presence of complex band structure prevents a more quantitative assessment.

From Table 4.4 the inference can be drawn that assuming O_2 is the only absorber it will introduce systematic errors no bigger than .2% and .3% in the effective absorption cross-section of SX and QT chambers respectively. Therefore, in the analysis no attempt was made to allow for the effects of the other absorbers.

Table 4.5 shows the contribution of atmospheric constituents other than O_2 to the absorption of $L\alpha$. It differs from Table 4.4 in

that the contribution is given at several heights. It can be seen that the significance of the other absorbers varies quite markedly with altitude. Two distributions of NO are included; that of Meira (1971) labelled A and that of Trinks *et al* (1978b) labelled B.

The $n(O_2)$ below 110 km is that derived from the Lα chambers of the present work. Because of the problems associated with the interpretation of data from these chambers the percentages were also calculated using the mass spectrometer results of Trinks *et al* (1978b). The differences in the percentages were small. The distributions for the other gases are as quoted for Table 4.4.

TABLE 4.5 THE POSSIBLE CONTRIBUTION OF ATMOSPHERIC GASES OTHER THAN O_2 TO THE ABSORPTION OF Lα

ALT	GAS	N_2	CO_2	H_2O	NO(A)	NO(B)
90		.4%	-		.06%	
92.5		.3%	1.2%	3%		
100		.3%	.8%	8%	1.5%	1.5%
105		.4%	.7%	21%	1.5%	4%
110		.3%	.3%	27%	10.8%	4.8%
120		.45%	.3%	53%		31%

The size of the possible contributions of the other gases to the absorption of Lα above 100 kms immediately makes it obvious why it was stated in 4.2.6. that problems with the non-monochromatic response of the ion chamber need not be the limiting factor in the use of LNO and MNO chambers. Ignoring the other absorbers in the absorption cross section adopted for Lα alone, could lead to large systematic errors and these, in general, increase as the altitude increases.

The magnitude of these errors will, however, vary significantly with the profiles assumed. For example, Hall (1972) assumed a water vapour concentration of 3 ppm. This would imply that water vapour would absorb < 4% of the Lα radiation at 110 kms. This contrasts strongly with the figure of 27% given in the Table. This figure is based on the $n(H_2O)$ measurements of Martynkevich (1972). A similar, though not as exaggerated effect, is seen with the two profiles adopted for n(NO).

It was found, however, that an effective absorption cross-section $\sigma_{EFF}(L\alpha)$ which allowed for the two most significant absorbers (H_2O and NO) did not produce a theoretical extinction curve which matched the experimental data. Nor did the implied molecular oxygen densities agree with the QT oxygen densities.

At the heights considered it has already been shown that the other wavelengths within the passband of the chamber must be taken into account (Section 4.2.6). Therefore $\sigma'_{EFF}(\lambda_1, \lambda_2)$ was calculated. This took into account what appeared to be the most significant gas-water vapour. $\sigma'_{EFF}(\lambda_1, \lambda_2)$ was 14% larger at 100 kms and 37% larger at 110 km than the $\sigma_{EFF}(\lambda_1, \lambda_2)$ described in the previous section.

But $\sigma_{EFF}(\lambda_1, \lambda_2)$ had produced a theoretical extinction curve which matched the experimental data reasonably well. If the water vapour profile* was correct the magnitude of $\sigma_{EFF}'(\lambda_1, \lambda_2)$ now required the density of molecular oxygen to be greatly reduced in order to obtain similar matching. In fact, allowing for the presence of H_2O in the atmosphere and, in addition, correcting for the non-Lyman-α response of the chamber, implied molecular oxygen densities significantly less than those derived from the QT data.

* This refers to the profile of Martynkevich, 1972.

From the considerations outlined in this section the following points arise :

1. the likely effect of other absorbers depends on the density profile assumed, and experimental determinations or theoretical estimates of these profiles are highly variable,

2. the effect of other absorbers did not appear to be able to explain the systematic differences observed between the results from the QT and Lα chambers.

Therefore, in this thesis, no attempt has been made to include the effect of the other absorbers when analysing the Lα ion chamber data. The possible but not necessarily probable magnitude of the systematic errors is given by the figures in Table 4.5. Some further discussion on this is included in Chapter 6. There the probable size of these systematic errors is considered in view of the close agreement that can be obtained between the QT and Lα implied molecular oxygen densities if $\sigma_{EFF}(\lambda_1, \lambda_2)$ (Section 4.2.6) only is used.

4.3 THE OPTICAL DEPTH FACTOR

The optical depth factor (F) has already been introduced in Section 4.1. In practical terms it relates the number of absorbing particles seen along the absorbing path to the vertical density of these particles.

This problem was first solved by Chapman (1931a, b). The approximations he derived for F are known as the Chapman functions and are functions of

(a) $X = (R_e + z)/H$ (4.28)

where R_e is the radius of the earth, z is the altitude and H is the scale height of the absorbing species defined by

$$H = kT/mg \tag{4.29}$$

m = mass of absorbing particle

g = gravitational acceleration

k = Boltzmann's constant

T = temperature

(b) Θ = the solar zenith angle

The function can be defined as

$$ch(X_p, \Theta_p) = \frac{1}{n_p H} \int_{S_p}^{\infty} n \, ds. \tag{4.30}$$

(Smith and Smith, 1972)

where the subscript denotes the observation point P. S_p is the distance co-ordinate measured positively in the solar direction and n is the concentration of the absorbing species.

In deriving his function, Chapman (1931b) assumed a constant scale height. In the real atmosphere H will vary, but Swider (1964), who carefully evaluated the optical depth factor for both constant and varying scale heights, concluded that for molecular oxygen the use of the Chapman function, $ch(X,\Theta)$, as an approximation to the optical depth factor would introduce a systematic error of $< 4\%$ if $X \geqslant 50$. Swider also noted that a mean earth radius could be used to evaluate X and in the present work R was given the value of 6378 km. Using this it was found that the X was always $\geqslant 50$.

Therefore a Chapman function has been used. As has been common practice (Smith and Smith, 1972; Weeks and Smith, 1968; Green

et al, 1964; Fitzmaurice, 1964 and Banks and Kockarts 1973) an analytical approximation is adopted.

For the first two rockets launched in the program, SL1005 and SL1207, all measurements were above 98 kms. Using the iterative procedure described later in this section to find the scale height H, X was evaluated. It ranged from 380 to 810. The rockets were flown at solar zenith angles of 38° and 50° respectively, and interpolation of the table published by Chapman (1931b) indicated that under these conditions the flat earth approximation sec Θ would differ from the Chapman function by < ½%.

Sec Θ is therefore used in the analysis. Θ is held constant. This introduces uncertainty but by adopting the apogee value of Θ the uncertainty is limited to < 1% for SL1005 and less than 1.3% for SL1207.

The third rocket, Aerobee 13.123IS was, however, launched at an approximate zenith angle of 85°. From the tables of Swider (1964) the use of sec Θ in this instance would have produced systematic errors ranging from 11% to 38%. For this rocket several approximations to the Chapman function were evaluated but that of Swider (1964) as quoted by Banks and Kockarts (1973) is the one used. For the conditions relevant to the Aerobee rocket, this formulation (given below) once again differs by < ½% from ch(X, Θ)

$$F(X, \Theta) \approx ch(X, \Theta) \approx - X \cos \Theta + [1 + X(1 + \sin \Theta]^{\frac{1}{2}} \qquad (4.31)$$

$$\{ [X (1 - \sin \Theta)]^{\frac{1}{2}} + (\pi^{\frac{1}{2}}/2)(1 - \mathrm{erf} [X (1 - \sin \Theta)]^{\frac{1}{2}})$$

$$\exp [X (1 - \sin \Theta)] \}$$ (page 107 of reference)

The optical depth factor proved to be sensitive to changes in Θ. For example, a .8% change in Θ implied a 12% change in F.

Therefore to minimise error Θ is re-evaluated for each determination of F. The algorithm for Θ allows for the changing geographical position of the rocket as well as the change in the local hour angle of the sun. It is estimated that the final uncertainty in F due to uncertainty in Θ is $\pm$ 2%.

Determination of X relies on knowing a set of values for the scale height. This is achieved by an iterative procedure. A set of scale heights is assumed, the $n(O_2)$ are calculated using the associated F, a new set of scale heights is determined from these results, then F is re-calculated. F is not very sensitive to changes in the scale height. The spread in scale heights implied by the results of the various chambers led to an uncertainty in the mean of $\pm$ 10% and this only implied an uncertainty of $\pm$ 1% in F.

In summary, the use of $ch(X, \Theta)$ for the optical depth factor implies a systematic error of $<$ 4% in $n(O_2)$. [$ch(X, \Theta)$ is greater than the true optical depth factor by up to 4%. This will result in an under-estimation of $n(O_2)$ by the same amount]. The use of an approximation to the Chapman function contributes an uncertainty of approximately ½% to the calculation of $n(O_2)$. The evaluation of the approximation adds further uncertainty. The use of a constant zenith angle for SL1005 and SL1207 implies uncertainties of 1.0% and 1.3% respectively, while uncertainties in Θ and H imply an uncertainty of 3% in the optical depth factor calculated for the Aerobee rocket.

4.4 THREE POSSIBLE METHODOLOGIES BASED ON THE USE OF THE BEER-LAMBERT LAW

4.4.1 Introduction

Equation 4.10 and 4.14 are the basic forms of the Beer-Lambert Law used in the present work. These are re-stated below:

$$n(z) = \frac{1}{F} \cdot \frac{1}{\sigma_{EFF}(z)} \cdot \frac{1}{I} \cdot \frac{dI}{dz} \tag{4.10}$$

$$I(z) = I(z + \Delta z)\, e^{-(F.\sigma_{EFF}(z).N.\Delta z)} \tag{4.14}$$

F and $\sigma_{EFF}(z)$ are common to both and have already been considered. Two of the methodologies to be discussed (Sections 4.4.2 and 4.4.3) used the differential form, equation 4.10, and the difference between them lies in their evaluation of $\frac{1}{I} \cdot \frac{dI}{dz}$, while the third used the integral form (Section 4.4.4). All three are discussed in detail. Examples of data are drawn from the plots of Chapter 5 and not reproduced in this Chapter.

4.4.2 Hand-Drawn Curves

I is the ion chamber signal. Use of actual data points will, however, unnecessarily introduce noise into the derived $n(O_2)$ profile, principally because of the noise in the telemetry (± 25 mV). The simplest way to obtain a smoother set of values that can be used in 4.10 is to plot the data points, draw by hand a curve (the extinction curve) through them, and to read the required values of this curve. Calling these values S, $\frac{1}{I} \cdot \frac{dI}{dz}$ is substituted for in the following manner.

$$\frac{1}{I} \cdot \frac{dI}{dz} = \frac{1}{S(z)} \cdot \frac{dS(z)}{dz} = \frac{1}{S(z)} \frac{S(z + \Delta z) - S(z - \Delta z)}{2\,\Delta z}$$

$$= \frac{\Delta S}{2S(z)\,\Delta z} \tag{4.32}$$

Evaluation of S(z) must take into account the amplifier offsets at the time of flight. These can usually be read straight from the plot of the raw data, and, if required statistical information can be obtained

by looking at the spread in the received signal that occurs before the chamber begins to respond to incident radiation. The value of S_{MAX} must be known to allow $j(z)$ $(j(z) = S(z)/S_{MAX})$ to be found and consequently used to ascertain the appropriate value of σ_{EFF} (Section 4.2) for equation 4.10. Provided the rocket obtains a height well above the absorbing layer, S_{MAX} can normally be read straight from the plot of the data or evaluated by averaging the signal at these heights over a period of seconds.

Drawing the curves by hand automatically smoothes out small scale fluctuations such as the scatter caused by the telemetry, but, with care, larger fluctuations representing possible atmospheric structure will not be removed. The method has the advantage of being suitable for both good and poor data. Computer-drawn plots of all the raw data received from the rocket experiments are given in Chapter 5. Figures 5.6 and 5.7 illustrate clearly the extremes of quality in the data obtained. While it is obvious that the method could be applied to the data of Figure 5.6, it is equally clear that despite the noise an extinction curve can be discerned in the data of Figure 5.7. It is quite easily drawn in by hand.

The visual display allows a quick assessment of the data. For example, Figure 5.20 shows clearly the changing sensitivity of the flight chamber SX 7 and indicates immediately that care must be observed when analysis of this chamber is undertaken. The suitability of some techniques that might be adopted can also be assessed. For example, it is seen immediately from the plot of the QT 204 downleg (Figure 5.7) that attempts to find S_{MAX} by averaging the signal observed during the time the rocket was above the absorbing layer would give S_{MAX} a value

systematically above the easily recognized level in the plot. In addition, the standard deviation, which would have to be associated with the mean would be disproportionately large, because of the noise spikes. S_{MAX} for this chamber, was, therefore, not found by averaging signal levels.

The major disadvantage of the method is the lack of formal information about the uncertainty or error associated with the results. Data quality permitting, the mean and standard deviation of both offset and S_{MAX} can sometimes be determined, but information of this type could not be obtained for the values read off the extinction curve itself. Averaging is not valid because of the rapidly changing value for the flux incident on the ion chamber as the rocket moves up through the absorbing layer. However, each data point is associated with an uncertainty of $\pm$ 25 mV (δ S), because of the telemetry, and the suitability of assigning the same uncertainty to the points read from the graph was investigated.

Assigning δ S to S(z) leads to apparent uncertainties of 100% or greater in ΔS at the extreme ends of the extinction curve. If Δz, the height interval, is increased so that ΔS remains large compared with δ S, information about possible structure is lost.

In the present work this was considered unavoidable and initially Δz was as large as 4 kms. It was found, however, that for most data, varying Δz from 2-4 kms had very little effect. The scatter in the derived $n(O_2)$ remained the same although the apparent error in ΔS was approximately halved. This supported the hypothesis that the smoothing implied by the hand-drawn curve invalidated the use of the 25 mV telemetry noise as an estimation of the uncertainty in the data.

It is considered that the only true estimation of the uncertainty in the number densities obtained in this way would come from the statistical variation in the results of several chambers. The discussion of the extent to which this type of information was available in the present work is left to Chapter 6.

Therefore in summary, the use of this technique involves the following steps :

(a) large scale plots of the raw data are drawn by a computer,

(b) a smooth curve is drawn by hand through the points,

(c) S is read off this curve at ½ km or 1 km intervals,

(d) $\frac{1}{I} \cdot \frac{dI}{dz}$ is evaluated using equation 4.32,

(e) if possible the amplifier offsets and S_{MAX} are read off each curve.

Where, as in some uplegs - for example - the upleg of QT 1 on Skylark SL1207 (Figure 5.13) - this is not possible, it is assumed that the amplifier offsets read off the downleg curve apply for the whole flight.

4.4.3 The Use of Weighted Differences

The inability of the method described in Section 4.4.2 to generate appropriate error information led to the development of a second methodology. This approach to the data relies on the use of averaged weighted differences to determine $\frac{dI}{dz}$.

The initial step involves choosing a specific, but arbitrary, interval of a number of consecutive points, dividing the data into these

intervals, and for each interval calculating the mean $(\overline{y}_k)$ and standard deviation $(\sigma_{y_k})^*$ of the points that make up the interval. Then in any one interval if a data point doesn't match the criterion

$$\overline{y}_k - 3\,\sigma_{y_k} < y_k < \overline{y}_k + 3\,\sigma_{y_k}$$

it is rejected. The choice of the number of points was not completely arbitrary. It was found that if the number chosen implied too great an interval, then the genuine changes in y_k led to a large σ_{y_k} and the criterion adopted failed to filter out noise spikes. The use of 10 points proved satisfactory.

Application of the above is followed by a re-calculation of the mean $(\overline{y}'_k)$ and the adoption of a new criterion

$$\overline{y}'_k - 2\,\sigma'_{y_k} < y_k < \overline{y}'_k + 2\,\sigma'_{y_k}$$

where σ'_{y_k} is the standard deviation associated with $\overline{y}'_k$. This removes most noise spikes in the data and is preferred because the remaining y_k are unmodified by the technique. This smoothed data set shall be referred to as y_m.

The next step is the generation of points at equally spaced height intervals. This is achieved by the following. At some height, z_{0_i},

$$y_{0_i} = \frac{\Sigma\, w_m\, y_m}{\Sigma\, w_m} \tag{4.33}$$

Where the summation is taken over the whole data set y_m and w_m is the weighting function given by

* Note that in this section $\sigma_{\text{PARAMETER}}$ implies the Gaussian standard deviation of that parameter. Because absorption cross-sections are not discussed in this section there is no conflict of notation.

$$w_m = e^{-x_m^2} \tag{4.34}$$

and

$$x_m = \frac{z_m - z_{0_i}}{\delta z_1} \tag{4.35}$$

where z_m is the height of the point y_m and δz_1 is the resolution, (this will be discussed in more detail later). In practice to restrict the summation to a more realistic average and to reduce computing time x_m is given the range $-2.5 \leqslant x_m \leqslant 2.5$, and no data point, y_m, is considered if its corresponding x_m falls outside the range.

The slope at z_{0_i} (i.e. $\frac{dI}{dz}$) is generated in a similar manner

$$g_{0_i} = \frac{\Sigma\, w_n'\, g_n}{\Sigma\, w_n'} . \tag{4.36}$$

where g_n is either given by

$$g_n = (y_{0_n} - y_{0_{(n-1)}})/\Delta z_0 \qquad \text{(Case 1)} \tag{4.37}$$

with a corresponding weight function of

$$w_n' = e^{-x_n^2} \tag{4.38}$$

or alternatively, around the point (z_{0_i}, y_{0_i}) of the previous step

$$g_n = \frac{y_{0_n} - y_{0_i}}{h_n - z_{0_i}} \quad n \neq i \qquad \text{(Case 2)} \tag{4.39}$$

where the y_{0_n} are also the weighted values of the previous step and h_n the altitude of y_{0_n}

For Case 2 the weighting function at $n=i$ must equal 0. A suitable weighting function is given by differentiating 4.38 i.e. w_n' becomes

$$w_n' = -2x_n\, e^{-x_n^2} \tag{4.40}$$

Figures 4.11 and 4.12 show sketches of the meaning of the different g_n

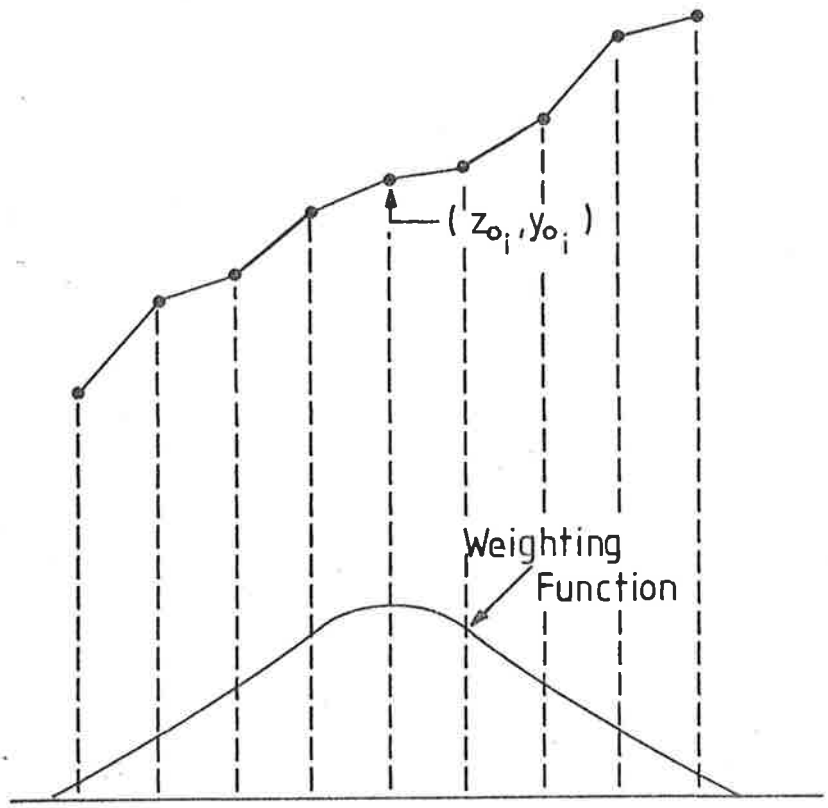

Fig 4.11 <u>Case 1</u>: the gradient at (z_{o_i}, y_{o_i}) is the weighted mean of the individual gradients between each pair of points. The weighting function shows the weighting for each gradient.

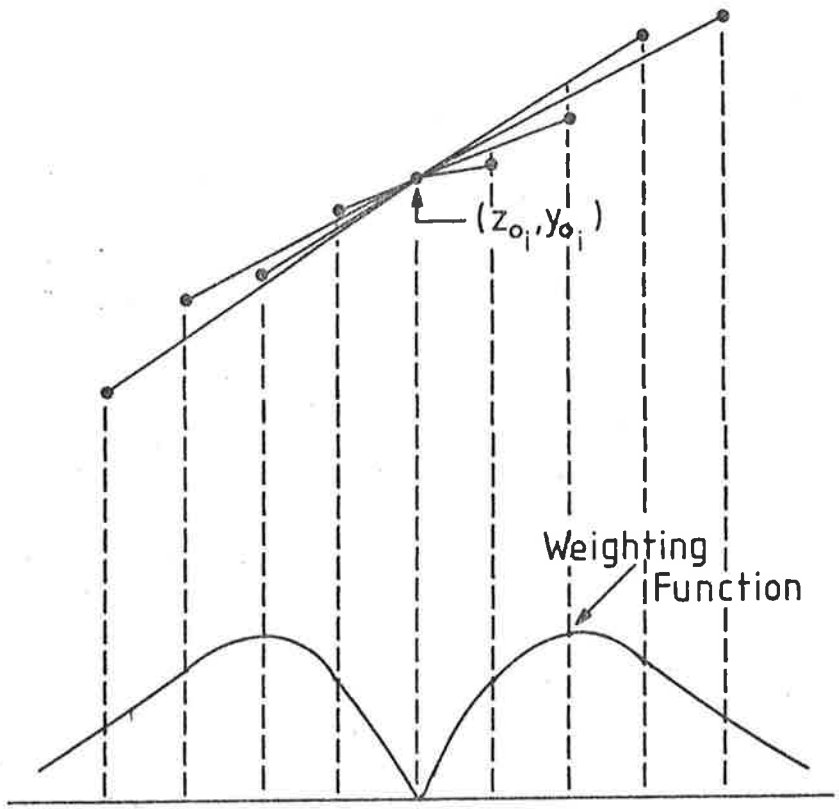

Fig. 4.12 <u>Case 2</u>: the gradient at $(z_{o\,i}, y_{o\,i})$ is the weighted mean of the gradients between each point and $(z_{o\,i}, y_{o\,i})$.

Also shown is a sketch of their assumed weighting function.

A variation of Case 2 may also be considered (Figure 4.13).

$$g_n = \frac{y_{0(i+n)} - y_{0(i-n)}}{\Delta h_n} \qquad \text{(Case 3)}$$

where $\Delta h_n = 2n\,\Delta z_0$ and the weighting will depend on the distance between y_{0_i} and $y_{0_{(i+n)}}$.

For Case 1, 2 and 3, the errors associated with g_0 are

$$\sigma_{g_0} = \sqrt{\frac{N_0\,\Sigma\, w_n'\,(g_n - g_0)^2}{(N_0-1)\,\Sigma\, w_n'}} \qquad (4.41)$$

where N_0 is the actual number of points used in the summation.

δz_1 was introduced as the resolution of y_{0_i} in equation 4.35.

$$\text{i.e.} \qquad x_m = \frac{z_m - z_{0_i}}{\delta z_1}$$

The chosen criterion for the choice of δz_1 was the desire for the normalized weighting functions of two adjacent points to intersect at

$$w_1 = w_2 = .5$$

The distance Δz_0 between the points is fixed by the data and in the present work the smallest Δz_0 that could be considered is .25 kms. At the point of intersection

$$z_m = z_{0_i} + \tfrac{1}{2}\,\Delta z_0$$

and

$$x_m = \frac{z_m - z_{0_i}}{\delta z_1} = \frac{\Delta z_0}{2\delta z_1}$$

$$\therefore \qquad e^{-\left(\frac{\Delta z_0}{2\delta z_1}\right)^2} = \tfrac{1}{2}$$

Taking the natural logarithm of both sides

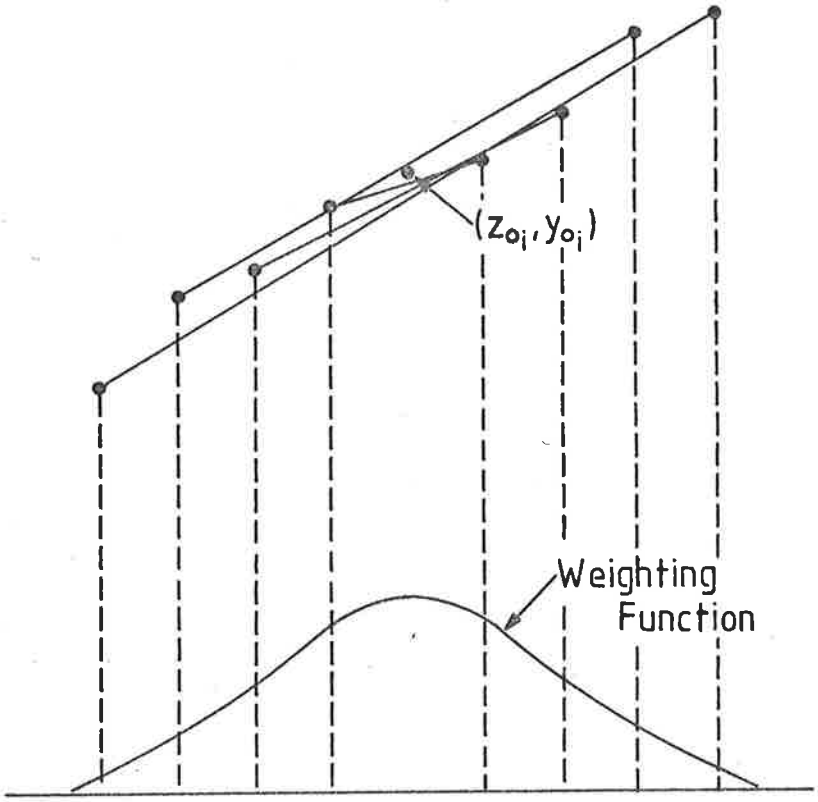

Fig. 4.13 <u>Case 3:</u> the gradient at $(z_{o\,i}, y_{o\,i})$ is the weighted mean of the gradients between points equidistant from $(z_{o\,i}, y_{o\,i})$.

$$\left(\frac{\Delta z_0}{2\delta z_1}\right)^2 = \ln 2$$

$$\therefore \quad \delta z = \Delta z_0 / 2\sqrt{\ln 2} \qquad (4.42)$$

Then if Δz_0 equals .25 kms

$$\delta z_1 = .15 \text{ kms.}$$

It is easily shown that the use of δz_1 is, however, inappropriate for the weighting function of g_n. If Case 2 is considered, the weighting function is given by equation 4.40. Therefore the maximum weighting will occur at

$$\frac{\partial}{\partial x}\left(-2xe^{-x^2}\right) = 0$$

$$\therefore \quad e^{-x^2}(4x^2 - 2) = 0$$

$$\therefore \quad x = \pm \frac{1}{\sqrt{2}}$$

but for g_n $\quad x_n = \dfrac{z_{0_n} - z_{0_i}}{\delta z_1}$

Taking $\Delta z_0 = .25$ kms again, and with $\delta z_1 = .15$ the maximum weighting will occur at $x = .106$ kms, i.e. .106 kms away from Z_{0_i}, but the first point occurs .25 kms away and a quick sketch (Figure 4.14) will show the unsuitability of the weighting inferred by $\delta z_1 = .15$.

Therefore x_n' is used in the weighting function for g_n; x_n' is defined as

$$x_n' = \frac{z_{0_n} - z_{0_i}}{\delta z_2} \qquad (4.43)$$

δz_2 is used to generate the smoothing of g_0 desired. If, for example, the maximum weighting is required for points $2\Delta z_0$ away, i.e. g_2.

$$\delta z_1 = 2 \times .25 / \frac{1}{\sqrt{2}} \approx .7 \text{ kms.}$$

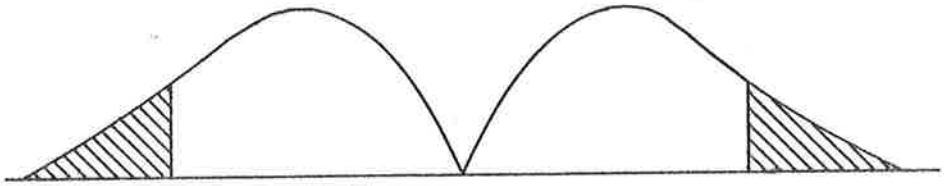

Fig. 4.14 If the resolution is too small, weighting occurs in the wings of the weighting function as illustrated by the shaded area above.

i.e. the smoothing for g_0 is significantly greater than that for y_0.

The method of weighted differences can only be used with smooth data. This prerequisite is a limitation and prevents application of the technique to many of the extinction curves given in Chapter 5 e.g. Figs. 5.7, 5.10 and 5.25. However, data like the extinction curve for QT204 upleg (Fig 5.6) is suitable and the analysis of this chamber's results is presented to illustrate the method.

Calculations were carried out for Δz_0 = .25 kms, .5 kms and 1 km. Therefore, δz_1 and δz_2 were as given in Table 4.6. δz_2 was generated by the criterion that g_2 should be the most significant. Values are given in km.

TABLE 4.6

Δz_0	δz_1	δz_2
.25	.15	.7
.5	.3	1.4
1.0	.6	2.8

The $n(O_2)$ profile obtained with Δz_0 = .25 kms is given in Fig. 4.15, with Δz_0 = .5 kms in Fig. 4.16 and with Δz_0 = 1 km in Fig 4.17. Although the values are plotted 1 km apart, the resolution of the graphs will be the corresponding δz_2 given in Table 4.6, the given value being at the midpoint of that interval.

All three profiles show scatter. Figs. 4.15, 4.16 and 4.17 were generated by first using 4.39 to generate g_n; and the altitude at which the scatter becomes apparent, 119 kms, 129 kms and 137 kms respectively,

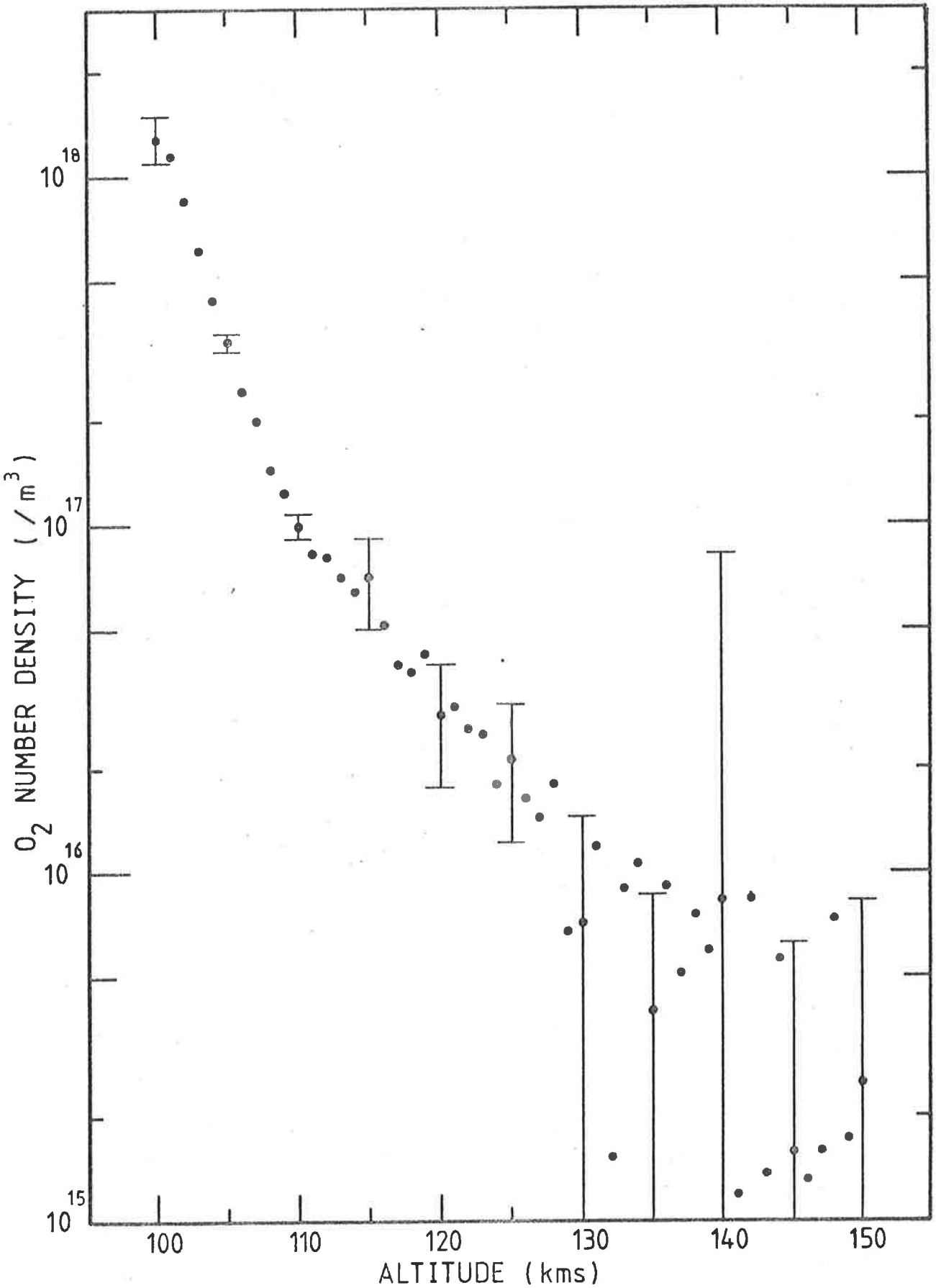

Fig. 4.15 $n(O_2)$ derived from telemetred signal shown in fig. 5.6. $\Delta z_0 = .25$ km.

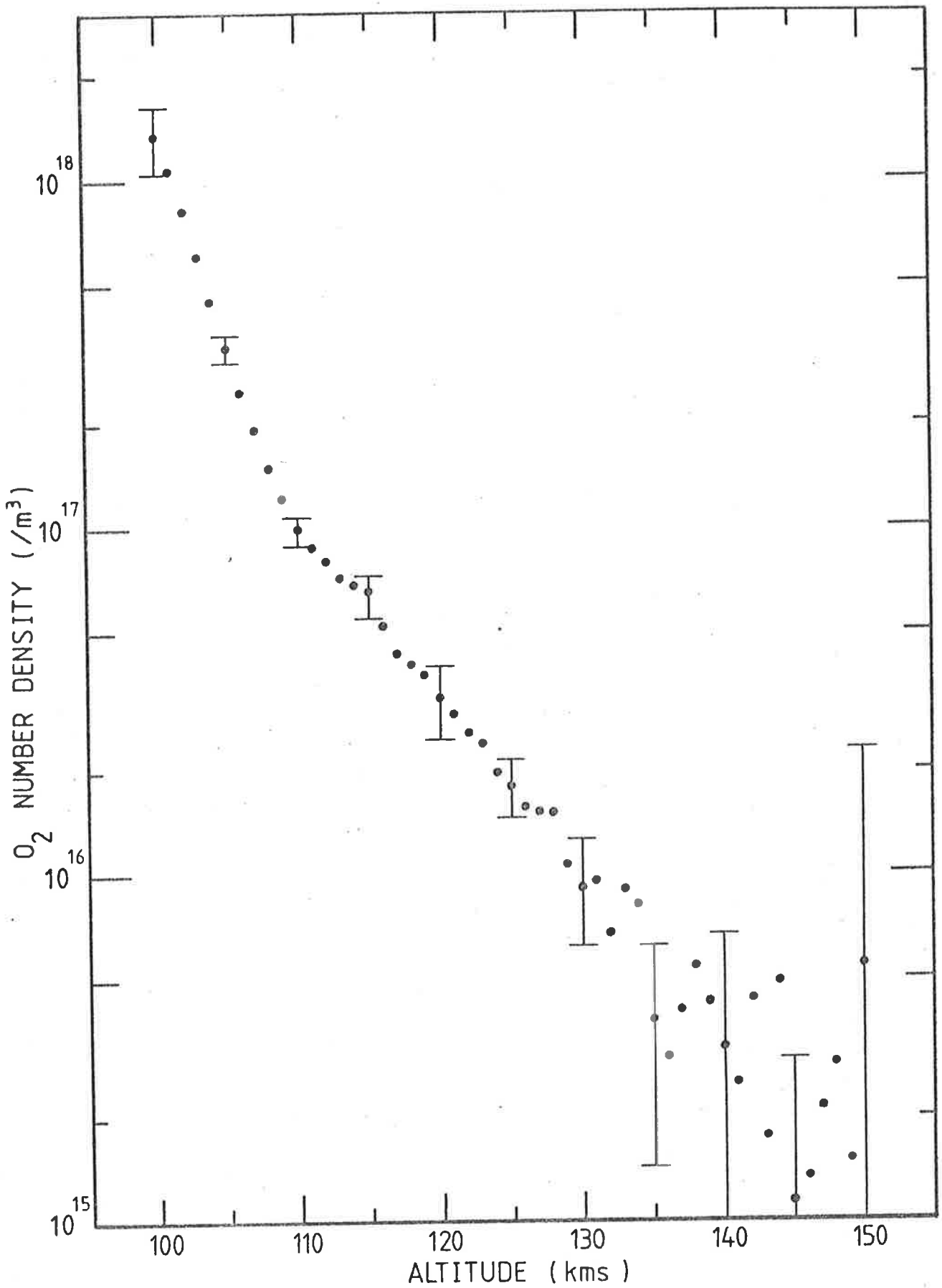

Fig. 4.16 $n(O_2)$ derived from telemetred signal shown in fig. 5.6. $\Delta z_0 = .5$ km.

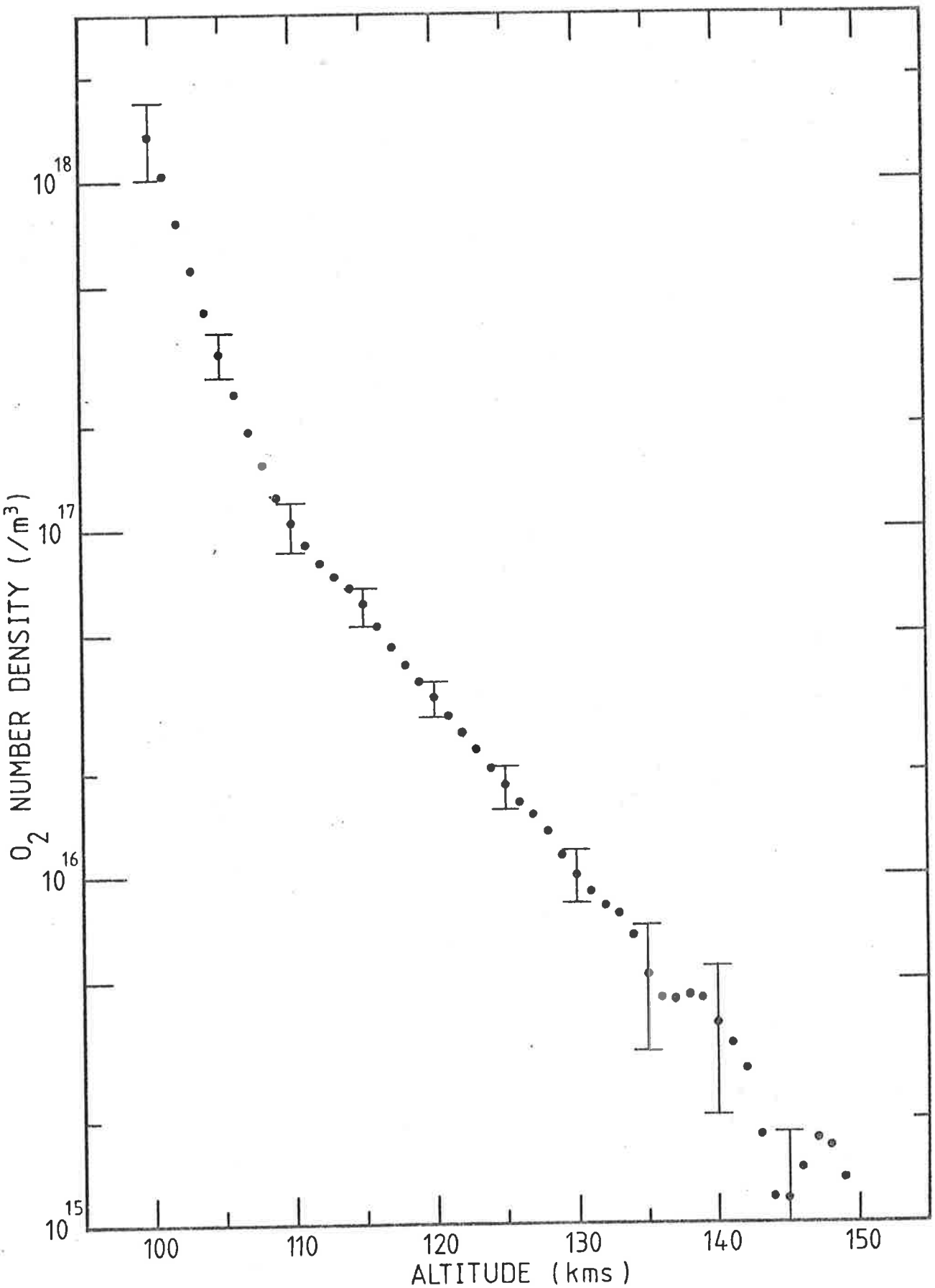

Fig. 4.17 $n(O_2)$ derived from telemetred signal shown in fig. 5.6. $\Delta z_0 = 1$ km.

corresponds well with the altitude at which $|y_{0_{(i+2)}} - y_{0_i}|$ becomes less than or approximately equal to the telemetry uncertainty δS. The correspondence to $|y_{0_{(i+2)}} - y_{0_i}|$ rather than $|y_{0_{(i+1)}} - y_{0_i}|$ is not unexpected since the maximum weighting in the generation of g_{0_i} (Equation 4.36) is given to g_2 (Equation 4.39). This result would suggest that the altitude resolution is limited by the telemetry uncertainty.

The start of the scatter is pronounced and clearly indicates where the viability of the adopted resolution ends, but an expression (Equation 4.41) was given for estimating the uncertainty (σ_{g_0}) associated with a particular evaluation of g_0, and the magnitude of σ_{g_0} is also of interest.

Although this magnitude shows great variation there are several general observations that can be made. These are

(1) uncertainties below the altitude where scatter becomes pronounced are on average considerably less than those above this altitude,

(2) uncertainties associated with g_0 at the upper limit of the extinction curve, on average, decrease as the resolution decreases. For example, at z_0 = 157 kms, $\sigma_{g_0} \approx 67\%$ for Δz_0 = 1 km, while for Δz_0 = .5 kms, $\sigma_{g_0} \approx 100\%$ at this same altitude,

(3) at some altitudes a decrease in resolution may increase σ_{g_0}. For example, at z_0 = 105 kms, σ_{g_0} for Δz_0 = .25 kms, .5 kms and 1 km equals 5.7%, 8.6% and 13.2% respectively.

These general observations may be seen graphically by referring to Figures 4.15, 4.16 and 4.17, where the uncertainty arising

from the uncertainty in g_0 (the uncertainty in $n(O_2)$ discussed in Sections 4.2 and 4.3 is for the moment ignored) is indicated at several different heights.

Points (1) and (2) are consistent with the appearance of the data. However, the increase in the magnitude of σ_{g_0} with a decrease in resolution prompted further investigation into the significance of σ_{g_0} and its calculated magnitude.

σ_{g_0} (Equation 4.41) is a weighted estimate of the uncertainty associated with g_0. The weighting function, w_n', in combination with the resolution δz_2, in effect, defines the smoothing being carried out in obtaining g_0, but it was found that σ_{g_0} was much more sensitive to the choice of these parameters than g_0 itself. In fact, calculations involving different w_n' and different altitude resolutions led to the conclusion that the magnitude of σ_{g_0} not only reflected the uncertainty in the data, but also the suitability of the chosen weighting function and the resolution.

This is consistent with the observation that a decrease in resolution could increase the uncertainty associated with g_0. A decrease in resolution is equivalent to an increase in smoothing and the g_n are calculated over much larger distances. If the slope of the curve is changing quickly, genuine systematic changes in g_n will enhance σ_{g_0}. It was found that the smoothing adopted had to be a compromise between averaging out purely statistical fluctuations and enhancing σ_{g_0} because of these genuine changes in g_n. Although there were exceptions at a few altitudes the compromise implied using a gradually decreasing resolution as the altitude increased.

The results are not given graphically, but the data was also analyzed using Δz_0 = 2 kms. Using the methods already outlined in this section to calculate y_0, and then g_0, the resolution of the final profile was 5.6 kms and the g_0 were calculated over distances as large as 14 kms. The calculated values of σ_{g_0} were consistent with the above results. At the lower altitudes genuine variation in g_n led to a σ_{g_0} some 3 or 4 times greater than that for Δz_0 = .25 kms, while, at the higher altitudes, where statistical fluctuations dominated, the increased smoothing led to a σ_{g_0} that was smaller than those calculated for the other spacings.

In summary, $\frac{dI}{dz}$ (i.e. g_0) can be calculated by the method of weighted differences provided the data is smooth and continuous. An estimate of the uncertainty (σ_{g_0}), associated with the evaluation of g_0 at any height, can be made, but the σ_{g_0} will reflect, not only the uncertainty of the data but also the suitability of the chosen resolution.

4.4.4 Curve Fitting and the Method of Maximum Likelihood

As well as drawing, by hand, a line of best fit through the data points, an attempt was made to find a mathematical function which described the extinction curve of the ion chamber. Polynominals were found which appeared to fit most of the data well but their usefulness was limited by their inability to describe the rapid changes in slope seen at the upper and lower limits of the data. It may have been possible to build up composite curves of polynominals which did adequately describe the data, but since the absorption is expected to be exponential it was considered more realistic to fit an exponential or a series of exponentials.

A technique was developed whereby the molecular oxygen density was used as a fitting parameter for an exponential of the form

$$y_i = ae^{-b \Delta x_i} \tag{4.44}$$

where a = the initial signal at height h; Δx_i = distance from h measured downwards (see Figure 4.18);

$$b = N . \sigma_{EFF} . F \tag{4.45}$$

N = molecular oxygen density at height h,

F = optical depth factor,

σ_{EFF} = effective absorption cross-section for the chamber at height h.

Problems with notation arise. However, in the following, σ with the subscript EFF (i.e. σ_{EFF}) represents the effective absorption cross-section of the chamber, σ with any other subscript, i.e. σ_B, represents the statistical uncertainty of the parameter identified by the subscript.

No attempt was made to find one set of parameters (a, b) which described all the data points. Holding N and σ_{EFF} constant this would not have been possible. Equation 4.44 was fitted to 30 data points at a time. This was a compromise between the need for adequate statistics and the desire for a useful height resolution. 30 data points corresponded to an interval of approximately 1 to 1½ kms.

To fit the exponential to the data the method of maximum likelihood is adopted. i.e. Chi-squared (χ^2) is minimized. For an exponential of the form given in 4.44.

$$\chi^2 = \sum_{i=1}^{n} \frac{[y_i - ae^{-b \Delta x_i}]^2}{\sigma_{y_i}^2} \tag{4.46}$$

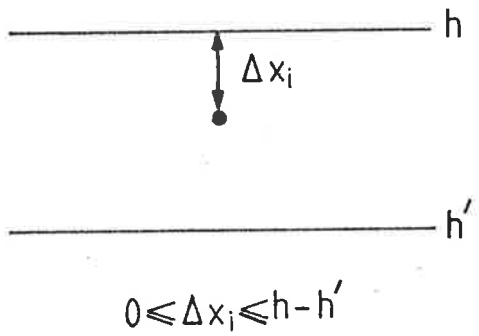

Fig 4.18 Basic assumptions for method of maximum likelihood.

For the purposes of this analysis the uncertainty in all y_i, σ_{y_i}, is taken to be equivalent. χ^2 is a minimum and the coefficients a and b are optimal at

$$\frac{\partial f}{\partial a} = \frac{\partial f}{\partial b} = 0 \qquad (4.47)$$

where f is the right hand side of 4.46 Taking $\sigma_{y_1} = \sigma_{y_2} = \sigma_{y_3} = \sigma_{y_i}$ = constant, 4.47 leads to

$$\Sigma \left[y_i - ae^{-b \Delta x_i} \right] \left[- e^{-b \Delta x_i} \right] = 0 \qquad (4.48)$$

$$\Sigma \left[y_i - ae^{-b \Delta x_i} \right] \left[+ ae^{-b \Delta x_i} . \Delta x_i \right] = 0 \qquad (4.49)$$

The magnitude of $b \Delta x_i$ ranges from 10^{-2} to 10^{-4}. Therefore the approximation $e^t = 1 + t$ can be used and (4.48) and (4.49) become

$$na - \Sigma_{y_i} - 2ab \Sigma \Delta x_i + b \Sigma \Delta x_i y_i = 0. \qquad (4.50)$$

and

$$\Sigma \Delta x_i y_i - b \Sigma \Delta x_i^2 y_i - a \Sigma \Delta x_i + 2 ab \Sigma \Delta x_i^2 = 0 \qquad (4.51)$$

respectively. Therefore, two equations are generated which contain a and b and solutions for a and b may be found.

The numerical calculations were carried out on a computer. The program used,and the method itself,were tested by finding a and b for a real function which had been used to generate y_i from a given set of x_i. The test function was

$$y_i = 2.00 \, e^{-(2.9 \times 10^{-5}) \Delta x_i}$$

The constants were chosen to approximate values that would occur if the method was applied to rocket flight data.

From 4.45 it is clear that $n(O_2)$ is derived from the value of b. Any uncertainty in the evaluation of b will add to the uncertainty in the derived $n(O_2)$. The test program suggested that errors in b would be of the order of 3½%. However, this was only for one specific choice of b and the error was expected to vary. Therefore the uncertainty in b is calculated for each value of b.

$$\sigma_b^2 = \Sigma \frac{\partial b}{\partial y_i} \sigma_{y_i}^2 \qquad (4.52)$$

Initially, σ_{y_i} was taken to be constant and equal to the uncertainty in the telemetry. $\frac{\partial b}{\partial y_i}$ was determined by manipulation of (4.50) and (4.51). The errors generated by this approach were too large.

The uncertainty for each interval is, therefore, estimated by looking at the way the data deviates from the theoretical expression calculated for that height interval.

$$\text{i.e.} \quad \sigma_j^2 = \frac{1}{n-2} \Sigma(y_i - a_j e^{-b_j \Delta x_j})^2 \qquad (4.53)$$

where the subscript j denotes a particular height interval and n is the number of data points in the interval. The uncertainty in b becomes

$$\sigma_{b_j}^2 = \Sigma \frac{\partial b_j}{\partial y_i} \sigma_j^2 \qquad (4.54)$$

Figure 4.19 shows the results obtained from the data of Fig 5.6. Use of σ_{b_j} produces reasonable behaviour in the calculated errors. They show a steady increase as the real change in signal over the 30 point interval (i.e. the change in the signal due to changing incident flux levels) approaches the telemetry uncertainty δS. It can be seen also that they are larger than the 3½% predicted by the test program. If a

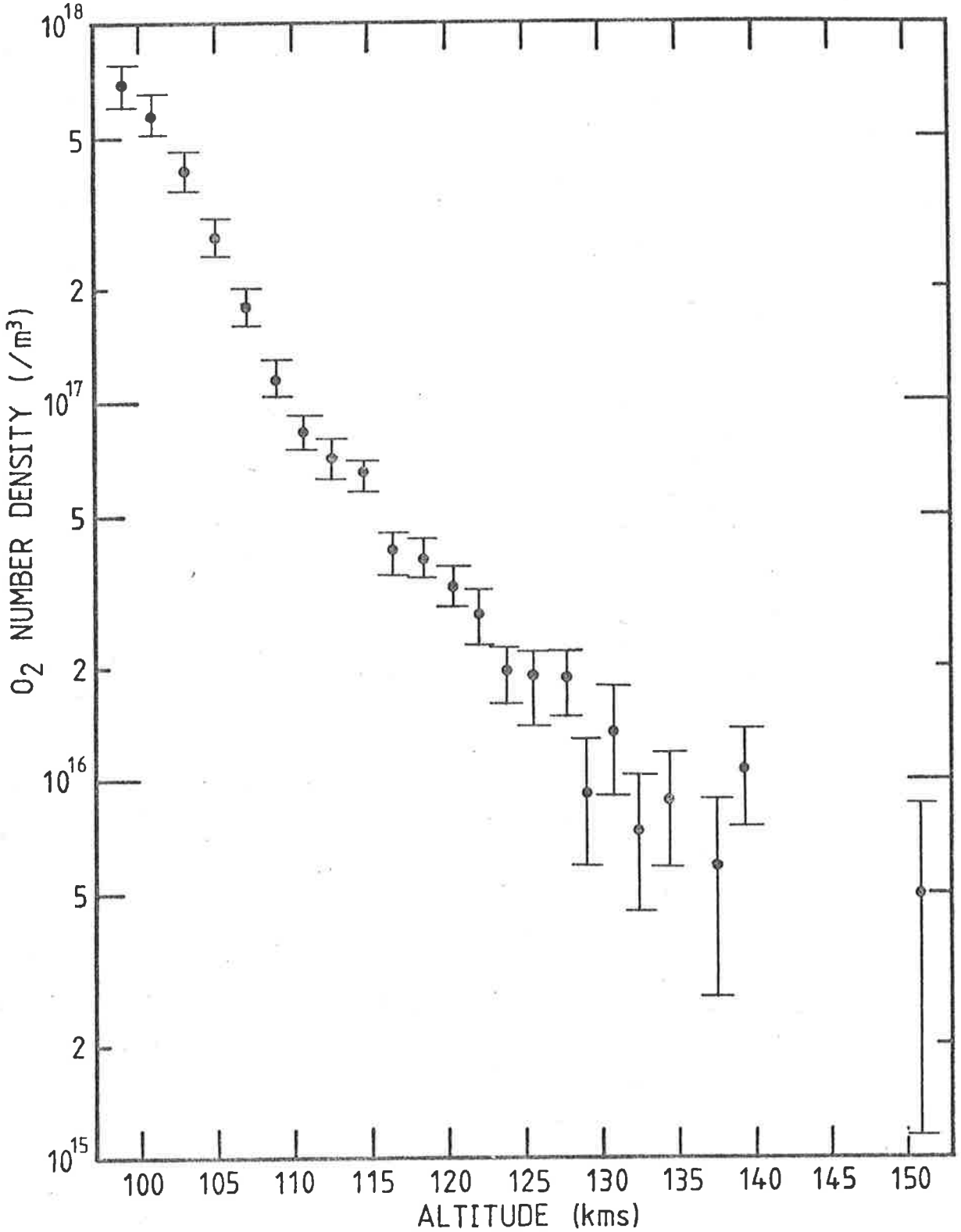

Fig 4.19 $n(O_2)$ derived from telemetred signal shown in figure 5.6 by adopting the method of maximum likelihood.

smaller interval is chosen, e.g. 10 pts. the errors increase, as would be expected, from the poorer statistics implied.

As with the other techniques discussed, the method of maximum likelihood has both advantages and disadvantages. The major advantage is the ability to extract error information from the data. Not only did σ_{b_j} indicate the uncertainty in the derived $n(O_2)$ that arose from the analysis method, but inference could be drawn from the behaviour of σ_{b_j}. Statistically σ_{b_j} would be expected to vary slowly from interval to interval. If σ_{b_j} varied strongly this could be indicative of atmospheric structure and such behaviour would clearly delineate regions where closer more careful analysis was warranted. Against the technique was the fact that, as with the method of weighted differences, the technique could not be applied to poor quality data, (Figure 5.7), or intermittant data, (Figure 5.25), or the data from the spectrophotometer, (Figure 5.10).

4.5 CHOICE OF METHODOLOGY

Three techniques for finding $\frac{dI}{dz}$ have been described. It was pointed out in sections 4.4.3 and 4.4.4 that neither the method of maximum likelihood nor the method of weighted differences could be used on poor quality or intermittant data. This contrasted with the capability, stated in Section 4.4.2, of the method of hand-drawn curves to handle all the data obtained in this research program. (see Chapter 5).

It is obvious, therefore, if only one method is to be used it must be that outlined in Section 4.4.2. However, in view of the error information that can be obtained from both of the other techniques, it was decided to investigate whether or not it was valid to compare

number densities determined by different techniques. If this was so then the use of the hand-drawn curves technique could be restricted to the data that could not be handled by the other two methods.

The data, from several QT and SX ion chambers, was analyzed using each of the techniques. An example of the results for a QT chamber is given in Figure 4.20, while Figure 4.21 displays the results from an SX chamber. The height resolution for all techniques is similar, approximately 1 - 2 kms. The flight data from which the $n(O_2)$ were derived is given in Figure 5.6 and Figure 5.18. Several features are immediately apparent. These are:-

(1) over the middle section of the profiles the number densities determined by each method are similar,

(2) at the lower altitude limit the results from the method of maximum likelihood appear to differ systematically from the other two profiles,

(3) and at the upper altitude limit all profiles show scatter, with the scatter being the most pronounced for the method of maximum likelihood.

The discrepancy between the $n(O_2)$ profile from the method of maximum likelihood and that from the method of hand-drawn curves immediately suggests that comparison between data analyzed by these two different methods would be invalid. As to which method should be used to give the better estimate of the atmospheric O_2 densities at the time of measurement, it is considered that the method of maximum likelihood cannot be regarded as reliable and should not be used. The rationale behind this conclusion follows.

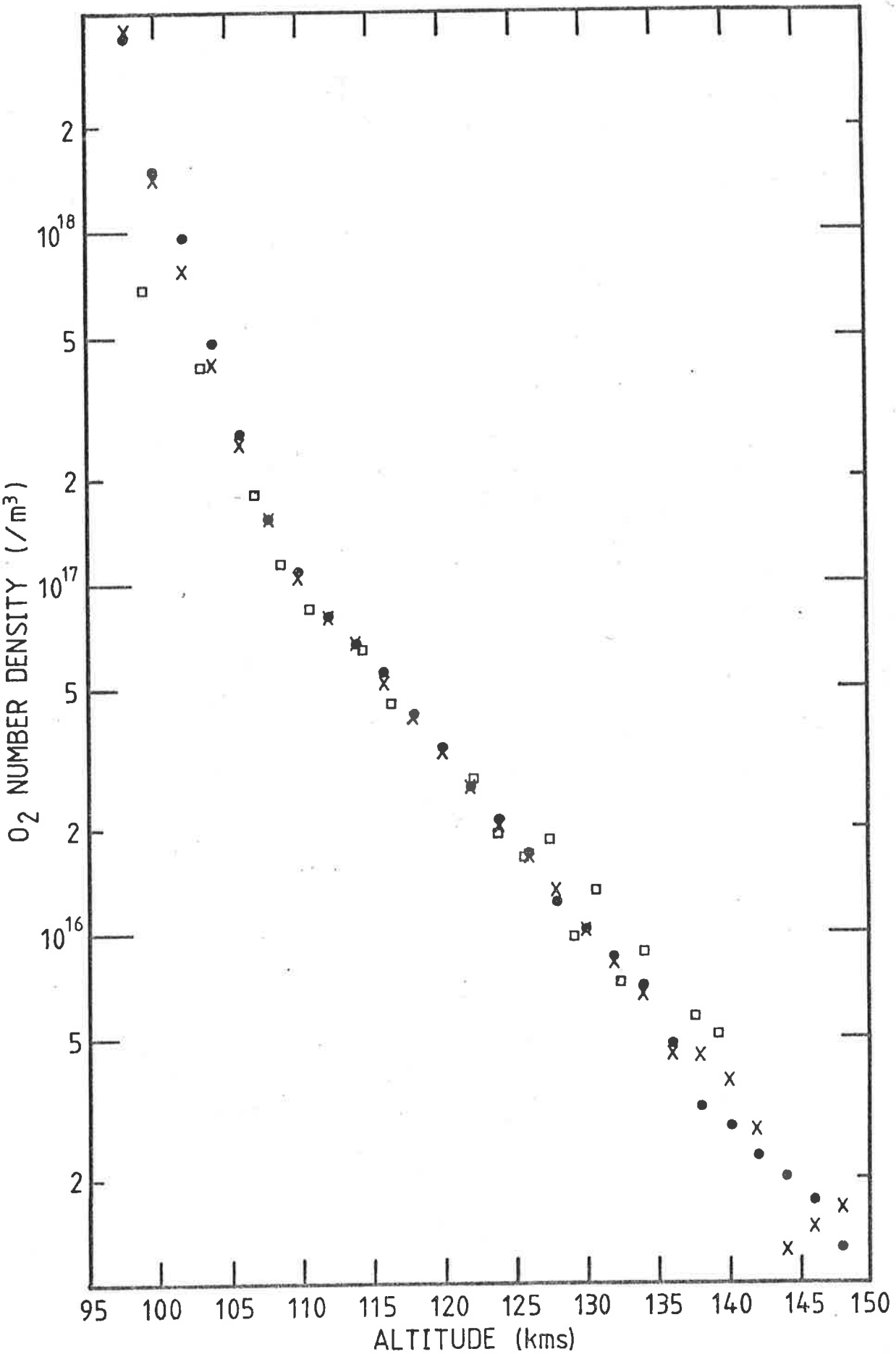

Fig 4.20 Comparison of $n(O_2)$ derived from data of figure 5.6 using the three different methodologies outlined in section 4.4.

- ● hand-drawn curve
- X method of weighted differences
- □ method of maximum likelihood.

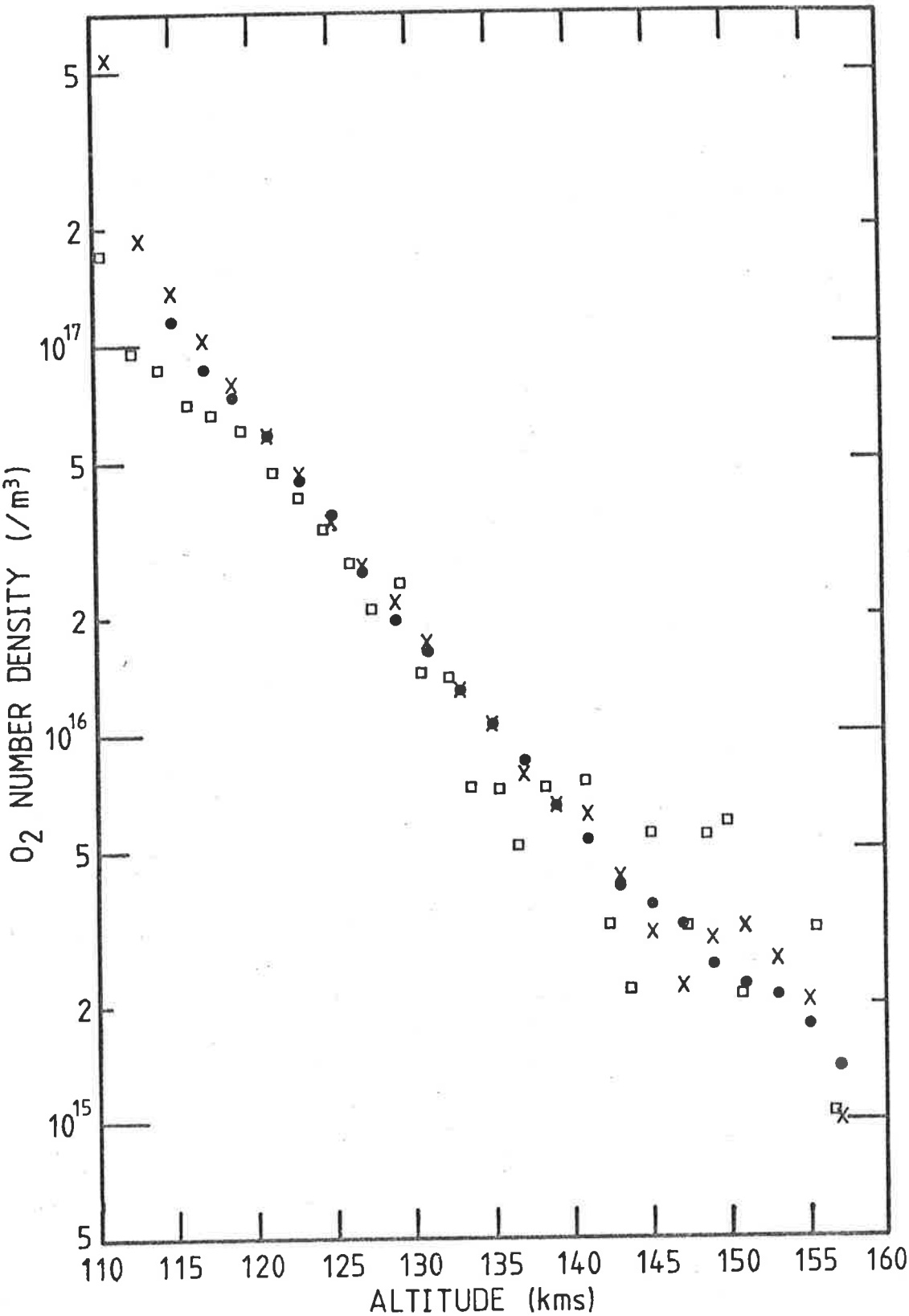

Fig 4.21 Comparison of $n(O_2)$ derived from data of figure 5.18 using the three different methodologies outlined in section 4.4.

- ● hand-drawn curve
- X method of weighted differences
- □ method of maximum likelihood.

Apart from the pronounced scatter, seen at the higher altitudes and suggesting an extreme sensitivity to statistical fluctuation in the data, it was found, on further investigation, that the number density obtained depended on the resolution chosen. At the lower altitude limit, for example, fitting the exponential to data from a smaller height range (½ kms rather than 1½ kms) gave a mean $n(O_2)$ well in excess of those shown on the graphs and very close to the other two profiles. The densities obtained were different again when a 2½ km interval was used.

This dependence could have been tolerated if some valid criterion for choosing the appropriate interval had been found. However, even the uncertainty associated with the number density could not be used to select the interval. In the above example, the uncertainty associated with the number density derived from fitting the exponential to a smaller interval, was larger, because of the poorer statistics afforded by fewer data points, yet the results appeared to be more satisfactory. The method of maximum likelihood was not considered any further.

In contrast to the method just discussed, the $n(O_2)$ from the method of weighted means shows close agreement with the $n(O_2)$ from the method of hand-drawn curves over most of the altitude range covered in Figures 4.20 and 4.21. Nor does the choice of resolution significantly affect the derived $n(O_2)$ as long as the chosen resolution does not exceed the quality of the data. However, at the upper limits of both profiles illustrated, the $n(O_2)$ profile displays an oscillatory pattern which is not duplicated in the $n(O_2)$ profile derived from the hand-drawn curves. This makes comparison between profiles from the two different methods suspect, but the more important question raised was

whether or not the oscillations represented genuine atmospheric conditions at the time of the measurement.

These oscillations have already been interpreted in Section 4.4.3, as signalling the point where the data could no longer support the chosen resolution and they are considered an artifact of the method. A more careful appraisal confirms this conclusion.

If the oscillations represented genuine atmospheric structure, the $n(O_2)$ profile derived, at the same resolution, from two different chambers flown on the same rocket, would be expected to behave in a similar manner. However, it is found that while the data from one chamber may lead to an oscillatory $n(O_2)$ profile, at the same height, the data from the second chamber may predict a smoothly varying profile. For each resolution adopted, the occurrence or otherwise of oscillations in the $n(O_2)$ profile derived from either of the ion chambers depends, as was stressed in Section 4.4.3, on the relative magnitudes of $|y_{0_{(i+2)}} - y_{0_i}|$ and δS, the telemetry uncertainty. It does not correlate with a particular altitude as would be expected if it were a genuine atmospheric phenomenon.

Figure 4.22 shows a composite profile determined by the method of weighted differences. The densities are plotted at 1 or 2 km intervals, but the resolution alters, as indicated on the graph, from .7 kms to 2.8 kms. The resolution is gradually decreased, with increasing altitude, in order to minimise the uncertainty (restricted to σ_{g_0} - Section 4.4.3) associated with the number density given. This uncertainty is given as error bars on the graph. The uncertainties discussed in 4.2 and 4.3 are not included since they affect all profiles

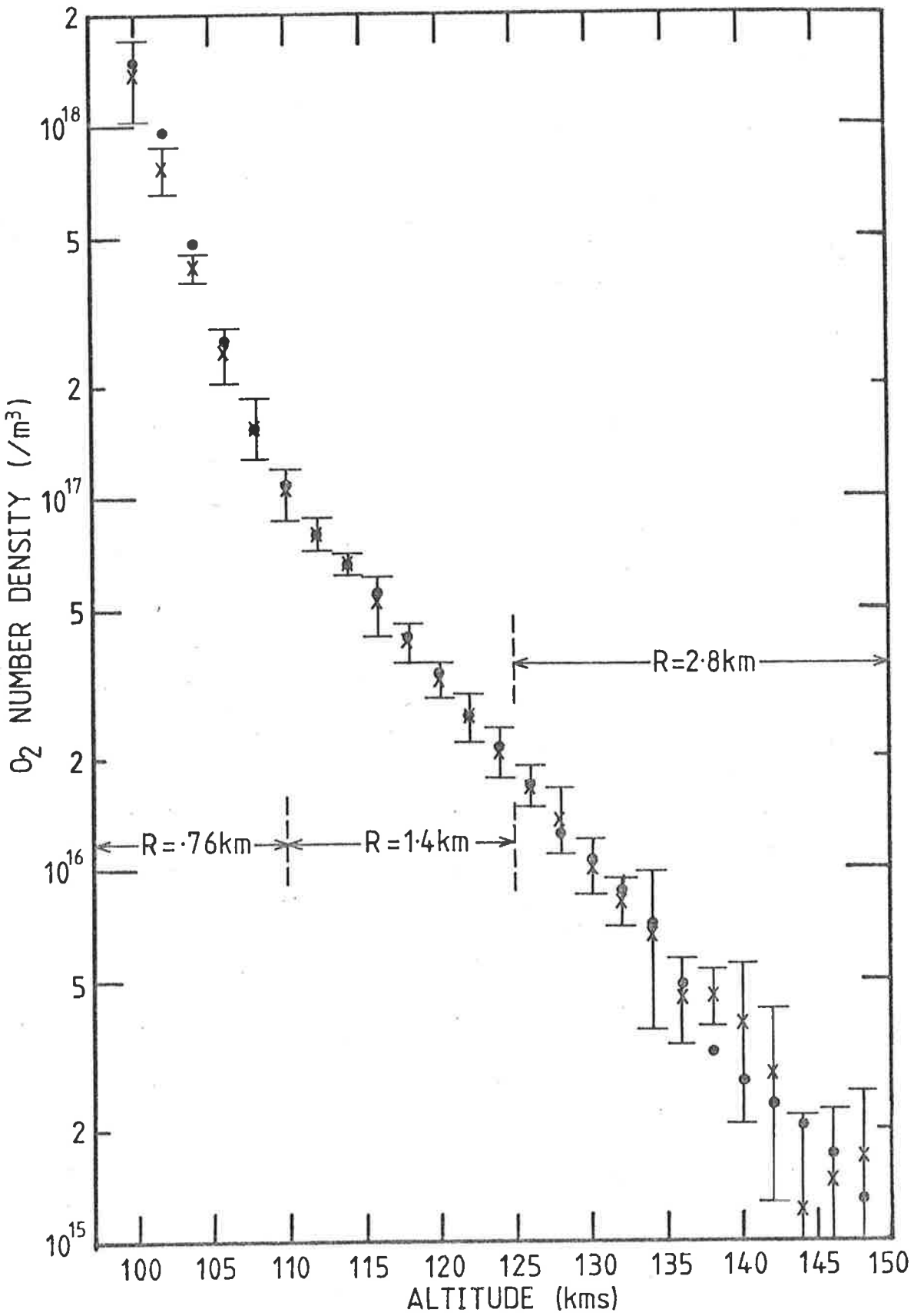

Fig 4.22 Comparison of $n(O_2)$ determined by hand-drawn curves and by the method of weighted differences. R is the altitude resolution.

● hand-drawn curves

method of weighted differences.

in the same way and the only purpose of 4.22 is to enable comparison between this profile and the second one drawn on the figure. The second profile was obtained by the method of hand-drawn curves.

Statistically the profiles cannot be said to disagree, since for the most part the $n(O_2)$ derived from the method of hand-drawn curves lies within the possible spread of values of the $n(O_2)$ from the method of weighted differences. Over most of the profile, there is no criterion which can be used to suggest which of the two values of $n(O_2)$, i.e. the mean value from the method of weighted differences or that from the method of hand-drawn curves, is the better estimate of the atmospheric $n(O_2)$. However, manipulation of w_n' and δz_2 (see Section 4.4.3) at the upper altitude limit suggested that the degree of smoothing required to remove the oscillation observed at these altitudes, even when $\Delta z_0 = 1$ km (Figure 4.17), systematically enhanced $n(O_2)$.

Because of this, and because the error information gained appeared to reflect the method of analysis as much as the genuine uncertainty in the data, it was considered more advantageous to adopt a method which, although it could not provide error information for a single curve, could be used on all the available data. This would prevent comparisons being made uncertain by possible systematic differences in the analysis methods.

Accordingly, all the data was analyzed by the method of hand-drawn curves outlined in 4.4.2.

4.6 SUMMARY OF UNCERTAINTY IN MOLECULAR OXYGEN PROFILE ARISING FROM METHODOLOGY

It has already been stated that information about the likely uncertainty of $\frac{1}{I}\frac{dI}{dz}$ derived from a hand-drawn curve is not available from a single curve and that statistical information can only be obtained

by considering several curves and their implied densities. This work is included in Chapter 6. However, in this chapter uncertainties arising from the use of the effective absorption cross-section and the optical depth factor have been discussed. Table 4.7 summarizes the magnitudes of the uncertainties and possible systematic errors associated with these factors.

It was shown in Section 4.2.6. that large scale systematic differences could arise in the $L\alpha$ results if the other wavelengths were ignored. Since correction factors were used these are not put in the table. However, the extra uncertainty which appeared in the mean of the molecular oxygen densities derived from the $L\alpha$ chambers is included. Although Table 4.5 shows other absorber contributions to the absorption of $L\alpha$ of up to 53% and $\sigma_{EFF}(\lambda_1, \lambda_2)$ calculated for an O_2/H_2O atmosphere showed an enhancement that reached 37% by 112 kms, these are not listed in Table 4.7. Use of these figures place the derived $n(O_2)$ below that independently obtained by the QT chambers and it is considered these values are unrealistic (see Chapter 8 for further discussion on water vapour profile). The figures quoted are based on a water vapour concentration of 3 ppm (Hall, 1972) and the NO density profile of Trinks *et al* (1978b).

The systematic error is quoted such that a negative value implies a under-estimation of $n(O_2)$.

TABLE 4.7 SUMMARY OF THE UNCERTAINTIES AND POSSIBLE SYSTEMATIC ERRORS ASSOCIATED WITH ION CHAMBER*

ROCKET	CHAMBER	UNCERTAINTY	POSSIBLE SYSTEMATIC ERROR
SL 1005	QT	± 12.8%	- 16%
	SX	± 7.5%	- 8%
	Spectrometer	± 7.5%	- 8%
SL 1207	QT 1 (special case see 4.2.5)	± 23%	- 16%
	SX	± 8%	- 8%
AEROBEE 13.123IS	LNO/MNO	± 29%	< + 5% at 90 kms < 10% at 110 kms
	QT	± 14.8%	- 16%
	SX	± 8.5%	- 8%

*Recent laboratory measurements by A.J. Blake (private communication) confirms that the possible systematic error in σ_{EFF} for SX chambers arising from Temp. dependence of absorption cross-section will be no more than the 4% allowed for in the table.

CHAPTER FIVE

THE ROCKET EXPERIMENTS

This Chapter describes the rocket-borne experiments used to measure molecular oxygen densities in the altitude region 80 kms to 170 kms. The discussion includes tabulation of relevant launch parameters; brief descriptions of the rockets and the environment they provided for the experiments; descriptions of the experiments themselves and presentation of the data. The data, which, apart from the removal of some noise spikes, is the raw data received at the ground station, is presented as signal *vs* altitude curves. Some discussion on the quality of the data is entered into.

Some mention is also made of the airglow photometer experiments (Section 1.3.3). The experiments are fully described in Chapter 7 but comments specifically connected with their rocket environment and their flight performance are included here for convenience.

5.1 SUMMARY OF ROCKET FLIGHTS

Three separate experiments were flown on three separate rockets during the current research program. All three rockets have been named previously. They were the Skylark rockets SL1005 and SL1207 and the Aerobee rocket, Aerobee 13.123IS. Table 5.1 tabulates the relevant launch and flight parameters.

5.2 THE SKYLARK ROCKETS

5.2.1 The Vehicle

The first two molecular oxygen experiments were flown on Skylark rockets. This section briefly describes these rockets and the

TABLE 5.1

NAME OF ROCKET	DATE OF FLIGHT	COORDINATES OF LAUNCHER	FIRING TIME (LOCAL)	FIRING TIME (UT)	SOLAR ZENITH ANGLE AT APOGEE	APOGEE (Kms)	K_p 6.7 HRS BEFORE LAUNCH
SL 1005	11.12.72	30.94S 136.52E	9.20 CST	00.00	38°	196	1^-
SL 1207	23.4.74	30.94S 136.523	10.33 CST	01.03	50°	177	4^+
AEROBEE 13.123 IS	22.2.77	30.94S 136.46E	6.36 CST	21.06 (21.2.77)	84.6°	177	3^-

environment they provided.

5.2.1.1 General Description

The Skylark rocket was designed and built for an upper atmosphere research programme that began in the International Geophysical Year 1957/1958. It was designed specifically to enable scientific groups to build and work on their experiments independently of other groups in a multi-experimental payload.

The general configuration of the vehicle is as shown in Diagram 5.1(a). It was a two stage solid fuel rocket with a 44 cm diameter payload section. The initial thrust was provided by a booster stage. This burnt for about 4 secs. and lifted the rocket to a height of 1.5 kms to 2 kms. A more sustained thrust was provided by the second/sustainer stage, which was ignited approximately six seconds after launch and burnt for about 30 seconds. To give the rocket stability during this early powered part of the flight, it was spun up to a rate of approximately 3.5 revs/sec. This was achieved by using a small motor fitted with lateral jets and sited between the booster motor and the sustainer stage. It was ignited at launch and burnt for about 4 secs.

The payload or head section consisted of a number of cast magnesium alloy body sections manacle-clamped together. The size, type and number of body sections used was determined by the requirements of the individual experimenter and by weight and stability considerations. This section was then clamped to the sustainer motor with another manacle ring. If payload recovery was required explosive bolts were fitted to the ring. When triggered they allowed 3 spring-powered plungers to operate. These plungers were capable of thrusting the payload away from the motor at a rate of 1-2 m/s.

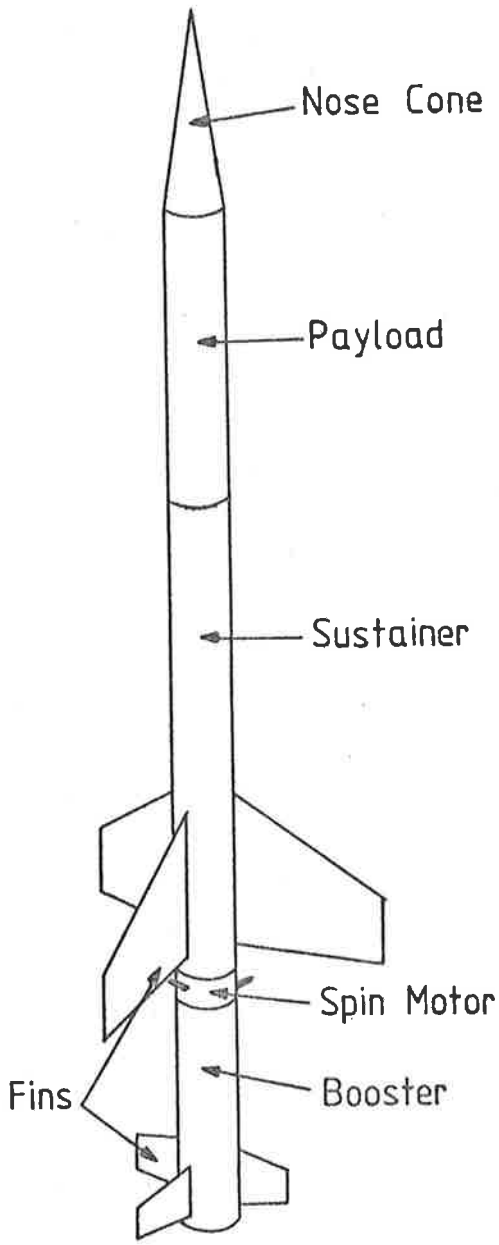

Fig. 5.1a General Configuration of Skylark Rocket.

The internal diameter of the body sections and therefore the space available for instrumentation was 39 cms. The body sections came in standard heights but if an experiment was too high to be accommodated in a standard bay, two or more could be bolted together. Transverse bulkheads, which could be fitted between body sections, provided the platform on to which the experiments were bolted. If required, special bulkheads were available which would pressure seal an experiment.

Apart from the experiments the head section of the rocket contained several standard instrumentation packages. Power for the experiments was provided by a 28V power supply capable of giving 15 amps for 10 minutes. Detector signals were telemetred back to the ground station by two E.M.I. type 465 senders. The rocket also carried a doppler transducer to provide velocity information for the tracking station and instrumentation such as roll rate gyroscopes to evaluate vehicle performance. Another standard piece of instrumentation was the flight program unit. In this unit specially made cams were used to mechanically trigger pulses that would carry out such in-flight functions as turning experiments on and off.

The Skylark rockets SL1005 and SL1207 had two other features:

(i) the rockets were attitude controlled;
i.e. the direction of look could be adjusted to an experimenter's needs and maintained throughout flight,

(ii) payload recovery was possible;

These features did however, carry penalties.

A bay was required for the attitude control unit instrumentation. During flight attitude control was achieved by using jets of high pressure

dry nitrogen. Therefore high pressure cylinders had to be carried and these were both weighty and bulky. Before the look direction could be adjusted the rocket had to be despun. This implied fitting a despin unit. Payload recovery meant a parachute had to be carried and this implied another large and heavy bay.

Stability could not be maintained if the head section became too long. Therefore the addition of the above bays restricted the space available for experiments. The relative space occupied by experiments and support systems can be seen in Figure 5.1(b). The extra weight of the bays reduced the apogee height that could be obtained.

In both rockets these penalties were carried by the secondary experiments and had a major effect on the design and performance of the experiments.

5.2.1.2 The Environment

The environment provided by the Skylark rocket was moderate in temperature, pressure and acceleration. Maximum expected longitudinal acceleration was 15g about 35 secs. after take-off. Vibrations were normally in the range 20 Hz-2 kHz with a maximum acceleration in the lateral and thrust axis of less than .6g rms. The internal lagging of the rocket was designed to keep experimental temperatures below 60°C. Thermistors flown on SL1207 indicated experimental temperatures were well below this and in fact remained within 10° of launch temperature throughout the flight. If it was necessary to pressure seal an experiment the specification met for the sealing was a leakage rate of no more than 1 lb/sq. in/hr.

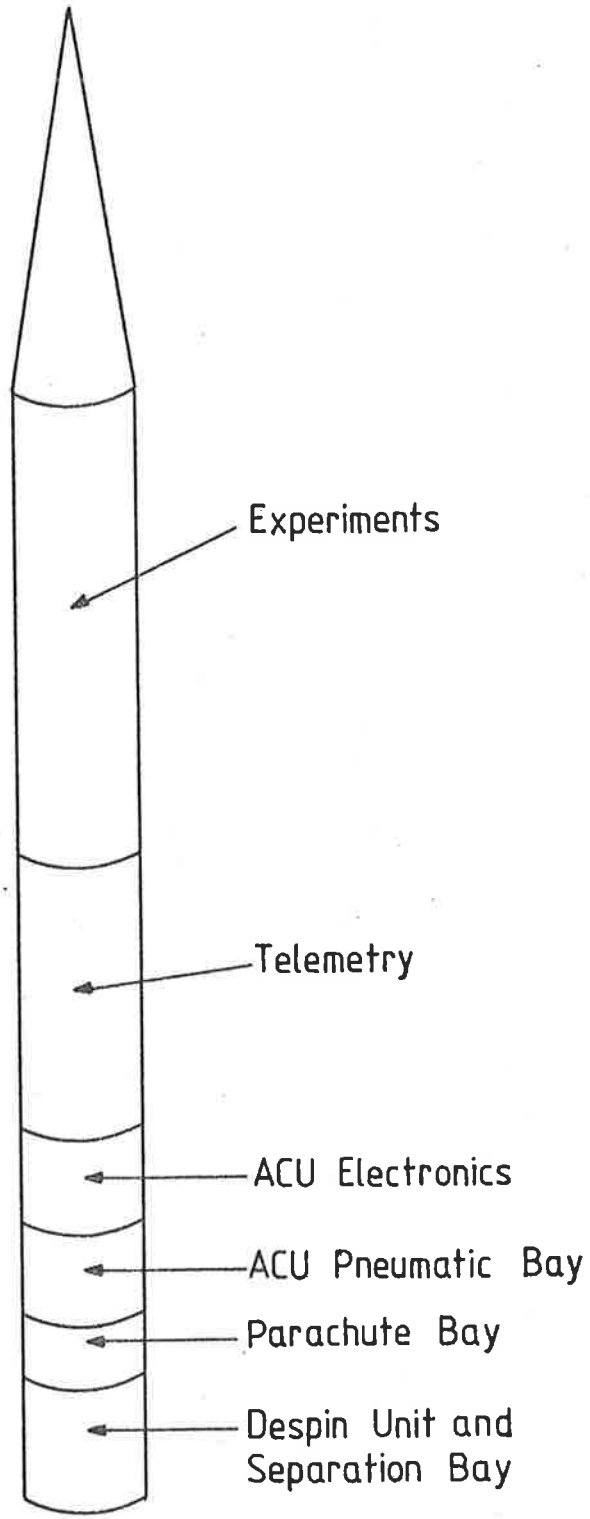

Fig 5.1b General Configuration of Skylark Payload

5.2.2 SL 1005

5.2.2.1 The Experiments

The Adelaide University experimental package had to share a bay with the sun sensor of the attitude control unit (ACU) and instrumentation flown for the U.K. Meteorological Office. This location severely restricted the possible size of the package, fig 5.2a. Therefore only four experiments were flown. Each had comparatively simple instrumentation and electronic hardware. The experiments were:

(a) two experiments to measure molecular oxygen,

  (i) 3 ion chambers, 1 SX and 2 QT

  (ii) the spectrophotometer designed to simulate an SX chamber

(b) 2 X-ray proportional counters to measure the total density profile (Bibbo, 1977).

(c) A photometer (Chapter 7) to measure the zenith intensities of the airglow at λ3914Å and λ5577Å.

A photograph and overlay showing the location of each experiment is given in Figure 5.2b.

With the exception of the airglow instrumentation the experiments were designed to view the sun. They were, therefore, mounted so that their common direction of look was parallel to that of the sun sensor of the ACU. Accuracy of alignment was achieved by the use of an auto collimator.

The photometers (Chapter 7) had to view zenith. The direction of look was made variable by mounting them in a rotatable block. This enabled zenith angles up to 45° to be accommodated. However, the block

Fig. 5.2a Location of Experimental package in SL 1005.

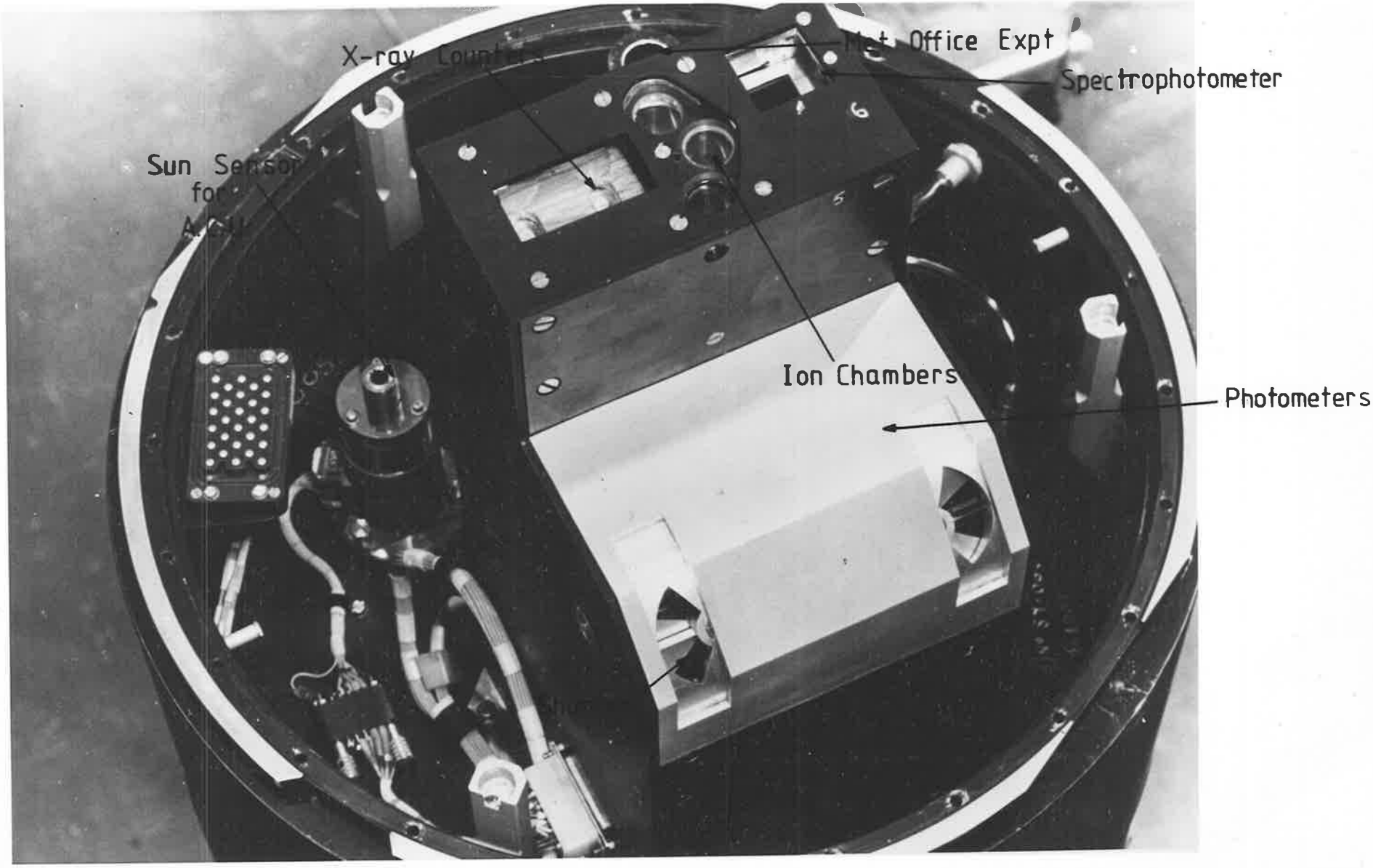
X-ray Counter
Met Office Expt
Spectrophotometer
Sun Sensor
for
Ion Chambers
Photometers

Fig. 5.2b Experimental package flown on SL 1005.

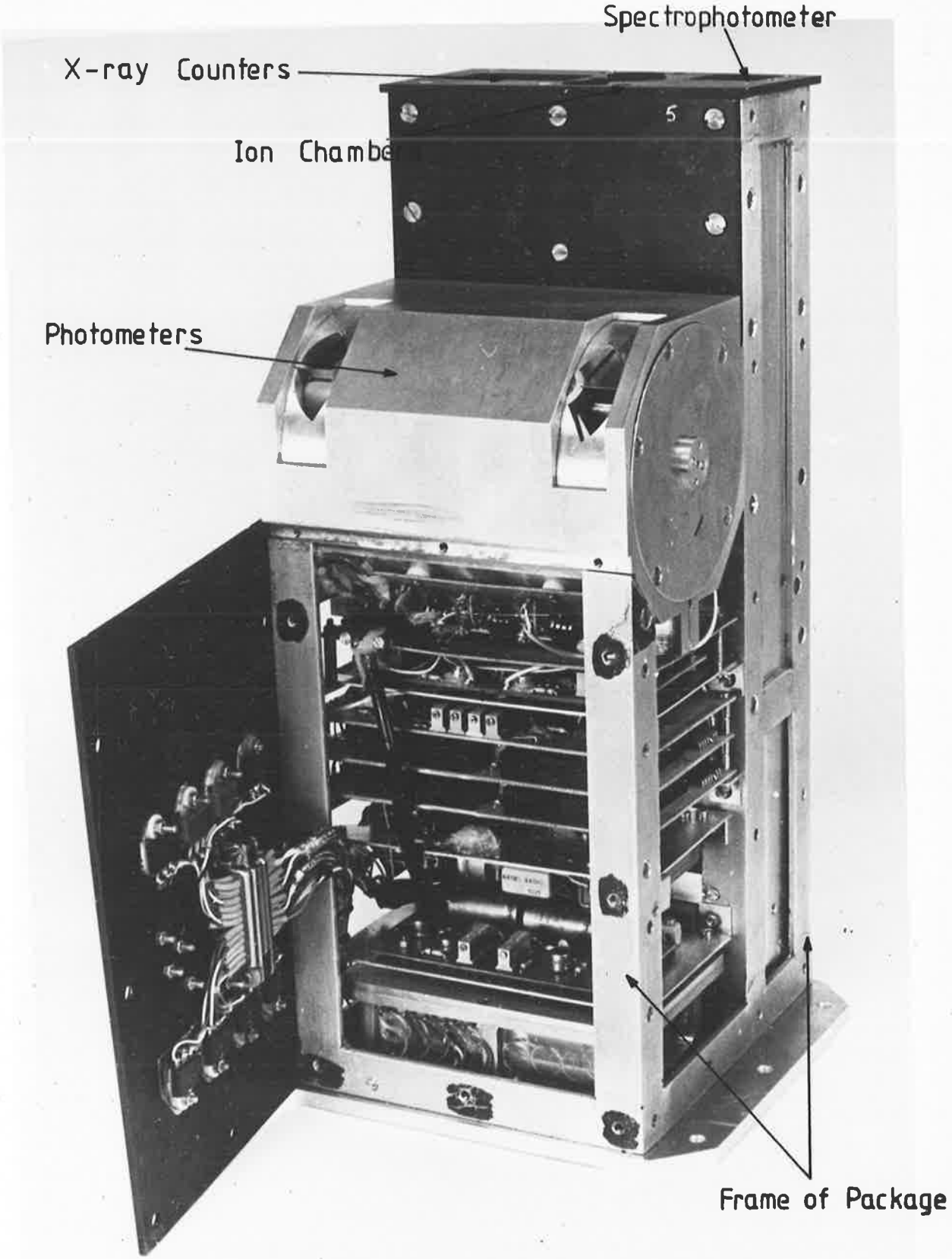
Spectrophotometer
X-ray Counters
Ion Chamber
Photometers
Frame of Package

was manually locked into place and therefore the zenith angle at which the rocket was to be launched had to be decided before the final build up of the head section.

The necessary power rails to the detectors of the photometers (2 EMI 9734 QNB photomultipliers) and the spectrophotometer (1 EMR 541-G-05M-14 photomultiplier) were supplied by DC-DC converters powered by the 28V power rail from the rocket batteries. The ion chambers were run at 37½V. This was the result of floating a 15V battery on top of the 22½V regulated power rail supplied by the vehicle.

Log amplifiers (Analog Devices Inc. 755p) were used on the outputs of the photomultipliers. With these set at 1V/decade and with a telemetry range of -3 to +3V signal currents over 5 orders of magnitude could be accommodated. The linear amplifiers (circuit diagram Figure 5.3) used for the ion chambers were set at 1.1×10^{-10} amps/volt.

The output of the amplifiers was sampled by the telemetry sender. The ion chambers and the spectrophotometer each had a sub-commutated channel which implied a sampling rate of 20 times/sec while each detector of the photometer had a half channel and its output was sampled 40 times/sec.

Unless needed for preflight checks the ion chambers were at all times kept in a sealed container with activated silicon gel. This provided protection against possible water vapour contamination. Once the final build up of the payload had been completed the bay housing the experiment was flushed with a dry gas to ensure continued protection.

Two gases were used. In an attempt to prolong the life of the X-ray proportional counters argon methane was flushed continuously

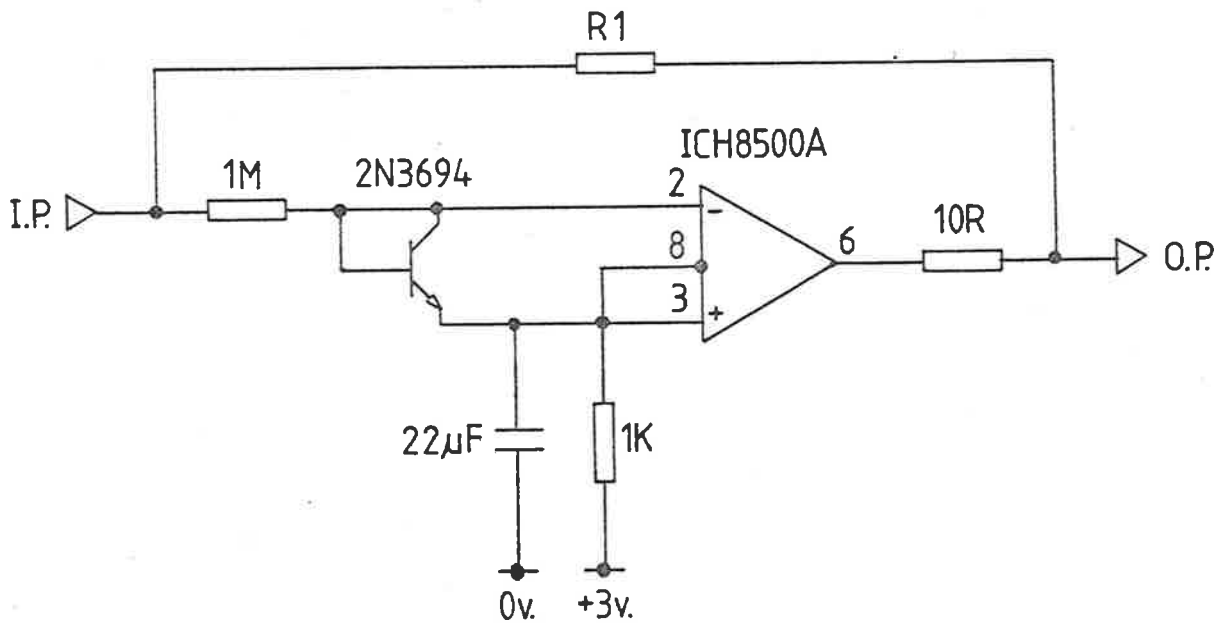

Fig. 5.3 Linear amplifier for Ion Chambers flown on SL 1005 and SL 1207. The gain is set by adjusting the value of the feedback resistor R1.

through the bay until 2 days before the scheduled launch (Bibbo, 1977). The flushing gas was then changed to dry nitrogen. A snatch connection was fitted to the bay and nitrogen flushing was continued until the launch.

The photometers were protected by a light proof, dust proof cover which was removed just before the final build up.

5.2.2.2. Preflight Checks

All experiments underwent preflight checks. For these the complete instrumentation head of the rocket was built up and the flight programme unit was run. Power for the experiments was provided by the vehicle and the data transmitted by the telemetry senders was recorded. The following were checked:

(a) that each experiment was unaffected by the other experiments the rocket carried

(b) that pulses from the flight programme unit, which in flight would trigger such events as forward separation and despin, had no detrimental effect on the experiments

(c) that the high tension was switched on and off at the correct time

(d) that a signal from each output was received through the telemetry sender and that this signal level was as expected.

Checks (a) to (d) were carried out several times. The last check was made as the rocket stood on the launcher.

5.2.2.3 The Flight

SL 1005 performed satisfactorily. Acquisition on to the sun to an accuracy of ± 1' of arc was obtained by 124 kms. This accuracy was maintained until 100 kms on the downleg of the flight.

The head section was lifted to an apogee of 196 kms at 224.84 sec. after launch and was above 100 kms for approximately 290 sec.

With the exception of the experiments described in this thesis the head section was recovered in good condition. The experiments of the present work were in an exposed position and suffered damage from re-entry as well as damage from the impact.

The vehicle was tracked and the final trajectory calculated to an accuracy of ± 20 metres.

5.2.2.4 The Results

The three ion chambers and the spectrophotometer all yielded data on both the upleg and the downleg sections of the flight. This data is given in graphical form in Figures 5.4 to 5.11. With the exception of the removal of some noise spikes from the telemetred upleg signal, the data has not been processed. The figures are labelled with the code name of the ion chamber which produced the signal and this labelling is utilized in the following.

The most striking thing about the data is the severe degradation in quality between the upleg and the downleg. The problem may have been associated with the performance of the telemetry sender but this is not known. However, as was pointed out in Section 4.4.2 extinction curves are still easily identified in the downleg data and it

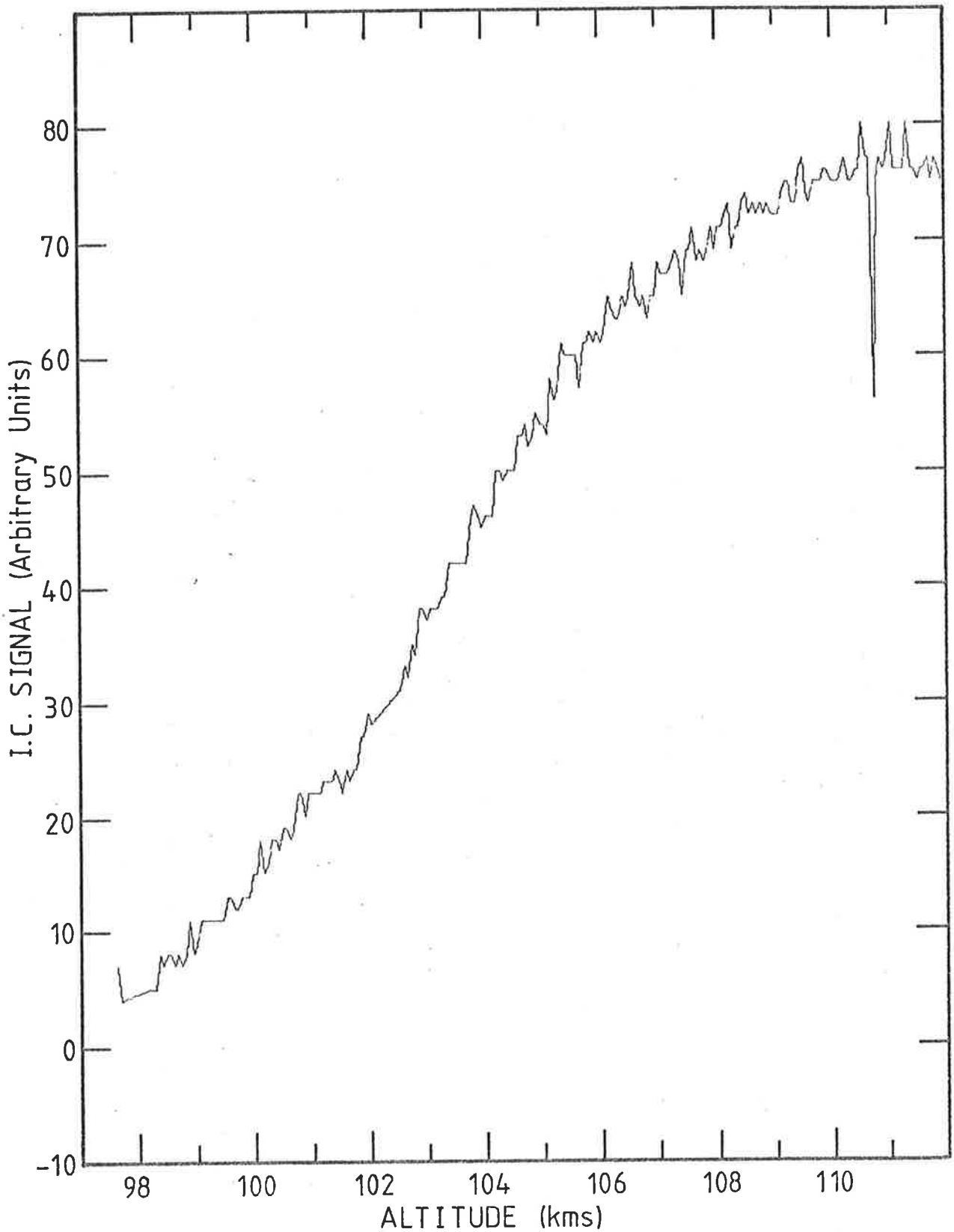

Fig 5.4 Telemetred signal from QT 203 flown on SL 1005 - upleg.

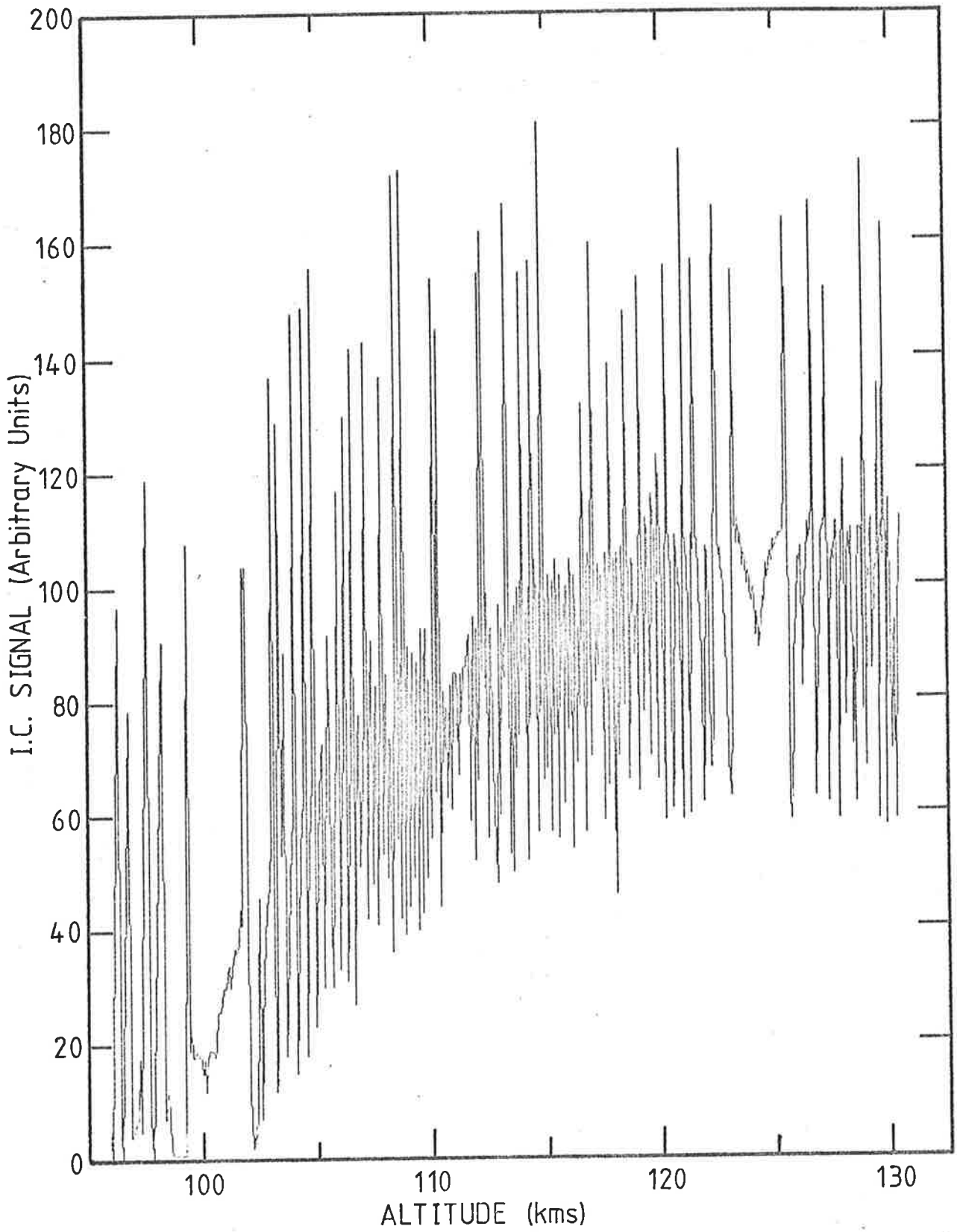

Fig 5.5 Telemetred signal from QT 203 flown on SL 1005 - downleg.

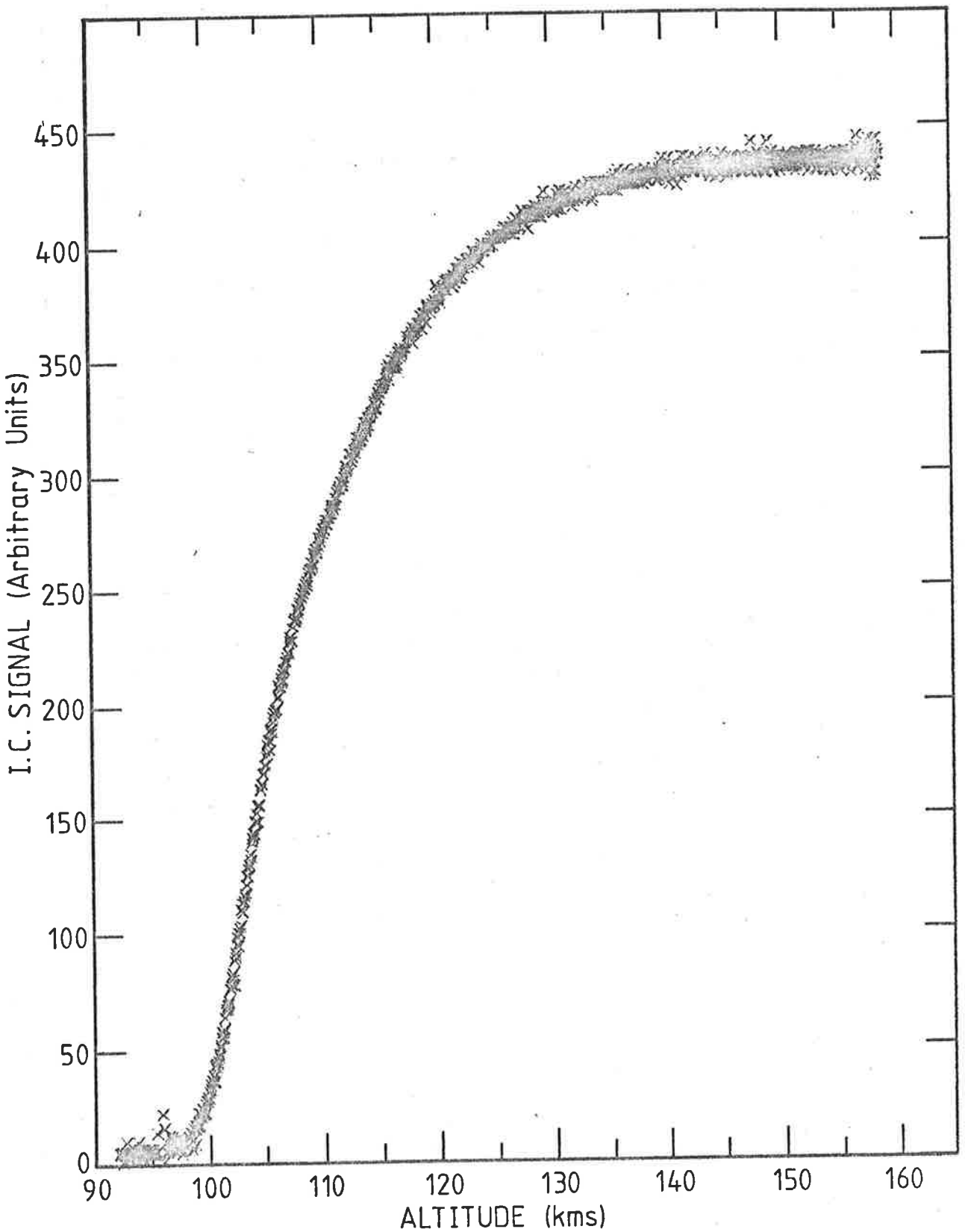

Fig 5.6 Telemetred signal from QT 204 flown on SL 1005 - upleg.

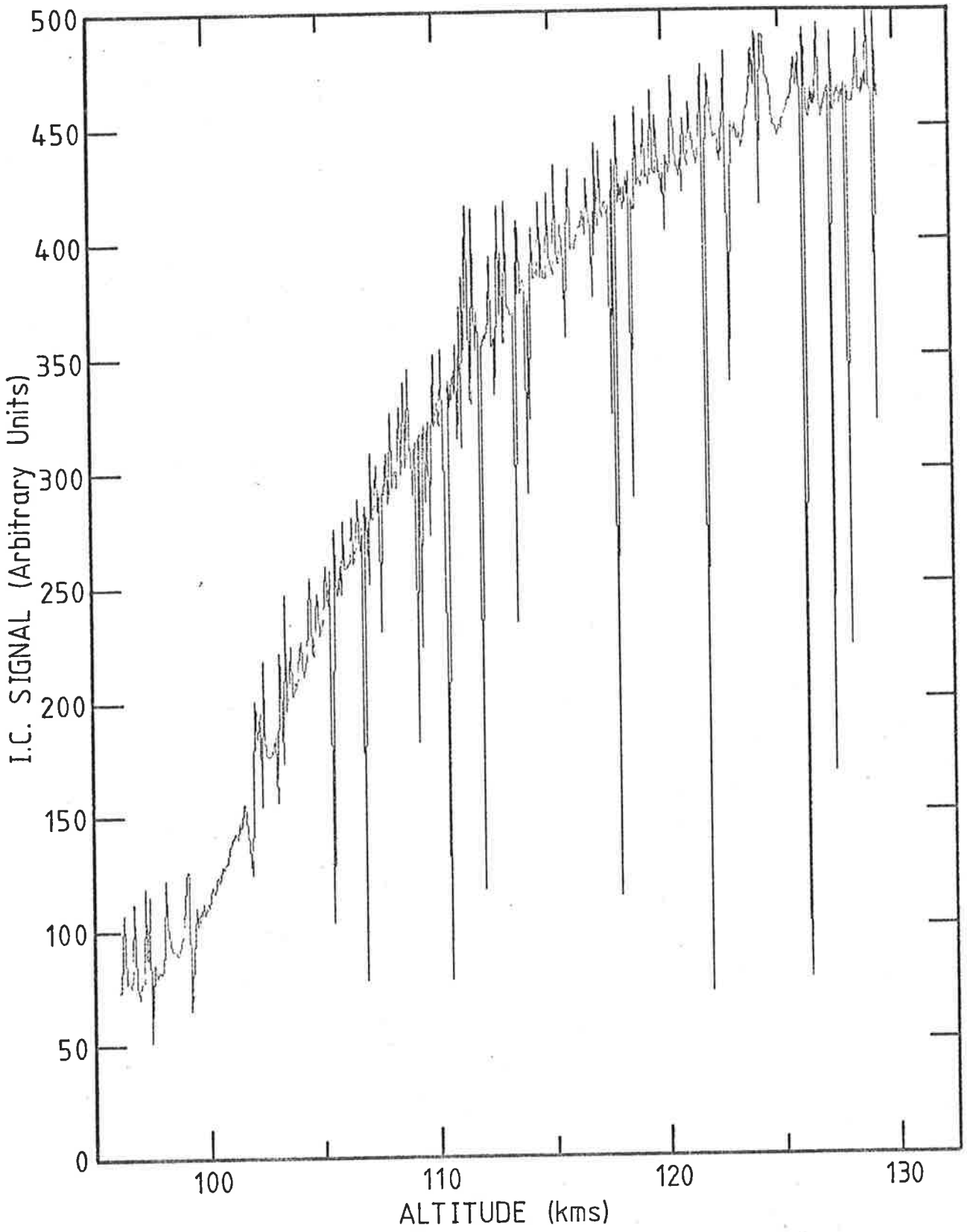

Fig 5.7 Telemetred signal from QT 204 flown on SL 1005 - downleg.

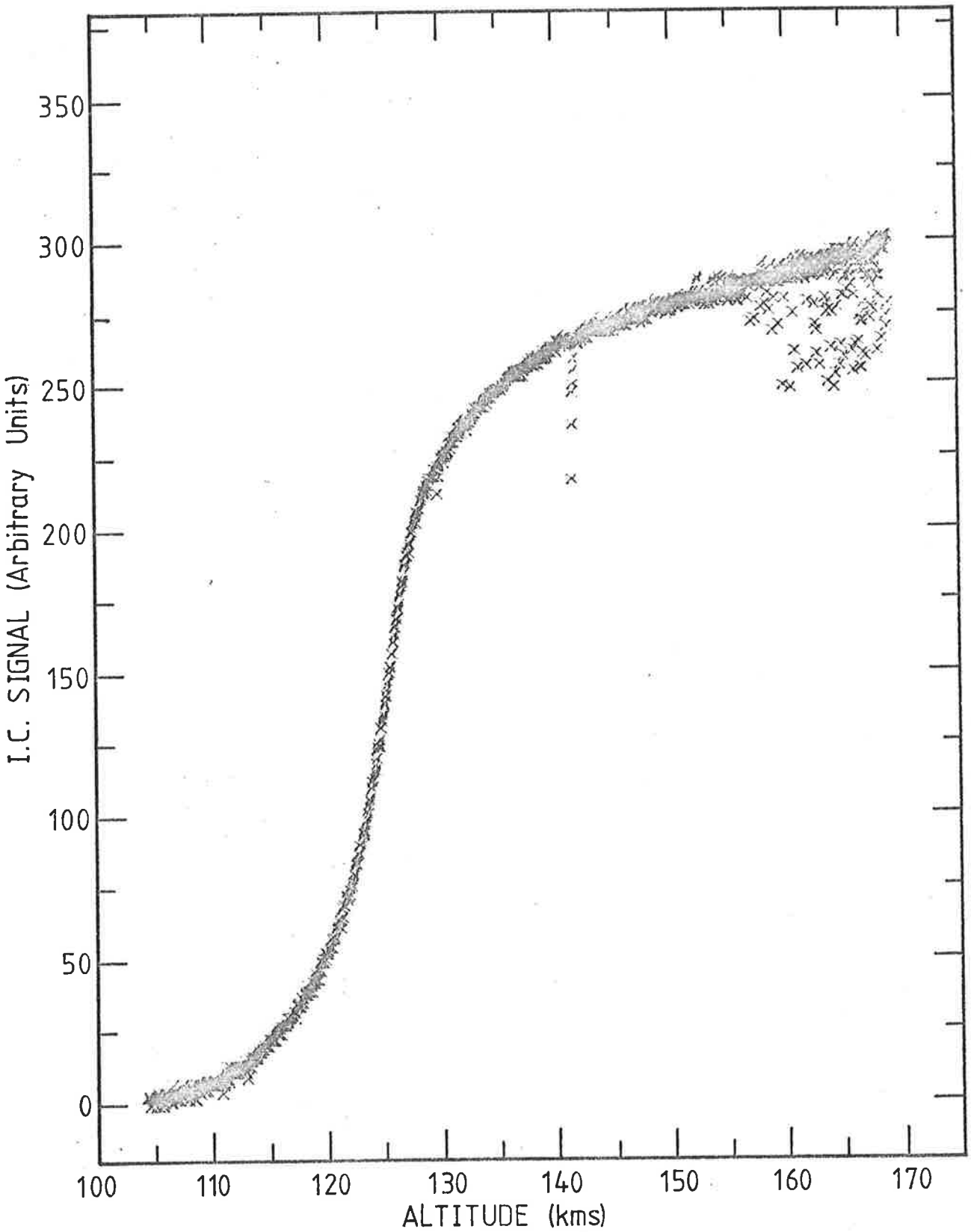

Fig 5.8 Telemetred signal from SX 3 flown on SL 1005 - upleg.

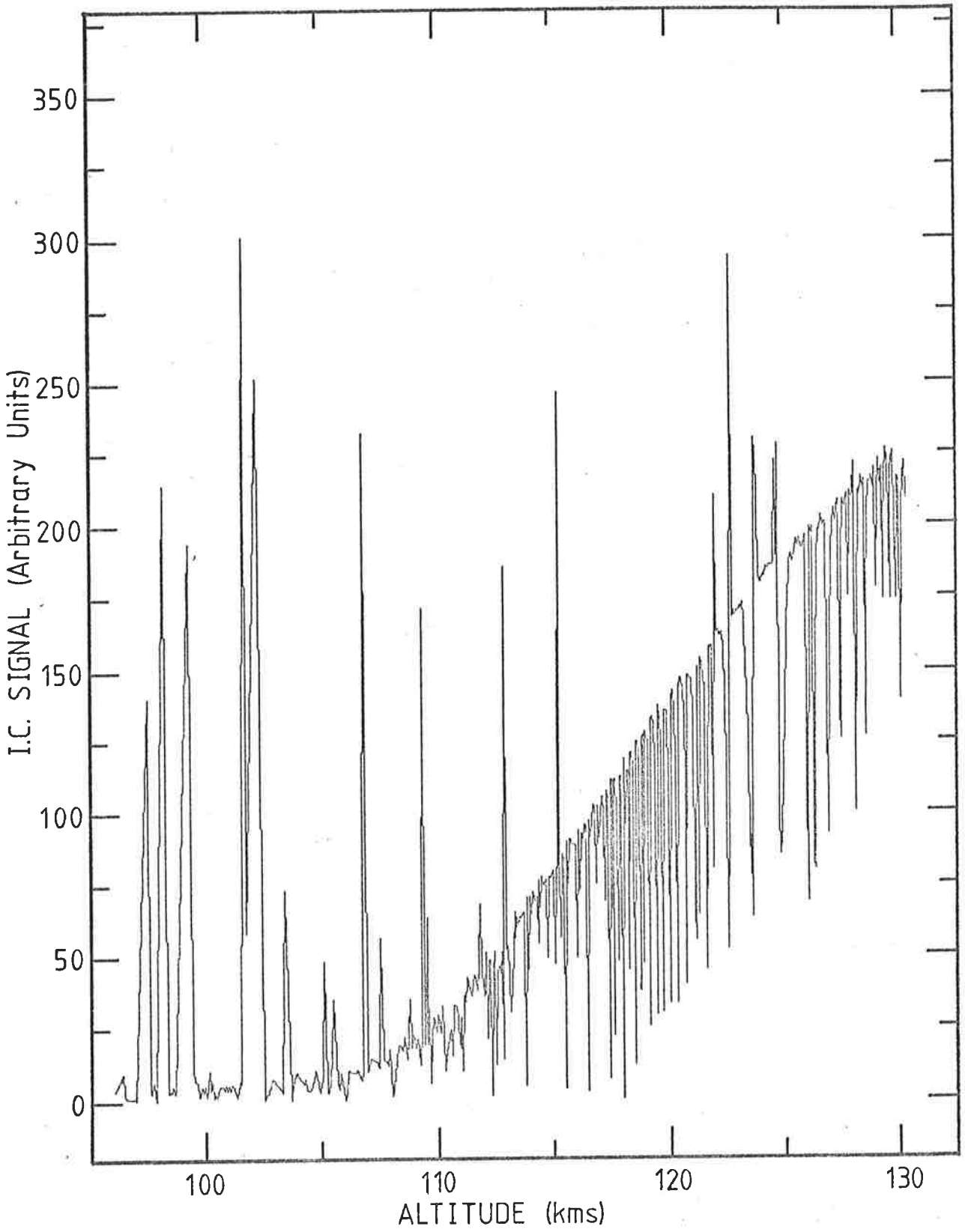

Fig 5.9 Telemetred signal from SX 3 flown on SL 1005 - downleg.

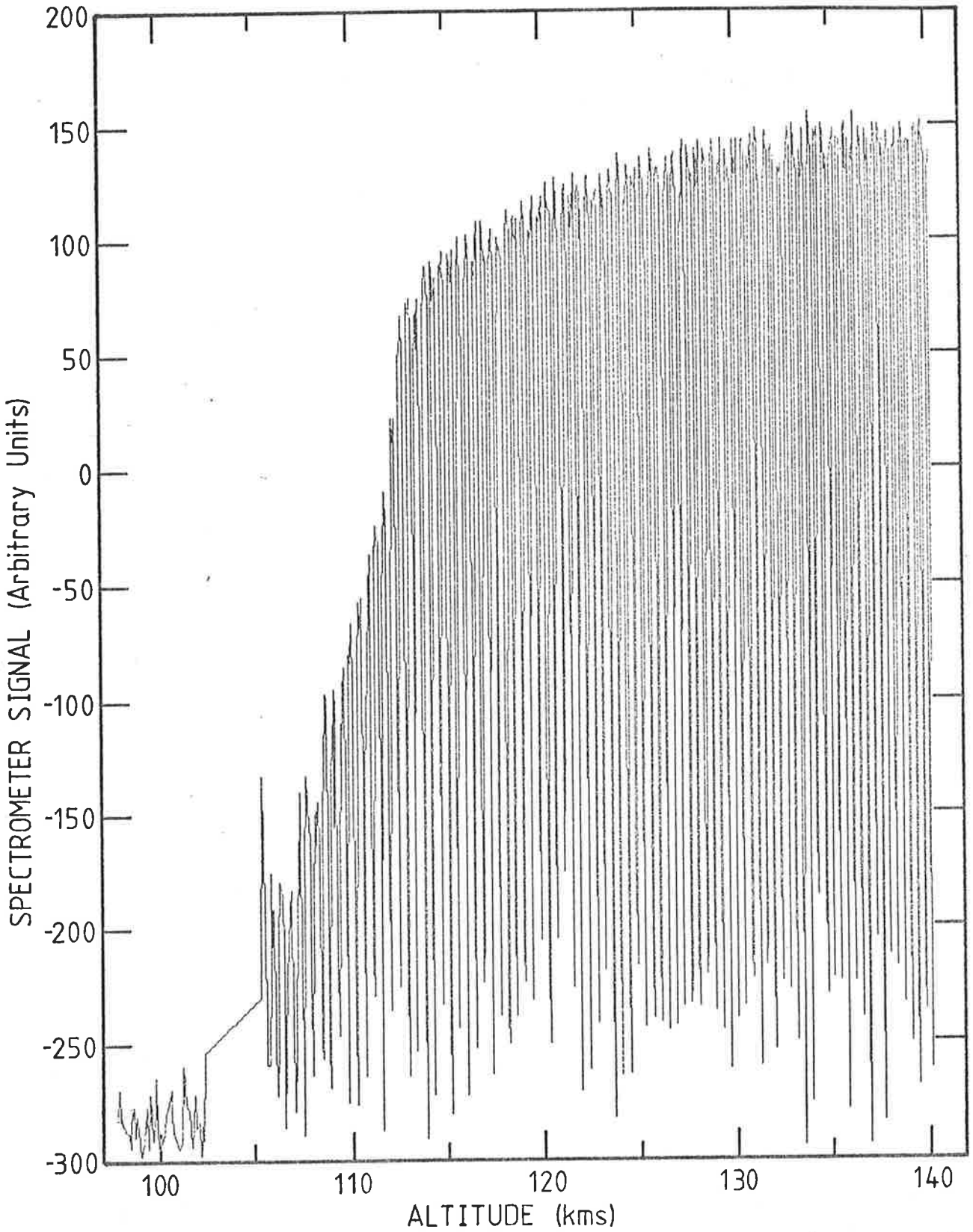

Fig 5.10 Telemetred signal from the Spectrophotometer flown on SL 1005 - upleg.

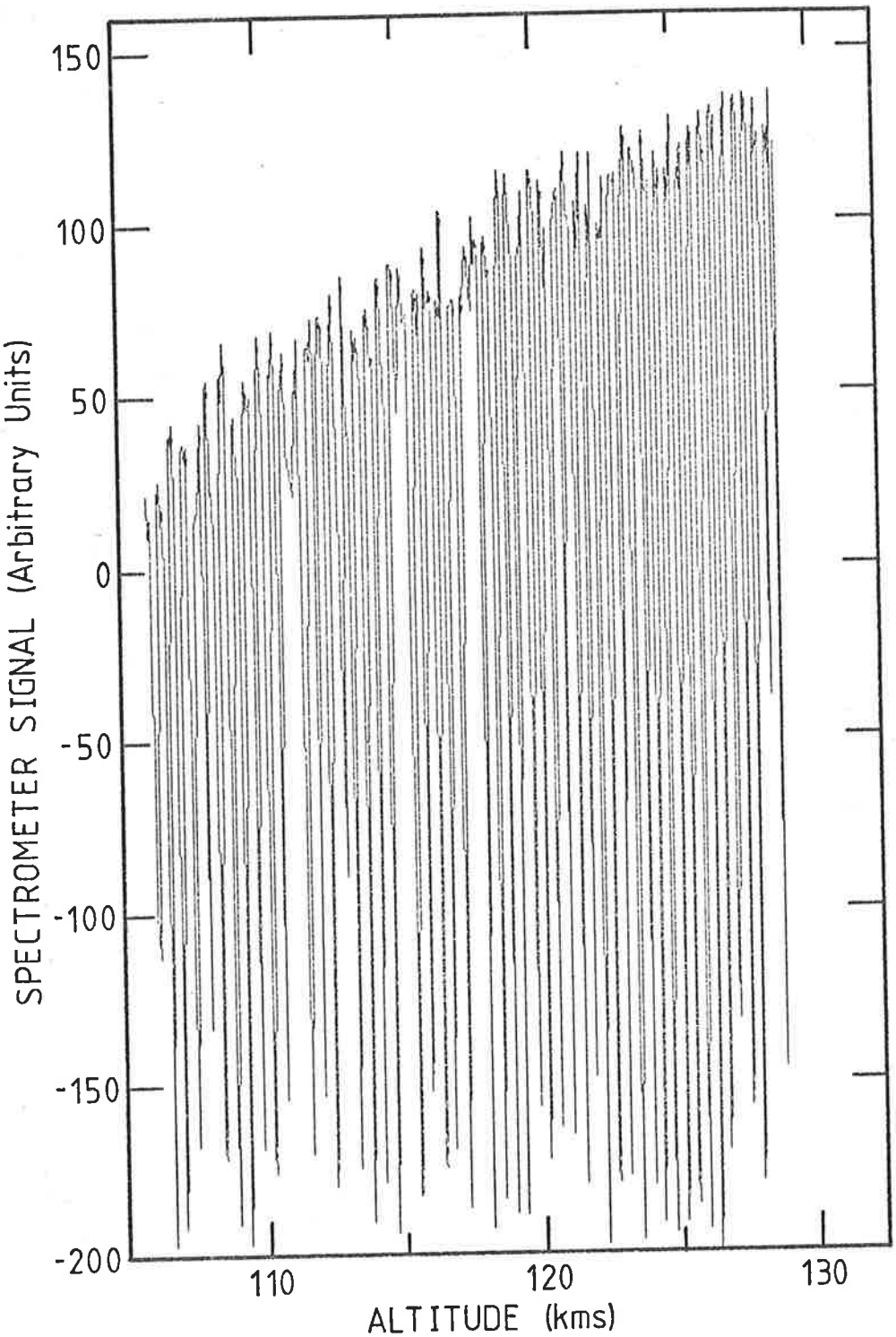

Fig 5.11 Telemetred signal from the spectrophotometer flown on SL 1005 - downleg.

was possible to obtain molecular oxygen densities.

The results of QT 203 were restricted by the chambers apparent loss of sensitivity, while those from the spectrometer would have been less uncertain had the telemetry sampling rate been faster. The sample rate of 20 times/sec was not fast enough to always ensure observation of the maximum signal reached each time the shutter rotated. The extinction curves (Figure 5.10, 5.11) are therefore, poorly defined. In contrast the extinction curve of QT 204 is extremely well defined and in terms of the signal-to-noise ratio is the highest quality data received throughout the programme.

No results were obtained from the photometers. Lack of space had prevented baffling being built into these instruments and it is thought this allowed scattered light to reach the detectors. They stayed in saturation throughout the flight. The photometers and their signal levels are discussed further in Chapter 7.

5.2.3 SL 1207

5.2.3.1 The Experiments

Figure 5.12 is a photograph of the experimental package flown on SL 1207. There were five experiments and these were

(a) four ion chambers (2 SX and 2 QT) to determine the molecular oxygen density profile,

(b) four photometers to measure the daytime zenith intensities of the airglow lines λ5577Å - OI, λ6300Å - OI, 5200Å - NI and the first negative band of N_2^+ - λ3914Å,

(c) a grazing incidence spectrometer to measure the intensity of the solar flux lines λ304Å, λ584Å and λ770Å (Bibbo, 1977),

Fig. 5.12 Experimental package flown on SL 1207.

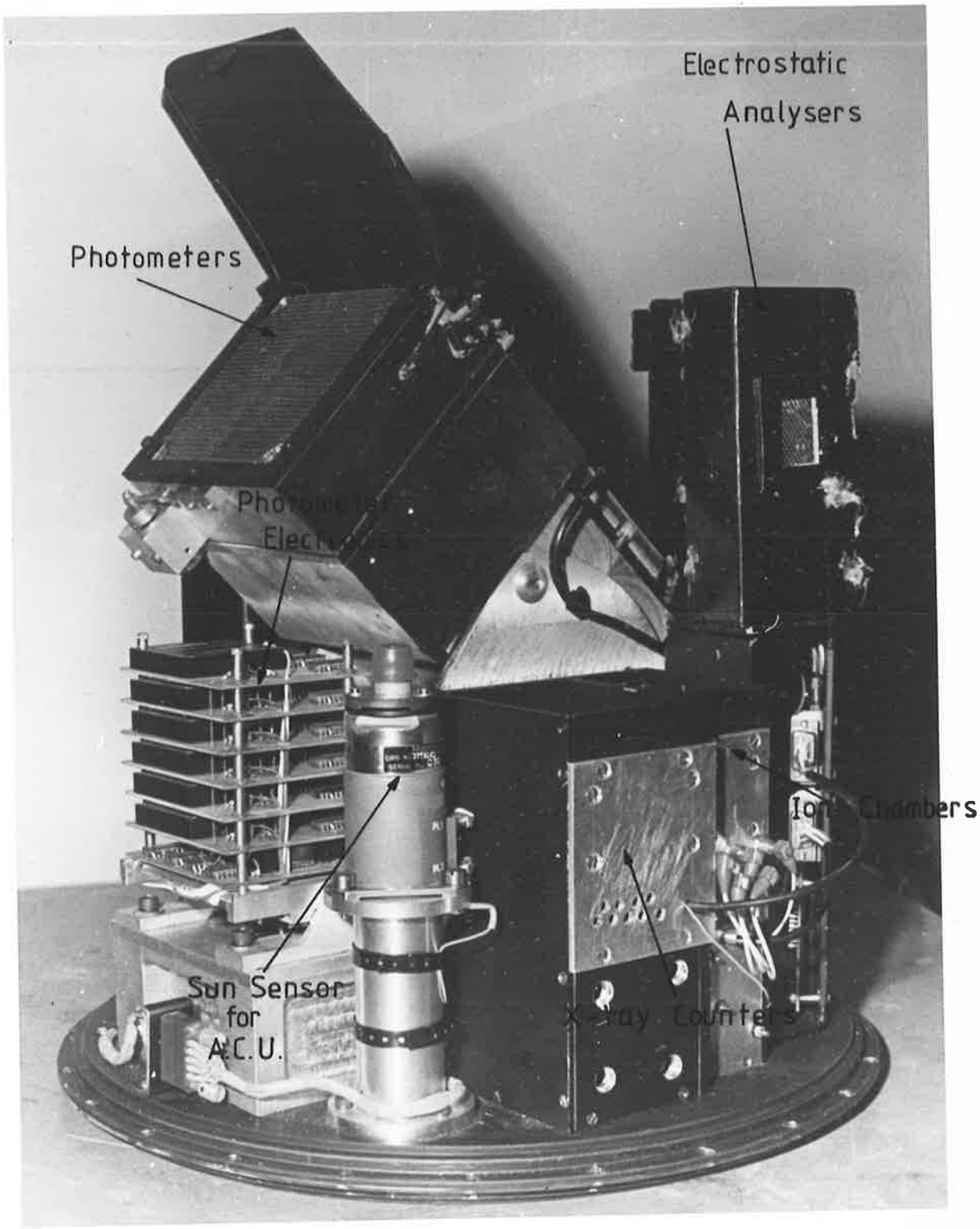
Electrostatic
Analysers
Photometers
Photometer
Electronics
Ion Chambers
Sun Sensor
for
A.C.U.
X-ray Counters

(d) 2 X-ray proportional counters to measure the solar flux in the wavelength ranges λλ1Å - 20Å and λλ44Å - 60Å (Bibbo, 1977),

(e) two electrostatic analysers looking in mutually perpendicular directions to measure the velocity profiles of thermal electrons and photo-electrons, (Bibbo, 1977).

The power rails to the ion chambers and the photometers were provided as described in Section 5.2.2.1. The outputs from the EMI 9734 QNB photomultipliers used as detectors in the photometers were fed into Analog Devices, 755P log amplifiers set at 1 volt/decade. The linear amplifiers (circuit diagram - Figure 5.3) used for the ion chambers were set at 1.0×10^{-10} amps/volt. The ion chambers were each sampled at 20 times/sec while each photometer was sampled at 40 times/sec.

The photometer (Chapter 7) was designed to view zenith and it was supported on a variable mount which could accommodate zenith angles up to 45°. It was locked at 45° before the final build up.

The ion chambers and the photometers were protected prior to launch in a manner similar to that described in Section 5.2.2.1. Preflight checks were identical to those listed in Section 5.2.2.2 for SL 1005.

5.2.3.2 The Flight

SL 1207 performed satisfactorily. The acquisition was accurate to ± 1 min of arc and it was maintained from 115 kms on the upleg to 85 kms on the downleg.

The head section was lifted to an apogee of 177.2 kms at 218.72 secs. and was above 100 kms for approximately 260 secs.

SL 1207 carried a parachute but post-flight calibration of the experiments was not possible because once again the experimental

package was in an exposed position and suffered damage through re-entry and impact.

Power was lost to the experiments 30 seconds early, but this did not degrade the results gained for this thesis.

The vehicle was tracked and the final trajectory calculated to an accuracy of ± 111 metres.

5.2.3.3 The Results

Two SX and one QT chamber yielded data on both the upleg and downleg. The quality of the data varied as can be seen by the computer drawn graphs (Figures 5.13 to 5.18). Figures 5.19 and 5.20 show some of the data again. This time the upleg and downleg are plotted on the same graph. Noticeable is the substantial agreement between the upleg and downleg QT chamber signals while the signals received from SX 7 vary dramatically, even over apogee. During this section of the flight the rocket should be above the absorbing layer and the signal would be expected to remain steady. This feature is discussed in Chapter 6.

The molecular oxygen experiment was degraded by the failure of a QT chamber and the poor signal-to-noise ratio for the chamber SX 5 (Figures 5.15 and 5.16). These chambers must have deteriorated during the time SL 1207 spent on the launcher. The present experiment was only one of several on the payload and the firing time was governed by the stringent criteria laid down for the flight weather conditions by the primary experiments. Access either for testing or replacing of chambers was not possible once the rocket was on the launcher and the criteria were not met for 20 days.

Requirements for the primary experiment also had deletorious effects on the photometer experiment. Unplanned-for pre-cooling of the

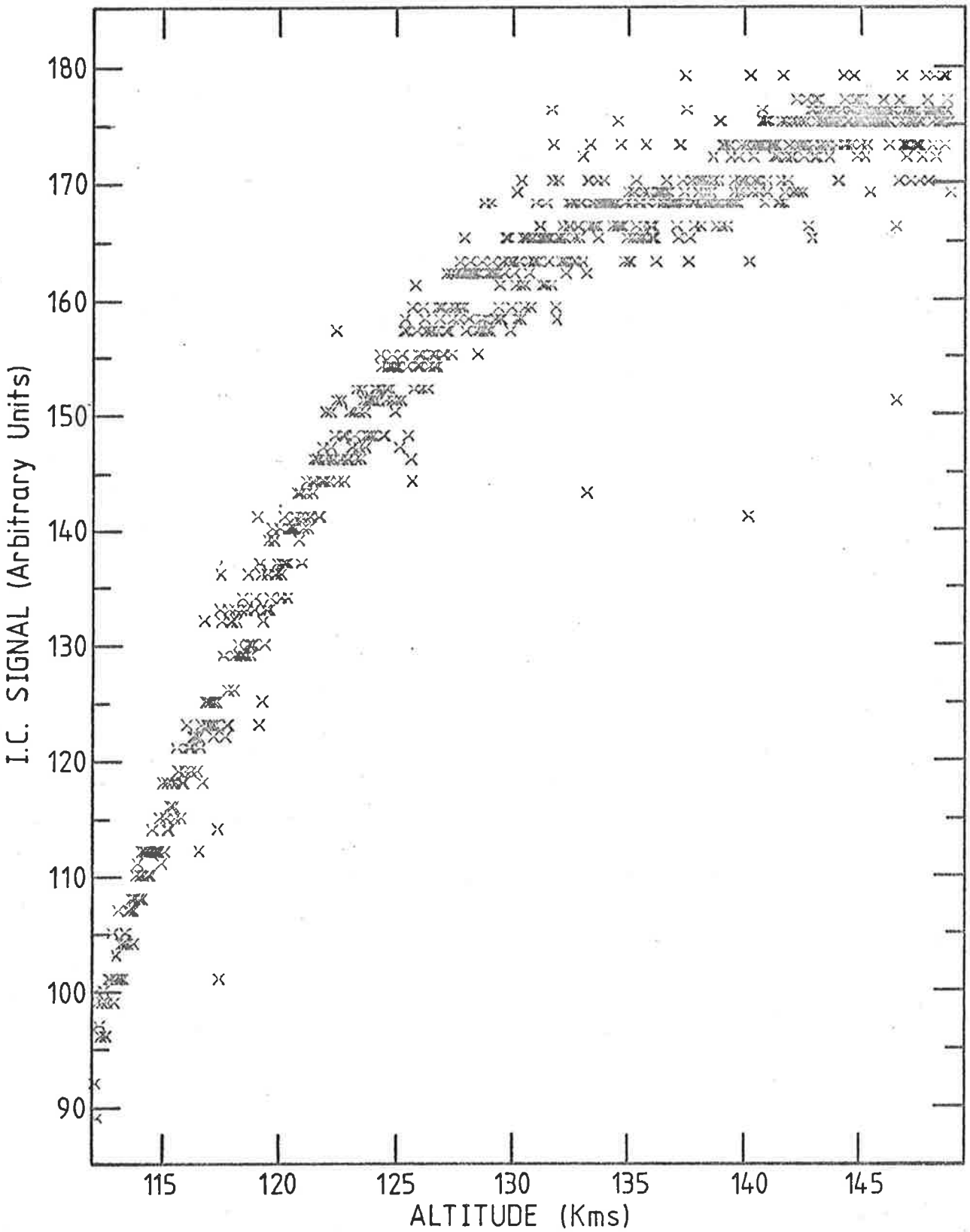

Fig 5.13 Telemetred signal from QT 1 flown on SL 1207 - upleg.

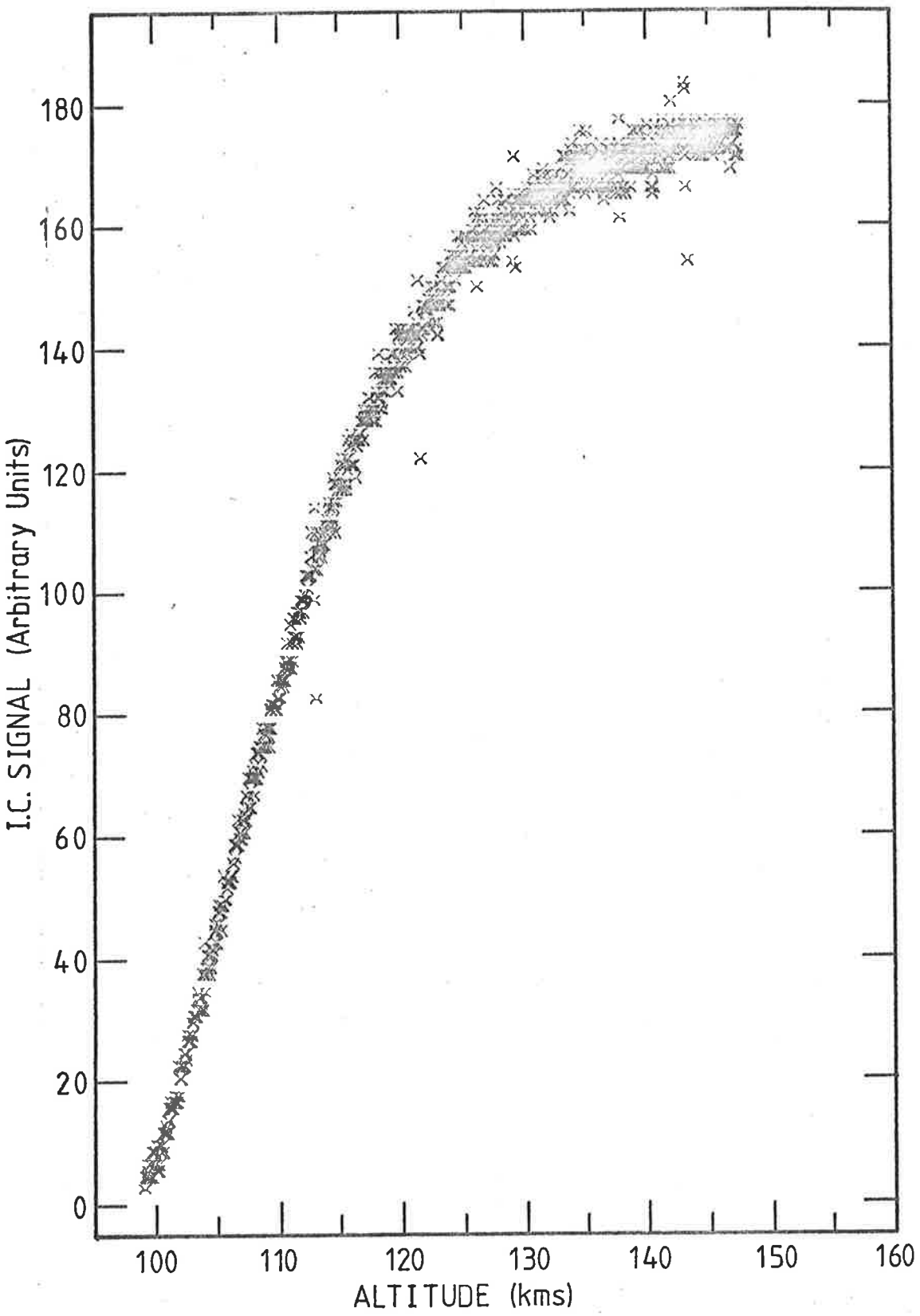

Fig 5.14 Telemetred signal from QT 1 flown on SL 1207 - downleg.

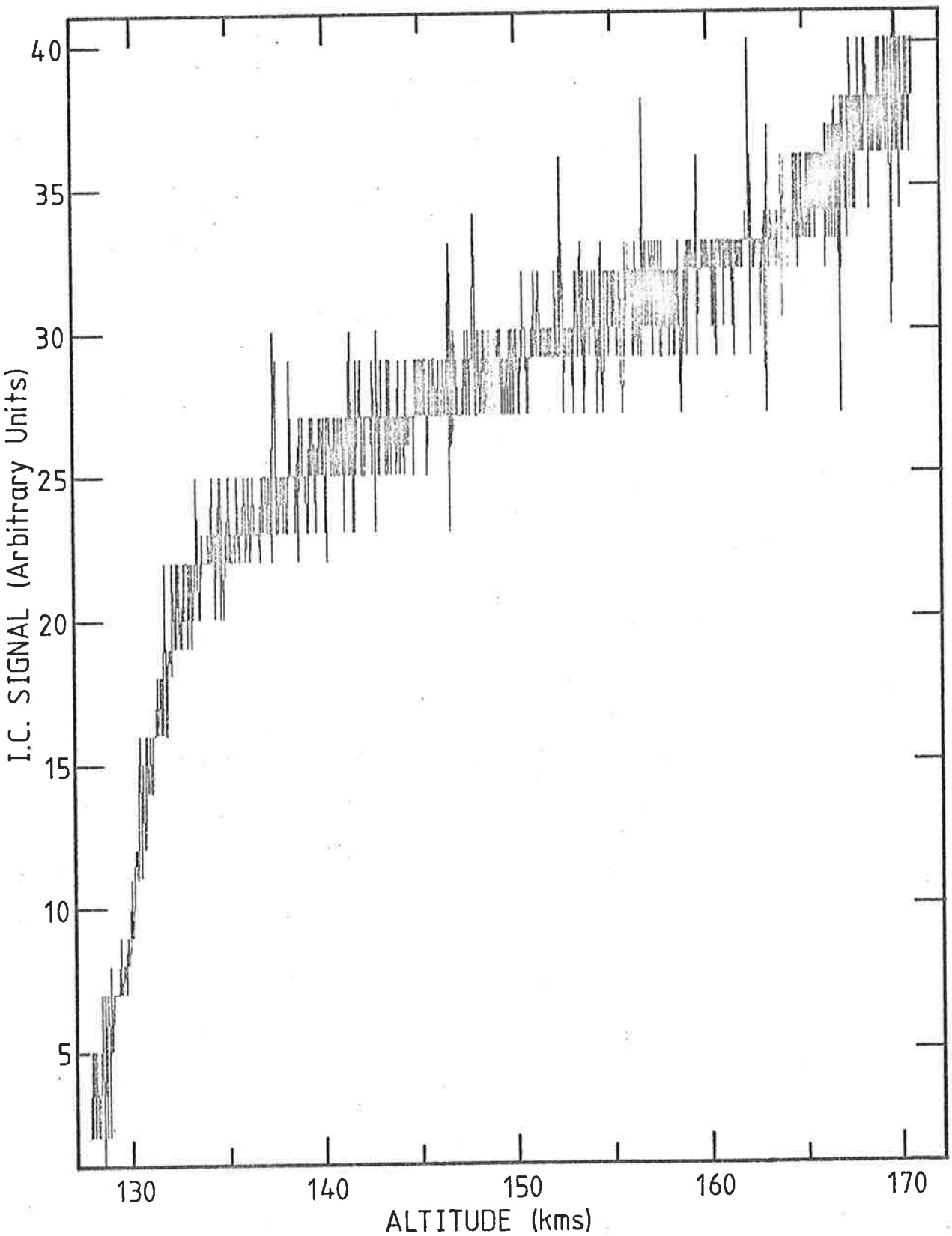

Fig 5.15 Telemetred signal from SX 5 flown on SL 1207 - upleg.

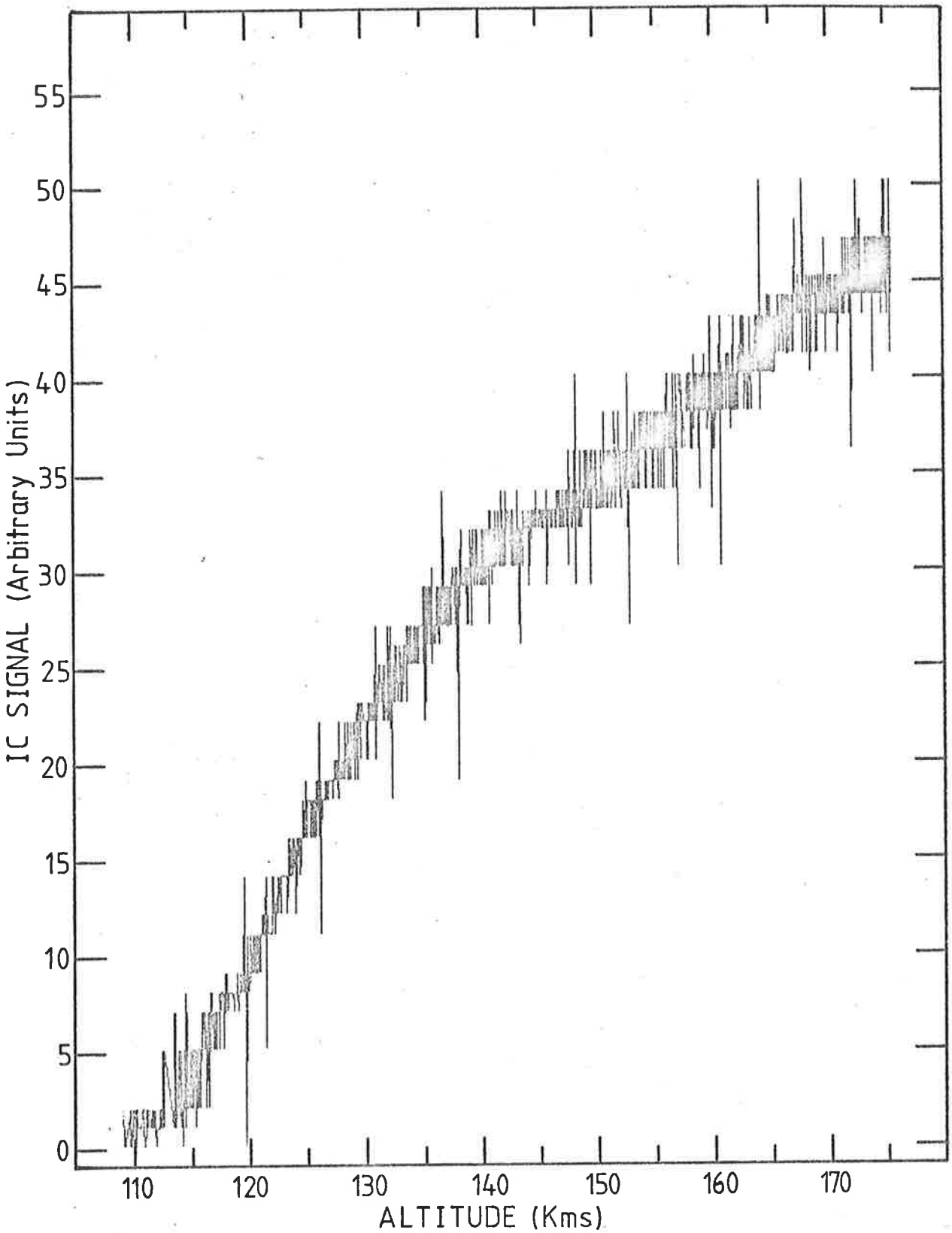

Fig 5.16 Telemetred signal from SX 5 flown on SL 1207 - downleg.

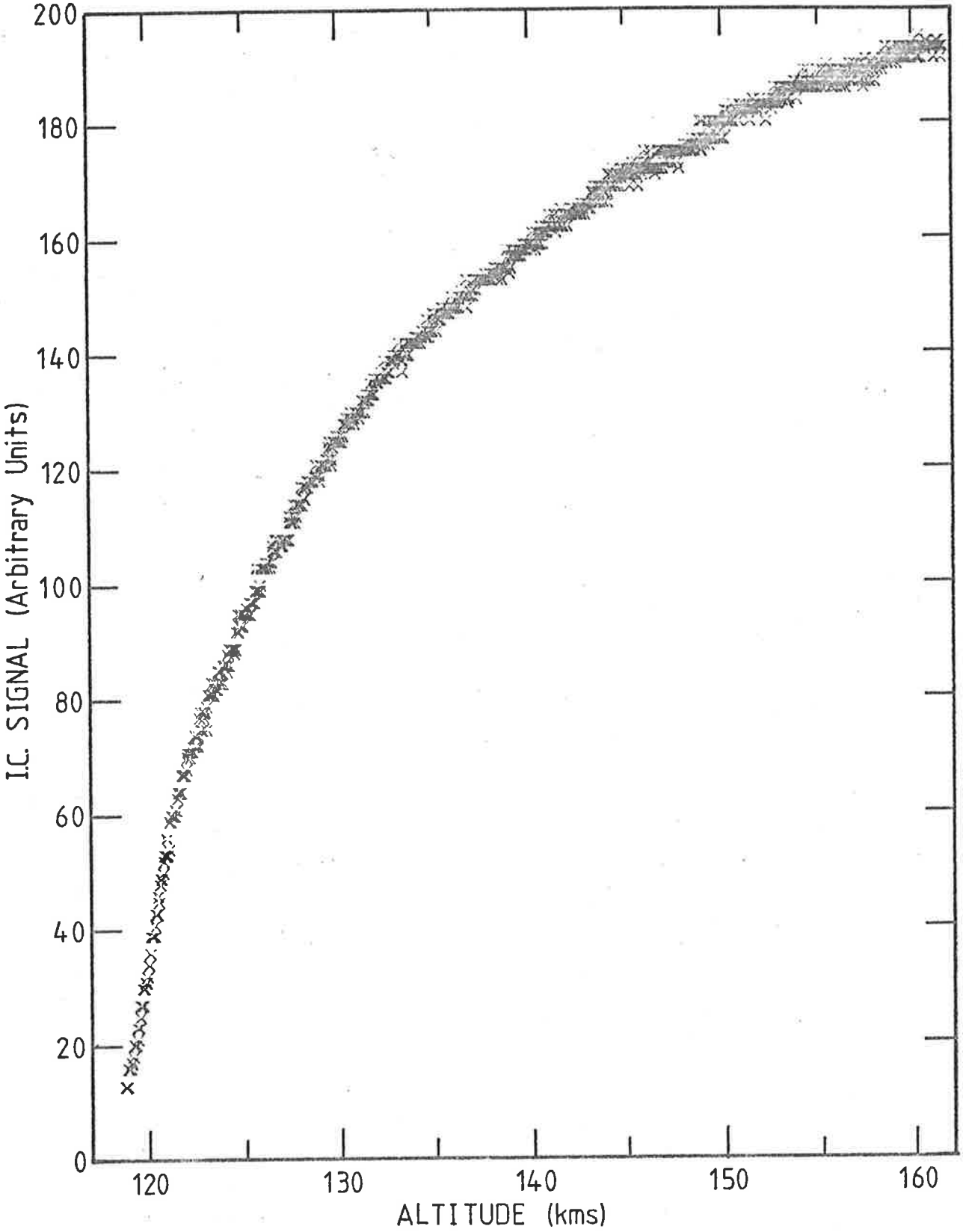

Fig 5.17 Telemetred signal from SX 7 flown on SL 1207 - upleg.

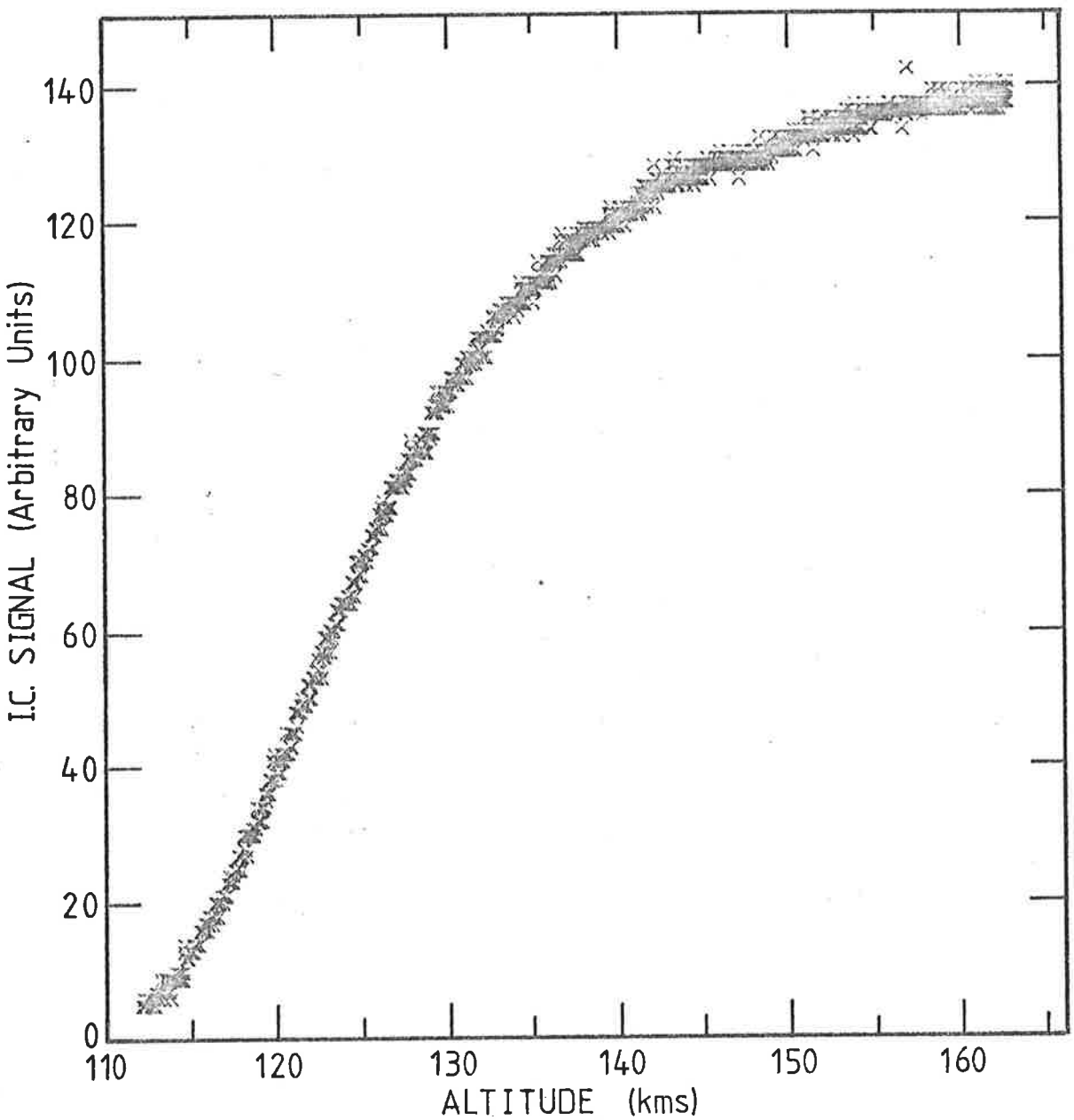

Fig 5.18 Telemetred signal from SX 7 flown on SL 1207 - downleg.

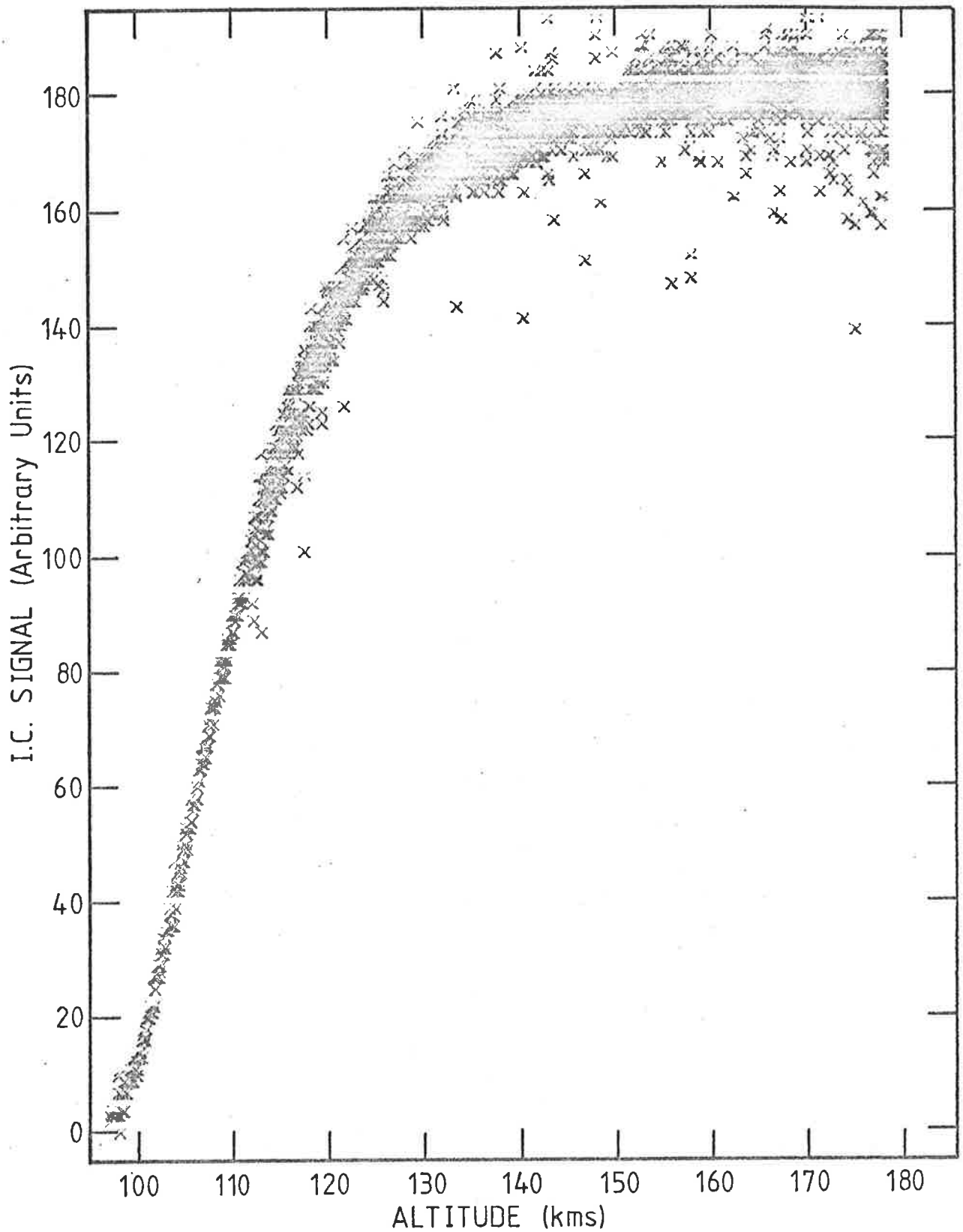

Fig 5.19 Telemetred signal from QT 1 flown on SL 1207. Signal levels for whole flight are shown.

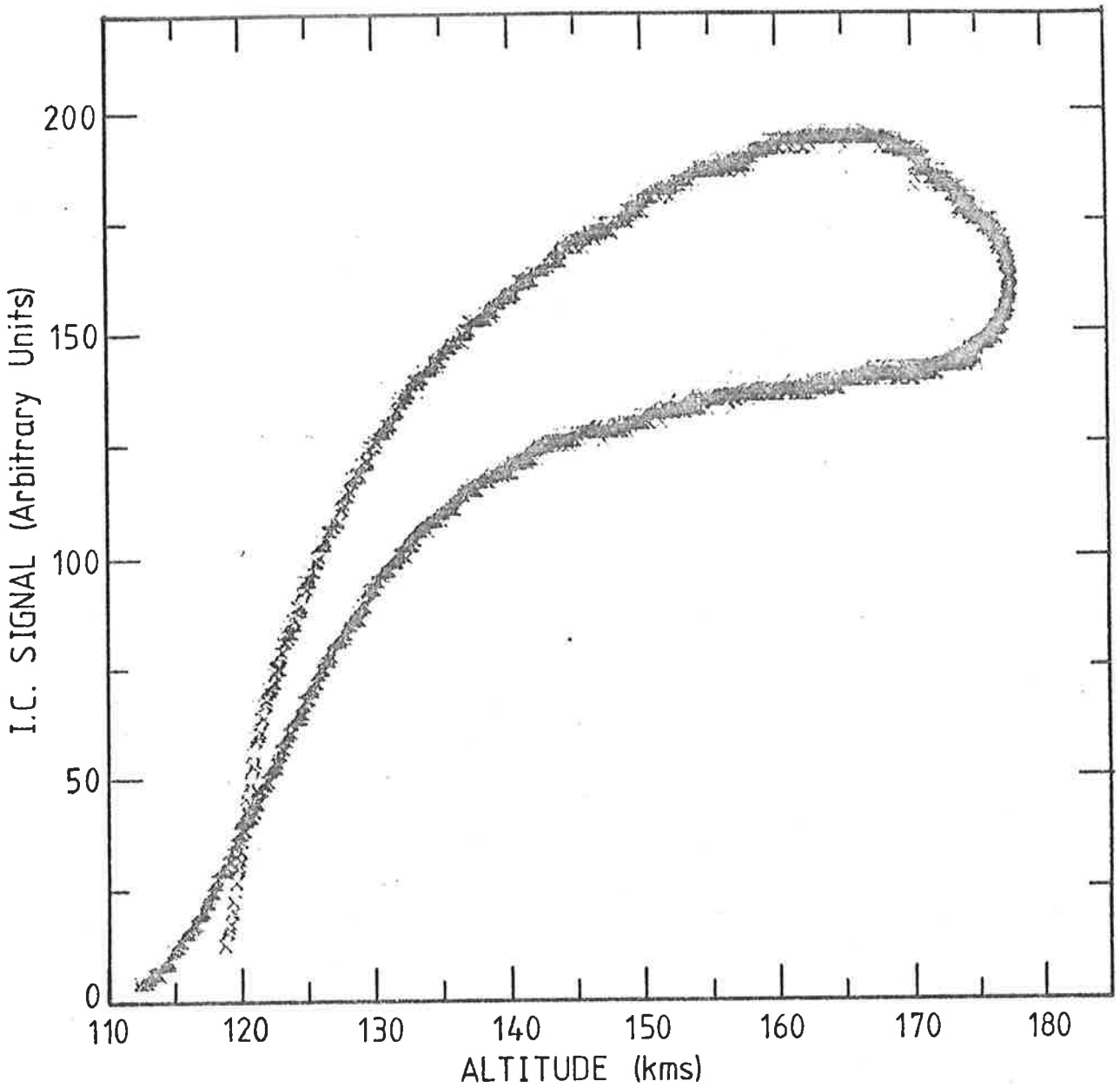

Fig 5.20 Telemetred Signal from SX 7 flown on SL 1207.
Signal levels are shown for whole flight.

whole head section implied the experimental temperature at launch was 19°C. It had been anticipated that for the planned date of launch (March-April) the likely temperature would be 35°C and the transmission of the airglow filters had been specified for this temperature (Chapter 7). As it was, the thermistors flown on the round indicated that the "massive" photometer block stayed within 5°C of its launch temperature for the whole flight and at 24°C the wavelengths of interest would have occurred in the wings of the transmission window rather than the peak. No meaningful information on zenith airglow intensities was obtained.

5.3 AEROBEE 13. 123 IS

5.3.1 The Vehicle

The Aerobee 13.123 IS was one of seven Aerobee 170/200's launched at Woomera in February 1977 by the Goddard Space Flight Division of the National Aeronautics and Space Administration of the United States of America.

The Aerobee 170/200 is a free flight fin-stabilized liquid propellant vehicle boosted by a fin-stabilized solid propellant booster. There are no physical restraints between the two stages and separation occurs after the booster has burnt out because of gravity and drag forces acting on the empty motor. Initial stability is achieved by centring fins to give a roll rate of approximately 2.5 revs/sec.

Aerobee 13.123 IS was attitude controlled and recovery of the payload was planned. As with the Skylark rockets this implied the need for a despin unit, gas cylinders, the Attitude Control System (ACS) instrumentation and a parachute. Similar penalties in loss of space and weight available for experiments were incurred.

The space available for instrumentation is a cylinder with a nominal diameter of 38 cms. The length of this cylinder is determined by the experimenter but the choice is constrained by weight and stability considerations. The body sections of an Aerobee rocket are not load bearing and experiments must be supported in a framework independent of the skin of the rocket.

In Aerobee 13.123 IS doors were cut into the skin. They were pyrotechnically removed during flight to expose the instrumentation.

5.3.2 The Experiments

The scientific objective of the Aerobee rocket flight was to measure simultaneously, a number of atmospheric parameters at a time (zenith angle 84.6°) when the atmosphere was changing rapidly. To achieve this the following were flown.

(a) 6 ion chambers (1 LNO, 1 MNO, 2 QT and 2 SX),

(b) 2 X-ray proportional counters to measure total density profiles, (Bibbo, 1977),

(c) one EUV grazing incidence monochromator scanning from 90Å to 1100Å to measure the density profiles of N_2, O_2 and O (Lean, 1980),

(d) one 1/8m Ebert fastie spectrometer scanning the wavelength range 1350 to 1750 to measure the molecular oxygen density profile (Lean, 1980),

(e) one cylindrical electrode energy analyser, one electron retarding potential analyser and one positive ion retarding potential analyser, to measure the velocity profiles of ions, thermal electrons and photo-electrons, (Bibbo, 1977),

(f) one multi-channelled airglow photometer, to measure the intensities of the airglow lines λ7620Å, λ6300Å, λ5577Å and the bands at λ3914Å and λ3370Å, (R. Schaeffer, private communication),

(g) one neutral particle and one positive ion quadrupole mass spectrometer to identify and measure the abundances of neutral particles and positive ions, (Bibbo, 1977).

The payload is shown in Figure 5.21.

The ion chambers flown on Aerobee 13.123 IS were the modified type shown in Figure 3.2. They were mounted so that their direction of look was parallel to that of the sun sensor of the ACS. They were run at + 45V. As with the Skylark chambers this was achieved by floating a 15V battery on top of the regulated voltage supplied by the vehicle; in this case ± 30 volts. The output from each chamber was fed into a 2 stage amplifier (Circuit diagram, Figure 5.22). The operational amplifier (ICH 8500Å) with its feedback resistor was placed on a separate board and bolted as close as possible to the back of the ion chamber it was serving. This helped to minimize noise. The gain of each stage was determined by the ratio of the resistances, i.e. $R_2/10K$ for the first stage and $R_3/10K$ for the second (see 5.22 for meaning of symbols).

The output of each stage was sampled by the PCM telemetry. The first stage at 40 times/sec. and the second stage at 80 times/sec. The more sensitive stage would saturate early but the increase in amplification allowed for a better signal-to-noise ratio for the chambers low altitude initial response to the solar flux. At these lower altitudes

Fig. 5.21 Aerobee 13.123 IS Payload.

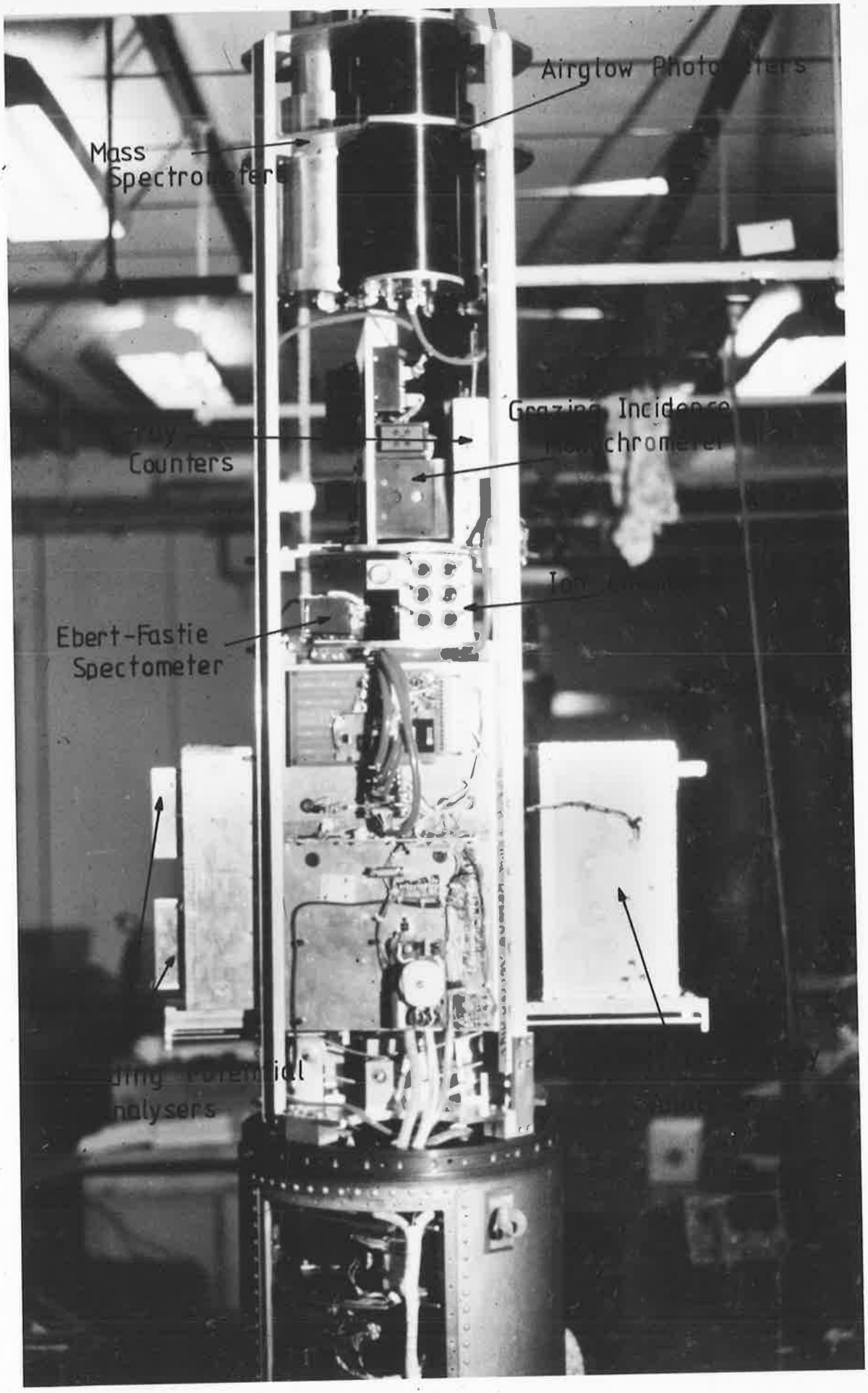
Airglow Photo
Mass
Spectro
Counters
Incidence
Ebert-Fastie
Spectometer

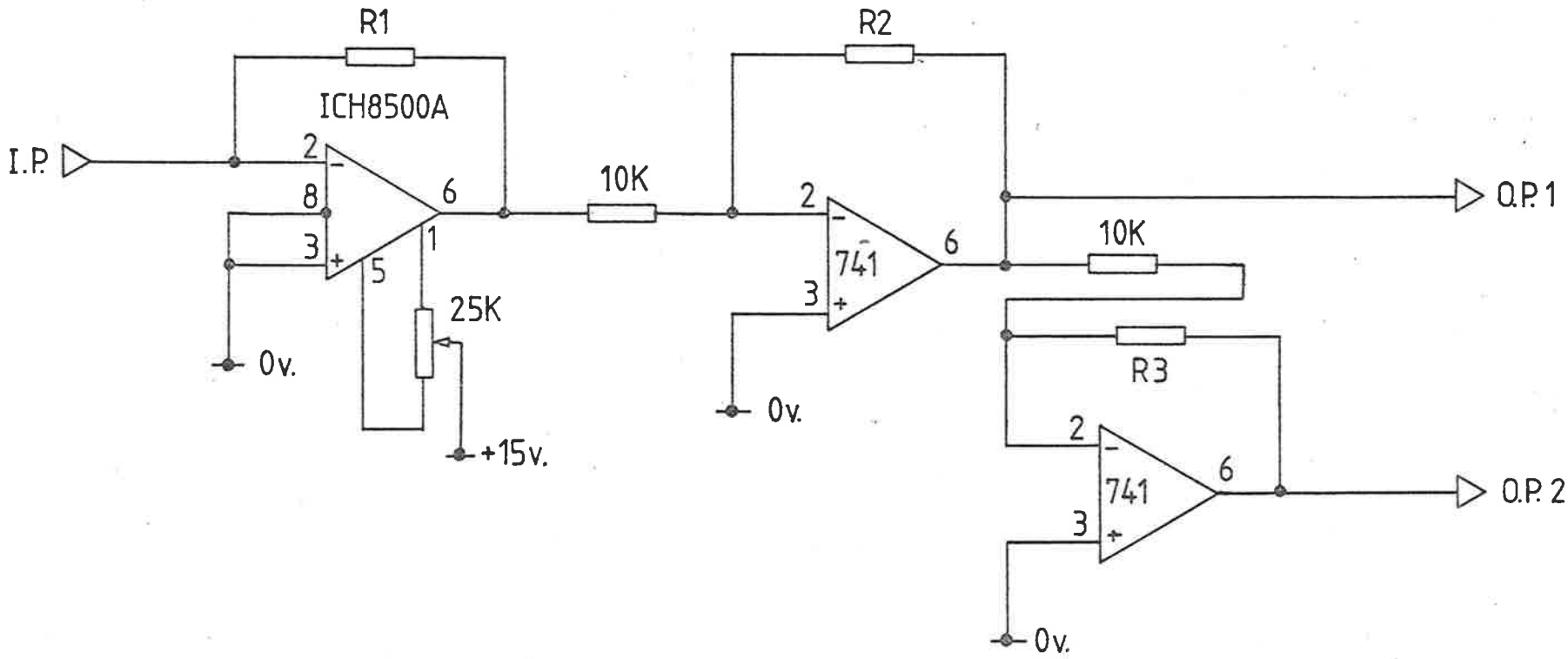

Fig. 5.22 Amplifier for Ion Chambers flown on Aerobee 13.123 IS. The gain is set by adjusting the values of the feedback resistors, R1, R2, and R3.

the rocket is travelling faster than it is at the heights where the less sensitive stage provides the data and therefore to maintain high resolution the more sensitive stage was sampled more frequently.

Preflight care of the ion chambers was similar to that described for Skylark SL 1005 (Section 5.2.2.1). Flushing was carried out up to an hour before launch. Preflight checks were similar to those described in Section 5.2.2.2.

5.3.3 The Flight

Acquisition on to the sun was obtained by 107 kms on the upleg and maintained until approximately 80 kms on the downleg.

The head section weighing 146 kg was lifted to a height of 177 kms at 222 secs. Data was recorded from 81 sec. to 365 sec, i.e. a total of 284 secs.

The parachute deployed late subjecting the payload to severe accelerations. This sheared some of the restraining bolts and part of the payload was lost. However, the ion chambers were recovered and post flight calibration was possible.

The telemetry was in the main satisfactory. However, sub-commutated channels all showed regular dropouts throughout the flight, 40% to 50% of the data transmitted through these channels was invalid.

The vehicle was satisfactorily tracked and the final trajectory calculated to an accuracy of ± 20 metres.

5.3.4 The Results

All six ion chambers yielded information on both the upleg and the downleg, but the signal strength from the LNO chamber was much less than expected. The LNO chamber survived impact and post flight calibration showed that its efficiency had decreased to ¼ of its

original value. The new efficiency was consistent with the signal strengths observed during flight. The window seal showed signs of deterioration but this may have been the result of re-entry heating. A spectral response curve taken during the post flight calibration indicated the chamber was contaminated but it is felt this occurred after recovery when the chambers were cleaned.

The most probable cause for the degradation was water vapour contamination, but this cannot be proved. Since useable data was still obtained, despite the decrease in sensitivity, further explanation was not sought.

The two SX chambers also survived impact. Post flight calibrations of these showed unchanged sensitivities but the band pass limits had shifted by $\lambda 1$Å to $\lambda 2$Å.

The upleg and downleg raw data of all chambers showed differences but some of this will be caused by the rapidly changing optical depth factor at the time of flight. Further discussion on these differences is left to Chapter 6.

All the ion chambers were on sub-commutated channels. Therefore much data was lost. However, as is shown by Figures 5.23 - 5.34 the "good" data could be isolated and useable extinction curves were obtained. The gaps in the data did influence the analysis method chosen and this has already been discussed in Chapter 4.

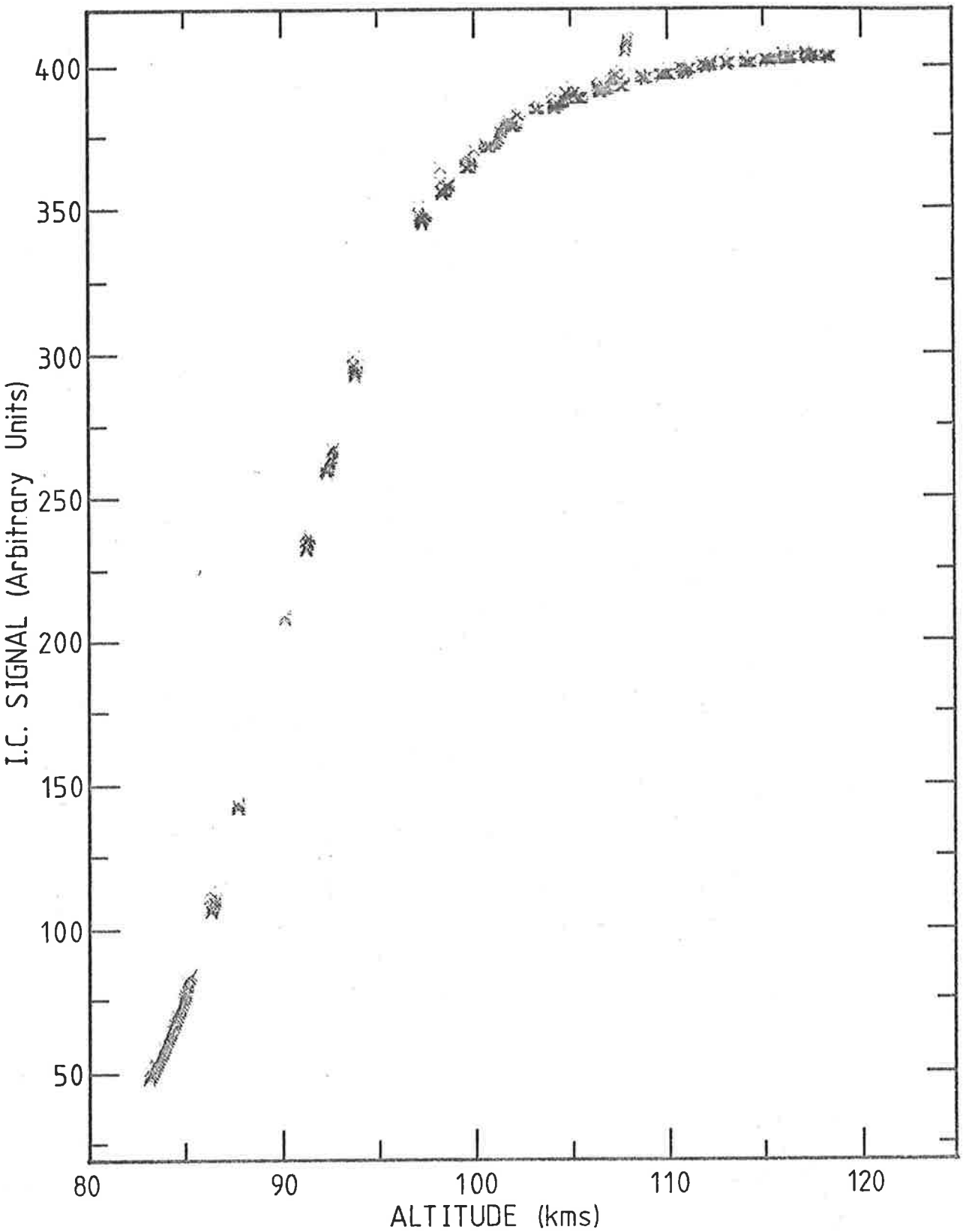

Fig 5.23 Telemetred signal from LNO 202 flown on Aerobee 13.123 IS - upleg.

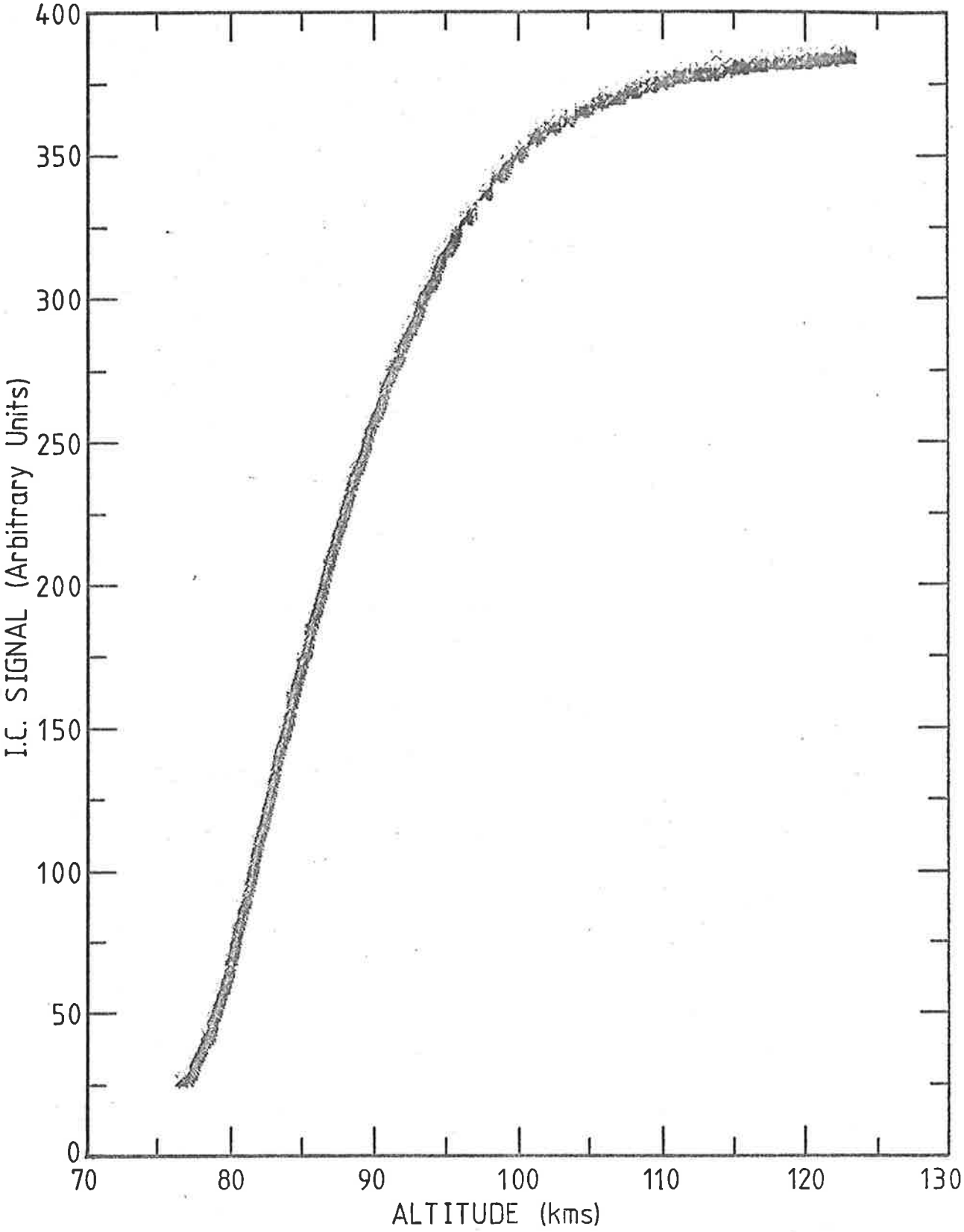

Fig 5.24 Telemetred signal from LNO 202 flown on Aerobee 13.123 IS - downleg.

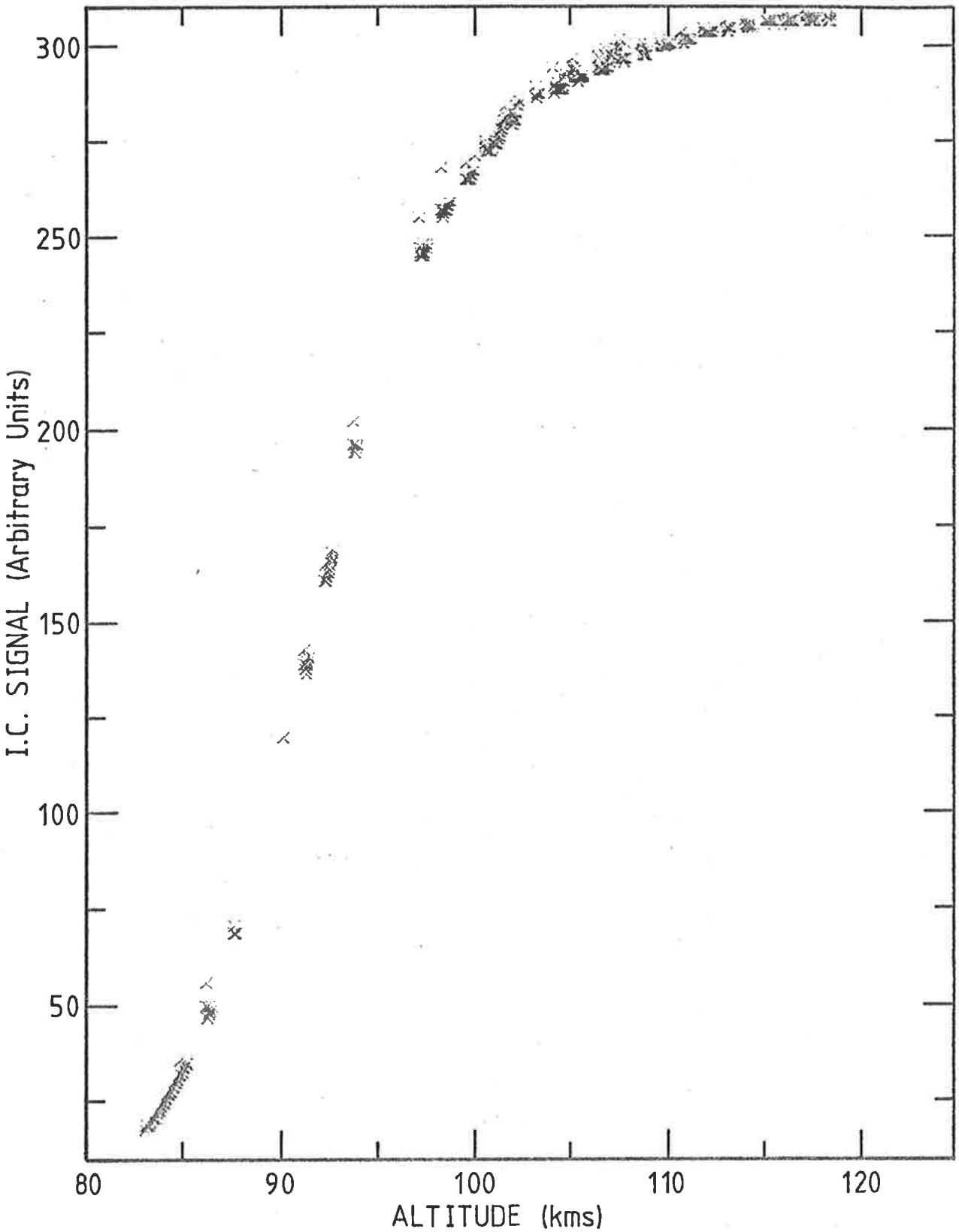

Fig 5.25 Telemetred signal from MNO 1 flown on Aerobee 13.123 IS - upleg.

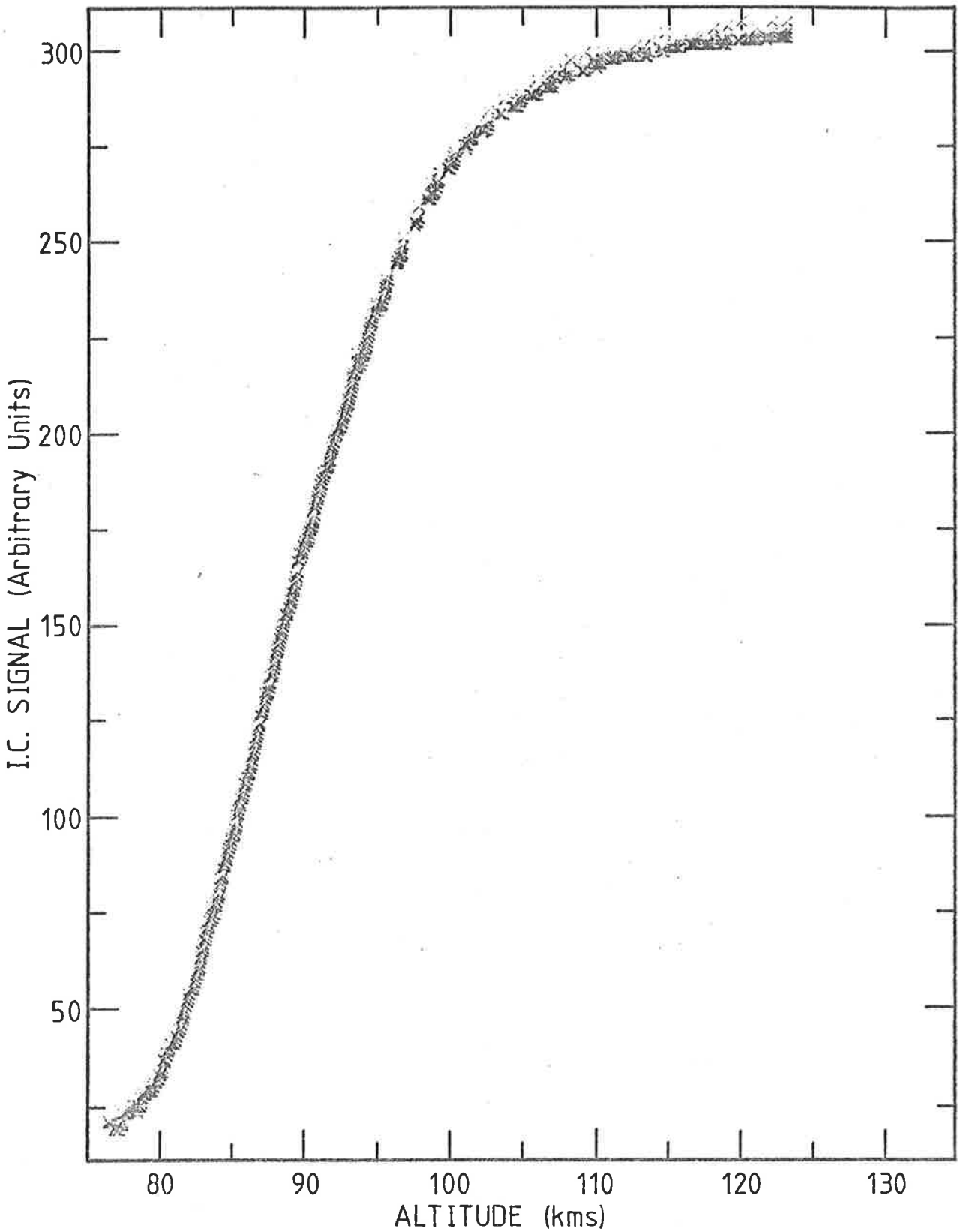

Fig 5.26 Telemetred signal from MNO 1 flown on Aerobee 13.123 IS - downleg.

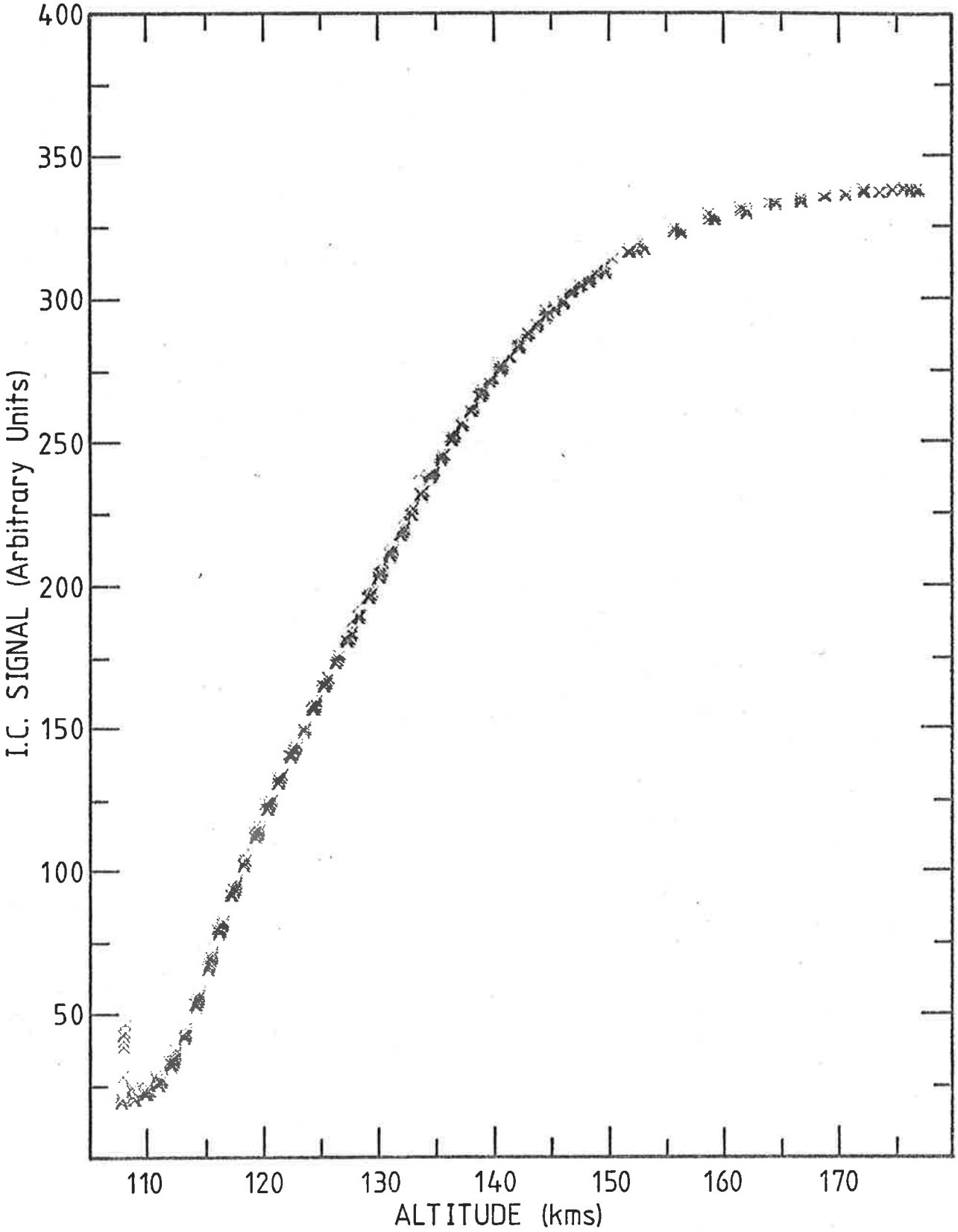

Fig 5.27 Telemetred signal from QT 202 flown on Aerobee 13.123 IS - upleg.

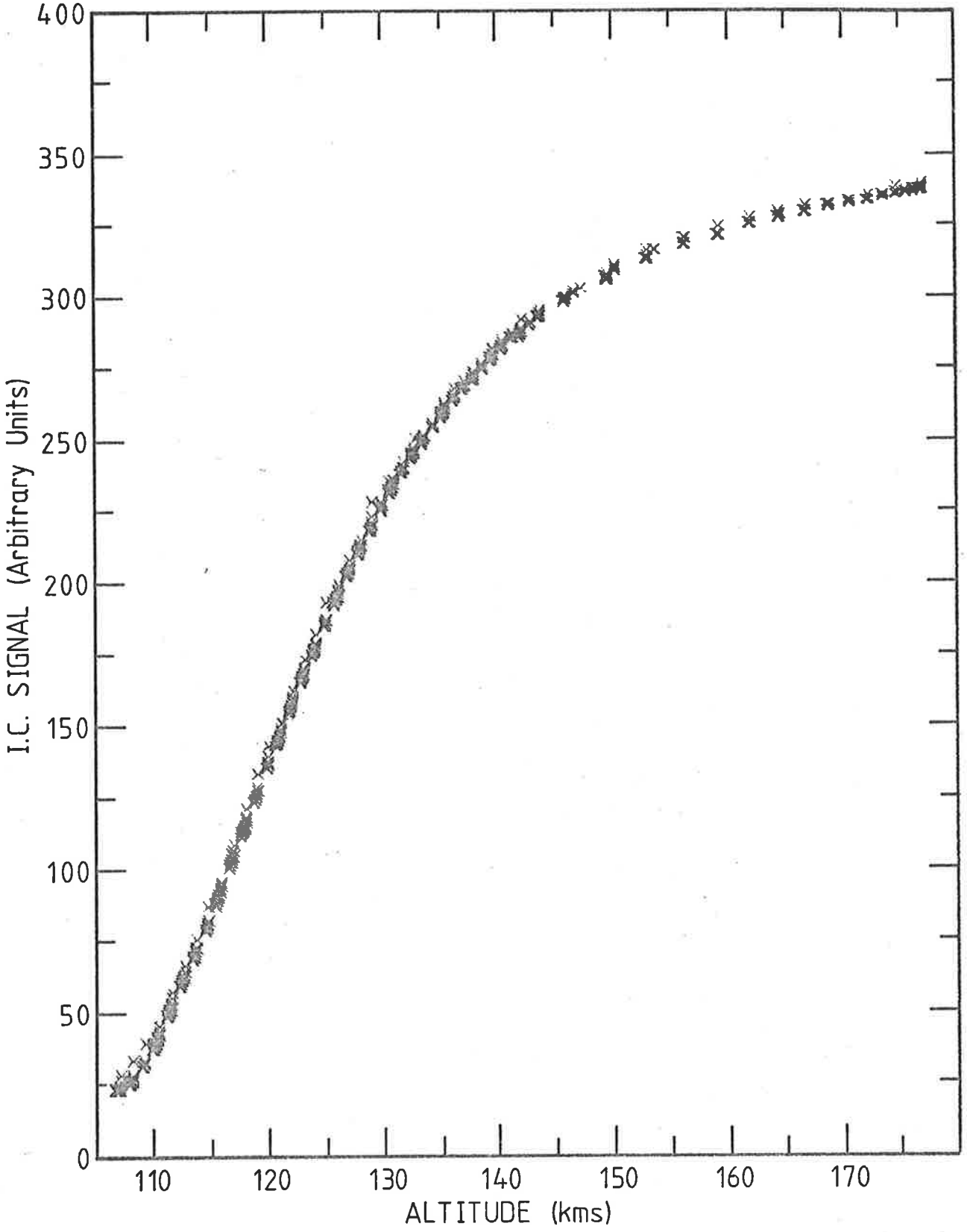

Fig 5.28 Telemetred signal from QT 202 flown on Aerobee 13.123 IS - downleg.

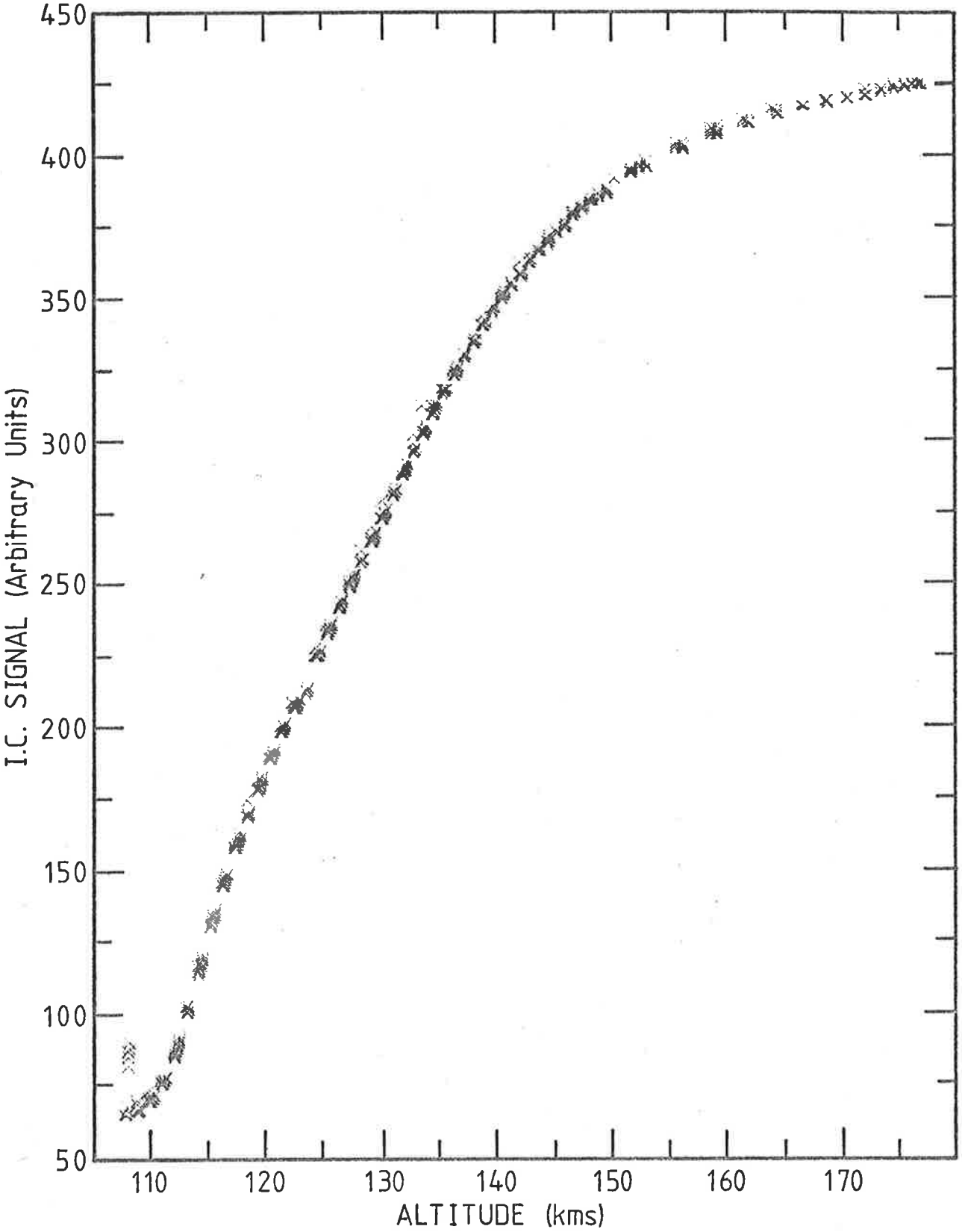

Fig 5.29 Telemetred signal from QT 5 flown on Aerobee 13.123 IS - upleg.

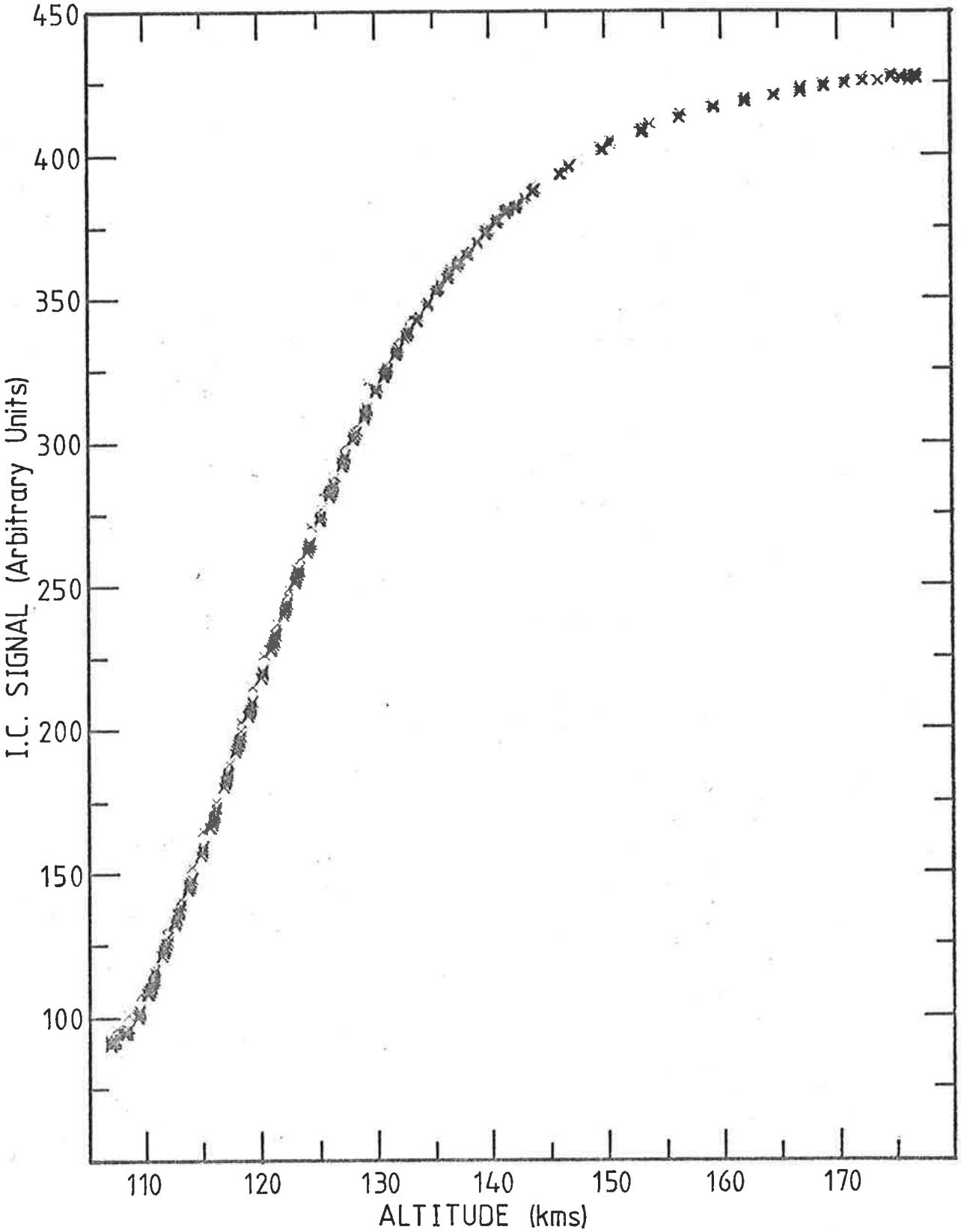

Fig 5.30 Telemetred signal from QT 5 flown on Aerobee 13.123 IS - downleg.

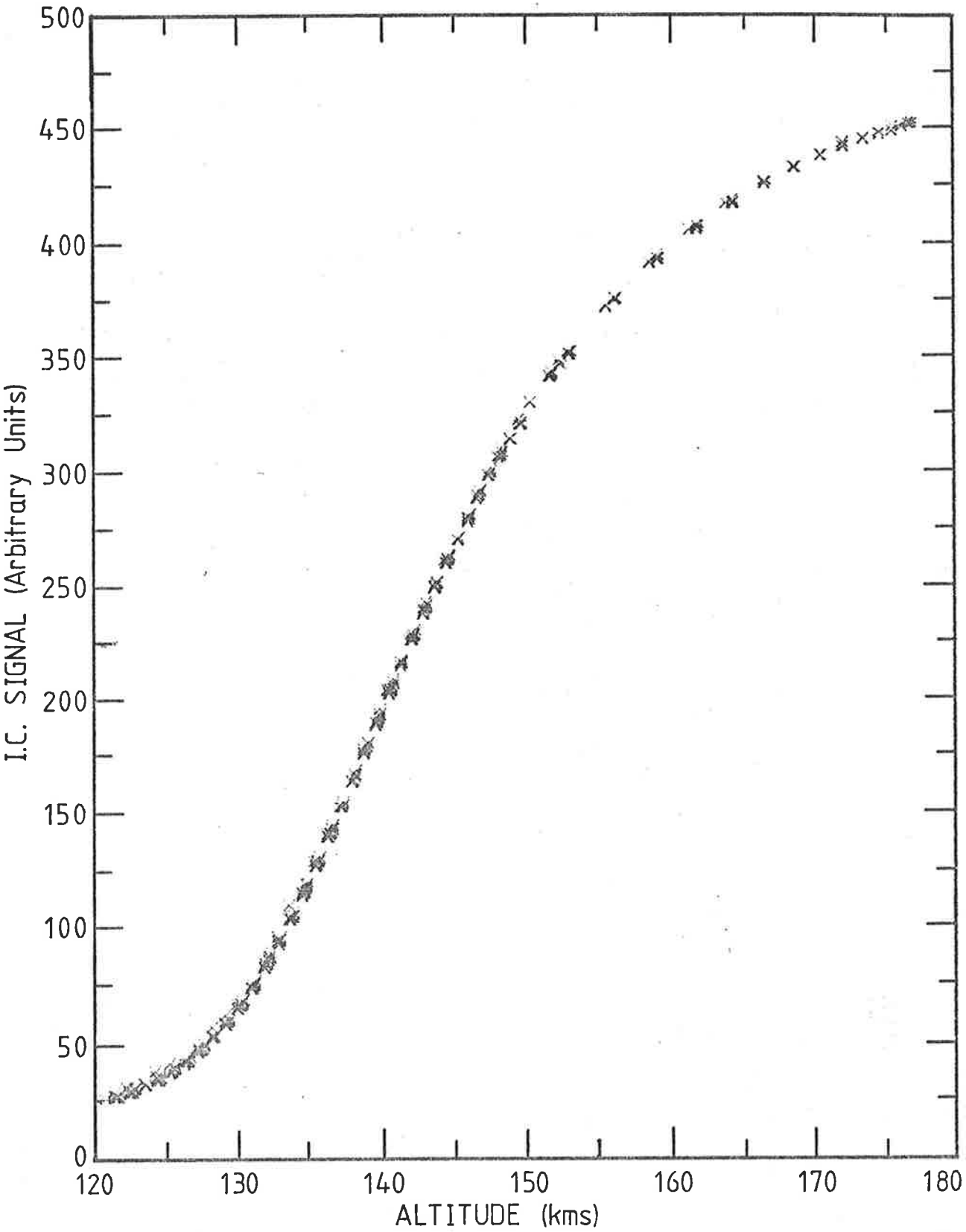

Fig 5.31 Telemetred signal from SX 202 flown on Aerobee 13.123 IS - upleg.

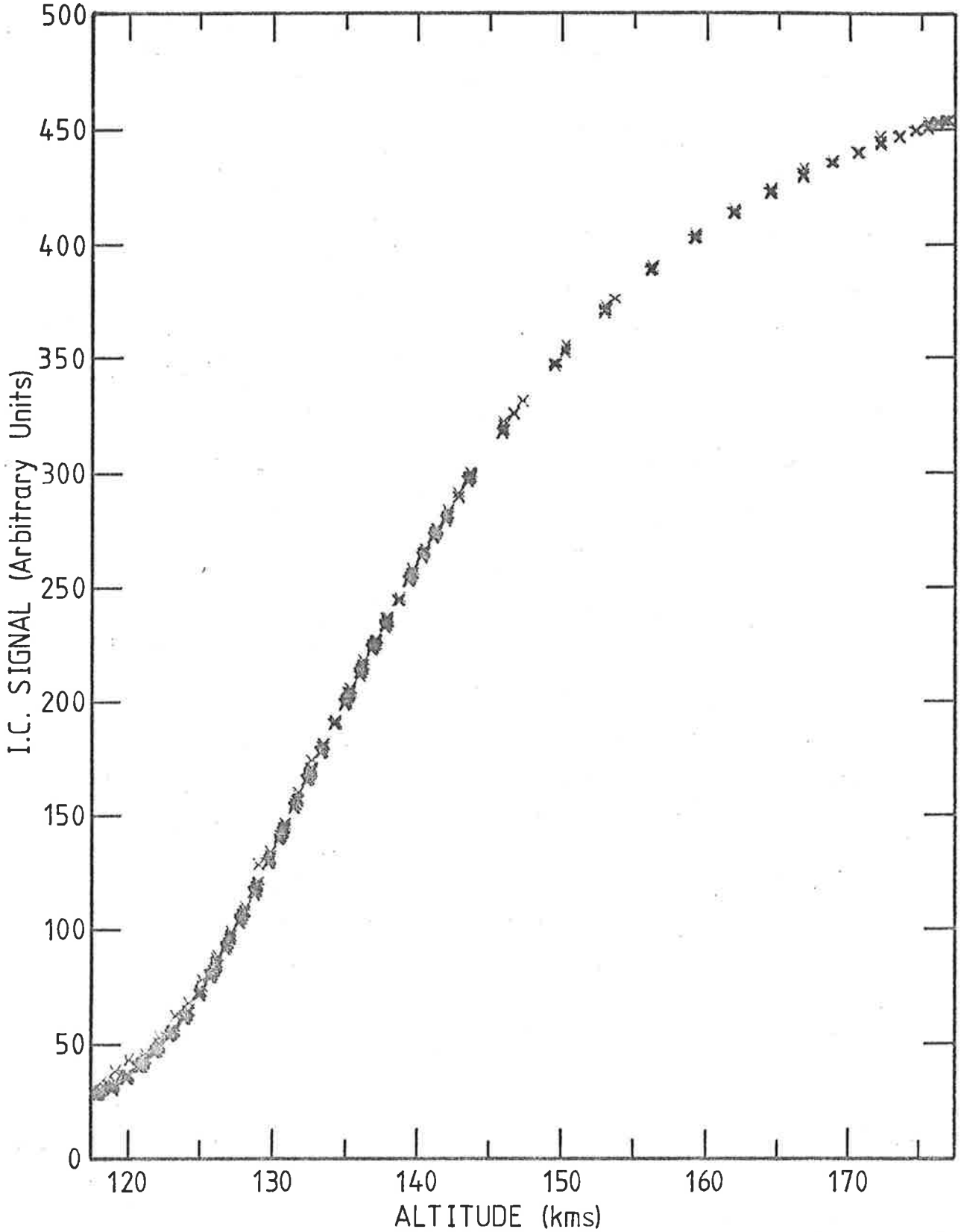

Fig 5.32 Telemetred Signal from SX 202 flown on Aerobee 13.123 IS - downleg.

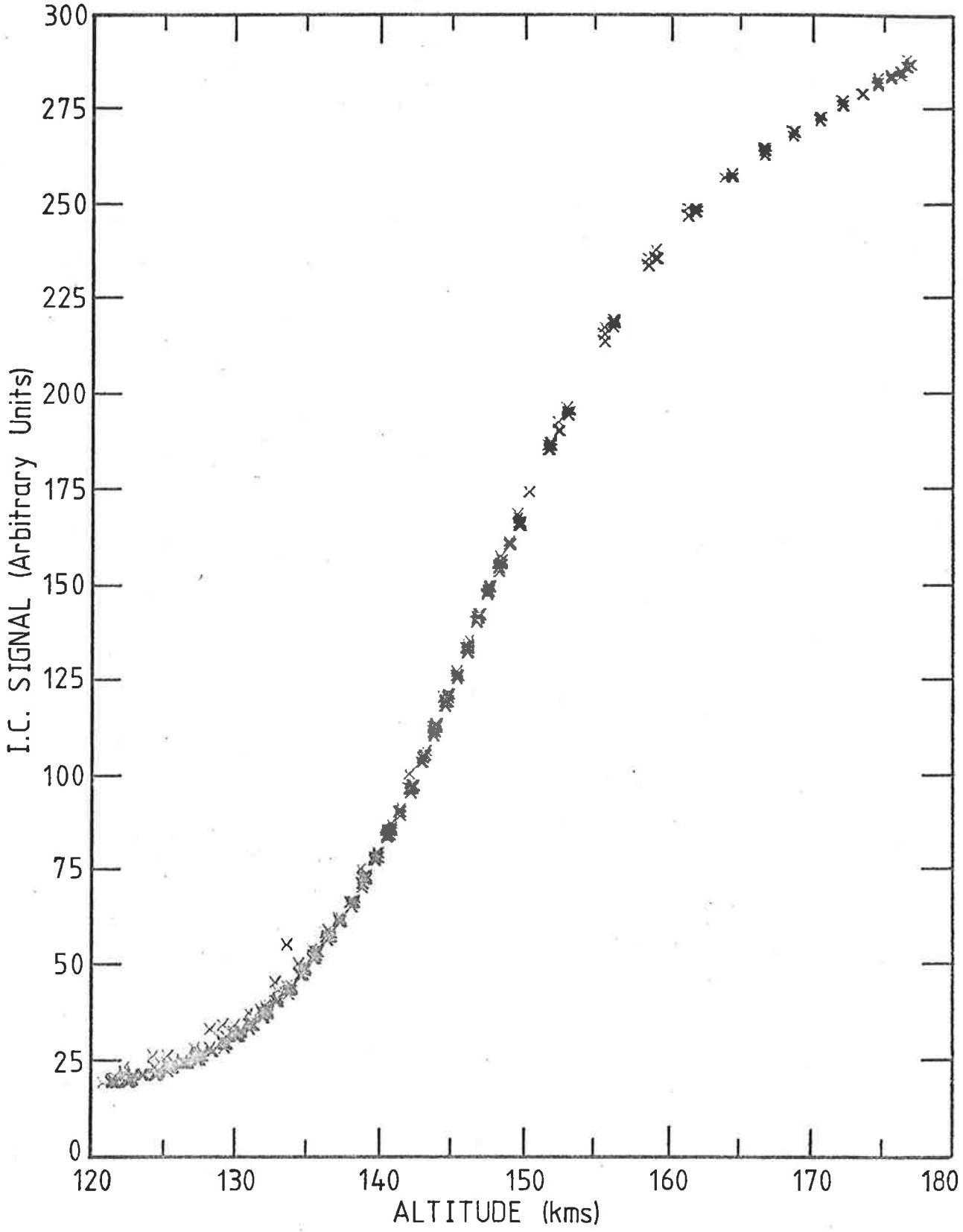

Fig 5.33 Telemetred signal from SX 204 flown on Aerobee 13.123 IS - upleg.

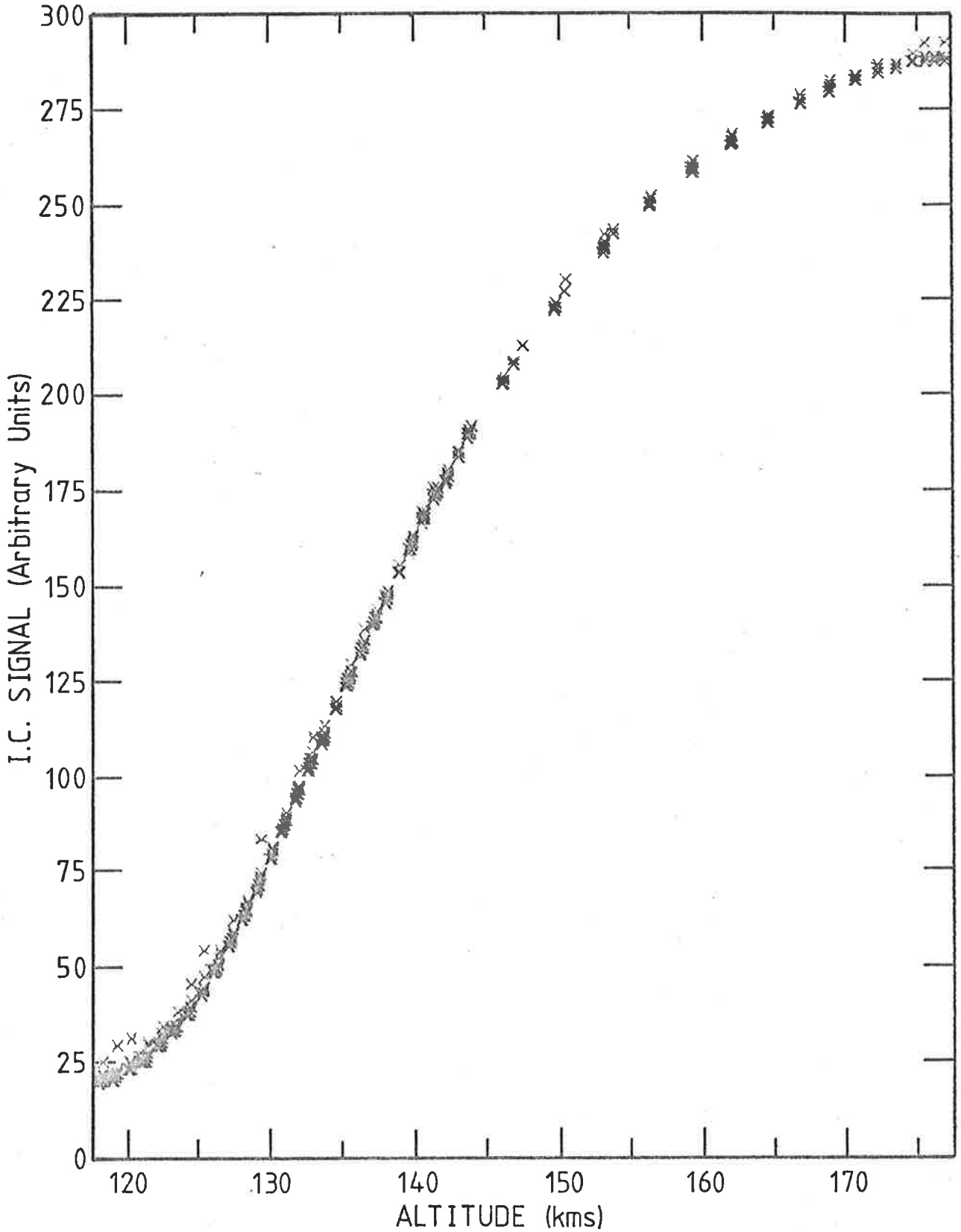

Fig 5.34 Telemetred signal from SX 204 flown on Aerobee 13.123 IS - downleg.

CHAPTER 6

LOWER THERMOSPHERIC MOLECULAR OXYGEN DENSITIES

This chapter presents the results obtained from the molecular oxygen experiments described in the preceding chapters. Each profile obtained is presented in graphical form in Section 6.1 (tabulations of the densities are given in Appendix 2). The discussion in Section 6.1 centres on the general appearance of these individual profiles and comparison between profiles made by different chambers on the same flight.

Mean profiles were calculated from the results of each rocket-borne experiment. These are given in Section 6.2 (tabulations of these can also be found in Appendix 2). The profiles were not just averages of the separate results from each chamber and the section contains the rationale for the method used to construct each mean. In the case of Aerobee, where the ion chambers were only one of three experiments to measure molecular oxygen, comparison is made between the three experiments. Comparison is also made between the molecular oxygen densities obtained in this work and those from earlier Woomera measurements.

Signal levels from the chambers at apogee allowed an estimation of the flux levels for the radiation within their passbands. A brief discussion on the magnitude and uncertainty of these estimations is also included in Section 6.1.

Section 2.4.2 discussed variations that could be expected in lower thermospheric molecular oxygen densities. In Section 6.3 the results obtained in this work are examined to see if they can either confirm, or deny such variations. Since the experiments were flown at widely spaced intervals and were always launched from Woomera, this capacity is limited,

but, for example, the magnitude of magnetic variations is commented on.

Attempts have been made to model molecular oxygen densities for over thirty years. In Section 6.4 the results are compared with two of the later models. In addition some comment is made on the suitability of such models.

Section 6.5 summarizes the results that have been achieved in the course of this programme and assesses them in view of the aims of the research that were set out in Chapter 1.

Section 6.6 looks at the future work to be done in the investigation of lower thermospheric molecular oxygen densities and how this is most likely to be achieved. Development of the techniques outlined in this work is also commented on.

6.1 THE RESULTS

6.1.1 Introduction

The molecular oxygen experiment was flown on three rockets. On each rocket $n(O_2)$ profiles were obtained on both the upleg and the downleg of the flight. This section considers the profiles obtained by each chamber.

The profiles are looked at in detail. Some general remarks are made in Section 6.1.2 while Sections 6.1.3 and 6.1.4 compare profiles determined by different chambers; $L\alpha$/QT in 6.1.3 and SX/Spectrophotometer/QT in Section 6.1.4.

The discussion in these latter two sections includes consideration of what extra information may be obtained because of the overlapping profiles and comments on the apparent systematic differences between molecular oxygen profiles determined by different chambers on the same flight.

Section 6.1.5 discusses the estimates made of the flux intensities.

6.1.2 Presentation of Individual $n(O_2)$ Profiles and General Comments

Figures 6.1 to 6.25 show each molecular oxygen density profile obtained. They are not complete lower thermospheric profiles (see Section 6.2) but the results obtained from individual ion chambers. The figures are identified by the code of the ion chamber, and whether it is derived from the upleg data or the downleg data. This identification links Figures 6.1 to 6.25 to the raw data given in Chapter 5 and the tabulations given in Appendix 2.

On each profile at one or two heights an error bar has been drawn. These do not represent the total uncertainty. They represent and illustrate the significance of the errors discussed in Chapter 4 and summarized in Table 4.7.

Figure 6.1 shows the profile from the quartz triethylamine chamber QT 203. The coverage is limited because the signals from this chamber broke up above 110 kms and an extinction curve could no longer be discerned. The downlegs of all the chambers on SL 1005 (Figs 6.3, 6.5 and 6.7) are limited to $z < 130$ kms. Once again signal break up was the limiting factor.

A change in slope is observed in QT derived profiles in the altitude range 105 to 120 kms. This could represent a change in scale height and be indicative of the fact that the atmosphere was changing from a region of mixing to a region where concentrations are the result of maintenance of diffusive equilibrium. This is considered more closely in Section 6.4.

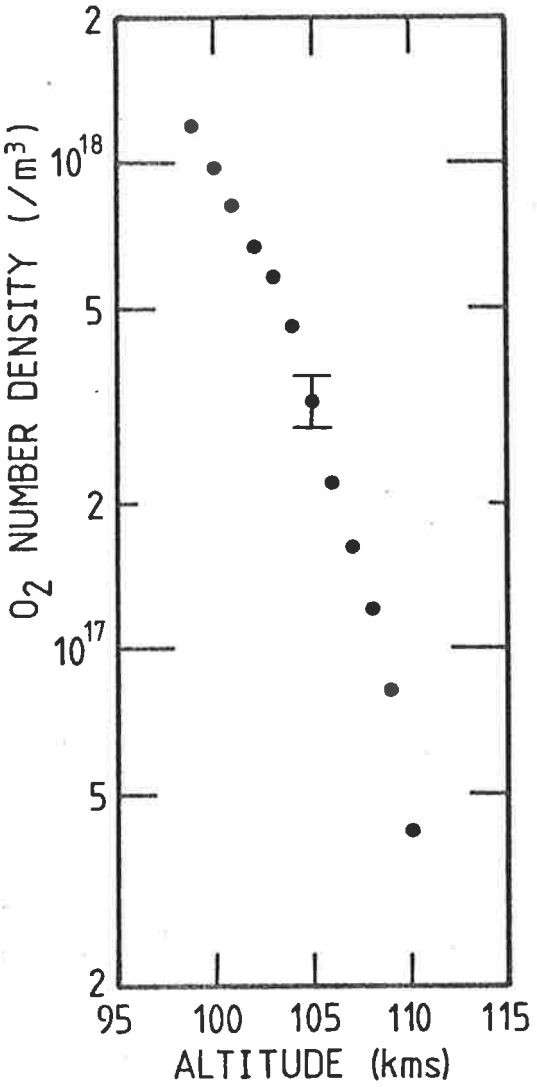

Fig. 6.1 $n(O_2)$ profile from the upleg data of QT203 flown on SL 1005.

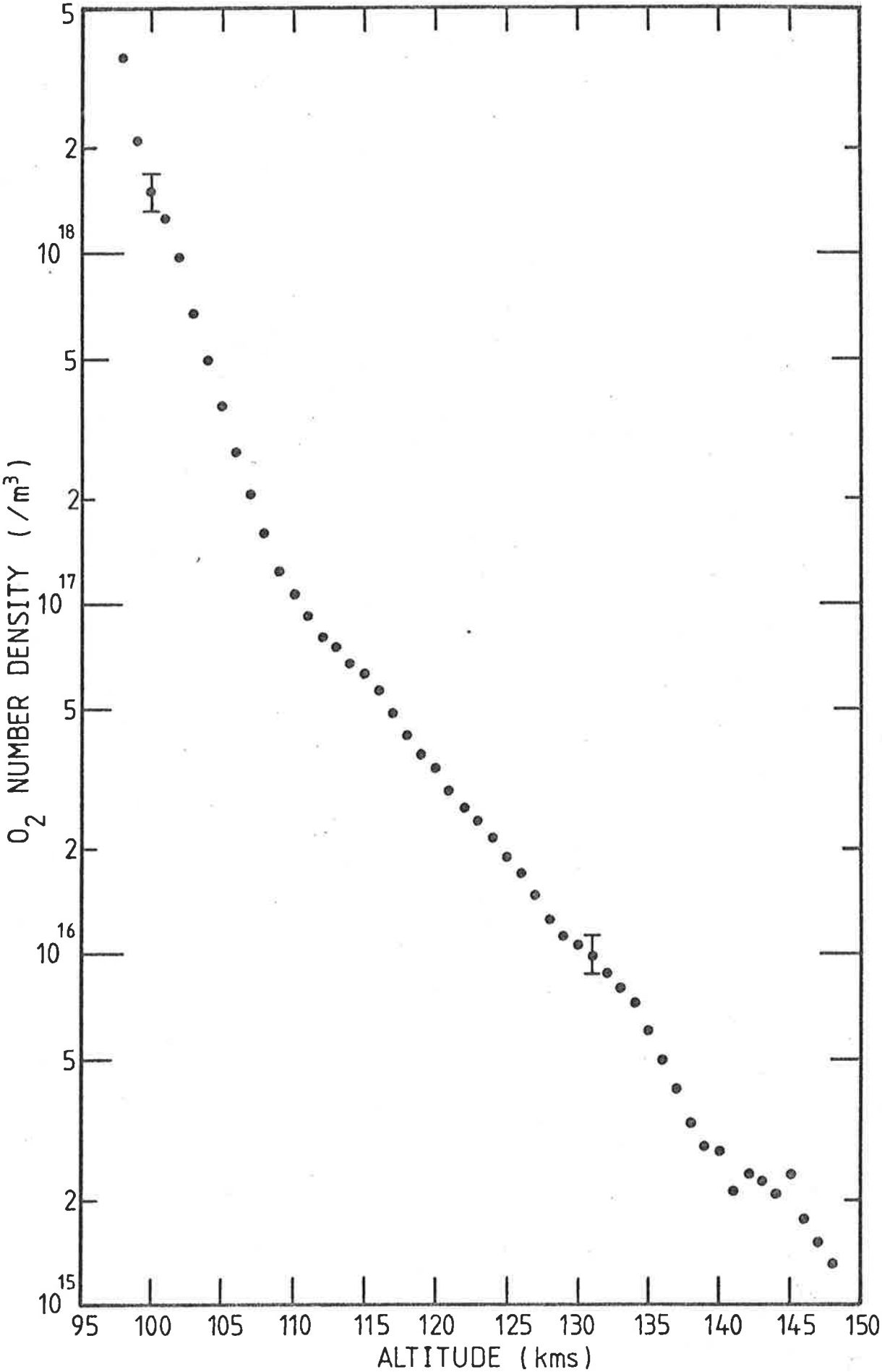

Fig. 6.2 $n(O_2)$ profile from upleg data of QT204 flown on SL 1005.

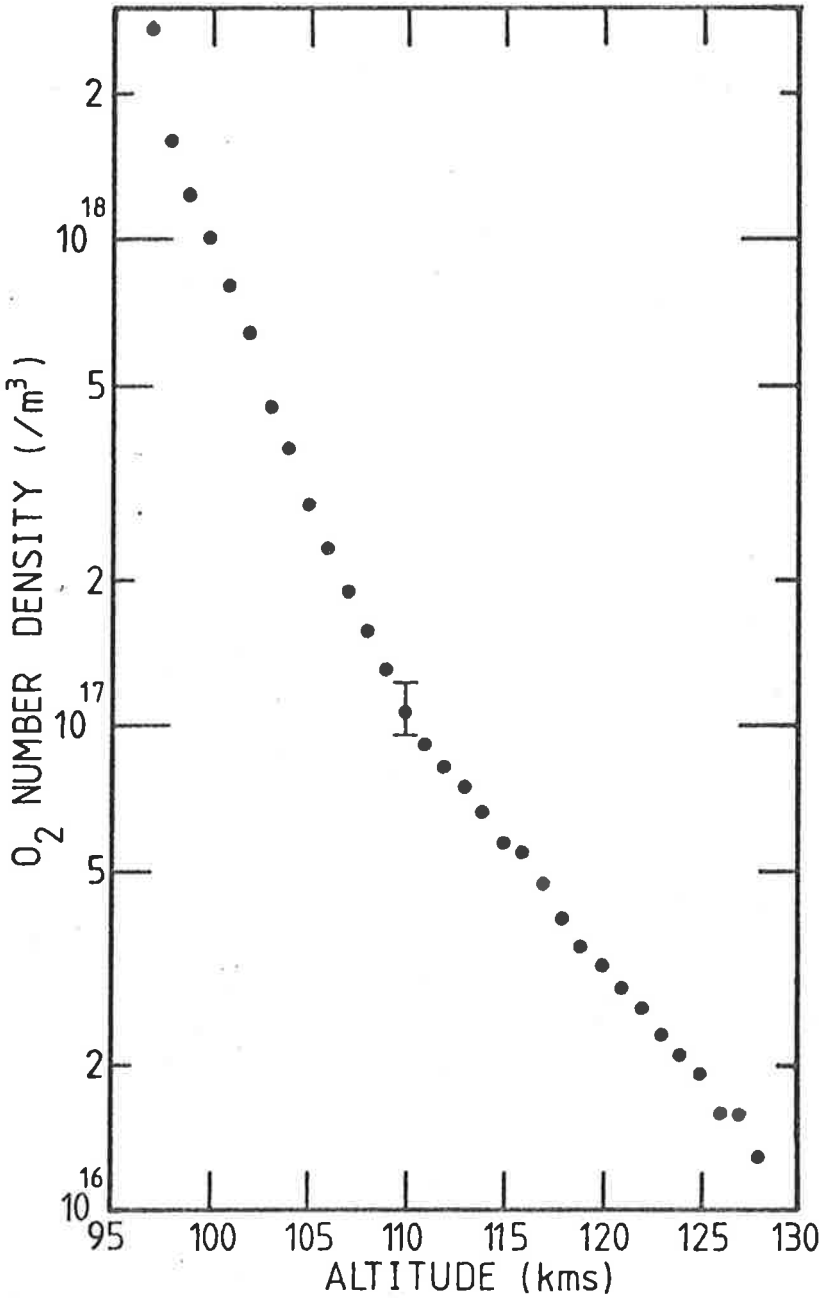

Fig. 6.3 $n(O_2)$ profile from downleg data of QT204 flown on SL 1005.

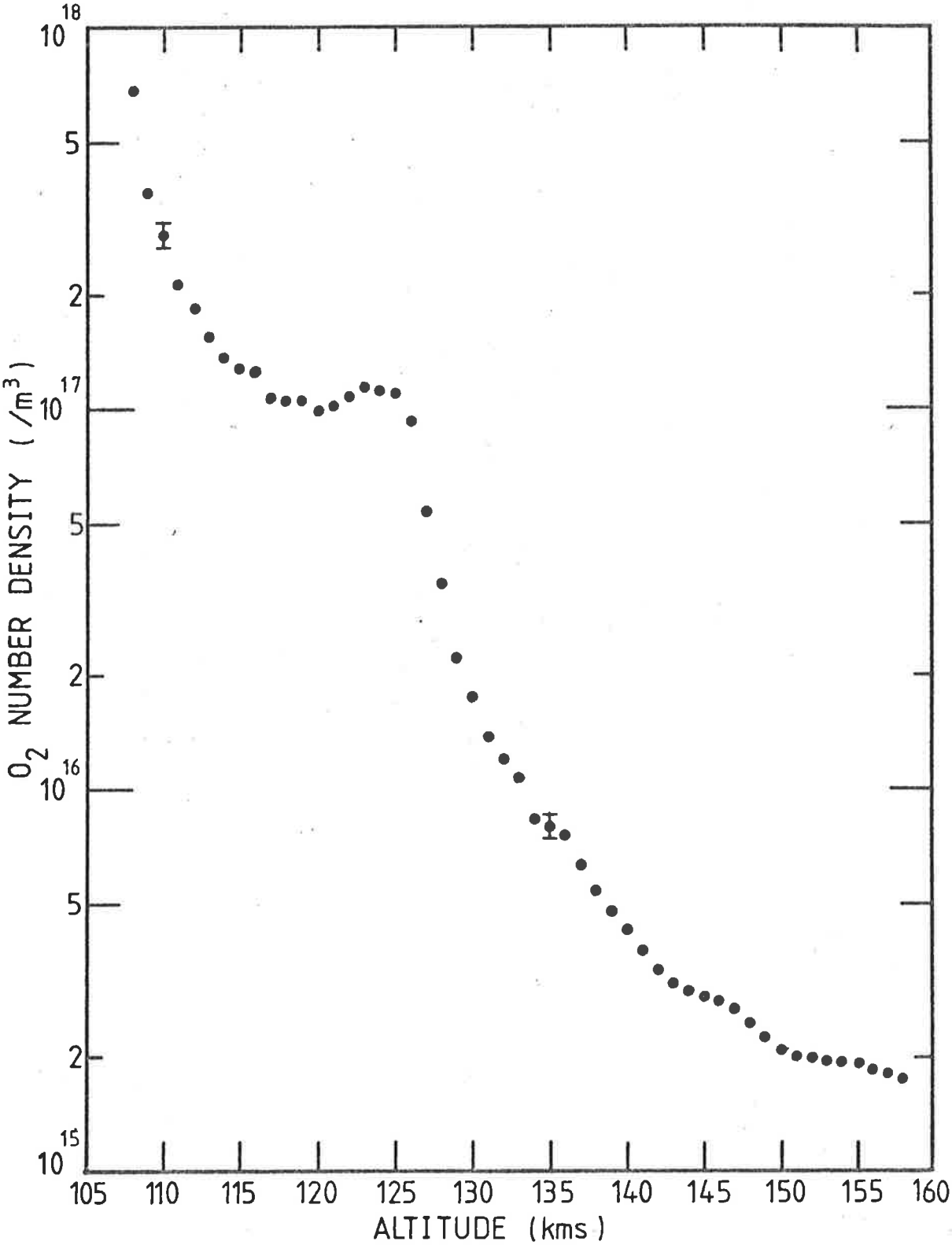

Fig. 6.4 $n(O_2)$ profile from upleg data of SX3 flown on SL 1005.

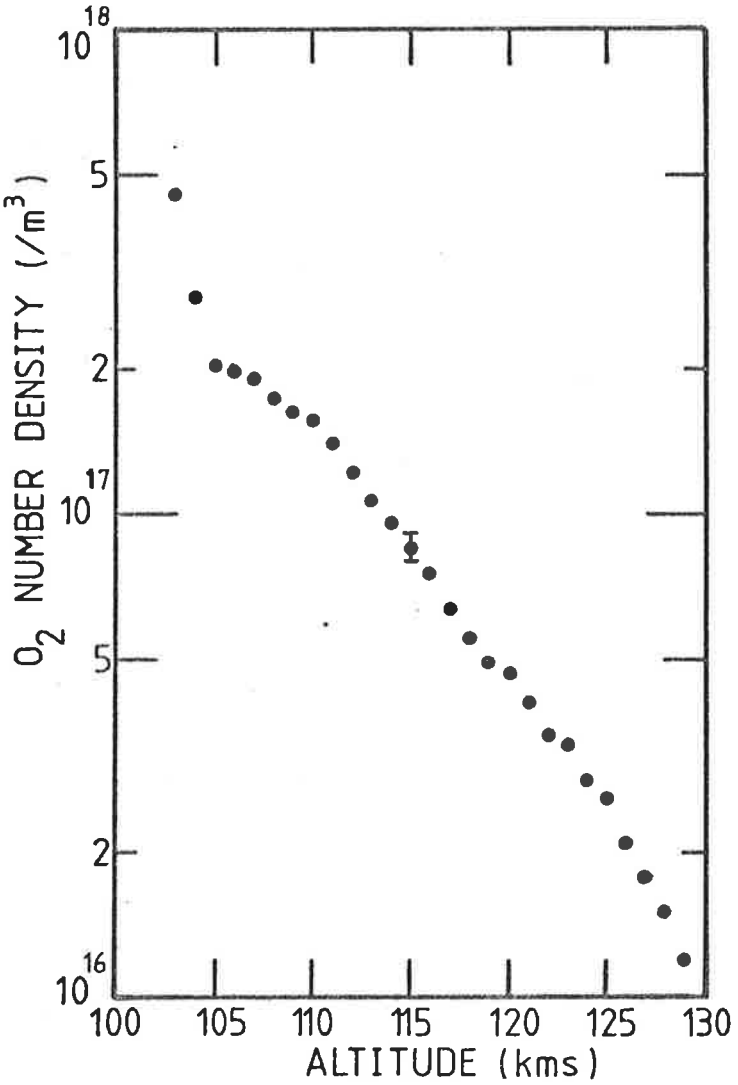

Fig. 6.5 $n(O_2)$ profile from downleg data of SX3 flown on SL 1005.

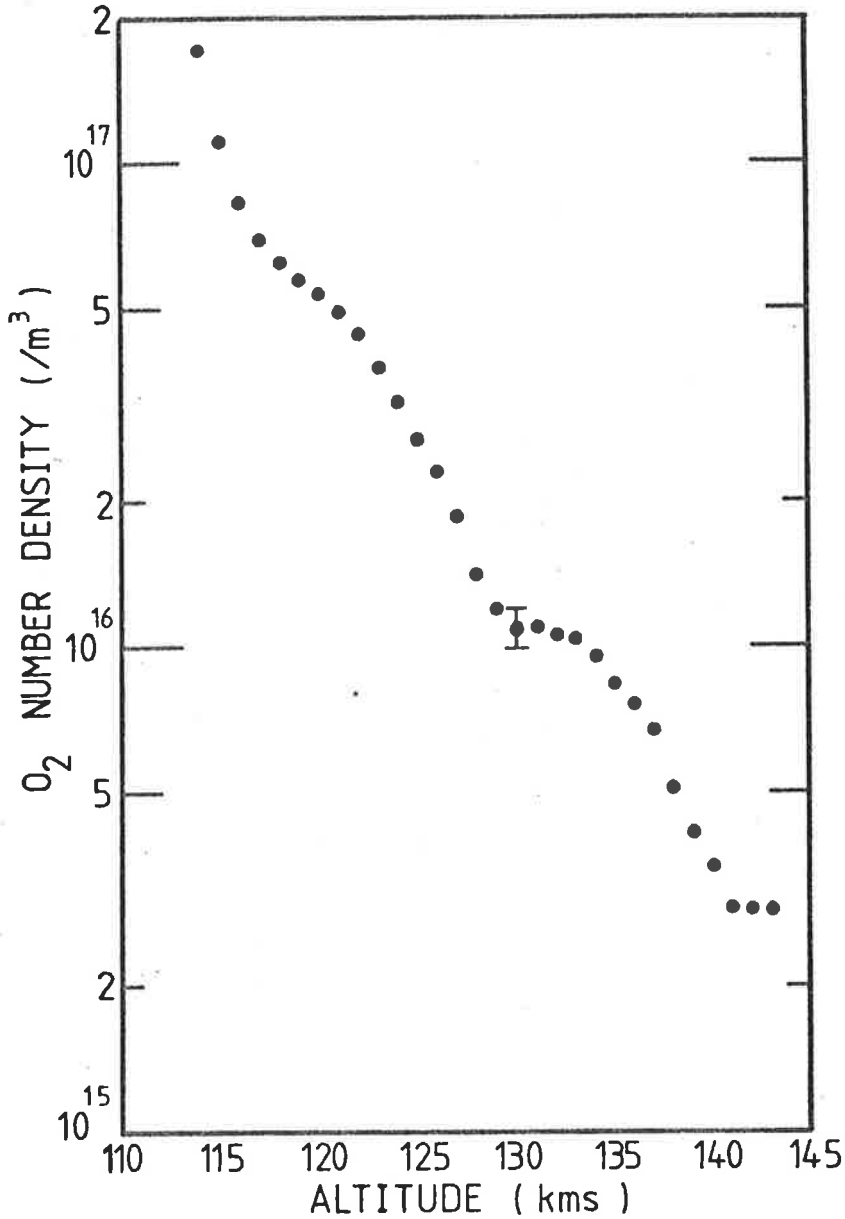

Fig. 6.6 $n(O_2)$ profiles from upleg data of Spectrometer flown on SL 1005.

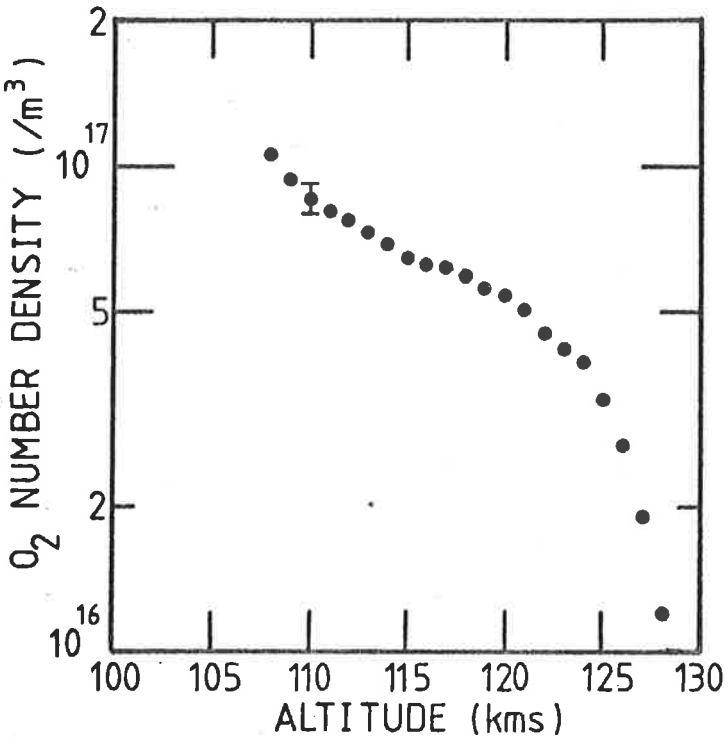

Fig. 6.7 $n(O_2)$ profile from downleg data of Spectrometer flown on SL 1005.

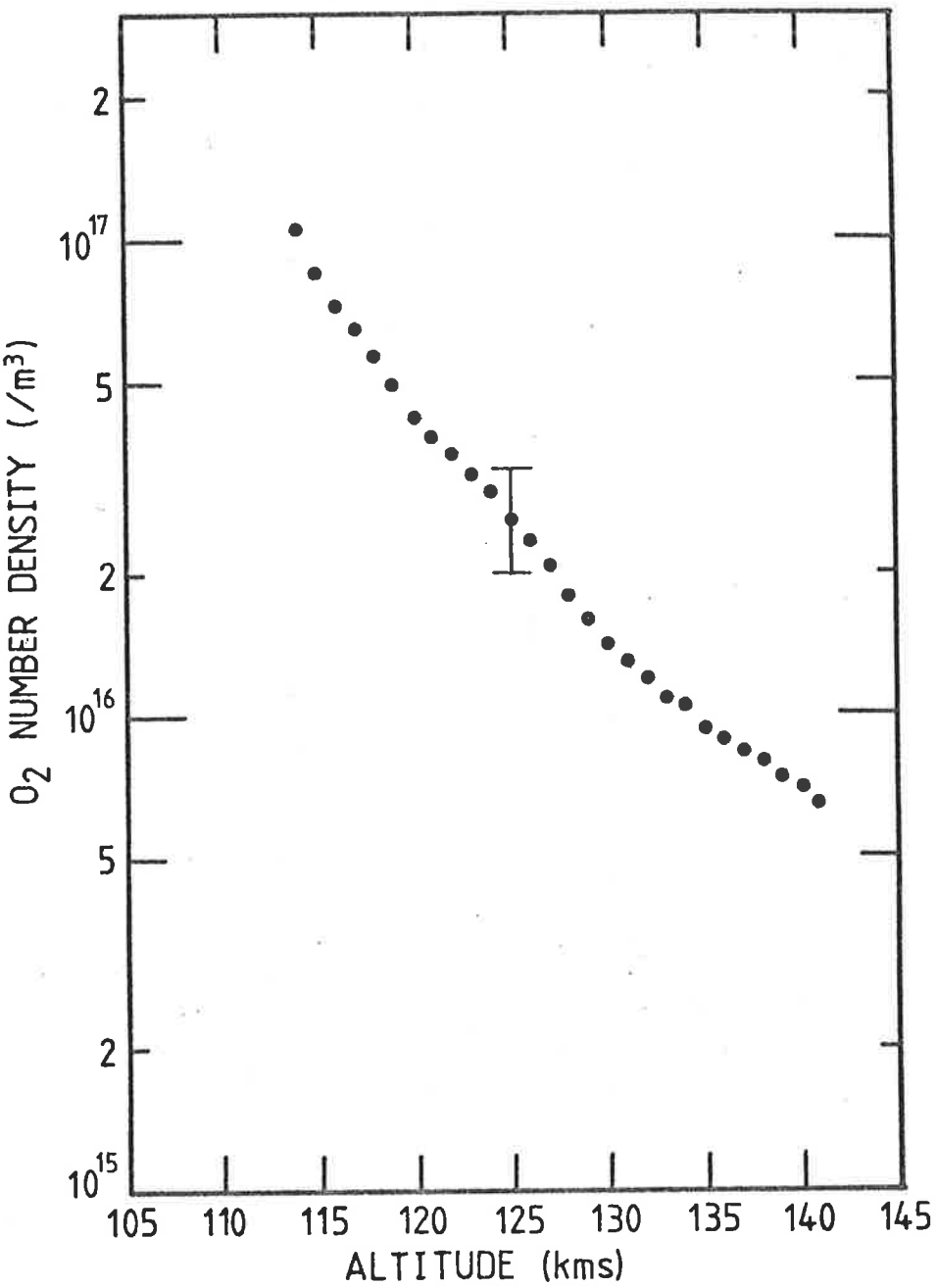

Fig. 6.8 $n(O_2)$ profile from the upleg data of QT1 flown on SL 1207.

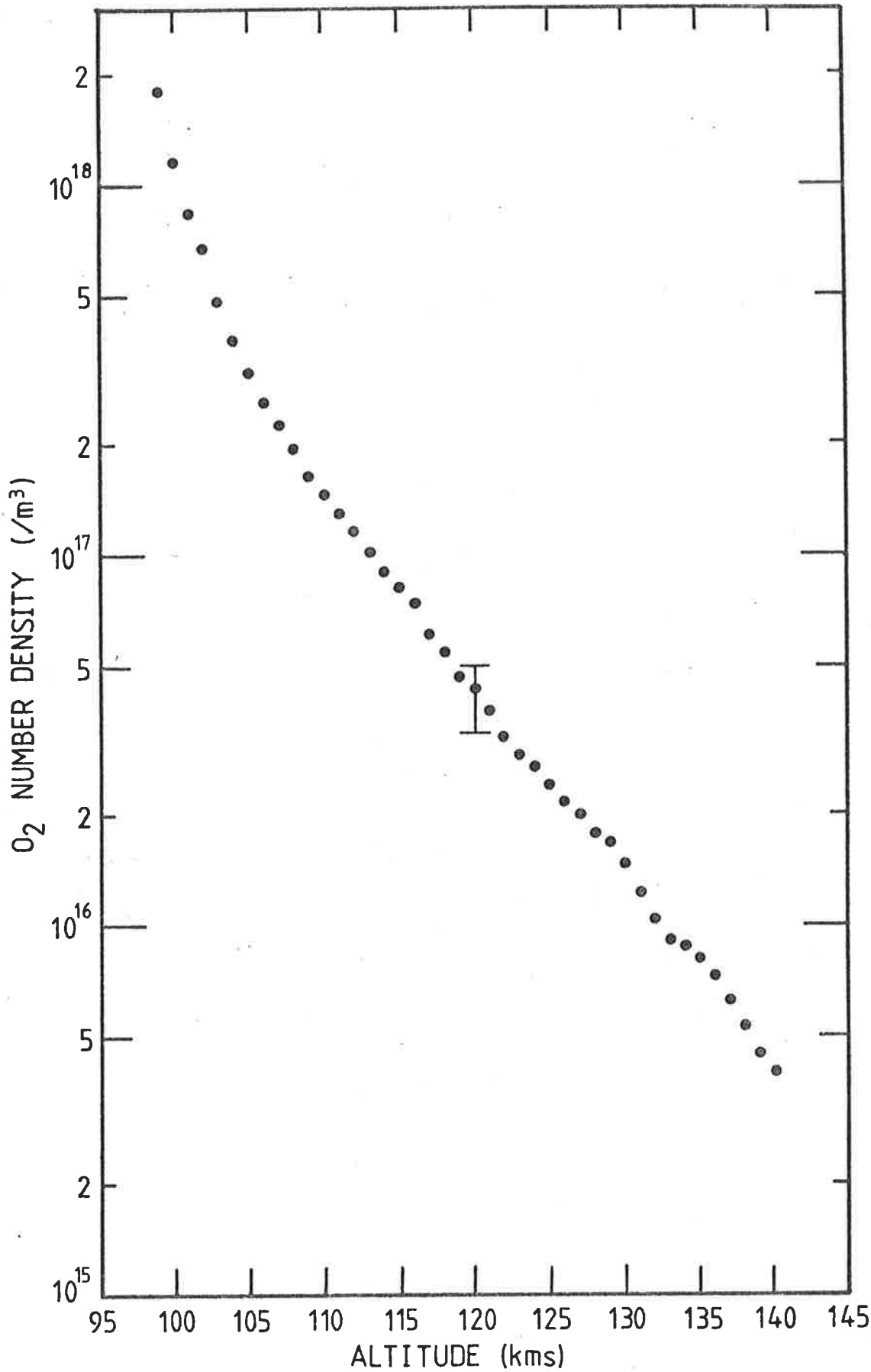

Fig. 6.9 $n(O_2)$ profile from the downleg data of QT1 flown on SL 1207.

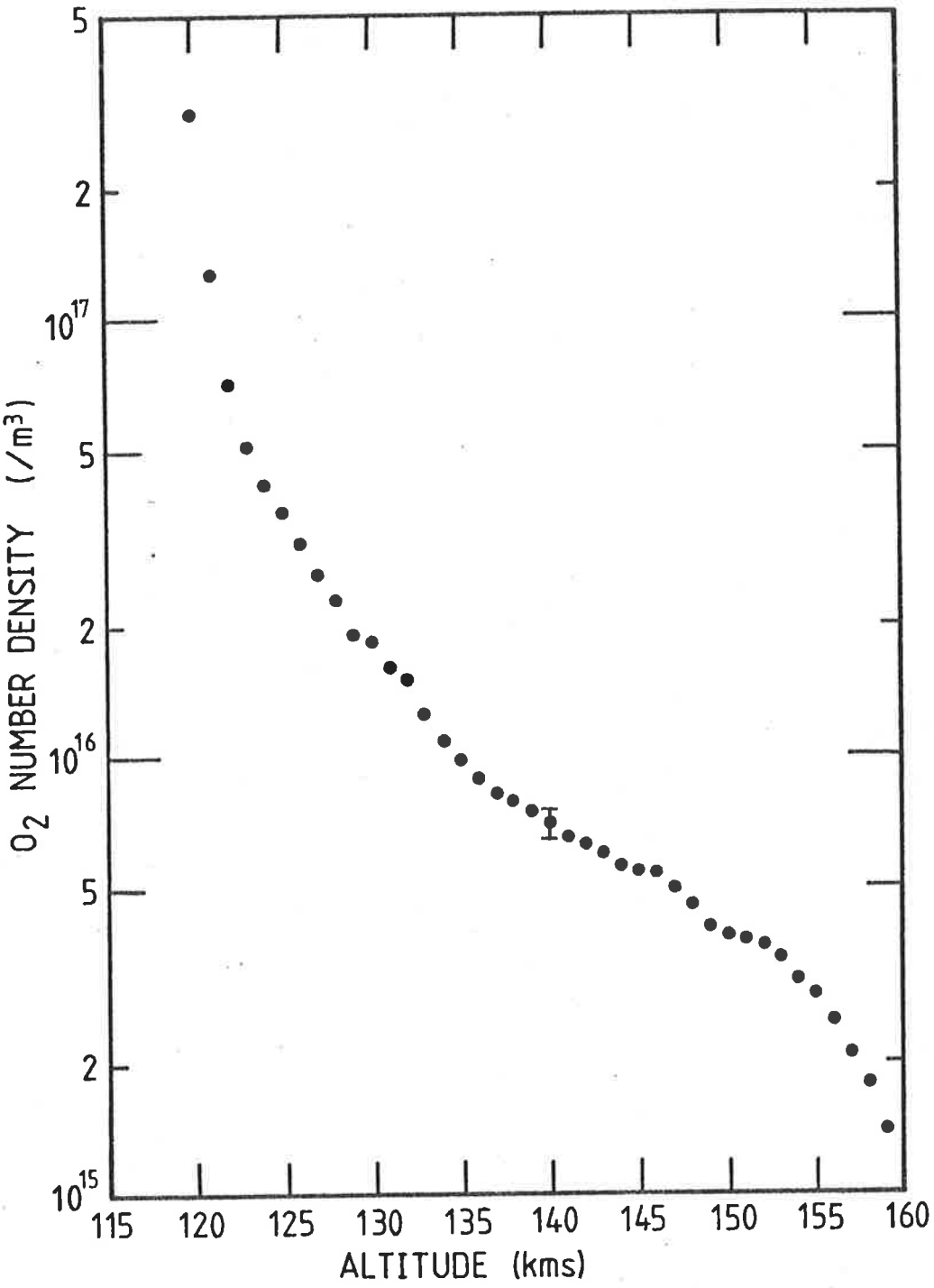

Fig. 6.10 $n(O_2)$ profile from upleg data of SX7 flown on SL 1207.

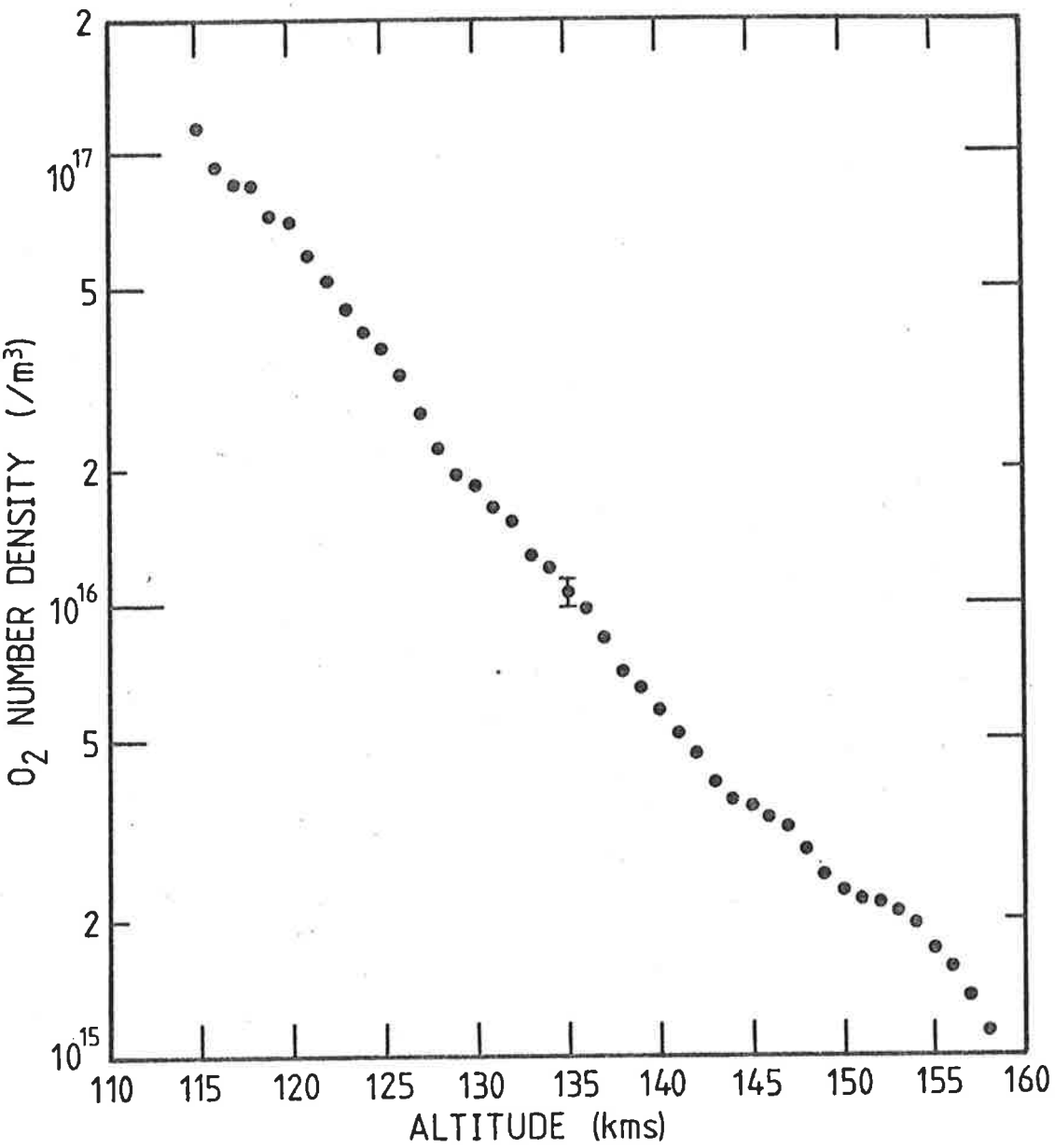

Fig. 6.11 $n(O_2)$ profile from downleg data of SX7 flown on SL 1207.

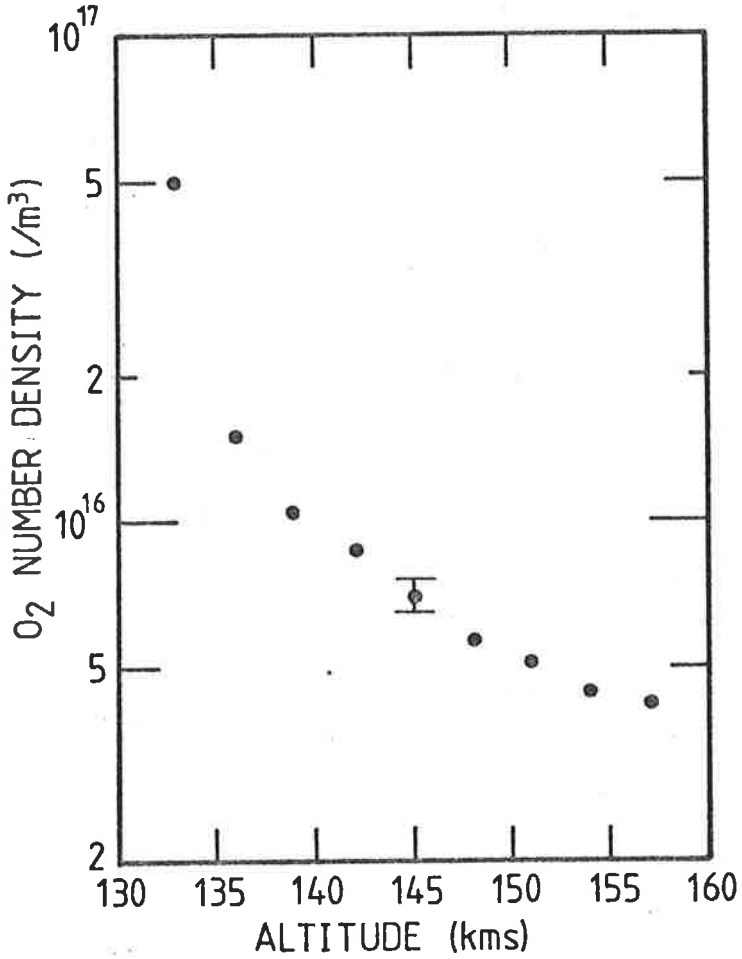

Fig. 6.12 $n(O_2)$ profile from the upleg data of SX5 flown om SL 1207.

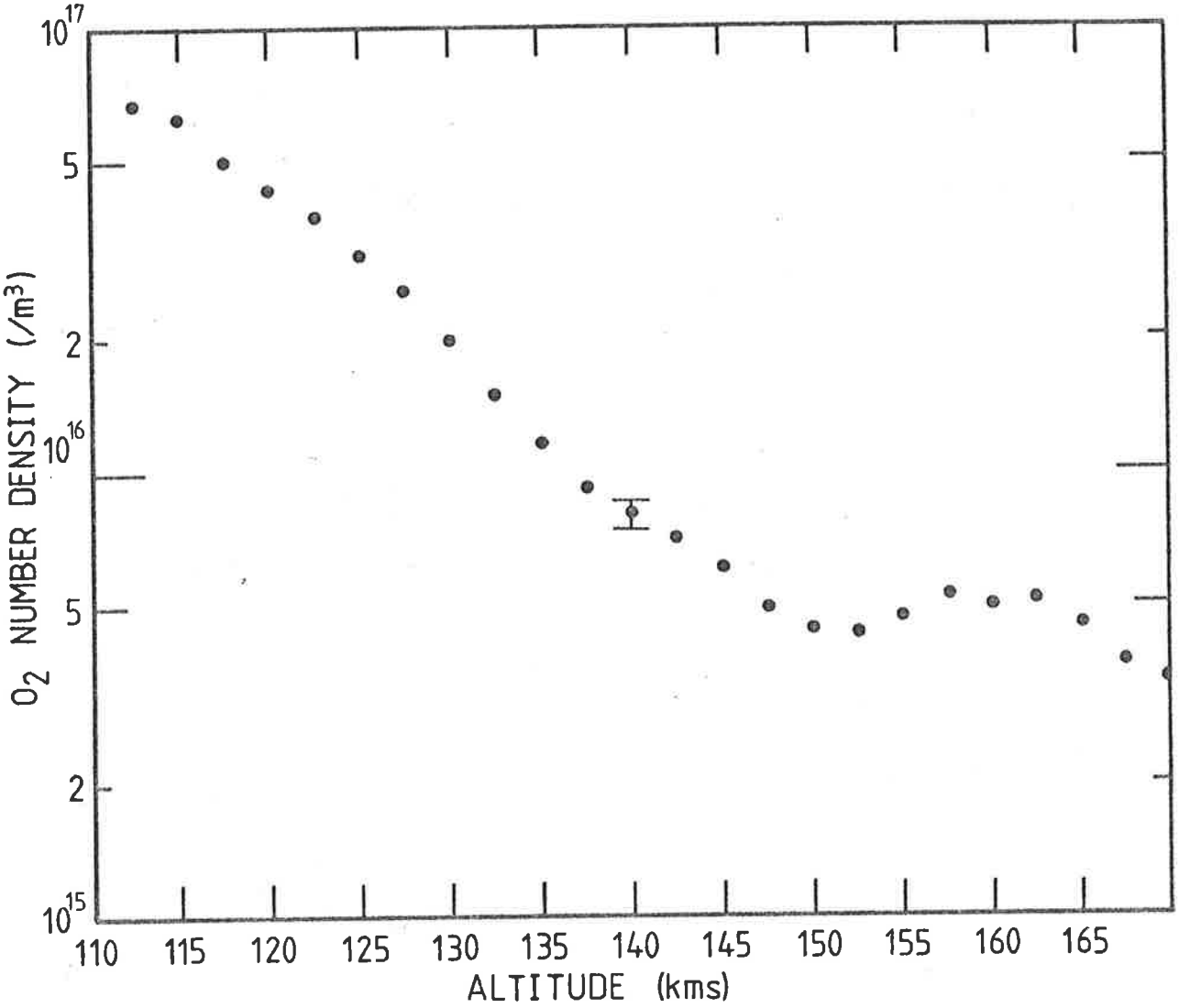

Fig. 6.13 $n(O_2)$ profile from downleg data of SX5 flown on SL 1207.

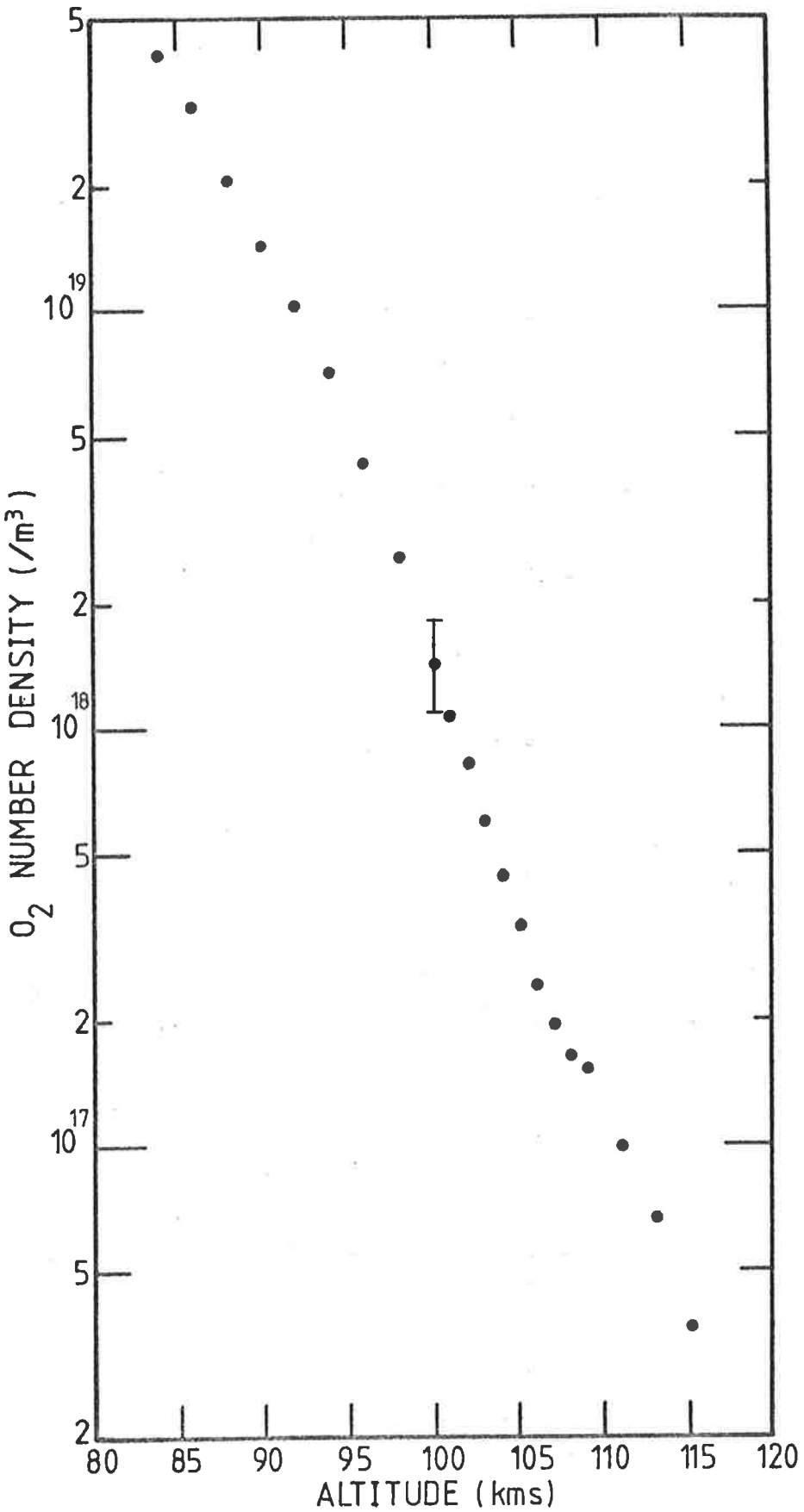

Fig. 6.14 $n(O_2)$ profile from the upleg data of LNO202 flown on Aerobee 13.123 IS

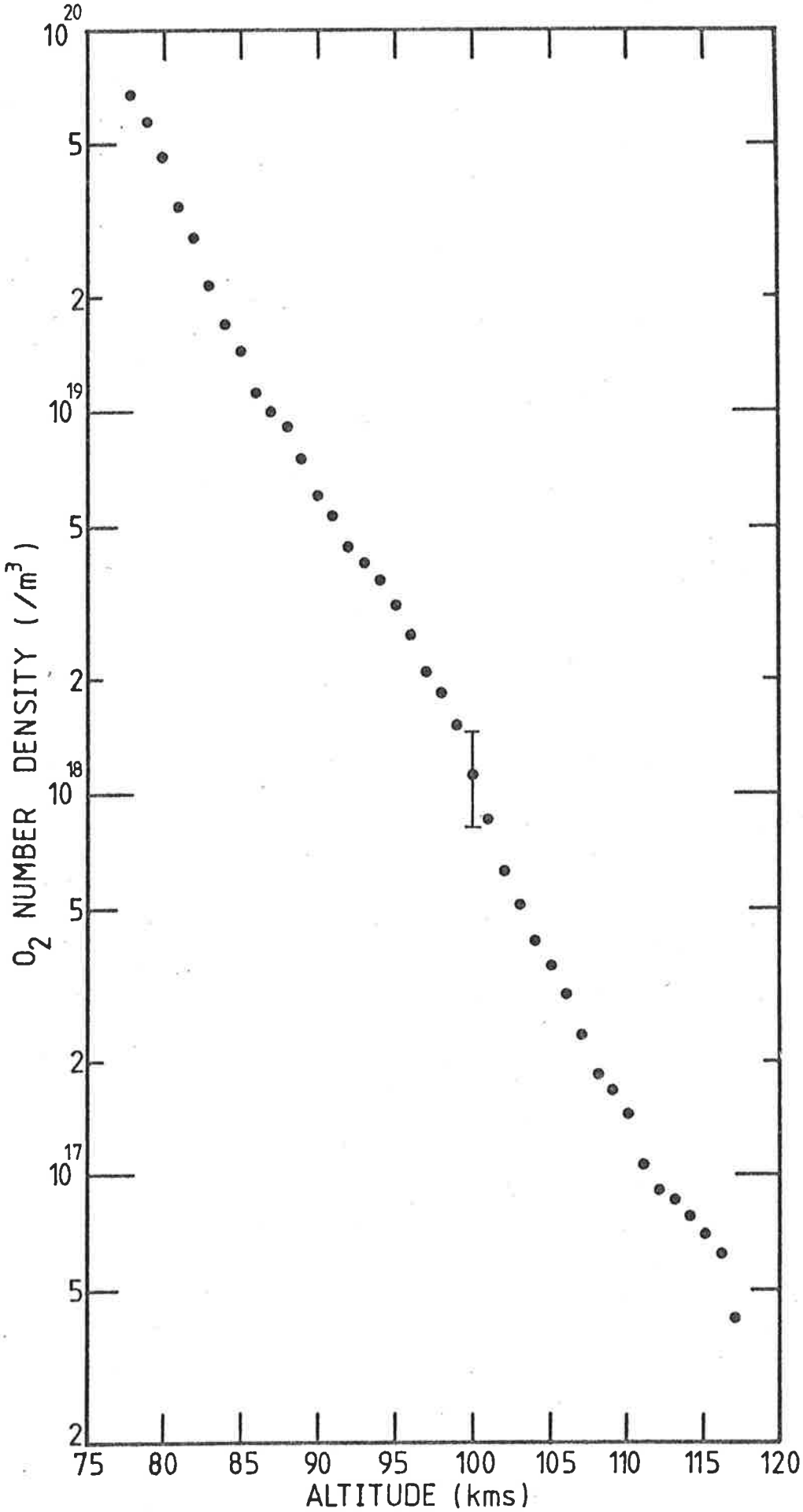

Fig 6.15 $n(O_2)$ profile from the downleg data of LNO202 flown on Aerobee 13.123 IS.

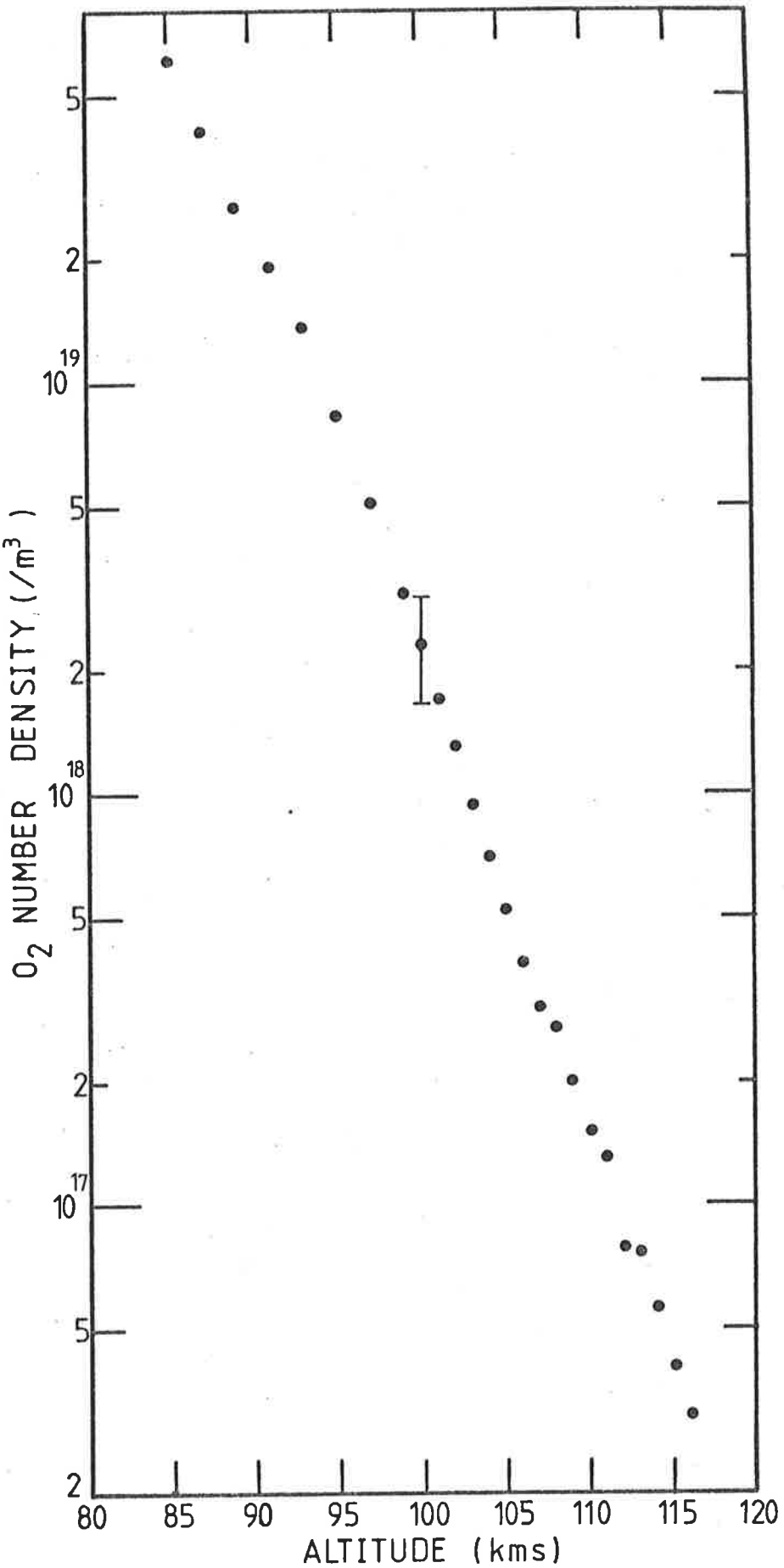

Fig. 6.16 $n(O_2)$ profile from the upleg data of MNO1 flown on Aerobee 13.123 IS.

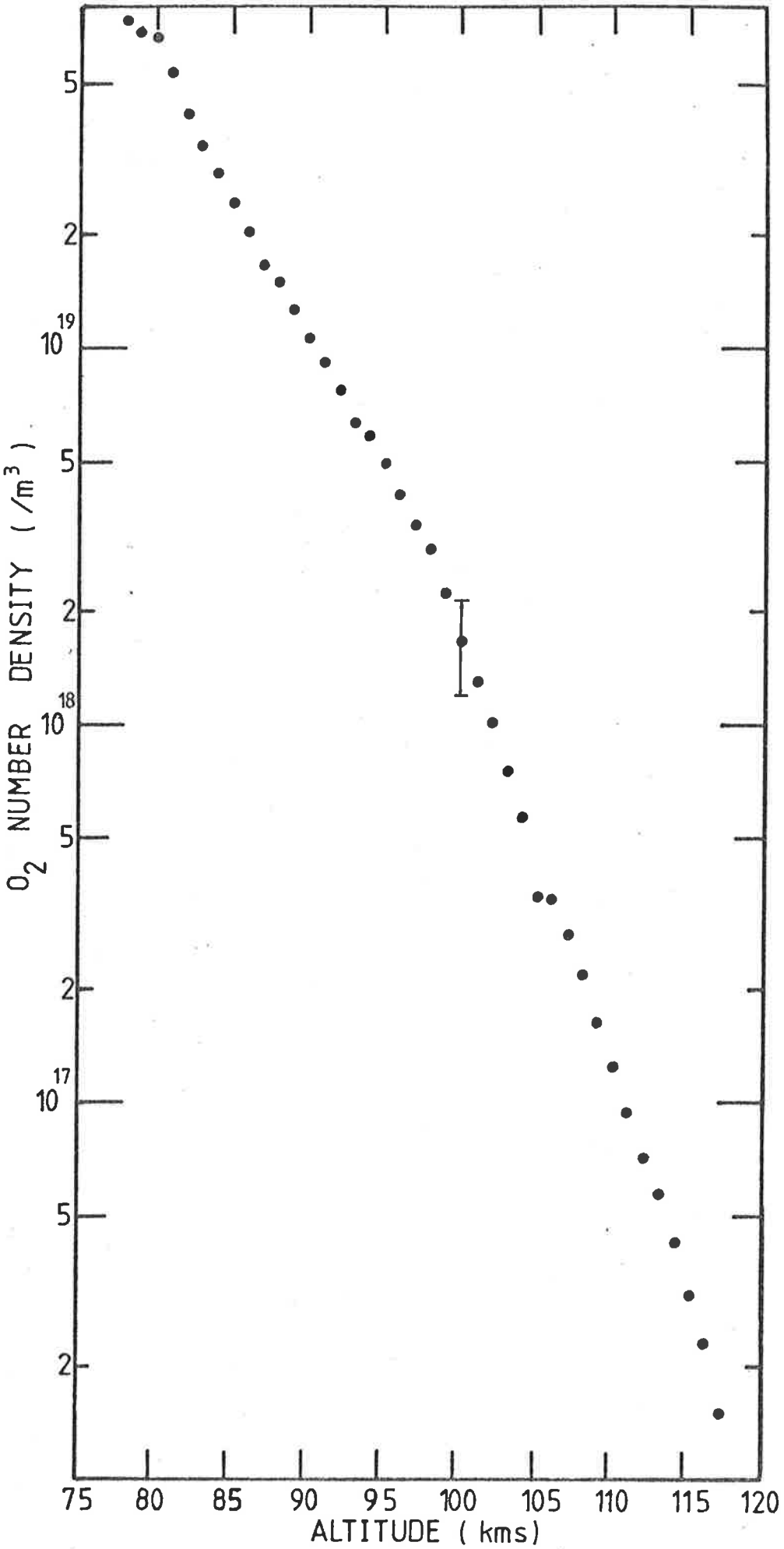

Fig. 6.17 $n(O_2)$ profile from the downleg data of MN01 flown on Aerobee 13.123 IS.

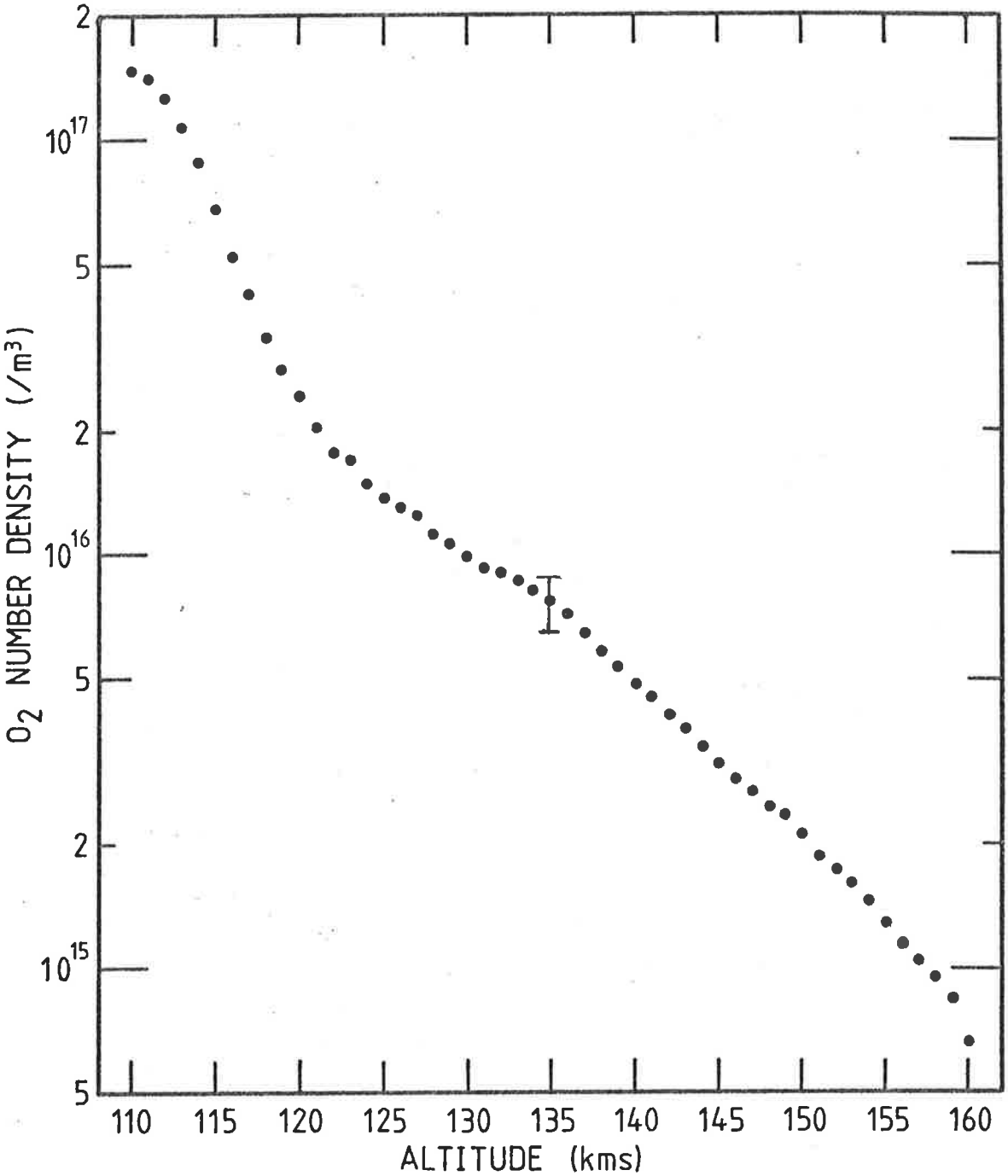

Fig. 6.18 $n(O_2)$ profile from the upleg data of QT202 flown on Aerobee 13.123 IS.

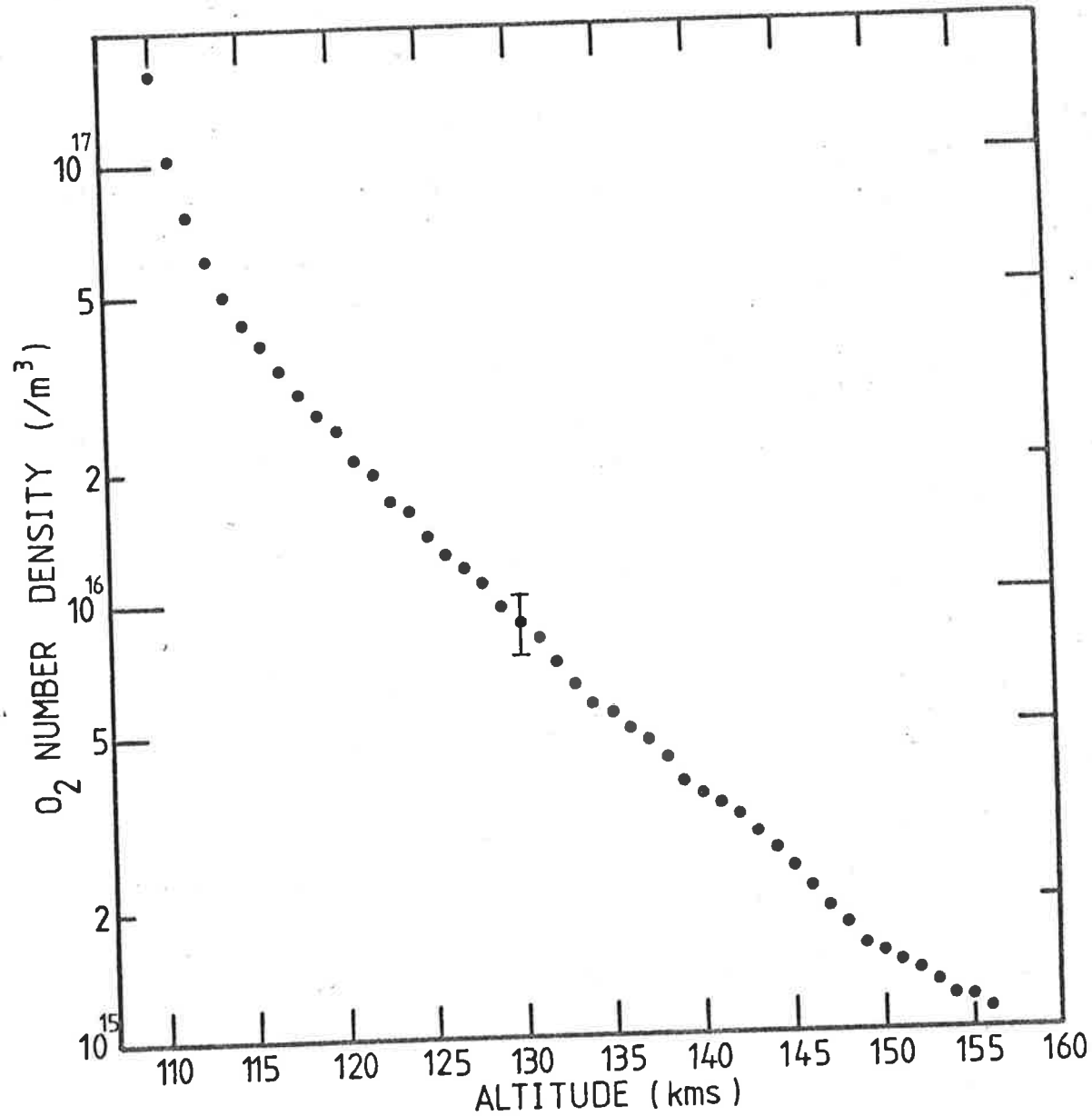

Fig. 6.19 $n(O_2)$ profile from the downleg data of QT202 flown on Aerobee 13.123 IS.

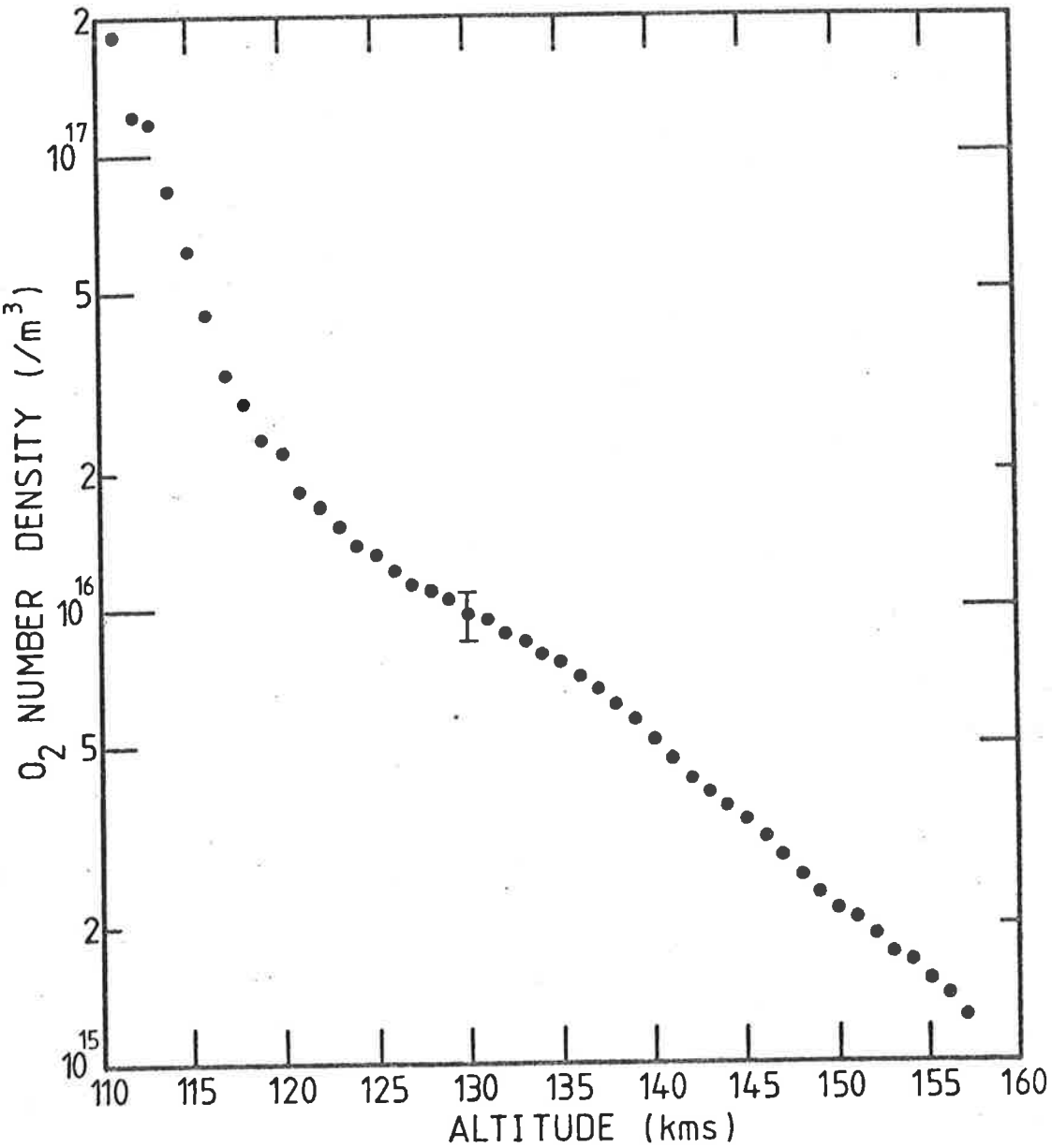

Fig. 6.20 $n(O_2)$ profile from the upleg data of QT5 flown on Aerobee 13.123 IS.

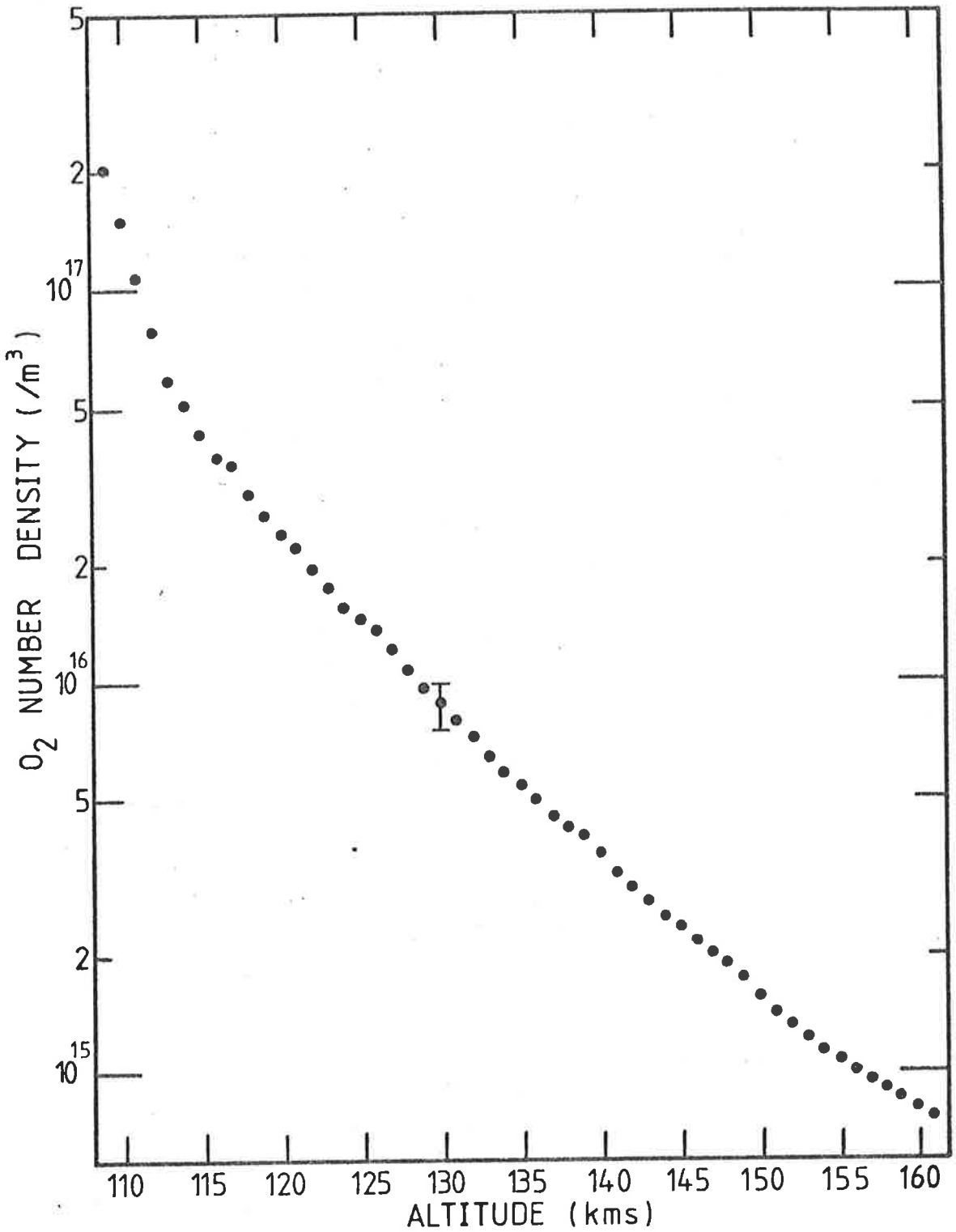

Fig.6.21 $n(O_2)$ profile from downleg data of QT5 flown on Aerobee 13.123 IS.

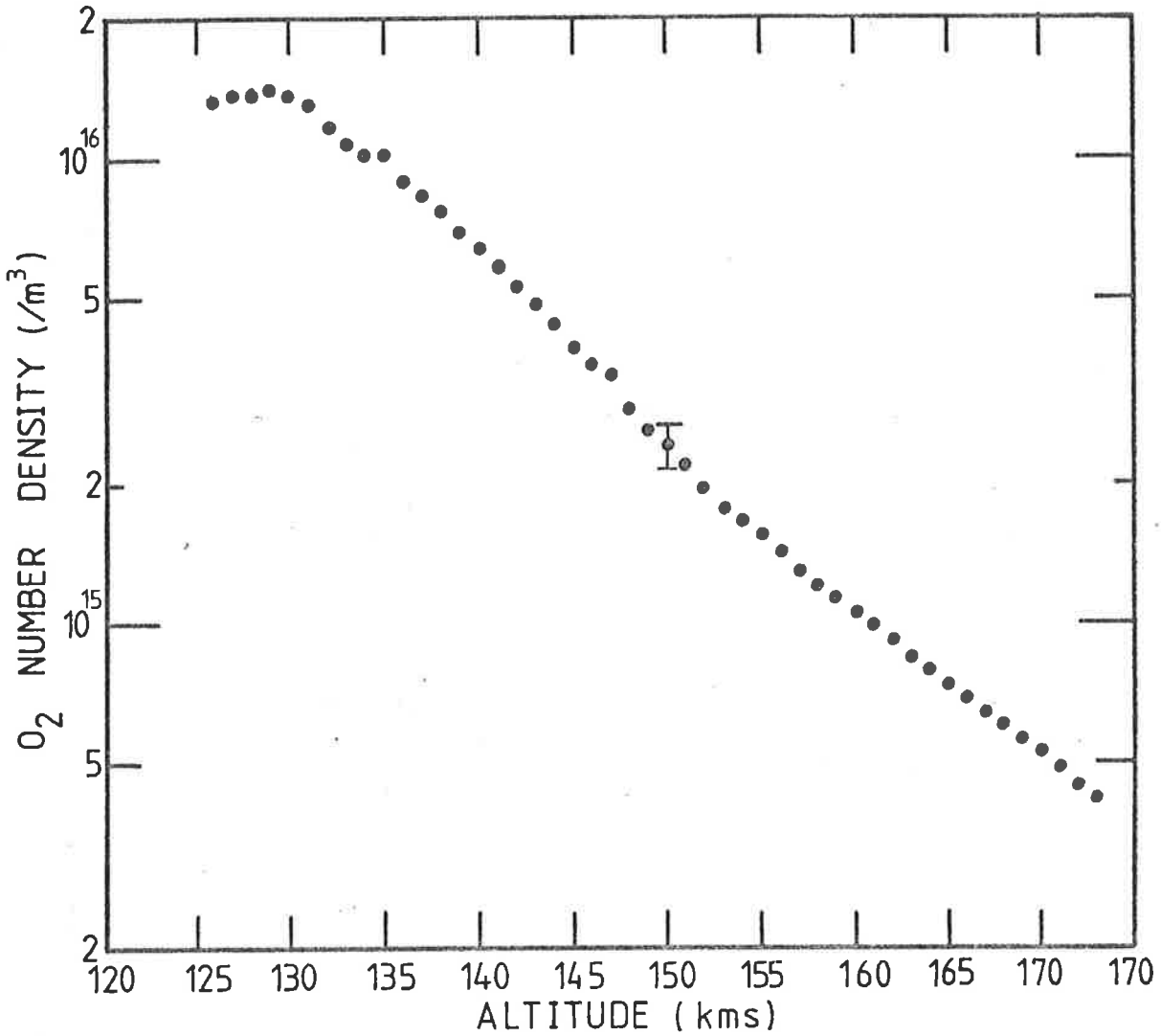

Fig. 6.22 $n(O_2)$ profile from the upleg data of SX202 flown on Aerobee 13.123 IS.

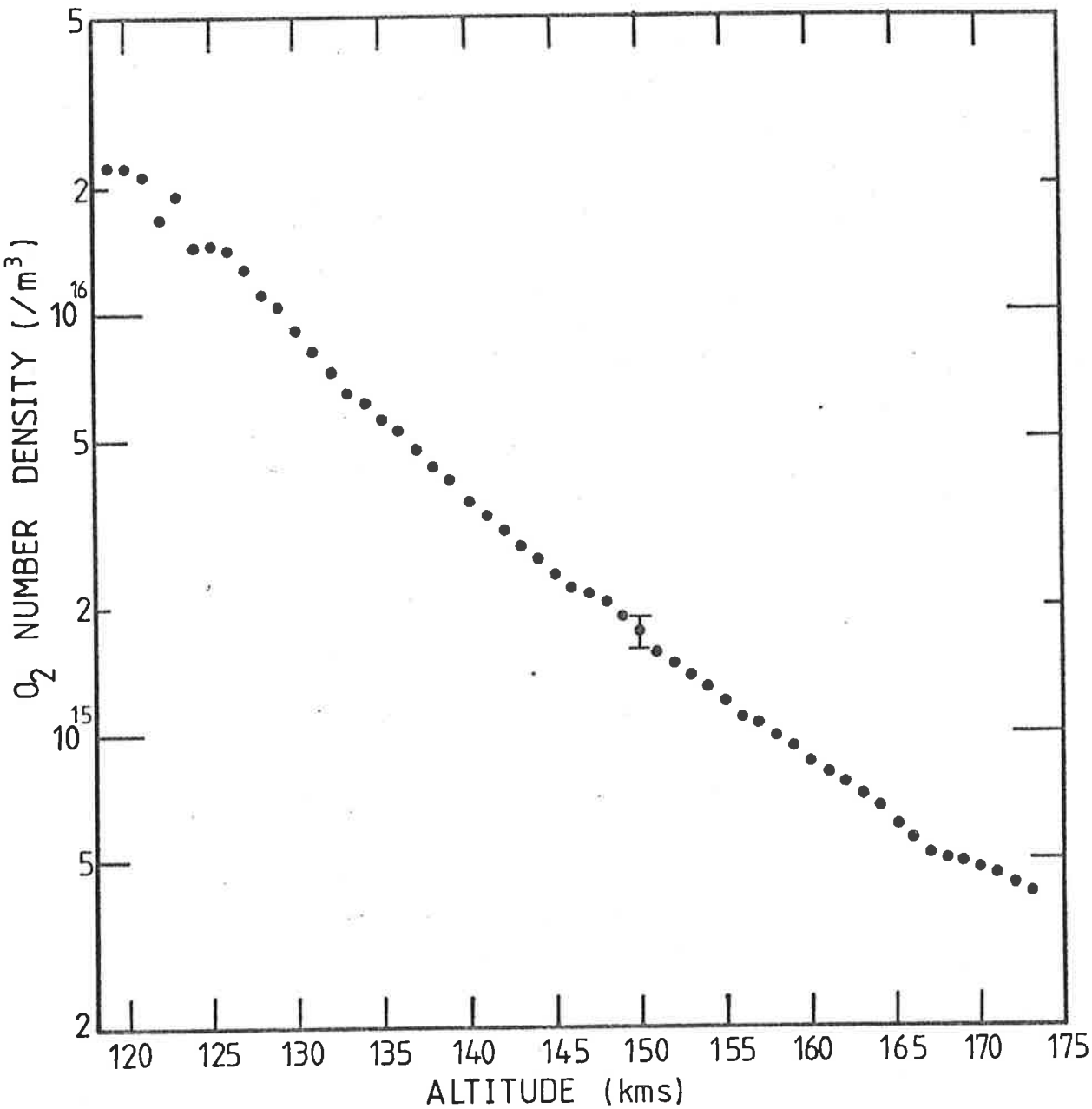

Fig 6.23 $n(O_2)$ profile from the downleg data of SX202 flown on Aerobee 13.123 IS.

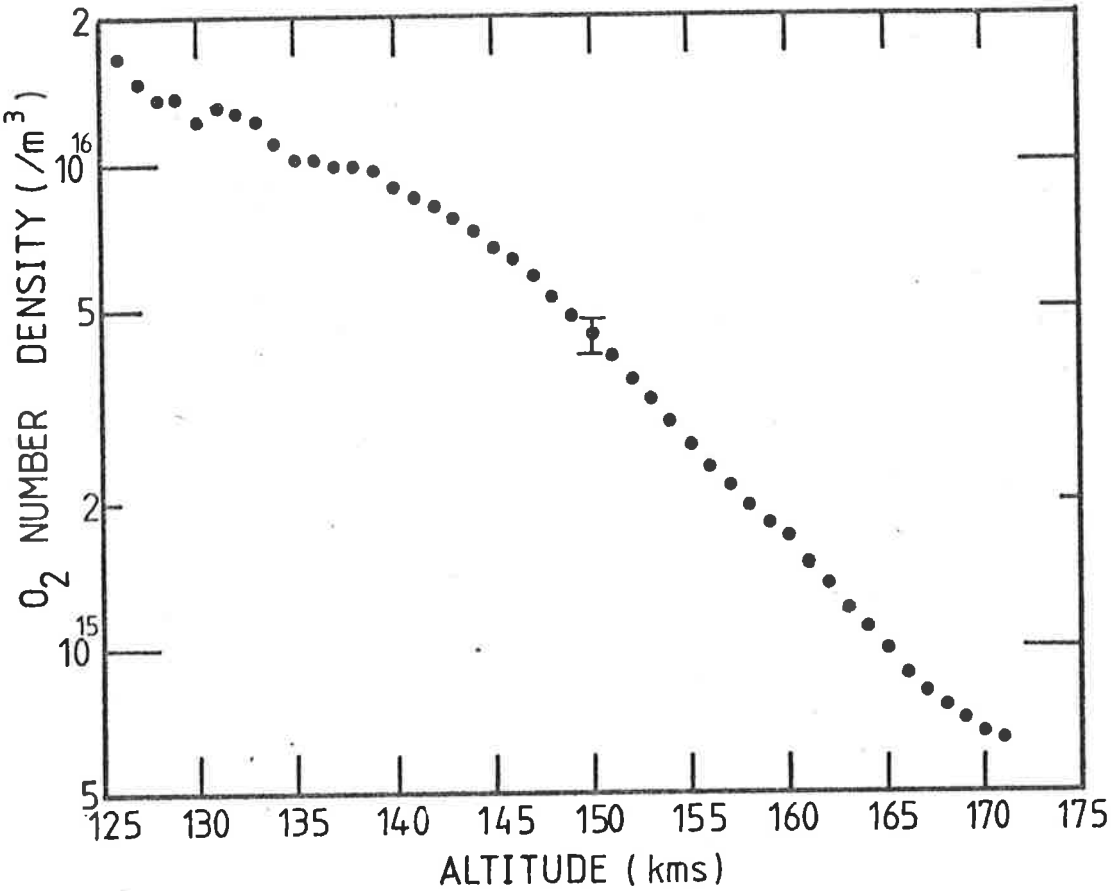

Fig. 6.24 $n(O_2)$ profile from the upleg data of SX204 flown on Aerobee 13.123 IS.

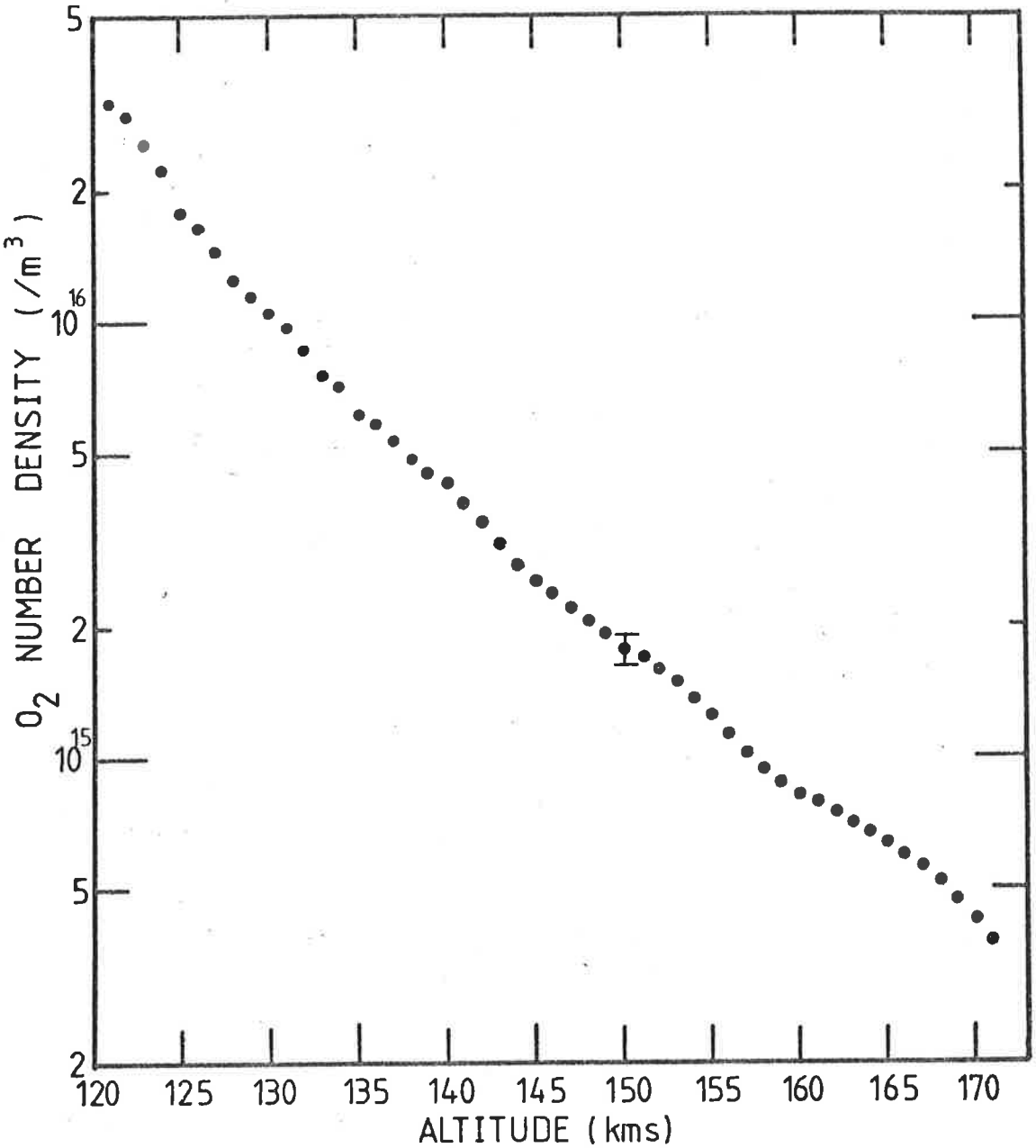

Fig. 6.25 $n(O_2)$ profile from the downleg data of SX204 flown on Aerobee 13.123 IS.

Profiles determined from the upleg data of three of the SX chambers (Figs 6.4, 6.22, 6.24) show steps at the lower altitude limit. These are not considered to be genuine. There is also an anomaly in the molecular oxygen densities derived from the downleg data of SX 5. Once again this is not considered to be genuine. Profiles derived from SX chambers are discussed again in Section 6.1.4.

Finally, where data has been collected over such an altitude range on both the upleg and downleg, as to make comparison possible, it is seen that at the lower altitude limits, upleg densities are always greater than the downleg densities. This feature is discussed further in Section 6.3.

6.1.3 Comparison of the Molecular Oxygen Density Profiles Determined by Lα and QT Chambers

In Section 4.2.6, an attempt was made to qualitatively assess the influence the non-Lα wavelengths in the passband of a Lα chamber had on the signal. This led to the calculation and use of an effective cross section for the whole chamber rather than just for Lα itself. Because of the overlap in the molecular oxygen density profiles determined by Lα and QT ion chambers, the method could be tested, and the agreement between the profiles, as illustrated in Fig 4.10, indicates its validity. It was claimed in Section 4.2.6. that if the downleg data only were used, the agreement was better. Fig 6.26 verifies this statement.

The error bar shown is that for the Lα chambers and it is derived from the error given in Table 4.7 with allowance made for the fact that two profiles have been averaged to obtain this curve. To avoid confusion, the error associated with the QT profile is not shown but it lies within that of the Lα chamber and agreement within error bars has

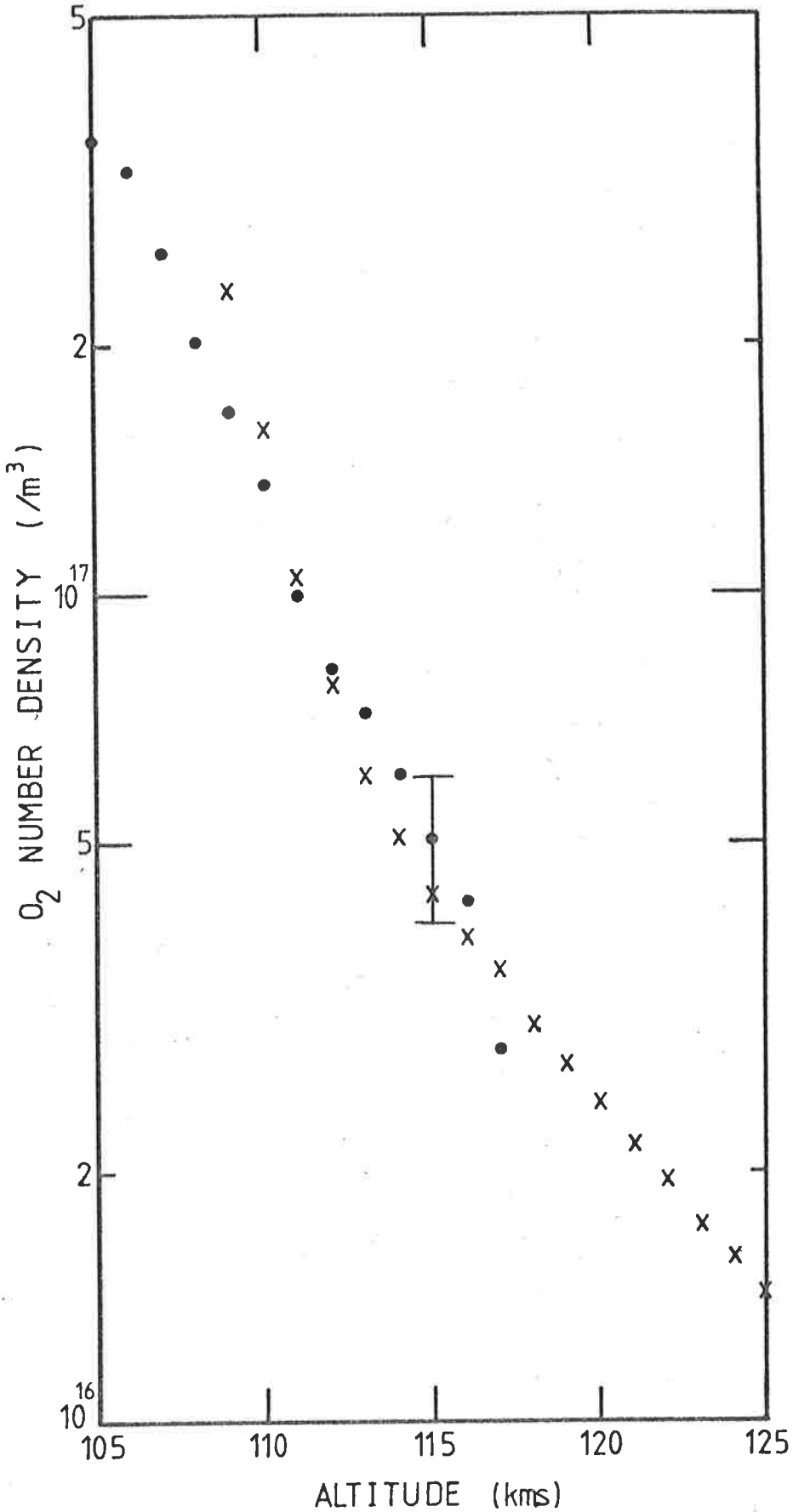

Fig. 6.26 Comparison of the corrected average $n(O_2)$ profiles derived from the downleg data of the Lα ion chambers with the average profile derived from the downleg data of the QT ion chambers on the same flight.

x - QT ion chamber
• - Lα ion chamber

been obtained.

The author, therefore, reiterates her conclusion that this technique should be adopted for the analysis of the data of Lα chambers, and feels that if the initial spectral response of the chamber is taken with higher resolution, then problems, such as the introduction of at least 15% uncertainty experienced in the present work, could be avoided.

Once the validity of the use of a total effective cross section had been accepted, the overlapping of the profiles could be further utilized in an attempt to assess the consequences of the decision made in Section 4.2.7,to ignore the effect of other absorbers.

The error in the molecular oxygen profile determined from the data of a QT chamber is not significant if the presence of the other atmospheric gases is ignored (Table 4.4). For molecular oxygen profiles derived from the data from Lα chambers it has been suggested the error could be quite large (Table 4.5). However, in the present work the size of this error must be curtailed in view of the agreement that has been obtained between Lα and QT results (Fig 6.26) by the use of $\sigma_{EFF}(\lambda_1, \lambda_2)$ (Section 4.2.6), (i.e. taking the whole of the passband into account).

In an extremely speculative proposition the residual difference at 115 kms has been used to make a very tentative comment on likely water vapour densities (Section 8.5.2) but it is felt by the author that statistical fluctuations or even the possible systematic error (excluding the effect of other absorbers) associated with each profile (Table 4.7) more likely accounts for the discrepancy.

As can be seen, the agreement is well within the combined uncertainties of the profiles, and is inconsistent with magnitude of the

errors suggested in Table 4.5. Hall (1972) suggested a total error of 7%. The present work can neither confirm or deny this estimate, but it is suggested that for the Aerobee flight this would represent the upper limit to the error.

Therefore, the decision made in 4.2.7 to ignore the effect of other absorbers is thought to introduce no more than 7% error in $n(O_2)$ derived from $L\alpha$ chambers.

6.1.4 Comparison of the $n(O_2)$ Profiles Determined by SX and QT Ion Chambers and by the Spectrometer

It can be concluded from the discussion in Section 3.10, that the upleg data from SX chambers is not reliable. This belief is strengthened by the appearance of the $n(O_2)$ profiles determined from the upleg data. The extinction curves determined by SX 3, SX 202 and SX 204 (Figs 5.8, 5.31 and 5.33) appear smooth and well defined, but the profiles all show a step. Steps in the profile of molecular oxygen densities have been observed (Groebecker, 1971), but as this phenomenon is not observed in the profiles determined by the Aerobee QT chambers, nor the upleg profile of the spectrometer on the same flight as SX 3, the step can only be considered an artifact of either the method of collecting the data, or the method of analyzing it.

Since the method of analysis was similar for the data from the QT ion chambers, the spectrometer (Section 3.3) and the downleg data of the SX ion chambers, the profiles of which do not show a similar step, it is not considered the analysis introduces the anomalies. This conclusion was tested by manipulating the values of the analysis parameters (for example, amplifier offsets, the value of the maximum signal) but the

subsequent changes in the derived $n(O_2)$ were inadequate to explain the anomaly.

It could, however, be explained by an increasing sensitivity in the ion chamber's response (see Section 3.10). This would also explain why at higher altitudes the $n(O_2)$ determined from the upleg data of SX 3, SX 204 and SX 202 appear systematically higher than that determined by QT chambers in the same payload. It does not explain why the upleg O_2 densities determined by the spectrophotometer should also be consistently greater. A continuing increase in the dark current, and therefore, in the signal, as the result of heating was considered, but heating was slight and the change in the dark current too small to be of significance.

The dichotomy has not been resolved and, as is discussed in Section 6.2.2., it is reflected in the uncertainty associated with the mean $n(O_2)$ profile derived from the experimental payload of SL 1005.

In contrast the systematic difference between the downleg O_2 densities from the ion chambers QT 1 and SX 7 flown on SL 1207, is consistent with a continuation of the decrease in sensitivity observed in SX 7 over apogee (Fig 5.20). However, once again no realistic correction can be made and the final profile (Section 6.2.1.2) must reflect the disparity in an enhanced uncertainty.

That these anomalies are the result of changes in the response of the SX chambers rather than systematic error in the assumed cross-sections (Section 4.2) is supported by the excellent agreement between the $n(O_2)$ profiles determined from the downleg data of the 2 SX and the 2 QT chambers flown on Aerobee 13.123 IS (Fig 6.29). The close agreement lends credence to the suggestion that the cross-sections for molecular

oxygen of Blake *et al* (1966) approximate quite well the lower thermosphere molecular oxygen absorption cross-sections (Section 4.2.4).

6.1.5 Broad Band Estimates of Flux Levels

The intensity of the solar flux in the passband of a broad band ion chamber can be estimated from the signal received at apogee, provided apogee is well above the absorbing layer for the radiation within the passband. Using the amplifier calibrations to convert the telemetred voltage V to a current I the total flux within the passband can be estimated by

$$n = I \cdot \frac{1}{A} \cdot \frac{1}{\varepsilon . W_{\frac{1}{2}}} \cdot \frac{1}{1.6 \times 10^{-19}} \qquad (6.1)$$

where A is the area of ion chamber window in cm^2

ε is the maximum sensitivity of the chamber, and

$W_{\frac{1}{2}}$ is the full width half maximum of the spectral response

n is in the units of photons/cm^2/sec/Å

Alternatively the flux may be expressed in the units ergs/cm^2/sec/Å. Calling this quantity ϕ

$$\phi = \frac{n.\ h.\ C}{\lambda} \qquad (6.2)$$

where n is the flux obtained from (6.1)

h is Planck's constant and

$= 6.62517 \times 10^{-27}$ erg/sec

C is the velocity of light (i.e. $C = 3.00 \times 10^{10}$ cms/sec), and

λ is 1.6×10^{-5} cms (i.e. 1600Å) for the QT ion chamber,

1.45×10^{-5} cms (i.e. 1450Å) for the SX ion chambers.

The Lyman-alpha chambers were not treated as broad band ion chambers. Section 4.2.6 described how an estimate of the Lα radiation's contribution to the total signal was made and once this was known then n was given by

$$n = I' \cdot \frac{1}{A} \cdot \frac{1}{1.6 \times 10^{-19}} \qquad (6.3)$$

where I' is the appropriate fraction of the max. signal. Equation (6.2) was still valid used with $\lambda = 1.216 \times 10^{-5}$ cms.

The flux levels obtained by the broad band ion chambers in the molecular oxygen experiment are given in Table 6.1.

TABLE 6.1 FLUX LEVELS

FLIGHT (Date of Launch)	$F_{10.7}$ Flux ($W.10^{-22}.m^{-2}Hz^{-1}$)	WAVELENGTH Å	FLUX (ergs/cm²/sec/Å
SL 1005 (11.12.72)	105	1425 - 1490 1560 - 1650	4.37×10^{-3} 1.87×10^{-2}
SL 1207 (23.4.74)	74	1425 - 1490 1560 - 1650	3.59×10^{-3} 6.84×10^{-3} *
AEROBEE (22.2.77)	76	Lα 1425 - 1490 1560 - 1650	4.41 6.1×10^{-3} 2.5×10^{-2}

* See comment in text.

The figures quoted in Table 6.1 must be treated with some caution. It has already been suggested that some of the SX chambers were undergoing changing sensitivities. This cast doubt on the validity of using laboratory measured efficiencies which, in themselves, for SL 1005 and SL 1207, had had to be estimated. (Section 3.6.2.4) In addition, both SL 1005 and SL 1207 spent several weeks on the launcher during which time the sensitivities of the chambers may have altered from their calibration values. It is considered that the apparently low value for the flux in the range λλ 1560Å - 1650Å for the SL 1207 flight reflects a deterioration in the chamber sensitivity rather than a genuine decrease in solar radiation.

The uncertainties associated with the flux estimates came from the uncertainty in the absolute calibration, the possible but unknown deterioration in sensitivity while the rocket is on the launcher, the change, if any, in sensitivity during the flight, and the possible contribution of solar lines to the broad band continuum. No attempt to give a quantitative assessment of this is made.

The values in Table 6.1 suggest that the $F_{10.7}$ flux is not a good indicator of the flux in the EUV wavelengths observed. This is consistent with the results of Hinteregger (1976) who showed correlation between $F_{10.7}$ and fluxes in the range λλ 1553 - 1791Å was poor.

Heroux and Higgins (1977) reported on a measurement of solar flux made on the 23.4.74. Their measurement at λλ 1400Å - 1500Å of $\approx 3.32 \times 10^{-3}$ ergs.sec/cm^2/Å is in quite good agreement with the estimation made from the data of the SX chambers flown on SL 1207. The agreement may be fortuitous since the rapidly changing sensitivities of

these chambers over apogee made approximation inevitable. However, the agreement between the SX values taken on the 11.12.72 and the measurements of Rottman, 2 days later, (as quoted in Delaboudiniere *et al* 1977), is reasonable as well, if Rottman's fluxes over the passband of the ion chamber are averaged.

The flux values estimated from the QT ion chamber data do not agree as well with values published in the literature. The value given by Heroux and Higgins (1977) for the 23.4.74 is some 74% larger, but as already suggested the apparently low value observed in this work may be due to equipment deterioration. The value for SL 1005 is over 20% larger than Rottman's average value.

The value of 4.41 ergs/cm^2/sec observed on Aerobee for Lα is within the range of values quoted by Heroux and Higgins (1977), though lower than most of them. It is also within the range of values given in the paper by Delaboudiniere *et al* (1977).

The flux values measured on the Aerobee for the wavelength ranges $\lambda\lambda$ 1425Å - 1490Å and $\lambda\lambda$1560Å-1650Å are high compared with the measurements of Delaboudiniere *et al* (1977). They also disagree with the comments made by Hinteregger (1979) about solar cycle 21. Aerobee 13.123 IS was flown at the start of solar cycle 21 and, in comparison to the flux values determined by SL 1005 and SL 1207, both launched during cycle 20, the flux values from Aerobee are much higher relative to the $F_{10.7}$ flux. Hinteregger (1979) claimed that while relative flux values for $\lambda < 1027$Å had greatly increased, relative values for $\lambda > 1250$Å showed little change.

However, the author has reasonable confidence in the flux values given. The SX chambers (1425Å to 1490Å) survived impact and were re-calibrated after launch. They were found to be within 10% of their original calibrations. In addition, during flight, they showed none of

the excessive changes in sensitivity displayed by the SX chambers on the earlier flights. The QT chambers also appeared to be stable.

It is suggested by the author that these results point to the need for continued measurements of the solar flux and the need for the development of a reliable solar flux index.

6.2 THE MEAN PROFILES

This section gives the rationale to the selection of profiles that make up the mean average profile for each rocket. The uncertainties associated with these profiles are discussed and they are then compared with previous measurements at Woomera. In the case of Aerobee,comparison is also made with measurements made by other instrumentation in the same payload.

6.2.1 Selection of Profiles for the Mean Profile

6.2.1.1 SL 1005

Figures 6.1 to 6.7 give the profiles obtained by the experimental payload flown on SL 1005. The mean profile given in 6.27 is the unweighted average of data in Figures 6.1, 6.2, 6.3, 6.5 and 6.7 plus the data in Fig 6.4 from $z = 133$ km upwards and Fig 6.5 from 118 km upwards.

The discussion in Section 6.1.4 has already indicated that the step in the profile of the SX 3 data is not considered to be genuine, and, as will be discussed in Section 6.3, nor is the enhancement in the upleg profile from the spectrometer below 118 kms. These have, therefore, been excluded.

Initially a weighted mean was calculated. The weighting factor used was $1/\sigma^2$ where σ is the uncertainty given in Table 4.7 for each type of detector. The appearance of this profile, together with the presence of anomalies in the SX derived profiles, suggested that

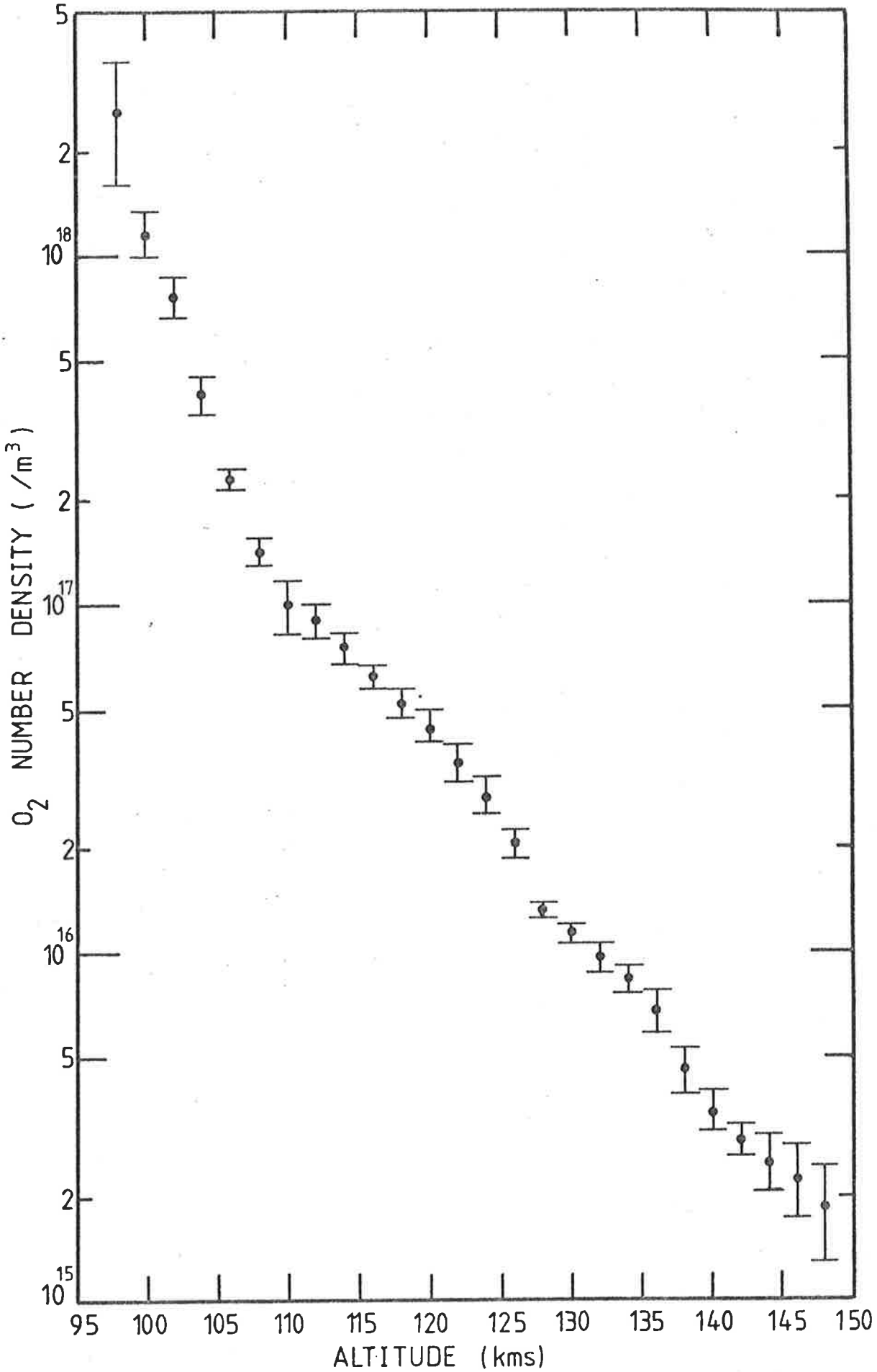

Fig. 6.27 Mean $n(O_2)$ profile from SL 1005

weighting the mean profile towards the SX results could not be justified. Therefore with no other realistic criteria on which to base weighting, (The weighting used in Aerobee - Section 6.2.1.3 - is not used because it once again biases the average towards the SX values) and with the source of the systematic error causing the difference between QT and SX derived profiles not known, an unweighted average was adopted.

6.2.1.2 SL 1207

Figures 6.8 to 6.13 give the profiles obtained by the experimental payload on SL 1207.

Once again the initially high densities from the SX chamber are not considered to be genuine and have been left out. The signal levels of SX 5 were low and the telemetred signal was noisy. It was difficult to discern the extinction curve and the appearance of the $n(O_2)$ profiles (Figures 6.12, 6.13) reflects this difficulty. The profiles are not thought to truly reflect atmospheric densities, and are therefore, left out of the calculations of the mean.

For similar reasons to those given in 6.2.1.1. the final profile is an unweighted average. This is shown in Figure 6.28.

6.2.1.3 Aerobee 13.123 IS

Figures 6.14 to 6.25 give the profiles obtained by the experimental payload flown on Aerobee 13.123 IS. The mean profile is given in Figure 6.29, and is the weighted average of the molecular oxygen profiles obtained from the downleg data of the ion chambers.

The weighting is combined of two parts. The first weights the results according to the uncertainty that must be associated with each type of chamber (Table 4.7). The second part relates to the uncertainty that arises from the telemetry uncertainty. It has already been stated in

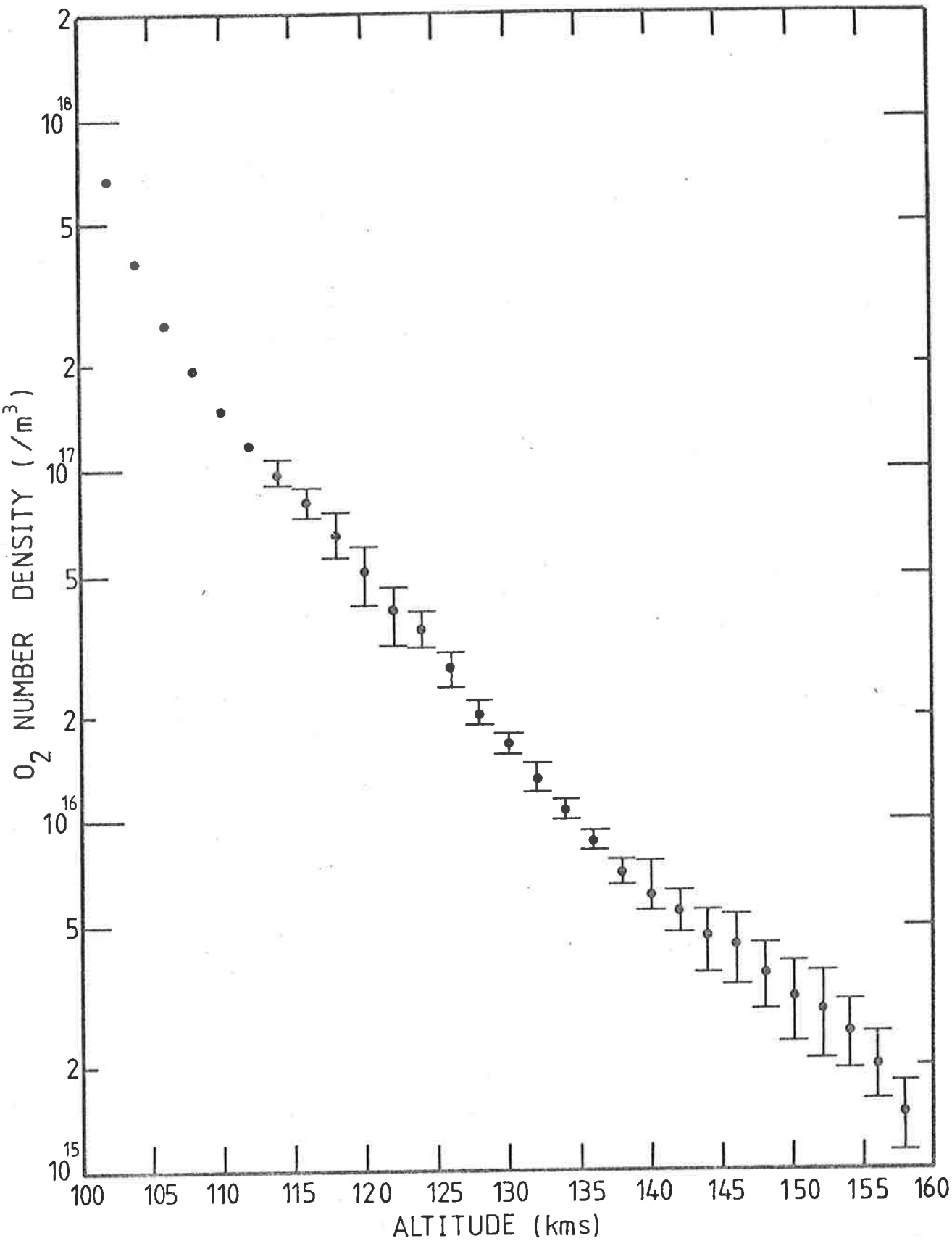

Fig. 6.28 Mean $n(O_2)$ profile for SL 1207.

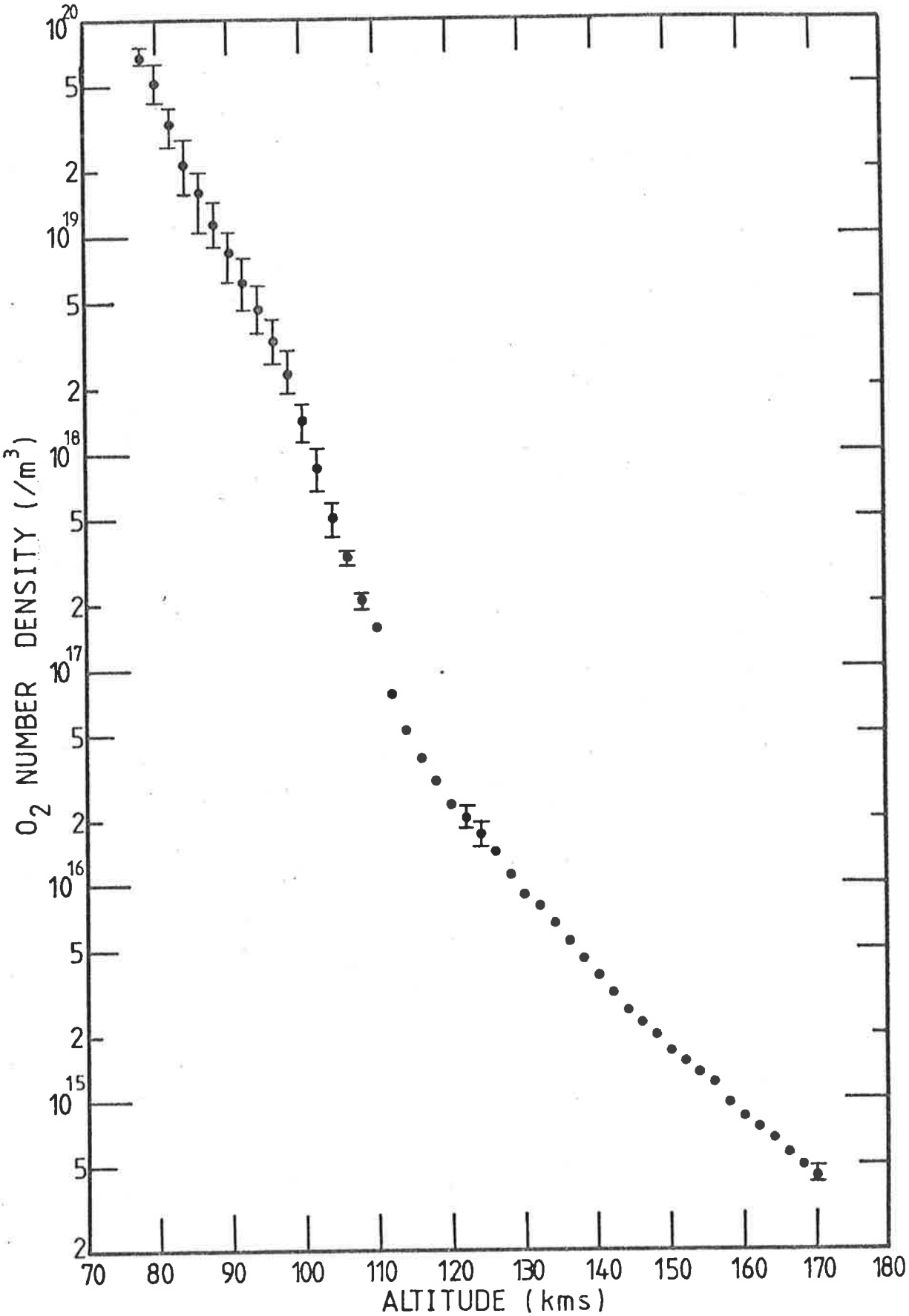

Fig. 6.29 Mean $n(O_2)$ profile from Aerobee 13.123 IS. Where error bars are not shown the error is $\leqslant$ 5%

4.4.2 that telemetry uncertainty cannot be directly related to the uncertainty in $n(O_2)$. However, where ΔS, the change in signal due to the change in the intensity of the flux reaching the detector, is large compared with the telemetry uncertainty, the extinction curve is also well defined. Intuitively it appears reasonable to suggest that the uncertainty in the derived $n(O_2)$ will, therefore, be less.

Accordingly the weighting function used was $\Delta S/\sigma^2$. There is a further advantage to using ΔS. Where a mean of several curves can be taken it discriminates against $n(O_2)$ derived from the lower altitude limit of an extinction curve. At this limit the uncertainty in S, the detector signal, can also be large because of the uncertainty in the amplifier offsets.

ΔS is still, however, an unsuitable weighting function for SL 1005 and SL 1207. Reference to fig. 2.1 most clearly illustrates this. Towards the upper limit of the QT curve, ΔS for this chamber will be smaller than that for the SX chamber, and therefore, once again the mean will be biased toward the results from the SX chambers.

The profiles from the upleg were not included. It will be argued in Section 6.3 that there was a systematic difference between the upleg and downleg, and therefore, averaging of all profiles is not valid. An average upleg profile is not regarded as a good estimate of the lower thermospheric oxygen densities at the time of the flight because of the possibility, as discussed in Section 6.1.4, of an instrument induced enhancement of the $n(O_2)$ derived from SX chambers.

6.2.2 Uncertainties Associated with Mean Profiles

It was stated in Section 4.4.2 that the only true estimate of the uncertainty of the number densities obtained from hand drawn curves would come from the statistical variation in the results of several chambers. The error bars drawn on Figs 6.27, 6.28 and 6.29 have been derived from such variation and represent the uncertainity in the means.

Error bars are not shown for $n(O_2)$ taken over the altitude range 100 kms to 113 kms by the experiment on SL 1207 (Fig 6.28). The given densities over this range are derived from the results of only one chamber, and therefore, the best estimate of the uncertainty is the 23% listed in Table 4.7. Error bars are also not shown over most of the altitude range 110 kms to 168 kms of the mean Aerobee profile, (Fig 6.29) but here, this is a reflection of the quality of the results obtained - see note in figure heading.

Apart from the given uncertainty each measurement is also associated with a systematic error. This will vary according to the source of the profiles averaged to obtain the mean. For example, at 100 kms on SL 1005, the profile is the average of $n(O_2)$ determined by QT chambers, and therefore, the systematic error is - 16% (Table 4.7), whereas at 165 kms on Aerobee, the profile is determined by SX chambers and the systematic error is - 8% (Table 4.7).

As an approximation the systematic errors are :

(1) for SL 1005 it varies from - 16% at 98 kms to - 10% at 148 kms,

(2) for SL 1207 it varies from - 16% at 100 kms to - 8% at 158 kms,

(3) for Aerobee 13.123 IS it varies from + 5% at 78 kms, peaks at - 12% over the altitude range 126 kms to 156 kms, then reduces to - 8% by 170 kms.

In the present work the accuracy of the height determination for SL 1005 and Aerobee 13.123 IS was ± 20 metres, while for SL 1207 this uncertainty was increased to ± 111 metres. No attempt has been made to quantitatively assess the uncertainty this implies in $n(O_2)$.

6.2.3 Comparisons of Densities obtained with Ion Chambers against those obtained with a Mass Spectrometer and a UV Spectrophotometer

Fig 6.30 shows the mean profile given in Fig 6.29 plus the $n(O_2)$ profiles obtained by the mass spectrometer (G. Bibbo - private communication) and the Ebert-Fastie spectrometer (J. Lean, 1980) which were also included in the same payload (Fig 5.21). For clarity error bars are not shown on Fig 6.30. All the profiles were determined on the downleg.

Agreement, within combined uncertainties, is obtained between the results from the ion chambers and the Ebert Fastie Spectrometer over the altitude range 123 kms to 157 kms. The agreement once again reinforced the belief that the cross-sections of Blake *et al* (1966) are a reasonable approximation to the atmospheric temperature affected cross-sections. This conclusion has been drawn because the results of Lean (1980) have been derived by using temperature dependent absorption cross-sections (Blake *et al* 1980) to analyse the extinction curve of each wavelength considered (1744Å, 1729Å, 1714Å and 1657Å).

At altitudes greater than 157 kms, the results from the spectrometer begin to drop away. The author considers the ion chamber results to be more reliable since they are derived from a more favourable part of their extinction curve, i.e. the change in signal due to the increase in flux is still large compared with the change possible because of the telemetry uncertainty. The extinction curves of the lines observed by the spectrometer have nearly reached their maximum and are changing very little.

The author does not know the cause of the discrepancies between the two profiles at the lower altitudes, but once again has confidence in the ion chamber results, and would point out that they are more consistent with model densities such as those proposed by Jacchia (1977).

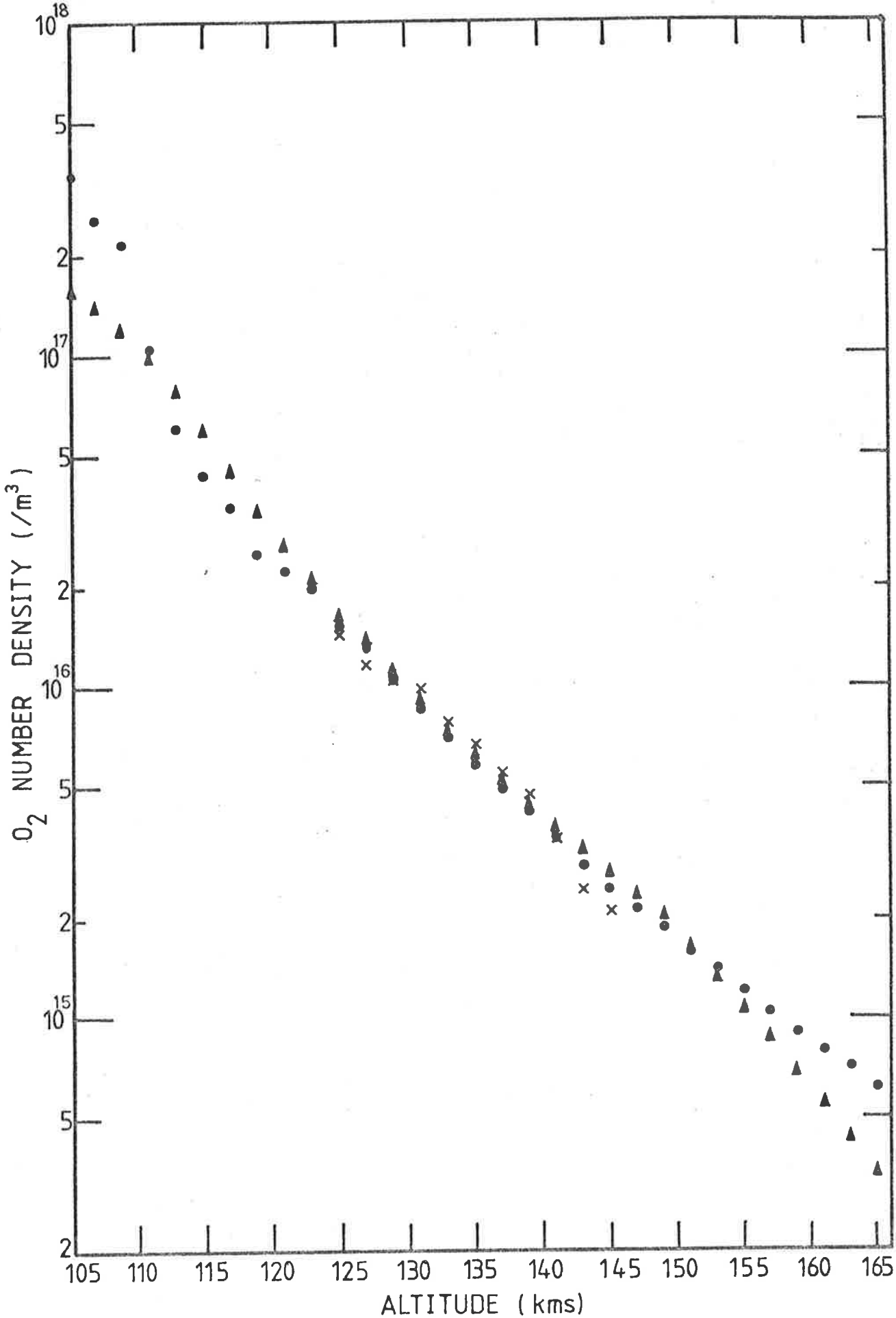

Fig. 6.30 Comparison of $n(O_2)$ profiles measured on Aerobee 13.123 IS.

● - Present results
x - Mass Spectrometer (G.Bibbo - private communication)
▲ - FUV Photometer (Lean, 1980)

A comparison of $n(O_2)$ profiles derived from UV and mass spectroscopic techniques was made in Section 2.4.1. The conclusion was reached that at least 15% to 20% of the atomic oxygen was recombining to form O_2 within the ion source of uncooled mass spectrometers.

The present work supports the concept that recombination occurred within the M.S. The agreement between the UV and mass spectroscopic techniques shown in Fig 6.30 was achieved by adopting a recombination level of 46%. (G. Bibbo, private communication). The uncertainty associated with the mass spectrometer results was large and the figure of 46% may be grossly over estimated. It is certainty far in excess of the 10% determined by Ackerman *et al* (1974) when they flew a mass spectrometer and an UV spectrometer in the same payload.

Nevertheless, large recombination factors have been reported in the literature. For example, Gross *et al* (1968) found that they required a recombination of 40% to reconcile their data. Therefore the value obtained is not considered unrealistic.

6.2.4 Comparison of $n(O_2)$ Profiles with Earlier Woomera Measurements

Determinations of atmospheric molecular oxygen densities have been carried out at Woomera since the early 1960's. (Carver *et al* 1964; 1966; 1969; Wildman *et al* 1969; Ilyas, 1976). It has been suggested the measured $n(O_2)$ show variation with the magnetic field or time of day (Carver *et al* 1978a). However, in this section, no attempt is made to isolate and identify such trends. The presentation is graphical and it is intended merely to show the range of profiles that have been measured at Woomera, and the position, with respect to this range, of the present results.

Fig 6.31 compares the $n(O_2)$ profiles derived from the $L\alpha$ chambers flown on Aerobee 13.123 IS with the $n(O_2)$ profiles obtained with similar instrumentation in previous years (Carver *et al* 1964; Carver *et al* 1969; Ilyas, 1976). With the exception of the Aerobee results, the numbers are taken from Carver *et al* (1977b) because Carver *et al* have re-analyzed their earlier measurements with the new temperature affected cross-sections for $L\alpha$ that were also adopted in the present work. The comparison is restricted to altitudes less than 90 kms in order to avoid the question of the significance of the other wavelengths. With the exception of the profile determined by the experimental payload carried on C 4018 (Ilyas, 1976), the present results are much lower than the other profiles. Further comment on these profiles is made in Section 6.3.3.

Fig 6.32 compares the $n(O_2)$ derived from the QT chambers flown during the present work with $n(O_2)$ profiles derived from the QT chambers flown by Ilyas (1976). The latter were flown on the small spin stabilized sounding rockets described in Section 8.4.1. Comparison is restricted to the results from the same type of chamber to avoid the possibility of the profiles reflecting differences in instrumentation rather than differences in atmospheric molecular oxygen densities. Because Ilyas (1976) used a standard spectral response curve to calculate the chamber's effective cross-section the author considers these profiles may contain systematic errors (see discussion in 4.2.5). No allowance can be made for them, however, since the required information, the spectral response curves of the chambers used by Ilyas (1976) is not available. Despite this the probable size of the error involved means the conclusions which may be drawn from Fig 6.32 are still valid.

This figure shows that with the possible exception of the molecular oxygen densities measured by the chambers flown on SL 1207 the

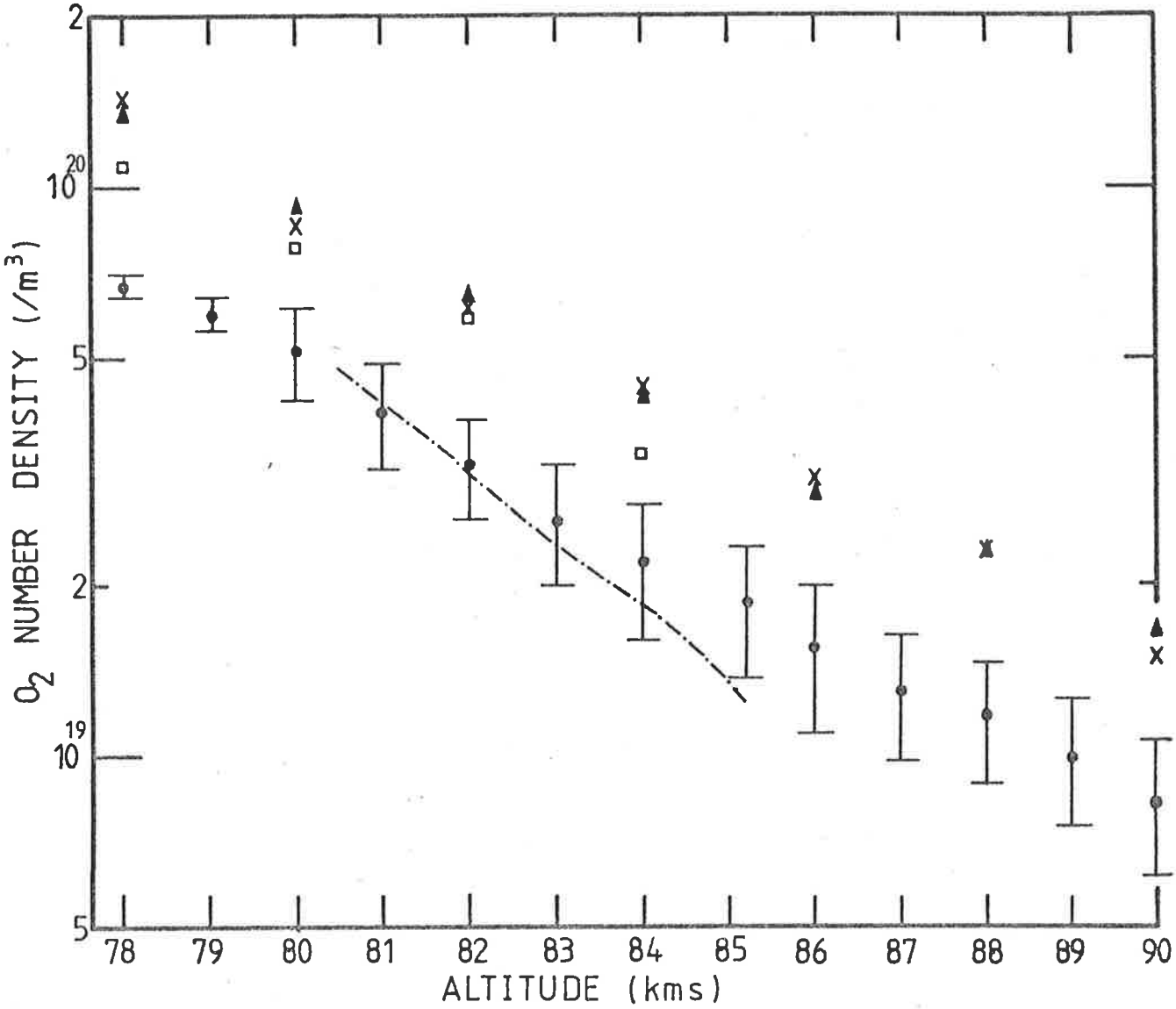

Fig. 6.31 Comparison of low altitude $n(O_2)$ profiles taken above Woomera. Figures in brackets give the k_p 6.7 hours before launch.

- ● - present results (3^-)
- —·— - C4018 29/4/75 (1^-)
- x - C4009. 2/10/74 (3^+)
- ▲ - rocket fired 11/11/66 (2)
- □ - rocket fired 6/12/63 (0)

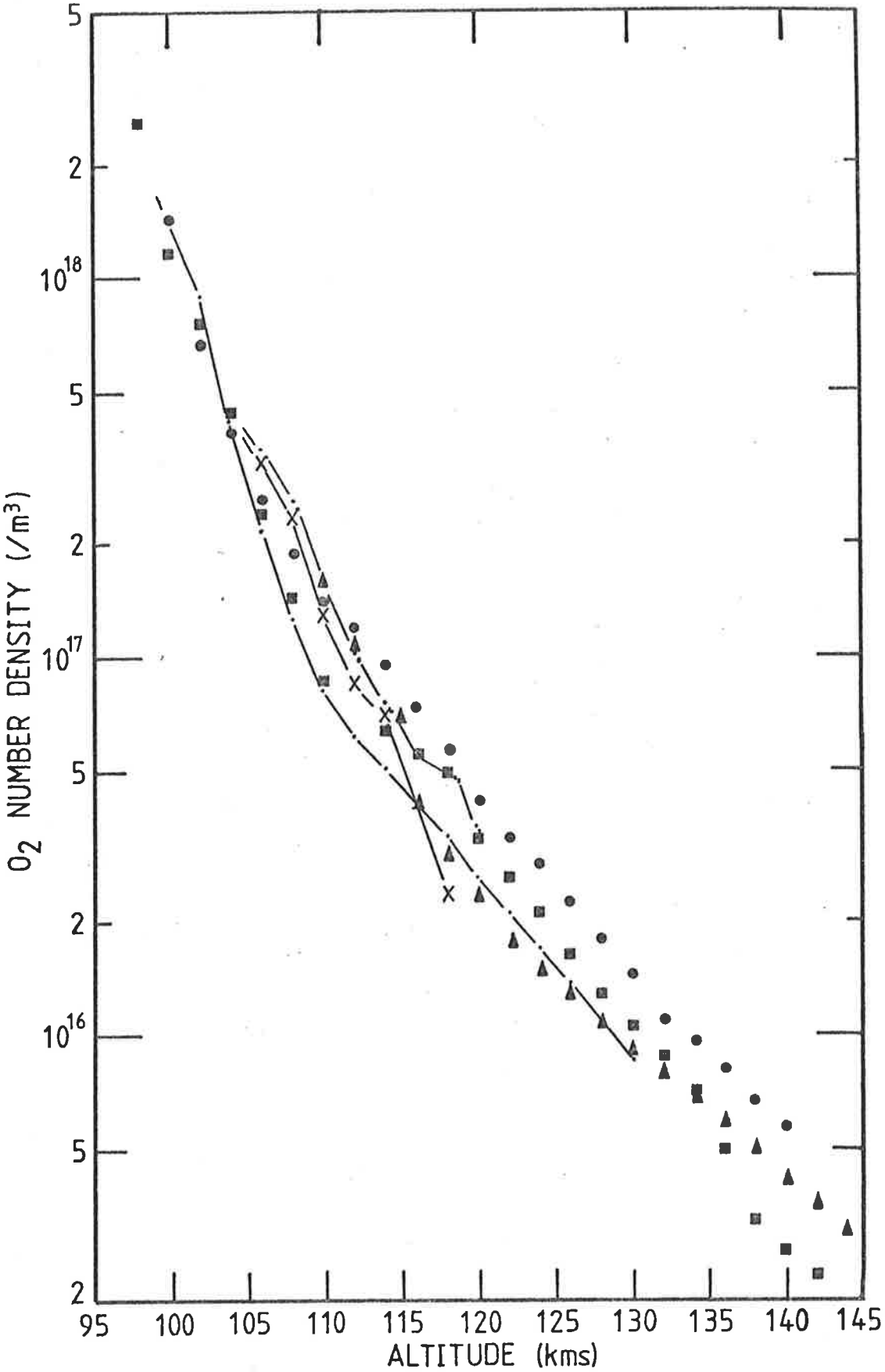

Fig. 6.32 Comparison of $n(O_2)$ profiles measured with QT ion chambers above Woomera.

—x— C4018 (Ilyas, 1976)
—·—- C1029 "" ""
—··—- C4009 "" ""
■ - SL 1005
● - SL 1207
▲ - Aerobee 13.123 IS

present results are well within the range of the previous measurements. Despite this, the profiles differ significantly in their slope. While the results from C 1029 show a change in slope similar to that observed in the present work, the profiles from C 4018 and C 4009 lack this feature entirely. The deviation at the higher altitude limit of the C 4009 profile is considered to reflect the uncertainty of the determination rather than an underlying change in the atmospheric structure.

However, it is suggested that the different slopes to the profiles measured at different times do reflect a changing atmospheric structure above Woomera.

The only high altitude measurements of $n(O_2)$ above Woomera that are available for comparison with the present results are those of Wildman *et al* (1969). Fig 6.33 shows this comparison. These were also taken with SX chambers, so once again the problems of differing instrumentation are avoided. In all cases the $n(O_2)$ are determined from the more stable downlegs. There is insufficient information to make any positive conclusions from Fig 6.33. All that can be said is that given the variation displayed in Fig 6.32, the present high altitude results would not appear to be inconsistent with the earlier data.

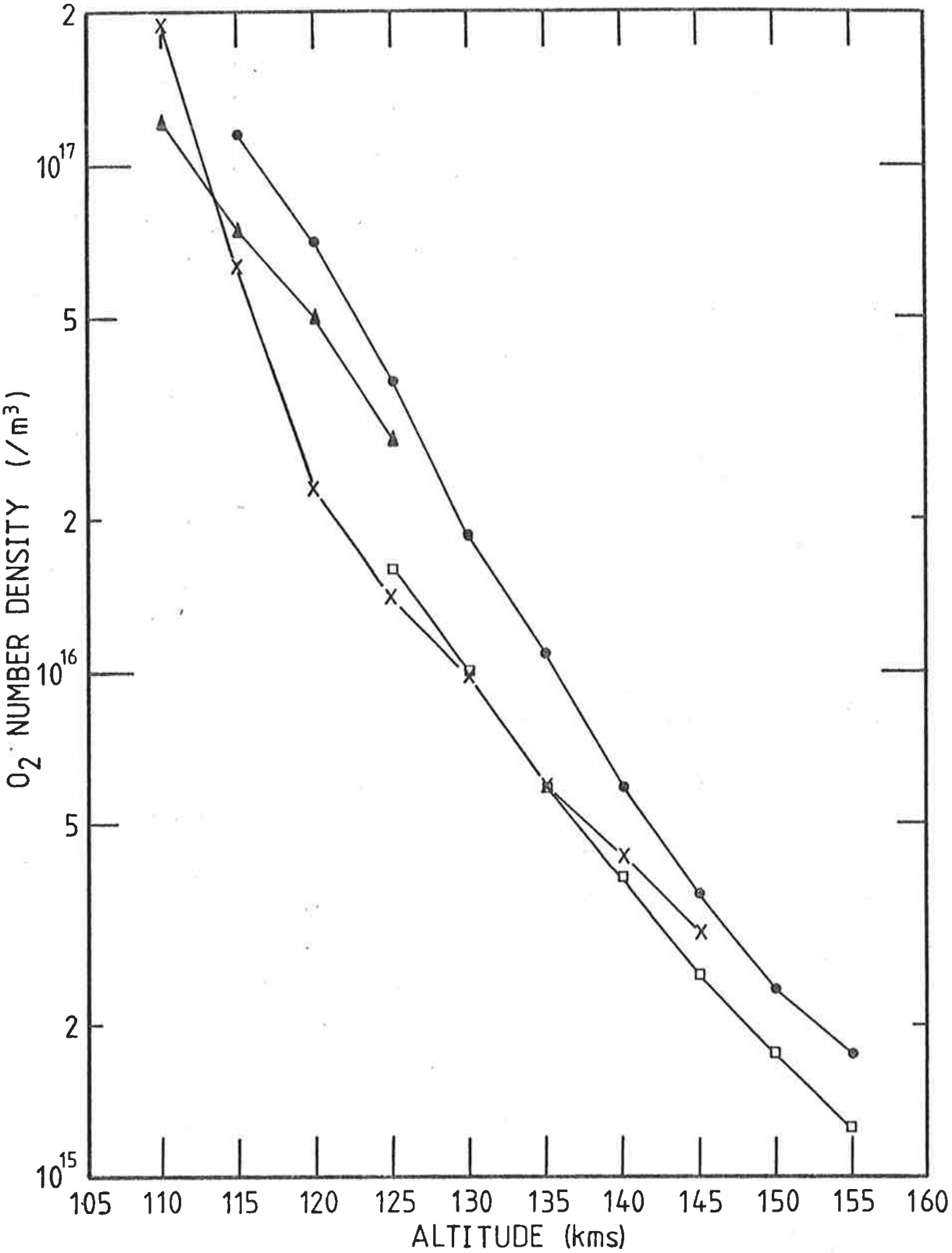

Fig. 6.33 Comparison of high altitude mean $n(O_2)$ measured with SX ion chambers.

—X— - Wildman *et al* (1969)
—●— - SL 1207
—▲— - SL 1005 - ave of downlegs only
—□— - Mean Aerobee 13.123 IS

6.3 OBSERVED VARIATIONS IN MOLECULAR OXYGEN DENSITIES

The variations that have been observed in lower thermospheric molecular oxygen densities were reviewed in Section 2.4.2. In this review, diurnal, seasonal, magnetic, semi-annual, annual, latitudinal and solar flux variations were discussed.

However, there were only three rockets flown in the present research programme, and since they were all launched from the same place and were widely spaced in time but not in season, it was not expected that comment on any of these variations would be possible. However, the timing of the launches has allowed comparison,both between measurements taken on magnetically Quiet and magnetically Disturbed days, and between measurements taken on the same day but $\approx 60°$ of latitude apart. These comparisons are discussed in 6.3.2 and 6.3.3.

On the last rocket the data was such that comparison between the densities derived from the upleg signals and the densities derived from the downleg signals was possible. This is discussed further in 6.3.1.

6.3.1 Horizontal Variations

The existence of semi-annual, annual and latitudinal variations (see Section 2.4.2.4) points to large scale horizontal structure in lower thermospheric molecular oxygen densities. The results of Aerobee 13.123 IS

suggest that small scale structure might also be observed.

Fig 6.34 shows the mean upleg and downleg densities determined by the QT chambers on the Aerobee rocket. The results from the SX chambers have not been included because of the possibility that derived upleg densities may be enhanced by the behaviour of the instrumentation. Discrepancy between the upleg and the downleg is noted over two altitude ranges, i.e. $z < 118$ and $z > 128$. The discrepancy at the lower altitudes is considered to be an artifact of the instrumentation. It has been noted that at their lower altitude limit all chambers show a similar discrepancy (Section 6.1.2) even where the results from another and different type of chamber show good upleg/downleg agreement. For $z > 128$ kms, however, the author considers the profiles shown in 6.34 reflect a genuine atmospheric phenomenon. The discrepancy is well outside combined uncertainties.

The scale of this phenomenon is small. The horizontal scale of acoustic-gravity waves, tidal waves, or planetary waves range from hundreds of kms to thousands of kms, (Mayr and Volland, 1971; Newton *et al* 1969; Yeh and Lui, 1974). Despite this it is suggested that such waves may account for the observation.

Trinks *et al* (1978a) proposed that deviations from the diffusive equilibrium models might be the result of tidal and gravity waves.

The upleg profile presents a far greater deviation from a diffusive equilibrium profile than does the downleg. The observation could be explained if the Aerobee rocket passed through the edge of an upward propagating disturbance on the upleg but descended outside its boundaries.

No statistically significant difference was observed in the upleg and downleg profiles of SL 1005 and SL 1207.

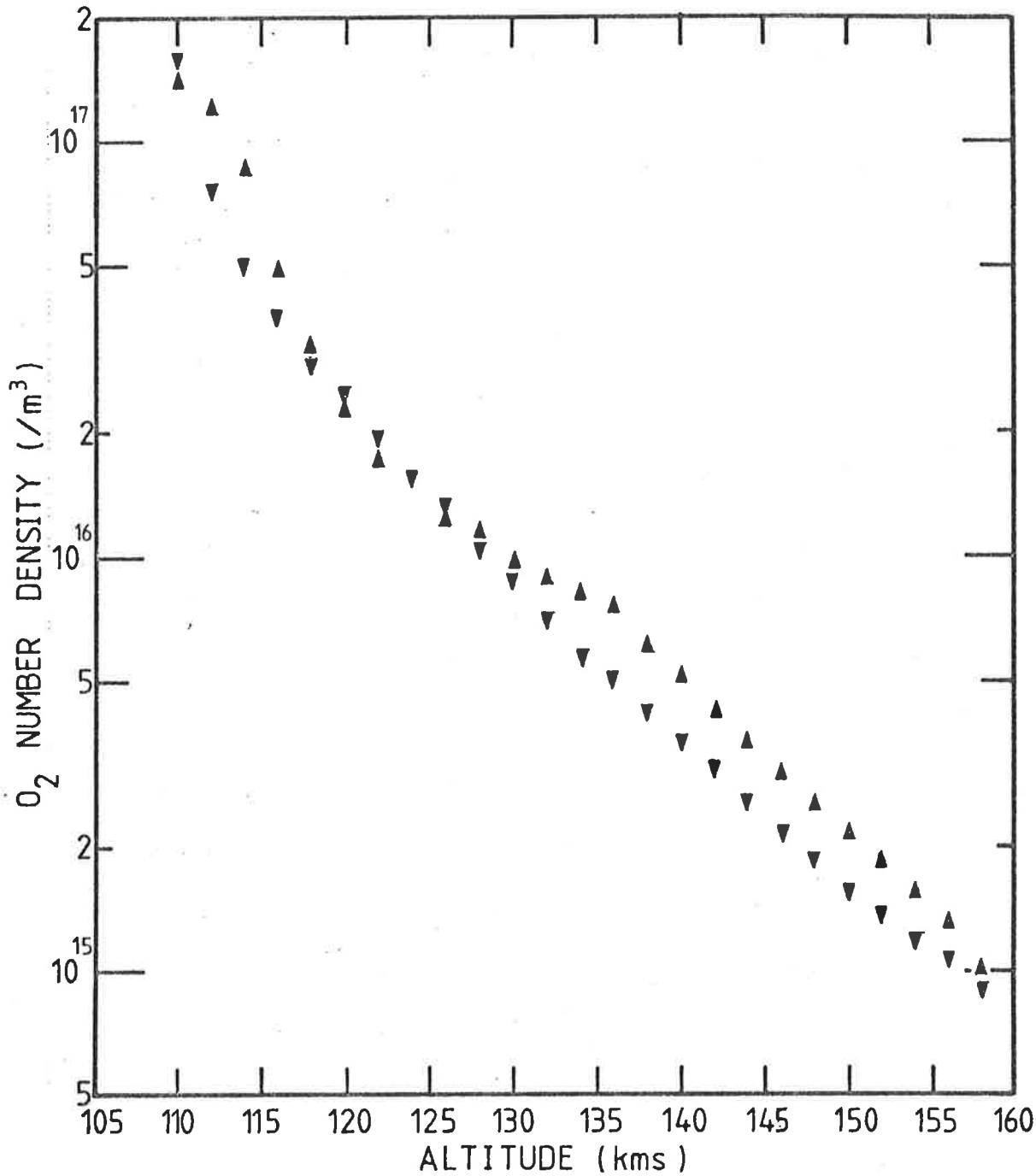

Fig. 6.34 Comparison of average $n(O_2)$ profiles derived from upleg and downleg data of QT chambers flown on Aerobee 13.123 IS.

▲ - upleg

▼ - downleg

6.3.2 Seasonal/Latitudinal Variations

Seasonal/latitudinal variations were discussed in 2.4.2.1. With only two measurements it is not possible to make any comment on the existence or magnitude of such variations, but for interest, the results of SL 1207 have been compared, graphically, with those of Higgins and Heroux (1977). The rockets were launched approximately 17.5 hours apart, from launch sites approximately evenly distant from the equator (32.4° N compared with 31.94° S) and the k_p indices 6.7 hours before launch were the same (i.e. 4^+). The two profiles are compared in Fig 6.35.

Above 120 kms the southern hemisphere results are significantly greater than the northern hemisphere results. However, the cause cannot be isolated from possibilities such as latitudinal effect, a seasonal effect or a latitudinal variation in the magnitude of the magnetic effect.

6.3.3 Magnetic Variations

The effect of magnetic activity on lower thermospheric molecular oxygen densities was discussed in Section 2.4.2.3. In the following, the $n(O_2)$ profiles measured in the present work, and profiles also measured at Woomera by other researchers (Carver *et al*, 1964, 1966; Ilyas, 1976) are discussed with the view to drawing some conclusion about the effect of magnetic activity on $n(O_2)$ at this location.

The fortuitous timing of SL 1005 and SL 1207 has already been mentioned. SL 1005 was flown on a magnetically quiet day while SL 1207 was flown on a disturbed day. In agreement with the suggestion that increased magnetic activity will enhance molecular oxygen densities the $n(O_2)$ determined by the SL 1207 experiment were up to 75% greater than the $n(O_2)$ determined by the SL 1005 experiment. The enhancement is plainly seen in Fig 6.32.

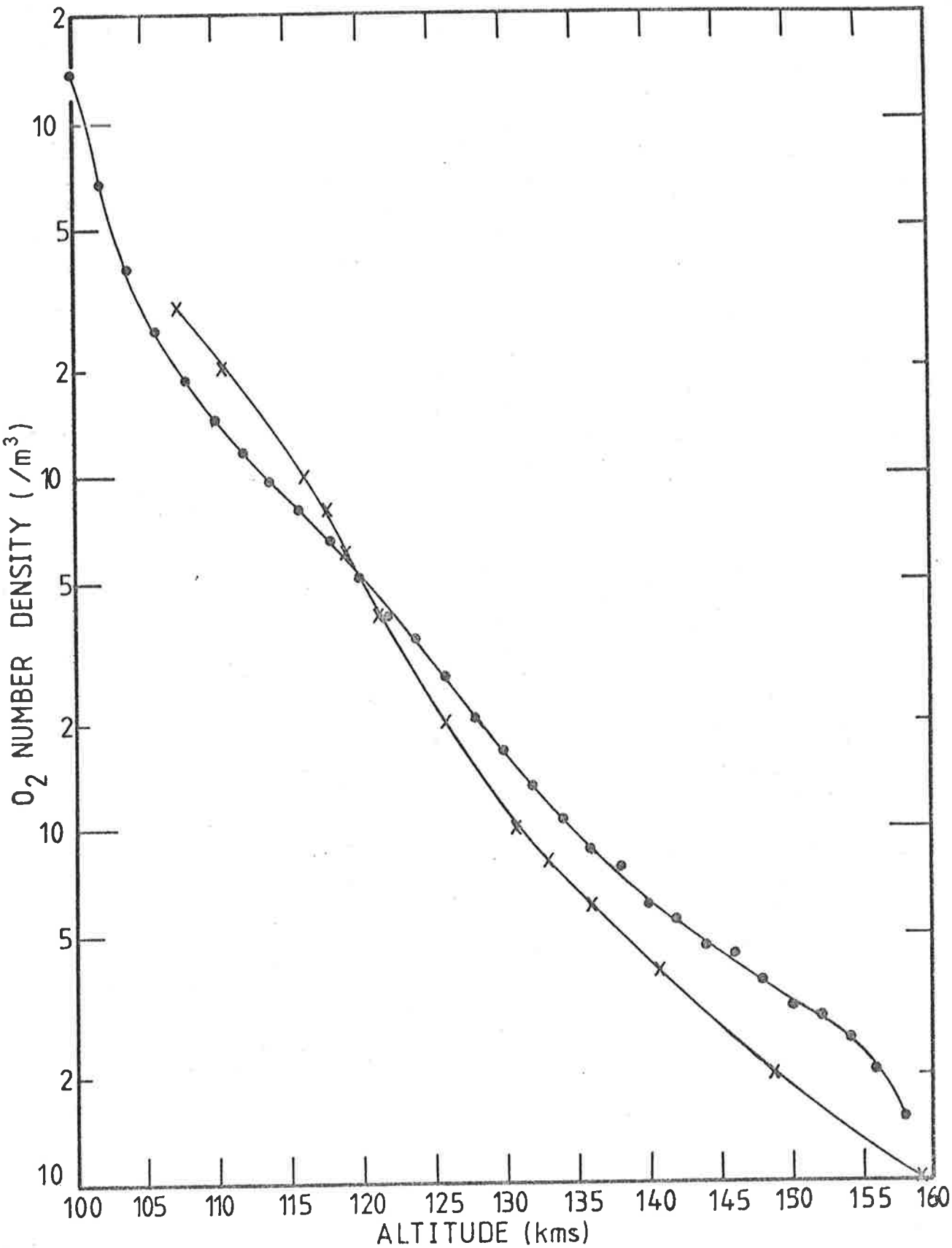

Fig. 6.35 Comparison of the $n(O_2)$ profile of Higgins and Heroux (1977) with the mean profile of SL 1207.

● - Present results

x - Higgins and Heroux (1977)

However, Fig 6.32 shows other features that are not consistent with the above example. C 1049 was also launched on a disturbed day, yet the measured $n(O_2)$ lie below those of SL 1005. Magnetic activity at the time of the Aerobee launching was intermediate between that for SL 1005 and SL 1207, yet for $z < 134$ kms the $n(O_2)$ determined by the Aerobee experiment lie below those from the SL 1005 experiment.

Fig 6.31 compares low altitude $n(O_2)$ determinations made at Woomera over a period of 14 years. The value of the k_p index, 6.7 hours before launch, has been given as the indication of magnetic activity for each flight. Consideration of these profiles and the magnetic activity at the time of their determination indicates that for the lower altitudes too, the picture of the response to magnetic activity is ambiguous.

Other factors may be obscuring the response to magnetic activity. For example, the profiles shown in Fig 6.31 are spread, in time, over more than one 11 year solar cycle. However, the conclusion that can be drawn from measurements taken at Woomera is that while enhancement in $n(O_2)$ may follow periods of magnetic disturbance, the magnitude of such enhancement will not be a simple function of k_p.

6.4 THE MODEL PROFILES

6.4.1 Comparison with CIRA 72 and Jacchia 77

Figures 6.36 and 6.37 show the mean profiles obtained in Section 6.2 compared with either CIRA 72 or Jacchia 77 (Jacchia, 1977).* The Jacchia profile has been calculated using the conditions relevant to the time of launch. Both these models assume that above a fixed height the concentrations of atmospheric constituents are controlled by diffusive equilibrium. The contrasting appearance of the mean profiles of SL 1005, SL 1207 and Aerobee 13.123 IS suggest that at the time of these determinations of lower thermospheric molecular oxygen densities, this

* as calculated by Lean (1980)

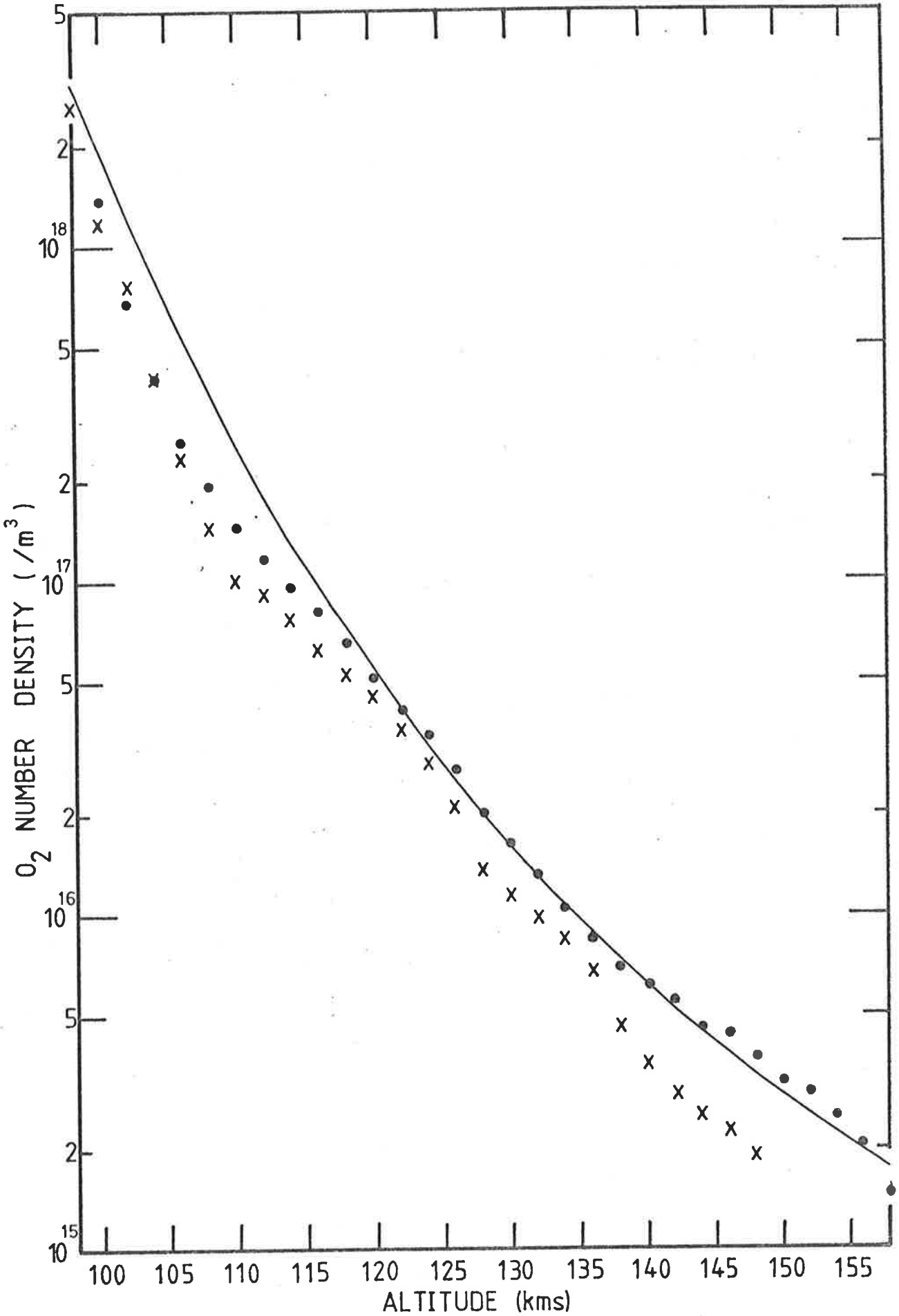

Fig. 6.36 Comparison of mean $n(O_2)$ profiles of SL 1005 and SL 1207 with CIRA 1972.

——- CIRA 1972
x - SL 1005
● - SL 1207

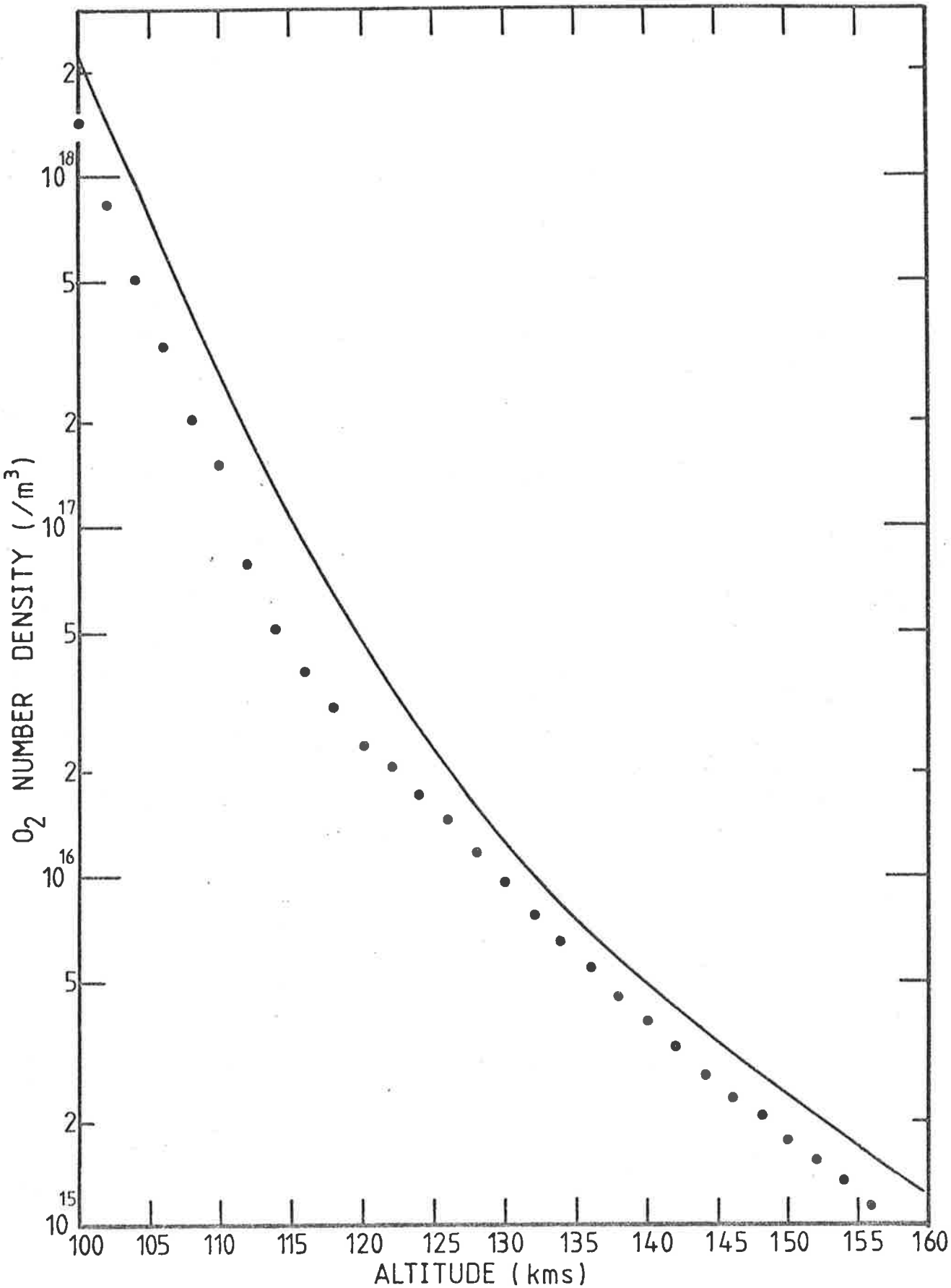

Fig. 6.37 Comparison of mean $n(O_2)$ profile from Aerobee 13.123 IS with the model of Jacchia (1977)

——— - model value

• - Present results.

atmospheric constituent was not in diffusive equilibrium.

The result is not inconsistent with the results from other research groups (Weeks 1975b; Atreya *et al*, 1976; Garriott *et al*, 1977; Trinks *et al* 1978a). Nor is it inconsistent with the work of Oran and Strobel (1976) who argued that photodissociation of O_2 would cause departures of $n(O_2)$ from diffusive equilibrium concentrations. Kayser (1980) argued similarly.

It could be argued that some of the discrepancy arises from the mismatching of the height of the turbopause, with it occurring at a different altitude than allowed for by the model. (The change in slope observed in the $n(O_2)$ profiles measured by the QT chambers could indicate the height of the turbopause). In fact quite a successful model has been built up which uses the exospheric temperature and the height of the turbopause as it's parameters (Blum *et al*, 1978).

An alternative explanation would suggest that the deviations, from the model, seen in the measured profiles are the result of upward propagating gravity waves. This has been proposed by Trinks *et al* (1978a) to explain the severe deviations, from J71 (Jacchia 1971), seen in their mass spectroscopically measured profile. The data of Atreya *et al* (1976) also lends itself to a similar explanation.

There would appear to be a systematic difference between the magnitudes of the $n(O_2)$ determined above Woomera and the model profile given by Jacchia (1977). (Fig 6.37). Since the model densities were calculated using atmospheric conditions relevant to the time of launch, the discrepancy argues that models, even with the level of sophistication of Jacchia's (1977) are still inadequate.

The results have not been compared with models such as MSIS (Hedin *et al*,1977a and 1977b) which have been constructed to fit a variety of

of experiments carried out over a relatively wide range of solar activity. However, it is noted that discrepancies existed between MSIS and the mass spectroscopically determined profiles of Trinks *et al* (1978a) above 140 kms.

The discrepancy shown in the present work could be, as argued by Trinks *et al* (1978a) within the natural variability of the atmosphere, but even if this is so, it points out clearly that present models cannot predict atmospheric behaviour accurately, and need further development.

6.4.2 Comments on Models

Many of the results have shown departures from diffusive equilibrium. Consideration of the photochemistry of the lower thermosphere (Oran and Strobel, 1976) argues that this is to be expected. The work by Mayr and Volland (1971; 1972) on wind-induced diffusion also leads to predictions of departures from diffusive equilibrium. This would lead to the conclusion that models which basically rely on the assumption of diffusive equilibrium (e.g. CIRA 72, Jacchia, 1971) have limited application.

The Jacchia models (Jacchia 1965, 1971 and 1977) use $F_{10.7}$ and $\overline{F}_{10.7}$ (i.e. average) flux to calculate the exospheric temperature. Schmidtke (1979) and Hinteregger (1977) both point out that the solar flux is poorly correlated with $F_{10.7}$ and $\overline{F}_{10.7}$. Therefore these models and any future models which calculates the exospheric temperature from $F_{10.7}$ and $\overline{F}_{10.7}$ will be limited in their suitability.

Finally, it is becoming increasingly clear that dynamics play a major part in the determination of the behaviour of the upper atmosphere (Mayr and Harris, 1977a; Mayr *et al*, 1978). Any future modelling must also include dynamic considerations.

6.5 SUMMARY

The basic research objective was stated as being the determination of lower thermospheric molecular oxygen profiles with good altitude resolution and small associated uncertainties. The mean profiles given in Section 6.2 for the most part represent the achievement of this aim.

Then, three core questions were posed: the first two were -

(a) was there a statistically significant difference between profiles obtained on the upleg and downleg ?

(b) did this difference denote observation of horizontal structure in the atmosphere ?

For SL 1005 and SL 1207 it was decided that these two questions had been answered in the negative. For Aerobee 13.123 IS it was concluded that answers were in the affirmative.

Measurements were taken at differing levels of magnetic activity and the present results showed enhancement in $n(O_2)$ occurred when magnetic activity, as indicated by the k_p index, increased. However, at Woomera the enhancement was not as large as had been reported by some research groups. Consideration of other Woomera measurements of $n(O_2)$ suggested that enhancement did not always occur.

Finally, the mean profiles were compared with 2 model profiles. Agreement was not close. It is considered that models must include dynamical considerations if they are to match experimental determinations.

6.6 FUTURE WORK

Carignan (1975) and Hedin (1979) both made the point that the behaviour of $n(O_2)$ was the least understood. The addition of results from 3 widely spaced (in time) rocket flights do not alter the truth of

these statements.

They have provided some valuable southern hemisphere data which, as has been stressed in Chapter 1, has been lacking, but they are inadequate, to help resolve the ambiguity arising over seasonal/annual/latitudinal effects (Chapter 2). They do reflect the inadequacies of the models (Section 6.4). Much more data is needed.

The majority of this data will be collected by satellite borne mass spectrometers. However, UV absorption techniques will still be used to enable determination of $n(O_2)$ at altitudes below satellite perigee. The UV instrumentation, however, will most likely be narrow band in order to avoid the uncertainties associated with the estimation of σ_{EFF} for a broad band instrument. Should broad band instrumentation be used on these long life vehicles, ion chambers would be discriminated against because, despite the improvements seen in the type 2 chambers, unpredictable failures still occur (e.g. the deterioration of the LNO chamber on Aerobee 13 123 IS).

Having said this the author still believes the justification of rocket-borne experiments given in Chapter 1 is valid and that ion chambers are viable instrumentation for these vehicles. Their small size, wide field of view and their ability to monitor the solar radiation continuously enable them to exploit this environment. In particular, their small size enables multiple numbers of chambers to be flown which improves the statistics of the experiment.

If ion chambers are to be used then it is desirable the uncertainties associated with them are reduced. This would require, for example, further investigation of the changing sensitivities of SX chambers and a better estimate of the effective cross-section of the $L\alpha$

chambers.

However, in conclusion, it is stressed that knowledge of the behaviour of lower thermospheric molecular oxygen is inadequate, and must be expanded, and while improvement of the instrumentation and methodologies outlined in this thesis is desirable, the experiment, as it stands, can still be exploited to achieve this purpose.

CHAPTER 7

THE AIRGLOW EXPERIMENTS

This chapter briefly discusses the two airglow experiments flown during the present research programme. The rationale behind their inclusion in the programme has already been discussed and will not be considered here.

The introduction, Section 7.1, covers the basic design principles behind both instruments. Sections 7.2.1 and 7.2.2 describe the individual instruments in more detail; that flown on the Skylark rocket SL1005 in Section 7.2.1 and that flown on the Skylark rocket SL1207 in Section 7.2.2.

Calibration techniques, which were similar for both photometers, are covered in Section 7.3. The discussion is not detailed, but limited to consideration of what factors had to be taken into account.

A brief comment about the photometer's flight performance was made in Chapter 5. This is elaborated in Section 7.4 but, as has already been stated, the experiments were not successful and no attempt is made to extract airglow intensities from the signals received.

7.1 INTRODUCTION

The measurement of day airglow is made difficult by the presence of a strong continuum background arising from the Rayleigh scattering of sunlight. Some means of measuring and subtracting this background is essential. The photometers described in Sections 7.2.1 and 7.2.2 were based on instrumentation developed by Dandekar (1969) to circumvent the problem of this background. A description of Dandekar's photometer is

given to illustrate the method he adopted, and therefore, the principle of the present photometers.

A schematic of the Dandekar instrument is given in Fig 7.1a. The light passed through the baffle systems, through the filters, and then, was folded by the use of right angled prisms, to fall onto a single detector through two apertures A and A'. The light was chopped by the shutter S. S, A and A' were machined precisely so that the total aperture onto the detector was always the same (Fig 7.1b).

The constant size of the aperture implied the rotation of the shutter would have no effect on the signal observed, if the light reaching A or A' was of the same intensity (Fig 7.1c). On the other hand an imbalance in the intensity of light reaching A or A' would give rise to a modulated signal, and the modulations would be synchronous with the shutter.

This was the principle of the instrument. One of the filters was centred at the airglow line, the other at a wavelength close enough so that the continuum intensity seen by both filters would be approximately the same, but far enough away so that the airglow line did not fall within its passband. By actually matching, with the aid of the diaphragms, the continuum intensity transmitted by both filters, the instrument would, when viewing a continuum plus the airglow line, register the intensity of the airglow line in the amplitude of the modulated signal superposed on the steady continuum signal.

While Dandekar's principle could be adopted, the photometers could not be replicas of his instrument. In neither rocket was there enough room. In addition, the fact that both were attitude controlled imposed an additional design criterion.

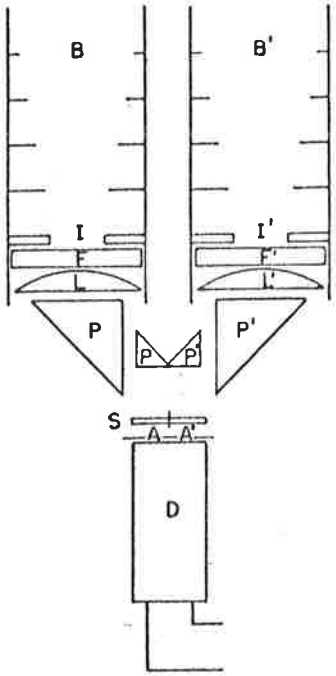

B, B' BAFFLE SYSTEMS
I, I' ADJUSTABLE IRIS DIAPHRAGMS
F, F' INTERFERENCE FILTERS
L, L' FIELD LENSES
P, P' PAIR OF RIGHT ANGLED PRISMS
S ROTATING SHUTTER
A, A' PAIR OF APERTURES
D DETECTOR

(a) Schematic of Rocket Photometer of Dandekar (1969)

A, A' APERTURES
S SHUTTER

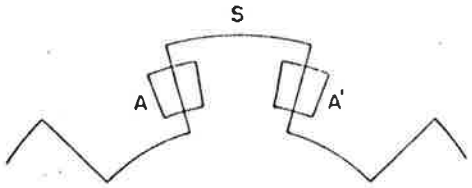

(b) Sketch showing constant area of illumination.

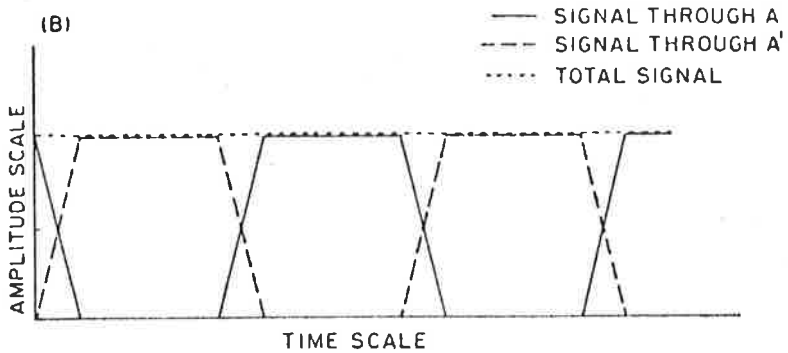

(c) Schematic representation of photometer output when illuminated by a continuum.

Fig. 7.1 Reproduced from fig.2a and fig. 2b of Dandekar(1969)

Both rockets carried sun sensors which provided the input into the attitude controlled units and kept the rocket pointed at the sun. The rockets orientation around its long axis could also be specified and maintained. Consequently, by suitably specifying this orientation, and setting up the instrumentation so that the angular separation between the look directions of the sun sensor and the photometers was equivalent to the solar zenith angle (SZA) at the proposed time of launch,it was possible to ensure the photometers viewed zenith throughout the controlled part of the flight.

However, the time of launch, and hence the expected SZA, could not be confirmed until a week or so before the launch. Therefore, the design had to incorporate a mechanism for altering the look direction of the photometers, in order that a variety of solar zenith angles could be accommodated.

In summary, therefore, the photometers incorporated

(a) a mechanism to enable different solar zenith angles to be accommodated

(b) a double filter system to allow the subtraction of the background

and the design was influenced strongly by the restricted space available.

7.2 THE PHOTOMETERS

This section describes the airglow photometers. The description is brief and no attempt is made to elaborate, beyond what has already been stated in Section 7.1, on why these particular designs were used.

7.2.1 The SL1005 Photometers

The SL1005 airglow experiment was designed to measure two airglow lines simultaneously. These, as has already been mentioned in Chapter 1, were 3914Å (N_2^+) and 5577Å (OI). To achieve this, a double photometer was built, but since the two halves of the instrument were

identical only one is now described.

Figure 7.2a is a schematic of the end view of the instrument and shows the optical system. Radiation entered the system through aperture A or A'. It was chopped by a shutter directly behind the aperture. The shutter was machined to exactly match the truncated sector shape of the apertures (Fig 7.2b). The apertures and the shutters behind them can be seen plainly in Figures 5.2a and 5.2b.

Light entering A passed through the filter F_A, and then was reflected by the mirror M_3, the beam splitter, the mirror M_4 and finally the mirror M_5. M_5 was set at 45° to the plane of the optics (equivalent to the plane of the page) and directed the light onto the photomultiplier which was at 90° to the plane of the optics.

Light entering A' was reflected off M_1 and M_2, passed through F_{A1}, then the beam splitter and was reflected off M_4 and M_5 before reaching the same detector as the light from aperture A.

Filter F_A was nominally centred at 5577Å, (3914Å in other photometer) and filter F_{A1} was nominally centred at 5600Å (4060Å). The shutter was driven by an Escap motor at 1 revolution/sec. resulting in the radiation being chopped approximately 3 times/km. The photomultipliers were EMI 9734 QNB and were chosen on the basis of the magnitude of their dark currents. The quietest most stable ones were used.

The interior of the optic system was sprayed matt black to reduce unwanted reflections.

It was stated in Section 7.1 that the angle between the direction of look of the instrument and the sun sensor had to be adjustable. This flexibility was achieved in the mounting of the double photometer. The instrument was held by an irregularly shaped section of aluminium (Fig 7.3), slotted to provide a clamp. The cylindrically shaped photometer block,

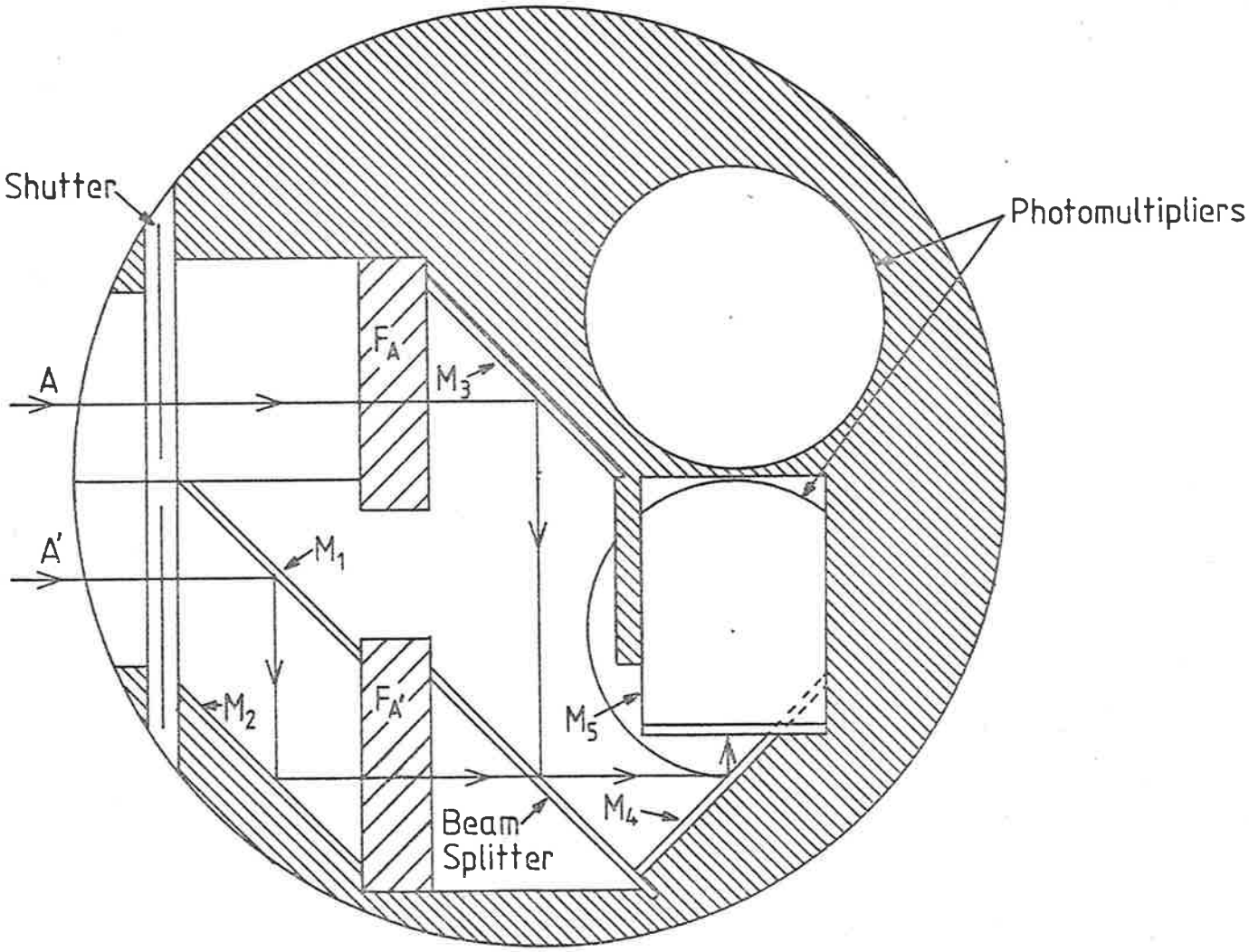

Fig. 7.2a Schematic of end view of Photometer-Optical System.

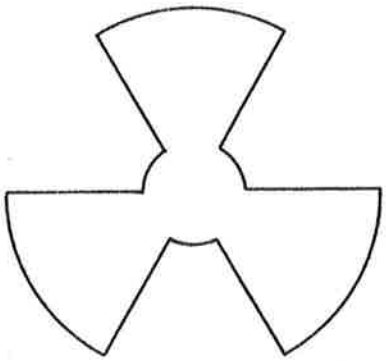

Fig. 7.2b Shape of shutter-showing truncated segments

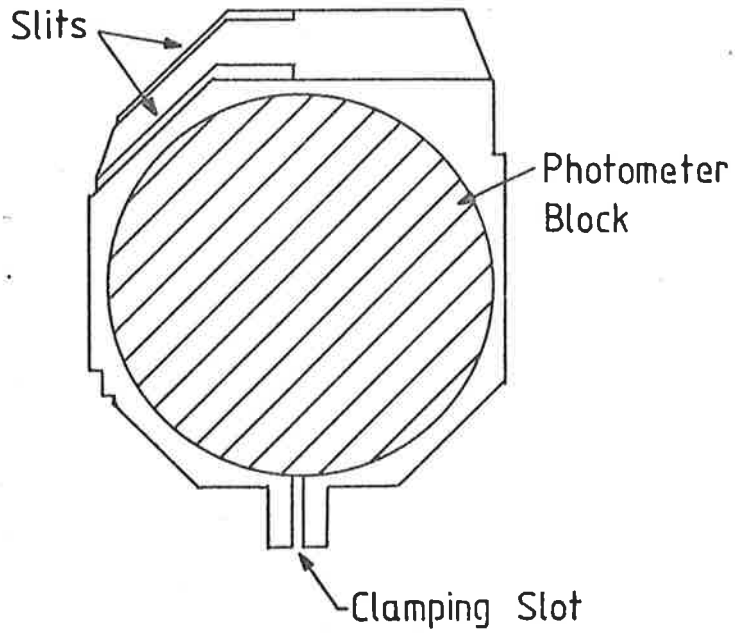

Fig. 7.3 Aluminium clamping section
for SL 1005 Photometer.

could be turned within this section, and the slits cut in the section allowed the look direction of the photometers to vary over 45° (see Fig 5.2a). The spectrophotometer, the ion chambers and the X-ray counters were all sun pointing, so the angle was determined with reference to their look direction, and then, the photometers were clamped into place. As stressed in Chapter 5, this adjustment was not possible once the rocket had been built up.

7.2.2 The SL1207 Photometers

The SL1207 airglow experiment differed strongly from the one just described. This was partly because more room was available, partly because it was desired to look at more lines (3914Å, 5200Å, 5577Å and 6300Å), and partly because it was sought to avoid the severe scattering problems experienced by the SL1005 instrumentation (Section 7.4).

Figs 7.4a and 7.4b are schematics of the side and end view of the system. The four photometers were grouped together and although they each had their separate optical systems they shared a single shutter. Once again the shutter had been precisely machined such that the segments removed exactly matched the shape of the apertures. This shutter, however, differed from the ones used in the SL1005 instrument in that a ¼ section (approx.) was left solid. This implied that every revolution, the dark current of the detector of each photometer could be checked since the solid section was large enough to cover both apertures of a photometer simultaneously.

Light passed through a 38 mm length of aluminium foil honeycomb, then through the filters set behind apertures which were in the shape of truncated segments, and was then chopped by the shutter already discussed. It then passed through a lens which focused it onto the EMI 9734 QNB photomultiplier used as the detector. These were not

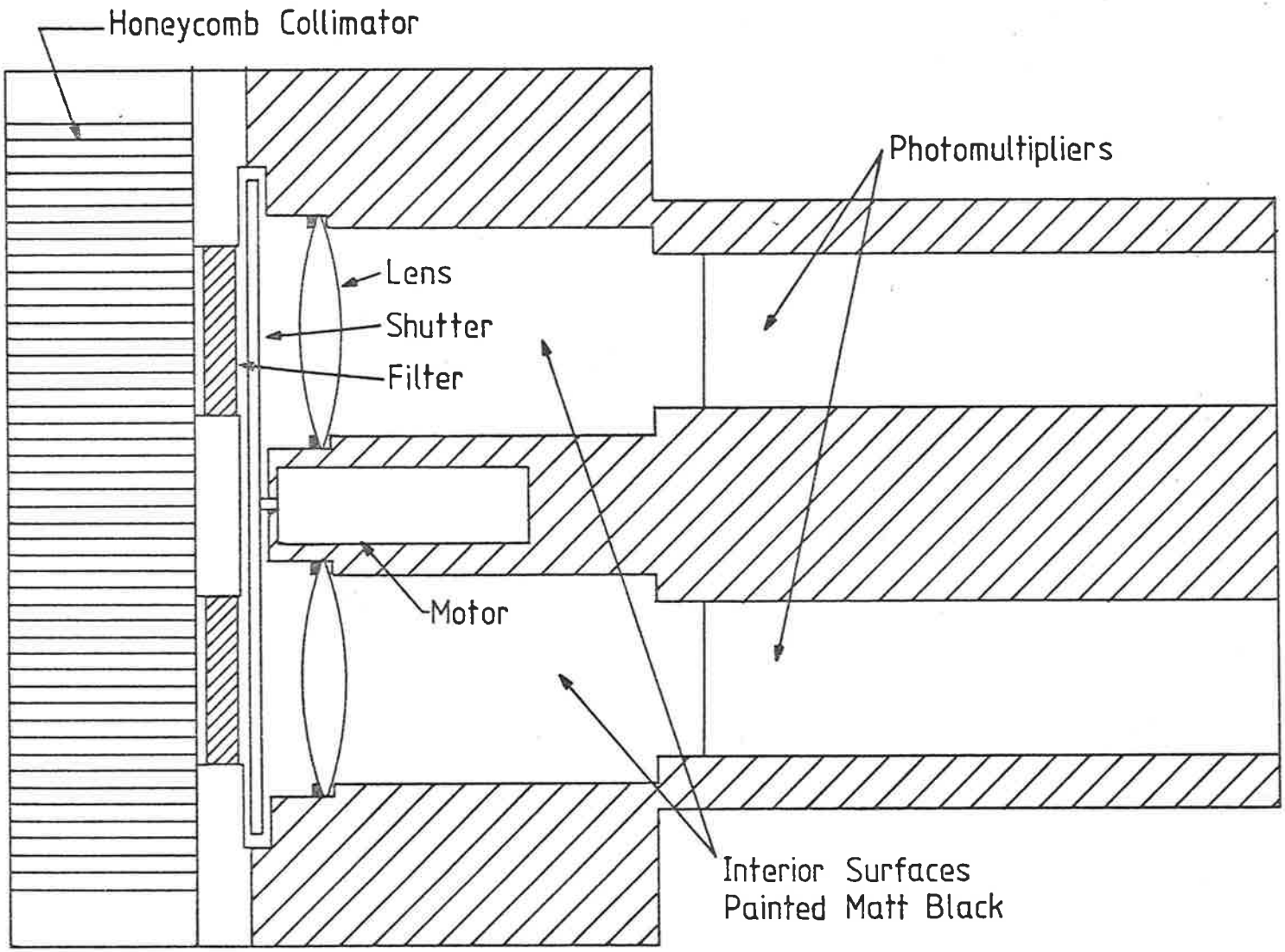

Fig. 7.4a Schematic of side view of SL 1207 Photometer.

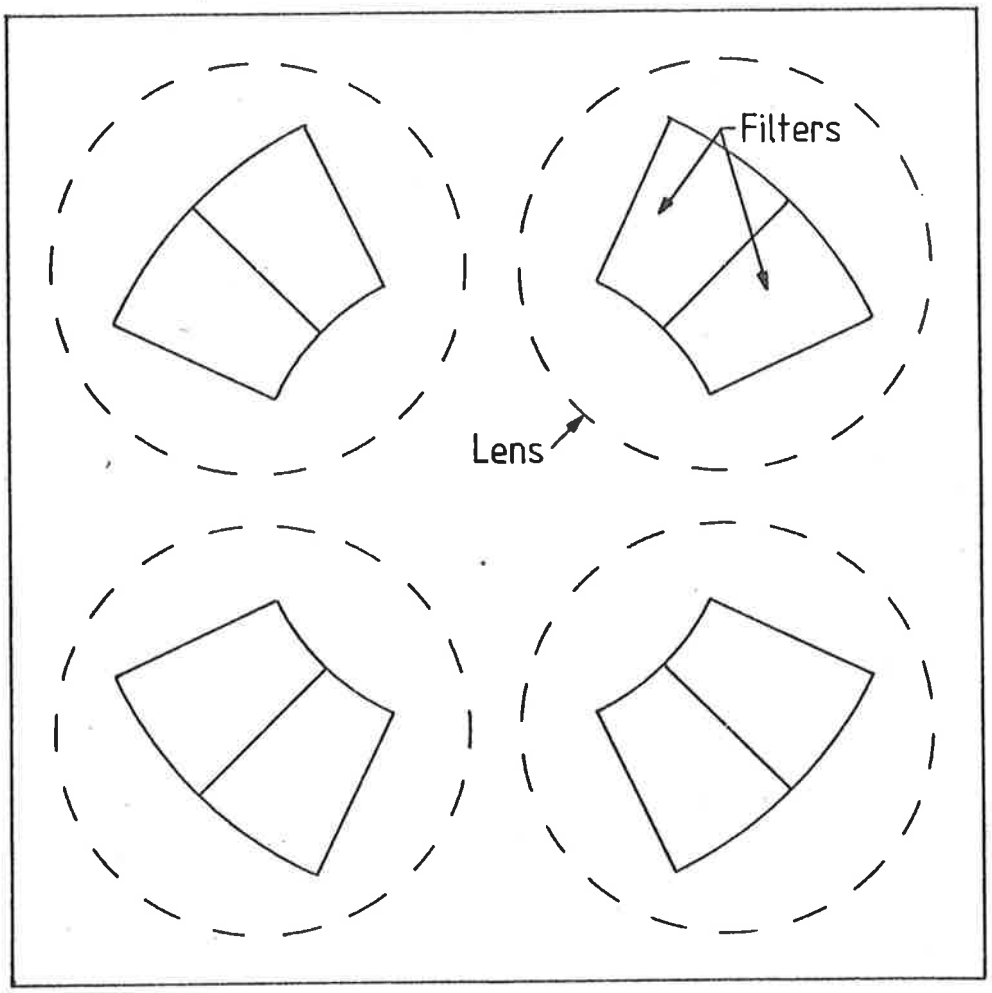

Fig 7.4b Schematic of end section of SL 1207 Photometer.
To improve clarity shutter not shown.

ideal detectors, because of their low response in the red (fig 7.5), but were used because of their small size, (30 mm nominal diameter, 100 mm long).

All interior surfaces were painted matt black to reduce scattered light.

Once again the mounting of the instrument provided the means to adjust the direction of look of the instrument. A schematic of the arrangement is given in fig 7.6. The photometer block was pivoted on Pin A. The slot had been machined precisely and could accommodate SZA's up to 45°. The scale was attached to help make adjustments easier and faster. The Pin B was first located with the aid of this scale, before being locked into place to secure the instrument.

In fig 5.12, a shield is seen on the instrument. This was spring loaded and opened when the nose cone was ejected. This was fitted shortly before launch as an extra - successful - precaution against scattered light and subsequent saturation of the detectors.

7.3 CALIBRATION OF THE PHOTOMETERS

The procedure for both instruments was similar, and therefore, in the following, no differentiation is made between them unless a technique or problem was unique to a particular instrument.

7.3.1 Alignment of Photometers

It was found for the SL1207 photometers that the use of the lens implied alignment was not critical and the accuracy of the original machining was sufficient.

For the SL1005 photometers it was found to be necessary to use a laser to align the mirrors. The light from a low powered laser (Metrologic : Model 420, .5 mW) was passed through a pair of beam splitters

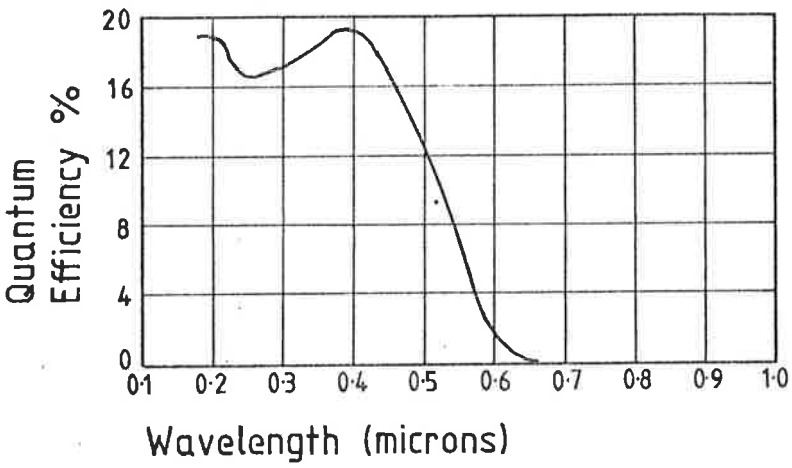

Fig. 7.5 Response of Cathode of EMI 9734QNB Photomultiplier. Reproduced from EMI Catalog.

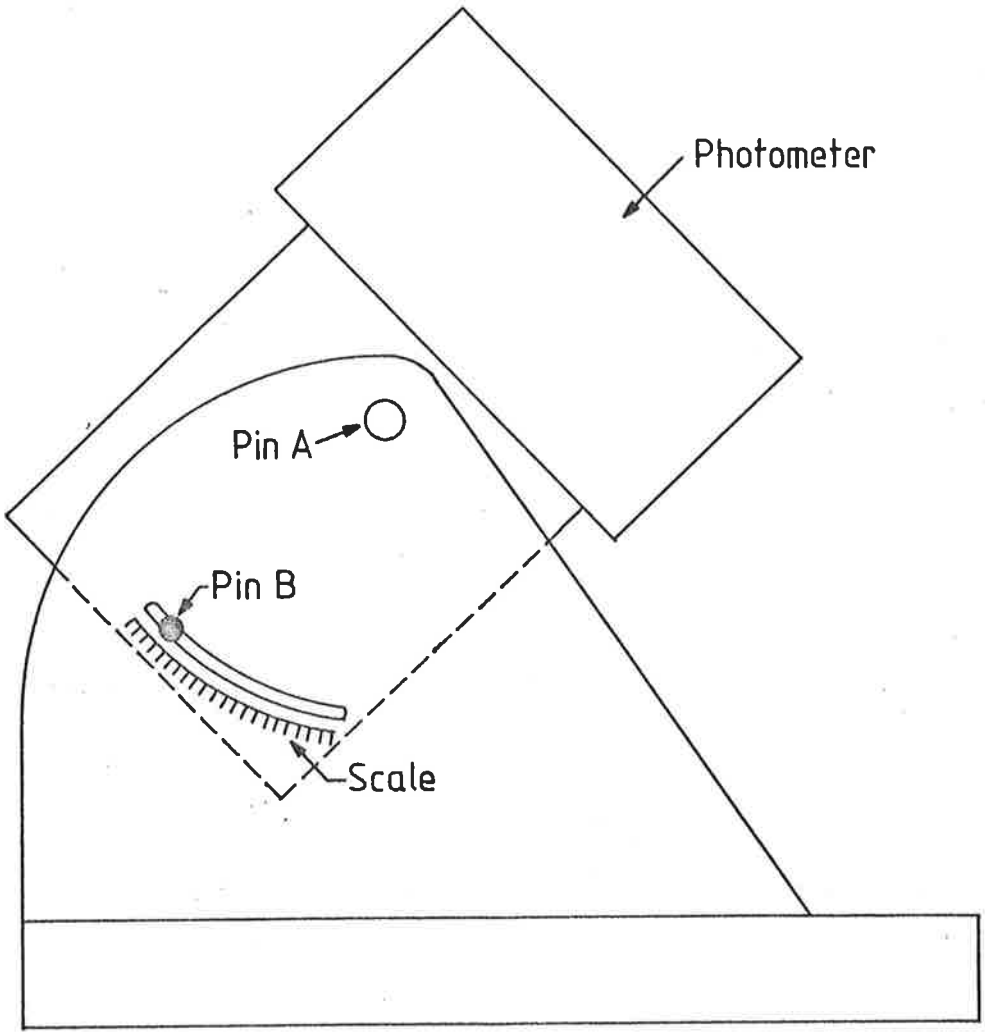

Fig. 7.6 Schematic of mounting of SL 1207 Photometer.

so that two beams were produced and apertures A and A' could be illuminated simultaneously. Cross hairs were centred in the cylinders bored out for the photomultipliers, and mirrors M_1, M_2 ... M_5 were adjusted until the light rays from A and A' were coincident on the centre of the cross hairs.

7.3.2 Filter Selection

Each photometer required two filters, one at the line in question, and one close to, whose response at the airglow line was negligible. Because the principle of the equipment relied on them transmitting a balanced intensity of continuum, these two filters also had to have similar transmission coefficients and this was one of the selection criteria.

The selection process was also influenced by the temperature coefficients of the filters. These were measured as mostly being in the range of a .2 to .3Å/°C shift in the wavelength of the maximum response. The choice was dictated by the expected wavelength of the maximum response (λ_{MAX}) at flight temperatures rather than λ_{MAX} measured during the selection process.

7.3.3 Angular Response

After the filters had been selected and placed in the instrument the angular response was checked. Once again this proved to be only critical for the SL1005 photometers (Section 7.2.1). The honeycomb section in the front of the SL1207 photometers implied a total angular field of view of approximately 10.5° and there were no anomalous side peaks or irregularities in the response.

The initial angular response of the SL1005 instrument showed

serious side peaks. These appeared to occur because of the distance between the filters and A and A' and because the filters were bigger than A or A'. Further masking of the filters themselves, produced a smooth angular response with a full width ½ max of 10° to 15°. The unmasked section of the filters still remained slightly bigger than the apertures.

7.3.4 White Light Calibration

White light calibration was not only essential so amplifier levels could be adjusted to accommodate expected continuum intensities, it was also necessary to enable balance of the continuum intensities being transmitted through the filters. In SL1005 balance was achieved by altering the reflectance/transmission ratio of the beam splitter (see fig 7.2a). In the SL1207 instrument this facility was not available, and despite careful selection of the filters, there was an imbalance. However, the ripple this imbalance caused in the signal was small, and remained constant as the intensity increased. It was, therefore, considered acceptable to measure the magnitude of this AC component and use it as a correction factor, rather than attempt to remove it by modifying the instrument.

7.3.5. Calibration for Airglow Lines

The final step was the calibration of the photometer's response to the airglow line. A monochromator with a Xenon lamp was used as the light source. A beam attenuator was also used to ensure the photomultipliers were not forced into the non-linear section of their response.

Use of a beam splitter in the path of the light enabled a photomultiplier, positioned at 90 degrees to the direction of the beam, to be set up as a secondary standard. The secondary standard was calibrated against a thermopile, then used to monitor the beam while measurements were taken of the photometers' response. A schematic of the experimental arrangement for the calibration is shown in fig 7.7. Comparison, through the secondary standard, between the photometer's response and the thermophile's output enabled absolute calibration.

7.4 FLIGHT PERFORMANCES

7.4.1 SL1005

Prior to the flight, the major concern had been whether or not the flight temperatures would reach the 50°C that had been allowed for in the making and selecting of the filters. This turned out to be an academic question. Scattered light drove the photometers into saturation as soon as they were exposed. Baffles had not been fitted to the instrument, mostly because there was not enough room, but partly because it was believed that with the narrow field of view (10° - 15°), and with the photometers being pointed at zenith, they were not necessary. In addition, the optical path was complex and the interior of the instrument had been blackened to reduce stray reflections.

The exposed nature of the apertures, however, still allowed scattered light to reach the photomultipliers and no useful data was obtained.

7.4.2 SL1207

More precautions against scattered light were taken with the SL1207 photometers, and the shield and the honeycomb already mentioned, were successful in preventing scattered light saturating the photomultipliers.

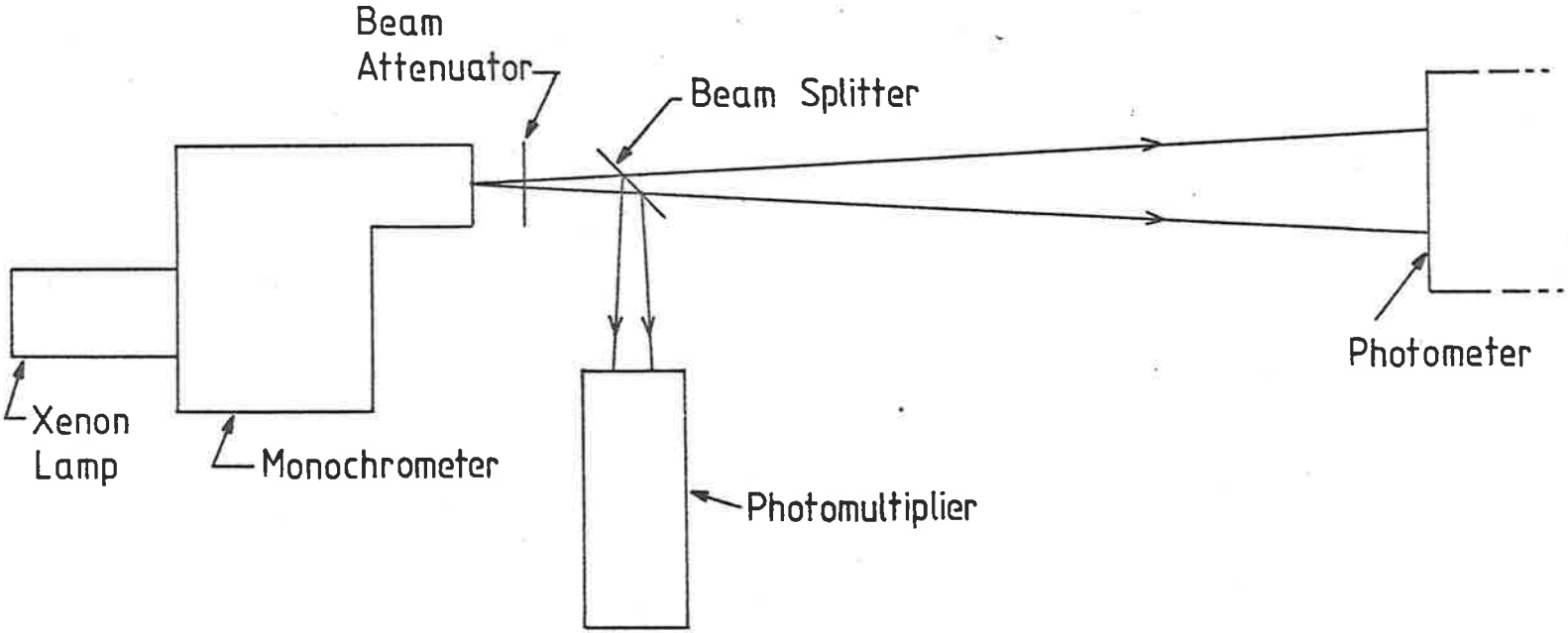

Fig. 7.7 Schematic of Experimental Apparatus for Calibration of Photometers.

However, although an AC ripple was seen on top of a DC level throughout the flight, the amplitude of this ripple remained constant and close to that observed during white light calibrations.

An explanation, consistent with conditions at the time of launch, can be found for this. The thermistors flown on SL1005 had shown that, even in the exposed position it occupied, the photometer block did not reach the 50°C expected. 35°C seemed a more reasonable temperature to expect. Therefore, the filters were ordered with the specification that at 35°C their maximum response should be at the nominated wavelength. The delivered filters did not meet this criterion. The temperature at which the desired response would occur varied between 40°C and 50°C. Lack of time forced the use of these components. It was hoped that careful analysis would yield useful information, even though the wavelength of the airglow line would be in the wings of the response rather than the maximum. However, with the temperature not rising above 24°C, (Section 5.3.3.3), it would be expected that the response at the airglow line would be too small for the subsequent signal to rise above the noise level. Under these conditions, the expected signal would resemble the white light calibrations, since the photometers would really only be responding to a continuum.

7.5 SUMMARY

This chapter briefly discussed two photometers constructed during the course of this work. The complexity of the first design was imposed by the extreme restrictions in space, and led to problems with the alignment and angular response of the instrument. The lack of space also prevented the fitting of baffles and the experiment failed because of

scattered light.

The experience of the first instrument led to the second photometer block being designed such that alignment was not critical, the angular response was smooth and regular, and the photometers didn't suffer the effects of scattered light. However, this experiment was not successful either, because of mismatching of filter parameters to the actual launch conditions.

CHAPTER 8

THE WATER VAPOUR EXPERIMENT

Since no useful data was obtained from the water vapour experiment, this chapter has been included principally so that this thesis may summarize the whole of the research programme undertaken. The presentation is limited.

A brief introduction (Section 8.1) looks at what initiated the interest in attempting to obtain a measure of the water vapour concentration, and the reason why photometric methods were adopted. Section 8.2 discusses the concept of the experiment while Section 8.3 considers the computer program written to test the feasibility of the concept. Section 8.4 gives a brief account of the vehicles used and the results obtained.

Recent detailed checking of the computer program revealed an error, the correction of which, badly affected the predicted sensitivity. The significance of this mistake, with respect to the viability of the experiment, is discussed in Section 8.5. In Section 4.2.7. it was decided that no allowance was to be made for other absorbers in the analysis of the ion chamber data. In view of the reason given for wishing to measure $n(H_2O)$ (Section 8.1) this decision is considered further in Section 8.5.

8.1 INTRODUCTION

Although water vapour features in the photochemistry of the upper mesosphere, lower thermosphere region (Hunt, 1972; Fukuyama, 1974), interest in this gas, in the present work, was limited to the effect its presence could have on the validity of determinations of $n(O_2)$ from the data of $L\alpha$ chambers.

Discussion in Section 4.2.7 has shown that, depending on the $n(H_2O)$ profile assumed, water vapour may absorb a significant proportion of the solar $L\alpha$. Therefore the derived $n(O_2)$ will be associated with large errors if the water vapour absorption is ignored. However, it is difficult to assess the size of such errors. While figures up to 53% are given in Table 4.5, these are only valid for the assumed profile (Martynkevich, 1972) and, as with all atmospheric parameters, the water vapour density profile would be expected to vary. Measurements (Martynkevich, 1972; Martynkevich and Shvidkovsky, 1971; Radford *et al*, 1977; and Sonnemann *et al*, 1977) do in fact show strong variation. Therefore, if this source of error was to be removed, a measurement of $n(H_2O)$ had to be made simultaneously with the measurement of $n(O_2)$ and the initial aim of the water vapour experiment was just this.

However, the physical limitations of the vehicles in which the experiments were to be flown forced a compromise.

Small sounding rockets were used (See Section 8.4 for description). Space for instrumentation was limited, and since it was not desired to seriously degrade the principle experiment which was the measurement of molecular oxygen densities, the physical restraints on the water vapour experiment were extreme. A scheme, however, had been suggested (J.H. Carver, private communication). This scheme utilized ion chambers. The choice of instrumentation had several advantages. The detectors were small, and since, in physical dimensions, they exactly matched the ion chambers used in the $n(O_2)$ experiments (see Chapter 3 for description of detectors) it was not necessary to alter the instrumentation block of the rocket. In addition, the necessary expertise and equipment for their construction and calibration was already available.

These advantages had to be weighed against the fact that computer simulation of the experiment implied that in this form the experiment could only give an upper limit to $n(H_2O)$. However, it was decided by the author, that despite this reduction in scope, useful information could still be obtained and the water vapour experiment described in the following sections was based on ion chambers.

The previously mentioned discovery of the error implies this decision was, in fact, based on incorrect information, but consideration of this is left to Section 8.5.

8.2 CONCEPT OF EXPERIMENT

The technique relies on the differences in the absorption cross-sections of water vapour and molecular oxygen. Consider solar radiation at two wavelengths λ_1 and λ_2. Let the absorption cross-sections for these wavelengths be as follows. (The actual values given have no significance and have been included only for illustrative purposes)

$$\lambda_1 \; : \quad \sigma_{H_2O} = 10^{-18}\,cm^2$$

$$\sigma_{O_2} = 10^{-18}\,cm^2$$

$$\lambda_2 \; : \quad \sigma_{H_2O} = 10^{-20}\,cm^2$$

$$\sigma_{O_2} = 10^{-18}\,cm^2$$

In a pure oxygen atmosphere the extinction coefficient at any altitude h will be identical for the two wavelengths since adapting Equation 4.20

$$\phi_h(\lambda_i) = \phi_\infty(\lambda_i) \; e^{(-\sigma_i N_T(O_2))} \tag{8.1}$$

which implies

$$j_{\lambda_i}(h) = \frac{\phi_h(\lambda_i)}{\phi_\infty(\lambda_i)} = e^{(-\sigma_i N_T(O_2))} \qquad (8.2)$$

where $\phi_h(\lambda_i)$ is the flux at $z = h$, for λ_i

$\phi_\infty(\lambda_i)$ is the flux at $z = \infty$, for λ_i

$N_T(O_2)$ is the total column density of O_2 above h.

The right hand side of 8.2 is the same for $i=1$ or $i=2$ for the cross-sections given. If, however, water vapour is present the power of the exponent becomes

$$(-(10^{-18}.N_T(O_2) + 10^{-18}.N_T(H_2O)))$$

for λ_1 and becomes

$$(-(10^{-18}.N_T(O_2) + 10^{-20}.N_T(H_2O)))$$

for λ_2. $N_T(H_2O)$ is the total column density of water vapour above $z=h$.

Therefore the right hand side of 8.2 will approach zero more rapidly for λ_2 than for λ_1 and $j_{\lambda_1}(z)$ will decrease more rapidly than $j_{\lambda_2}(z)$.

From the above $j_{\lambda_i}(z)$ will be affected by water vapour, but it will also depend on the molecular oxygen density. Therefore in any computer simulation of the experiment (Section 8.3) the calculated $j_{\lambda_i}(z)$ will depend on the model densities chosen. Comparison of theoretical and experimental $j_{\lambda_i}(z)$ will not be useful since any difference between them could be caused by a difference between the model $n(O_2)$ and the $n(O_2)$ at the time of the experiment, as well as the presence of water vapour.

However, if the ratio $R(z) = j_{\lambda_1}(z)/j_{\lambda_2}(z)$ is considered, the mol. oxygen term in the exponent cancels, and the parameter is independent of the model $n(O_2)$ densities. From the previous discussion on the behaviour of $j_{\lambda_1}(z)$ and $j_{\lambda_2}(2)$ it will reflect the presence of water vapour. If the behaviour of the ratio can be calibrated in some way against the concentration of water vapour, then, experimental determination of the extinction coefficients of λ_1 and λ_2 will enable a measure of $n(H_2O)$.

The technique was less simple in practice. The use of broad band detectors where one detector saw the broad band equivalent of λ_1, and the other the broad band equivalent of λ_1 and λ_2, meant that σ_{EFF} had to be used. This parameter was not the same for the two chambers. Therefore the ratio was not independent of the assumed model $n(O_2)$ density. Computer simulation of the experiment, however, showed that the ratio was far more sensitive to the presence of water vapour than changes in $n(O_2)$. The above ratio still varied with $n(H_2O)$ but the sensitivity of the experiment was less.

As has already been stated in Chapter 3, LEB, MEB and LEC ion chambers (see Table 3.1, page 72 for explanation of code) were used in the water vapour experiment. In addition, on the last pair of rockets (Section 8.4.2.3) the results of LNO and MNO ion chambers were considered. The initial experiment involved the comparison of the extinction curves of LEB and LEC chambers. (Their spectral response is given in 3.11c and 3.11d). The sensitivity of the ratio of their extinction coefficients to water vapour arose from lines such as $\lambda = 1126$Å where $\sigma_{H_2O}/\sigma_{O_2} \approx 47$. For the last pair of rockets application of the technique was based on the difference in the absorption cross-sections at $L\alpha$. From Table 4.3, $\sigma_{H_2O}/\sigma_{O_2} \approx 1490$.

8.3 COMPUTER SIMULATION OF EXPERIMENT

It was mentioned in the previous section that it was necessary to calibrate, in some way, the behaviour of the ratio $R(z)$ against $n(H_2O)$. It was decided to simulate the experiment on the computer, using model $n(O_2)$ and fixed values of water vapour concentrations, i.e. 1 ppm, 10 ppm, 100 ppm, and 1000 ppm, and to compare the subsequent theoretical $R(z)$ with the flight $R(z)$ when it became available. This approach had the advantage that the programme could be initially used to test the feasibility of the experiment.

Discussion of the molecular oxygen experiment has shown that a rocket-borne experiment is associated with unavoidable uncertainties. Therefore, if, for example, 10 ppm of water vapour were to be detected the difference between $R'(z)$ for 10 ppm and $R(z)$ for a pure oxygen atmosphere would have to be greater than the expected uncertainty associated with the experimental $R(z)$. The conclusions drawn from the theoretical ratios are discussed in Section 8.5.

The programme was, in many ways, similar to the calculation of the effective absorption cross section programme discussed in Section 4.2.4. The theoretical signal and extinction coefficient, at any height $z = h_k$, was calculated by a step by step calculation of the absorption from $z = 200$ kms down to $z = h_k$. Using a variation of 4.15

$$\phi(\lambda, h_k) = \phi(\lambda, h_{k+1}).e^{-(F.\ \sigma'(\lambda).\Delta h)} \tag{8.3}$$

and the signal

$$S(h_k) = \int_{\lambda_2}^{\lambda_2} \phi(\lambda, h_k).\varepsilon(\lambda).d\lambda$$

and the extinction coefficient $\quad j(h_k) = \dfrac{S(h_k)}{S(200)}$

since $z = 200$ was taken as infinity,

λ_1, λ_2 are the passband limits.

$\varepsilon(\lambda)$ is the sensitivity - the spectral response curves of the flight chambers were used,

F = optical depth factor,

Δh = path length taken as 1 km,

$\phi(\lambda,200)$ the flux from Brinkman *et al* (1966)

and $\sigma'(\lambda)$ is the absorption cross section which allows for the presence of water vapour

$$\sigma'(\lambda) = \sigma_{H_2O}(\lambda).n(H_2O) + \sigma_{O_2}(\lambda).n(O_2).$$

Once $j(h_k)$ had been determined for each chamber the relevant ratios were calculated.

8.4 THE ROCKET EXPERIMENTS

The water vapour experiment was flown on six rockets fired during the years 1973 to 1975. Table 8.1 summarizes the appropriate launch parameters.

The rockets used were known as Cockatoo rockets and a brief description of this vehicle is given in Section 8.4.1. These rockets were not attitude controlled and some means of determining detector aspect was essential. Discussion of this is not relevant to this chapter, but a description of the methods employed has been given in Appendix 3. The flight performance of each rocket and payload is given in Section 8.4.2.

8.4.1 Description of the Cockatoo Vehicle

The Cockatoo rocket was a two stage, solid propellant, spin stabilized rocket, capable of carrying an eighteen kilogram payload to a height of approximately 130 kms. The instrumentation head was the same

TABLE 8.1 DETAILS OF ROCKETS INVOLVED IN WATER VAPOUR RESEARCH PROGRAMME. ALL WERE LAUNCHED FROM WOOMERA (30.94° S, 136.52° E)

Name of Rocket	Date of Flight	Firing* Local (UT)	Apogee
C1044	15/8/73	9.01CST (23.31)	124
C1046	26/6/74	9.15CST (23.45)	120
C4009	2/10/74	8.20CST (22.50)	132
C4007	2/10/74	17.25CST (07.55)	137
C4018	29/4/75	9.15CST (23.45)	133.5
C4017	29/4/75	16.55CST (07.25)	-

* UT times for C1044, C1046, C4009 and C4018 refer to previous day.

diameter as the second stage motor and provided a cylinder of 12.7 cm o.d. and 75 cms long for experimental payloads. The nose cone was generally not available for use by experimenters as this housed a battery pack and magnetometers. The general configuration of the vehicle can be seen in Figure 8.1.

The telemetry system was an EMI TM5H. This provided 24 data channels which could be sampled either 80 or 160 times per second. The greater speed was used for the Cockatoo rockets from C4009 onwards. A feature of the system was the capability of subcommutating channels, so that up to 8 different outputs could be looked at on a single channel. On the Cockatoos being discussed two channels were subcommutated. The outputs from power supply monitors, thermisters and the calibration voltages of the telemetry system were usually given these 1/8 channels as they could tolerate the slower sampling rate.

The telemetred signals received by the ground station were recorded on magnetic tape and film. Chart recorders were used to give real time displays of flight transmission.

The vehicles were launched from a single rail launcher at approximately 85° elevation. Azimuth was typically 320°. Both azimuth and elevation were, however, determined by local weather conditions and constraints imposed on the allowable range and bearing of the impact points of the first and second stages of the rocket.

At zero time the first stage motor and the second stage igniter delay fuse were ignited. The first stage burnt for approximately 2.5 seconds, providing a maximum acceleration of the order of 100 g. At +3 seconds, the first stage was separated from the second stage and the

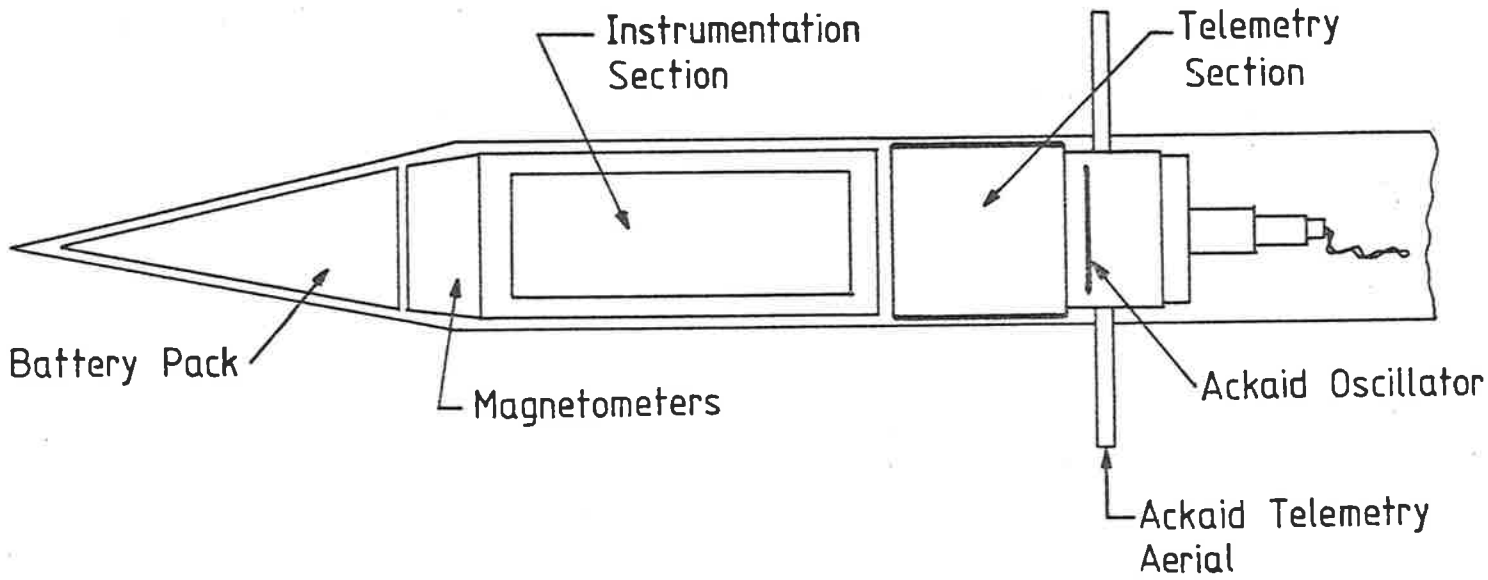

Fig. 8.1 General configuration of Cockatoo Rocket.

instrumentation head. This section coasted until the second stage ignited at approximately + 20 secs. The second stage was burnt out by + 26 secs but remained with the instrumentation head. The covers were released from the experiments at + 30 sec. Low tension power supplies were on at launch, but the switching on of the high tension supplies, should they be required, could be delayed to suit the convenience of the experimenter.

Some rockets were fitted with an Ackaid Oscillator, which assisted the radar tracking of the vehicle, but irrespective of this, the tracking gave a nominal accuracy to the altitude determination of ± ½ km.

Nominal apogee was at 130 km at approximately +2 mins 55 secs. Parachutes were not used and destructive impact occurred at approximately 6 mins.

8.4.2. Performance of Vehicles

All the Cockatoo rockets carried similar experimental payloads. A schematic of a typical instrumentation head is given in Fig. 8.2. The experiments included were

(a) UV photometers to measure ozone density profiles,

(b) Ion chambers to measure molecular oxygen profiles from 70 kms to apogee. The ion chambers used were LNO, MNO and QT (Ilyas, 1976),

(c) X-ray detectors to measure total density profiles, (Bibbo, 1977),

(d) Ion chambers to determine an upper limit to the water vapour density. The ion chambers used were either LEC and LEB or LEB and MEB.

The electronic circuitry used to convert the ion chamber signal to one suitable for the input of the telemetry sender, the prelaunch care

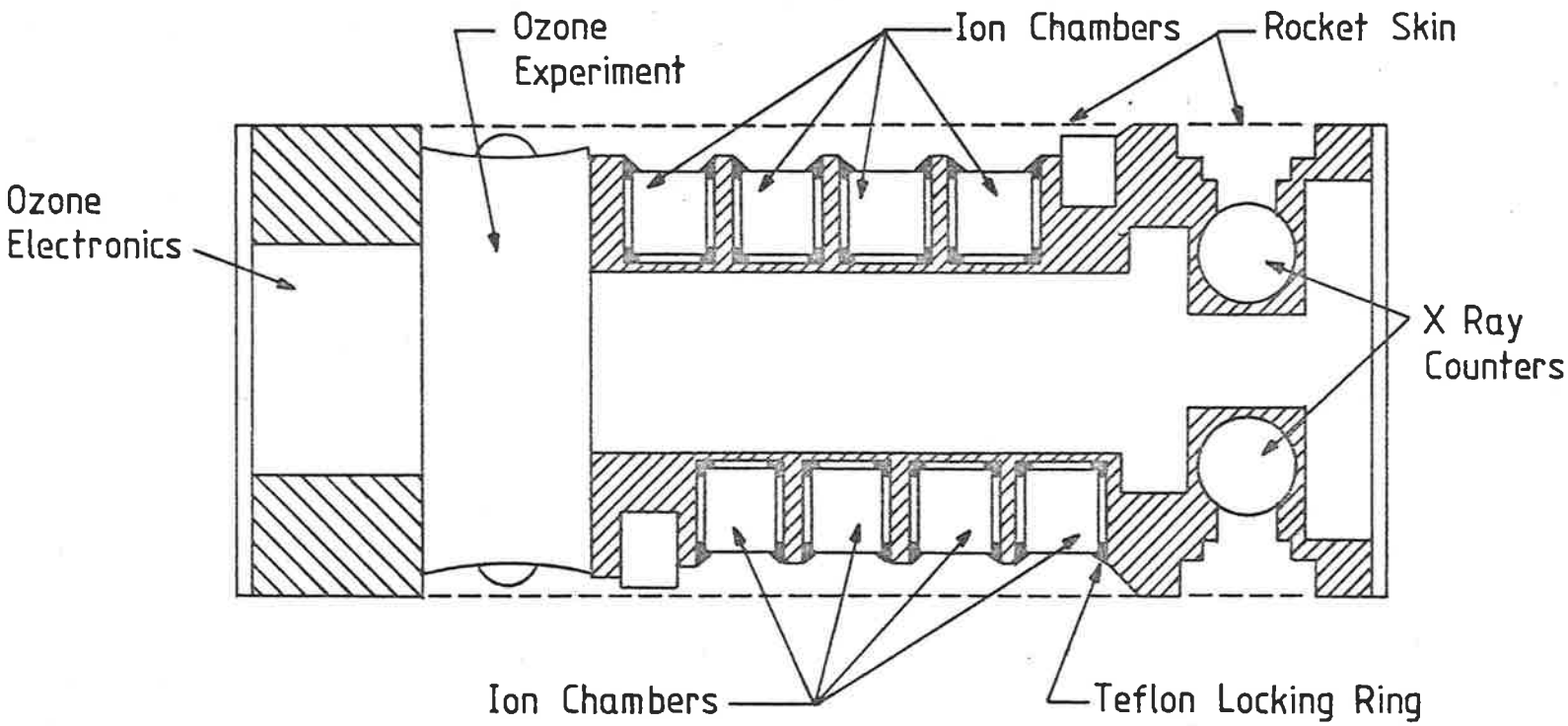

Fig. 8.2 Instrumentation Head for Cockatoo Rocket.

and the testing of the ion chambers of experiment (d) was practically identical to that given in Chapter 5 for the molecular oxygen experiments flown on the Skylark rockets and is, therefore, not described again.

As with the other rockets the payloads were flushed continuously with dry nitrogen once the rocket was on the launcher.

8.4.2.1 C1044 and C1046

Cockatoo rockets were intended to be spin stabilized vehicles. Both C1044 and C1046 failed to spin up successfully after launch. The spin rate obtained, $\approx$ 1 to 2 revs/min, was insufficient for stability and the subsequent motion of the vehicle prevented the acquisition of useful data.

8.4.2.2 C4009 and C4007

Launched in the morning and evening of the same day both C4009 and C4007 performed satisfactorily. They reached a spin rate of 8.4 revs/sec and their motion consisted of a stable precession with a coning angle of approximately 25°.

However, the LEC chambers used failed, showing excessive noise and long wavelength sensitivity. Information from only one set of chambers, in this case LEB's, was inadequate for the technique and no estimations of water vapour were possible.

8.4.2.3 C4017 and C4018

Because of motor malfunction C4017 was only airborne for 30 secs, and only reached a height of 30 kms. It is not considered further.

C4018 was stable spinning at 11 revs/sec, and precessing with a coning angle of $\approx 30°$. The water vapour experiment on this round had been modified. LEC's had not been used because of their failure on C4009 and C4007, and it was hoped to use the results from the LNO, MNO chambers of (b) in combination with those from LEB and MEB chambers.

Both LEB's and LNO chambers had been flown on C4009 and C4008, but here no useful information had been gained because the LNO chambers exhibited changing sensitivities (Ilyas, 1976) which led to uncertainties that were too large for the technique. However, the chambers in C4018 were type II ion chambers, and with their improved stability. (Section 3.2.10), it was hoped to obtain data of sufficient quality.

The data was not obtained. The chambers, although stable during flight, had apparently deteriorated before launch or at launch. Signal levels were low. The telemetry uncertainty therefore introduced a large uncertainty and the quality of the data was insufficient to enable any determination of water vapour densities.

8.5 THE VIABILITY OF THE WATER VAPOUR EXPERIMENT AND SOME COMMENTS ON LIKELY DENSITIES

8.5.1 Viability of Experiment

It was stated in 8.3 that if a particular concentration of water vapour was to be detected, then the difference between $R'(z)$, the ratio with the water vapour, and $R(z)$, the ratio in a pure oxygen atmosphere, would have to be greater than the uncertainty associated with the experimental ratio, $R_E(z)$.

In the computer programme, the extinction coefficient $j(h_k)$ of the chamber was effectively defined as

$$j(h_k) = \frac{\int_{\lambda_1}^{\lambda_2} \phi(\lambda, h_k).\ \varepsilon(\lambda).d\lambda}{\int_{\lambda_1}^{\lambda_2} \phi(\lambda,\infty).\varepsilon(\lambda).d\lambda}$$

The $j(h_k)$ calculated by the flight data is given by

$$j(h_k) = \frac{V(h_k)}{V(\infty)} = \frac{\beta.\int_{\lambda_1}^{\lambda_2} \phi(\lambda, h_k).\varepsilon(\lambda)d\lambda}{\beta \int_{\lambda_1}^{\lambda_2} \phi(\lambda, H).\varepsilon(\lambda).d\lambda}$$

V is the telemetred voltage, H is well above the absorbing layer and β allows for the amplifier calibrations, the efficiency and the window area of the chamber. Since β cancels, and on the above definition of H, $\phi(\lambda, H)$ will be equivalent to $\phi(\lambda, \infty)$, the two definitions are equivalent, enabling valid comparison. In addition, and of importance also, independence of β implies that the $j(h_k)$ for either chamber, and therefore, the experimental ratio

$$R_E = \frac{j_A(h_k)}{j_B(h_k)} \tag{8.5}$$

where A and B denotes either LEC and LEB, LEB and LNO, or MEB and MNO, will not be affected by uncertainties in amplifier calibration, efficiencies and window areas.

R_E is independent of aspect. Equation 8.5 equals

$$\frac{V_A(h_k).\ A(h_k)}{V_A(\infty).\ A(\infty)} \Big/ \frac{V_B(h_k).\ A(h_k)}{V_B(h_k).\ A(\infty)} \tag{8.6}$$

where V_A, V_B are the telemetred voltages of the chambers and A allows for a change of aspect between $z = \infty$ and $z = h_k$ and corrects the signal back to zero aspect to allow a true evaluation of $j_A(h_k)$ and $j_B(h_k)$. Equation 8.6 reduces to

$$\frac{V_A(h_k)}{V_B(h_k)} \cdot \frac{V_B(\infty)}{V_A(\infty)}$$

Therefore uncertainties in the determination of the aspect or the calibration of the angular response of the chambers will not contribute to the uncertainty of the experimental ratio.

It was considered the only significant source uncertainty in the ratio was the result of the telemetry uncertainty ($\delta V \approx 25$ mV). The effect of this was much reduced in this instance. In the molecular oxygen experiment where ΔV (i.e. the change in signal) was required, δV rapidly became the limiting factor as it approached, and exceeded the magnitude of ΔV, thereby forcing a lessening of the resolution of the analysis. However, for the water vapour experiment, where the ratio depends on V not ΔV, results from the present work imply that under favourable conditions the uncertainty in the ratio would range from 2% to 12%.

With these size uncertainties, the results of the feasibility studies suggested 10 ppm could be detected. Although Hall (1972) had suggested 3 ppm, the Martynkevich (1972) profile was consistent with, for example, approximately 10 ppm at 100 kms and it appeared the experiment would provide useful information about water vapour densities.

Through equipment failure, however, no useful data was obtained (Section 8.4), but even if good quality signals had been received a concentration as low as 10 ppm could not have been detected. The previously mentioned mistake in the computer program, when corrected, raised the minimum detectable concentration from 10 ppm to 50 to 100 ppm. Although concentrations of this magnitude have been observed (for example, Sonnemann *et al*, 1977, reported a concentration of 500 ppm at 115 kms) most theoretical and experimental estimates of $n(H_2O)$ at upper mesospheric heights are far less (e.g. Radford *et al*, 1977; Anderson and Donahue, 1975; Fukuyama, 1974).

From this it can only be concluded that it is unlikely the water vapour experiment would have provided data of any significance and that

the experiment must be considered of doubtful viability.

8.5.2 A Comment on Likely Densities

Despite the failure to obtain information about $n(H_2O)$ at 70 kms to 100 kms a tentative suggestion about the water vapour concentrations over the altitude range $\approx$ 110 to 118 kms, can be made. This does not necessarily have general application since the figures are restricted to those drawn from the data of a single rocket flight above Woomera (30.94° S, 136.52° E) on 22/2/77.

The molecular oxygen profiles derived from the QT and LNO ion chambers overlap. Initially, the two profiles showed gross disagreement. Since, as tables 4.4 and 4.5 showed, QT results are not affected by the presence of water vapour while $L\alpha$ ion chamber results are, an explanation was sought for the difference by assuming the presence of water vapour. At some altitudes concentrations of H_2O of 100 ppm were required to reconcile the two profiles. It is interesting to note that had the water vapour experiment been flown successfully on this rocket, it would have, even with the reduced sensitivity, confirmed or denied this solution.

Then it was shown that the other wavelengths of the $L\alpha$ chamber should be taken into account (Section 4.2.6). This also reconciled the two profiles and the presence of water vapour was not necessary.

Despite this conclusion, drawn because agreement between the two profiles was well within their combined uncertainties (Fig 4.10), water vapour could still have been present. However, even if the residual differences between the two profiles (the more reliable downleg data was considered) were caused by water vapour rather than statistical fluctuations, then the concentration of water vapour, for example at 115 kms, had an upper limit of 5 ppm.

APPENDIX 1

THE EFFECT OF CONTAMINATION ON THE STANDARD ION CHAMBER CALIBRATIONS

It was stated in Section 3.2.6.4 that a systematic error may occur in the standard ion chamber calibration as the result of the contamination of the nitric oxide. This appendix attempts to identify likely contaminants and their effect on the calibration.

The gas was supplied by the Matheson Corporation through C.I.G. Australia. C.I.G. listed possible contaminants as Nitrous Oxide (N_2O) [.05%], Nitrogen dioxide (NO_2) [.05%], Carbon dioxide (CO_2) [.2%] and Nitrogen (N_2) [.05%]. Other users of this gas (Stober, 1962; Melia, 1965) also listed nitrous acid (HNO_2), oxygen (O_2), water (H_2O), nitrous anhydride (N_2O_3), nitric pentoxide (N_2O_5) and nitrogen tetroxide (N_2O_4).

The slush mixture used during the purification process was at - 80° C and removed such contaminants as NO_2, CO_2, N_2O_5, N_2O_3, H_2O and N_2O_4. Because of its unstable state there appears to have been few measurements of the physical constants of HNO_2 (Jones, 1973) and it is unclear whether the slush mixture would remove this contaminant. However, Melia (1965) only lists this as a trace element and does not suggest it will cause problems. It is not considered further. From the specifications set out by C.I.G. and Melia (1965), it surmised that the concentrations of N_2 or O_2 will be $\ll$ .05% and at these concentrations neither gas is expected to significantly affect the response of the chamber.

From the above the only significant contaminant would appear to be N_2O. Melia (1965) found evidence to suggest that at the pressures normally found in commercially supplied gas cylinders, the N_2O concentration would be increased by 2% to 3% per month. The likely reaction

was

$$3NO \rightarrow N_2O + NO_2$$

The cylinder of nitric oxide used in the present work was 8 years old. The initial contamination of N_2O could be considered to be within the .05% suggested by C.I.G. and the 1% measured by Melia (1965). From this and from the range of accumulation rates (2% to 3%) the likely contamination by N_2O was 1% to 7%.

The absorption coefficient, for N_2O, at $L\alpha$ is almost identical to that of NO (Watanabe *et al*, 1953). Therefore, in the standard ion chamber, it would be expected that the relative amount of the incoming $L\alpha$ radiation absorbed by N_2O would be approximately equal to the relative level of contamination, i.e. if N_2O makes up 7% of the gas then it will absorb 7% of the incident radiation.

There will be no contribution to the signal from the absorption of $L\alpha$ radiation by N_2O since the ionization threshold of N_2O occurs at approximately 967Å. Absorption of $L\alpha$ will result in photolysis, the products of which will be NO, N, O and N_2. Some fluorescence will occur, for example at 5577Å from $O('S) \rightarrow O('D)$ transition of atomic oxygen but such radiation will not be detected by the standard ion chamber.

Referring back to Section 3.2.6.4 this will imply an under-estimation of the current measured at total absorption, I_{ABS}. From equation 3.4, repeated below,

$$Q_L = 81 \times \frac{I_L}{I_{ABS}}$$

an under-estimation of I_{ABS} leads to an over-estimation of Q_L, where Q_L is the efficiency of the chamber/photodiode being calibrated. I_L is the signal from the chamber/photodiode.

It is noted that the likely upper limit to the effect, i.e. 7%, would be sufficient to explain the discrepancy between the efficiency of the photo-diode, as stated in the accompanying National Bureau of Standards calibration, and the measurement made with the standard ion chamber.

APPENDIX 2

TABULATIONS OF MOLECULAR OXYGEN DENSITIES.

CHAMBER / ALT(kms)	QT 203 UPLEG	QT 204 UPLEG	QT 204 DOWNLEG	SX 3 UPLEG	SX 3 DOWNLEG		Spectro meter DOWNLEG
98		3.58(18)	1.58(18)				
99	1.20(18)	2.09(18)	1.22(18)				
100	9.67(17)	1.50(18)	1.01(18)				
101	8.10(17)	1.25(18)	8.02(17)				
102	6.74(17)	9.74(17)	6.42(17)				
103	5.87(17)	6.74(17)	4.46(17)		4.48(17)		
104	4.66(17)	4.87(17)	3.72(17)		2.80(17)		
105	3.22(17)	3.66(17)	2.83(17)		2.02(17)		
106	2.21(17)	2.68(17)	2.28(17)		1.98(17)		
107	1.62(17)	2.03(17)	1.87(17)		1.91(17)		
108	1.21(17)	1.55(17)	1.54(17)	6.79(17)	1.77(17)		1.05(17)
109	8.22(16)	1.23(17)	1.29(17)	3.62(17)	1.62(17)		9.56(16)
110	4.24(16)	1.07(17)	1.06(17)	2.86(17)	1.56(17)		8.63(16)
111		9.11(16)	9.11(16)	2.11(17)	1.38(17)		8.10(16)
112		7.98(16)	8.24(16)	1.81(17)	1.21(17)		7.76(16)

TABLE A.2a. Molecular Oxygen Densities from Skylark SL1005

CHAMBER / ALT(kms)		QT 204 UPLEG	QT 204 DOWNLEG	SX 3 UPLEG	SX 3 DOWNLEG	Spectro meter UPLEG	Spectro meter DOWNLEG
113		7.49(16)	7.48(16)	1.54(17)	1.05(17)	3.53(17)	7.30(16)
114		6.70(16)	6.61(16)	1.33(17)	9.60(16)	1.70(17)	6.93(16)
115		6.27(16)	5.77(16)	1.28(17)	8.40(16)	1.10(17)	6.45(16)
116		5.59(16)	5.46(16)	1.23(17)	7.51(16)	8.21(16)	6.23(16)
117		4.87(16)	4.73(16)	1.03(17)	6.32(16)	6.88(16)	6.29(16)
118		4.20(16)	3.96(16)	1.04(17)	5.50(16)	6.26(16)	6.01(16)
119		3.69(16)	3.55(16)	1.02(17)	4.90(16)	5.75(16)	5.64(16)
120		3.40(16)	3.21(16)	9.70(16)	4.76(16)	5.37(16)	5.45(16)
121		2.91(16)	2.85(16)	9.89(16)	4.13(16)	4.91(16)	5.04(16)
122		2.62(16)	2.60(16)	1.06(17)	3.55(16)	4.41(16)	4.54(16)
123		2.41(16)	2.32(16)	1.14(17)	3.33(16)	3.82(16)	4.29(16)
124		2.14(16)	2.09(16)	1.09(17)	2.82(16)	3.19(16)	3.95(16)
125		1.90(16)	1.92(16)	1.10(17)	2.46(16)	2.68(16)	3.31(16)
126		1.69(16)	1.57(16)	9.18(16)	2.12(16)	2.30(16)	2.68(16)
127		1.47(16)	1.55(16)	5.35(16)	1.78(16)	1.85(16)	1.94(16)

TABLE A.2a Continued.....

CHAMBER / ALT(kms)		QT 204 UPLEG	QT 204 DOWNLEG	SX 3 UPLEG	SX 3 DOWNLEG	Spectro meter UPLEG	Spectro meter DOWNLEG
128		1.25(16)	1.30(16)	3.43(16)	1.51(16)	1.41(16)	1.21(16)
129		1.13(16)		2.21(16)	1.20(16)	1.35(16)	
130		1.06(16)		1.74(16)		1.27(16)	
131		9.82(15)		1.35(16)		1.12(16)	
132		8.77(15)		1.19(16)		1.06(16)	
133		7.84(15)		1.05(16)		1.02(16)	
134		7.14(15)		8.42(15)		9.58(15)	
135		5.91(15)		7.98(15)		8.30(15)	
136		4.91(15)		7.74(15)		7.65(15)	
137		4.13(15)		6.35(15)		6.70(15)	
138		3.26(15)		5.54(15)		5.10(15)	
139		2.82(15)		4.85(15)		4.14(15)	
140		2.70(15)		4.29(15)		3.51(15)	
141		2.05(15)		3.84(15)		2.88(15)	
142		2.37(15)		3.41(15)		2.88(15)	

Table A.2a continued.....

CHAMBER / ALT(kms)		QT 204 UPLEG		SX 3 UPLEG			
143		2.26(15)		3.13(15)			
144		2.04(15)		2.96(15)			
145		2.36(15)		2.84(15)			
146		1.72(15)		2.78(15)			
147		1.50(15)		2.66(15)			
148		1.28(15)		2.45(15)			
149				2.24(15)			
150				2.08(15)			
151				1.98(15)			
152				1.97(15)			
153				1.96(15)			
154				1.95(15)			
155				1.95(15)			
156				1.87(15)			
157				1.81(15)			

Table A.2a continued.....

CHAMBER / ALT(kms)	QT 1 UPLEG	QT 1 DOWNLEG	SX 7 UPLEG	SX 7 DOWNLEG
100		1.14(18)		
101		8.44(17)		
102		6.72(17)		
103		4.79(17)		
104		3.88(17)		
105		3.09(17)		
106		2.58(17)		
107		2.25(17)		
108		1.93(17)		
109		1.64(17)		
110		1.44(17)		
111		1.30(17)		
112		1.17(17)		
113		1.01(17)		
114	1.04(17)	8.89(16)		
115	8.50(16)	8.26(16)		1.15(17)
116	7.32(16)	7.43(16)		9.55(16)
117	6.55(16)	6.07(16)		8.77(16)
118	5.76(16)	5.47(16)		8.38(16)
119	4.93(16)	4.68(16)		7.32(16)
120	4.26(16)	4.04(16)	2.97(17)	7.03(16)
121	3.88(16)	3.81(16)	1.27(17)	5.90(16)
122	3.52(16)	3.19(16)	7.10(16)	5.26(16)
123	3.19(16)	2.88(16)	5.25(16)	4.54(16)
124	2.95(16)	2.70(16)	4.28(16)	3.99(16)
125	2.68(16)	2.41(16)	3.68(16)	3.73(16)
126	2.32(16)	2.17(16)	3.09(16)	3.21(16)

Table A.2b Molecular oxygen densities from Skylark SL1207.

CHAMBER / ALT(kms)	QT 1 UPLEG	QT 1 DOWNLEG	SX 7 UPLEG	SX 7 DOWNLEG
127	2.06(16)	1.99(16)	2.64(16)	2.65(16)
128	1.78(16)	1.76(16)	2.30(16)	2.26(16)
129	1.61(16)	1.69(16)	1.92(16)	1.96(16)
130	1.42(16)	1.47(16)	1.84(16)	1.86(16)
131	1.32(16)	1.22(16)	1.63(16)	1.63(16)
132	1.21(16)	1.02(16)	1.51(16)	1.55(16)
133	1.08(16)	9.13(15)	1.26(16)	1.29(16)
134	1.04(16)	8.84(15)	1.10(16)	1.22(16)
135	9.34(15)	8.07(15)	9.78(15)	1.07(16)
136	8.92(15)	7.32(15)	8.96(15)	9.86(15)
137	8.38(15)	6.34(15)	8.34(15)	8.42(15)
138	7.97(15)	5.38(15)	7.89(15)	7.02(15)
139	7.45(15)	4.90(15)	7.46(15)	6.51(15)
140	7.05(15)	4.42(15)	7.05(15)	5.84(15)
141	6.54(15)		6.59(15)	5.18(15)
142			6.29(15)	4.68(15)
143			5.99(15)	4.02(15)
144			5.58(15)	3.73(15)
145			5.51(15)	3.61(15)
146			5.44(15)	3.41(15)
147			4.98(15)	3.22(15)
148			4.54(15)	2.86(15)
149			4.11(15)	2.51(15)
150			3.95(15)	2.33(15)
151			3.85(15)	2.27(15)
152			3.69(15)	2.18(15)
153			3.47(15)	2.10(15)

Table A.2b continued.....

CHAMBER ALT(kms)			SX 7 UPLEG	SX 7 DOWNLEG
154			3.08(15)	1.96(15)
155			2.87(15)	1.74(15)
156			2.49(15)	1.58(15)
157			2.12(15)	1.35(15)
158			1.81(15)	1.13(15)
159			1.38(15)	

Table A.2b continued.....

ALT(kms)	SX5 DOWNLEG		ALT(kms)	SX 5 DOWNLEG
112.5	6.86(16)		142.5	7.10(15)
115	6.30(16)		145	6.15(15)
117.5	5.02(16)		147.5	4.93(15)
120	4.34(16)		150	4.53(15)
132.5	3.78(16)		152.5	4.34(15)
125	3.12(16)		155	4.72(15)
127.5	2.57(16)		157.5	5.38(15)
130	1.98(16)		160	5.02(15)
132.5	1.49(16)		162.5	5.08(15)
135	1.15(16)		165	5.23(15)
137.5	9.23(15)		167.5	4.56(15)
140	7.98(15)		170	3.76(15)
			172.5	3.40(15)

Table A.2c Molecular oxygen numbers from Skylark SL1207

ALT(kms)	SX 5 UPLEG	SX 5* DOWNLEG
133	4.92(16)	1.43(16)
136	1.50(16)	1.06(16)
139	1.06(16)	8.14(15)
142	8.90(15)	7.0 (15)
145	7.02(15)	5.8 (15)
148	5.66(15)	4.8 (15)
151	5.26(15)	4.4 (15)
154	4.63(15)	4.5 (15)
157	4.32(15)	5.0 (15)

Table A.2d.

* Numbers read of graph to enable direct comparison of upleg and downleg.

CHAMBER / ALT(Kms)	MNO 1 UPLEG UNCORRECTED	MNO 1 UPLEG CORRECTED	MNO 1 DOWNLEG UNCORRECTED	MNO 1 DOWNLEG CORRECTED	LNO 202 UPLEG UNCORRECTED	LNO 202 UPLEG CORRECTED	LNO 202 DOWNLEG UNCORRECTED	LNO 202 DOWNLEG CORRECTED
78			7.39(19)	7.36(19)			6.66(19)	6.62(19)
79			6.82(19)	6.79(19)			5.82(19)	5.78(19)
80			6.70(19)	6.67(19)			4.62(19)	4.59(19)
81			5.36(19)	5.32(19)			3.49(19)	3.46(19)
82			4.19(19)	4.16(19)			2.83(19)	2.80(19)
83			3.45(19)	3.42(19)			2.17(19)	2.15(19)
84			2.92(19)	2.89(19)	4.04(19)	4.01(19)	1.71(19)	1.69(19)
85	6.09(19)	6.06(19)	2.42(19)	2.39(19)			1.45(19)	1.43(19)
86			2.04(19)	2.01(19)	3.05(19)	3.02(19)	1.15(19)	1.13(19)
87	4.10(19)	4.06(19)	1.67(19)	1.64(19)			1.03(19)	1.00(19)
88			1.51(19)	1.48(19)	2.06(19)	2.03(19)	9.30(18)	9.05(18)
89	2.76(19)	2.73(19)	1.27(19)	1.24(19)			7.81(18)	7.57(18)
90			1.06(19)	1.04(19)	1.43(19)	1.40(19)	6.36(18)	6.14(18)
91	1.95(19)	1.92(19)	9.53(18)	9.26(18)			5.57(18)	5.35(18)
92			7.95(18)	7.69(18)	1.05(19)	1.02(19)	4.67(18)	4.46(18)

TABLE A.2e Molecular oxygen numbers from Aerobee 13.123 IS

CHAMBER / ALT(Kms)	MNO 1 UPLEG UNCORRECTED	MNO 1 UPLEG CORRECTED	MNO 1 DOWNLEG UNCORRECTED	MNO 1 DOWNLEG CORRECTED	LNO 202 UPLEG UNCORRECTED	LNO 202 UPLEG CORRECTED	LNO 202 DOWNLEG UNCORRECTED	LNO 202 DOWNLEG CORRECTED
93	1.37(19)	1.33(19)	6.61(18)	6.36(18)			4.24(18)	4.01(18)
94			6.10(18)	5.83(18)	7.21(18)	6.90(18)	3.84(18)	3.61(18)
95	8.62(18)	8.30(18)	5.16(18)	4.88(18)			3.38(18)	3.13(18)
96			4.37(18)	4.10(18)	4.57(18)	4.27(18)	2.81(18)	2.56(18)
97	5.41(18)	5.10(18)	3.71(18)	3.42(18)			2.34(18)	2.08(18)
98			3.22(18)	2.88(18)	2.83(18)	2.51(18)	2.14(18)	1.83(18)
99	3.47(18)	3.12(18)	2.61(18)	2.24(18)			1.84(18)	1.48(18)
100	2.70(18)	2.33(18)	2.08(18)	1.67(18)	1.82(18)	1.42(18)	1.53(18)	1.14(18)
101	2.15(18)	1.72(18)	1.80(18)	1.32(18)	1.49(18)	1.06(18)	1.26(18)	8.54(17)
102	1.79(18)	1.30(18)	1.59(18)	1.03(18)	1.28(18)	8.11(17)	1.01(18)	6.31(17)
103	1.49(18)	9.48(17)	1.36(18)	7.71(17)	1.04(18)	5.91(17)	8.85(17)	5.07(17)
104	1.28(18)	7.07(17)	1.16(18)	5.74(17)	8.51(17)	4.36(17)	7.92(17)	4.15(17)
105	1.07(18)	5.21(17)	9.89(17)	3.47(17)	7.09(17)	3.31(17)	7.33(17)	3.53(17)
106	9.02(17)	3.86(17)	8.91(17)	3.45(17)	5.69(17)	2.43(17)	6.66(17)	2.95(17)
107	7.85(17)	3.01(17)	8.15(17)	2.79(17)	4.86(17)	1.94(17)	5.63(17)	2.30(17)

TABLE A.2e Continued.....

CHAMBER / ALT(Kms)	MNO 1 UPLEG UNCORRECTED	MNO 1 UPLEG CORRECTED	MNO 1 DOWNLEG UNCORRECTED	MNO 1 DOWNLEG CORRECTED	LNO 202 UPLEG UNCORRECTED	LNO 202 UPLEG CORRECTED	LNO 202 DOWNLEG UNCORRECTED	LNO 202 DOWNLEG CORRECTED
108	7.98(17)	2.73(17)	7.21(17)	2.20(17)	4.44(17)	1.65(17)	4.76(17)	1.82(17)
109	6.46(17)	1.99(17)	6.18(17)	1.64(17)	4.29(17)	1.50(17)	4.67(17)	1.67(17)
110	5.90(17)	1.49(17)	5.27(17)	1.26(17)			4.27(17)	1.43(17)
111	5.46(17)	1.33(17)	4.28(17)	9.30(16)	3.20(17)	9.81(16)	3.35(17)	1.05(17)
112	3.65(17)	7.82(16)	3.59(17)	7.10(16)			3.04(17)	9.08(16)
113	4.00(17)	7.64(16)	3.20(17)	5.75(16)	2.37(17)	6.61(16)	3.03(17)	8.62(16)
114	3.20(17)	5.56(16)	2.61(17)	4.35(16)			2.87(17)	7.72(16)
115	2.57(17)	4.04(16)	2.03(17)	3.11(16)	1.43(17)	3.66(16)	2.72(17)	6.96(16)
116	2.13(17)	3.11(16)	1.59(17)	2.32(16)			2.56(17)	6.20(16)
117			1.06(17)	1.49(16)			1.81(17)	4.16(16)
118								

TABLE A.2e continued....

CHAMBER / ALT(kms)	QT 202 UPLEG	QT 202 DOWNLEG	QT 5 UPLEG	QT 5 DOWNLEG		SX 202 DOWNLEG		SX 204 DOWNLEG
109		2.41(17)		2.02(17)				
110	1.47(17)	1.63(17)		1.48(17)				
111	1.41(17)	1.02(17)	1.83(17)	1.05(17)				
112	1.26(17)	7.63(16)	1.23(17)	7.83(16)				
113	1.07(17)	6.05(16)	1.19(17)	5.87(16)				
114	8.73(16)	5.04(16)	8.29(16)	5.07(16)				
115	6.80(16)	4.36(16)	6.13(16)	4.27(16)				
116	5.23(16)	3.88(16)	4.46(16)	3.76(16)				
117	4.25(16)	3.40(16)	3.26(16)	3.60(16)				
118	3.37(16)	2.98(16)	2.84(16)	3.01(16)				
119	2.82(16)	2.67(16)	2.34(16)	2.68(16)		2.26(16)		
120	2.42(16)	2.48(16)	2.22(16)	2.36(16)		2.27(16)		
121	2.05(16)	2.14(16)	1.83(16)	2.18(16)		2.14(16)		3.16(16)
122	1.78(16)	1.94(16)	1.69(16)	1.94(16)		1.69(16)		2.95(16)
123	1.69(16)	1.71(16)	1.51(16)	1.73(16)		1.91(16)		2.54(16)

Table A2.f Molecular oxygen numbers for Aerobee 13.123 IS

CHAMBER / ALT(kms)	QT 202 UPLEG	QT 202 DOWNLEG	QT 5 UPLEG	QT 5 DOWNLEG	SX 202 UPLEG	SX 202 DOWNLEG	SX 204 UPLEG	SX 204 DOWNLEG
124	1.50(16)	1.61(16)	1.38(16)	1.54(16)		1.43(16)		2.22(16)
125	1.37(16)	1.41(16)	1.33(16)	1.44(16)		1.43(16)		1.77(16)
126	1.31(16)	1.29(16)	1.21(16)	1.35(16)	1.31(16)	1.41(16)	1.67(16)	1.65(16)
127	1.24(16)	1.19(16)	1.14(16)	1.22(16)	1.38(16)	1.25(16)	1.48(16)	1.45(16)
128	1.14(16)	1.10(16)	1.09(16)	1.06(16)	1.36(16)	1.11(16)	1.37(16)	1.25(16)
129	1.05(16)	9.57(15)	1.03(16)	9.55(15)	1.40(16)	1.02(16)	1.39(16)	1.14(16)
130	9.86(15)	8.85(15)	9.78(15)	8.75(15)	1.37(16)	9.13(15)	1.23(16)	1.04(16)
131	9.39(15)	8.18(15)	9.39(15)	7.91(15)	1.30(16)	8.18(15)	1.31(16)	9.72(15)
132	9.02(15)	7.19(15)	8.87(15)	7.17(15)	1.16(16)	7.29(15)	1.28(18)	8.59(15)
133	8.57(15)	6.38(15)	8.37(15)	6.46(15)	1.09(16)	6.82(15)	1.23(16)	7.47(15)
134	8.16(15)	5.74(15)	7.92(15)	5.83(15)	1.01(16)	6.14(15)	1.10(16)	7.10(15)
135	7.67(15)	5.45(15)	7.59(15)	5.42(15)	1.02(16)	5.65(15)	1.02(16)	6.15(15)
136	7.18(15)	5.13(15)	7.16(15)	4.97(15)	8.90(15)	5.30(15)	1.02(16)	5.80(15)
137	6.52(15)	4.77(15)	6.56(15)	4.55(15)	8.33(15)	4.75(15)	9.84(15)	5.28(15)
138	5.87(15)	4.31(15)	6.10(15)	4.24(15)	7.66(15)	4.31(15)	9.89(15)	4.78(15)

Table A.2f continued.....

CHAMBER / ALT(kms)	QT 202 UPLEG	QT 202 DOWNLEG	QT 5 UPLEG	QT 5 DOWNLEG	SX 202 UPLEG	SX 202 DOWNLEG	SX 204 UPLEG	SX 204 DOWNLEG
139	5.42(15)	3.78(15)	5.66(15)	3.99(15)	6.92(15)	4.02(15)	9.76(15)	4.51(15)
140	4.92(15)	3.56(15)	5.15(15)	3.66(15)	6.44(15)	3.64(15)	8.92(15)	4.21(15)
141	4.55(15)	3.40(15)	4.68(15)	3.27(15)	6.89(15)	3.32(15)	8.55(15)	3.87(15)
142	4.15(15)	3.19(15)	4.26(15)	2.97(15)	5.36(15)	3.03(15)	8.18(15)	3.44(15)
143	3.81(15)	2.94(15)	3.95(15)	2.74(15)	4.88(15)	2.81(15)	7.69(15)	3.09(15)
144	3.45(15)	2.67(15)	3.65(15)	2.52(15)	4.42(15)	2.60(15)	7.25(15)	2.77(15)
145	3.15(15)	2.43(15)	3.39(15)	2.37(15)	3.92(15)	2.41(15)	6.74(15)	2.54(15)
146	2.91(15)	2.17(15)	3.15(15)	2.18(15)	3.64(15)	2.26(15)	6.35(15)	2.38(15)
147	2.69(15)	1.94(15)	2.86(15)	2.02(15)	3.40(15)	2.17(15)	5.86(15)	2.19(15)
148	2.50(15)	1.79(15)	2.58(15)	1.90(15)	2.91(15)	2.05(15)	5.31(15)	2.06(15)
149	2.35(15)	1.61(15)	2.36(15)	1.72(15)	2.61(15)	1.91(15)	4.87(15)	1.92(15)
150	2.15(15)	1.56(15)	2.17(15)	1.58(15)	2.43(15)	1.74(15)	4.39(15)	1.78(15)
151	1.92(15)	1.49(15)	2.07(15)	1.45(15)	2.20(15)	1.57(15)	3.99(15)	1.69(15)
152	1.74(15)	1.39(15)	1.91(15)	1.34(15)	1.97(15)	1.47(15)	3.59(15)	1.59(15)
153	1.59(15)	1.32(15)	1.77(15)	1.25(15)	1.78(15)	1.38(15)	3.25(15)	1.50(15)

Table A.2f continued.....

CHAMBER / ALT(kms)	QT 202 UPLEG	QT 202 DOWNLEG	QT 5 UPLEG	QT 5 DOWNLEG	SX 202 UPLEG	SX 202 DOWNLEG	SX 204 UPLEG	SX 204 DOWNLEG
154	1.46(15)	1.22(15)	1.65(15)	1.16(15)	1.68(15)	1.30(15)	2.92(15)	1.37(15)
155	1.28(15)	1.20(15)	1.53(15)	1.09(15)	1.57(15)	1.20(15)	2.62(15)	1.25(15)
156	1.16(15)	1.14(15)	1.41(15)	1.01(15)	1.44(15)	1.12(15)	2.37(15)	1.13(15)
157	1.06(15)		1.28(15)	9.70(14)	1.30(15)	1.05(15)	2.17(15)	1.02(15)
158	9.48(14)			9.17(14)	1.22(15)	9.84(14)	1.96(15)	9.40(14)
159	8.50(14)			8.65(14)	1.15(15)	9.27(14)	1.81(15)	8.77(14)
160	7.71(14)			8.23(14)	1.06(15)	8.50(14)	1.69(15)	8.19(14)
161	6.93(14)			7.86(14)	9.94(14)	8.12(14)	1.49(15)	7.94(14)
162					9.22(14)	7.59(14)	1.36(15)	7.45(14)
163					8.54(14)	7.18(14)	1.21(15)	7.11(14)
164					7.93(14)	6.72(14)	1.10(15)	6.73(14)
165					7.36(14)	6.04(14)	9.90(14)	6.39(14)
166					6.85(14)	5.58(14)	8.80(14)	6.00(14)
167					6.42(14)	5.21(14)	8.07(14)	5.63(14)
168					6.05(14)	4.97(14)	7.57(14)	5.19(14)

Table A.2f continued.....

CHAMBER ALT(kms)					SX 202 UPLEG	SX 202 DOWNLEG	SX 204 UPLEG	SX 204 DOWNLEG
169					5.64(14)	4.89(14)	7.13(14)	4.70(14)
170					5.33(14)	4.74(14)	6.70(14)	4.24(14)
171					4.94(14)	4.62(14)	6.47(14)	3.77(14)
172					4.55(14)	4.46(14)		
173					4.25(14)	4.22(14)		

Table A.2f continued.....

TABLE A2.g

The final mean O_2 profile

from SL1005

ALTITUDE	MEAN $n(O_2)$ (m^{-3})	ERROR IN MEAN	ERROR IN MEAN (%)
98	2.58(18)	1.00(18)	39
99	1.50(18)	2.93(17)	20
100	1.16(18)	1.71(17)	15
101	9.54(17)	1.48(17)	16
102	7.63(17)	1.06(17)	14
103	5.39(17)	5.59(16)	10
104	4.01(17)	4.75(16)	12
105	2.93(17)	3.48(16)	12
106	2.29(17)	1.46(16)	6.4
107	1.86(17)	8.62(15)	4.6
108	1.42(17)	1.29(16)	9.1
109	1.18(17)	1.39(16)	12
110	9.95(16)	1.83(16)	18
111	1.00(17)	1.28(16)	13
112	9.02(16)	1.03(16)	11
113	8.19(16)	7.70(15)	9.4
114	7.46(16)	7.17(15)	9.6
115	6.72(16)	5.77(15)	8.6
116	6.20(16)	4.69(15)	7.6
117	5.55(16)	4.35(15)	7.8
118	5.19(16)	4.69(15)	9.1
119	4.71(16)	4.67(15)	9.9
120	4.44(16)	4.79(15)	11
121	3.97(16)	4.71(15)	12
122	3.54(16)	4.18(15)	12
123	3.23(16)	3.86(15)	12

ALTITUDE	MEAN $n(O_2)$ (m^{-3})	ERROR IN MEAN	ERROR IN MEAN (%)
124	2.84(16)	3.47(15)	12
125	2.45(16)	2.62(15)	11
126	2.07(16)	2.03(15)	9.8
127	1.72(16)	8.95(14)	5.2
128	1.34(16)	5.49(14)	4.1
129	1.23(16)	6.43(14)	5.2
130	1.14(16)	7.50(14)	6.6
131	1.05(16)	6.90(14)	6.6
132	9.69(15)	9.15(14)	9.4
133	9.02(15)	1.18(15)	13
134	8.38(15)	7.05(14)	8.4
135	7.40(15)	7.49(14)	10
136	6.77(15)	9.29(14)	14
137	5.73(15)	8.05(14)	14
138	4.63(15)	6.98(14)	15
139	3.94(15)	5.95(14)	15
140	3.50(15)	4.59(14)	13
141	2.92(15)	5.17(14)	18
142	2.89(15)	3.00(14)	10
143	2.70(15)	4.35(14)	16
144	2.50(15)	4.60(14)	18
145	2.60(15)	2.40(14)	9.2
146	2.25(15)	5.30(14)	24
147	2.08(15)	5.80(14)	28
148	1.87(15)	5.85(14)	31
149	2.24(15)	N/A	N/A

ALTITUDE	MEAN $n(O_2)$ (m^{-3})	ERROR IN MEAN	ERROR IN MEAN (%)
150	2.08(15)	N/A	N/A
151	1.98(15)	N/A	N/A
152	1.97(15)	N/A	N/A
153	1.96(15)	N/A	N/A
154	1.95(15)	N/A	N/A
155	1.95(15)	N/A	N/A
156	1.87(15)	N/A	N/A
157	1.81(15)	N/A	N/A

TABLE A2.h

The final mean O_2 profile

from SL1207

ALTITUDE	MEAN $n(O_2)$ (m^{-3})	ERROR IN MEAN	ERROR IN MEAN (%)
100	1.40(18)	N/A	N/A
101	8.44(17)	N/A	N/A
102	6.72(17)	N/A	N/A
103	4.79(17)	N/A	N/A
104	3.88(17)	N/A	N/A
105	3.09(17)	N/A	N/A
106	2.58(17)	N/A	N/A
107	2.25(17)	N/A	N/A
108	1.93(17)	N/A	N/A
109	1.64(17)	N/A	N/A
110	1.44(17)	N/A	N/A
111	1.30(17)	N/A	N/A
112	1.17(17)	N/A	N/A
113	1.01(17)	N/A	N/A
114	9.65(16)	7.55(15)	7.8
115	9.42(16)	1.04(16)	11
116	8.10(16)	7.26(15)	9.0
117	7.13(16)	8.32(15)	12
118	6.54(16)	9.26(15)	14
119	5.64(16)	8.41(15)	15
120	5.11(16)	9.62(15)	19
121	4.53(16)	6.85(15)	15
122	3.99(16)	6.42(15)	16
123	3.54(16)	5.10(15)	14
124	3.48(16)	3.86(15)	11
125	3.13(16)	3.40(15)	11

ALTITUDE	MEAN $n(O_2)$ (m^{-3})	ERROR IN MEAN	ERROR IN MEAN (%)
126	2.70(16)	2.64(15)	9.8
127	2.34(16)	1.80(15)	7.7
128	2.03(16)	1.48(15)	7.3
129	1.80(16)	8.57(14)	4.8
130	1.65(16)	1.17(15)	7.1
131	1.45(16)	1.06(15)	7.3
132	1.32(16)	1.26(15)	9.5
133	1.14(16)	8.75(14)	7.7
134	1.06(16)	6.99(14)	6.6
135	9.47(15)	5.47(14)	5.8
136	8.77(15)	5.28(14)	6.0
137	7.87(15)	5.10(14)	6.5
138	7.07(15)	6.01(14)	8.5
139	6.58(15)	6.03(14)	9.2
140	6.09(15)	6.26(14)	10
141	6.10(15)	4.62(14)	7.6
142	5.49(15)	8.05(14)	15
143	5.01(15)	9.85(14)	20
144	4.66(15)	9.25(14)	20
145	4.56(15)	9.50(14)	21
146	4.43(15)	1.02(15)	23
147	4.10(15)	8.80(14)	21
148	3.70(15)	8.40(14)	23
149	3.31(15)	8.00(14)	24
150	3.14(15)	8.10(14)	26
151	3.06(15)	7.90(14)	26
152	2.95(15)	7.55(14)	26

ALTITUDE	MEAN $n(O_2)$ (m^{-3})	ERROR IN MEAN	ERROR IN MEAN (%)
153	2.79(15)	6.85(14)	25
154	2.52(15)	5.60(14)	22
155	2.31(15)	5.65(14)	25
156	2.04(15)	4.55(14)	22
157	1.74(15)	3.85(14)	22
158	1.47(15)	3.40(14)	23
159	1.38(15)	N/A	N/A

TABLE A2.i

The final mean O_2 profile from Aerobee 13. 123 IS.

ALTITUDE	MEAN $n(O_2)$ (m^{-3})	ERROR IN MEAN	ERROR IN MEAN (%)
78	6.76(19)	2.88(18)	4.3
79	6.02(19)	4.27(18)	7.1
80	5.17(19)	9.33(18)	18
81	4.06(19)	8.71(18)	21
82	3.27(19)	6.46(18)	20
83	2.63(19)	6.16(18)	23
84	2.19(19)	5.91(18)	27
85	1.85(19)	4.76(18)	26
86	1.54(19)	4.39(18)	29
87	1.30(19)	3.19(18)	25
88	1.18(19)	2.87(18)	24
89	9.97(18)	2.42(18)	24
90	8.30(18)	2.13(18)	26
91	7.39(18)	1.95(18)	26
92	6.15(18)	1.61(18)	26
93	5.23(18)	1.17(18)	22
94	4.77(18)	1.11(18)	23
95	4.05(18)	8.74(17)	22
96	3.38(18)	7.69(17)	23
97	2.80(18)	6.68(17)	24
98	2.38(18)	5.24(17)	22
99	1.87(18)	3.80(17)	20
100	1.41(18)	2.65(17)	19
101	1.10(18)	2.33(17)	21
102	8.48(17)	1.99(17)	23
103	6.50(17)	1.32(17)	20

ALTITUDE	MEAN $n(O_2)$ (m^{-3})	ERROR IN MEAN	ERROR IN MEAN (%)
104	4.99(17)	7.94(16)	16
105	3.50(17)	3.00(15)	8.6
106	3.20(17)	2.50(16)	7.8
107	2.56(17)	2.45(16)	9.6
108	2.03(17)	1.89(16)	9.3
109	2.18(17)	1.30(16)	6.0
110	1.54(17)	4.88(15)	3.2
111	1.04(17)	1.12(15)	1.1
112	7.75(16)	1.13(15)	1.5
113	5.99(16)	1.82(15)	3.0
114	5.08(16)	1.72(15)	3.4
115	4.33(16)	1.71(15)	3.9
116	3.84(16)	1.53(15)	4.0
117	3.50(16)	8.73(14)	2.5
118	3.00(16)	1.50(14)	.5
119	2.52(16)	1.42(15)	5.6
120	2.36(16)	6.07(14)	2.6
121	2.26(16)	1.84(15)	8.1
122	2.06(16)	2.77(15)	13
123	2.00(16)	1.86(15)	9.3
124	1.69(16)	1.89(15)	11
125	1.52(16)	8.79(14)	5.8
126	1.45(16)	7.36(14)	5.1
127	1.33(16)	4.97(14)	3.7
128	1.14(16)	4.02(14)	3.5
129	1.04(16)	3.92(14)	3.8

ALTITUDE	MEAN $n(O_2)$ (m^{-3})	ERROR IN MEAN	ERROR IN MEAN (%)
130	9.47(15)	3.72(14)	3.9
131	8.66(15)	4.30(14)	5.0
132	7.71(15)	3.63(14)	4.7
133	6.98(15)	2.17(14)	3.1
134	6.41(15)	2.91(14)	4.5
135	5.79(15)	1.56(14)	2.7
136	5.44(15)	1.59(14)	2.9
137	4.92(15)	1.52(14)	3.1
138	4.47(15)	1.32(14)	2.9
139	4.18(15)	1.46(14)	3.5
140	3.84(15)	1.60(14)	4.2
141	3.52(15)	1.53(14)	4.3
142	3.19(15)	1.14(14)	3.6
143	2.91(15)	7.87(13)	2.7
144	2.66(15)	4.94(13)	1.9
145	2.46(15)	3.68(13)	1.5
146	2.29(15)	3.97(13)	1.7
147	2.16(15)	3.46(13)	1.6
148	2.04(15)	3.56(13)	1.8
149	1.89(15)	4.30(13)	2.3
150	1.74(15)	3.28(13)	1.9
151	1.61(15)	4.08(13)	2.5
152	1.51(15)	4.13(13)	2.7
153	1.42(15)	4.03(13)	2.8
154	1.32(15)	3.00(13)	2.3

ALTITUDE	MEAN $n(O_2)$ (m^{-3})	ERROR IN MEAN	ERROR IN MEAN (%)
155	1.21(15)	2.05(13)	1.7
156	1.12(15)	1.43(13)	1.3
157	1.04(15)	1.47(13)	1.4
158	9.65(14)	1.66(13)	1.7
159	9.07(14)	1.79(13)	2.0
160	8.38(14)	1.06(13)	1.3
161	8.04(14)	6.71(12)	.8
162	7.57(14)	2.42(12)	.3
163	7.15(14)	3.39(12)	.5
164	6.72(14)	4.89(11)	.1
165	6.18(14)	1.71(13)	2.8
166	5.75(14)	2.07(13)	3.6
167	5.39(14)	2.07(13)	3.8
168	5.06(14)	1.08(13)	2.1
169	4.82(14)	9.22(12)	1.9
170	4.56(14)	2.40(13)	5.2
171	4.31(14)	4.09(13)	9.5
172	4.46(14)	N/A	N/A

APPENDIX 3

THE DETERMINATION OF DETECTOR ASPECT

The need to determine detector aspect did not arise in the work carried out in this thesis since the molecular oxygen experiments were flown on attitude controlled vehicles, and the required ratio in the water vapour experiment was independent of the aspect. Nevertheless some quite extensive work was carried out on the properties of one type of aspect detector, in preparation for the possible flight of molecular oxygen experiments on spin stabilized vehicles, and this is discussed in the following sections.

A.3.1 Introduction

The technique of broad band absorption spectrophotometry is based on the assumption that any change observed in the detector signal is due solely to a change in the amount of absorber between the detector and the source of radiation. This assumption is not valid for the raw data received from a detector flown on a spin stabilized rocket. On this type of rocket the angle between the sun vector and the look direction of the detector i.e. the aspect, varies throughout the flight and if the detectors used are ion chambers, the non-uniform angular response of these instruments (Figure 3.14) introduces variations in the observed signal that are independent of the amount of absorber.

Gross and Heddle (1964) described a device for measuring the aspect. A modified version of this device (Lockey, 1972) known as sunslits, was flown on C1044 and C1046 (Chapter 8). However, the sunslits are not described in this appendix. They were unsuitable for use in fast spinning rockets and this lead to the investigation of a new type known as quad aspect sensors.

In the following sections, quad aspect sensors are first described, and then their calibration, and the uncertainties associated with their use, are discussed.

A.3.2 Description of Quad Aspect Sensors

The quad aspect sensors were modified PIN-SPOT/4D quadrant detectors from United Detector Technology Incorporated. The basic device consisted of four discrete photo-cathode elements on a single substrate with an active output lead from each element. The device was encapsulated in a TO-5 type package with a glass window. The appearance and dimensions of the device are shown in Figure A.3.1.

The device was modified by evaporating gold onto part of the window surface, leaving only a 2.7 mm square, directly above the photo-cathode elements, capable of transmitting light through to them.

A.3.3 Calibration of Quad Aspect Sensors

During a rocket flight if the sun was anything else but directly overhead, this mask would cast a shadow over part of the photo-cathodic area of the device. Figure A.3.2 is a simplified sketch of the effect of the Sun being at an angle. Part of element "a" is in shadow. This will reduce the signal from element "a", and the ratio, signal from "a"/signal from "b", will be less than 1, the expected value when the Sun is directly overhead. Calibration can link the value of this ratio with the angle of the Sun. From Figure A.3.2 it can also be seen that the largest angle these devices can measure will be the one corresponding to both element "a and b" being in shadow and that the value of this angle will be determined by the dimension h. From experience it was found that the value of h given in the data sheet was a nominal value only and that h had to be deduced from calibration procedures.

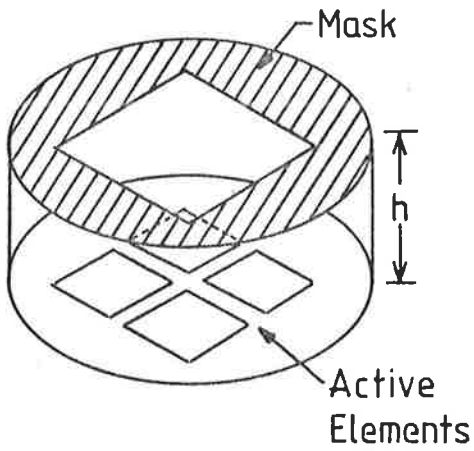

Fig A.3.1a View of location of mask above the active area of the detector.

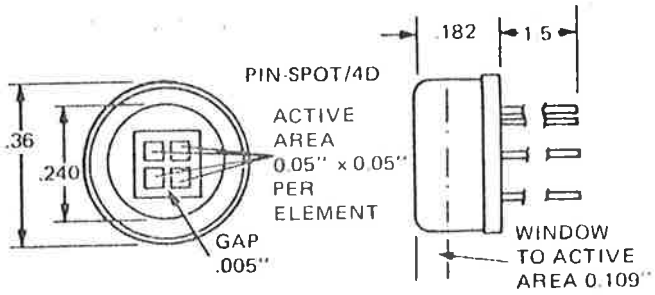

Fig A.3.1b Dimensions of Quad Aspect Sensors.

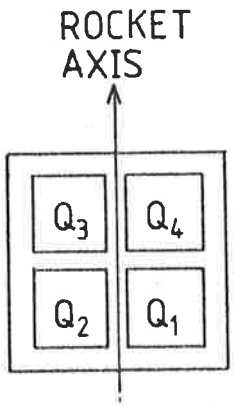

Fig A.3.1c Identification of active areas.

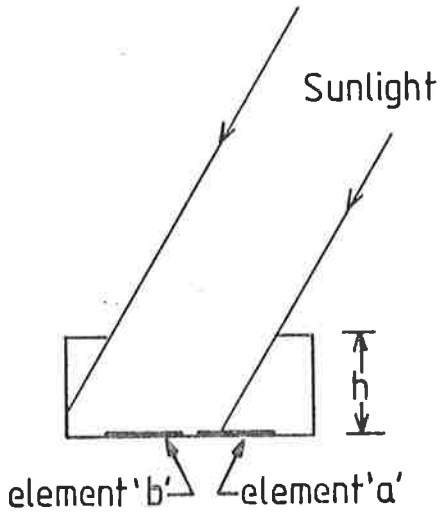

Fig. A.3.2 The shadow thrown by the mask when the sun is at an angle.

Calibration procedures, therefore, had two aims -

1. matching the angle of the source of light to the ratio it produced.
2. determining the largest angle which could be measured and hence the value of h .

The value of h was then used to construct a function $A(R)$ where R was the ratio of the signals. The use of a function to determine the angle from the ratio R was more efficient for computing than using a look table based on the discrete measurements of (1). The measurements of (1) were used to check $A(R)$.

A quartz halogen spot light was used as a light source. The aspect sensor was mounted in the experimental payload such that one axis was parallel to the long axis of the payload. This implied that the one axis of the device would be parallel to the roll axis of the rocket during flight. The payload was mounted on a rotating table such that the axis of rotation was in the plane of the sensor and passed through the middle of it. The table scale was adjusted to zero degrees and the spot light placed directly in front of, but some metres away from the device.

The signals from all elements were recorded every $5°$ from $+90$ to -90 for two cases

(a) the axis of rotation is $||$ to the roll axis of the rocket.

(b) the axis of rotation is $\perp$ to the roll axis of the rocket.

If the elements are defined as shown in Figure A.3.1c and the signal from element i is called Qi then for case (a) the ratios Q_2/Q_1 and

and Q_3/Q_4 were expected to be similar. For case (b) Q_1/Q_4 and Q_2/Q_3 were expected to be similar. Calibration showed that they were. In addition calibration showed that while individual devices varied slightly the mean limiting angle was $\pm 50°$. If the original evaporation of the mask had not been done with sufficient accuracy this was indicated by offsets, i.e. equal signals from all four elements occurring off zero degrees, and non-symmetrical response curves.

The calibration, as described, does limit the use of the detectors. The signals from the four elements can be used to uniquely determine the sun's position anywhere within the device's field of view. However, if the device has only been calibrated along the axes, it is essential, for aspect determination, that the aspect along one of these axes is zero. In the rocket this is achieved as the rocket spins around its long axis.

The maximum signals Q_1, Q_2, Q_3, Q_4 from each element in any one revolution of the rocket will correspond to the aspect being zero in the plane $\perp$ to the long axis, for that element. If the device, for example, was positioned in a rocket similar to the way it was positioned in the calibration, either Q_1 and Q_4, or Q_2 and Q_3 would be expected to peak simultaneously and their ratios, i.e. Q_1/Q_4 or Q_2/Q_3 would determine the aspect.

A.3.4 Uncertainties in the Aspect Determination

There were 2 significant sources of uncertainty in the use of the quad aspect sensors described. The first involved resulted from the accuracy with which the mask could be evaporated on to the device. (This source was removed in later devices by placing the device in an accurately machined holder in order to produce the desired masking, rather than using

evaporative techniques). Table A.3.1 shows the size of the expected uncertainty. Although the errors in the angle could be quite significant, because of the shape of the ion chamber's angular response the final correction was small and could be ignored.

TABLE A.3.1 UNCERTAINTY INTRODUCED BY MIS-ALIGNMENT OF MASK

Angle	Error in Calculated Angle	Error in Corrected Ion Chamber Signal
5°	20%	.5%
20°	1%	negligible
30°	negligible	negligible

The second source of uncertainty arose from the limitations of the telemetry. The telemetry uncertainty has already been cited as a source of uncertainty in all rocket experiments. It also affected the accuracy of the aspect determination. Table A.3.2 gives the size of the introduced uncertainties. Once again the shape of angular response of the ion chambers reduces the effect.

TABLE A.3.2 UNCERTAINTY INTRODUCED BY UNCERTAINTY IN THE TELEMETRY

Angle	Uncertainty in Q_1/Q_4 ratio	Uncertainty in calculated angle	Uncertainty in corrected I.C. signal
3°	± 4%	± 1½°	± .3%
20°	± 5.4%	± 1°	± 1.7%
32°	± 18%	± 1°	± 3.6%

PUBLICATIONS

Bibbo, G., J.H. Carver, L.A. Davis, B.H. Horton and J.L. Lean, 1979. "U.V. Extinction and Mass Spectrometer Rocket Measurements of Atmospheric Composition over Woomera" Space Res. XIX, 255.

Carver, J.H., L.A. Davis, B.H. Horton and M. Ilyas, 1978. "Ultraviolet Extinction Measurements of Molecular Oxygen Density", J. Geophys. Res. 83, 4377.

BIBLIOGRAPHY

Ackerman, M., P. Simon, U. von Zahn, and U. Laux, 1974. J. Geophys. Res. 79, 4757.

Alcayde, D., P. Bauer, C. Jaeck, and J.L. Falin, 1972. J. Geophys. Res. 77, 2368.

Alcayde, D., P. Bauer, and J. Fontonari, 1974. J. Geophys. Res. 79, 629.

Allison, R., J. Burns, and A.J. Tuzzolino, 1964a. J. Opt. Soc. Amer. 54, 747.

Allison, R., J. Burns, and A.J. Tuzzolino, 1964b. J. Opt. Soc. Amer. 54, 1381.

Anderson, J.G. and T.M. Donahue, 1975. J. Atmos. Terr. Phys. 37, 865.

Atreya, S.K., T.M. Donahue, N.E. Sharp, B. Wasser, J.G. Drake, and G.R. Riegler, 1976. Geophys. Res. Lett. 3, 607.

Banks, P.M. and G. Kockarts, 1973b. Aeronomy Part B. Academic, New York.

Barlier, F., P. Bauer, C. Jaeck, G. Thuillier, and G. Kockarts, 1974. J. Geophys. Res. 79, 5273.

Barth, C.A. 1964. Ann. Geophys. 20, 182.

Barth, C.A. and A.F. Hildebrandt, 1961. J. Geophys. Res. 66, 985.

Bibbo, G., 1977. Ph.D Thesis, University of Adelaide.

Bibbo, G., J.H. Carver, L.A. Davis, B.H. Horton and J.L. Lean, 1979. Space Res. XIX, 255.

Bitterberg, W., K. Bruchausen, D. Offerman, and U. von Zahn, 1970. J. Geophys. Res. 75, 5528.

Black, G., R.L. Sharpless, T.G. Slanger and D.C. Lorents, 1975. J. Chem. Phys. 62, 4266.

Blake, A.J., J.H. Carver, and G.N. Haddad, 1966. J. Quant. Spectros. Radiat. Transf. 6, 451.

Blake, A.J., D.G. McCoy, H.P.F. Gies, and S.T. Gibson, 1980. Interim Sci. Rep. 15 Sept 1978 - 30 Nov 1979, Air Force Geophys Lab., Hanscom, AFB, MA.

Blum, P.W., K.G.H. Schuchardt, and U. von Zahn, 1978. J. Atmos. Terr. Phys, 40, 1131.

Brannon, P.J. and J.M. Hoffman, 1971. J. Geophys. Res. 76, 4630.

Brinkman, R.T., A.E.S. Green, and C.A. Barth, 1966. Tech. Rept. No. 32-951, Jet Propulsion Lab. Cal. Inst. Tech. Pasadena, California.

Byram, E.T., T.A. Chubb, and H. Friedman, 1954. J. Opt. Soc. of Amer. 44, 353.

Byram, E.T., T.A. Chubb, and H. Friedman, 1955. Phys. Rev. 98, 1594.

Byram, E.T., T.A. Chubb, H. Friedman, and J.E. Kupperian. Jr., 1956. Astrophys. J. 124, 480.

Byram, E.T., T.A. Chubb, H. Friedman, J.E. Kupperian. Jr., R.W. Kreplin, 1958. Astrophys. J. 128, 738.

Canfield, L.R., R.G. Johnston and R.P. Madden, 1973. Applied Optics. 12, 1611.

Carignan, G.R., 1975. Rev. Geophys. Space Phys. 13, 885.

Carrick, I., 1971. Honours Report, University of Adelaide.

Carver, J.H., 1969. Ann. I.Q.S.Y. 6, 259.

Carver, J.H., L.A. Davis, B.H. Horton and M. Ilyas, 1978a. J. Geophys. Res. 83, 4377.

Carver, J.H., P.J. Edwards, P.L. Gough, A.G. Gregory, B. Rofe and S.G. Johnson, 1969. J. Atmos. Terr. Phys. 31, 563.

Carver, J.H., H.P.F. Gies, T.I. Hobbs, B.R. Lewis, and D.G. McCoy, 1977a. J. Geophys. Res. 82, 1955.

Carver, J.H., G.N. Haddad, T.I. Hobbs, B.R. Lewis, and D.G. McCoy, 1978b. Applied Optics. 17, 420.

Carver, J.H., B.H. Horton, M. Ilyas, and B.R. Lewis, 1977b. J. Geophys. Res. 82, 2613.

Carver, J.H. and P. Mitchell, 1964. J. Scient. Instrum. 41, 555.

Carver, J.H. and P. Mitchell, 1967. J. Opt. Soc. Amer. 57, 738.

Carver, J.H., P.N. Mitchell, and E.L. Murray, 1966. Space Res. 6, 373.

Carver, J.H., P. Mitchell, E.L. Murray and B.G. Hunt, 1964. J. Geophys. Res. 69, 3755.

Champion, K.S.W., 1965. Planet. Space Sci. 13, 325.

Champion, K.S.W., 1970. Space Res. 10, 450.

Chandra, S., and A.K. Sinha, 1973. Planet. Space Sci. 21, 593.

Chapman, S., 1931a. Proc. Phys. Soc. 43, 26.

Chapman, S., 1931b. Proc. Phys. Soc. 43, 483.

Chapman, S., 1931c. Proc. Roy. Soc. A132, 353.

Chubb, T.A., and H. Friedman, 1955. Rev. Sci. Instrum. 26, 493.

CIRA, 1972. Cospar International Reference Atmosphere, Akademie-Verlag, Berlin.

Colegrove, F.D., W.B. Hanson, and F.S. Johnson, 1965. J. Geophys. Res. 70, 4931.

Dalgarno, A., W.B. Hanson, N.W. Spencer, and E.R. Schmerling, 1973. Radio Sci. 8, 263.

Dalgarno, A. and James G.G. Walker, 1964. J. Atmos. Sci. 21, 463.

Dandekar, B.S., 1969. Planet. Space Sci. 17, 1609.

Davis, R.J., 1966. J. Opt. Soc. Amer. 56, 837.

Delaboudiniere, J.P., R.F. Donnely, H.E. Hinteregger, G. Schmidtke and P.C. Simon, 1977. Report to Working Group IC, COSPAR, Tel Aviv.

Evans, J.S., and G.J. Schexynader, 1961. Nasa. Tech. Rep. R92.

Evans, J.V., 1972. J. Atmos. Terr. Phys. 34, 175.

Felder, W., and R.A. Young, 1972. J. Chem. Phys. 56, 6028.

Felske, D., R. Knuth, W. Lippert, and G. Sonnemann, 1974. J. Atmos. Terr. Phys. 36, 1355.

Felske, D., L. Martini, B. Stark, and J. Taubenheim, 1972. Space Res. 12, 651.

Felske, D., and G. Sonnemann, 1976. Space Res. XVI. 241.

Fitzmaurice, J.A., 1964. Appl. Opt. 3, 640.

Friedman, H., T.A. Chubb, J.E. Kupperian, and J.C. Lindsay, 1958. Annals of I.G.Y. 6, 316.

Friedman, H., S.W. Lichtman, and E.T. Byram, 1951. Phys. Rev. 83, 1025.

Fukuyama, K., 1974. J. Atmos. Terr. Phys. 36, 1297.

Garriott,O.K., R.B. Norton and J.G. Timothy, 1977. J. Geophys. Res. 82, 4973.

Giraud, A., 1973. J. Geophys. Res. 78, 332.

Giraud, A., G. Scialom, and A.A. Pokhunkov, 1972. J. Geophys. Res. 77, 1251.

Green, A.E.S., C.S. Lindenmyer, and M. Griggs, 1964. J. Geophys. Res. 69, 493.

Groebecker, A.J., 1971. Trans Amer. Geophys. 52, 876.

Gross, M.J., and D.W.O. Heddle, 1964. Proc. Roy. Soc. A279, 523.

Gross, J., D. Offerman, and U. von Zahn, 1968. Space Res. VIII, 920.

Haasz, A.A., J.H. de Leeuw, and W.E.R. Davies, 1976. J. Geophys. Res. 81, 2383.

Hall, J.E., 1972. J. Atmos. Terr. Phys. 34, 1337.

Hall, L.A., G.W. Chagnon, and H.E. Hinteregger, 1967. J. Geophys. Res. 72, 3425.

Hall, L.A., W. Schweizer, and H.E. Hinteregger, 1965. J. Geophys. Res. 70, 105.

Hall, L.A., W. Schweizer and H.E. Hinteregger, 1963. J. Geophys. Res. 68, 6413.

Harris, I., and W. Priester, 1962a. Nasa Tech Note. TND 1443.

Harris, I., and W. Priester, 1962b. Nasa Tech Note. TND 1444.

Hays, P.B., A.F. Nagy, and R.C. Roble, 1969. J. Geophys. Res. 74, 4162.

Heath, D.F., 1973. J. Geophys. Res. 78, 2779.

Heath, D.F., and P.A. Sacher, 1966. Applied Optics. 5, 937.

Hedin, A.E., 1979. Rev. Geophys and Space Phys. 17, 477.

Hedin, A.E., C.P. Avery, and C.D. Tschetter, 1964. J. Geophys. Res. 69, 4637.

Hedin, A.E., B.B. Hinton and G.A. Schmitt, 1973. J. Geophys. Res. 78, 4651.

Hedin, A.E., and A.O. Nier, 1965. J. Geophys. Res. 70, 1273.

Hedin, A.E., and A.O. Nier, 1966. J. Geophys. Res. 71, 4121.

Hedin, A.E., C.A. Reber, G.P. Newton, N.W. Spencer, H.C. Brinton, and H.G. Mayr, 1977a. J. Geophys. Res. 82, 2148.

Hedin, A.E., J.E. Salah, J.V.Evans, C.A. Reber, G.P. Newton, N.W. Spencer, D.C. Kayser, D. Alcayde, P. Bauer, L. Cogger, and J.P. McClure, 1977b, J. Geophys. Res. 82, 2139.

Heroux, L., and J.E. Higgins, 1977. J. Geophys. Res. 82, 3307.

Heroux, L., and R. Swirbalus, 1976. J. Geophys. Res. 81, 436.

Herzberg, G., 1966. Electronic Spectra and Electronic Structure of Polyatomic Molecules. New York, Van Nostrand.

Hickman, D.R., and A.O. Nier, 1972. J. Geophys. Res. 77, 2880.

Higgins, J.E., and L. Heroux, 1977. J. Geophys. Res. 82, 3295.

Hinteregger, H.E., 1962. J. Atmos. Sci. 19, 351.

Hinteregger, H.E., 1976. J. Atmos. Terr. Phys. 38, 791.

Hinteregger, H.E., 1977. Geophys. Res. Lett. 4, 231.

Hinteregger, H.E., 1979. J. Geophys. Res., 84, 1933.

Hinteregger, H.E., and L.M. Chaikin, 1977. Space Res. XVII. 525.

Hudson, R.D., 1971. Rev. Geophys. Space Phys. 9, 305.

Hudson, R.D., and V.L. Carter, 1968. J. Opt. Soc. Amer. 58, 1621.

Hunt, B.G., 1972. Tellus XXIV, 1, 47.

Hunten, D.M., and M.B. McElroy, 1966. Rev. Geophys. 4, 303.

Ilyas, M., 1976. Ph.D Thesis, University of Adelaide.

Jacchia, L.G., 1965. Smithson. Astrophys. Obs. Special Rep. 170.

Jacchia, L.G., 1970. Smithson. Astrophys. Obs. Special Rep. 313.

Jacchia, L.G., 1971. Smithson. Astrophys. Obs. Special Rep. 323.

Jacchia, L.G., 1977. Smithson. Astrophys. Obs. Cambridge. Mass. Special Report 375.

Jacchia, L.G., J.M. Slowey, and U. von Zahn, 1978. Space Res. 18 199.

Johnson, F.S., and B. Gottlieb, 1970. J. Atmos. Terr. Phys. 18, 1707.

Johnston, F.S., K. Watanabe, and R. Tousey, 1951. J. Opt. Soc. Amer. 41, 702.

Jones, K., 1973. Pergamon Texts in Inorganic Chemistry, VOL II, The Chemistry of Nitrogen.

Jursa, A.S., Y. Tanaka, and F. Le Blanc, 1959. Planet. Space Sci. 1, 161.

Jursa, A.S., M. Nakamura, and Y. Tanaka, 1963. J. Geophys. Res. 68, 6145.

Jursa, A.S., M. Nakamura, and Y. Tanaka, 1965. J. Geophys. Res. 70, 2699.

Kasprzak, W.T., D. Krankowsky, and A.O. Nier, 1968. J. Geophys. Res. 73, 6765.

Katyushina, V.V., and G.S. Ivanov-Kholodny, 1971. Geomag. Aeron. 11, 775.

Kayser, D.C., 1980. J. Geophys. Res. 85, 695.

Kayser, D.C., and W.E. Potter, 1976. Geophys. Res. Lett. 3, 455.

Kayser, D.C., and W.E. Potter, 1978. J. Geophys. Res. 83, 1147.

Keneshea, T.J., S.P. Zimmerman, and C.R. Philbrick, 1979. Planet. Space Sci. 27, 385.

King-Hele, D.G., and D.M.C. Walker, 1969. Planet. Space Sci. 17, 1539.

Kirby-Docken, K., and M. Oppenheimer, 1977. J. Geophys. Res. 82, 3503.

Knapp, R.A., and A.M. Smith, 1964. Appl. Opt. 3, 637.

Knuth, R., G. Sonnemann, D. Felske, L. Martini, and B. Stark, 1976. Space Res. XVI, 245.

Krankowsky, D., W.T. Kasprzak, and A.O. Nier, 1968. J. Geophys. Res. 73, 7291.

Kupperian, J.E., E.T. Byram, and H. Friedman, 1959. J. Atmos. Terr. Phys. 16, 174.

Lake, L.R., and A.O. Nier, 1973. J. Geophys. Res. 78, 1645.

Lean, J.L. 1980. Ph.D Thesis, University of Adelaide.

Lee, L.C., L. Oren, E. Phillips, and D.L. Judge, 1978. J. Phys. B. Atom. Molec. Phys. 11, 47.

Lockey, G.W.A., 1972. Ph.D Thesis, University of Adelaide.

Lockey. G.W.A., B.H. Horton, and B. Rofe, 1969. Nature (Lond). 223, 387.

Mahajan, K.K., 1977. Space Res. XVII. 309.

Marmo, M.M., 1953. J. Opt. Soc. Amer. 43, 1168.

Martynkevich, G.M., 1972. Space Res. XII, 1311.

Martynkevich, G.M., and E.G. Shvidkovsky, 1971. Space Res. 11, 865.

Masuoka, T., and T. Oshio, 1974. Rev. Scient. Instrum. 45, 1012.

Mauersberger, K.D., D. Müller, D. Offerman, and U. von Zahn, 1968. J. Geophys. Res. 73, 1071.

Mauersberger, K., and A.O. Nier, 1973. J. Geophys. Res. 78, 330.

Mayr, H.G., P. Baeur, H.C. Brinton, L.H. Brace, and W.E. Potter, 1976. Geophys. Res. Lett. 3, 77.

Mayr, H.G., and I. Harris, 1977a. J. Geophys. Res. 82, 2628.

Mayr, H.G., and I. Harris, 1977b. Space Res. XVII. 293.

Mayr, H.G., and I. Harris, 1977c. Space Res. XVII. 301.

Mayr, H.G., I. Harris, and N.W. Spencer, 1974. J. Geophys. Res. 79, 2921.

Mayr, H.G., I. Harris, and N.W. Spencer, 1978. Rev. Geophys. Space Phys, 16, 539.

Mayr, H.G., and K.K. Mahajan, 1971. J. Geophys. Res. 76, 1017.

Mayr, H.G., and H. Volland, 1971. Ann. Geophys. 27, 513.

Mayr, H.G., and H. Volland, 1972. J. Geophys. Res. 77, 6774.

Mayr, H.G., and H. Volland, 1976. J. Geophys. Res. 81, 671.

Meadows, E.B., and J.W. Townshead. Jr., 1956. J. Geophys. Res. 61, 576.

Meadows, E.B., and J.W. Townshead. Jr., 1960. Space. Res. I. 175.

Meadows-Reed, E., and C.R. Smith, 1964. J. Geophys. Res. 69, 3199.

Meier, R.R., 1969. J. Geophys. Res. 74, 6487.

Melia, T.P., 1965. J. Inorganic Nucl. Chem. 27, 95.

Miera, L.J. Jr., 1971. J. Geophys. Res. 76, 202.

Moe, K., 1973. J. Geophys. Res. 78, 1633.

Moe, M.M., and K. Moe, 1969. Planet. Space Sci. 17, 917.

Müller, D., and G. Hartman, 1969. J. Geophys. Res. 74, 1287.

Newton, G.P., W.T. Kasprzak, and T. Pelz, 1974. J. Geophys. Res. 79, 1929.

Newton, G.P., D.T. Pelz, and H. Volland, 1969. J. Geophys. Res. Space Phys, 74, 183.

Nicolet, M., 1954. J. Atmos. Terr. Phys. 5, 132.

Nicolet, M., 1961. Smithson. Astrophys. Special Rep. 75.

Nier, A.O., 1970. J. Vac. Sci and Tech. 7, 247.

Nier, A.O., 1972. Space Res. XII. 881.

Nier, A.O., J. Hoffman, C. Johnson and J. Holmes, 1964. J. Geophys. Res. 69, 979.

Nier, A.O., W.E. Potter, and D.C. Kayser, 1976. J. Geophys. Res. 81, 17.

Nier, A.O., W.E. Potter, D.C. Kayser, and R.G. Finstad, 1974. Geophys. Res. Lett. 1, 197.

Nishi, K., K. Higashi, A. Yamaguchi, and T. Masuoka, 1976. Jap. J. Appl. Phys. 15, 2269.

Norton, R.B., and R.G. Roble, 1974. J. Geophys. Res. 79, 3876.

Norton, R.B., and R.G. Roble, 1977. J. Geophys. Res. 82, 3659.

Norton, R.B., and J.M. Warnock, 1968. J. Geophys. Res. 73, 5798.

Noxon, J.F., and A.E. Johanson, 1972. Planet. Space Sci. 20, 2125.

O'Conner, G., 1973. Ph.D Thesis, University of Adelaide.

Offerman, D., 1972. J. Geophys. Res. 77, 6284.

Offerman, D., 1974. J. Geophys. Res. 79, 4281.

Offerman, D., and K.U. Grossman, 1973. J. Geophys. Res. 78, 8296.

Offerman, D., and H. Tatarczyk, 1973. Rev. Sci. Instrum. 44, 1569.

Offerman, D., and H. Trinks, 1971. Rev. Scientific Instrum. 42, 1836.

Offerman, D., and U. von Zahn, 1971. J. Geophys. Res. 76, 2520.

Ogawa, M., 1968. J. Geophys. Res. 73, 6759.

Opal, C.B., H.W. Moos, 1969. J. Geophys. Res. 74, 2398.

Oppenheimer, M., A. Dalgarno, and H.C. Brinton, 1976. J. Geophys. Res. 81, 4678.

Oran, E.S., P.S. Julienne, and D.F. Strobel, 1975. J. Geophys. Res. 80, 3068.

Oran, E.S., and D.F. Strobel, 1976. J. Geophys. Res. 81, 257.

Parker, A.E., and K.H. Stewart, 1972. J. Atmos. Terr. Phys. 34, 1223.

Patterson, D.A., and W.H. Vaughan, 1963. J. Opt. Soc. Amer. 53, 851.

Pokhunkov, A.A., 1962. Planet. Space Sci. 9, 269.

Potter, W.E., D.C. Kayser, H.C. Brinton, L.H. Brace, and M. Oppenheimer, 1977. J. Geophys. Res. 82, 5243.

Potter, W.E., D.C. Kayser, and A.O. Nier, 1979. J. Geophys. Res. 84, 10.

Prinz, D.K., and G.E. Brueckner, 1977. J. Geophys. Res. 82, 1481.

Purcell, J.D., and R. Tousey, 1960. J. Geophys. Res. 65, 370.

Quessette, J.A., 1970. J. Geophys. Res. 75, 839.

Radford, H.E., M.M. Litvak, C.A. Gottlieb, E.W. Gottlieb, S.K. Rosenthal, and A.E. Lilley, 1977. J. Geophys. Res. 82, 472.

Rawer, K., G. Emmenegger, and G. Schmidtke, 1979. Space Res. XIX. 199.

Reber, C.A., and P.B. Hays, 1973. J. Geophys. Res. 78, 2977.

Reed, E.I., and S. Chandra, 1975. J. Geophys. Res. 80, 3053.

Reid, R.H.G., and G.L. Withbroe, 1970. Planet. Space Sci. 18, 1225.

Roble, R.G., and R.B. Norton, 1972. J. Geophys. Res. 77, 3524.

Rogers, P., 1979. Honours Report., University of Adelaide.

Rusch, D.W., W.E. Sharp, and P.B. Hays, 1975. J. Geophys. Res. 80, 1832.

Samson, J.A.R., 1964. J. Opt. Soc. Amer. 54, 6.

Schaefer, E.J., 1969. J. Geophys. Res. 74, 3488.

Schaefer, E.J., and M.H. Nichols, 1964a. Space Res. IV, 205.

Schaefer, E.J., and M.H. Nichols, 1964b. J. Geophys. Res. 69, 4649.

Schaeffer, R.C., P.D. Feldman, and W.G. Fastie, 1971. J. Geophys. Res. 76, 3168.

Schaeffer, R.C., and J.F. Noxon, 1975. Planet. Space Sci. 23, 1413.

Schmidtke, G., 1979. Space Res. 19, 193.

Scholz, T.G., and D. Offerman, 1974. J. Geophys. Res. 79, 307.

Slanger, T.G., and G. Black, 1977. Planet. Space Sci. 25, 79.

Smith, L.G., and K.L. Millar, 1974. J. Geophys. Res. 79, 1965.

Smith, F.L. III., and C. Smith, 1972. J. Geophys. Res. 77, 3592.

Sonnemann, G., D. Felske, R. Knuth, L. Martini, and B. Stark, 1977. Space Res. XVII. 265.

Spencer, N.W., L.H. Bruce, and D.W. Grimes, 1973. Radio Sci. 8, 267.

Stewart, K.H., and P.J.L. Wildman, 1969. Proc. Royal Soc. A311. 591.

Stoker, A.K., 1962. Nasa Tech. Note D1180.

Stober, A.K., R. Scolnik, and J.P. Hennes, 1963. Applied Optics, 2, 735.

Subbaraya, B.H., S. Prakash, V. Kuma, and P.N. Pareek, 1974. Space Res. XIV, 173.

Subbaraya, B.H., S. Prakash, and P.N. Pareek, 1972. J. Atmos. Terr. Phys. 34, 1141.

Swider, W., 1964. Planet. Space Sci. 12, 761.

Taeusch,D.R., G.R. Carignan and C.A. Reber, 1971. J. Geophys. Res. 76, 8318.

Townshead, J.W., E.B. Meadows, and E.C. Pressly, 1954. Rocket Exploration of the Upper Atmosphere edited by R.L.F. Boyd and M. Seaton, Inter-Science Publishers Inc, New York. pp 169-188.

Trinks, H., and K.H. Fricke, 1978. J. Geophys. Res. 83, 3883.

Trinks, H., D. Offerman, U. von Zahn, and C. Steinhauer, 1978a. J. Geophys. Res. 83, 2169.

Trinks, H., U. von Zahn, C.A. Barth, and K.K. Kelly, 1978b. J. Geophys. Res. 83, 203.

Vernazza, J.E., P.V. Foukal, M.C.E. Huber, R.W. Noyes, E.M. Reeves, E.J. Schmahl, J.G. Timothy and G.L. Withbroe, 1975. Astrophys. J. Letts. 199, L123.

Vidal-Madjar, A., 1975. Solar Phys. 40, 69.

von Zahn, U., 1968. Adv. in Mass Spectroscopy. 4, 869

von Zahn, U., 1970. J. Geophys. Res. 75, 5517.

von Zahn, U., and J. Gross, 1969. J. Geophys. Res. 74, 4055.

Walker, W.C., N. Wainfar, and G.L. Weissler, 1955. J. Appl. Phys. 26, 1366.

Wallace, L., and M.B. McElroy, 1966. Planet. Space Sci. 14, 677.

Watanabe, K., and E.C.Y. Inn, 1953. J. Opt. Soc. Amer. 43, 32.

Watanabe, K., 1958. Advan. Geophys. 5, 153.

Watanabe, K., F.M. Matsunaga, and H. Sakai, 1967. Applied Optics. 6, 391.

Watanabe, K., T. Nakayama, and J. Mottl, 1962. J. Quant. Spectrosc. Radiat. Transfer. 2, 369.

Watanabe, K., M. Zelikoff, and Edward C.Y. Inn, 1953. Geophys. Res. Papers No. 21. Geophysics Research Directorate, A.F. Cambridge Research Centre.

Weeks, L.H., 1975a. J. Geophys. Res. 80, 3655.

Weeks, L.H., 1975b. J. Geophys. Res. 80, 3661.

Weeks, L.H., and L.G. Smith, 1968. J. Geophys. Res. 73, 4835.

Wildman, P.J.L., M.J. Kerley, and M.S. Shaw, 1969. J. Atmos. and Terr. Phys. 31, 951.

Yeh, K.C., and C.H. Liu, 1974. Rev. Geophys. Space Phys. 12, 193.

Young, R.A., and G. Black, 1966. J. Chem. Phys. 44, 3741.